ROLLING CONTACT FATIGUE OF CERAMICS

By

Mark Hadfield

BEng CEng MIMechE MIMarE

A Thesis submitted for the degree of

Doctor of Philosophy

Department of Mechanical Engineering

Brunel University

1993

ABSTRACT

Ceramic/ceramic and ceramic/steel contacts under lubricated rolling conditions are studied. This work is of interest to ball bearing manufacturers as the use of ceramics in the design of these components has some advantages over traditional bearing-steel materials. Low density and increased stiffness are the mechanical properties which gas-turbine and machine tool manufacturers are most likely to realise. Much research over the past two decades on material structure, quality control and manufacturing techniques has produced a material which can seriously challenge bearing steel in ball-bearing design. This is especially the case for hybrid ball-bearings, ie ceramic balls with steel bearing races which are now used as standard components.

The purpose of this study is to examine the rolling contact fatigue failure modes of ceramics. This study concentrates on silicon nitride as this material has most potential for use by industry. The primary reason for studying ceramic balls is because of interest in ball-bearing applications, hence a modified four-ball machine is employed which correctly models ball motions and precisely defines ball load. Experimental and theoretical kinematic analysis of ball motion during modified four ball machine tests is presented. The kinematic analysis reveals that in practice, lower ball tracking exists at high speeds.

Test conditions of lubricated contacts under high compressive stress show delamination type failures. Delamination failures are classified in terms of propagation and initiation from scanning electron microscope observations. Residual stresses are measured on delaminated surfaces, which implies plastic deformation of the ceramic. Also, chemical analysis implies that disruption of silicon, nitrogen and oxygen levels may take place on delaminated surfaces. Experiments illustrating various fatigue failure modes using artificially pre-cracked ceramic balls in contact with a steel upper ball are presented.

PUBLICATIONS RESULTING FROM THESIS

[1] "Analysis of Silicon Nitride Ball Failure Due To Rolling Contact Fatigue"
By M.Hadfield, T.A.Stolarski and S.Tobe
Submitted to ICR 92 Conference, Birmingham
Submitted February 1992
Accepted for publication April 1992
Presented at conference September 1992

[2] "Delamination of Ceramic Balls in Rolling Contact"
By R.T.Cundill, M.Hadfield and T.A. Stolarski
Submitted to Ceramics International Journal
Submitted April 1992
Accepted for publication June 1992

[3] "Residual Stresses In Failed Ceramic Rolling Contact Balls"
By G.Fujinawa, M.Hadfield, T.A.Stolarski and S.Tobe
Submitted to Ceramics International Journal
Submitted July 1992
Accepted for publication October 1992

[4] "Failure Modes of Pre-Cracked Ceramic Elements Under Rolling Contact"
By R.T.Cundill, M.Hadfield, S.Horton and T.A.Stolarski
Submitted to Wear Journal
Submitted September October 1992

[5] "Failure Modes of Ceramic Elements With Ring-Crack Defects"
By R.T.Cundill, M.Hadfield, S.Horton and T.A.Stolarski
Submitted to Tribology International Journal
Submitted October 1992
Accepted for publication November 1992

ACKNOWLEDGEMENTS

Many people have encouraged and supported my research during the period of this study.

My supervisor, Dr T.A. Stolarski, has been always ready to provide encouragement, inspiration and guidance.

My industrial supervisor at SKF (ERC) Ltd, Dr R.T. Cundill, has given much advise of material aspects of technical ceramics. Dr S. Horton has also been an invaluable source of information on material aspects. Staff from SKF (ERC) Ltd have all contributed to this study by giving support and enthusiasm.

My supervisor at SKF (U.K.) Ltd, Mr N Stimson, also Mr P Tindale and staff provided insights to ball bearing technology and advise during rig modifications.

Several Technicians have helped with test rig modifications and setting up preparation and inspection equipment, including Clive Barrett, Tom Gates and Len Soans.

Visiting academic Dr S. Tobe of Tokyo Metropolitan University provided much expert knowledge. Dr Gillian Smith of NEI Parsons Ltd provided time, equipment and expertise with measurements of residual stress. Mr Go Fujinawa of Rigaku Corporation also provided expert knowledge.

Staff at the Experimental Techniques Centre, Brunel University have contributed to electron microscopy and interpretation.

The Department of Mechanical Engineering and Head of Department, Professor A.J. Reynolds have given constant support and encouragement.

Finally, last but not least, friends, family and Caroline have all contributed support and encouragement.

CONTENTS Page

CONTENTS CONTINUED

CONTENTS CONTINUED

NOMENCLATURE

The following notation is used in the mathematic model of the contact kinematics, chapter three, section [3.2].

a - Contact radius (mm)
r_c - Radius of cup (mm)
r_e - External radius of cup (mm)
r_l - Radius of lower ball (mm)
r_u - Radius of upper ball (mm)
v - Upper-ball linear velocity (mm/s)
v_p - Lower-ball linear velocity (mm/s)
v_s - Lower-ball spin linear velocity (mm/s)
α - Angle (degrees)
β - Angle (degrees)
γ - Angle (degrees)
ω_p - Lower-ball angular velocity (rads/s)
ω_s - Lower-ball spin angular velocity (rads/s)
ω_u - Upper-ball angular velocity (rads/s)

The following notation is used in the theoretical contact stress analysis of the model contact, appendix two.

E - Elastic modulus
L - Stress cycle factor
M - Mass applied at lever arm
P - Point force
p - Pressure load
p_o - Maximum contact pressure
R_A - Radius of driving ball
R_P - Radius of planet balls
s - distance from deflection point
w - Deformation
z - Number of planet balls
ϵ - Normal strain
θ - Angle of elemental area
θ_1 - Contact angle between driving and planet balls
ν - Poisons ratio
σ - Normal stress
ϕ - Airy stress function
ω_A - Angular velocity of driving ball
ω_P - Angular velocity of planet balls about driving shaft axis
ω_R - Relative angular velocity

The following notation is used in the theoretical thin film lubrication regime calculations, appendix four.

E' - Effective elastic modulus
g_e - Elasticity parameter
g_l - Load parameter
g_s - Speed parameter
g_v - Viscosity parameter
h_2 - Minimum film thickness
R - Relative Radius
V - Relative surface velocity
α - Pressure-viscosity coefficient
μ_0 - Lubricant viscosity
ϖ - Normal load

The following notation is used in scanning electron microscope calculations of stereo depth measurement and coating thickness, appendix seven.

K - Gas constant
Kv - Voltage (KV)
ma - Current setting (mA)
Mg - Magnification
P - Measured difference
T - Thickness of coating (Å)
t - Time (minutes)
Z - Objective height
α' - First image SEM angle
α'' - Second image SEM angle

The following notation is used in derivation of residual stress measurements by diffraction of x-rays, appendix eight.

d - Interplaner spacing in the crystal
E - Elasticity modulus
n - Positive integral number indicating the order of diffraction
ϵ - Quantity of strains
θ - Diffraction angle
θ_0 - Diffraction angle in a stress free condition.
λ - X-ray wavelength
ν - Poisson's ratio
ψ - Angle between the normal of the sample and the normal of the crystal plane

ABBREVIATIONS

ADC Analogue to Digital Converter

DAC Digital to Analogue Converter

ED Energy Dispersive

EHT EMF High Tension

EPMA Electron Probe Microanalysis

FEA Finite Element Analysis

FWHM Full Width of Half Maximum

HIP Hot Isostatically Pressed

IP Institute of Petroleum

ISO International Standards Organisation

LED Light Emitting Diode

NB Norton Corporation (U.S.A.)

PEEK Peek shift

SEM Scanning electron Microscope

TS Toshiba Corporation (Japan)

UB UB Industries (Japan)

WD Wavelength Dispersive

Chapter 1
INTRODUCTION

1.1 General Background

The use of ceramic materials for elements of rolling contact bearings shows some practical advantages over traditional bearing steels. The properties of ceramics, specifically low density and high stiffness, are of most interest to gas-turbine, Hamberg et al (1980) and machine tool manufacturers, Aramaki et al (1988). Also high hardness, low coefficient of thermal expansion and high temperature capability are properties suited to rolling element bearing materials. Silicon nitride has been found to have the optimum combination of properties suitable for this application. Much research over the past two decades on its structure, quality control and manufacturing techniques has produced material which can seriously be considered for rolling contact bearing design. This is especially true for hybrid ball-bearings, ie., ceramic balls with steel bearing races which are now used as a standard configuration in the bearing industry.

At present there is little information on load carrying capacity, wear, surface fatigue and failure modes of ceramics when used as a material in rolling contact bearings. It is particulary important that any new material considered for use in these applications should fail by a non-catastrophic mode. The only way, at present, to find out about these factors is to test the potentially useful material experimentally.

An experimental method is therefore essential for obtaining the information required about ceramic bearings. An experimental approach hence dominates the work described in this thesis. It is supplemented by an analysis using contact mechanics theory, elastohydrodynamic theory and finite element method.

A model contact consisting of three lower balls driven by a fourth contacting upper ball, simulates conditions within a standard deep-groove ball bearing. The upper ball models the inner bearing race, while the cup simulating the bearing outer race and the three planetary balls represents the balls within a ball bearing. In this way many more stress cycles are applied to a fixed contact area on the upper ball

and hence fatigue experimentation time is reduced.

The work was financed by the Science and Engineering Research Council with industrial support from SKF Ltd as a C.A.S.E. award scheme. Close liaison with the sponsoring company located at SKF U.K. and the SKF Engineering and Research Centre in the Netherlands took place during the project.

1.2 Objective and Scope of Research Work

The main objective of the study presented in this thesis was to investigate the failure modes of technical ceramics produced by the experimental model contact. The scope of this study includes altering tribological conditions under ambient temperature with ceramic/ceramic and ceramic/steel contacts. The influence of artificially produced cracks on the failure modes of ceramic balls was also studied.

1.3 Outline of Thesis

In Chapter one, general background information, and previous experimental and theoretical work related to this subject is described. Chapter two reports a detailed description and modifications of the experimental test rig. Chapter three describes the tribological contact zone conditions and stress analysis, by Hertz theory and analytical modelling. Upper and lower ball kinematic analysis is also presented in this chapter. Chapter four describes the main program of experimental testing. Section one is concerned with manufacturing, finishing and quality of the test specimens. Section two describes the lubricants used during testing. Section three outlines test procedure, preparation, initial microscopic inspection and test verification. In section four, scanning Electron Microcopy (SEM) and Electron Probe Micro Analysis (EPMA) are described. Section five covers the X-ray residual stress measurement, its theory and procedure, preparation and measurement verification. The final section deals with procedure, classification and inspection of pre-cracked ceramic test specimens.

Experimental results are presented in Chapter five. Test results on silicon nitride balls under various loads and lubricants are presented as section one. The lubricants used in these tests include base oil, standard oil, high viscosity oil, low

viscosity oil and emulsified water with brake fluid. Section two describes results with pre-cracked silicon nitride balls simulating a hybrid steel/ceramic contact bearing under lubricated conditions. A supplementary test using a 'Polymet' disc-on-rod machine with steel/ceramic lubricated contact is described in section three.

Analysis and interpretation of results is given in Chapter six. Section one reports on visual inspection including microscopic analysis, SEM and EPMA analysis and failure classification. Quantification of failure dimensions by Talysurf and SEM stereo analysis measurements are presented in section two. Residual stress results are shown in section three; this includes using different radiation sources and comparison with failure thickness. Conclusions and recommendations of further research topics resulting from this present study are outlined in Chapter seven.

1.4 Literature Survey

The research programme was preceded by a study of literature pertinent to the area of investigation. This literature survey is structured from a test-rig configuration type view point. Many test-rig types are used to study rolling contact fatigue, ie., modified four-ball, five-ball, balls-on-rod, disc-on-rod, contacting rings, ball-on-plate and full scale test. The test-rig type does have an influence on failure mode, which is the reason for the survey structure.

1.4.1 Experimental Research

a) Modified Four-Ball Machine

Preliminary work using a modified four-ball machine to asses hot-pressed silicon nitride as a rolling bearing material was reported by Scott and Blackwell (1973). Unlubricated contact was studied at different temperatures at 1500 r.p.m. and maximum Hertzian stress of 5.8 GPa. Lubricated contact was also studied at 7.7 GPa and ambient temperature. Under unlubricated conditions upper ball wear after 30 minutes was measured as 0.6 milligrams, the wear track on the ball surface retained modest surface quality. In the case of lubricated contact, failure occurred to the upper ball after 20 seconds and failure mode being wear and fracture. Silicon nitride upper ball was tested in contact with En31 steel lower ball and this increased

time to failure to 70 seconds. Using steel/steel contacts under lubricated conditions failure mode, occurring after 100 minutes, was fracture by a single small pit on the upper ball.

Silicon nitride manufactured by the hot pressed method could, on this basis, be regarded as a good wear resistant material although not a suitable alternative to steel under heavily loaded, lubricated conditions. Also, during testing, catastrophic failure was experienced during some lubricated tests. Although discouraging these results show a considerable improvement from similar tests, eg. Scott et al (1971), on silicon nitride manufactured from a reaction bonded process. These earlier tests produced even poorer lubricated rolling contact fatigue resistance with modest unlubricated wear resistance. Failure mode was reported as an excessive wear, catastrophic shattering or lower ball spalling. Lower ball spalling or flaking occurred on reaction bonded silicon nitride lower ball when tested with a hot-pressed upper-ball.

b) Five-Ball Machine

Fatigue life of high-speed ball bearings with hot pressed silicon nitride balls was investigated by, Parker and Zaretsky (1975). Lubricated contact was studied with 12.7 millimetre diameter balls, Hertz stresses ranging from 4.3 to 6.2 GPa, shaft speed of 9600 r.p.m. and contact angle of 30 degrees. Failures of upper balls showed no evidence of wear, only fatigue spalls similar to that found on steel ball failures. Life predictions showed that ceramic-steel contacts compared equally to steel-steel contacts. Edge cracking was not detected on any region near spalled areas or along contact path.

The spalling mode of failure with increased comparative fatigue life differed greatly with earlier four-ball machine experiments. The significance of material porosity, inclusion content and finishing procedure were suggested as factors causing life inconsistencies. Although these factors may have some influence on results, it is more likely however, that tribological differences of the two machines were more significant. The contact angle used for five-ball testing produces a greater spin-roll ratio and the increased dynamic effects has a large influence on ceramic materials.

c) Balls on Rod Machine

Comparative rolling fatigue studies of hot-pressured silicon nitride, hot isostatically pressed (HIP) silicon nitride, sialon and M50 bearing steel were reported by Lucek (1990). A rod type fatigue testing machine in which three half-inch diameter steel balls orbit a rotating 0.375 inch diameter cylindrical test specimen was used. At peak contact stress of 6.4 GPa, synthetic turbine oil at ambient temperature provided a boundary lubrication. The specimen speed was set at 3600 r.p.m. or 8600 stress cycles per minute. Results showed that the predominant fatigue failure mechanism in silicon nitride involves the slow growth of circumferential cracks from the edges of the contact path driven by tensile stresses. Spalling occurred when material in the compressive zone was insufficiently supported. Weibull life slopes were calculated for all materials and showed that hot-isostatically pressed silicon nitride compared better than M50 steel. Hot-pressed silicon nitride showed an order of magnitude reduction in fatigue life compared with HIP silicon nitride. Sialon fatigue mode was due to intergranular surface wear in the contact compressive area.

These relatively recent test results show some particulary interesting results compared with other test methods. The spalling mechanism of silicon nitride was different to that found during five-ball testing as no contact edge cracking was detected in the latter. Also, hot-pressed silicon nitride did not compare favourably as found in five-ball testing; this seems to confirm earlier work using four-ball machines.

d) Disc on Rod Machine

Rolling contact fatigue data, Cundill (1990), of good quality silicon nitride produced by the HIP technique was compared with poor quality silicon nitride and M50 steel. Poor quality silicon nitride being defined as material of high porosity and containing inclusions. A cylindrical rod test specimen similar to balls-on-disc machine was rotated at 12,500 R.P.M. between two steel discs which were drip lubricated. The test pressure was 5.4 GPa for ceramic/steel contact and 4.8 GPa for steel/steel contact produced by equal force.

The results showed that good quality silicon nitride outperforms M50 steel although poorer quality material severely reduces life. Fatigue mode of the ceramic in all cases being spalling as was the case of steel. Edge cracks as found in balls-on-disc machine were not reported, confirming that this may not be the only mechanism. Earlier work using this machine was performed by Lucek and Cowley (1978) using a hot-pressed ceramic test specimen. At that stage of the materials development results were not so as impressive as recent comparisons with bearing steel. All failures were of a spalling non-catastrophic nature and test loads varied from 4.1 to 5.5 GPa. Cone cracks were found on surfaces due to manufacturing errors which would reduce fatigue life. Surface quality was studied as a function of fatigue life, in particular, the method of specimen finishing. It was found that test specimen finishing by different honing and lapping techniques influenced rolling contact fatigue results. The fact that finishing techniques were found to be influential on test results is not surprising as directional topographic changes will influence frictional effects. Also sharpness of asperity slope is a function of finishing technique; ceramic materials may be sensitive to this parameter.

e) Contacting Ring Machine

Rolling and sliding wear mechanism experiments were performed by Braza et al (1989). This work involved the use of a large diameter cast iron roller contacting with a smaller diameter silicon nitride roller with an internal steel pin lubricated with a standard lubrication oil. Contact pressure was small, ie., 1.37 GPa, and three types of silicon nitride were tested:- hot pressed, pressureless sintered and reaction bonded. The wear rate for reaction bonded type was higher, the wear mode by 'grain pullout'. The other two types had similar wear rates, the mode of wear being sub-micron chipping. Rolling contact friction coefficients were found to be 0.0056 and all similar.

Wear properties of silicon nitride in rolling-sliding conditions were studied by, Akazawa and Kato (1988) using ring-on-roller test machine. Under no lubrication and a maximum Hertzian pressure of 1.1 GPa, results showed thin flake-like wear particles which were rich in oxygen.

Wear properties of silicon nitride were examined in dry rolling contact by Akazawa et al (1986). A ring-on-disk method was used to compare wear rates of pure rolling and rolling-sliding under contact pressures between 1.1 and 1.8 GPa. In the initial stages, wear rate was two orders of magnitude greater than the steady wear stage. Three types of wear debris were identified:- thin flake-like, glassy film and crystalline.

Dry rolling tests by Kim et al (1986) on several ceramics concluded that silicon nitride wear-rate was the smallest. A ring-on-disk testing machine was used, maximum Hertz stress ranged from 2.5 MPa to 5 GPa. A relation between wear rate and a mechanical properties was attempted without success, suggesting that a combination of material properties and roughness were needed. Brittle fracture mechanism was concluded to be the dominant wear mode.

f) Ball on Plate Machine

Experimental work performed by Fujiwara et al (1989) examined the dynamic and static load rating of silicon nitride as a bearing material. Steel balls revolving around an inner race were loaded against a flat test piece. The maximum contact stress was 6.4 MPa, rotational test speed was 1400 r.p.m and the lubricant was a turbine mineral oil. The test was stopped by vibration cut-out when spalling occurred on the silicon nitride test piece. Fatigue life results showed the ceramic performed better than steel although the scatter was greater due to longer lives. Spalling was identified as the most common long term mode of failure; two other modes which occurred in very short times were 'cave-in' and peeling. The two short-term modes of failure were attributed to material voids. Conclusions reached were that hot-pressed silicon nitride with a high rigidity containing yttrium and alumina as sintering additives was superior to bearing steel on the rolling fatigue life. In order to ensure rolling fatigue life reliability of silicon nitride, it is important that voids and segregation of sintering additives must be excluded.

Rolling fatigue life of ceramics was tested by Kikuchi et al (1984) using steel balls loaded on a flat test piece. Sintered and hot-pressed silicon carbide and silicon nitride were tested and compared with bearing steel. The results found poor

performance of the ceramic materials, although the hot pressed silicon nitride showed some favourable features; also the scatter of results was great. The failure modes included all forms of flaking, three of which were identified which varied in size and depth.

g) Full Scale Testing

The temperature performance of hybrid ball bearings with silicon nitride balls for a high-speed machine tool spindle, was studied by Aramaki et al (1988). Two different sized test spindles were used with 11.1 millimetre and 7.1 millimetre diameter silicon nitride balls. The results found that the ceramic balls showed a lower temperature rise and higher speed capacity relative to steel ball bearings. Frictional losses calculated analytically were in a good agreement with theoretical results.

Silicon nitride hybrid bearings were tested by Morrison et al (1984) using 12.7 millimetre diameter balls, M50 steel rings and a brass cage. Contact pressure ranged between 1.95 and 2.44 GPa, and the film parameter was approximately 3.5 for all tests. Spalling was identified as the only mode of failure, in no cases did the silicon nitride balls fracture. Statistical analysis showed that bearing life varies in accordance with a power law model.

Advantages of using silicon nitride as a bearing material was described by, Cundill (1983). Research activities within S.K.F. Ltd regarding the use of different materials in high speed, high temperature applications have concluded that silicon nitride offers most potential. Hot isostatic processing technique was described. It was reported that less power was lost due to ball spin and lower running temperatures compared with steel bearings.

A silicon nitride roller bearing was fitted to a J-402 gas-turbine engine main-shaft. Hamburg et al (1980), then ran the engine under test conditions for a program involving six engine tests. The main problems encountered were misalignment of the inner race caused during high thermal gradients and accelerations. Rolling contact fatigue tests using a disk system under lubricated conditions and contact stress of 5.5 GPa were carried out. Failures occurred at ten million stress cycles but

the majority were suspended at twenty-five million stress cycles; these results compared favourably to steel rollers.

A hybrid angular contact bearing fitted with 7.9 millimetre diameter balls was assembled on a high speed test rig. The tests produced by Reddecliff and Valori (1976) involved turbine driven shaft speeds to 71,500 r.p.m. and forced lubrication. The tests demonstrated that silicon nitride can operate satisfactorily under the current gas turbine engine speed, load, and lubrication conditions.

1.4.2 Theoretical Research

Sliding and rolling wear of ceramics was reviewed by Fischer (1990); particularly the relationship between material properties and the importance of tribochemical effects were identified. The dominant wear mechanism in silicon nitride was identified as micro-fracture; an equation for abrasive wear was stated. Silicon nitride was shown as having better rolling performance than other ceramics. An equation for wear rate of ceramics under rolling conditions was discussed. Tribochemical effects were discussed, in particular the wear of silicon nitride lubricated by paraffin. Water lubrication showed wear by chemical dissolution producing ultra flat surfaces.

In a review by Kato (1990), the fundamental frictional and wear properties of ceramics were discussed. A sliding wear mode diagram was introduced with particular reference to silicon nitride. Removal of material due to various types of crack propagation, ie., Hertzian, lateral, median and radial were discussed. Flake removal which were formed by lateral cracks initiated at the plastic zone of the subsurface could be identified. Wear volume removal due to flaking could be estimated by theoretical models described. Tribochemical wear of silicon nitride in a water environment was identified. Unlubricated contacts showed the generation of filmy silicon oxide wear particles. Surface finishing was also discussed, the problem of grinding with diamond wheels and powder producing surface cracks were identified. The recent understanding of tribochemical wear of silicon nitride in water suggests new finishing techniques should be investigated such as magnetic fluid grinding currently in use.

An examination of theoretical studies into ceramic wear mechanisms was made by Braza et al (1989). Mechanical aspects of wear were discussed without regard to tribochemical effects. Cracking types, ie., transgranular and intergranular were discussed, although, in theory, all cracks should be intergranular (along grain boundaries). As the surface energy along grains is reduced by grain boundary energy the actual practice is transgranular cracks. It was stated that transgranular cracks occur due to material flaws present either before or after loading. Silicon nitride may show intergranular cracking caused by glass phases at the grain boundaries produced from sintering additives. In the case of brittle materials, cracks may occur on the surface due to tension (mode I) or subsurface crack parallel to contact path due to shear (mode II). Friction in rolling and sliding contact can arise from asperity interlock, adhesion or abrasion by debris trapped between the contacting surfaces and viscous drag of the lubricant.

Ceramic tribology was reviewed by Crammer (1987); in particular, unlubricated contacts were discussed. Wear and friction was attributed to either adhesion, abrasion, delamination and micro-fracture, or a combination of these modes. Theories were considered and models discussed, including delamination of sliding contact. Silicon nitride was identified as a particularly difficult material to characterise due to varying manufacturing methods and sintering additives.

1.5 State of Art Resulting from Literature Survey

The advantages of using ceramic ball bearings have been confirmed from extensive full-scale turbine and machine tool testing. Various rolling contact tests methods have been employed to examine the fatigue life performance of ceramics. The test methods resulted in fatigue spalling in most cases, comparisons of life with steel materials have been evaluated. Since the early eighties, modified four and five ball spin rigs have not been used, and therefore correct simulation of rolling element bearings has not been considered. Detailed fatigue modes of spalling have not been adequately explained at this stage. Also the affect of damaged ceramic ball surfaces on fatigue failure modes have not been dealt with.

Chapter 2
TEST-RIG MODIFICATIONS

This chapter presents background work carried out as a preparation to experiments. The modified four ball machine was adapted to allow more sophisticated and flexible contact loading, to control lubricant flow into the contact zone and to allow machine temperature regulation to increase safety. Electronic, digital and mechanical components required for these modifications were designed and manufactured by the author with departmental assistance.

2.1 Test-Rig Modifications

2.1.1 Modified Load System Design

The test-rig contact load system was modified to allow variation of contact loads during experiments without constant supervision and also, to provide flexibility during overnight testing. A feasibility study was carried out of alternative designs to facilitate the optimum load system modification. The overall design problem was to replace the simple method of placing dead weights on the loading arm, shown in appendix one, by a controllable system. It was considered unnecessary to replace the lever-arm itself as it already provides an efficient method of transmitting an applied load. Three main design proposals were considered:

(i) Design one; a stepper-motor providing load variation by gradually extending or releasing a spring attached to the machine lever-arm.

(ii) Design two; a linear actuator either driven by a stepper motor or electro-magnet. The linear actuator would provide proportional movement to a spring attached to the lever-arm.

(iii) Design three; a pneumatic system, with an air cylinder rigidly fixed to the lever-arm. Air pressure within the cylinder is directly proportional to applied force for a given cylinder diameter. Air pressure would be controlled by a proportional solenoid valve driven from controllable current regulator.

All of the three designs have various advantages and disadvantages. The first design was considered to be the least expensive of the three as only two mechanical components are required. The main disadvantages with this system are: the design problem needs a changing load with no movement, as ball contact is maintained constant, therefore, a spring or similar component providing displacement is required. Also a profiled camshaft would be required to provide proportional movement from the stepper-motor drive to the spring. This would create a complicated mechanism with doubtful accuracy and sensitivity to an experiment requiring precise load increments.

The second design solved the problem of complication and accuracy by using a linear actuator. A spring would still be required to provide the mechanism with the necessary displacement. The main disadvantage with this system is financial cost of the non-standard linear actuator.

The third system was thought to be the most elegant design solution to the main criteria of function, simplicity, reliability and cost. As a pneumatic system responds to pressure changes then movement of the air cylinder is not necessary. The pressure regulator controlled by a current regulator has an in-built feed-back control system which reduces cost and complexity.

The schematic diagram and photograph, shown as figure 2.1, describes the basic loading system configuration and components. The pneumatic components supplied by 'Festo Ltd' consist of:- Air cylinder (DNU-32-2), Proportional pressure regulator (MPP-3-1/8), Current regulator (MPZ-1-24 DC) and Filter regulator unit (LFR-1/8-B). The components are located on a mild steel table which is also used to provide reaction to the pneumatic cylinder pulling force. The table is thus designed robustly to increase weight and is located fast to the floor with a suitable adhesive. Compressed air pressure from laboratory mains, which is well above operating pressure (alternating between 80 and 100 psi), supplies the pneumatic system. A filter regulator reduces the mains pressure to system operating pressure via a diaphragm screw adjustment valve. The filter removes excessive moisture and large particles from the air supply. Occasional water drainage is required from this unit. The filtered air at constant pressure is connected to a pressure regulator which

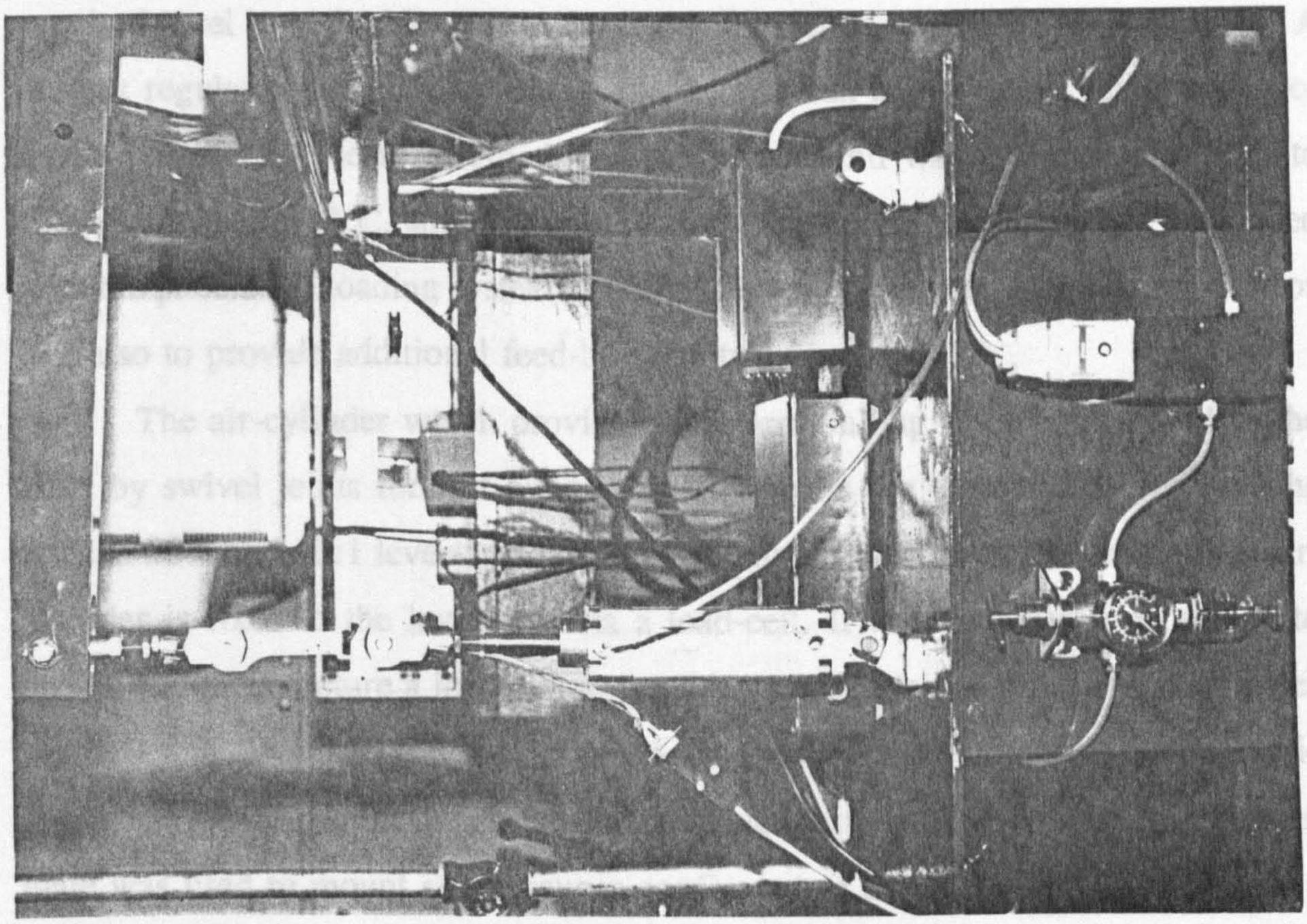

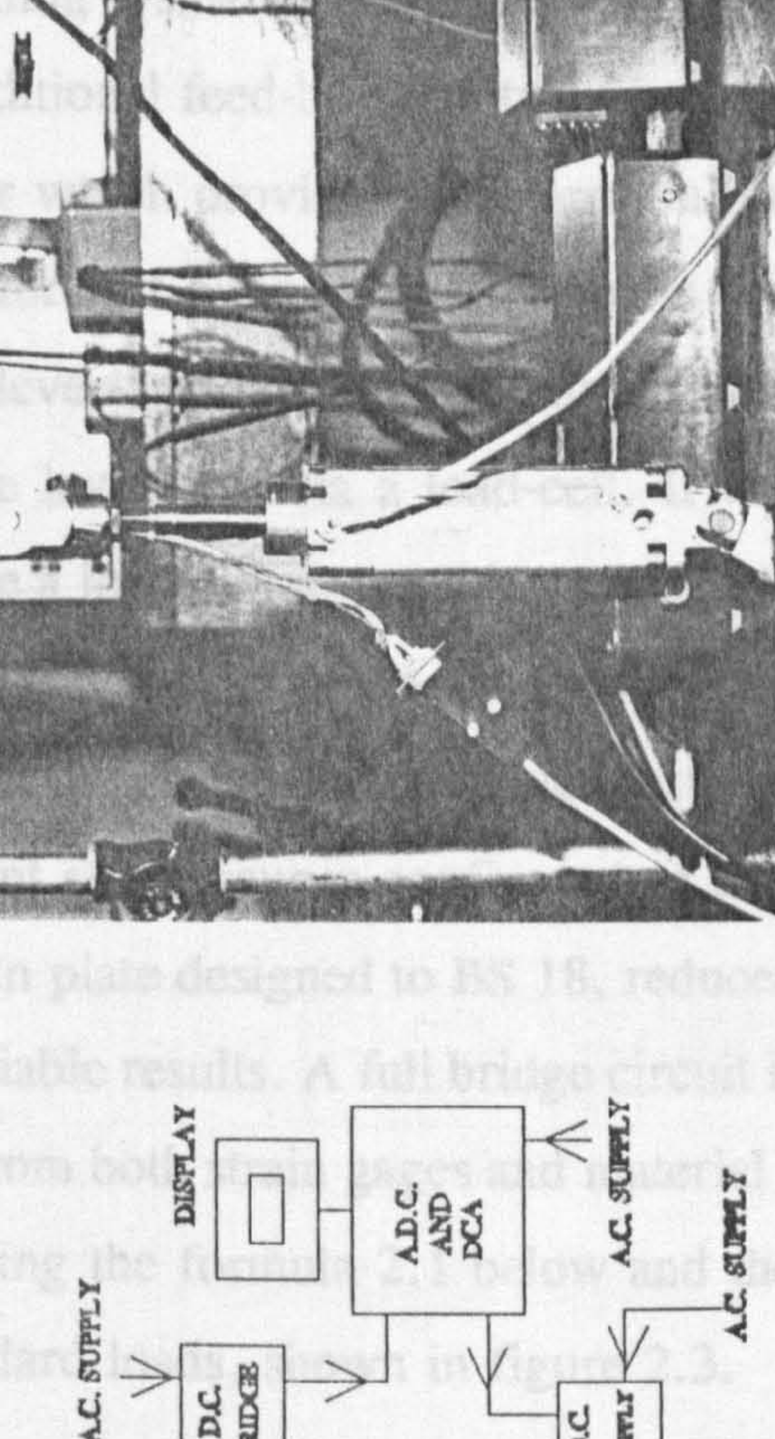

Figure 2.1 Pneumatic loading system

pressurises the air-cylinder. The pressure regulator adjusts the operating air to the required level by a double-acting piston valve which is positioned by a solenoid. A current regulator plugged into the solenoid valve can adjust the pressure regulator to the correct set pressure. An A.C. rectification unit was designed and built to provide a constant D.C. supply to the current regulator. A computer was interfaced with the pneumatic loading system to permit flexibility in lever-arm load application and also to provide additional feed-back control.

The air-cylinder which provides lever-arm pulling force is anchored to the table by swivel joints for self alignment. Two joints are permanently fixed to the table at 20:1 and 10:1 lever-arm positions. A simple short stroke double acting air-cylinder is fixed to the lever-arm via a load-cell. It was considered necessary to design and manufacture a load-cell to provide an accurate measurement of cylinder pressure and electronic feedback of lever-arm load and also to provide an automatic unloading mechanism in the event of a completed test. A standard aluminium strain plate was used to mount strain gauges configured as a 'full bridge' circuit, shown in figure 2.2. The strain plate designed to BS 18, reduces any stress concentrations which may cause unreliable results. A full bridge circuit is chosen as this maximises the strain gauge gain from both strain gages and material Poisson's ratio. The gauge output is calculated using the formula 2.1 below and the measured output voltage is calibrated with standard loads, shown in figure 2.3.

$$\frac{E_0}{E} = \frac{Fe(1-\nu)E-3}{2+Fe(1-\nu)E-6} \qquad (2.1)$$

The equipment required for interfacing the loading system analogue signals to a digital computer was provided by a 'Thinklab' system from '3D Ltd'. The following interface cards were used:- R-8PGA (eight instrument amplifiers followed by a multiplexer and gain programmable amplifier), R-12ADS (twelve-bit integrating ADC plus sign bit and over-range bit) and R-12DAC4 (twelve-bit, four channel DAC, output voltage switch selectable 0-10 V).

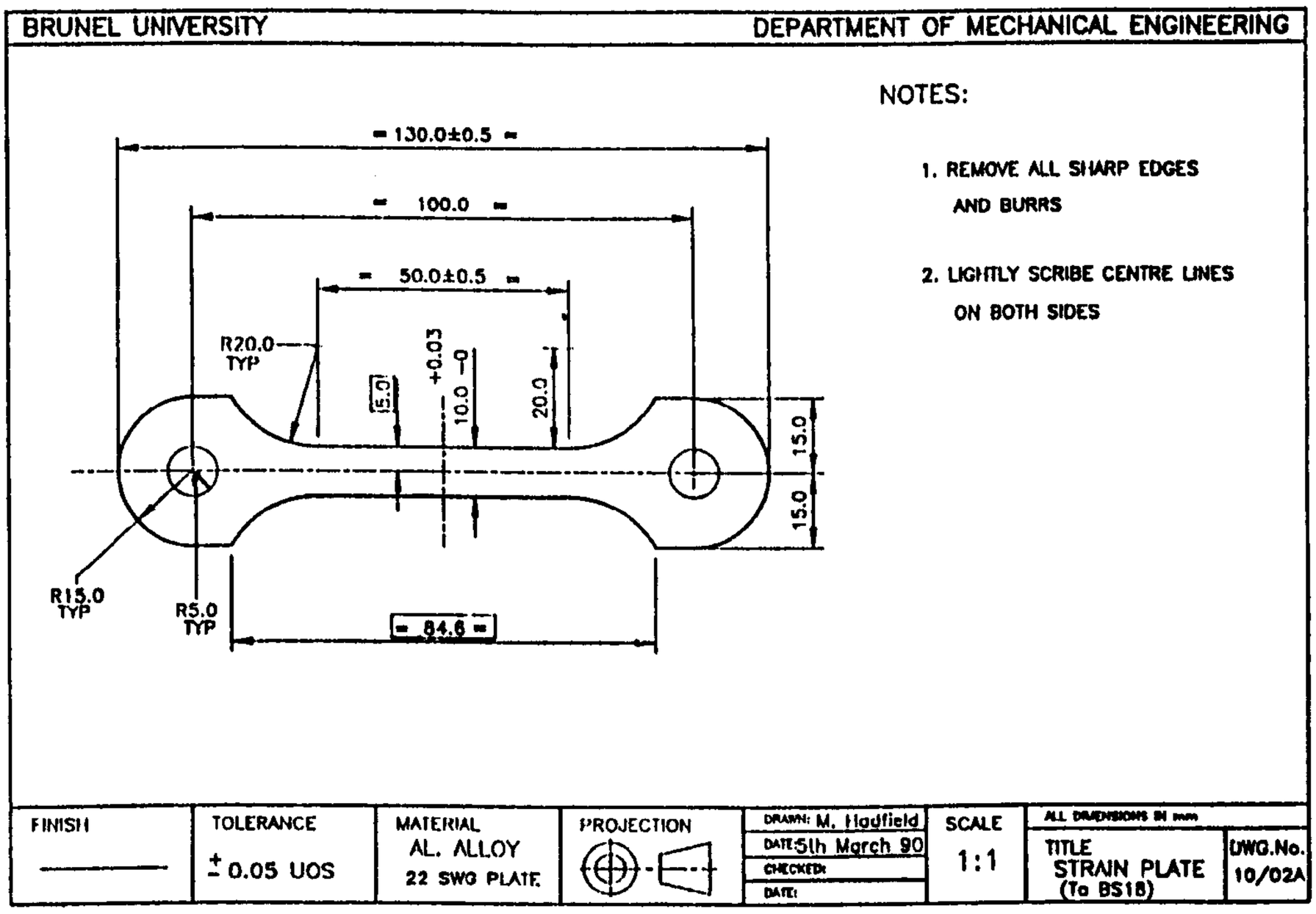

Figure 2.2 Strain plate

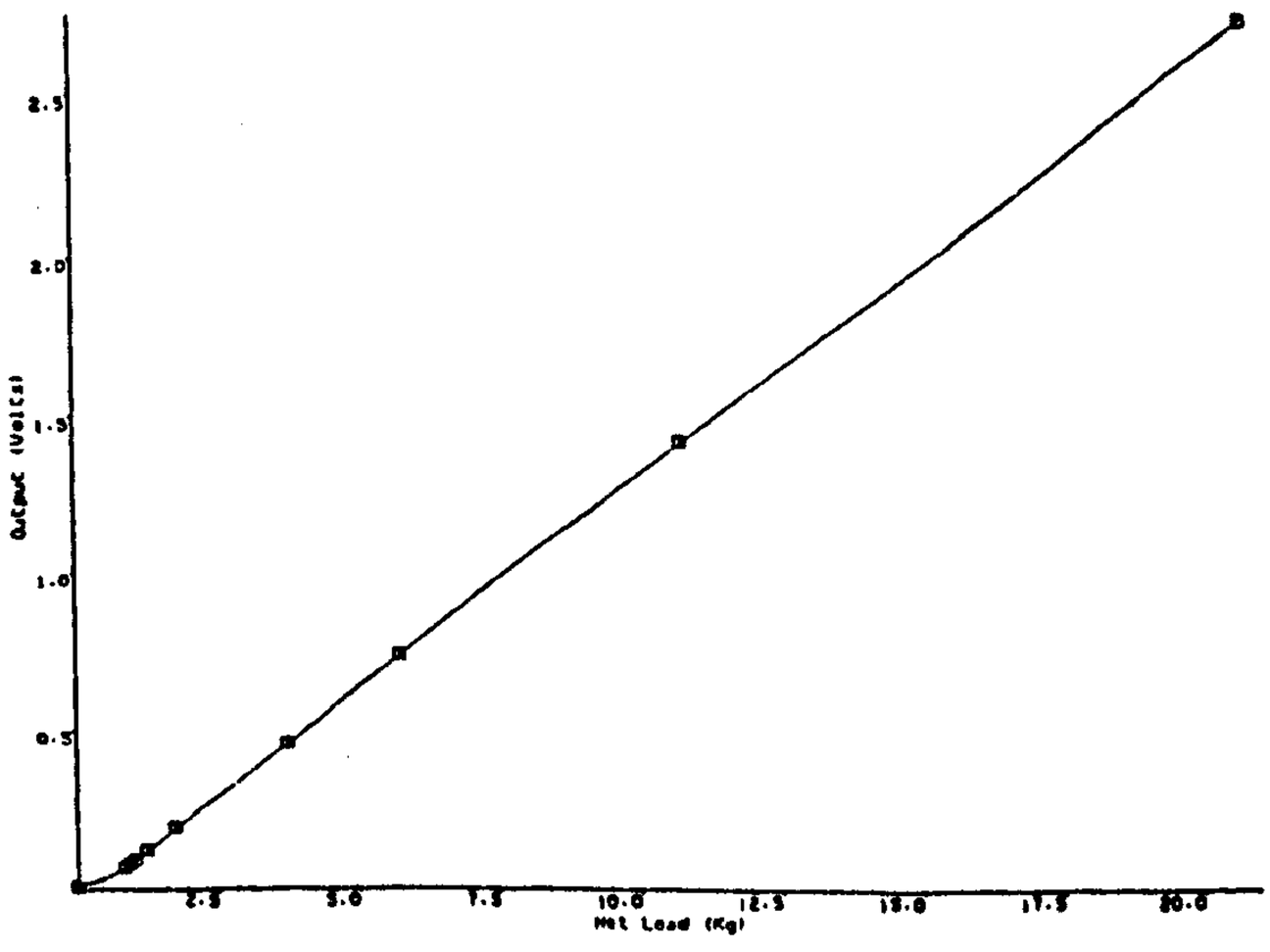

Figure 2.3 Load cell calibration

2.1.2 Feed Lubrication System Design

A splash lubricating system was designed and installed as an alternative to the standard machine 'enclosed' lubricating system. It is necessary for some experiments to use an alternative lubricating system for many reasons. Failure mode may be a function of lubrication method, wear debris may build up in an enclosed system which again may affect failure mode, lubricant temperature may change which affects lubrication regime, lower ball kinematics may also be affected by an 'enclosed' system due to lubricant viscosity. The splash lubrication also creates more flexibility when using emulsified lubricants as frequent replenishment is often required when using an 'enclosed' system.

Design of the splash lubrication system considered that the lubricant should be mechanically pumped to the contact zone by a controlled process. Two types of lubricant pump were appraised; a peristaltic pump and a micro pump. Both pumps have the advantage of the lubricant not contacting any internal mechanisms which allows for a recirculating option. The peristaltic pump is much cheaper but has several disadvantages compared to the micro pump. Limitation of lubricant temperature, restricted maximum head pressure, high minimum flow rate and restricted control of volumetric flow rate, are the main reasons why a micro pump was selected. The pump was supplied by ProMinent, a type 4.1 with a stainless steel chamber which was selected to resist any corrosion and debris damage. This pump operates from a diaphragm and swash-plate which enables both stroke volume and stroke rate to be adjusted, giving great flexibility and control of volumetric flow rate. After fixing the pump to the test-rig, oil suction piping was fitted, and flexible discharge piping was directed to the ball contact area; a hypodermic syringe assists exact positioning of outlet lubricant. The pump feed rate was calibrated from manufactures data; the pump range is from maximum 1170 cc/hr (100% membrane action with 120 pulses per minute) to minimum 1.2 cc/hr (20% membrane action with 2 pulses per minute).

To allow the splash system to drain contaminated lubricant away from the contact zone it was necessary to redesign the steel cup assembly housing, shown in figure 2.4, and manufacture additional hardened steel cups, shown in figure 2.5.

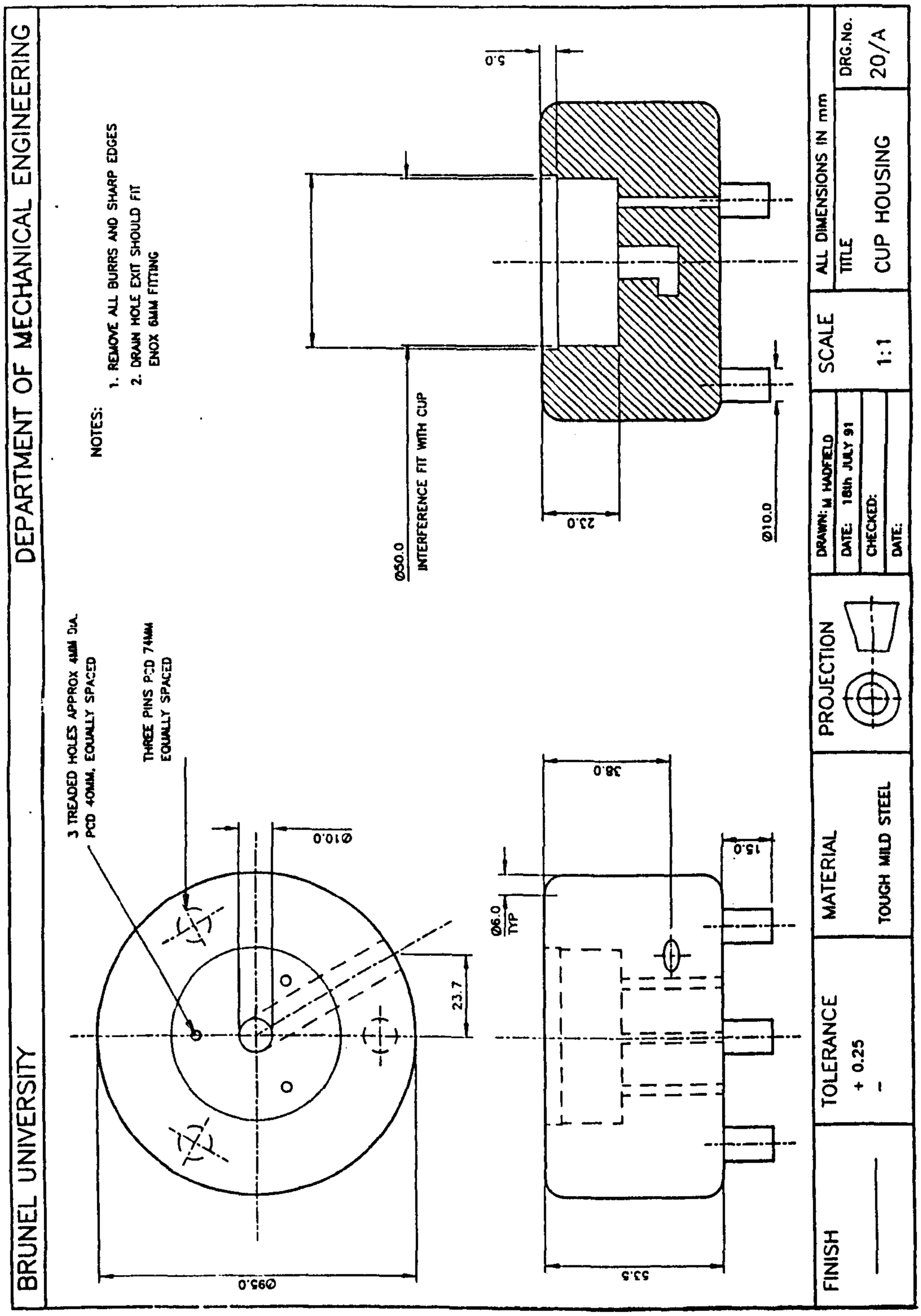

Figure 2.4 Cup assembly housing

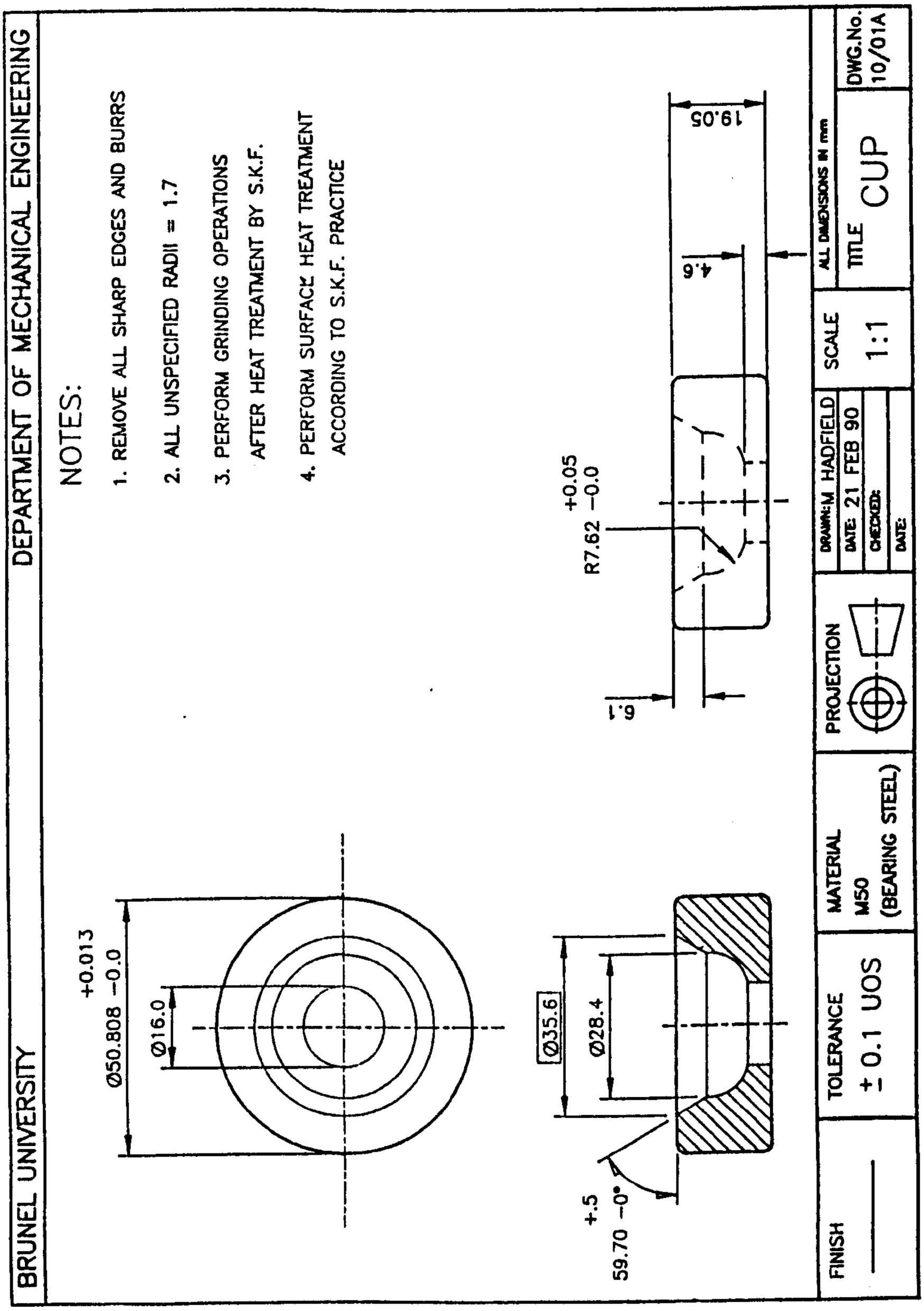

Figure 2.5 Hardened steel cup

The most efficient method of removing spent lubricant is a gravity drain system. This drainage system requires the cup housing assembly consisting of a heated pad to be redesigned. The new design of cup housing also allows steel cups to be pressed in and removed as required. Lubricant is drained through a right-angled hole drilled through the centre and side of the housing, a flexible pipe is attached to the hole outlet and drained below into a container. Schematic diagram of the feed lubrication system is shown in figure 2.6.

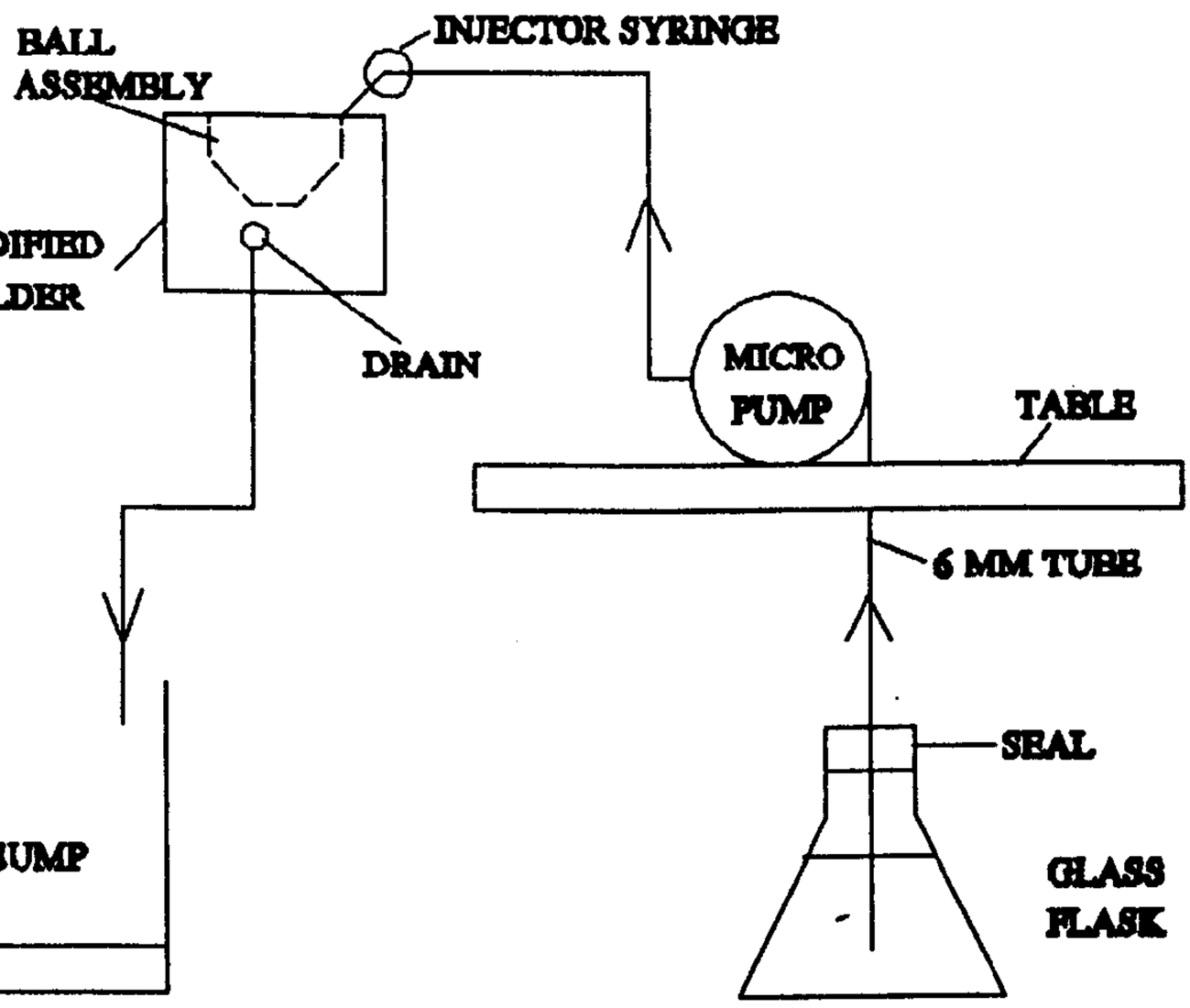

Figure 2.6 Schematic of feed lubrication system

2.1.3 Temperature Regulation

To enable the machine to be run unattended overnight additional safety devices were required to prevent excessive damage in the event of test-rig failure. Drive spindle-bearing temperature was monitored and a suitable cut-out designed and fitted to prevent major damage to the machine in the event of spindle-bearing failure. Temperature sensors of a semi-conductor type (LM35CZ) supplied by 'R.S. Ltd' were fitted into drilled holes close to each of the two spindle bearings. An electronic cut-out circuit and sensor power supply was built and linked to the original vibration sensor cut-out circuit. The link enables the machine to cut-out in the same mode as excess vibration, when the spindle bearing temperature reached an unacceptable level. Each temperature sensor was calibrated using suppliers data and the test-rig thermocouple. The sensors were set to stop the test-rig when spindle bearing temperature reached 85°C.

Chapter 3
CONTACT ANALYSIS

Analytical models of ball stress fields are presented to increase understanding of failure modes, compare the effect of materials on surface stress and provide the basis of further more refined analysis. A finite element analysis method is adopted to provide model flexibility under various loads and configurations. Theoretical kinematic analysis of the lower balls complex motion is also presented. Results derived from kinematic relationships are compared with experimental observations.

3.1 Finite Element Model

3.1.1 Background and Objectives

Previous work involving the use of an elastic analytical model for contact analysis was carried out by Hartnett (1978). This model presents a force-displacement method of predicting contact stress and can be solved without the use of digital computer. Much later, finite elements were used to predict contact stresses, and a displacement-force method was employed, which is particularly suited for digital computers as it requires a systematic solution of multiple simultaneous equations. Elastic-plastic rolling contacts were studied by Bhargaval et al (1989), Ham et al (1988) and Bhargaval et al (1985). A finite element crack propagation study of high speed roller bearings was performed by Tunca and Laufer (1987).

The finite element analysis (FEA) is an approximate displacement method which involves discretisation of a physical problem into 'elements' which are solved analytically. The basic principle of this method is an extension of the displacement method of stress analysis. Nodes which couple elements together by a stiffness matrix are used to solve the governing equation.

$$\{ P \} = [K]\{ p \} \tag{3.1}$$

The three main objectives for development by the analytical models of the contact problem are listed:-

(i) Prediction of dry frictionless contact stresses under static loads.

(ii) Stress field and surface contact pressure comparison of different materials.

(iii) Investigation of model sensitivity to specific contact volume analysis.

3.1.2 Model Description

Lubrication regime is studied using elastohydrodynamic theory. Results found, (see appendix four), show that full film exists implying that a frictionless model is valid. It is also recognised that lubricant film will influence surface deformation. For this case, however, a thin film exists and hence Hertz theory is valid. In the case of a typical ball bearing, friction coefficient is extremely low and hence its influence on stress fields is limited.

The model of ceramic upper-ball contacting with ceramic lower-ball is shown in figure 3.1. The model is axisymmetric which simplifies the geometric requirements to a plane model, rotated about the load axis. This type of model is accurate for symmetrical problems where out of plane strains are not significant, circumferential or 'hoop' strains are, however, included. Inclination contact angle between upper and lower balls, is taken into account by applying a vertical point component force to the upper-ball model, this force represents the lever-arm load. The contact model is restrained along the load axis of symmetry in the perpendicular direction, the lower ball is also restrained along the perpendicular axis in the load axis direction.

Element aspect ratio is important for the accuracy of the calculated displacements. It can been seen in figure 3.1 that some elements have poor aspect ratio; their position, however, is remote to the contact zone. The important area within the contact zone, figure 3.2, has an adequate aspect ratio. The mesh has 356 quadratic type elements; mesh density increases around the contact region as Hertz stresses are maximum fractionally below or on the surface.

It can been seen, figure 3.2, that the initial geometry considers the balls contacting at a point. To solve this contact problem, the model must accommodate material deformation to produce a contacting circle between balls. Surface nodes in the contact region are thus assigned together with model deformation of the balls.

The solution is found iteratively by gradually increasing the contact area and thus including additional assigned nodes and coupling them together within the stiffness matrix until equilibrium is achieved.

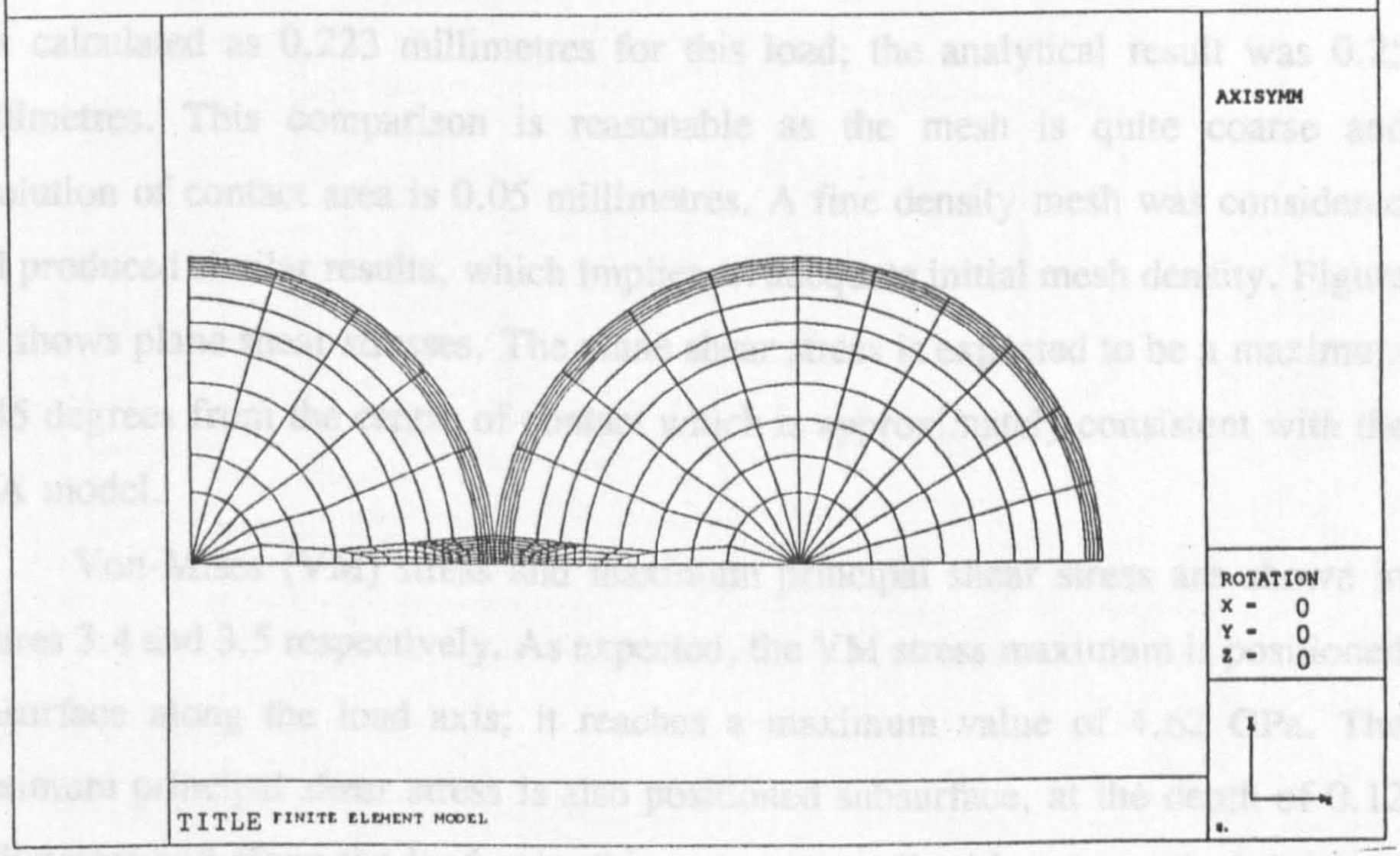

Figure 3.1 Finite element model

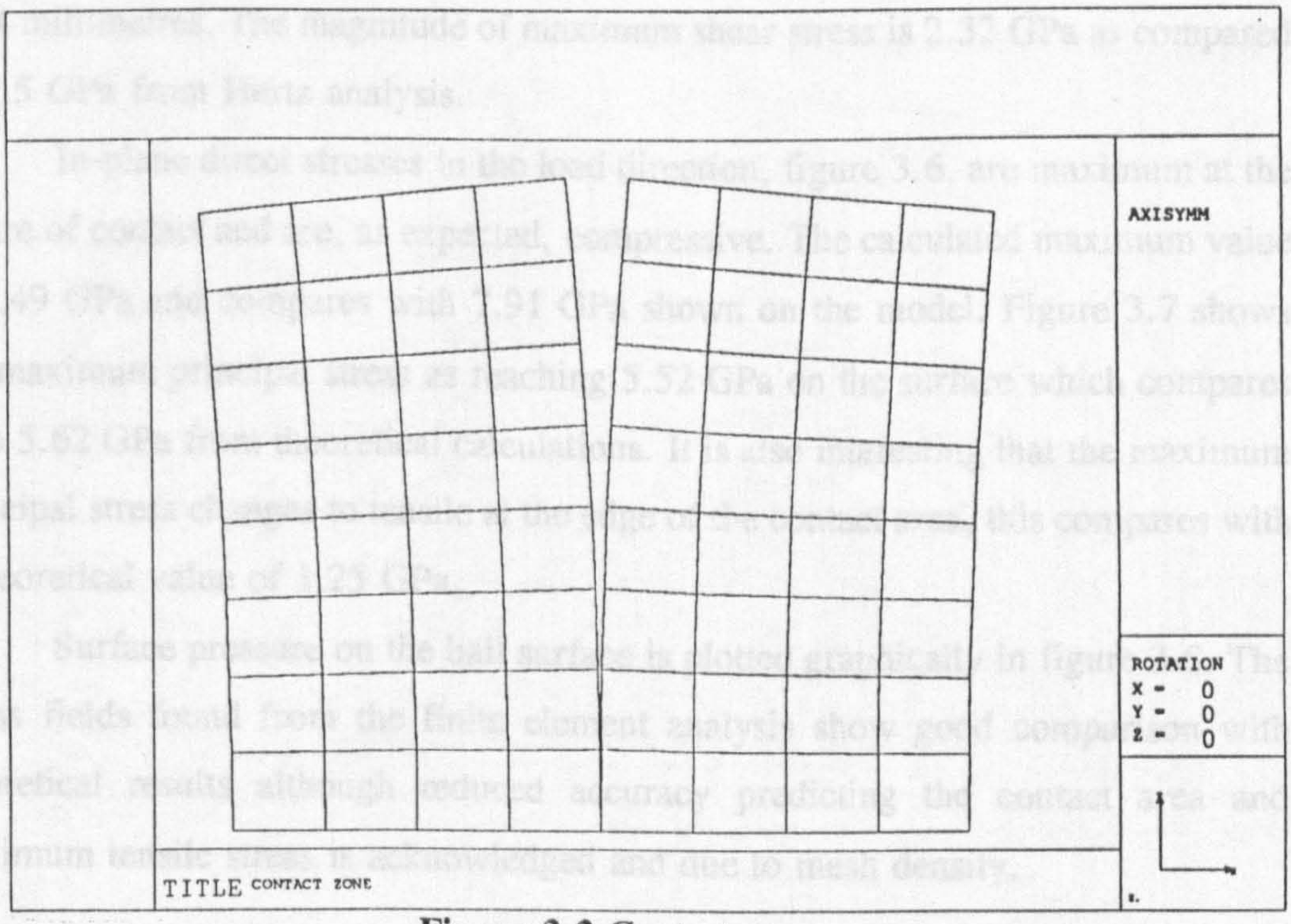

Figure 3.2 Contact zone

3.1.3 Results Analysis of Typical Load Case

The load case studied represents a lever-arm load of 10 kg or contact force of 800 N. Calculations with this typical load using Hertz theory are explained in appendix two, and the results are used to validate the FEA model. The analysis converged after five FEA iterations, gradually increasing contact area to reach equilibrium by increasing coupled surface nodes in the contact. Hertz contact radius was calculated as 0.223 millimetres for this load; the analytical result was 0.25 millimetres. This comparison is reasonable as the mesh is quite coarse and resolution of contact area is 0.05 millimetres. A fine density mesh was considered and produced similar results, which implies an adequate initial mesh density. Figure 3.3 shows plane shear stresses. The plane shear stress is expected to be a maximum at 45 degrees from the centre of contact which is approximately consistent with the FEA model.

Von-Mises (VM) stress and maximum principal shear stress are shown in figures 3.4 and 3.5 respectively. As expected, the VM stress maximum is positioned subsurface along the load axis; it reaches a maximum value of 4.62 GPa. The maximum principal shear stress is also positioned subsurface, at the depth of 0.12 millimetres and along the load axis, this compares well with a theoretical depth of 0.14 millimetres. The magnitude of maximum shear stress is 2.32 GPa as compared to 2.5 GPa from Hertz analysis.

In-plane direct stresses in the load direction, figure 3.6, are maximum at the centre of contact and are, as expected, compressive. The calculated maximum value is 7.49 GPa and compares with 7.91 GPa shown on the model. Figure 3.7 shows the maximum principal stress as reaching 5.52 GPa on the surface which compares with 5.62 GPa from theoretical calculations. It is also interesting that the maximum principal stress changes to tensile at the edge of the contact area, this compares with a theoretical value of 1.25 GPa.

Surface pressure on the ball surface is plotted graphically in figure 3.8. The stress fields found from the finite element analysis show good comparison with theoretical results although reduced accuracy predicting the contact area and maximum tensile stress is acknowledged and due to mesh density.

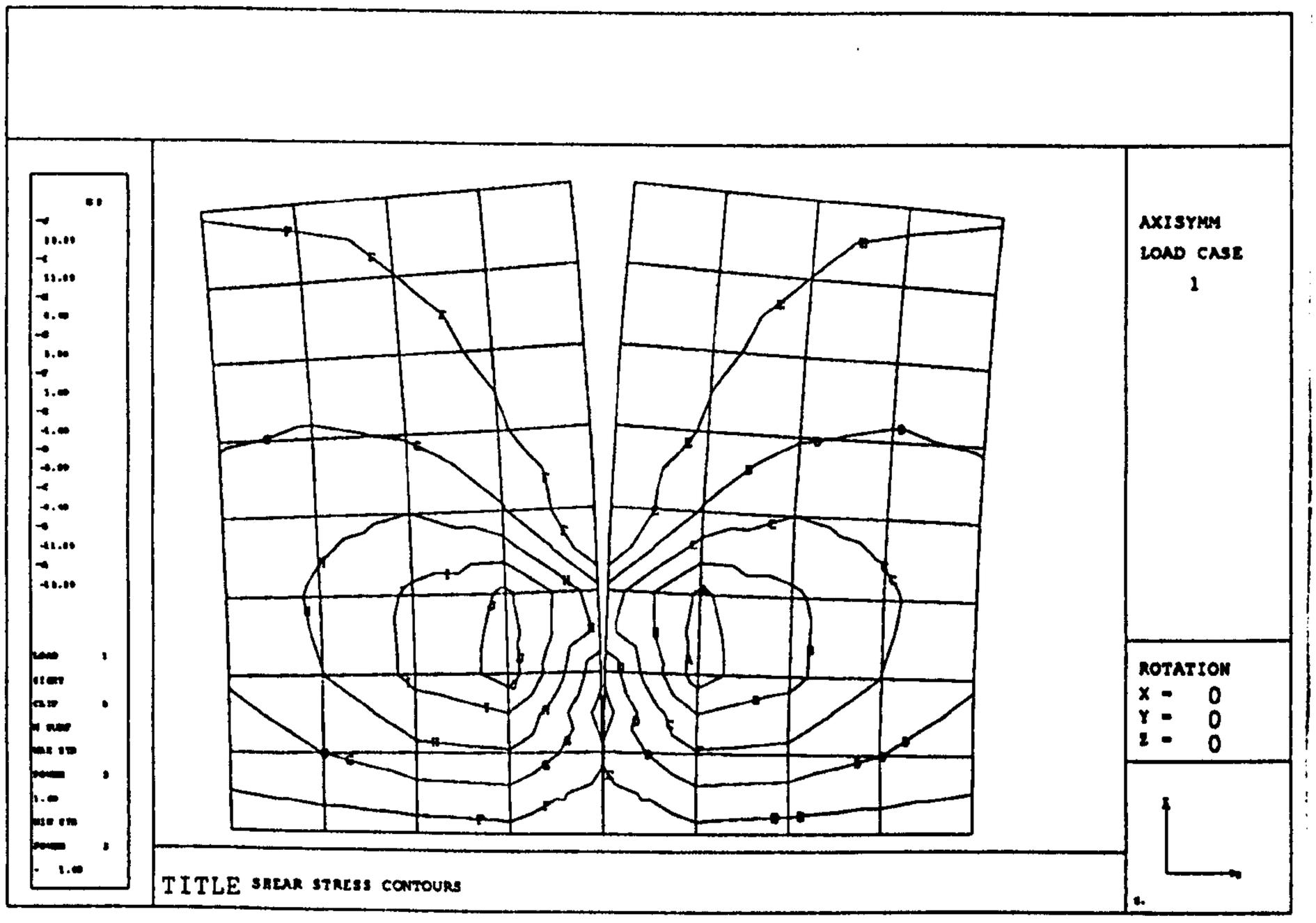

Figure 3.3 Shear stress contours

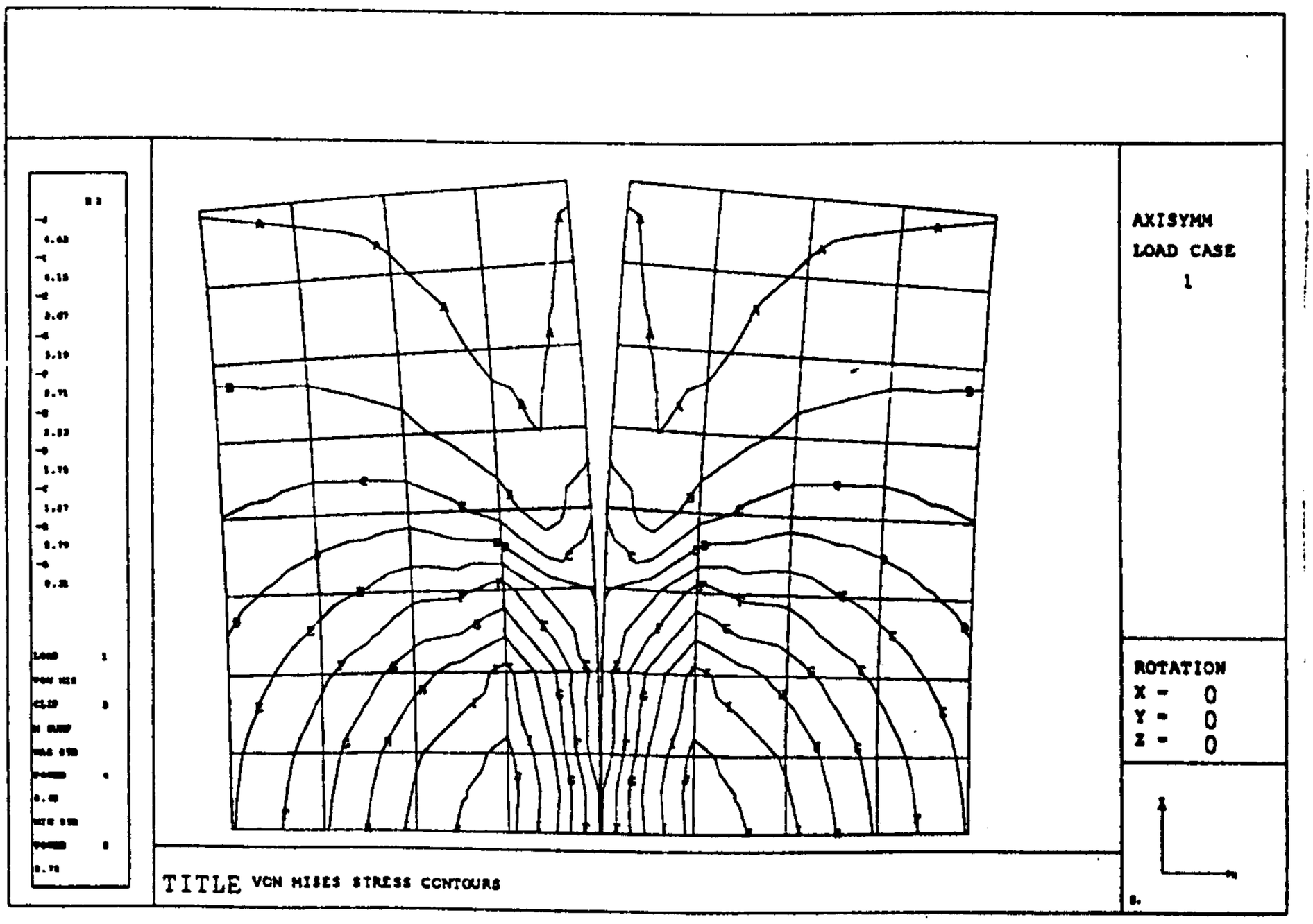

Figure 3.4 Von Mises stress contours

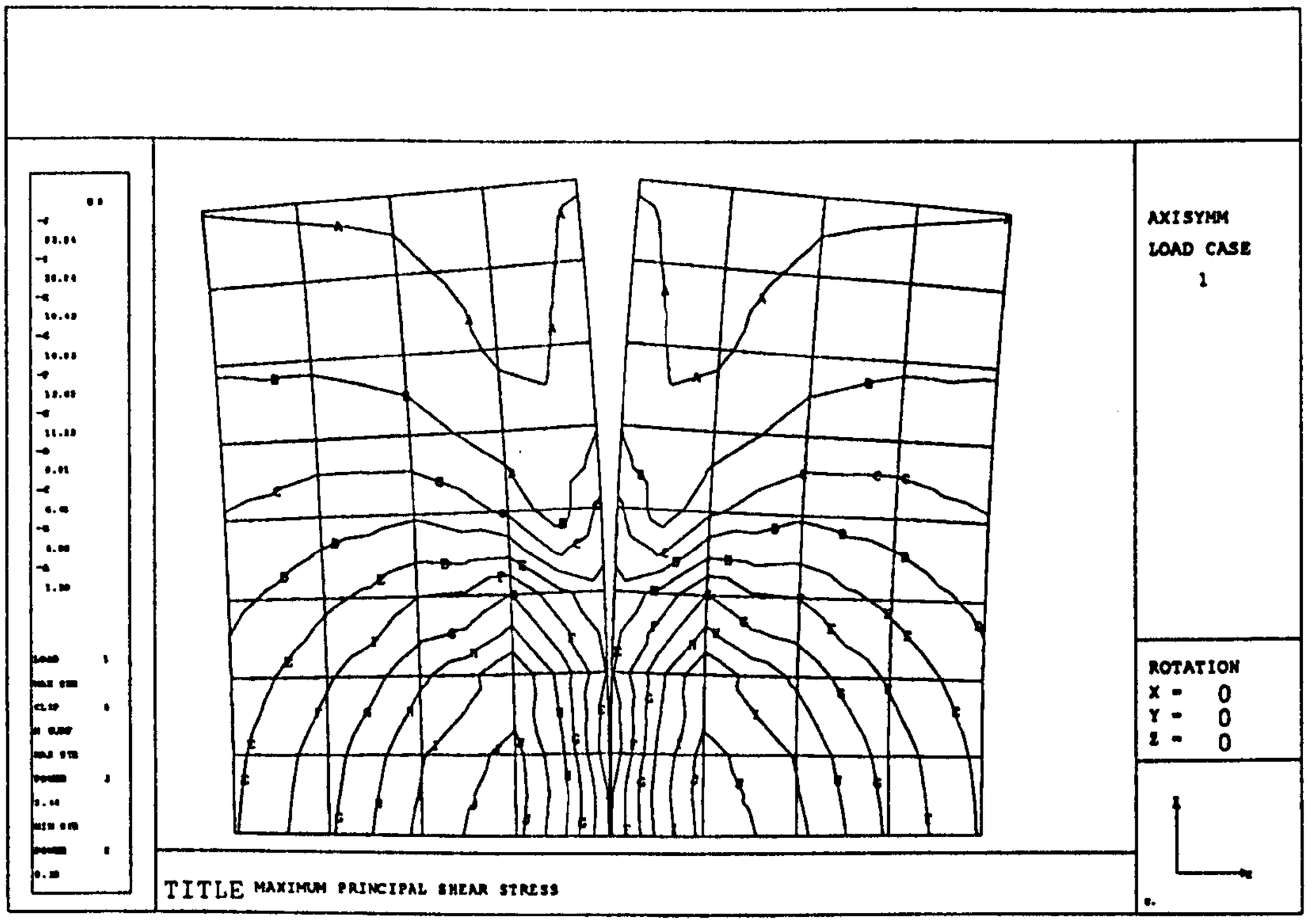

Figure 3.5 Maximum principal shear stress

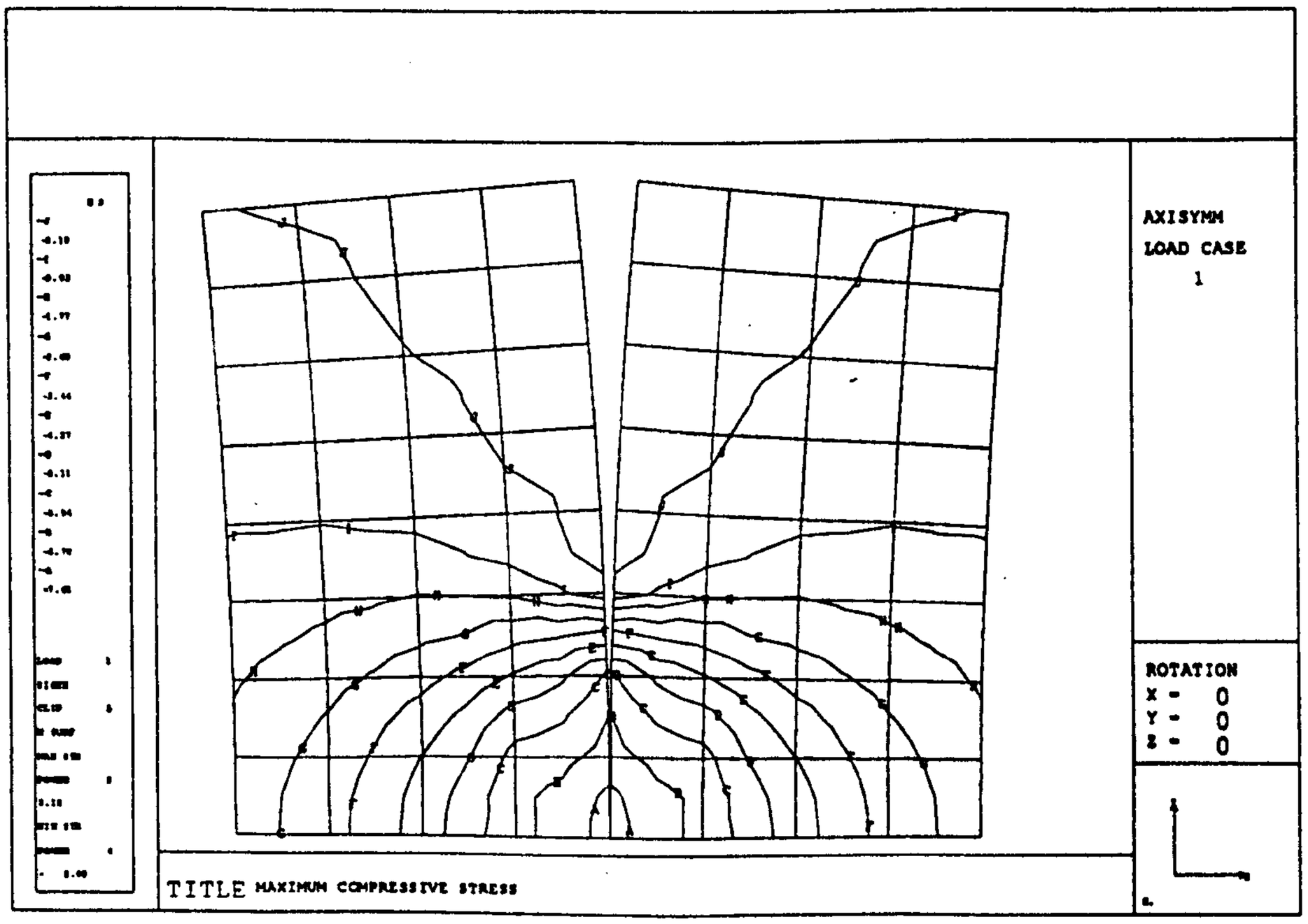

Figure 3.6 Maximum directional compressive stress

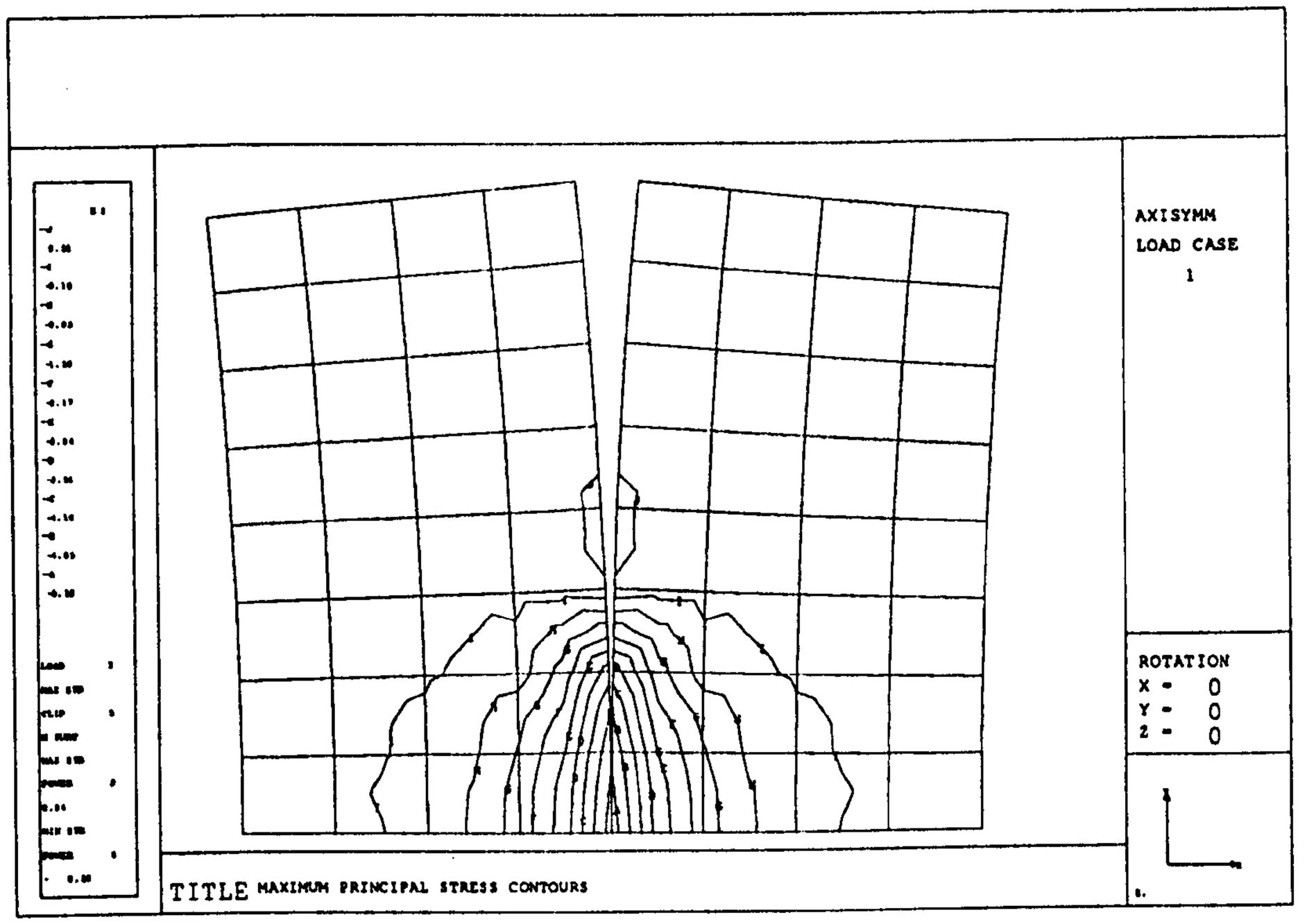

Figure 3.7 Maximum principal stress contours

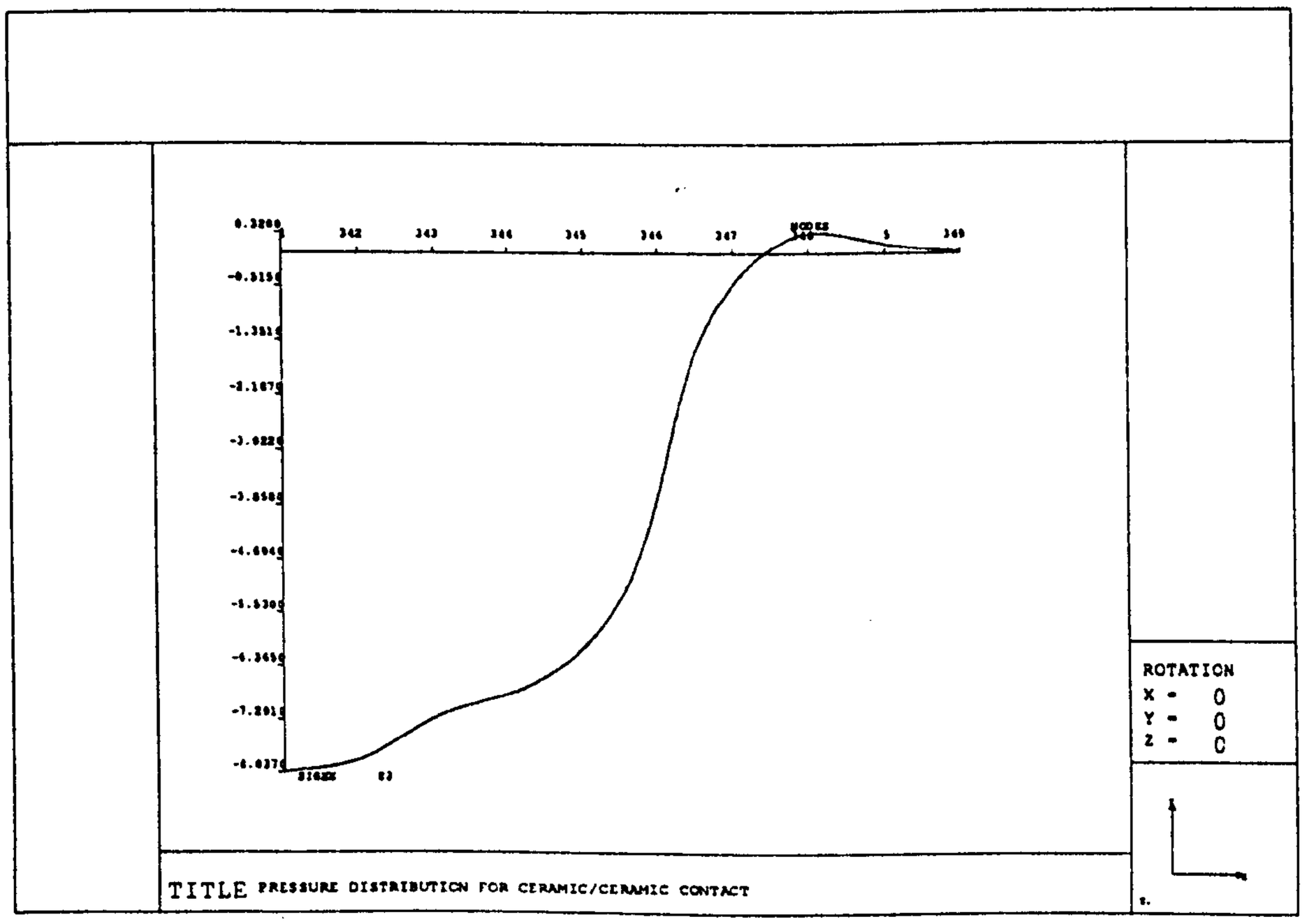

Figure 3.8 Pressure distribution on contact surfaces

3.1.4 Results Analysis of Different Contact Materials

The second objective of the model is to consider effect of materials on the stress fields and surface pressure. It is recognised that an apparent disadvantage with ceramic material is that its stiffness is higher than steel. Ceramic stresses are therefore correspondingly greater compared with steel materials for a given load. The effect of using ceramic materials on either ceramic/ceramic or ceramic/steel contacts is examined and stress analysis results compared with steel/steel contact. An identical load on ceramic/ceramic contact, considered in the previous section, is compared with other material combinations.

Steel/ceramic or hybrid contact is of particular interest to current practical bearing applications. Figure 3.9 shows maximum principal stress contours. The left ball is ceramic and shows high concentration levels compared to the steel ball shown on the right side. Stresses within the ceramic are lower than at the ceramic/ceramic contact; maximum level of 2.0 GPa compared to 2.32 GPa. High stress levels exist within the steel ball although with smaller gradient from the surface compared with the ceramic material. Pressure distribution on the contact surfaces, figure 3.10, suggests increased contact area and lower maximum pressure. Pressure profile is less intensive over a larger area compared with ceramic/ceramic contact, which is shown previously in figure 3.8.

Steel/steel contact is presented in figures 3.11 and 3.12, illustrating maximum principal shear stress and surface pressure distribution. Maximum principal stress contours show expected decreased levels with reduced gradient over a larger contact area. Maximum surface pressure is also reduced and distributed over a wider area compared with ceramic/ceramic and ceramic/steel contacts. Theoretical results for various loads and material configurations are presented in appendix three and compare reasonably with FEA results.

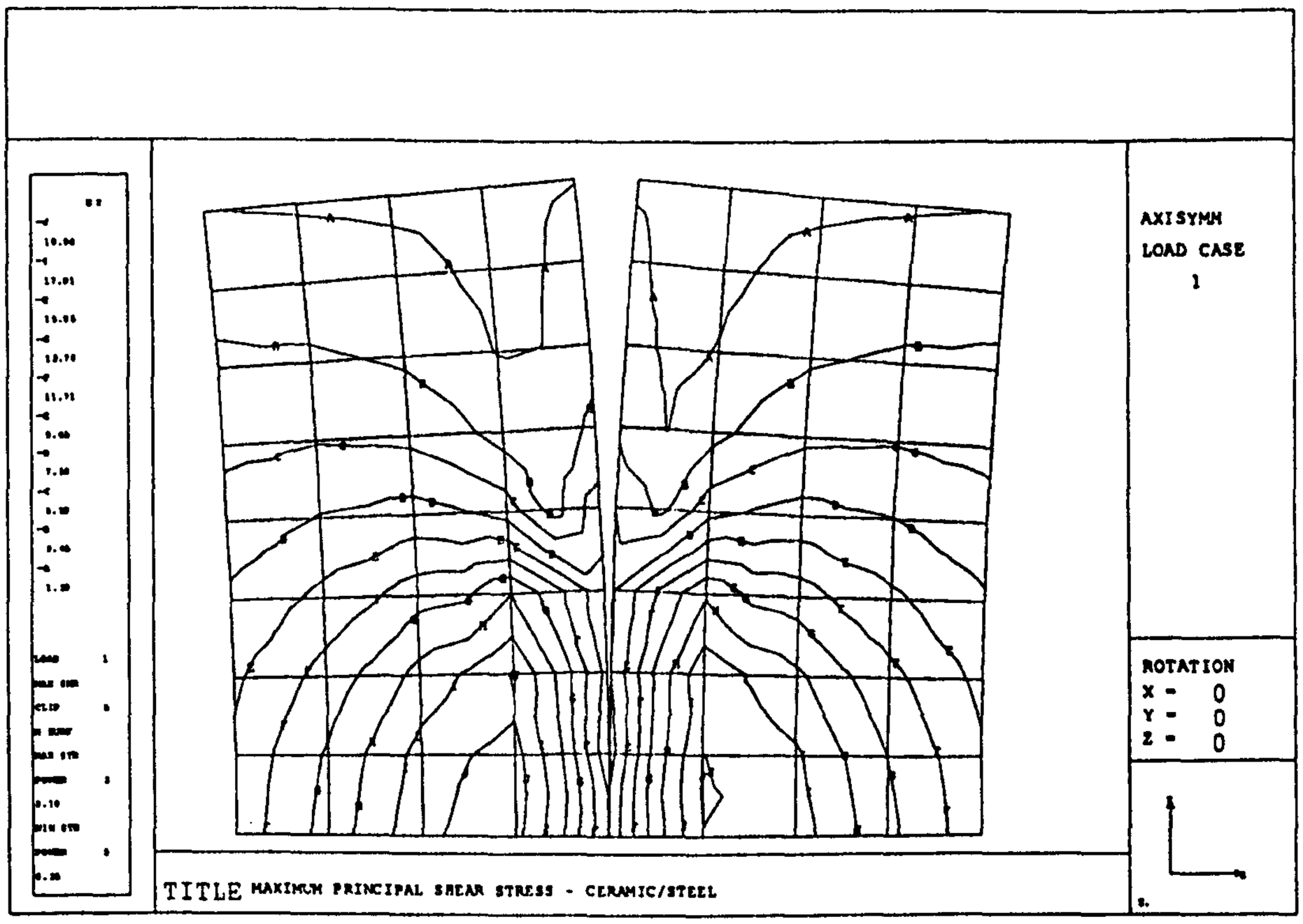

Figure 3.9 Maximum principal shear stress for ceramic/steel contact

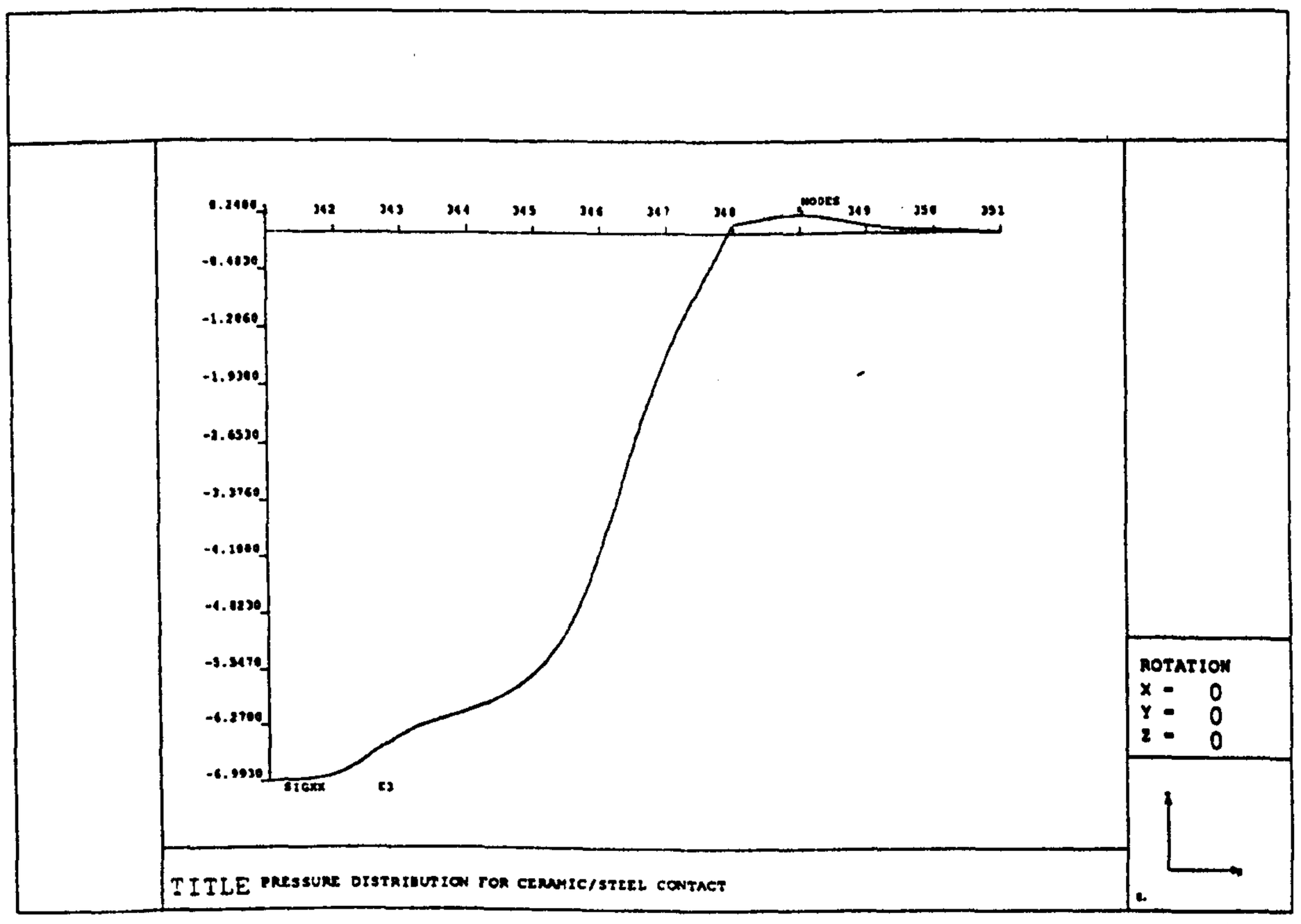

Figure 3.10 Pressure distribution for ceramic/steel contact

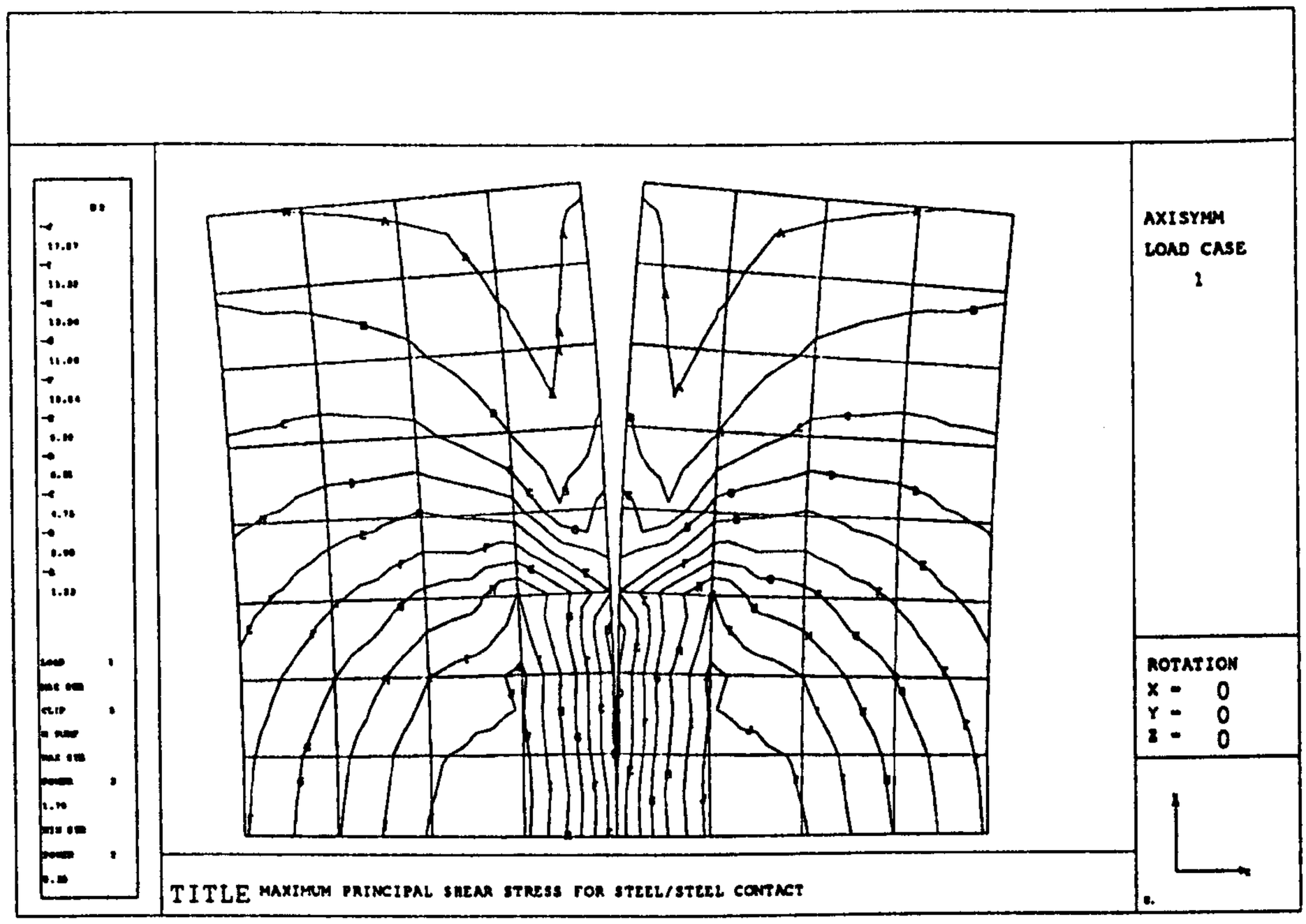

Figure 3.11 Maximum principal shear stress for steel/steel contact

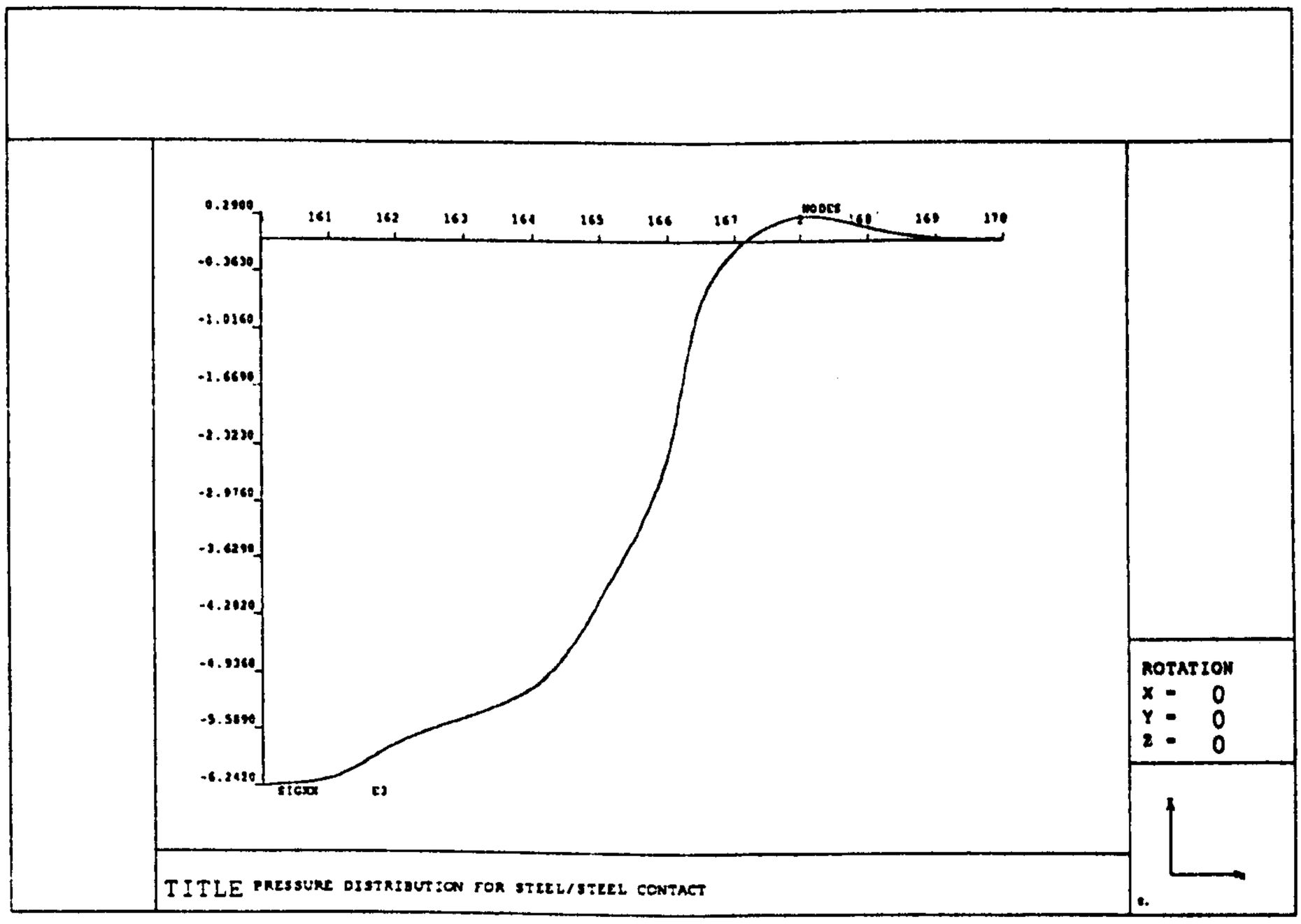

Figure 3.12 Pressure distribution for steel/steel contact

3.1.5 Results Analysis of Prescribed Displacements

The third objective of the finite element analysis is to model the contact volume only in order to perform a more detailed analysis. It is necessary only to model one contact volume as they are both identical. Displacements from the initial model, with increased mesh density, are extracted from around the contact zone and applied to the contact volume model. The displacements are interpolated where necessary due to the increase of nodal positions. This model requires no restraining or applied load along the boundary as the prescribed displacements provide strain and hence calculate stress.

Results from the contact volume model are shown in figure 3.13. Maximum principal shear stress pattern is shown to be similar to the initial model. The maximum value is 2.25 GPa and compares well with 2.32 GPa from previous results. This model using prescribed displacements can therefore be assumed as reasonable in assessing theoretical theories of fatigue failure, described in appendix three.

A preliminary fracture model is presented in figure 3.14. The effect of porosity on stress field may also be studied using the concentrated volume model. A crack is positioned at the same location and depth as the maximum principal shear stress shown in figure 3.14. The crack length is similar to the minimum detectable crack size using standard quality control procedures, described in chapter 4. This basic model using crack-tip elements shows calculated values for stress concentration factors. The advantage of this model compared with theoretical calculation is that the crack position within the stress field may be easily changed.

It can be seen that the FEA crack propagation technique can be used to predict stress intensity factors (mode 1 and 2) and show the resulting stress contours. This model is a preliminary investigation into crack tip analysis, further model development is required after extensive experimental analysis is complete. Elements near the crack tip do not show stress level due to the singularity involved in crack tip analysis by the J integral method.

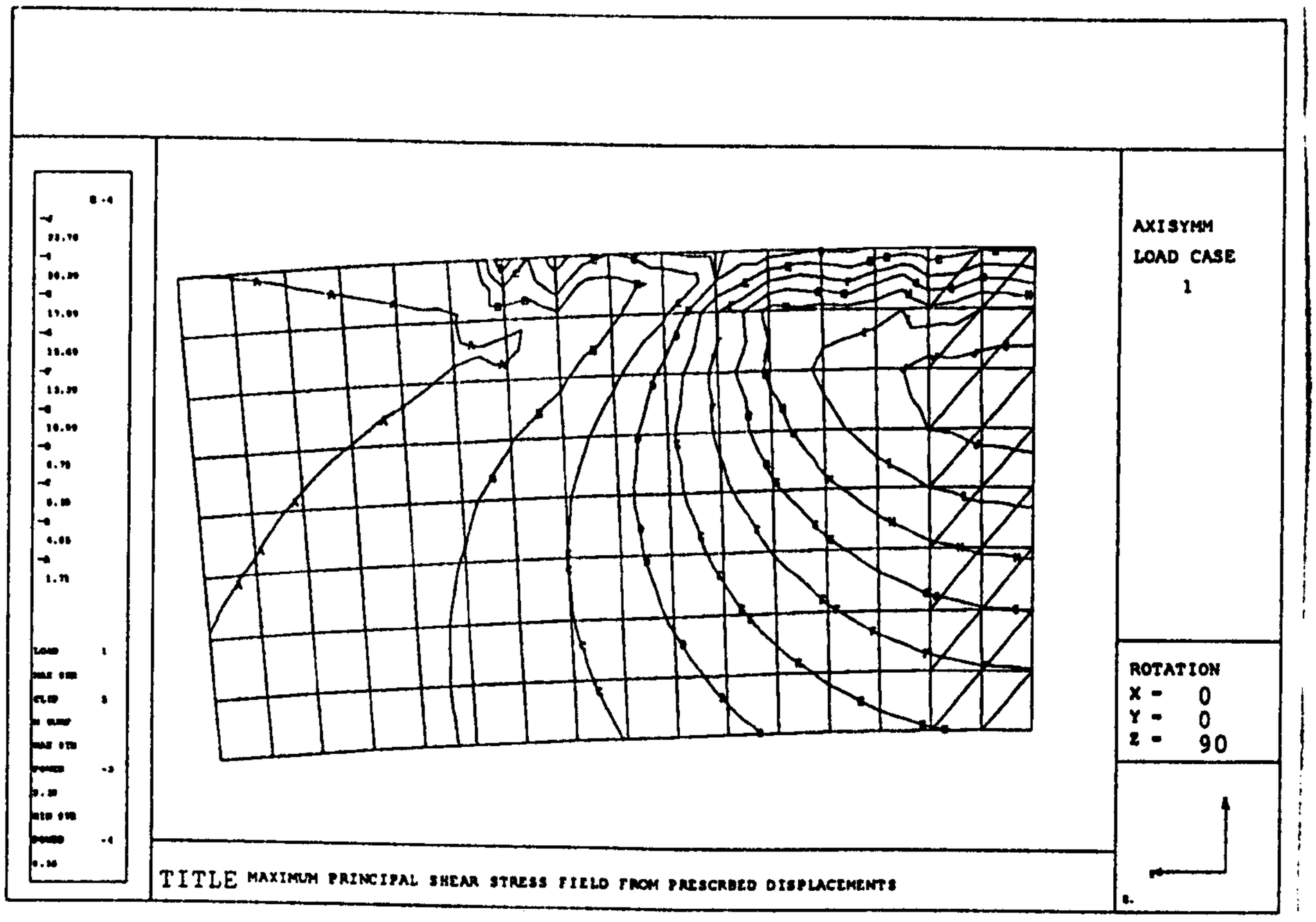

Figure 3.13 Maximum principal shear stress from prescribed displacements

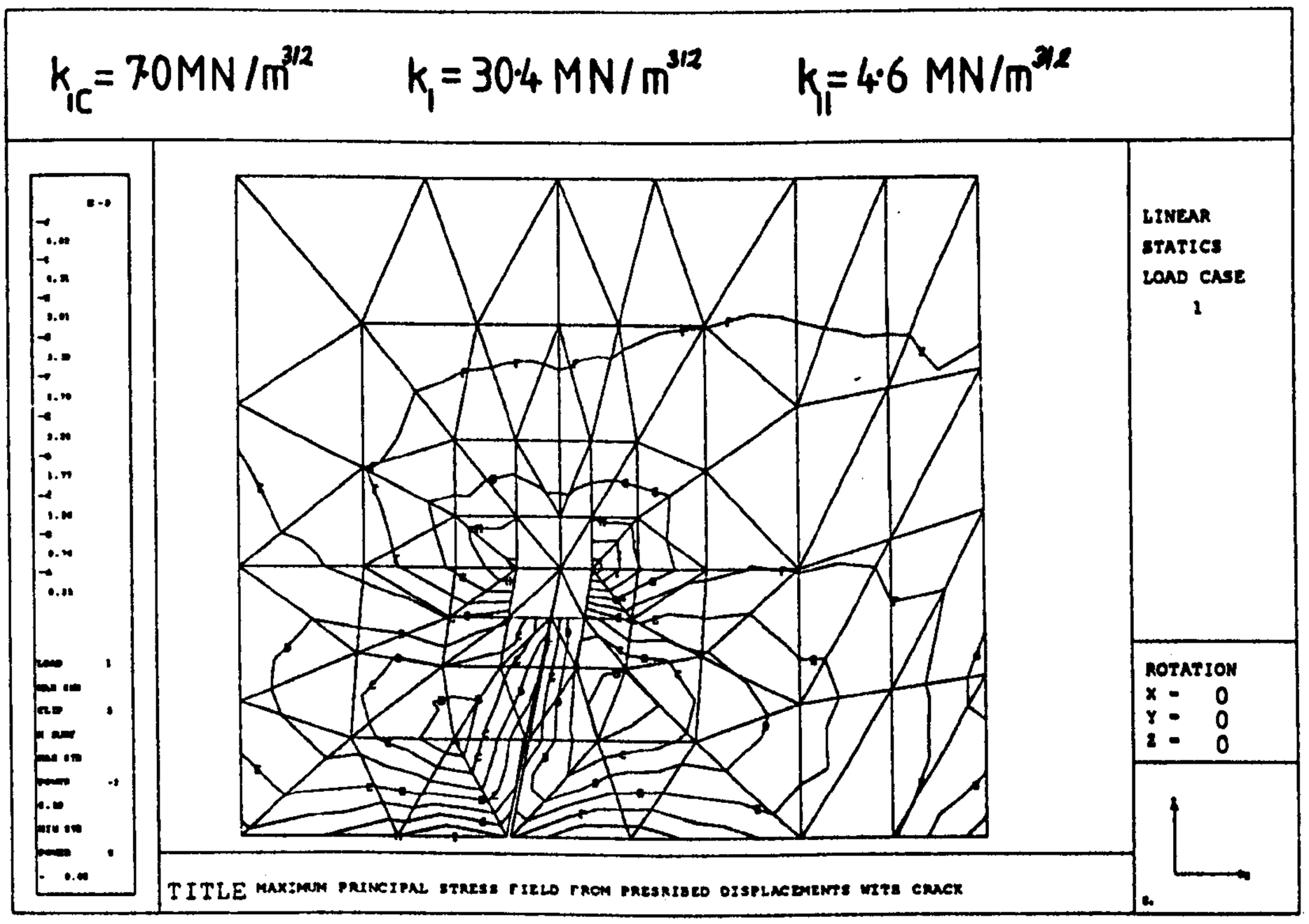

Figure 3.14 Maximum principal shear stress contours with crack

3.2 Kinematic Analysis

3.2.1 Background and Objectives

Kinematic analysis of lubricated rolling contacts is important for establishing mechanisms of fatigue failure. Lubrication regime is strongly related to the relative motion between the upper and lower balls. The lubrication regime has a strong influence on rolling contact fatigue failure modes and time to failure. Kinematics also has an influence on heat generated by material hysteresis, this as a function of frequency, which also influences fatigue failure. Slip or relative motion either by material deformation or general motion within contact surface has great influence on contact stress, lubricant traction, and heat generation. Ball-bearing kinematics has had much attention due to the tribological effects, notably Todd (1987), Harris (1971), Hirano (1965) and (1961).

The objective of the kinematic analysis on the four-ball machine is to establish geometric contact angles, calculate linear and angle velocity motion, describe lower-ball displacement and calculate slip due to material deformation. Experimental visualisation of relative velocity and displacement is presented concurrently with theoretical analysis.

3.2.2 Geometric Relationships

Geometric relationships are important as ball diameters and cup dimensions affect the kinematics and contact load. Figure 3.15 shows the geometric arrangement; angle 'alpha' is the basic contact angle assuming no dynamic effect, and is a function of ball and cup dimensions. Trigonometric relationships may be used to find this angle:

$$\alpha = \arcsin\left(\frac{(r_e - r_c)}{(2r_l + r_u - r_c)}\right) \tag{3.2}$$

Angle 'beta' is the angle between the lower-ball centroid and the vertical axis and is a function of upper and lower ball dimensions and the contact angle 'alpha'. Equation 3.3 is derived from trigonometric relationships:

$$\beta = \arctan\left(\frac{\sin(90-\alpha)}{\frac{r_1}{(r_u+r_1)\sin\alpha} - \cos(90-\alpha)}\right) \tag{3.3}$$

The final angle, 'gamma' is a function of angles 'alpha' and 'beta', and is given by equation 3.4. This is the angle between the lower-ball centroid and the cup tangent on the vertical upper-ball axis.

$$\gamma = 90-(\alpha+\beta) \tag{3.4}$$

All three contact angles are calculated and shown in appendix five for a standard experiment.

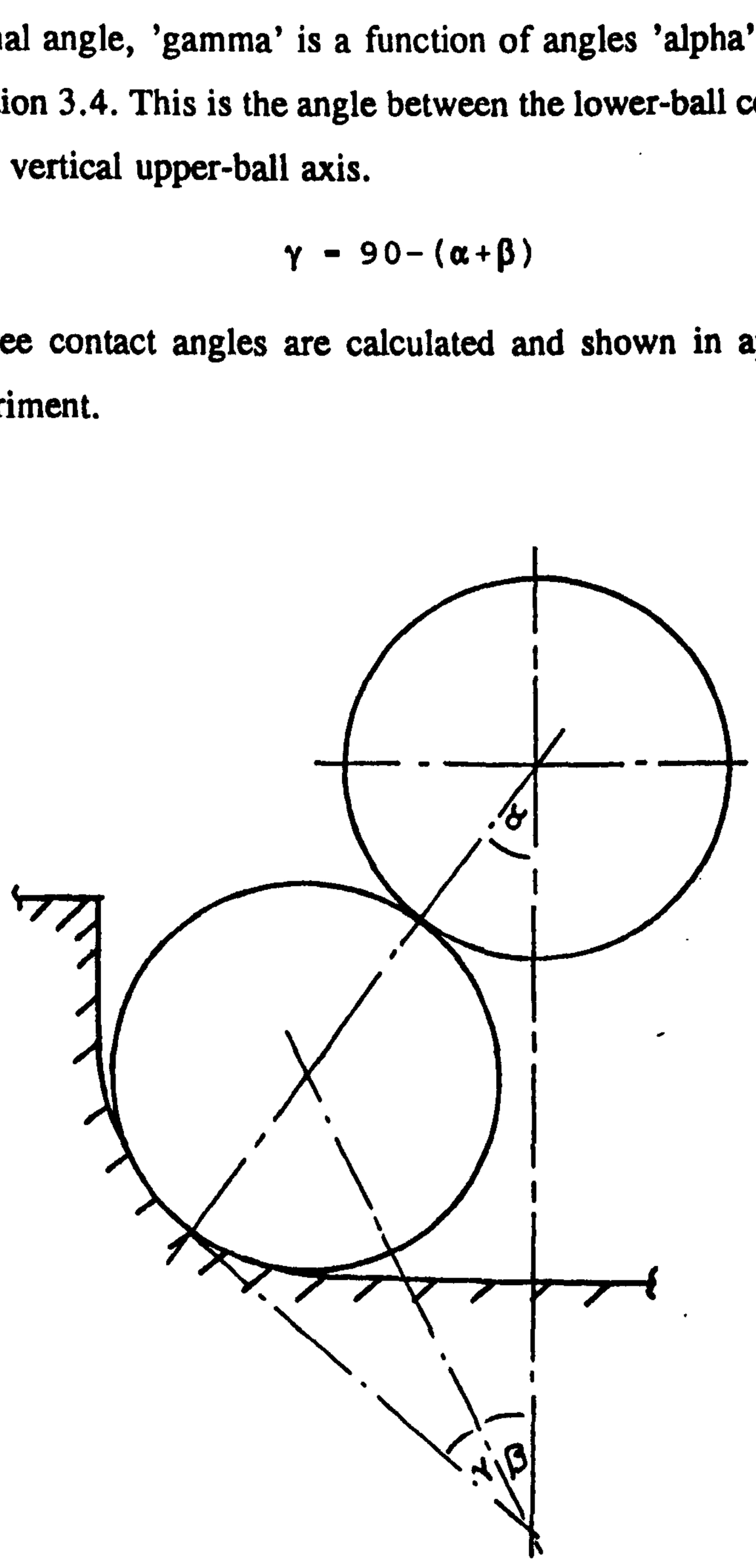

Figure 3.15 Upper and lower ball geometric relationship

3.2.3 Ball Velocity

Upper and lower ball linear and angular velocity is analyzed considering instantaneous motion. The upper ball drives the three lower balls around a steel cup (figure 3.16). Linear and angular velocity for upper ball may be established from machine spindle velocity and contact angle, equations 3.5 and 3.6, as upper-ball is fixed to the machine spindle directly.

Lower-ball motion is complicated as cup dimensions affect rotation, this motion is described by two components, rotation about spindle axis (planetary) and rotation about lower-ball axis (orbiting). By considering the instantaneous velocity for rolling contact, the velocity at the upper to lower ball interface is known. The velocity at the lower-ball to cup interface is zero and hence the velocity at the lower-ball centroid is half the former velocity. Lower-ball angular velocity about the vertical axis may thus be formulated. Upper-ball to lower-ball linear velocity about the vertical axis may also be formulated, equations (3.7) and (3.8). If no relative motion between upper and lower-ball is assumed then the sum of lower-ball velocities must equal that of the upper-ball, (3.9). Lower-ball orbiting linear and angular velocity may then be found from equilibrium at the ball interface, (3.10) and (3.11).

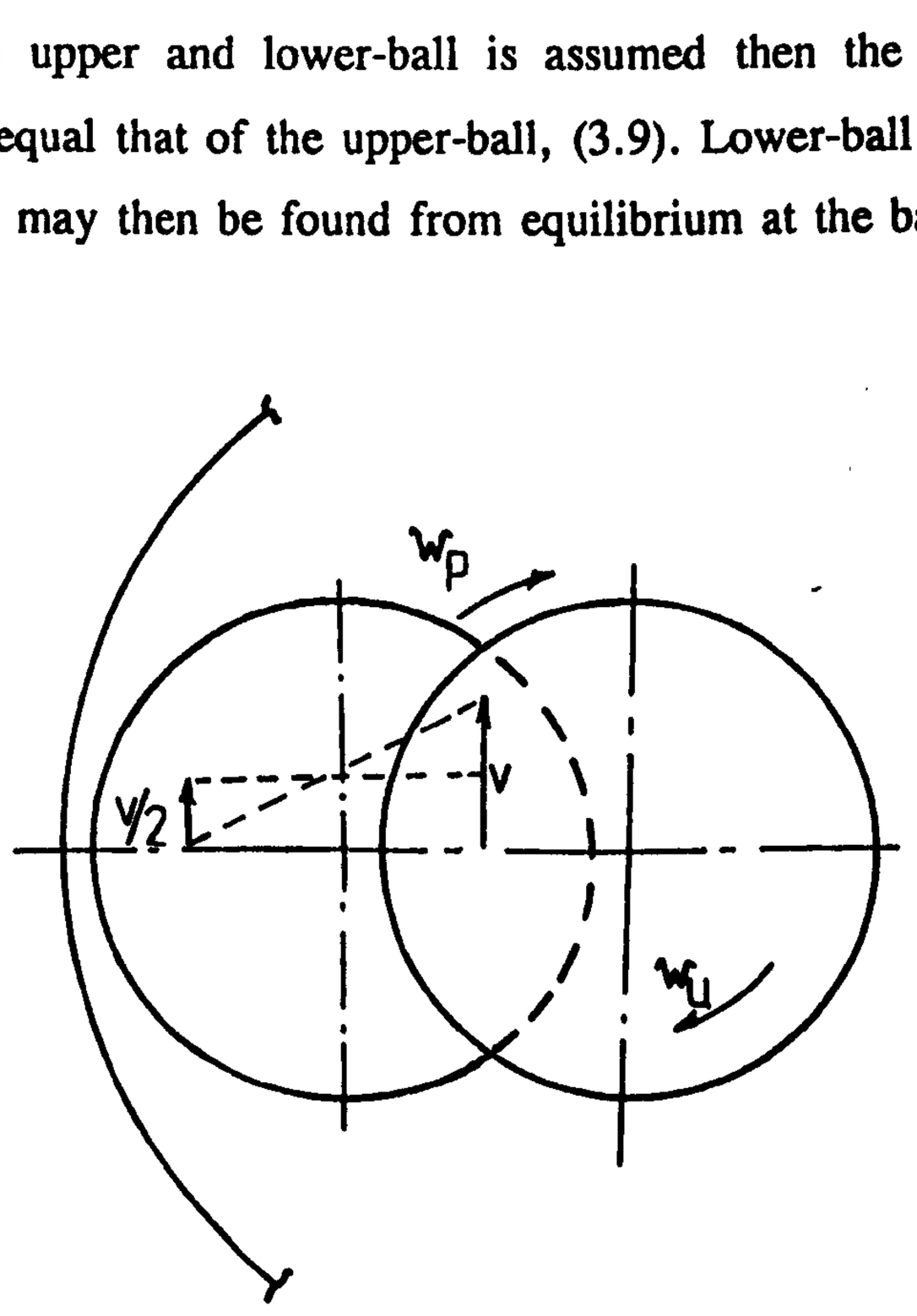

Figure 3.16 Instantaneous velocity

(i) Upper-ball:

$$v=\omega_u r_u \sin(\alpha) \tag{3.5}$$

$$\omega_u = R.P.M.\ \frac{2\pi}{60} \tag{3.6}$$

(ii) Lower-ball: *a) Motion about upper-ball vertical axis*

$$v_p=\frac{\omega_u r_u^2 \sin(\alpha)}{2(r_u+r_l)} \tag{3.7}$$

$$\omega_p=\frac{\omega_u r_u}{2(r_u+r_l)} \tag{3.8}$$

b) Motion about angle 'beta'

$$v_s=v-v_p \tag{3.9}$$

$$v_s= \omega_u r_u \sin(\alpha)\left(1-\frac{r_u}{2(r_u+r_l)}\right) \tag{3.10}$$

$$\omega_s=\frac{\omega_u r_u \sin(\alpha)}{r_l \sin(\gamma)}\left(1-\frac{r_u}{2(r_u+r_l)}\right) \tag{3.11}$$

Calculations of linear and angular velocities are shown in appendix five for typical machine spindle speed. The equations are also used to find average velocity required for lubrication calculations appendix four and five. Stress cycle factor (stress cycles received by upper ball) is a function of relative angular velocities and hence ball diameters, calculations are also shown in appendix five. The three motions of upper and lower balls, which are described by the previous calculations are illustrated in figure 3.17.

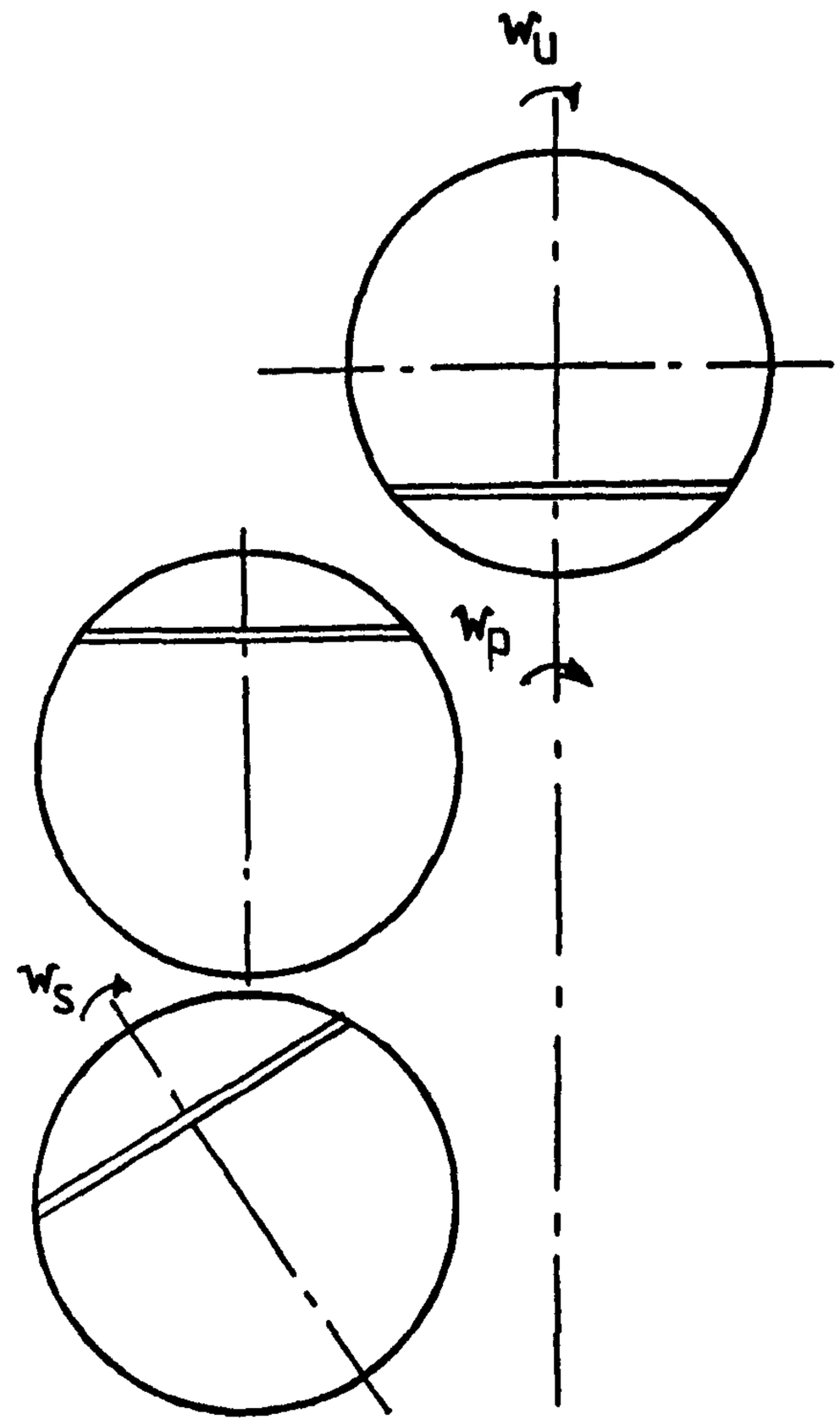

(a) Upper ball

(b) Lower ball (vertical axis)

(c) Lower ball (orbit)

Figure 3.17 Upper and lower ball velocity

3.2.4 Ball Displacement

Displacement of ball motion is analyzed to understand frequency of lower ball stress cycles. Upper-ball displacement may be easily calculated by summation of angular velocity over a suitable time step. Lower ball displacement is more complicated and may be described as the summation of combined planetary and orbiting angular velocity over suitable time step, equation 3.12.

An analytical solution for lower-ball displacement may be obtained by considering that a displacement vector must always satisfy the surface equation of a sphere. The displacements from planetary and orbiting motions may be considered separately then coupled together after each time increment. At each time increment the new coupled position vector is found on the ball surface. The next position

vector may be found from iterating the calculation from the new position. The results of a computer program which solves equation (3.12) numerically over a suitable time increment are shown in, figure 3.18.

$$[\theta_p+\theta_s]\Big|_{\theta_1}^{\theta_2} = \int_{t_1}^{t_2} \frac{\omega_u r_u}{2(r_u r_1)} + \frac{\omega_u r_u \sin(\alpha)}{r_1 \cos(\gamma)} \left(1-\frac{r_u}{2(r_u+r_1)}\right) dt \quad (3.12)$$

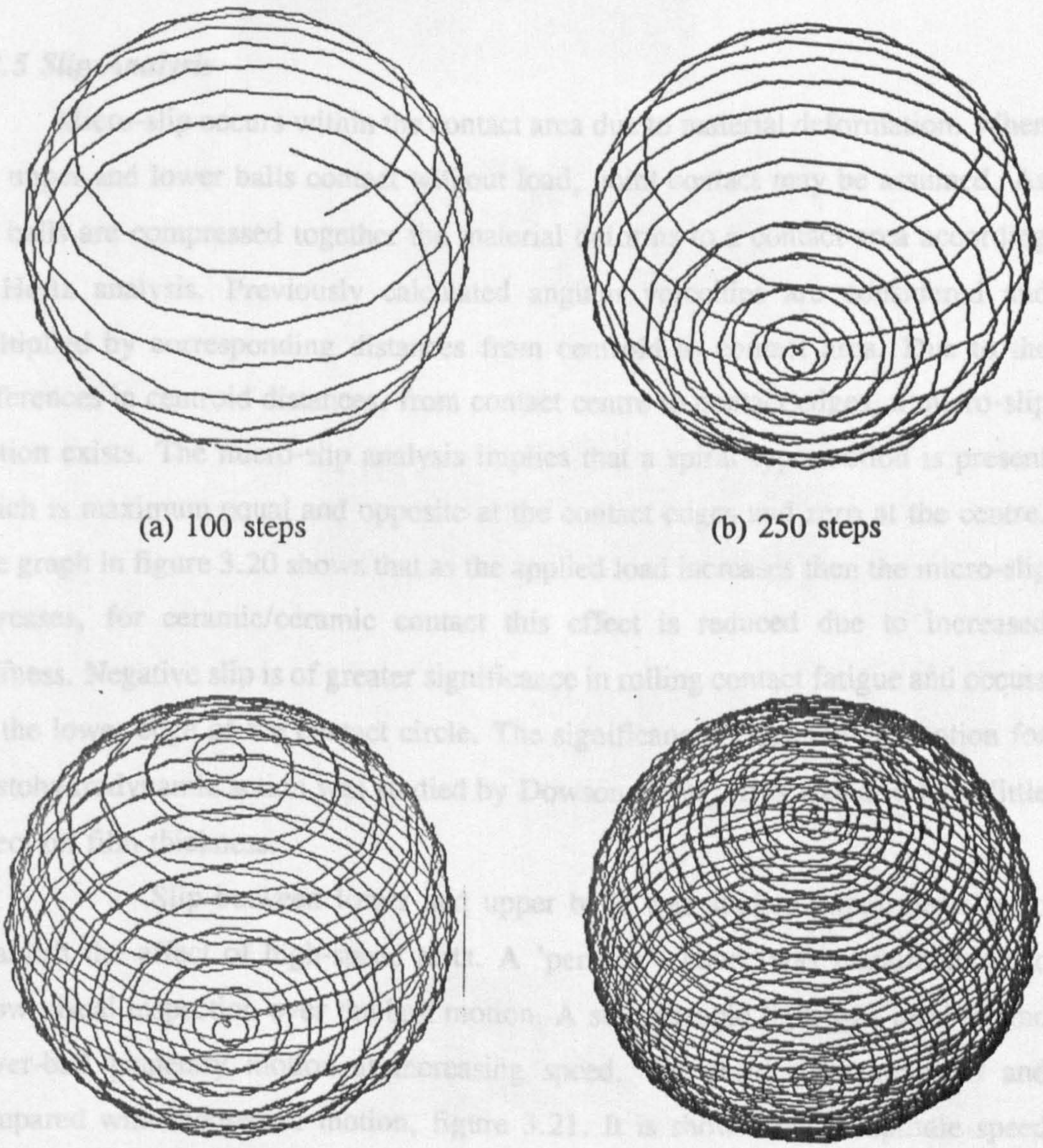

(a) 100 steps

(b) 250 steps

(c) 500 steps

(d) 1000 steps

Figure 3.18 Lower ball displacement (time interval 0.5 ms)

Lower-ball displacement was also studied experimentally by covering steel balls with a thin film of 'engineers blue'. A light load was applied to the assembly and the machine speed is set at 200, 2000, and 10,000 RPM. A stroboscopic lamp was used to view the motion. The results obtained are shown in figure 3.19. It can be seen than the experimental information contradicts the analytical model. Also it can be seen that the lower balls at 200 RPM do rotate in a manner that the entire ball surface passes through the contact zone. As the machine spindle speed increases the lower balls are held to a single rotating position. The experimental results imply that centrifugal effects may have influence on contact lower-ball displacement.

3.2.5 Slip Analysis

Micro-slip occurs within the contact area due to material deformation. When the upper and lower balls contact without load, point contact may be assumed. As the balls are compressed together the material deforms to a contact area according to Hertz analysis. Previously calculated angular velocities are considered and multiplied by corresponding distances from centroid to contact area. Due to the differences in centroid distances, from contact centre to contact edges, a micro-slip motion exists. The micro-slip analysis implies that a spiral type motion is present which is maximum equal and opposite at the contact edges and zero at the centre. The graph in figure 3.20 shows that as the applied load increases then the micro-slip increases, for ceramic/ceramic contact this effect is reduced due to increased stiffness. Negative slip is of greater significance in rolling contact fatigue and occurs on the lower edge of the contact circle. The significance of spiral type motion for elastohydrodynamic action was studied by Dowson (1991). It is found to have little effect on film thickness.

Slip between lower and upper balls was studied experimentally to establish the effect of high-speed tests. A 'perspex' cover was manufactured to allow visual inspection over the ball motion. A stroboscopic light was used to find lower-ball planetary motion at increasing speed. The results are analyzed and compared with theoretical motion, figure 3.21. It is shown that as spindle speed increases from zero to 10,000 RPM the lower ball slip increases to three percent.

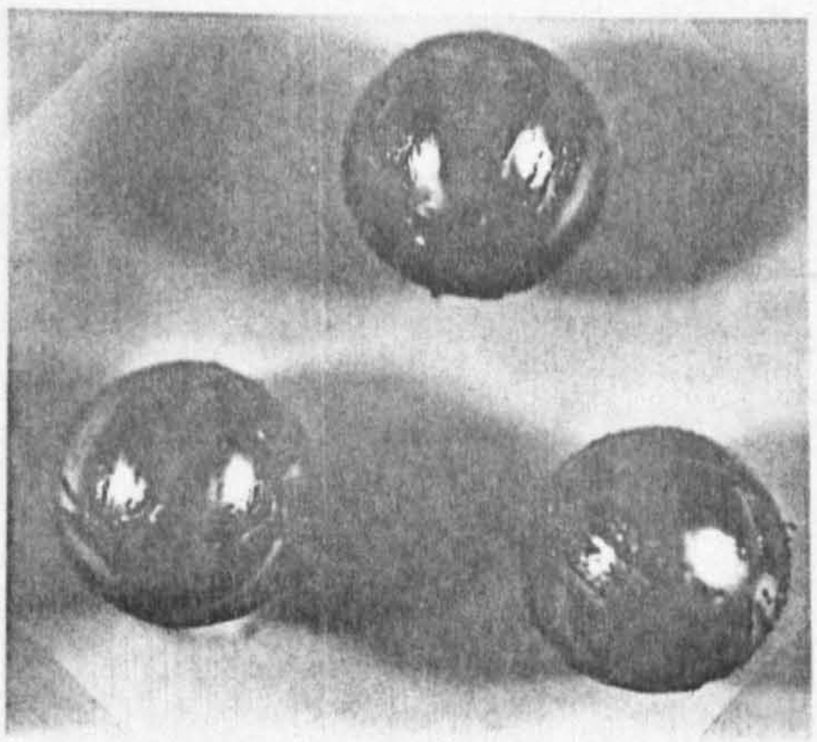

(a) 200 r.p.m.

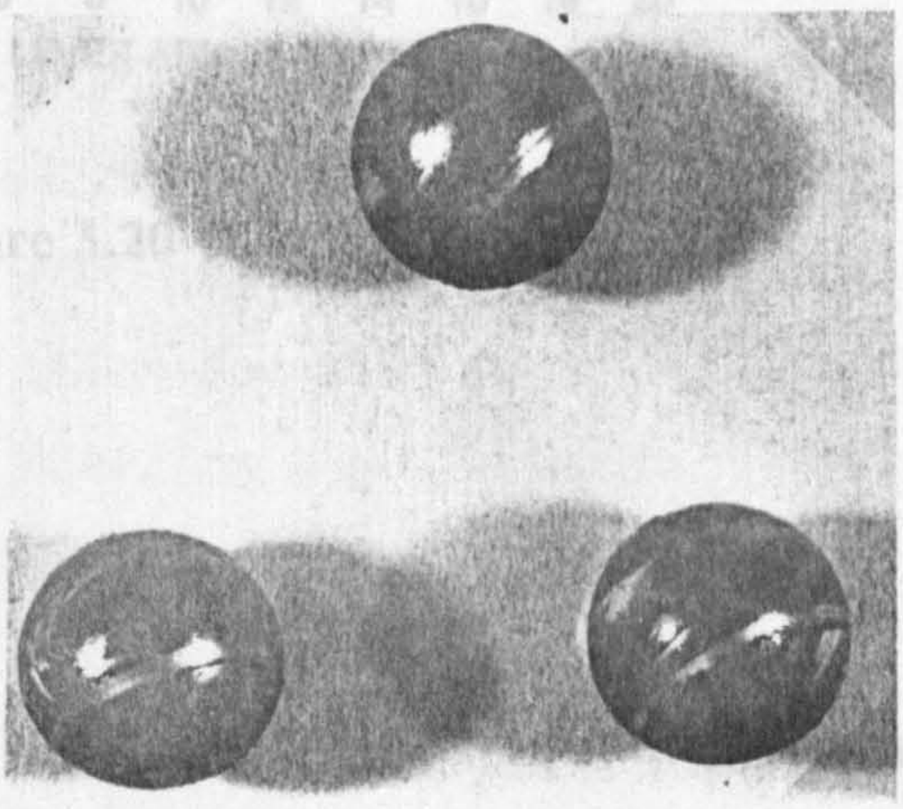

(b) 2,000 r.p.m.

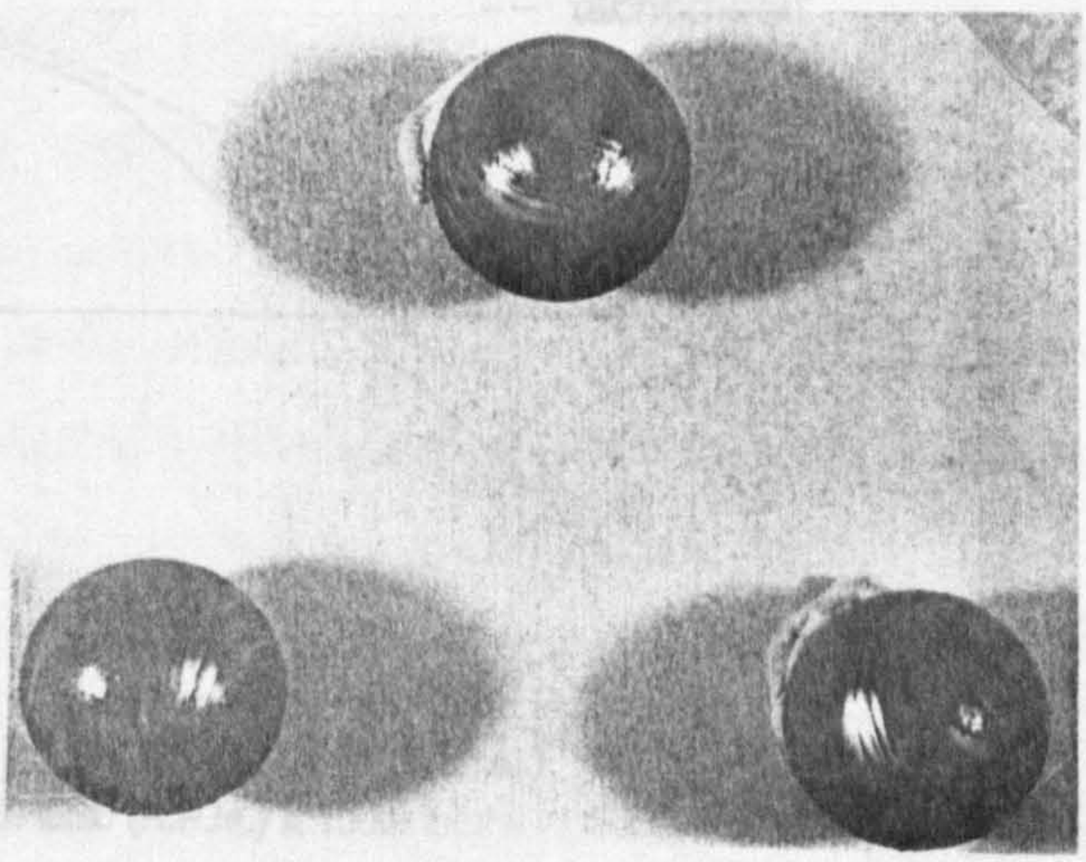

(c) 10,000 r.p.m.

Figure 3.19 Experimental contact path analysis

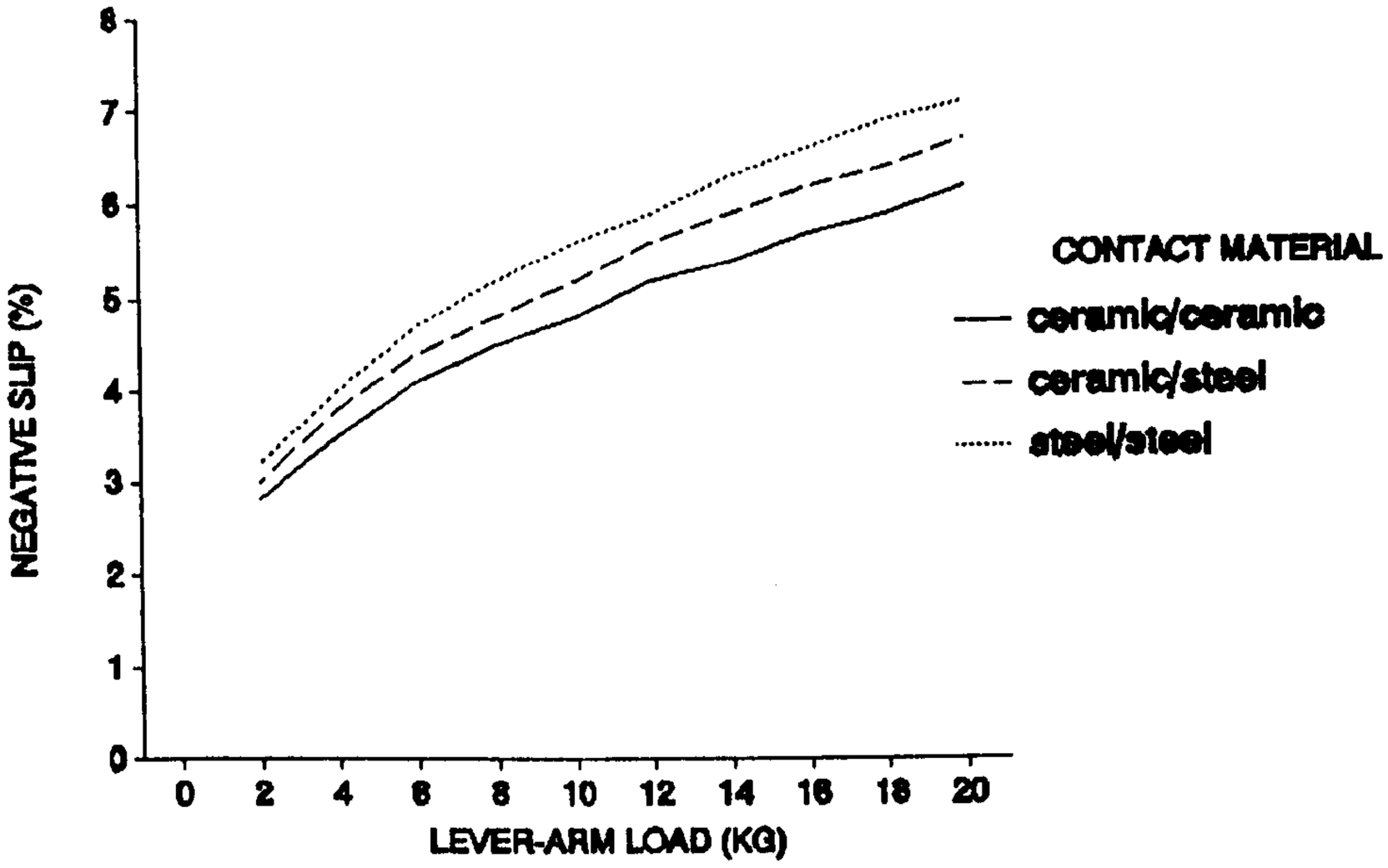

Figure 3.20 Theoretical contact slip

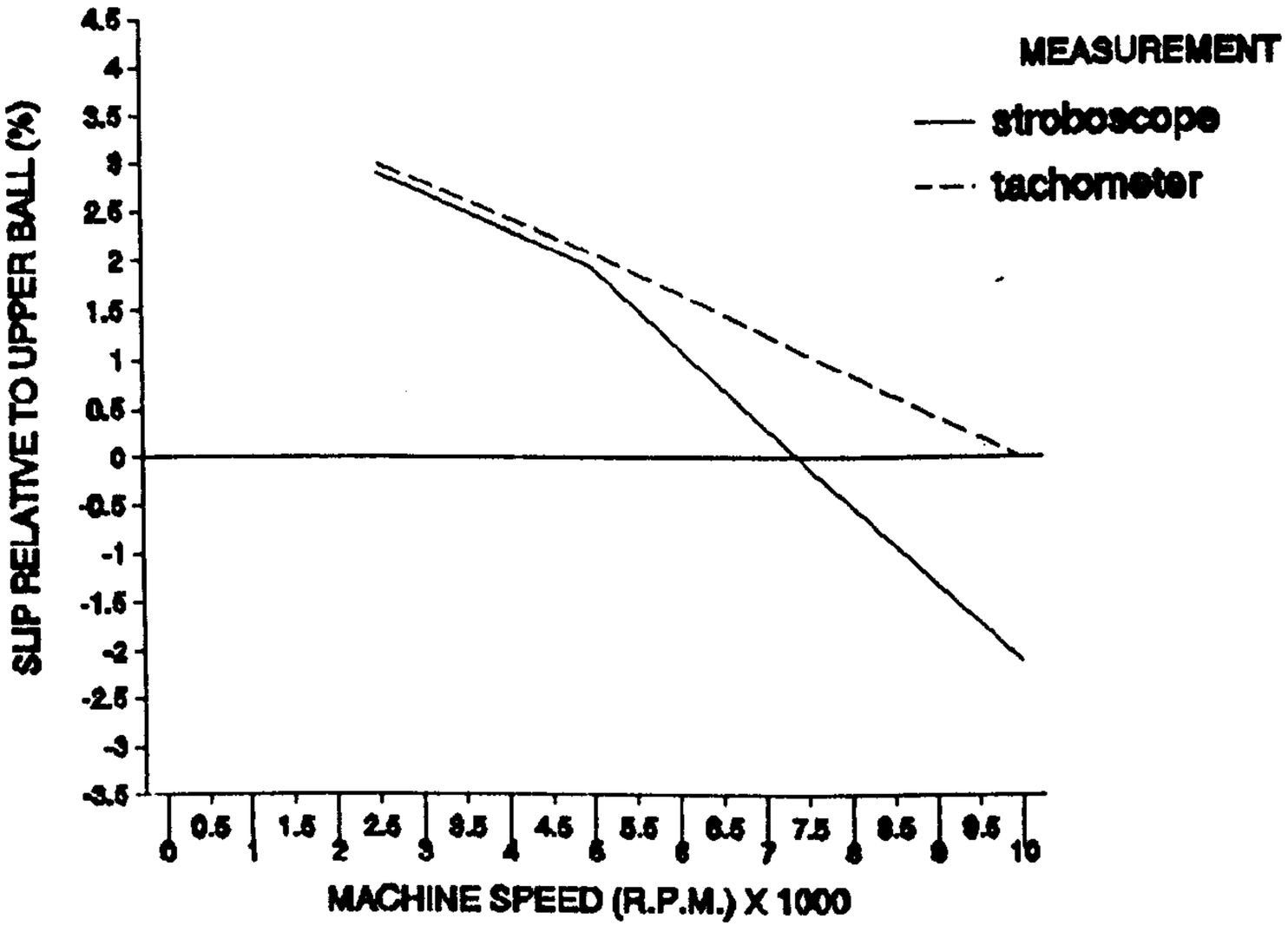

Figure 3.21 Visual slip analysis

Chapter 4
EXPERIMENT SPECIFICATIONS

This chapter presents specifications related to experimental research. Ceramic test materials are described with regard to manufacture, surface preparation and procedure for inducing artificial surface cracks. Test preparation, procedure, verification and lubricants are described. Post test surface analysis, using scanning electron microscopy and X-ray residual stress measurement, is also described.

4.1 Test Materials

4.1.1 Ball Manufacture

Silicon nitride and sialon ceramic materials are manufactured from fine powders. The (fine) powder used for silicon nitride manufacture is produced by a variety of techniques, such as direct nitridation, vapour phase reaction and carbothermal reduction. Powder particle size is of particular interest from an engineering view-point due to its influence on mechanical properties. Good quality silicon nitride powder is typically less than 1 μm in size.

Silicon-nitride material is (produced from powder) densified by liquid phase sintering. The degree of densification has a large influence on mechanical properties; maximisation is achieved through the use of sintering compounds. Sintering additive also has an influence on mechanical properties, such as hardness and toughness. Increasing additive volume, reduces hardness and increases toughness. Choice of sintering additive is, therefore, complex as although an additive may aid densification, it can have a counter-productive influence on material properties. In addition to the problem of choosing correct type and amount of sintering additive the technique will influence densification, material structure, amount of required additive and hence mechanical properties.

Most of the silicon nitride material used for this research was manufactured by Hot Isostatic Pressing (HIP) of 'green' preformed powder. The basic additives required for this technique are magnesium and yttrium oxides. Other additives; titanium, tantalum and zirconium, may also be used to customise material

properties. Preformed 'green' ball blanks are produced by die compaction or cold isostatic pressing after blending, milling and agglomeration operations. Geometry of preformed blanks may be improved by soft machining by standard operations at this stage. Densification of ball blanks is achieved by HIP at pressures of 200-300 MPa and temperatures of 1750-1900°C. Densification of silicon nitride by HIP is preferred to other methods such as hot-pressing, gas pressure sintering and pressureless sintering, as greater control and superior quality of material properties is available.

Sialon (Silicon Aluminium Oxygen Nitrogen) material is densified at lower pressures than silicon nitride. The production of sialon by pressureless sintering reduces manufacturing costs and time whilst increasing manufacturing safety. Aluminium oxide, aluminium silicon oxynitrides, calcium oxide and yttrium oxide are sintering additives used in the formation and densification of Sialon materials.

Manufacturers may improve post-densification ball blank geometry by hard machining. Centreless form grinding or a loose diamond abrasive method of machining are methods employed to hard machine densified ceramics. Material structure is complex and unique, as each manufacturer uses different manufacturing techniques and sintering additives. General material composition may be defined as hexagonal crystal structure with covalent bonded atoms, although some ceramics are impossible to classify by this simplistic format. The stoichiometric molecular weight of silicon-nitride (Si_3N_4) is 140 g/mol with 60 to 40 percent of silicon to nitrogen.

4.1.2 Material Quality

Material quality was monitored for all tested materials to identify possible failure causes and to ensure test consistency. During ball manufacture, each procedure may influence the material quality. For this reason attention to detail at each production stage is very important for high material quality. A sample ball from each tested batch is sectioned, polished and analyzed. The polished sample is then inspected with a light microscope; various techniques are used to improve visual appearance. Illuminated light intensity, dark field and Nomarsky interference are examples of light microscope techniques. The entire sample is first scanned

under low magnification to locate any obvious local inconsistencies. A more detailed analysis of any interesting areas is then performed to find inclusions, ceramic phases, metallic phases and porosity, (a typical area is classified to compare with other materials, phases are quantified using ISO 4505 "Hardmetals - Metallographic determination of porosity and uncombined carbon").

It is difficult to section and polish ceramics due to the high hardness and moderate toughness of the material. A 'Struers' cutting machine incorporating a diamond wheel with sample rotation facility is used to section a ball. Sample feed rate is set at 0.2 millimetres per minute, the cutting wheel head is lubricated with water. Once sectioned, the sample is mounted in a thermosetting polymer cup with a steel ring to facilitate grinding. Once mounted and cooled, the sample is flattened using a rotating water lubricated diamond-resin wheel. Silicon carbide paper (500, 800 and finally 1000 grade) is used to grind and smooth the sample surface. The surface is polished by using a cloth wheel and diamond spray (6, 3 and finally 1μm). At the final polishing stage, a light microscope is required to examine the sample for scratches.

A section of silicon nitride is shown in figure 4.1. The specimen is not typical as unusually high porosity exists, shown as the black areas on the section. The worst area of porosity is in the region of 10 μm in length and represents a very poor quality of material. Typical test material quality has zero porosity with fine ceramic or metallic phases.

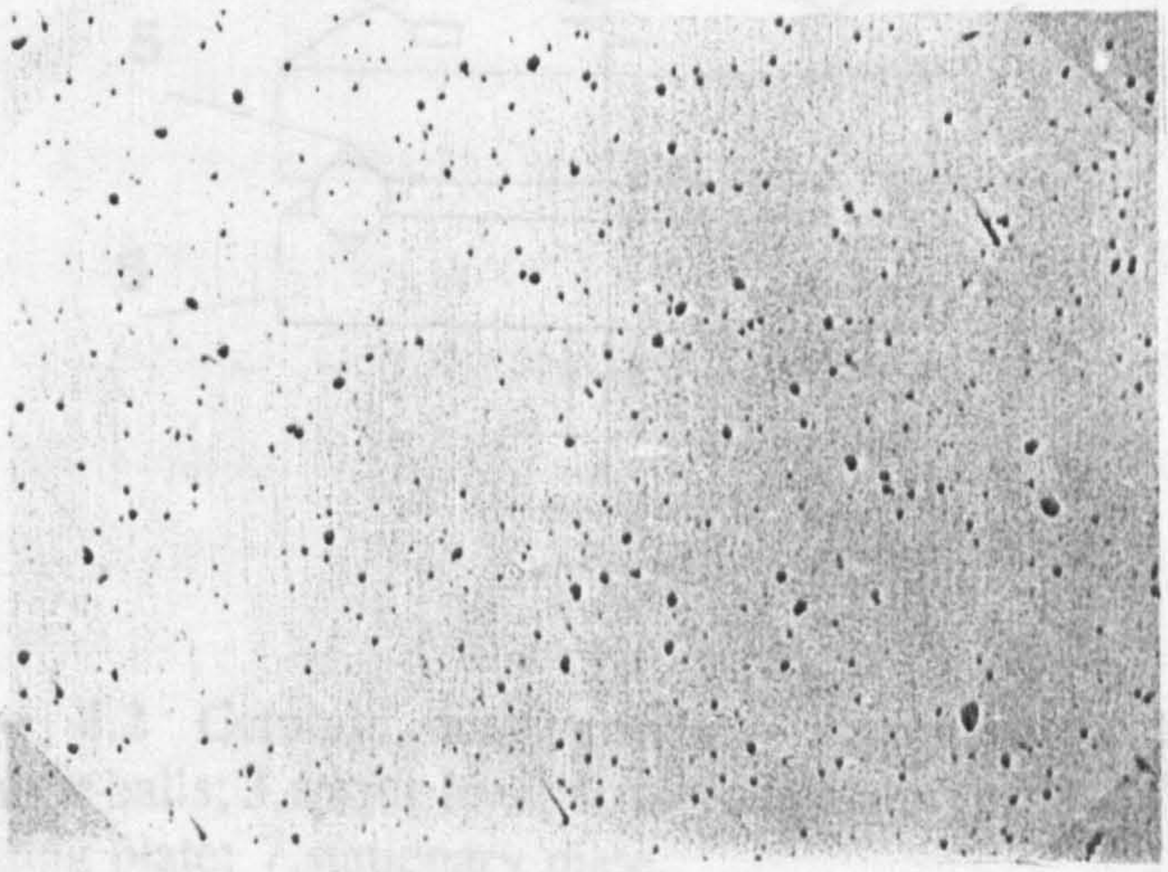

Figure 4.1 Material quality inspection (x115)

4.1.3 Ball Finishing

Densified ceramic ball blanks were received from manufacturers with typically 0.5 mm stock allowance and rough ground surfaces of 0.15 μm Ra (oversized to 13.23 mm in diameter). In preparation for fatigue tests, ball blanks were ground and polished to ISO standard geometry and surface roughness. Figure 4.2, illustrates the apparatus used for ball finishing. The lower rotating plate of the ball grinding apparatus is driven by an electric motor at low speed. An upper stationary plate is loaded by an adjustable spring. Both the upper and lower mild steel plates have machined 'V'- grooves to locate the ceramic balls. A micro-switch safety device stops the drive-motor in the event of high machine vibration. Ball on groove contact areas are splash lubricated, by a micro-pump. The machine may be adjusted to stop after a time period or set number of revolutions. Diamond abrasive paste is needed due to the high hardness of silicon nitride. It is evenly distributed around the ceramic balls before the machine is started. The grade and amount of diamond paste is varied depending on wear rate and surface quality required. Initially, coarse diamond abrasive (40 μm) is used until the ceramic balls are close to required size. Then the abrasive grade is then successively reduced; 25, 10, 5 and 1 μm, to produce a fine finish.

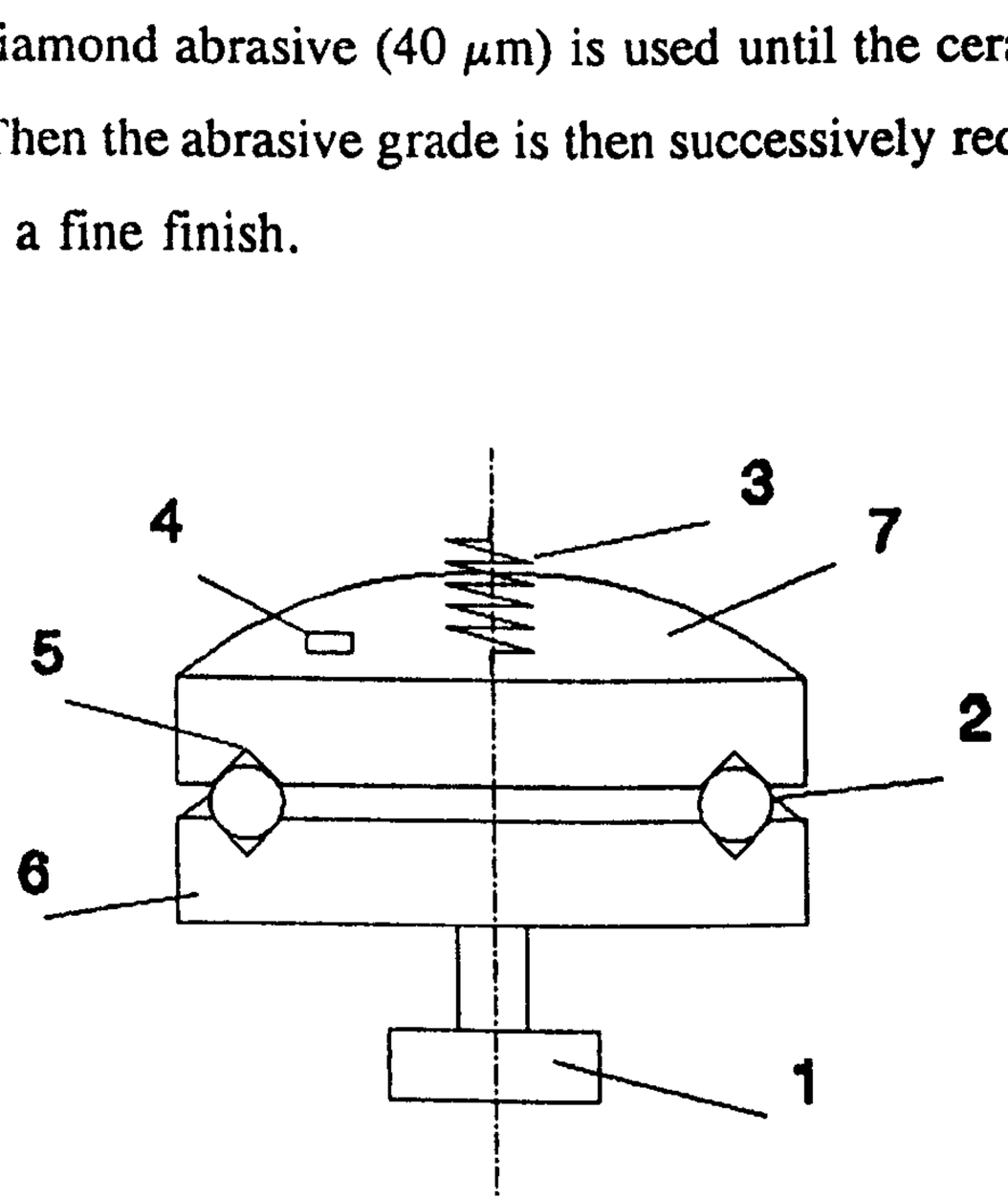

Figure 4.2 Ceramic ball grinding apparatus: 1,drive-motor; 2,ceramic balls; 3,spring load; 4,micro-switch cut-out; 5,'V'-groove; 6,rotating plate; 7,stationary plate.

The ball finishing operation is quite slow. For example, figure 4.3, shows total time of 148 hours to grind 43 silicon nitride balls to size. In the case illustrated in figure 4.3, the objective was to rough lap ball blanks to 12.7 mm diameter at a surface roughness of 0.05 μm Ra. During set time intervals wear rate, wear distribution, roughness, lubrication rate and condition of 'V'- grooves are monitored. Ceramic ball wear rate varies considerably with wear of the 'V'- grooves as this reduces contact stress. Balls are randomised at intervals related to wear rate distribution. Diamond paste breaks down to small grains which also reduces wear-rate, this may be detected as ball roughness reduces.

The majority of fatigue tests involved highly polished balls to surface roughness of below 0.01 μm. To achieve this high quality finish, polishing involved carefully monitoring loads, lubrication rate and abrasive grade. After a final polishing operation the ceramic balls are cleaned to remove all abrasive debris.

To ensure repeatable test conditions, final ball diameter, roundness, weight, and roughness were checked. Final ball diameter was measured on each ball with a dial test indicator to ensure consistent polishing. A precision balance was used to measure the weight of each ball to five decimal places of a gramme. Ball roundness and roughness was measured with 'Talyrond' and 'Talysurf' measuring instruments. Typical results are shown in figure 4.4.

4.1.4 Ball Surface Inspection

After final polishing and inspection checks, the ball surface quality was optically checked using light microscopy. Light microscopic techniques, described in section [4.1.2], were used to observe the ball surface. A customised manipulator positions each ball without manual contact interference. Figure 4.5, illustrates the result of a typical inspection; surface scratches are seen at low magnification, small scratches and general material features are seen at higher magnification. This example shows a high quality silicon nitride ceramic; the material has no porosity and hence is fully dense. The black area, shown in figure 4.5 under low magnification, indicates some ceramic phases which are a feature of processing and sintering additives.

GRINDING OPERATION

OBJECT: Grind silicon nitride ball blanks to 12.7 mm dia. with surface roughness 0.05 - 0.1 microns Ra.

BALL BLANK DATA:
Code UBQ
Initial roughness 0.15 microns Ra
Initial size 13.2246mm
Initial weight 4.0423gms

OPERATION DATA
43 ball ground per batch
Load variable
Grinding medium 45 micron diamond paste
Lubrication water with diamond paste and ceramic debris mixed and recirculated via micro-pump, drip feed

(I)
Initial roughness

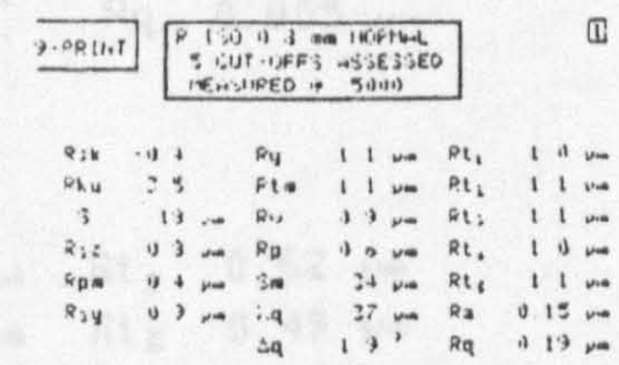

GRINDING OPERATION-FINAL MEASUREMENT

Final measurements after 147.9 hours, load 800N +120N (plate), 45 micron paste.

(F)
Roughness

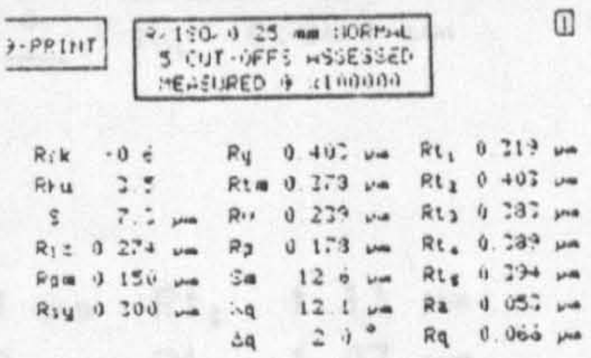

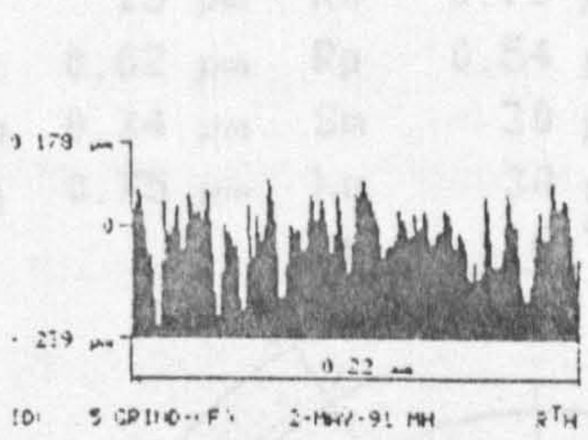

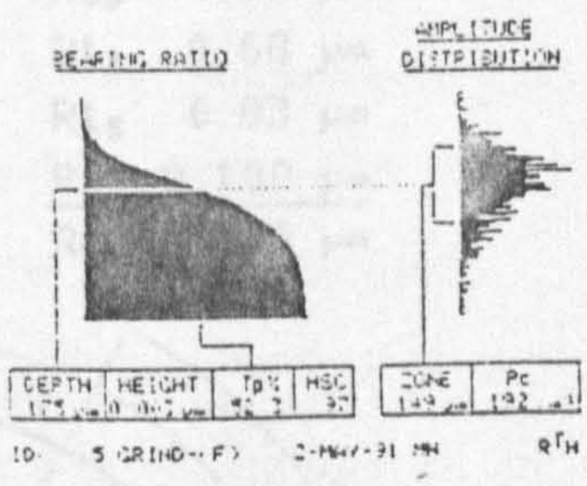

12.70

measured diameters (mm)
positions around wheel groove

12.70 12.70

12.70

Average diameter 12.70 mm
Average rate of material removal during test period 3.58 microns per hour
Width of top groove (90 degree) = 6mm
Width if bottom groove (90 degree) = 11mm
Mean groove dia. = 180 mm

Figure 4.3 Starting and final grinding data

Rsk	1.1	Ry	0.079 μm	Rt_1	0.079 μm
Rku	18.4	Rtm	0.053 μm	Rt_2	0.028 μm
S	18 μm	Rv	0.039 μm	Rt_3	0.059 μm
R_3z	0.016 μm	Rp	0.053 μm	Rt_4	0.021 μm
Rpm	0.030 μm	Sm	55 μm	Rt_5	0.078 μm
R_3y	0.018 μm	λq	32 μm	Ra	0.004 μm
		Δq	0.1 °	Rq	0.005 μm

(a) Standard roughness

Rsk	-2.4	Ry	0.94 μm	Rt_1	0.62 μm
Rku	17.4	Rtm	0.62 μm	Rt_2	0.49 μm
S	13 μm	Rv	0.73 μm	Rt_3	0.38 μm
R_1z	0.30 μm	Rp	0.21 μm	Rt_4	0.94 μm
Rpm	0.15 μm	Sm	26 μm	Rt_5	0.66 μm
R_3y	0.36 μm	λq	30 μm	Ra	0.056 μm
		Δq	1.0 °	Rq	0.080 μm

(b) Medium roughness

Rsk	-0.9	Ry	1.11 μm	Rt_1	1.11 μm
Rku	5.8	Rtm	0.92 μm	Rt_2	1.03 μm
S	15 μm	Rv	0.78 μm	Rt_3	0.93 μm
R_3z	0.62 μm	Rp	0.54 μm	Rt_4	0.68 μm
Rpm	0.34 μm	Sm	30 μm	Rt_5	0.83 μm
R_3y	0.75 μm	λq	30 μm	Ra	0.100 μm
		Δq	1.6 °	Rq	0.135 μm

(c) High roughness

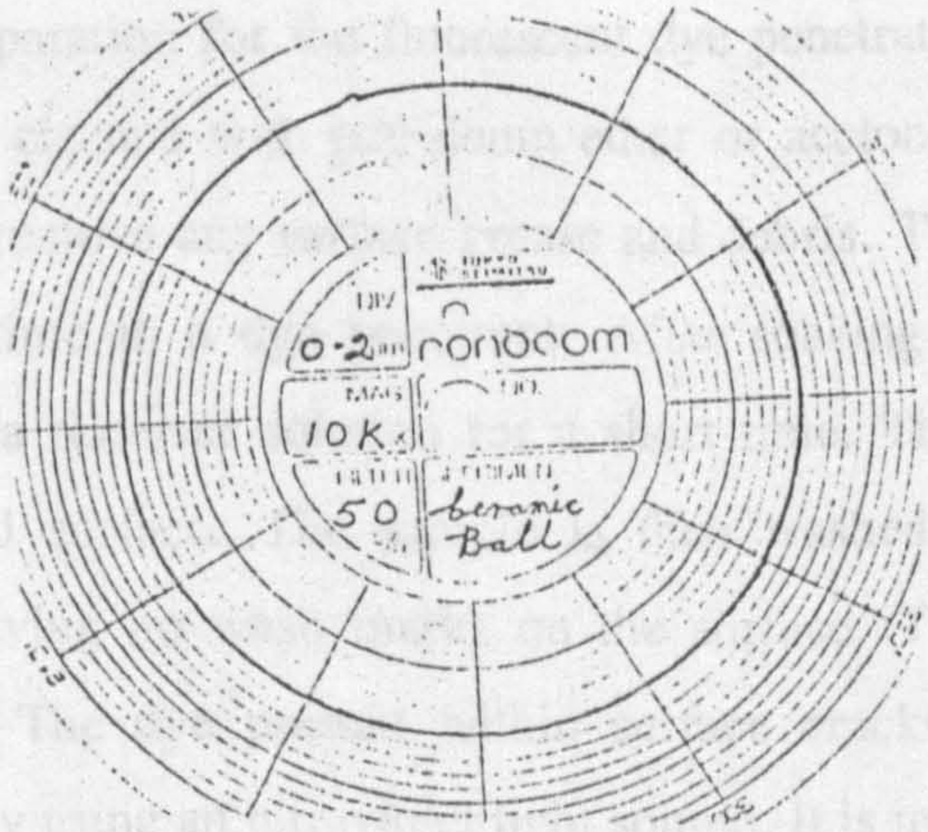

(d) Ball roundness

Figure 4.4 Typical roughness and roundness measurements

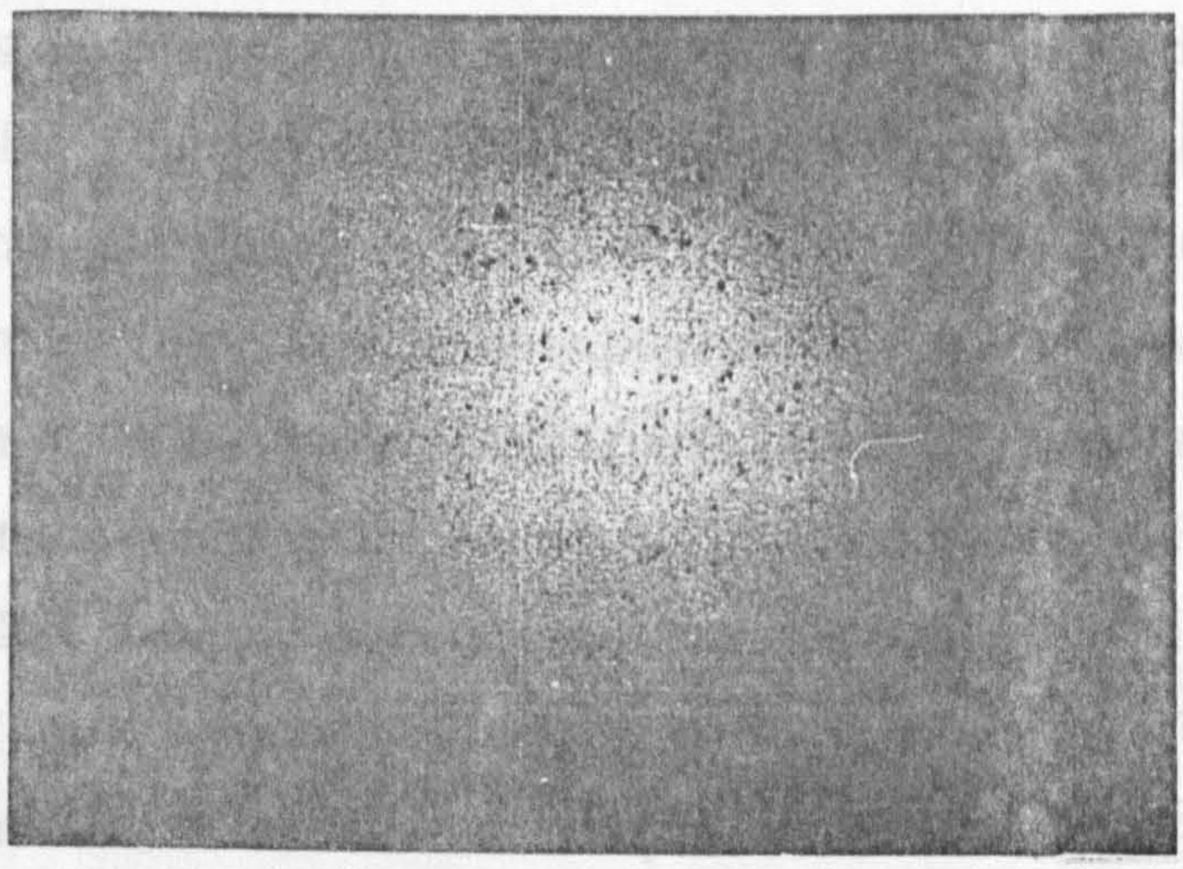

Figure 4.5 Ball surface inspection (x 57)

Ceramics are brittle materials, consequently manufacturing faults and transportation handling may cause surface cracks. Surface cracks are difficult to observe on ceramic surfaces even under high microscopic magnification, other non-destructive test techniques such as X-ray radiography and ultrasonics are of restricted use for screening operations. To enable quick and effective surface crack screening, a fluorescent dye penetration technique is used.

In preparation for the fluorescent dye penetration examination, the sample is thoroughly cleaned with petroleum ether or acetone in an ultrasonic bath. It is important to remove any surface grease and debris. The sample is then soaked for a period of time in a dye penetrant. After soaking and draining the sample is immersed in a remover solution for a short time. This process removes any dye from the ball surface. The sample is then washed thoroughly and then dried carefully, leaving no wash marks on the surface. The sample is then ready for examination. The dye present within surface cracks may be observed under a microscope by using an ultraviolet light source. It is important to inspect the sample as quickly as possible due to (fluorescent) degradation or fading of the chemical.

4.1.5 Pre-Cracked Balls

Surface cracks may exist on finished ceramic balls, due to poor manufacturing process or impact during transportation. The most common types of surface cracks are cone and ring types caused by a Hertzian stress field. These circular cracks have been studied since an initial analysis by, Hüber (1904) and more recently by, Ying and Hills (1991). Surface cracks caused by a sharp indentor are called lateral and radial types, described by, Ueda (1989). Although these cracks are not as common, they are found occasionally on ceramic balls, Cundill (1990), hence research of their influence on fatigue failure mode is necessary.

The surface cracks described, were artificially created so their influences on the fatigue failure mode could be studied, under controlled conditions. Radial and lateral cracks were produced on the ball surface by using a Vickers diamond pyramid indentor. Standard hardness test procedure was adopted according to ISO 146, various loads (5, 2.5 and 0.5 kg) were applied for 5 seconds. The indentations caused both radial and lateral cracks. At low loads, however, no cracks were apparent. Figure 4.6 shows typical radial cracks caused by a 5.0 kg indentor load. The figure 4.6 is a microscopic photograph of the impression under normal light conditions.

Figure 4.6 Radial and lateral cracks: normal light (x280)

Figure 4.7 illustrates the same pre-crack as figure 4.6; in this example the ball surface is treated with fluorescent dye as described in section 3.1.4. It can be seen that the radial cracks have extended beyond that observed under normal light. The lateral cracks which previously were not observed are shown clearly in this figure. The reason why the lateral cracks are not observed under normal light is that they exist subsurface. The ultra-violet light illuminates the fluorescent dye to show these cracks. This is also an example of the translucency of the silicon nitride. Radial crack length and impression width were measured using a calibrated viewing scale; in this case, tip-to-tip crack length is 0.143 mm and impression half diagonal is 0.071 mm.

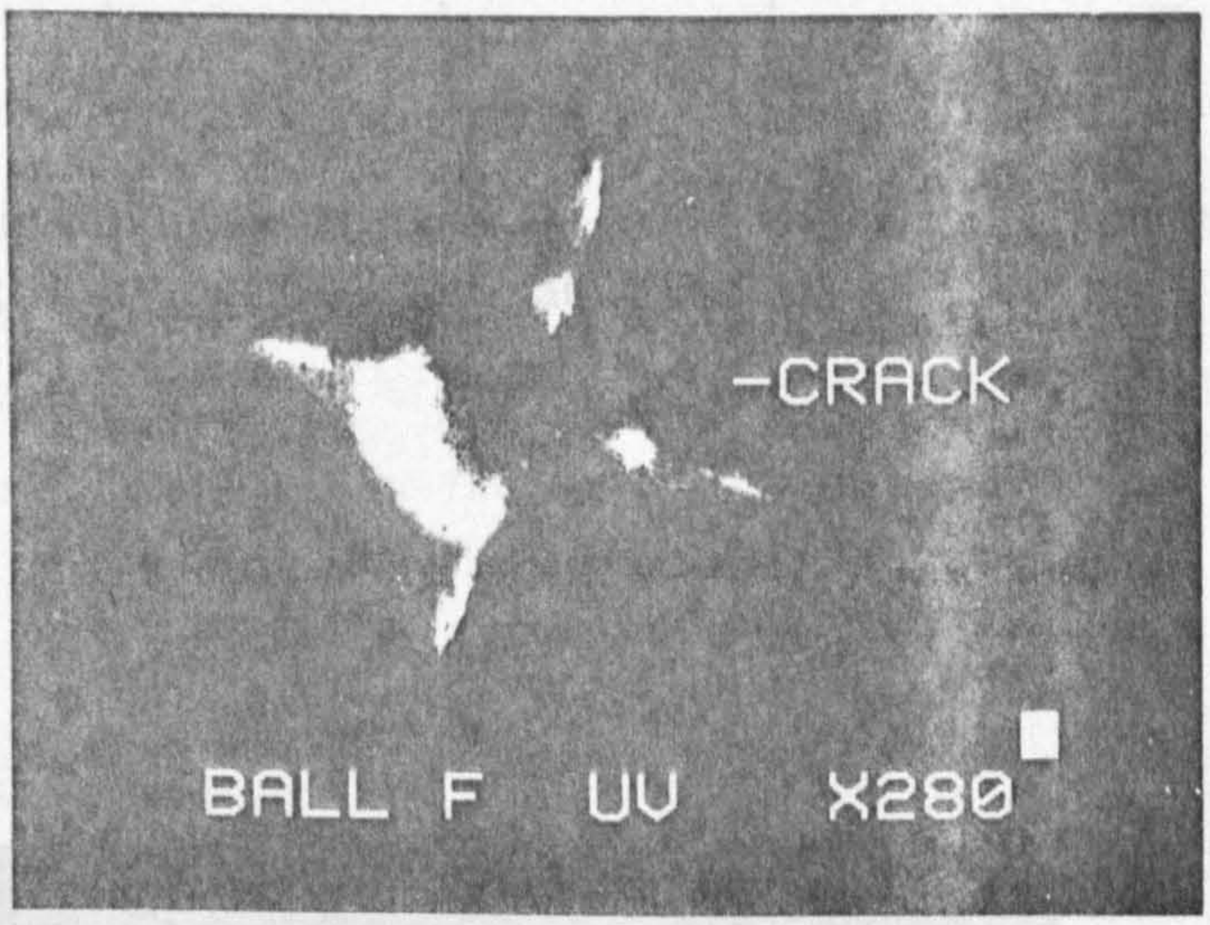

Figure 4.7 Radial and lateral cracks: ultra violet light (x280)

Ring or cone cracks were propagated on the ball surface by blunt impact load. A finished ceramic ball was placed in the recess of the mild-steel base with a tungsten carbide ball (½, ⅜ or ¼ inch diameter) on top, shown as figure 4.8. Tungsten carbide material was used as high hardness is required to avoid local plastic deformation. A mass is dropped under gravity through the alignment tube, impacting on the ball assembly. A typical ring crack, produced by a 158 gramme load, dropped from a height of 488 mm, using a ¼ inch tungsten carbide top ball, is shown as figure 4.9. The photograph shown was taken under ultra-violet light; the ring-crack diameter is 0.65 mm, this dimension corresponds to the theoretical Hertz circle diameter for this load condition.

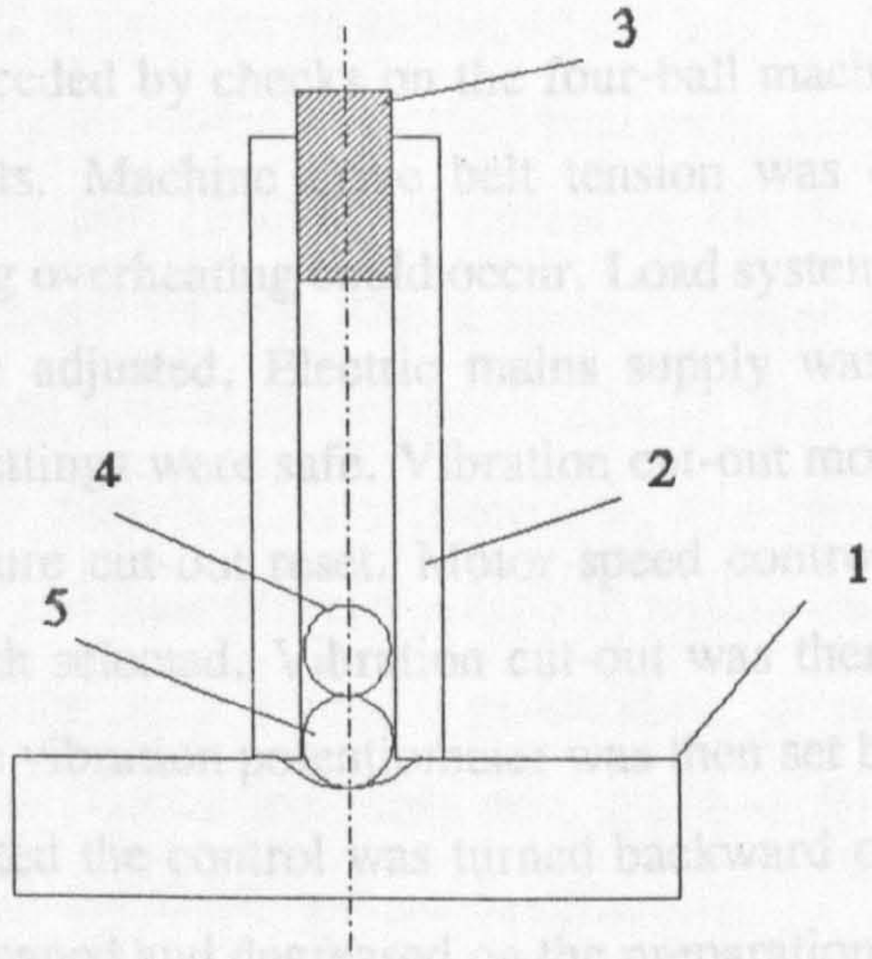

Figure 4.8 Schematic of impact drop test: 1, mild-steel base; 2,alignment tube; 3, drop load; 4,tungsten carbide ball; 5,ceramic ball.

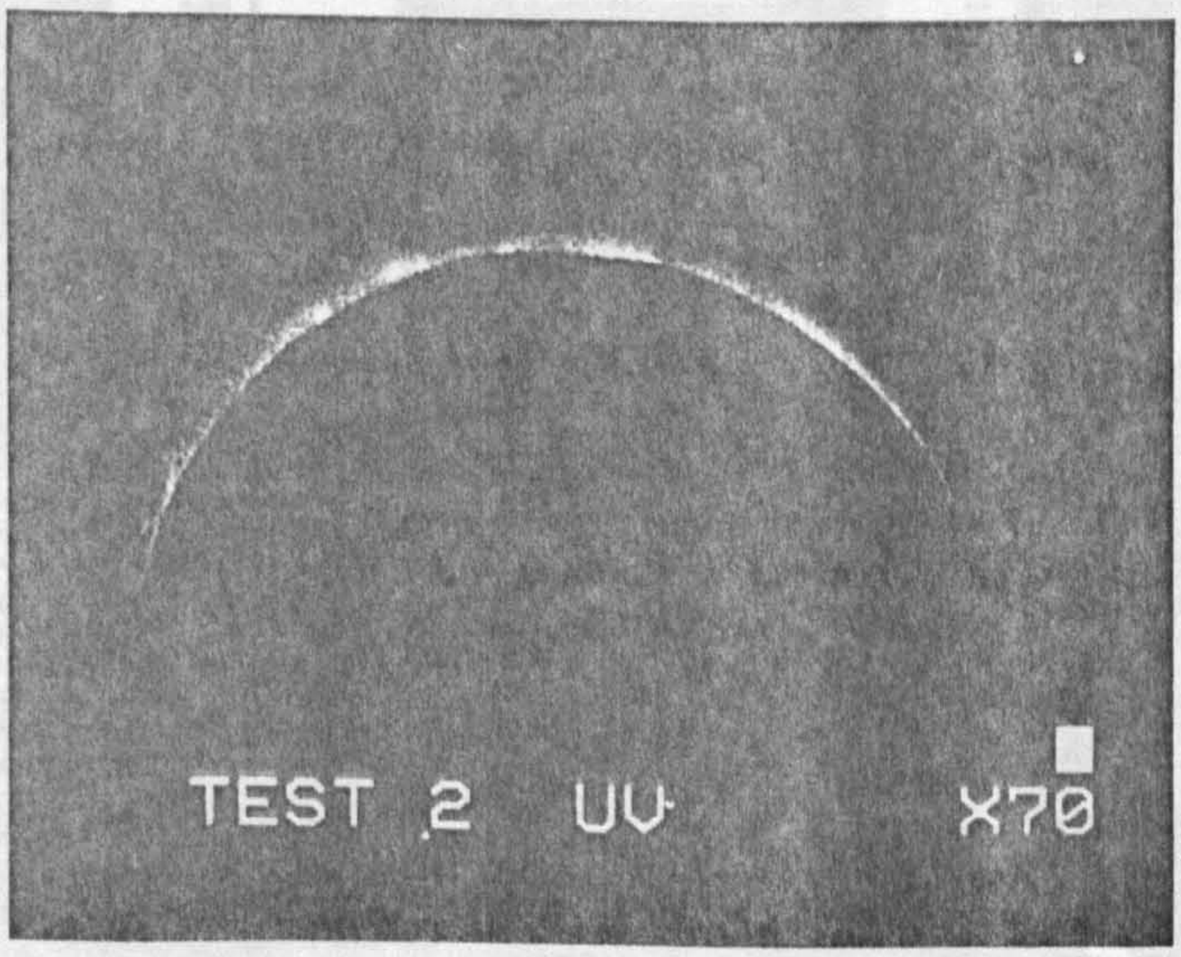

Figure 4.9 Ring crack: ultra violet light (x 70)

4.2 Modified Four-Ball Machine

4.2.1 Test Preparation

Each test was preceded by checks on the four-ball machine and cleaning of cup assembly components. Machine drive belt tension was checked, otherwise slipping or spindle bearing overheating could occur. Load system was calibrated and lever-arm counterbalance adjusted. Electric mains supply was switched on after checking initial control settings were safe. Vibration cut-out mode was selected and spindle bearing temperature cut-out reset. Motor speed controller was set to zero and 'motor enable' switch selected. Vibration cut-out was then checked using the vibration test switch. The vibration potentiometer was then set by adjustment, when a LED was just illuminated the control was turned backward one revolution.

Test balls were cleaned and degreased on the preparation bench, figure 4.10, using acetone and then 'Genklene' in an ultrasonic cleaner for 5 minutes. Cup assembly components were all cleaned in 'Genklene' in the ultrasonic cleaner for 10 minutes. All cleaned components were dried with a fan heater for 15 minutes to remove all cleaning agents and then cooled.

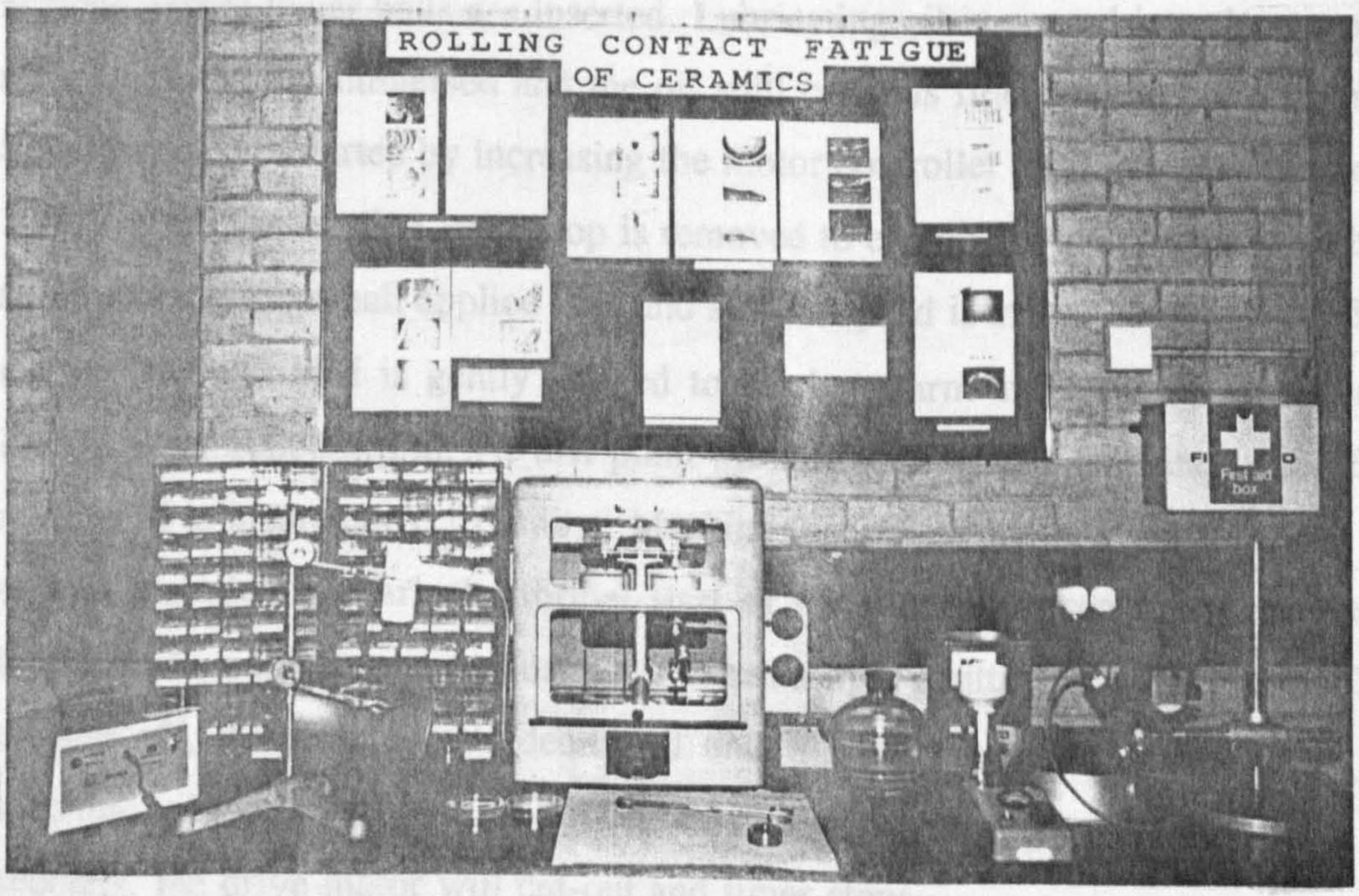

Figure 4.10 Preparation and inspection bench

Periodically, drive-spindle eccentricity was checked using a dial test indicator fixed to the machine cover. After the drive belt was removed, a ball and collet were fitted to the spindle. The maximum deviation of the ball as the spindle is revolved is 0.0076 mm, according to manufacturer's tolerances. Loading piston to drive-spindle concentricity was also checked by mounting the dial test indicator to the drive spindle using a special fixture. The thrust-race cover was removed and the spindle rotated, measuring around the thrust-race bore. The maximum deviation is 0.025 mm, according to manufacturer's tolerances. The measurements confirmed that spindle eccentricity and concentricity were just within tolerance, although with belt tension these readings were altered considerably. In addition, the steel cup which is pressed into the heater assembly was checked for flatness with a dial indicator, results showed that there was no deviation.

4.2.2 Test Procedure

The upper-ball is pushed into a spring steel tapered collet and marked to insure no relative movement. The collet assembly is pressed into the drive spindle after aligning the keyway and the ball is again cleaned with acetone. Cup assembly is fitted on to the heater pad and loading piston slots. The cup is finally cleaned with acetone before lower balls are inserted. Lubricating oil is poured into the cup until all lower balls are immersed and the oil spill cover is fitted on the cup assembly. Spindle motor is started by increasing the motor controller until the spindle reaches 1000 r.p.m. The loading lever stop is removed to enable the lower and upper balls to contact under a small applied load and spindle speed is increased quickly to 5000 r.p.m. Full test load is gently applied to the lever-arm and the spindle speed in increased to 10000 r.p.m. At this point the vibration of the machine is carefully monitored to insure correct running. Machine timer and counter is started, time and date is recorded to mark the formal start of test. Vibration sensitivity reading is increased by potentiometer adjustment. When a light emitting diode begins to flash on and off, the sensitivity is decreased until the off mode is reached. When the machine vibrates such that the diode remains in the on mode for more than two seconds, the drive motor will cut-out and timer stops.

During each test, spindle speed is monitored and adjusted until temperatures reaches equilibrium. Figure 4.11, shows a typical bulk temperature plot at the start of test, after three minutes the temperature has risen 34°C above ambient, it will take several more minutes to reach equilibrium temperature. Heat generation is due to elastic hysteresis when there is no asperity contact and slip is negligible. Spindle speed is readjusted after 30 minutes as increased lubricant and bearing temperatures reduce viscosity and inertia load. Lubricating oil is replenished during long-term tests as some lubricant is lost due to rotational forces. The machine is run overnight if necessary without supervision. Test is terminated due to completion of set cycles or increased vibration. At this point temperature, time and machine cycles are recorded.

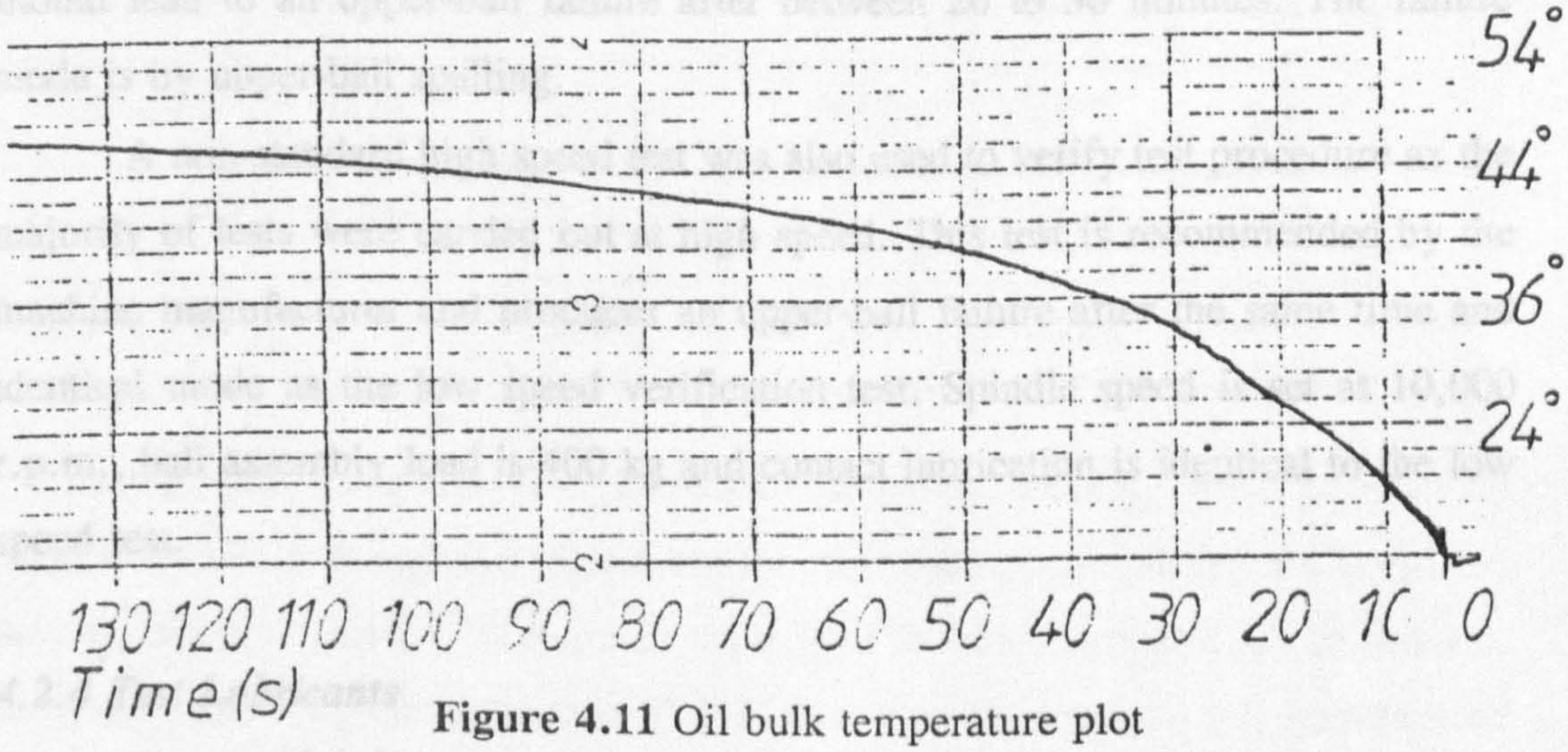

Figure 4.11 Oil bulk temperature plot

After test completion, cup assembly is allowed to cool before lower balls are removed from the cup and cleaned in acetone. Upper ball is inspected, if failed it is pushed out of the collet and cleaned in acetone. Lower and upper balls are examined under a light microscope, any failures are marked with permanent red ink. Lubricant within the cup is filtered through hardened ashless, grade 541 filter paper into a Buchner vacuum flask. Filter paper is examined under a light microscope and stored after marking position of debris. Surface crack analysis using dye penetrant and ultra violet light is performed using procedure described in section 4.1.4. Surface cracks seen under ultra violet light are marked with fluorescent ink. Balls

and debris requiring further analysis are stored in a desiccator, other samples are stored in a sample file. All machine components are cleaned in 'genklene' after test completion, steel cup is inspected for surface damage and replaced if necessary.

4.2.3 Test Verification

The test procedure and machine function were verified at regular intervals by two standard four-ball tests. The standard Institute of Petroleum test, IP 300, was used to verify the correct operation of the modified four-ball machine using standard quality SKF-3 bearing steel balls. This is a low speed tests in which spindle speed is set at 1450 r.p.m., unheated Shell Talpa 20 is used as a lubricant. The cup assembly is loaded by 600 kg and standard procedure is adopted. These conditions should lead to an upper-ball failure after between 20 to 30 minutes. The failure mode is by upper-ball spalling.

A non-standard high speed test was also used to verify test procedure as the majority of tests were carried out at high speed. This test is recommended by the machine manufacturer and produces an upper-ball failure after the same time and identical mode as the low speed verification test. Spindle speed is set at 10,000 r.p.m., ball assembly load is 400 kg and contact lubrication is identical to the low speed test.

4.2.4 Test Lubricants

Four test lubricants were used, which are detailed and specified in table 4.1. A highly refined straight naphthenic mineral oil, Shell Talpa 20, was used to examine effects of using a lubricant without additives. A formulated mineral oil, Shell Tellus 68, was used to assess the effects of a standard lubricant. A low viscosity synthetic oil, Exxon 2389, was used to examine effects of extremely thin films and a synthetic base. A high viscosity hydrocarbon research oil, B.P. HiTec 174, was used to examine possible effects of viscosity and increased film thickness.

Pressure-viscosity coefficient is an important property of the test lubricants when calculating lubrication regime, detailed in chapter 3. This property is temperature dependent and requires specialist high pressure equipment to measure.

To assess the necessity for this measurement a survey of existing literature was conducted on similar lubricants. It was concluded that the deviation in pressure-viscosity index could not justify exact experiments. The range of pressure-viscosity index showed that full film separation exists even when the minimum value for this property from other lubricants is applied.

Table 4.1 Lubrication properties

Lubricant	Specific Gravity at 15°C	Flash Point (°C)	Pour point (°C)	Kinematic Viscosity (c.s.°C)	
				40°C	100°C
Talpa 20	0.899	216.0	-33.0	94.6	8.8
Tellus 68	0.88	223.0	-30.0	68.0	8.6
Exxon 2389	0.955	220.0	-65.0	12.46	3.19
HiTec 174	0.95	255.0	-20.0	200.0	40.0

Lubricant compressibility is also an important property when considering traction forces. Although the calculation for slip at the contact surfaces was carried out, the effect of slip is a measure of the degree to which lubricant is compressed. A survey of existing literature showed that most lubricants become fully compressed at 2.5 GPa. As most testing was carried out between 6.0 and 9.0 GPa it can be assumed that the lubricants were fully compressed at test pressures and hence maximum shear stress easily reached. Non-Newtonian analysis of lubricant shear strength illustrates that the tractive force is proportional to maximum pressure. If slip occurs, the nature of the lubricant at the pressures may influence failure mode.

In addition to the above lubricants described in table 4.1, distilled water and emulsified oil were also used during tests. Emulsified oil was produced by mixing distilled water and brake fluid, in proportion of 50 percent each by volume.

4.3 Surface and Microscopy Studies

4.3.1 Preparation

Sample preparation is directly related to the quality of electron microscopic analysis. Good electrical conductivity is required to prevent 'charging' of the specimen which may result in variation in brightness or signal strength. Sample cleanliness from dust or grease is important for image clarity and chemical analysis. It is also important to make the sample mechanically stable for remote manipulation within the microscope.

Selected ball samples which had been examined with a light microscope, are mounted on special metallic stubs. Ball samples are held to the stubs with conductive adhesive, debris are placed on double sided adhesive paper before mounting on the stubs. A conductive path is necessary from the sample and stub to the goniometer to prevent electron charge saturation. Silver paint is spread on the metallic stub, adhesive and sample to increases conductivity.

Ceramic materials have low electric conductivity and hence require a thin coating of conductive material. The type of coating influences image quality and resolution. For ceramic balls gold is the most suitable material. A diode splutter method of coating is employed. The coating should be as thin as possible which does not cause charging in the electron microscope. Calculation for a typical coating thickness is shown in appendix 7. The sample is coated in a clean vacuum to improve the consistency and reduce debris on the surface.

Coating the sample to ensure high distribution and adhesion especially for spherical samples is quite time consuming. The sample is placed in a vacuum chamber and pumped out to 0.1 torr pressure. Argon is then released into the chamber and the vacuum is increased to 0.2 torr. Pressure is released to 0.1 torr whilst flooding the chamber with argon gas. The chamber is pumped out again and the process of argon flooding is repeated. Finally, the chamber is sealed and pumped out to 0.7 torr pressure. Electric power is applied to the gold diode and gas is released from the chamber to control charging rate and position. After approximately 5 minutes the power is stopped and vacuum released, the sample is place in a desiccator ready for analysis.

4.3.2 Machine Description

Two Scanning Electron Microscopes (SEM), Cambridge S250 and Joel 840A, were used for surface analysis. High resolution and large depth of field are features of SEM analysis. Magnifications of x30,000 are available for ceramic ball samples, generally, the machines are capable of x10 to x100,000 range. The basic principle of the scanning electron microscope is the use of a fine beam of electrons interacting with a specimen to produce a variety of signals and images. The electron probe is produced by an electron gun and focused along an electron column by condenser lenses.

The microscopes may be considered as five distinct systems:- electron gun source, condenser system, scanning system, detection facility and display system. The majority of images were produced on the Cambridge S250 machine as this has a reasonable working distance (25 mm), large tilt angles and is relatively straight forward to operate. The Joel 840A machine was used for quantitive line chemical analysis and digitised stereo images.

4.3.3 Surface Examination

Thorough visual surface examination of all ball failures and some test debris was performed using the scanning electron microscope. The basic procedure in setting the microscope up for surface examination is as follows:- a) fix the mounted sample on to the geometer and seal chamber, b) pump chamber out to required vacuum, c) select:- spot size 6, align, maximum amplitude, auto brightness, medium optibeam, correct EHT and minimum filament current, d) turn EHT and filament on, e) slowly increase filament current until saturation level is reached and e) align gun and aperture, check working distance is set at 11 millimetres.

A standard developed method of failure analysis is adopted during the initial stages viewing. The first stage is to record an overall view of the failure and to photograph a superimposed grid on the failed, for reference purposes. After all failure sections have a grid reference assigned, careful analysis of the failure extremes is recorded. At this time any feature requiring more detailed analysis is recorded. During detailed analysis at high magnification the microscope requires

tuning, such as adjustment of: aperture, astigmatism, scan speed, working distance and focus. Examination of failed areas also requires the sample to be manoeuvred within the chamber; this is useful for examining edges of failed areas.

All images are recorded by taking photographs of the display using a conventional camera. Monochrome film development and printing of the micrographs are processed shortly after the surface investigation. The main procedure for recording micrographs is:- a) focus image at high magnification, b) switch screen to graph mode to adjust contrast and brightness and c) switch to normal raster with slow scan speed (to reduce noise).

4.3.4 Stereo Microscopy

Stereo pair technique was used to quantify topographic heights on failed rough surfaces. The Cambridge S250 microscope allows stereo images to be recorded from the screen by examining the same area, with some angular difference between. The specimen is tilted between exposures; angles normally used are 35 and 45 degrees giving a difference of 10 degrees. When tilting the specimen on the goniometer stage, specific image features are drawn on the screen in ensure correct realignment. At both angles, the image is recorded using a standard camera.

A stereo viewer is used to analyze the micrographs. This is a system of mirrors and lenses which presents one image to each eye. The micrographs are moved until the image is fused together on a known reference point, where the relative height is known, for example, the edge of a failure. The image is positioned to a peak or valley of the rough surface, and then realigned by tilting the mirror; this tilt is calibrated with a micrometer. The micrometer reading is then used to calculated the depth. A typical calculation is shown as appendix 7.

An alternative to taking a photograph of the tilted specimen is to digitise the image. The two digitised images may be superimposed on a screen using a computer. Special red and green glasses may then be worn to perceive a three-dimensional image.

4.3.5 Chemical Analysis

Chemical analysis was performed whilst observing images of failed surfaces using the Cambridge S250 microscope with a Energy Dispersive (ED) system. The Joel 840A machine was used to perform chemical analysis by a Wavelength Dispersive (WD) method. The basic principle of both these systems is the detection of x-rays, which are generated by the interaction of the electron beam with the specimen.

The sample is usually un-coated or coated with carbon when the WD method is used, as gold coating interferes with accurate quantitive chemical analysis. The ED method is much quicker at qualitative analysis than the WD method, but if quantitive analysis is required then the WD system must be used.

4.4 Residual Stress Measurement

4.4.1 Measuring Equipment

The X-ray stress measurement method is the only non-destructive means of finding residual stress. The stress in the material can be directly measured in a non-contact manner. Residual stress is measured on failed ball surfaces to investigate stress distribution at failure time and proof of plastic strain existence. Also this measurement is of interest from a fracture mechanics viewpoint, stress intensity differential (ΔK) is related to high compressive residual stresses and hence proportional to crack growth rate, Kodama et al, (1990).

The measurement of residual stress was performed on a 'Rigaku Strainflex MSF-2M' machine. The basic measurement principles are described in appendix 8, and a machine schematic diagram is shown as figure 4.12. The X-ray tube is typically copper or chromium, with maximum load of 30 kV and 8 mA, incident and receiving parallel slits direct the beam. A goniometer enables a detector scanning range of 120 to 170 degrees and, with standard stepper motor control, accuracy is within standard tolerances. The detector is a scintillation counter probe type, in which the rate meter transforms the count rate to direct current voltage which is fed into the recorder.

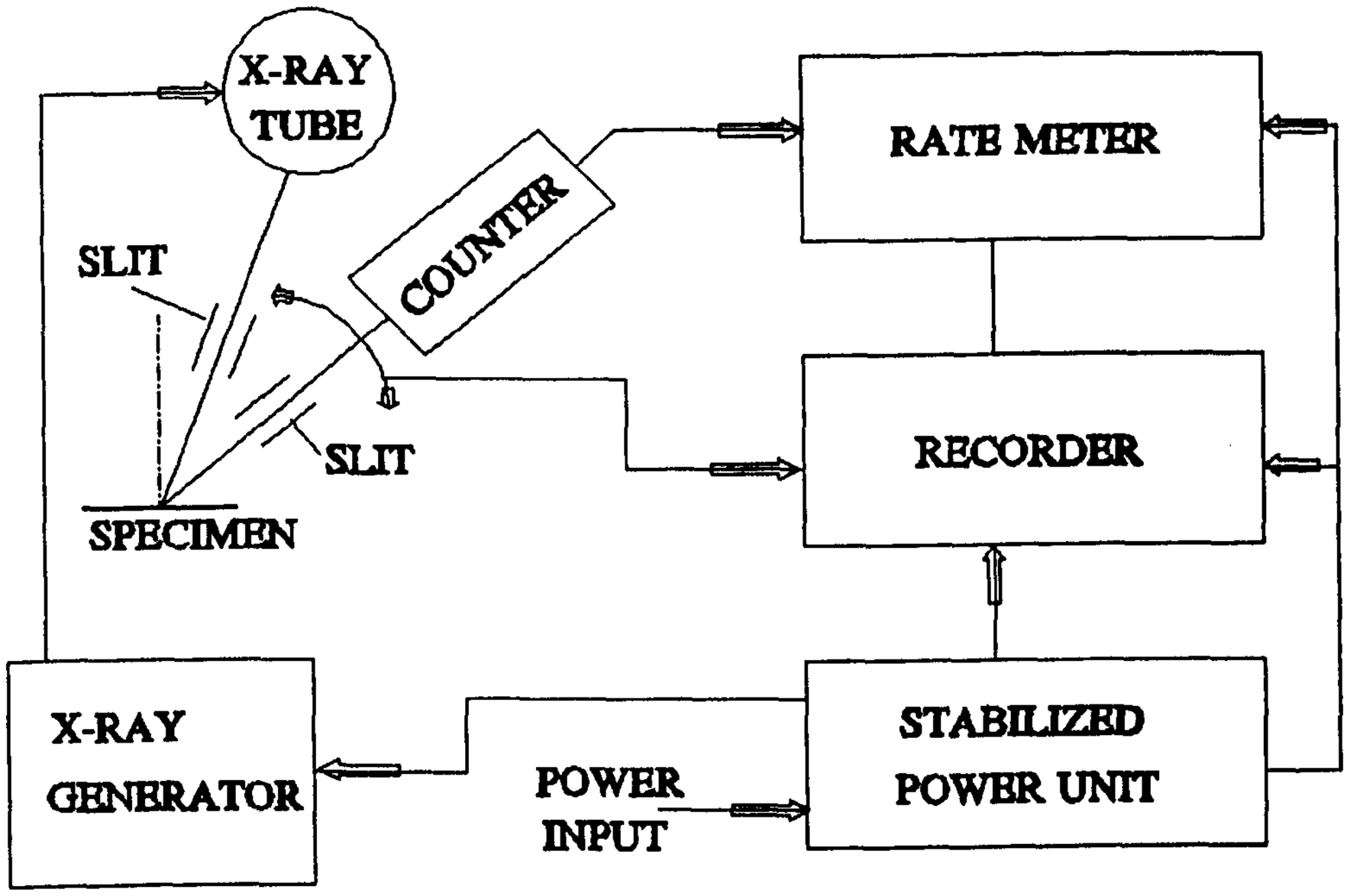

Figure 4.12 Diagram of x-ray apparatus

4.4.2 Measurement Preparation

Ideally, the specimen surface should be clean and smooth. Ball surface is cleaned with an ultrasonic method with acetone agent. Also, it is recommended for standard measurement that the surface should be electrolytically polished. The surface on ball samples are not polished, as surface effects on ceramics are reduced due to a large measurement depth and to enable further surface analysis. The sample is position before measurement is such a way that the centre of failure surface area corresponds to the incident X-ray beam centre, to reduce ball curvature effects.

The choice of characteristic X-ray influences the depth of measurement, measurement time and diffraction plane, shown as table 4.2. For the case of Cr-Kα and Cu-Kα radiation sources, measurement depth is 548 and 175 μm respectively. The X-ray source may be interchanged to estimate the stress gradient. The filter should be suitable for detecting alpha radiation and be compatible with the X-ray beam.

Sample to emitter distance is set to a standard distance. The irradiated area is adjusted using the parallel beam slits. Decreasing the irradiated area affects

reliability as this reduces the number of irradiated crystals; hence if area is decreased then measuring time should be increased. X-ray beam area on the sample surface may be checked by using fluorescent paper.

Table 4.2 X-ray stress measurement parameters

Measurement	1	2	3	4
Characteristic X-ray	Cr-Kα	Cr-Kα	V-Kα	Cu-Kα
Diffraction plane	(411)	(321)	(411)	(323)
Diffraction angle	125.54	117.40	152.0	141.73
Irradiation area (mm^2)	0.2	0.07	1.0	0.2
X-ray wavelength (Å)	2.29	2.29	2.51	1.54

4.4.3 Measurement Procedure

The optimal stress-free diffraction angle is found by scanning the incident X-ray from 120 to 170 degrees on an unstressed material section. During this initial scan, ψ is set at zero. Figure 4.13(a) and 4.13(b) show general scan results for Cu-Kα and Cr-Kα respectively. It can be seen from these graphs that Cu-Kα has, in this case, greater peaks, the maximum occurring at 141.6 degrees. Peak positions of silicon nitride using a Cu-Kα are shown in more detail in figure 4.13(c).

The goniometer is then set with the X-ray incidence angle set at zero. The first measurement is recorded and then counter reading for a fixed time and diffraction angle is measured. The incident angle is then moved 10 degrees and measurements are recorded. Peak shift of diffraction profile is then converted to strain as described in appendix 8. The peak shift of diffraction profile may be calculated by the centre of Full Width of Half Maximum intensity (FWHM) or peak position angle. In this case the peak position angle method is used.

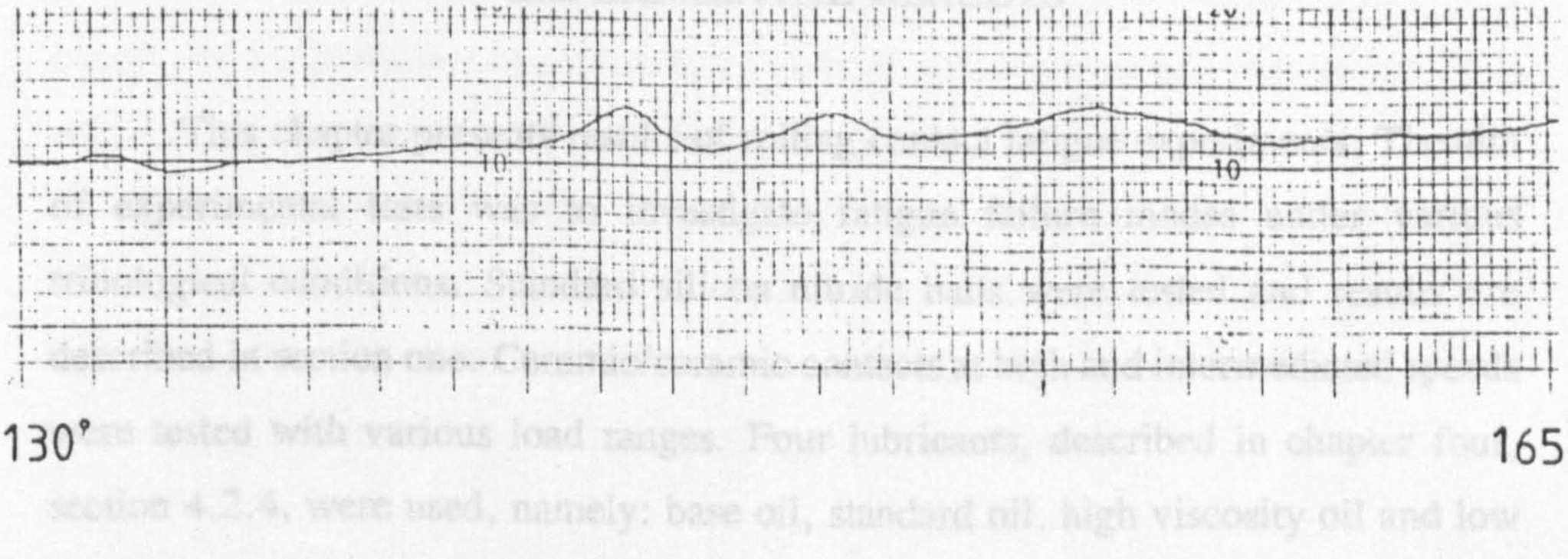

(a)

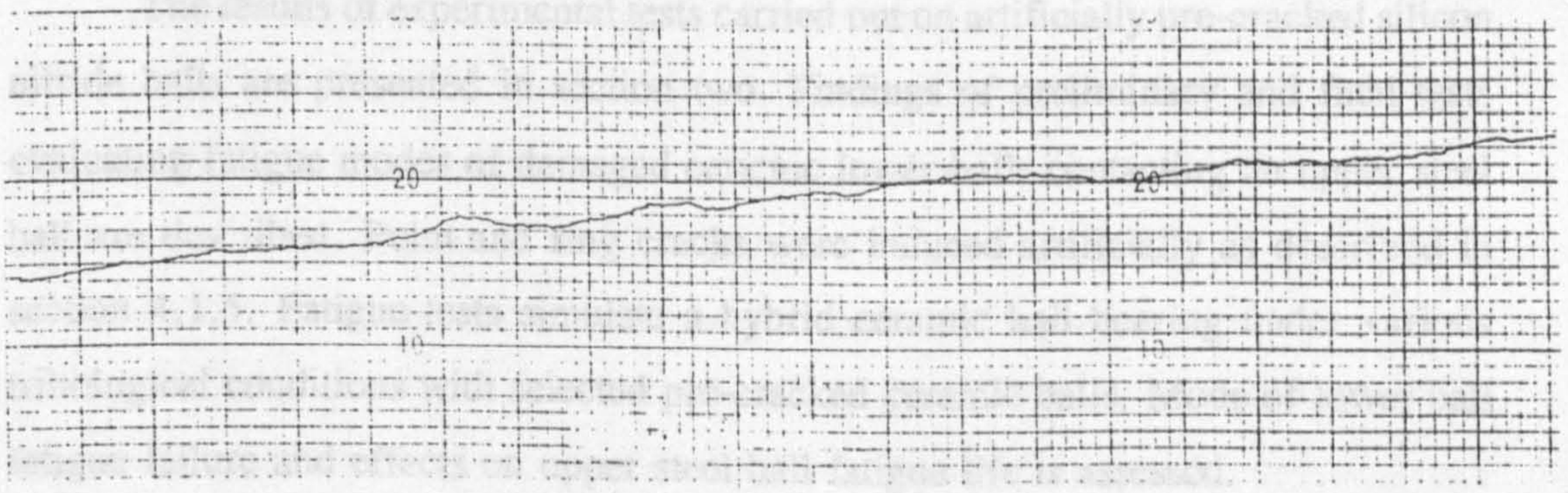

(b)

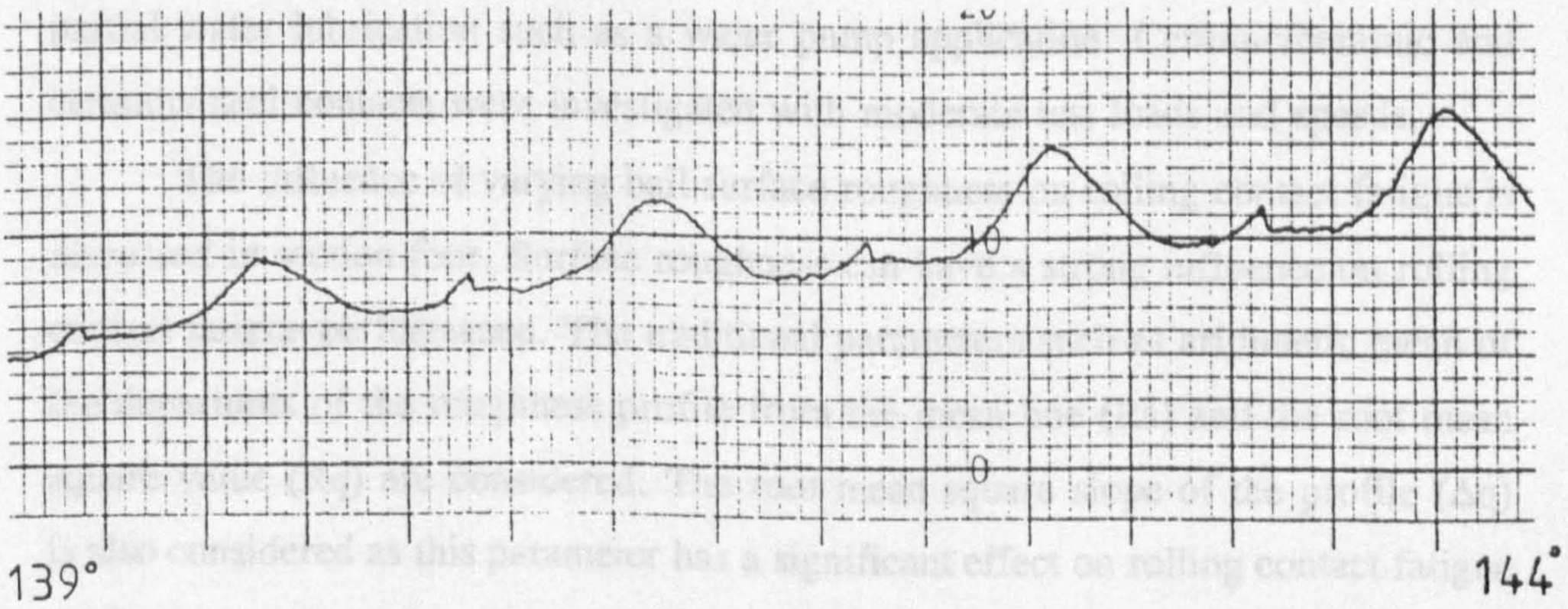

(c)

Figure 4.13 X-ray diffraction scans

Chapter 5
EXPERIMENTAL RESULTS

This chapter presents results of rolling contact fatigue experiments. The aim of experimental tests was to investigate fatigue failure modes under various tribological conditions. Standard silicon nitride balls were tested and results are described in section one. Ceramic/ceramic contacts at high and intermediated speeds were tested with various load ranges. Four lubricants, described in chapter four, section 4.2.4, were used, namely: base oil, standard oil, high viscosity oil and low viscosity oil. The effect of the tribological parameters on rolling contact fatigue failure mode is considered.

The results of experimental tests carried out on artificially pre-cracked silicon nitride balls are presented in section two. Findings of preliminary and final tests evaluating fatigue modes of damaged ceramic lower-balls contacting an upper steel ball are described. Point and ring cracks were induced artificially as described in section 4.1.5. Fatigue tests simulate a hybrid ceramic ball bearing under various tribological conditions with selected pre-cracked ceramic balls. Mode of lower ball fatigue failure and effects on upper steel ball fatigue life is assessed.

Emulsified oil experiments are described in section three. Emulsified oil with water is important for assessing the material performance under an unexpected lubricant regime. The work is also important when considering the material for partial water lubrication such as a water pump application. Ceramic/ceramic and ceramic/steel contacts were investigated with moderate test loads and speeds.

The influence of varying ball surface roughness on rolling contact fatigue is discussed in section four. Surface roughness can have a strong influence on rolling contact fatigue performance. The traditional parameters such as arithmetic mean of the departures of the roughness profile from the mean line (Ra) and the root mean square value (Rq) are considered. The root mean square slope of the profile (Δq) is also considered as this parameter has a significant effect on rolling contact fatigue performance. In the case of ceramics, Δq may have a greater influence due to tensile stresses caused by hydrostatic pressures within asperity valleys.

Sialon - an alternative ceramic material for ball bearing applications is described in chapter four, section 4.1. Sialon balls tests under various tribological conditions are presented in section five. Tests of ceramic/steel and ceramic/ceramic contacts are discussed and failure modes analysed.

A supplementary rolling contact fatigue test on silicon nitride is described in section six. This test enables failure mode to be compared with the modified four ball machine results. Standard tests on ceramic/steel contacts are carried out, effects of porosity, lubricant and surface roughness are considered.

5.1 Standard Silicon Nitride Ball Tests

5.1.1 Base Oil Lubrication

Conditions of low load ceramic/ceramic contact tests lubricated by a base lubricant are listed in table 5.1. Initial tests at moderate loads applied to standard ceramic contacts were suspended to over two million load cycles. Each test was conducted at a high speed of 10,000 r.p.m.

Results from ceramic/ceramic contact tests with base oil lubrication at low loads are shown as figure 5.1. Number of cycles to failure or suspension, and theoretical lubrication regime, expressed by parameter lambda, are illustrated. It can be seen that despite increasing maximum compressive stress considerably, the effect on lambda is small and well within the completely separated surface region. As the actual minimum film thickness is extremely thin, sensitivity to very slight changes in roughness or kinematic relationship will, in practice, have a large influence on the lambda parameter.

The first four tests, described in table 5.1, and figure 5.1, were suspended after reaching high numbers of stress cycles. An upper-ball wear path was not evident on all the first four tests after lubricant residual was removed by alumina paste. Surface roughness measurements of all three lower ceramic balls and close examination showed no damage or change in surface topography.

Table 5.1 Test Conditions

Test (10000 r.p.m.)	Maximum Compressive Stress (GPa)	Ball Roughness (Ra,μm)	Material	Temperature Start/Final (˚C)	Lubricant
1	6.0	0.008	UB	19/57	Talpa 20
2	6.0	0.008	UB	21/56	Talpa 20
3	6.4	0.008	UB	20/57	Talpa 20
4	6.75	0.008	UB	20/58	Talpa 20
5	7.1	0.008	UB	21/66	Talpa 20
6	7.1	0.008	UB	60/60	Talpa 20
7	7.1	0.008	UB	57/62	Talpa 20

The failure in test five failure was due to an upper-ball wear path and lower-ball delamination after six million upper-ball stress cycles. As temperature gradually increases with load, film thickness reduces due to viscosity effects. The lubricant is pre-heated to sixty degree celsius, to enable examination of lubricant film thickness sensitivity to temperature. Lubricant pre-heating resulted in much earlier failures, in tests six and seven, at approximately one million stress cycles. Lubricant viscosity effects and the absence of lubricant extreme pressure additives results in the ball surfaces being particularly vulnerable to partial film separation and hence causing a wear type failure mode. Roughness measurements of all lower-balls of tests five to seven showed no sign of damage to the highly polished ceramic surfaces, despite delamination and hence debris present within the lubricant.

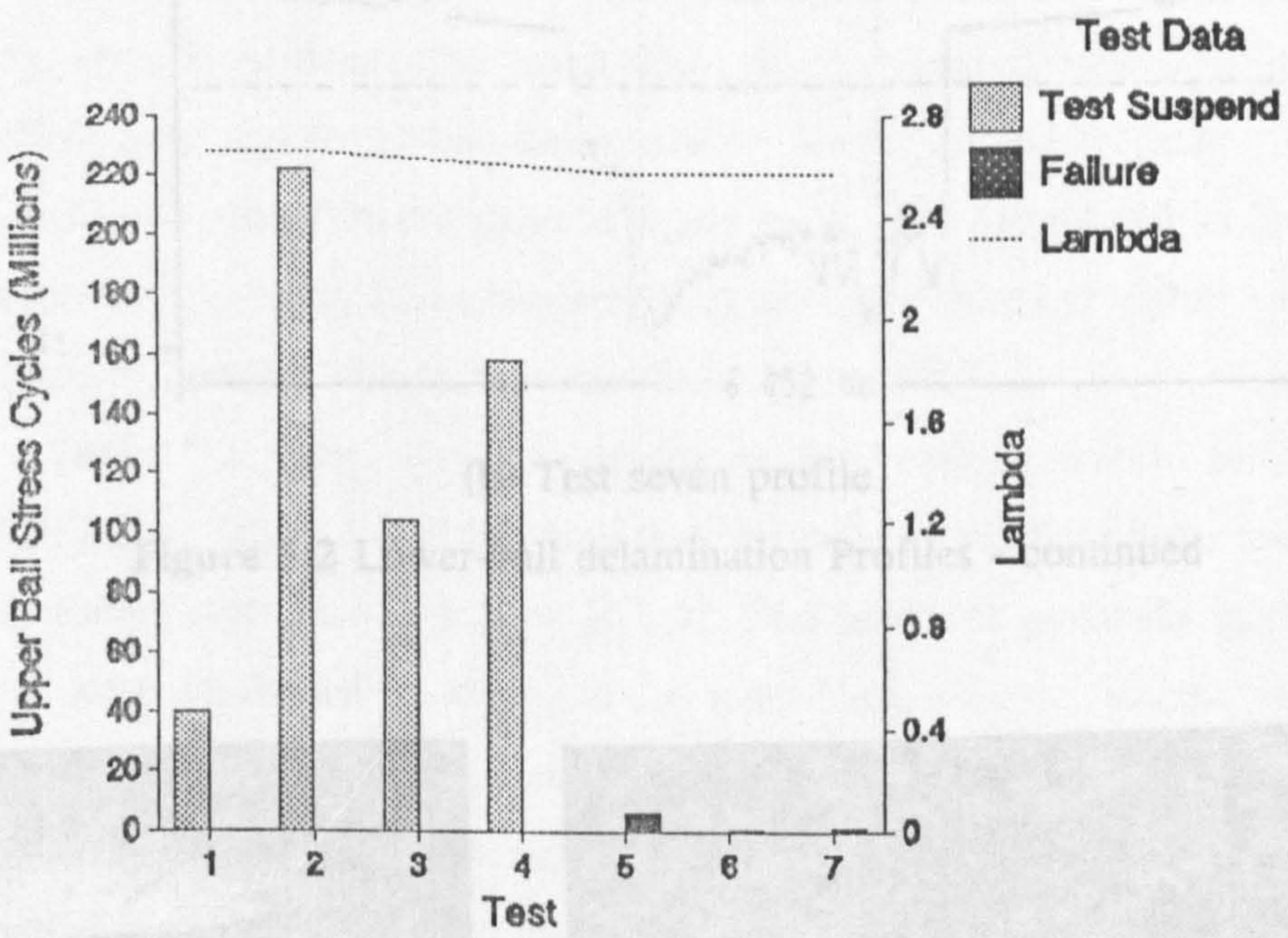

Figure 5.1 Base oil lubrication results

Figure 5.2 shows lower-ball profiles of delamination from test six, caption (a) and test seven, caption (b). Depth of delamination is shallow, averaging four microns; maximum theoretical shear stress position is approximately one hundred microns below the ball surface. Microscopic examination of test six upper-ball wear path is shown in figure 5.3. Caption (a) shows upper-ball wear path overview, minor spalling is shown in caption (b). High magnification of contact path edge, caption (c), shows no evidence of subsurface damage or micro-cracks.

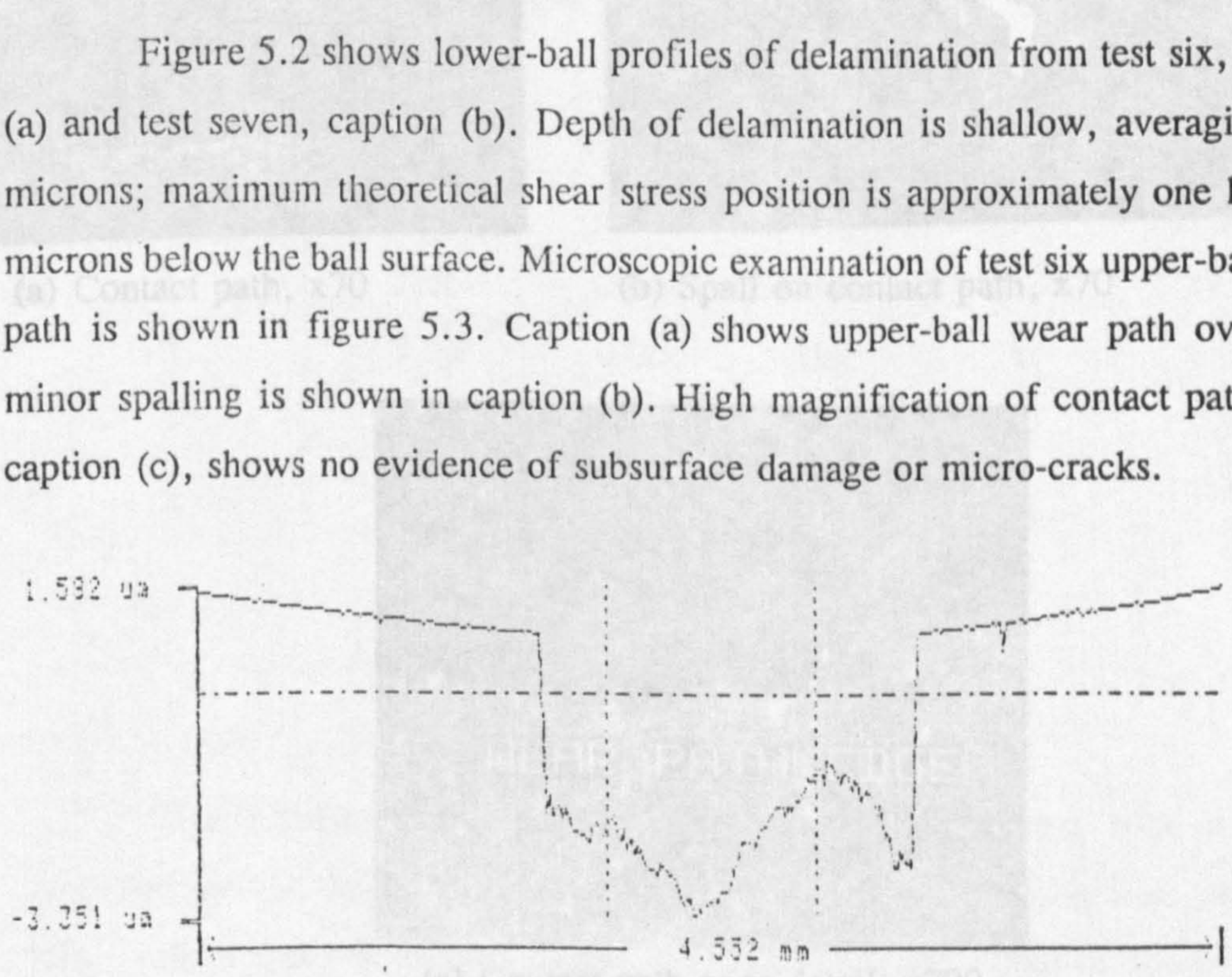

(a) Test six profile

Figure 5.2 Lower-ball delamination Profiles

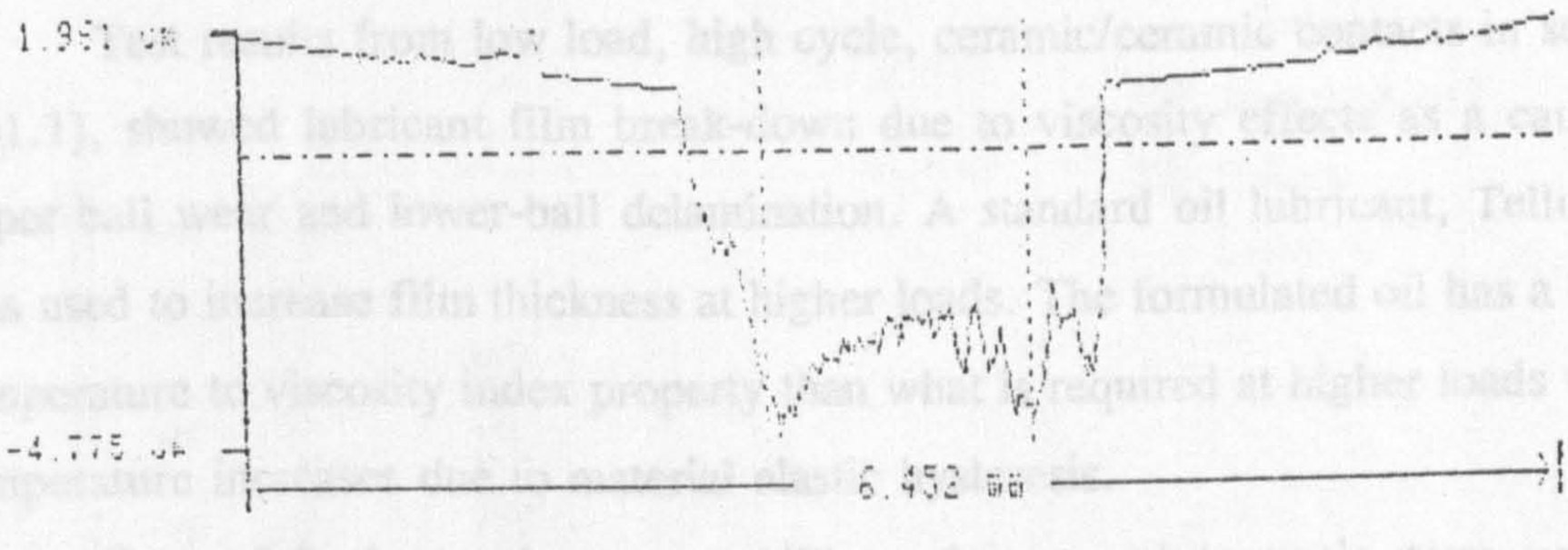

(b) Test seven profile

Figure 5.2 Lower-ball delamination Profiles - continued

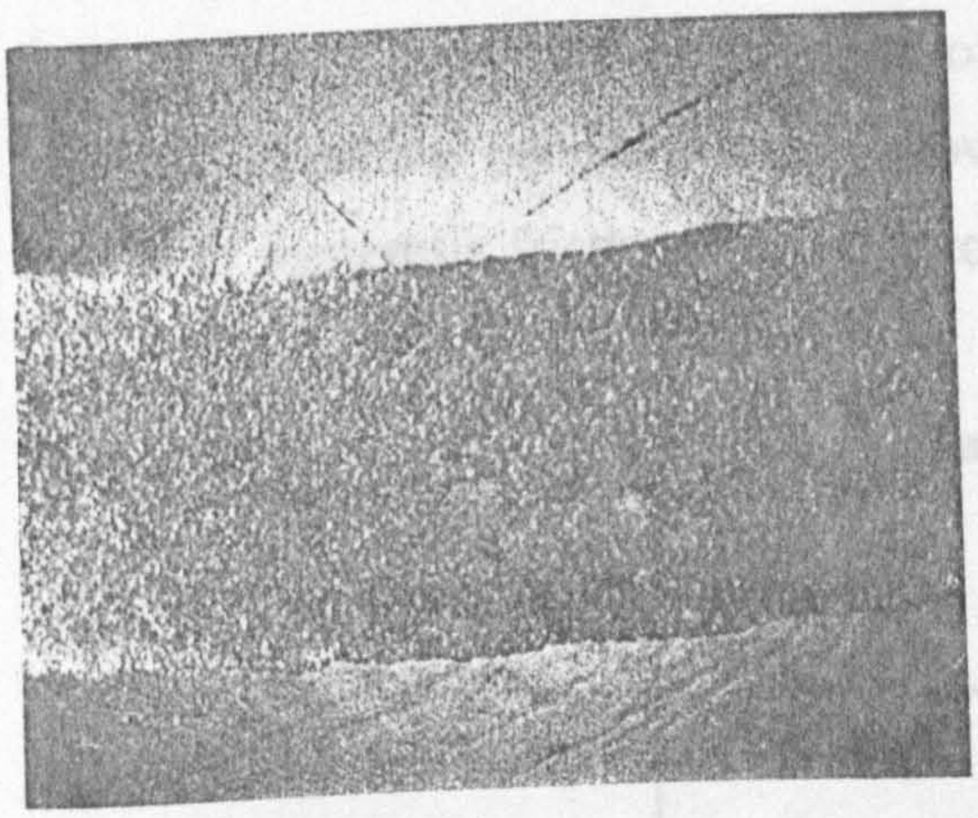

(a) Contact path, x70

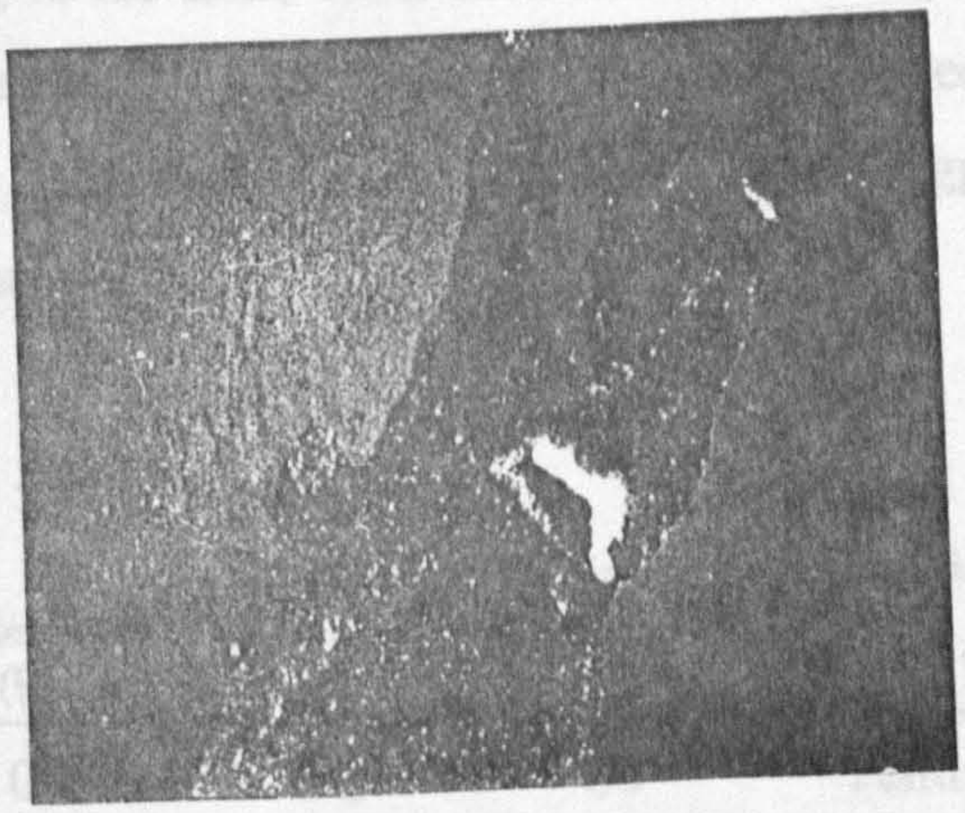

(b) Spall on contact path, x70

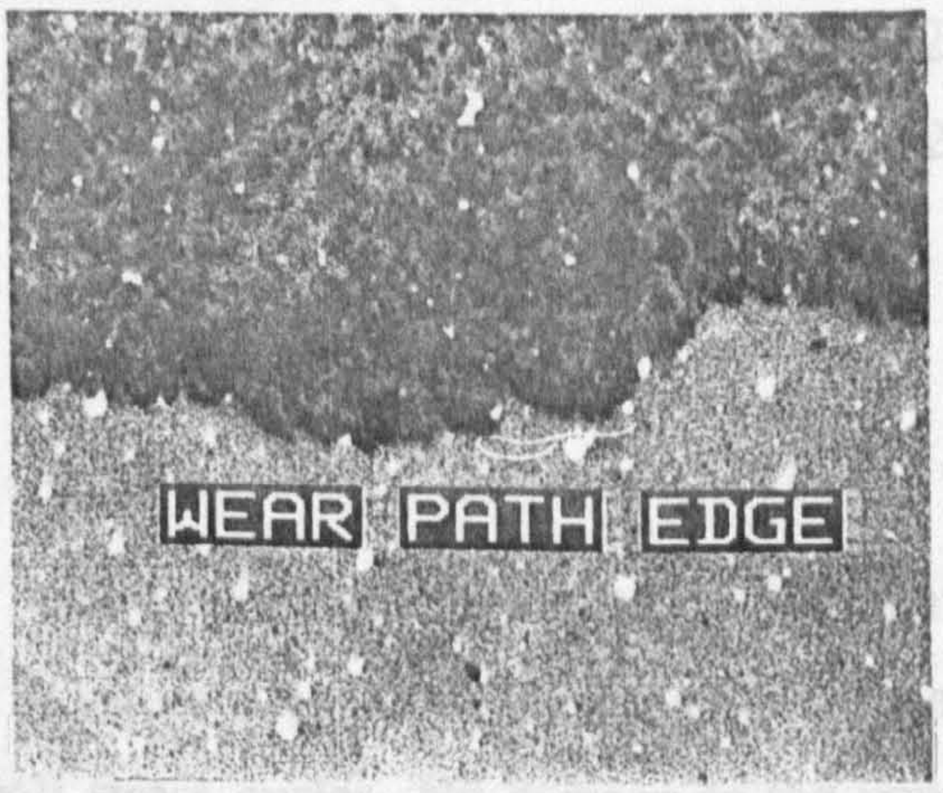

(c) Contact path edge detail, x700

Figure 5.3 Microscopic analysis of test six contact path

5.1.2 Standard Oil Lubrication

Test results from low load, high cycle, ceramic/ceramic contacts in section [5.1.1], showed lubricant film break-down due to viscosity effects as a cause of upper-ball wear and lower-ball delamination. A standard oil lubricant, Tellus 68, was used to increase film thickness at higher loads. The formulated oil has a better temperature to viscosity index property than what is required at higher loads where temperature increases due to material elastic hysteresis.

Table 5.2 shows the test conditions for ceramic/ceramic tests using a standard oil lubricant. Initial test load was the same as the final three tests of base oil lubrication described in section [5.1.1]. Test load was gradually increased and failures were confirmed by testing at the same load. Identical silicon nitride balls were used to base oil tests of section [5.1.1]. Temperature was recorded after reaching equilibrium and showed a gradual increase with load. This suggests a hysteresis friction effect due to material deformation.

Table 5.2 Test Conditions

Test (10000 r.p.m.)	Maximum Compressive Stress (GPa)	Ball Roughness (Ra,μm)	Material	Final Temperature ($^{\circ}$C)	Lubricant
1	7.1	0.008	UB	60	Tellus 68
2	7.35	0.008	UB	68	Tellus 68
3	7.35	0.008	UB	68	Tellus 68
4	7.6	0.008	UB	72	Tellus 68
5	7.6	0.008	UB	72	Tellus 68

Test results from ceramic/ceramic contact lubricated with a standard lubricant are shown in figure 5.4. Test one was suspended after one hundred and fifty million upper-ball stress cycles. No damage to the upper or lower balls was observed after microscopic analysis under white and ultra violet light. This first test

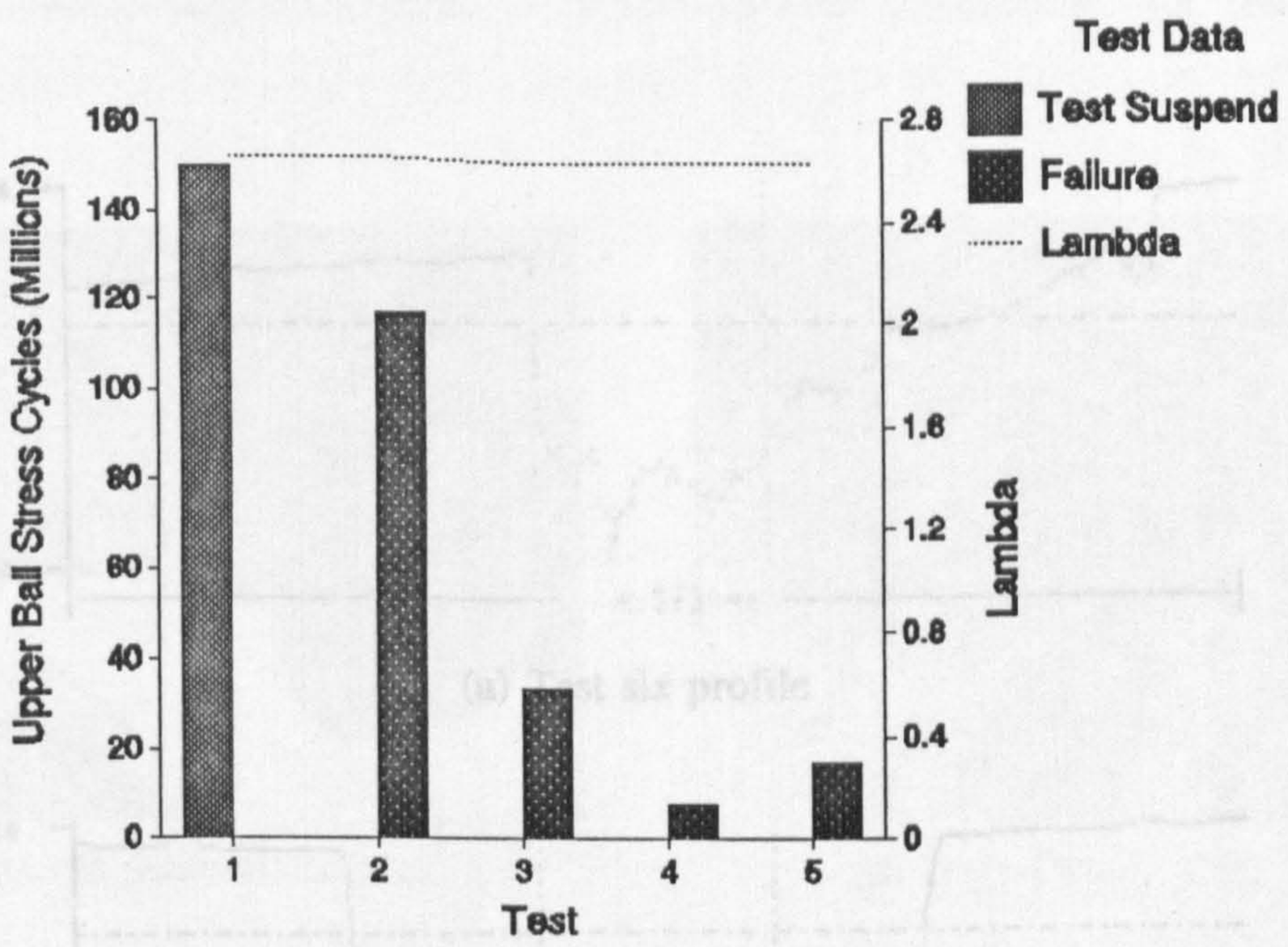

Figure 5.4 Standard oil lubrication results

was conducted at the same conditions under which base lubricant failed. This confirms that the mode of previous failure was due to a too thin film. Similar final temperature was also recorded which was ascribed to frictional effects of the material deformation hysteresis. The second test was conducted at a higher load level of 7.35 GPa and failure occurred by lower-ball delamination mode after 117 million upper-ball stress cycles; again higher bulk oil temperature was recorded. Microscopic examination of the upper-ball confirmed that no damage due to wear or surface cracks had occurred and therefore lower-ball delamination did not result from direct surface contact. Also, cycles to failure in excess of one hundred million implies a genuine fatigue failure mode. The lower ball delamination of test two was a heart shape with dimensions three by two millimetres. Surface profiles of the delamination is shown in figure 5.5, captions (a) and (b). It can be seen that the delamination depth varies from six to twenty-six microns with a generally constant gradient, although at the deepest peak the gradient increases before the delamination edge.

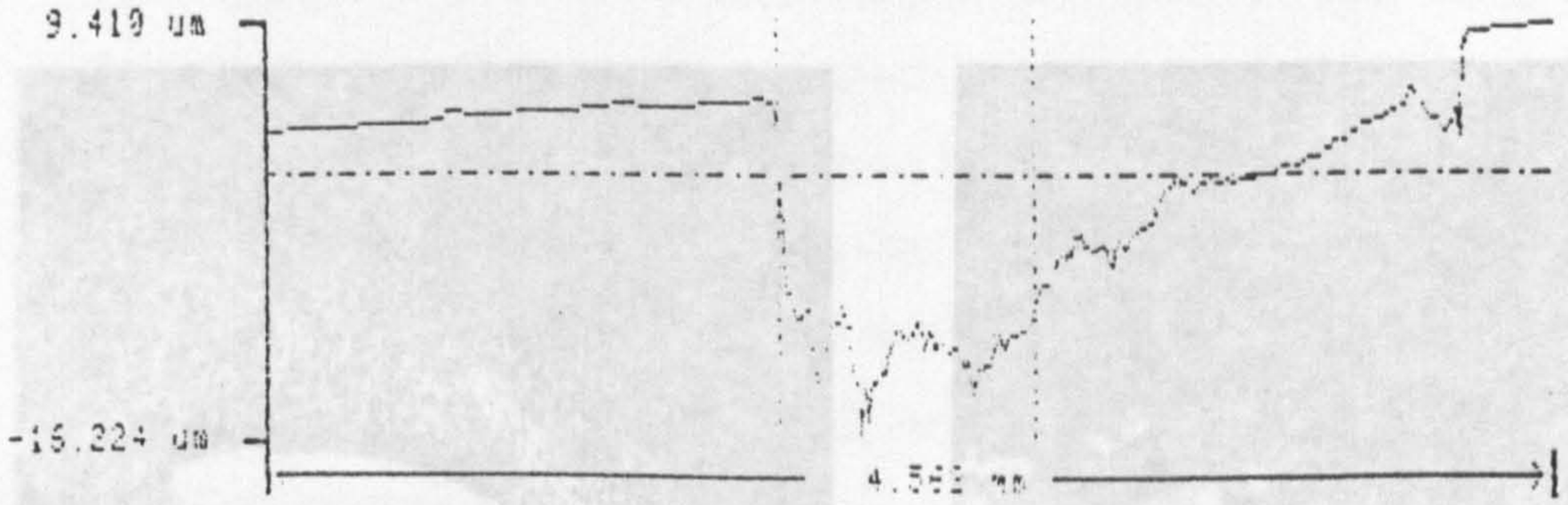

(a) Test six profile

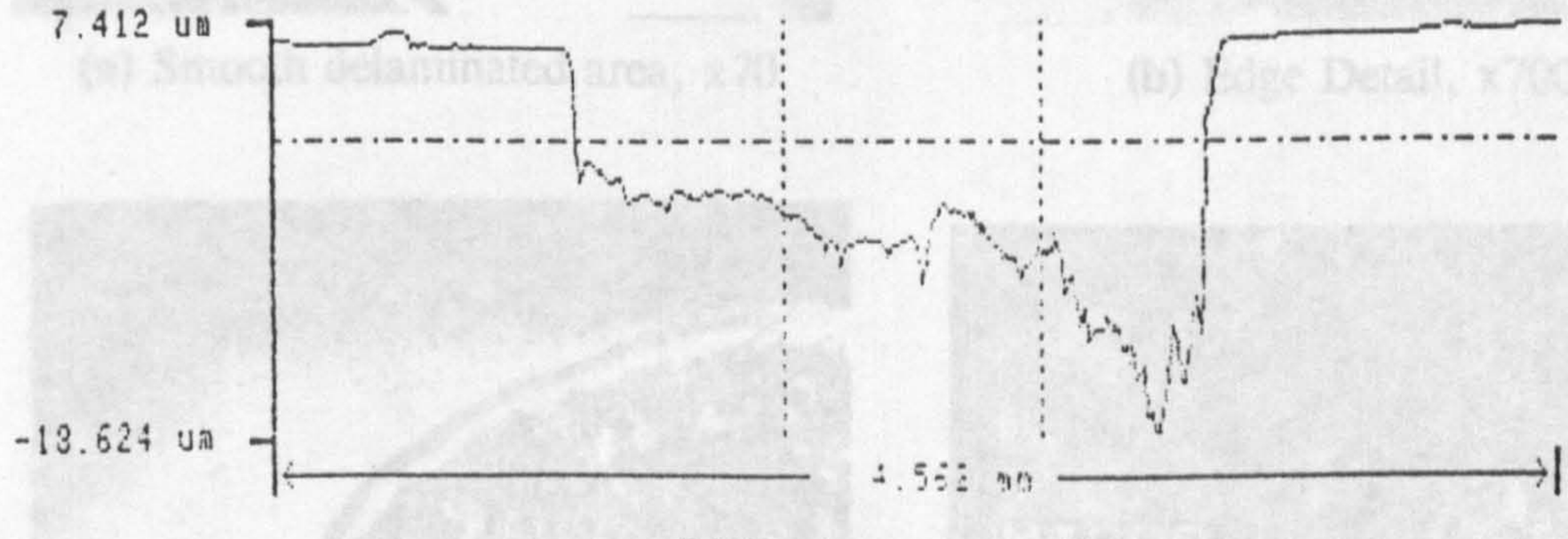

(b) Test seven profile

Figure 5.5 Lower-ball delamination profiles

Microscopic examination of the delamination and adjacent surface is illustrated in figure 5.6, captions (a) to (d). Caption (a) shows a section of smooth surface texture of the delamination. Edge of the smooth section is shown in caption (b), the absence of edge cracks is significant. A section opposite the smooth texture area shows increased roughness and undulations on the delaminated surface. the edge of the undulated surface is shown as caption (d), micro-cracks are present on the ball surface.

The smooth surface shown in caption (a), figure 5.6, is an area of shallow depth. The undulated surface of caption (c), figure 5.6, is an area of much deeper depth. It is also apparent from caption (c), figure 5.6, that the undulated surface crack propagates under the ball surface in a fatigue mode. Lubricant is a significant factor to the delamination mode, as base oil failures have smooth surface topography

and shallower depths compared to the failures when standard oil was used.

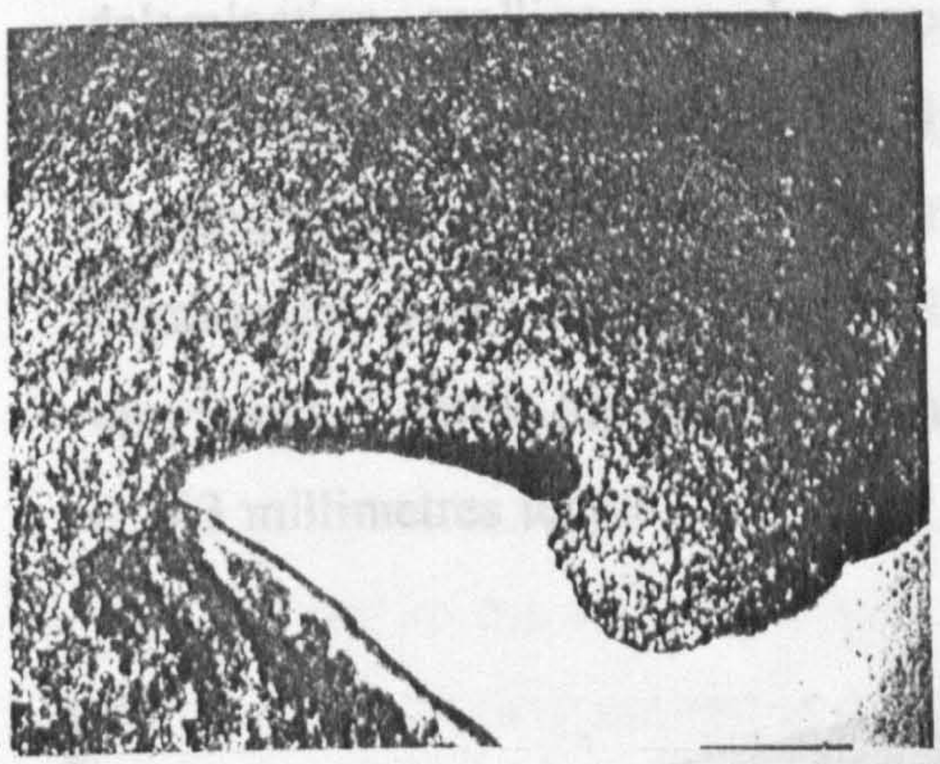

(a) Smooth delaminated area, x70

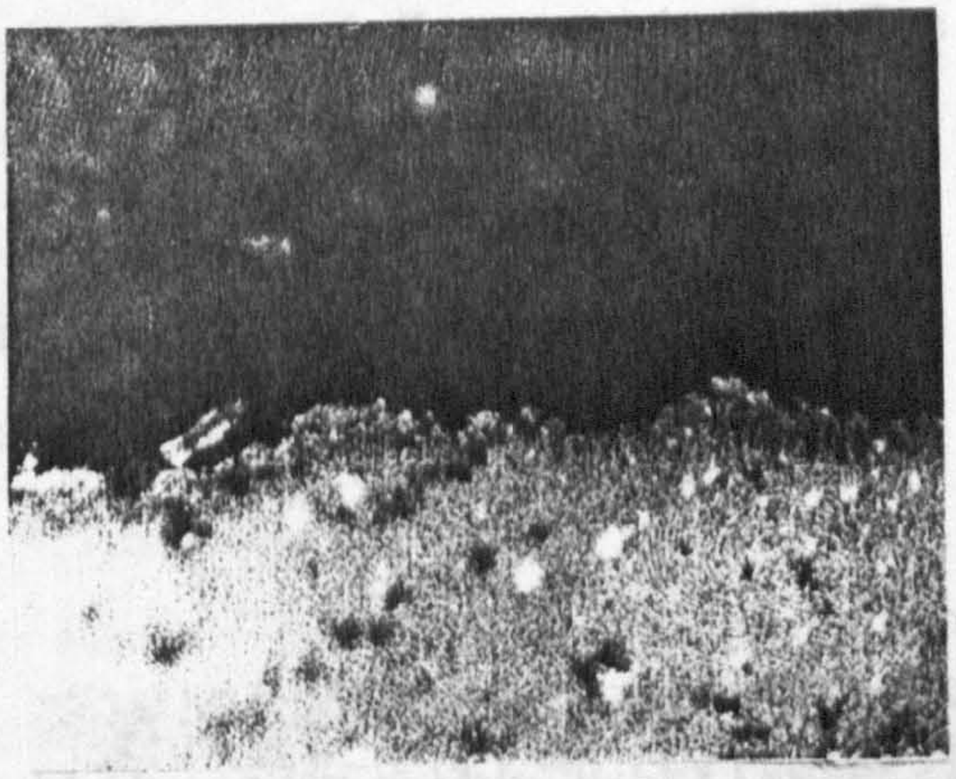

(b) Edge Detail, x700

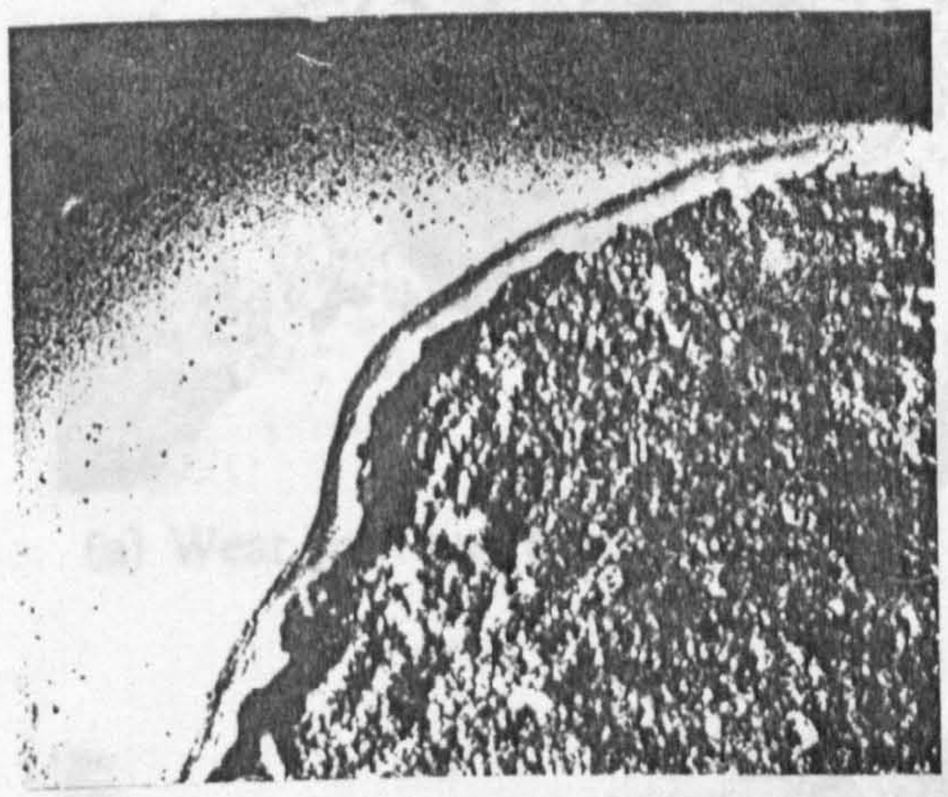

(c) Undulated delaminated area, x70

(d) Edge Detail, x700

Figure 5.6 Microscopic analysis of test two delaminated lower-ball

Test two result and failure mode was confirmed by a repeated experiment, test three, as shown in figure 5.4. Although the number of cycles to failure was less, over thirty million upper-ball stress cycles were reached before failure occurs. Higher test loads were applied and results are shown in figure 5.4. Test temperature again increased with increasing load and the number of cycles to failure was also reduced compared to the previous tests. Mode of failure was by lower-ball delamination with no upper-ball damage. Depth and nature of lower-ball

delamination was the same as in the case of tests two and three. Test four result was confirmed by test five, failure occurring after seventeen million upper-ball stress cycles. Upper-ball wear occurred during test five. In addition to lower-ball delamination, spalling was also apparent on the upper-ball wear path. Test five upper-ball contact path and spall analysis is shown as figure 5.7, captions (a) to (d). Caption (a) shows the wear path overview and spall, caption (b) the spall overview. Caption (c) shows the mounted ball section after cutting, grinding and polishing operations. Caption (d) shows the spall section, measured at sixty microns depth and 0.243 millimetres length.

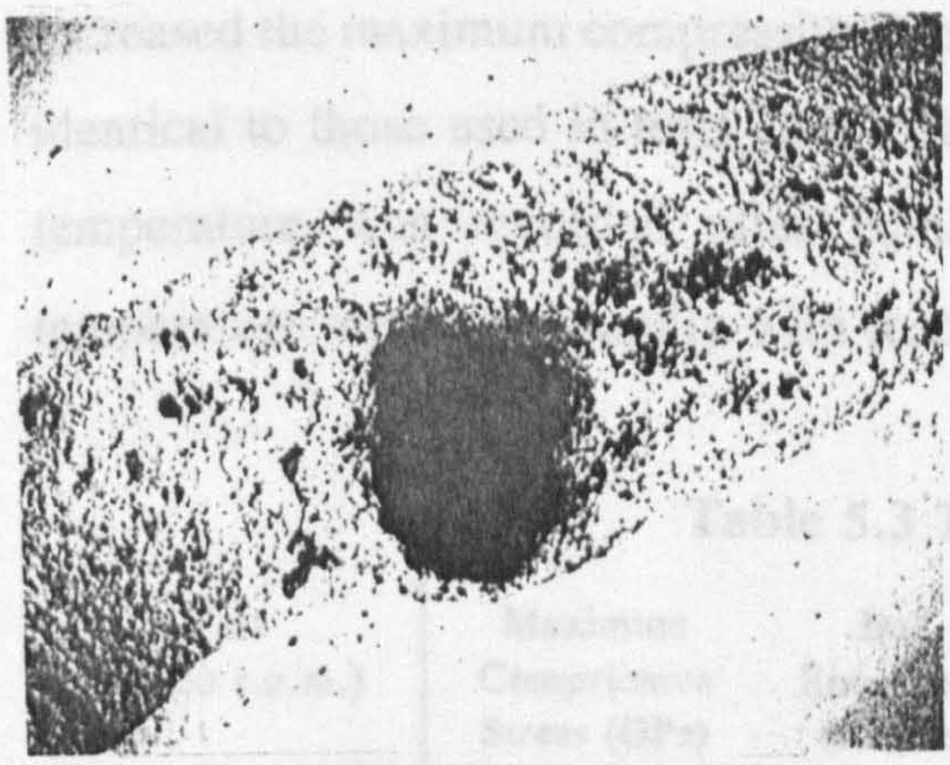

(a) Wear path and spall, x70

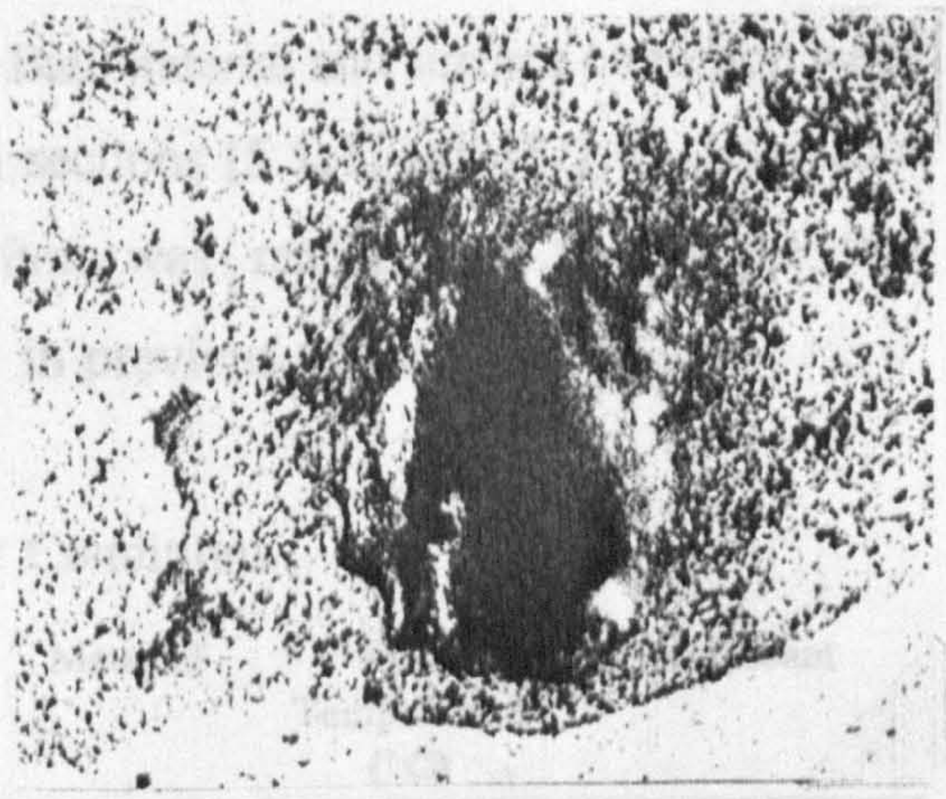

(b) Spall overview, x140

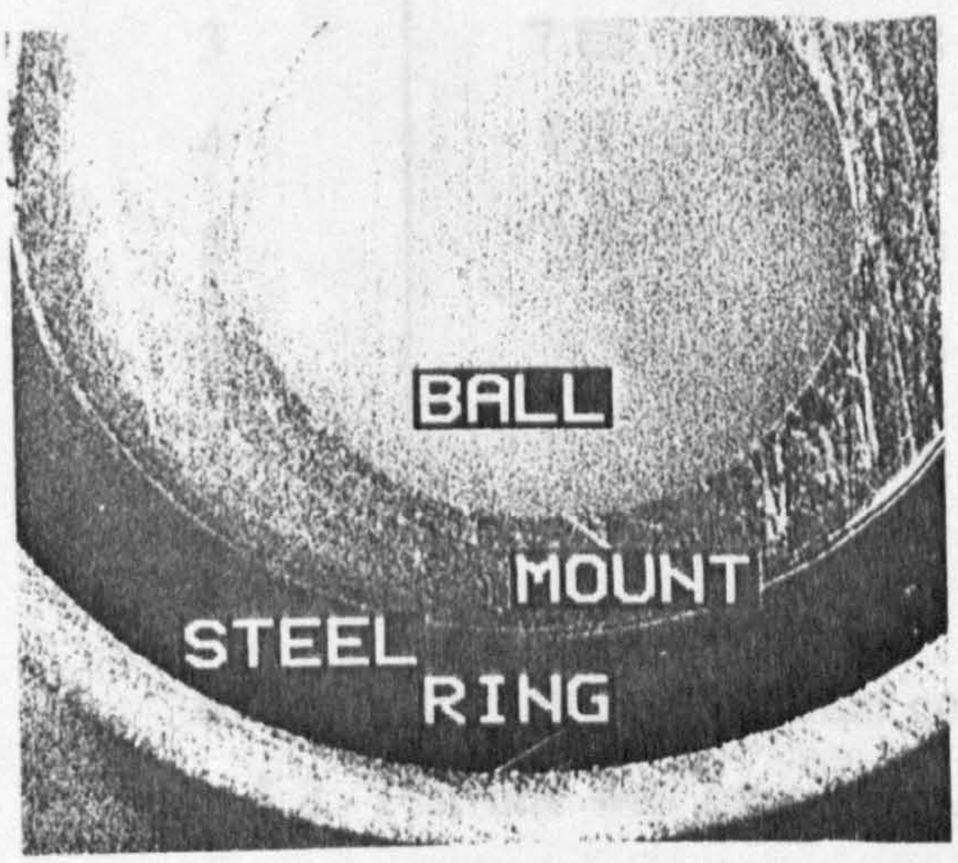

(c) Mounted section, x3.75

(d) Spall section - dark field, x140

Figure 5.7 Microscopic and section analysis of test five upper-ball

5.1.3 High Viscosity Oil Lubrication

Results from previous sections, [5.1.1] and [5.1.2], of ceramic/ceramic contact at steadily increasing loads, describe how lubricant viscosity is a limiting test factor. A lubricant with high viscosity at the test operating temperature was used to run ceramic/ceramic tests at increased loads. The non-commercial lubricant, HiTec 174, was provided by the British Petroleum Research Centre at Sunbury.

Test conditions for ceramic/ceramic contact with high viscosity lubricant are described in table 5.3. Maximum compressive stress commenced from the level at which the standard lubricant tests failed at relatively low cycles. Test two was repeated due to the unusual nature of the failure. Tests four to seven gradually increased the maximum compressive stress. Ball material and surface condition were identical to those used in tests described in sections [5.1.1] and [5.1.2]. Lubricant temperature was recorded after equilibrium was reached. It is evident that temperature increases steadily with load as in previous tests.

Table 5.3 Test Conditions

Test (10000 r.p.m.)	Maximum Compressive Stress (GPa)	Ball Roughness (Ra,μm)	Material	Final Temperature (°C)	Lubricant
1	7.6	0.008	UB	74	HiTec 174
2	7.85	0.008	UB	78	HiTec 174
3	7.85	0.008	UB	78	HiTec 174
4	8.1	0.008	UB	82	HiTec 174
5	8.7	0.008	UB	83	HiTec 174
6	9.1	0.008	UB	85	HiTec 174
7	9.6	0.008	UB	89	HiTec 174

Results from ceramic/ceramic contact with high viscosity oil are described in figure 5.8. Test one was suspended after 200 million upper-ball stress cycles. This compares with less than twenty million cycles to failure from the previous tests at the same load with a standard oil lubrication, section [5.1.2]. This result confirms

the sensitivity of the delamination fatigue failure mode to lubricant film thickness. Test two failed due to lower-ball spall and subsequent extensive delamination. The unusually low number of cycles may be caused by a ball defect or test procedure allowing debris into the enclosed oil sump. Test three was a repeat of test two and was suspended after 200 million upper-ball stress cycles. This confirms the unusual nature of test two failure.

Test four, figure 5.8, was suspended after 200 million stress cycles and after increasing maximum compressive stress to 8.7 GPa. After increasing load still further, test five, two lower-ball delaminations occurred after fifty million upper-ball stress cycles. Initial observations and roughness measurements showed no damage to the upper-ball and no secondary damage to lower-balls. Test six failed due to lower ball delamination after only 1.5 million upper-ball stress cycles at increased load again. Test seven failed after 0.5 million upper-ball load cycles after another load increase. Surface roughness of test six and seven lower balls were unaffected by failures.

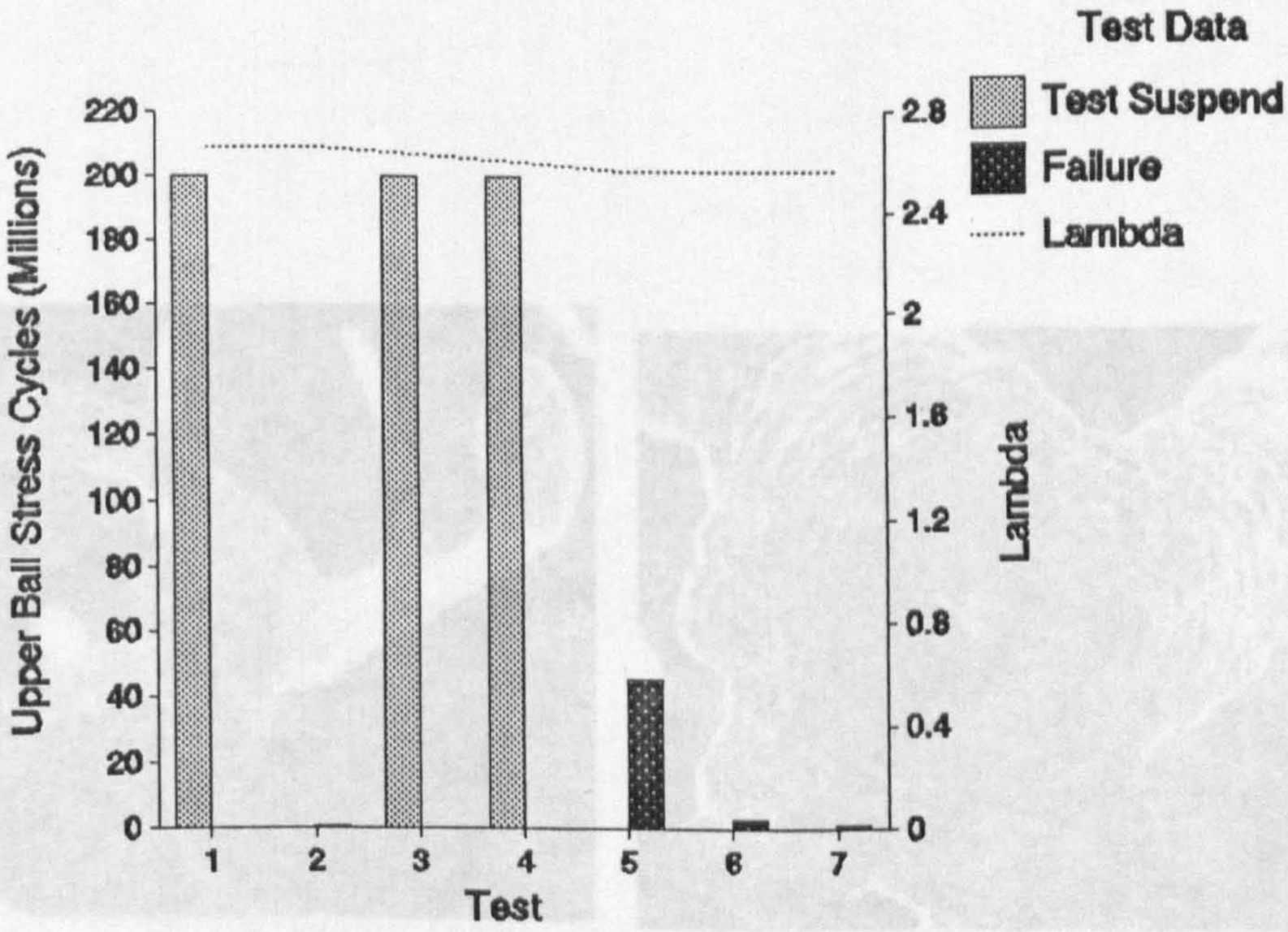

Figure 5.8 High viscosity oil lubrication results

The unusual failure of lower-ball from test two is shown as figure 5.9, captions (a) to (d). Caption (a) shows the lower-ball delamination overview, a central pit and four delamination paths are evident. The main body of the delamination is shown as caption (b). Concentric undulations from the central pit can be seen; these undulations maintain curvature and concentricity along the paths. Undulation height appears to increase at the path mouth, which suggests that energy may be a limiting factor to complete the circles. Also, theoretical analysis which considers undulation height as a function of fracture energy may describe this form of delamination failure. Caption (c) shows the central spall and secondary spall with the beginning of the undulations propagating concentrically. The central spall was measured as 36 microns deep, 100 microns top diameter and 40 microns base diameter. The delamination surface adjacent to the central pit is twenty microns from the ball surface. Dents were seen on the ball surface which is adjacent to the delaminated area, shown as caption (d). The dents illustrate that the ceramic, at these high hydrostatic pressures, behaves in a plastic deformation mode.

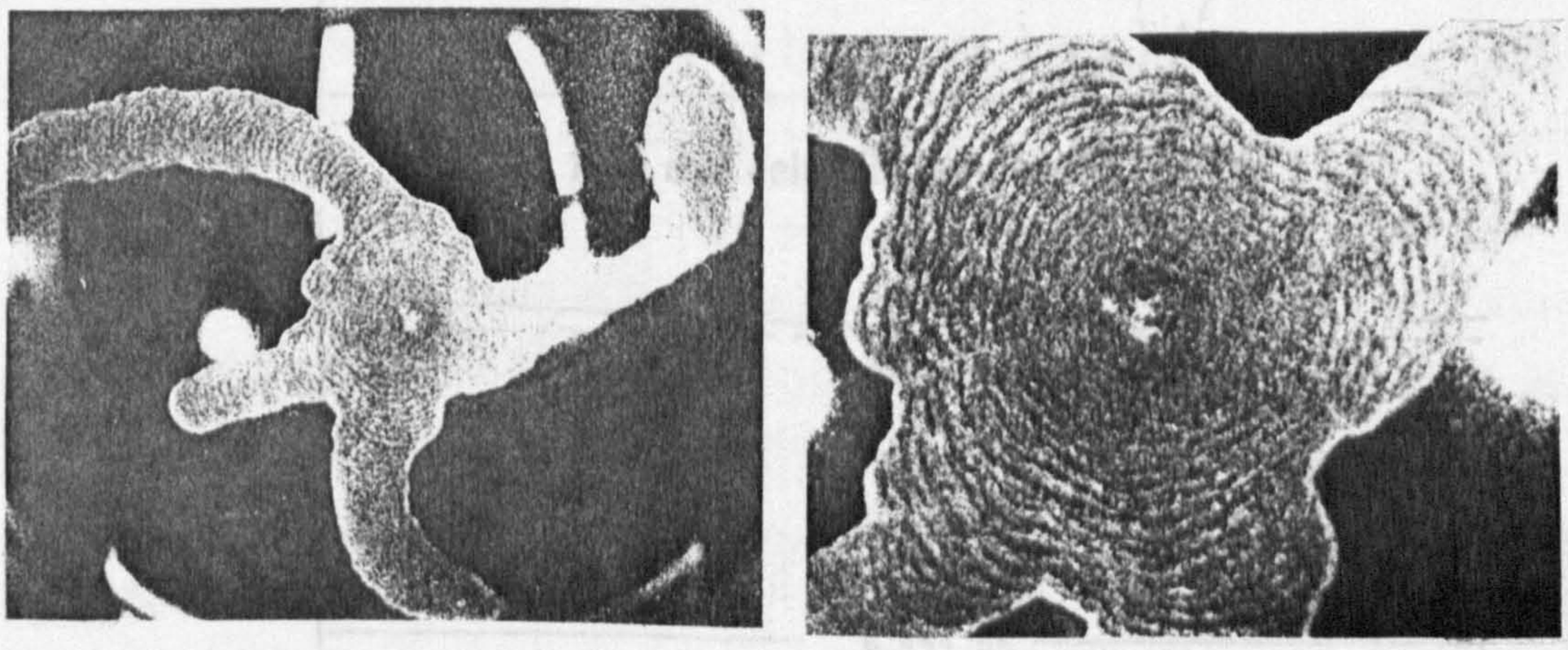

(a) Failure overview, x 7.5 **(b)** Central area, x 20

Figure 5.9 Microscopic analysis of test two lower-ball - captions (a) to (d)

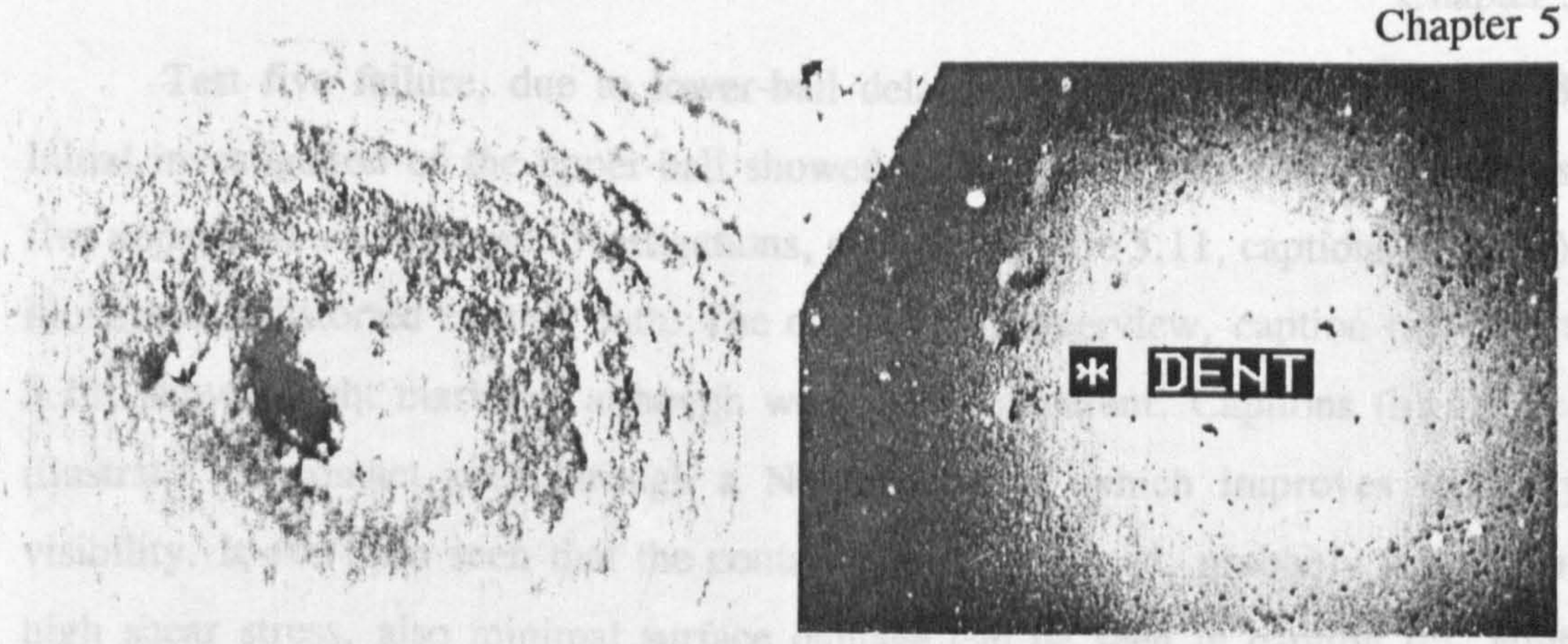

(c) Central spall and concentric undulations, x70 **(d)** Overview of dents, x70

Figure 5.9 Microscopic analysis of test two lower-ball - continued

Surface profiles of test two lower-ball delamination failure are shown as, figure 5.10, captions (a) and (b). Caption (a) shows the profile at the end of a delamination path, the tapered profile is typical for this type of area. Depth of failure is significantly greater than profiles from other lubricants. Caption (b) shows the profile across a delamination path, this reaches twenty microns depth and is, as expected, constant.

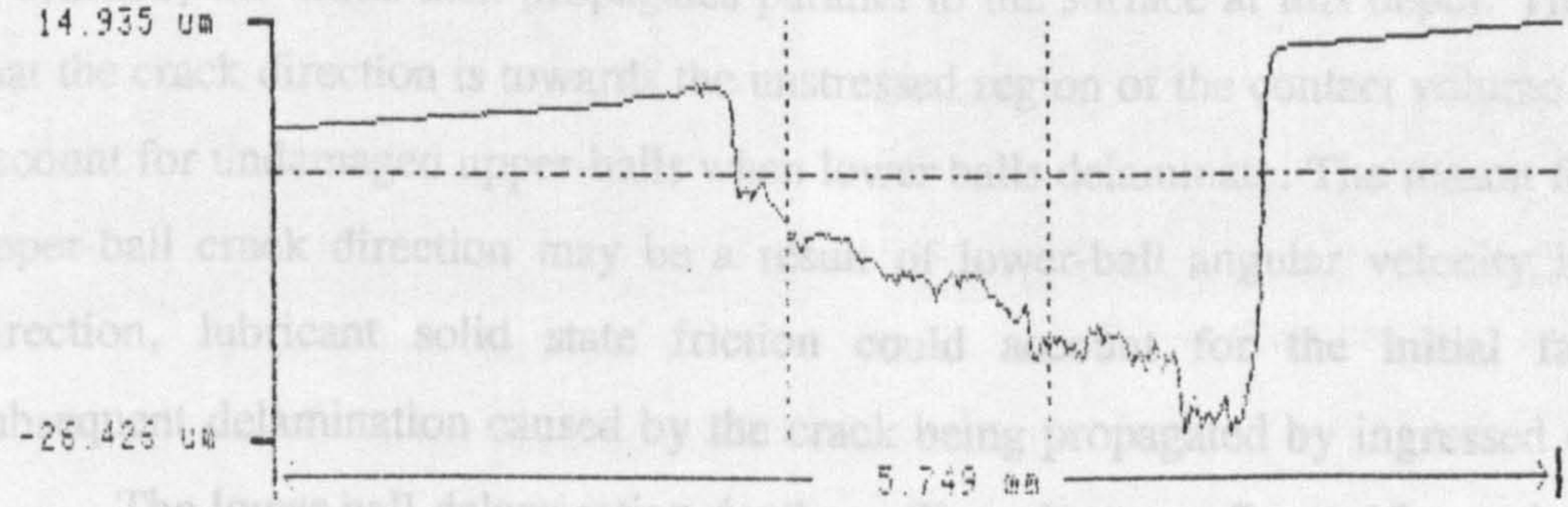

(a) Path end delamination profile

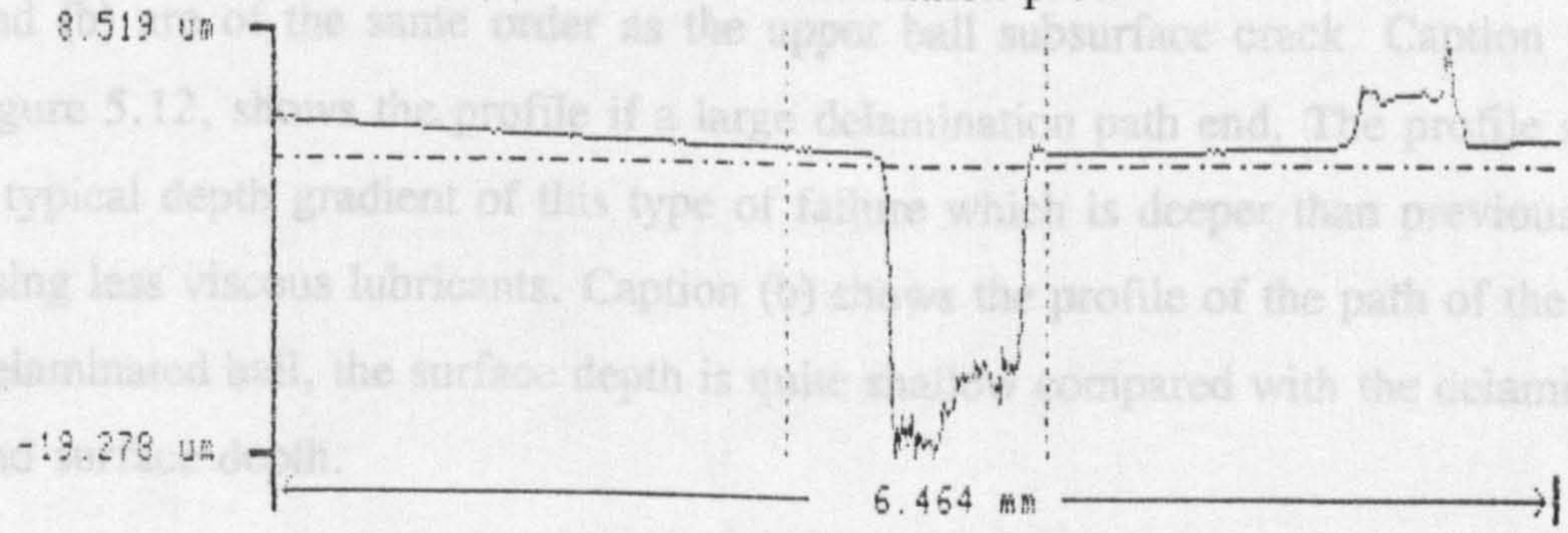

(b) Delaminated path profile

Figure 5.10 Test two lower-ball delamination profiles

Test five failure, due to lower-ball delamination, is shown in figure 5.8. Initial investigation of the upper-ball showed no apparent wear path. Further test five upper-ball microscopic investigations, shown as figure 5.11, captions (a) to (d), illustrated a distorted contact path. The contact path overview, caption (a), figure 5.11, shows slight markings although wear is not apparent. Captions (b) and (c) illustrate the contact path through a Nomarski lens, which improves topology visibility. It can been seen that the contact path is distorted, probably a result of high shear stress, also minimal surface damage can be seen in caption (c). High shear stresses are caused by subsurface contact stresses or solid state friction transmitted through the fully compressed lubricant by relative upper to lower ball surface velocity such as micro-slip.

The upper-ball was sectioned across the intact contact path, and then mounted, ground, polished and treated by the dye-penetrant process. Microscopic analysis under white and ultra violet light showed a subsurface crack which propagated from the surface at a direction, ninety degree to the contact path tangent line. The crack depth propagated into the material until a depth of twenty microns is reached, the crack then propagates parallel to the surface at this depth. The fact that the crack direction is towards the unstressed region of the contact volume could account for undamaged upper-balls when lower balls delaminate. The reason for the upper-ball crack direction may be a result of lower-ball angular velocity in this direction, lubricant solid state friction could account for the initial failure, subsequent delamination caused by the crack being propagated by ingressed oil.

The lower ball delamination depth profiles, shown as figure 12, captions (a) and (b) are of the same order as the upper ball subsurface crack. Caption (a) of figure 5.12, shows the profile if a large delamination path end. The profile shows a typical depth gradient of this type of failure which is deeper than previous tests using less viscous lubricants. Caption (b) shows the profile of the path of the same delaminated ball, the surface depth is quite shallow compared with the delaminated end surface depth.

Chapter 5

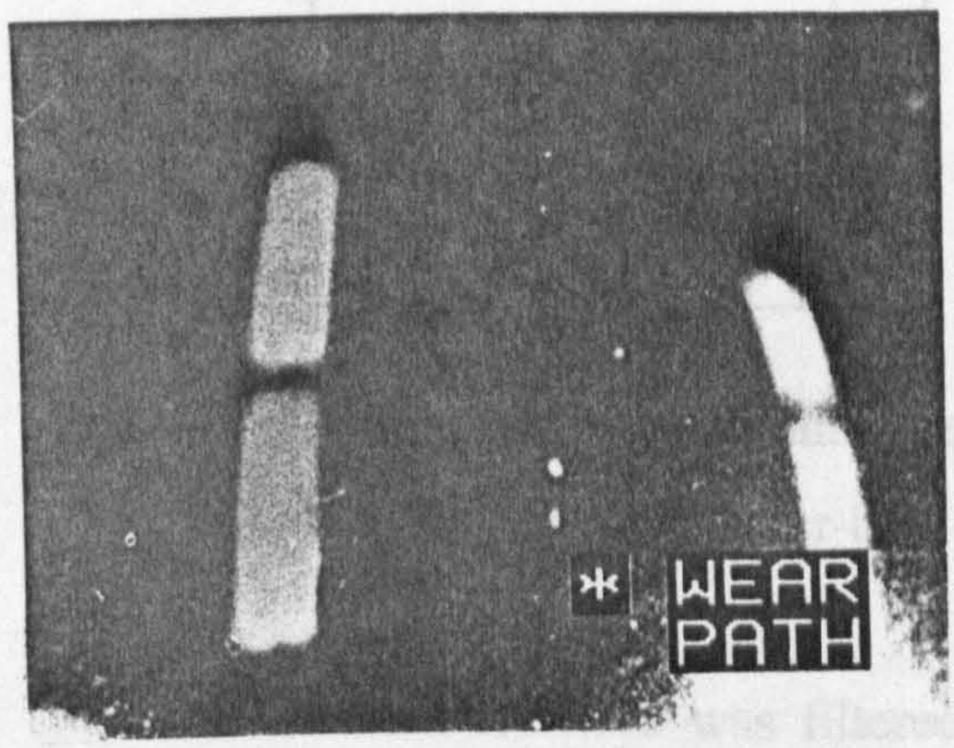

(a) Contact path overview, x 15

(b) Contact path detail, x 70

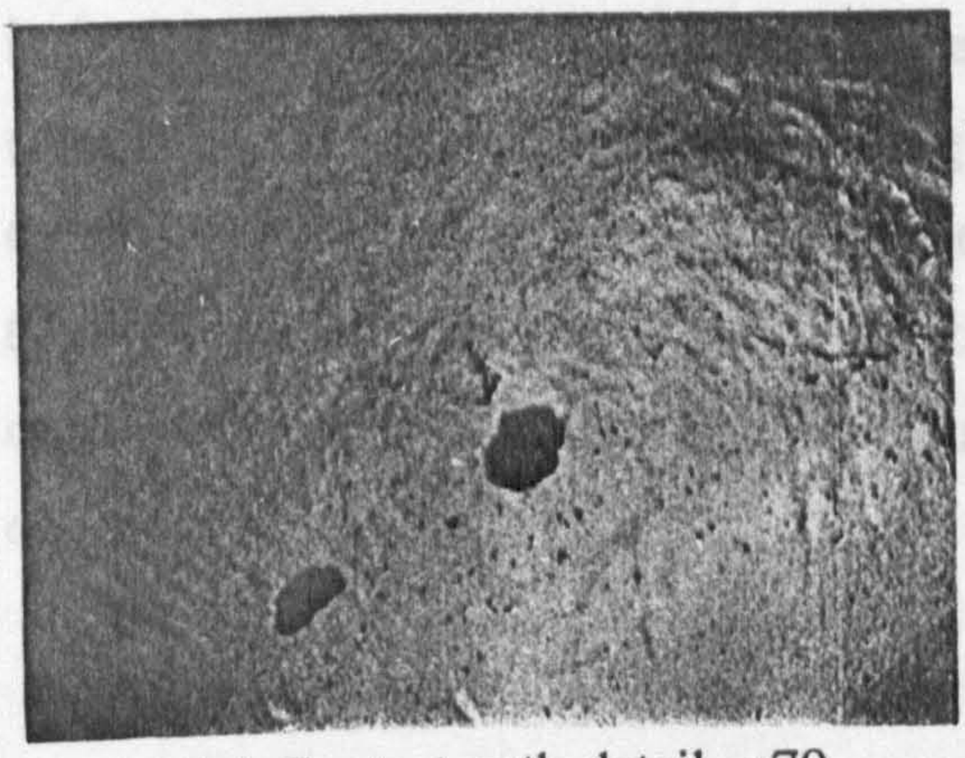

(c) Contact path detail, x70

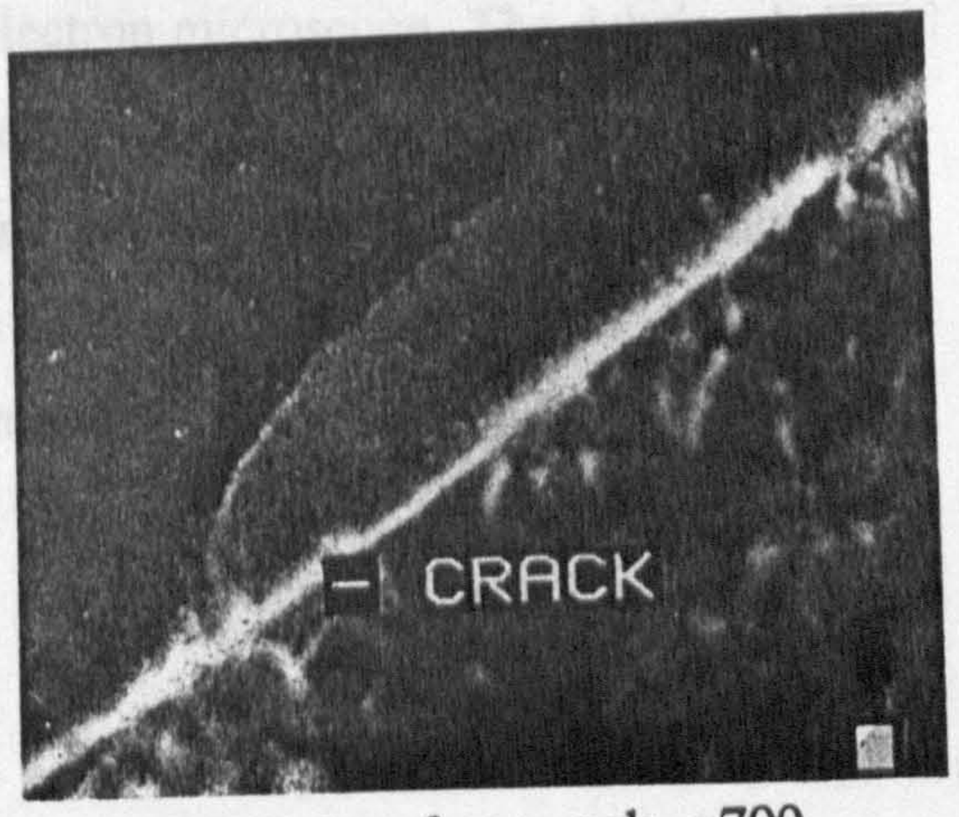

(d) Subsurface crack, x700

Figure 5.11 Microscopic analysis of test five upper-ball - captions (a) to (d)

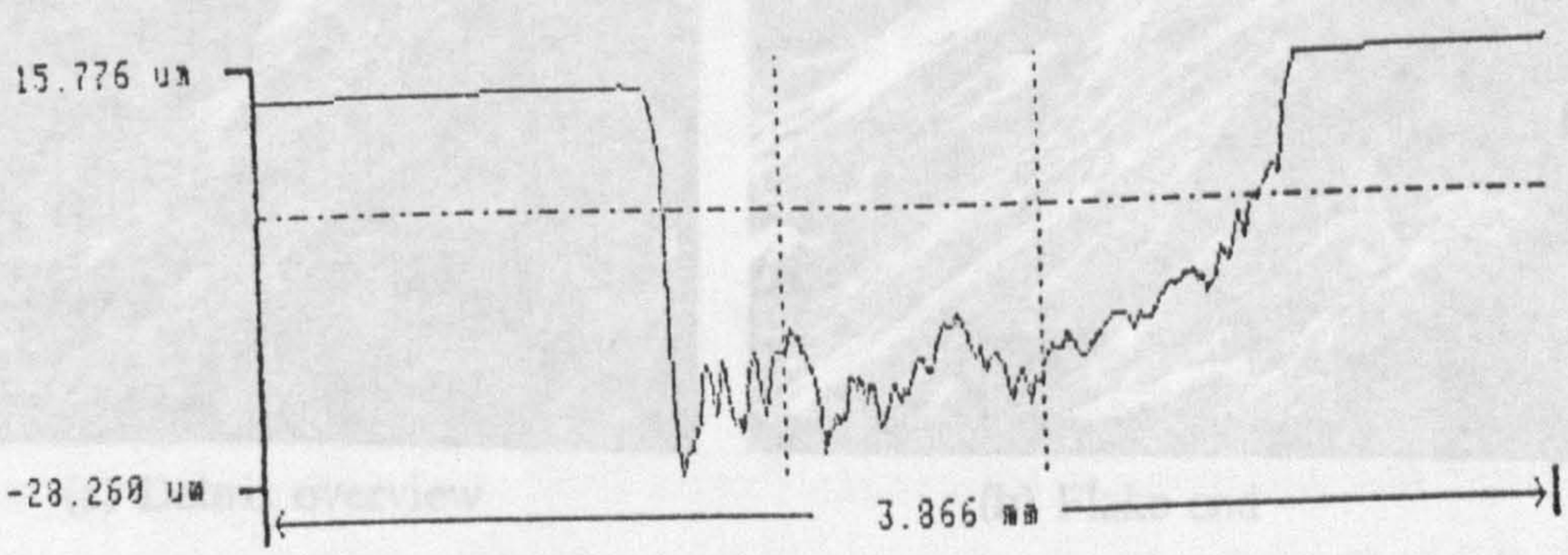

(a) Path end delamination profile

Figure 5.12 Test five lower-ball delamination profiles - captions (a) and (b)

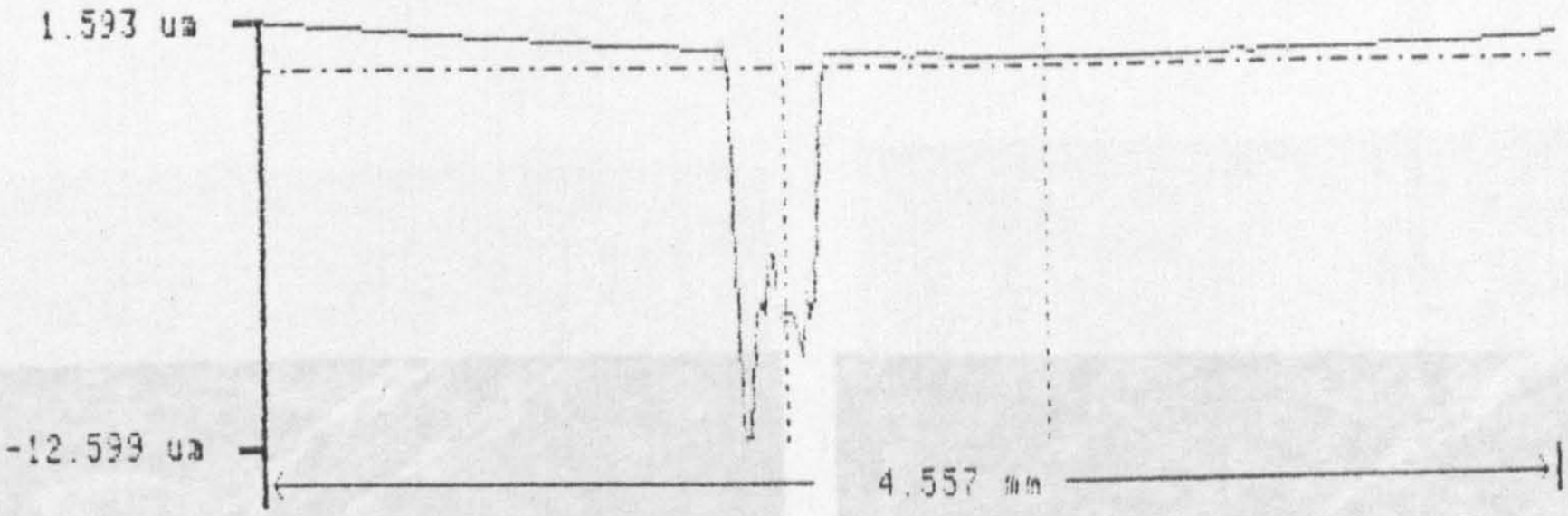

(b) Delaminated path profile

Figure 5.12 Test five lower-ball delamination profiles - continued

Debris from test five was filtered from the lubricant and microscopically inspected. A particularly large piece of debris was chemically cleaned, mounted on adhesive tape and viewed using a scanning electron microscope. The debris, shown in figure 5.13, captions (a) to (d) is from a delaminated ceramic lower-ball. Caption (a) shows the flake overview measuring one hundred by five hundred microns. Caption (b) shows the deformed ends of the flake edge. Captions (c) and (d) show the flake surface texture with features characteristic for brittle fracture. Observations of this large particle suggest brittle fracture although isolated parts of it may have deformed plastically.

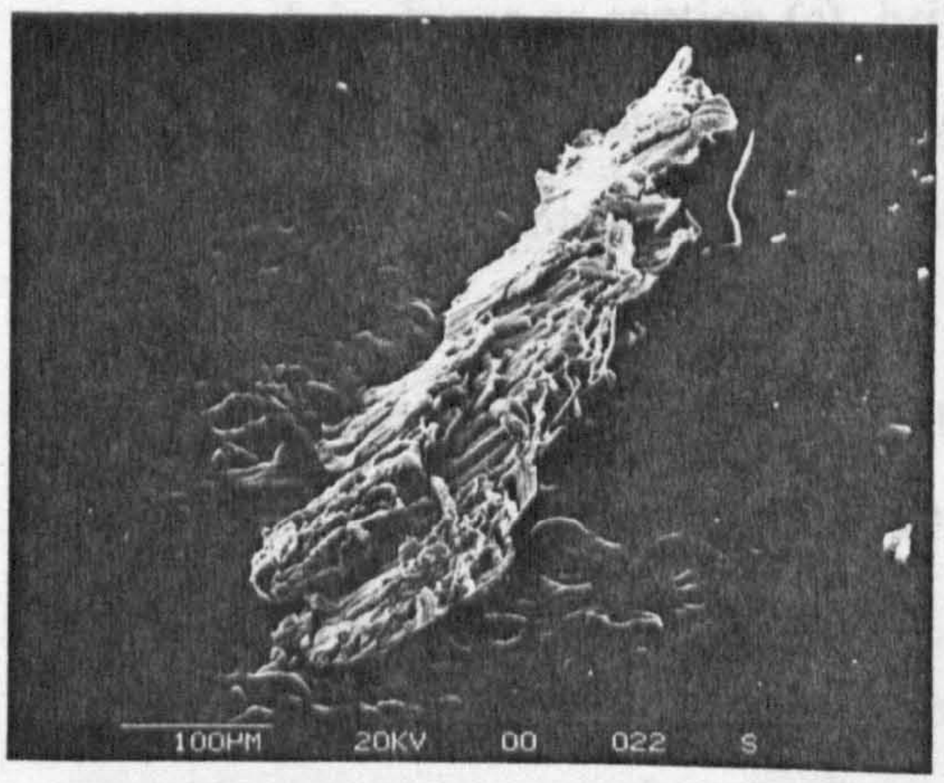

(a) Debris overview

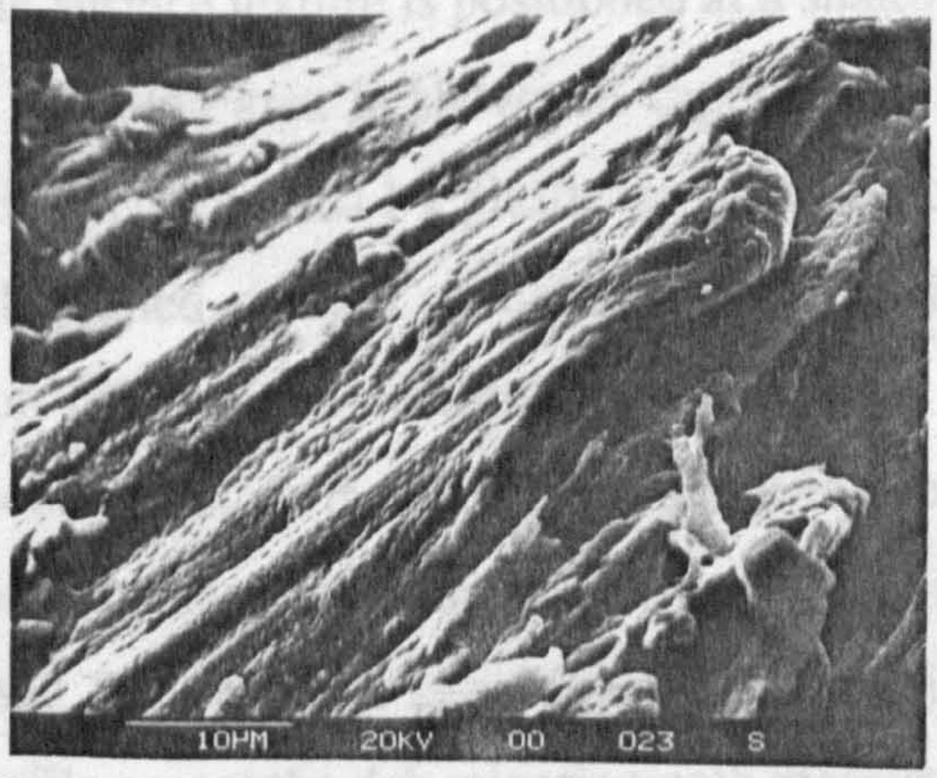

(b) Flake end

Figure 5.13 Micrographs of ball five ceramic debris - captions (a) to (d)

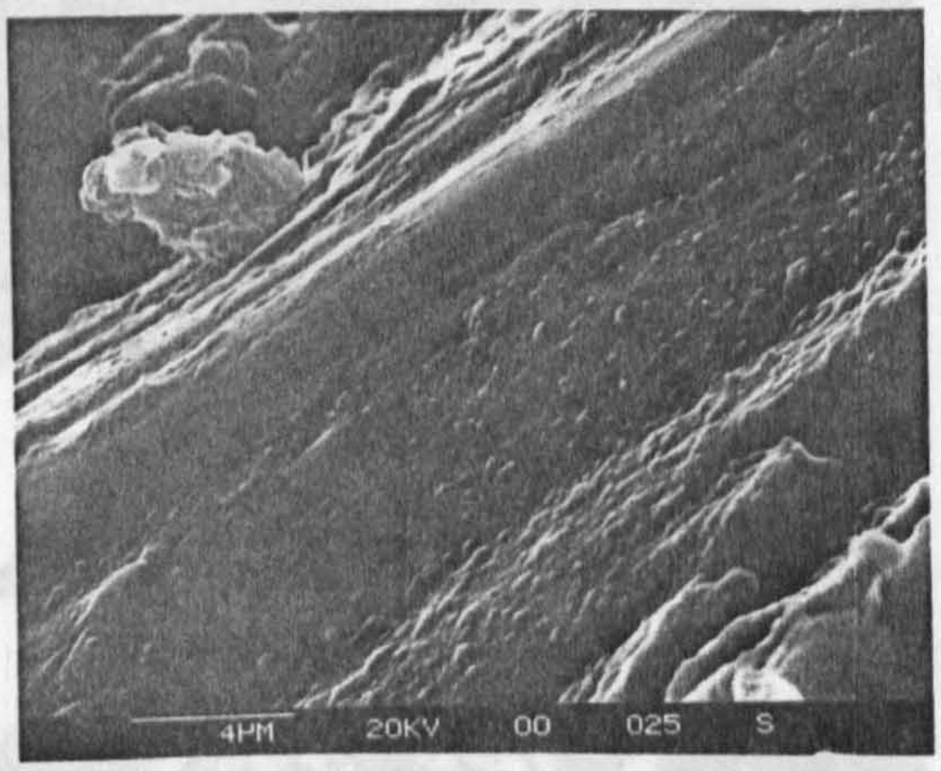

(c) Debris surface texture

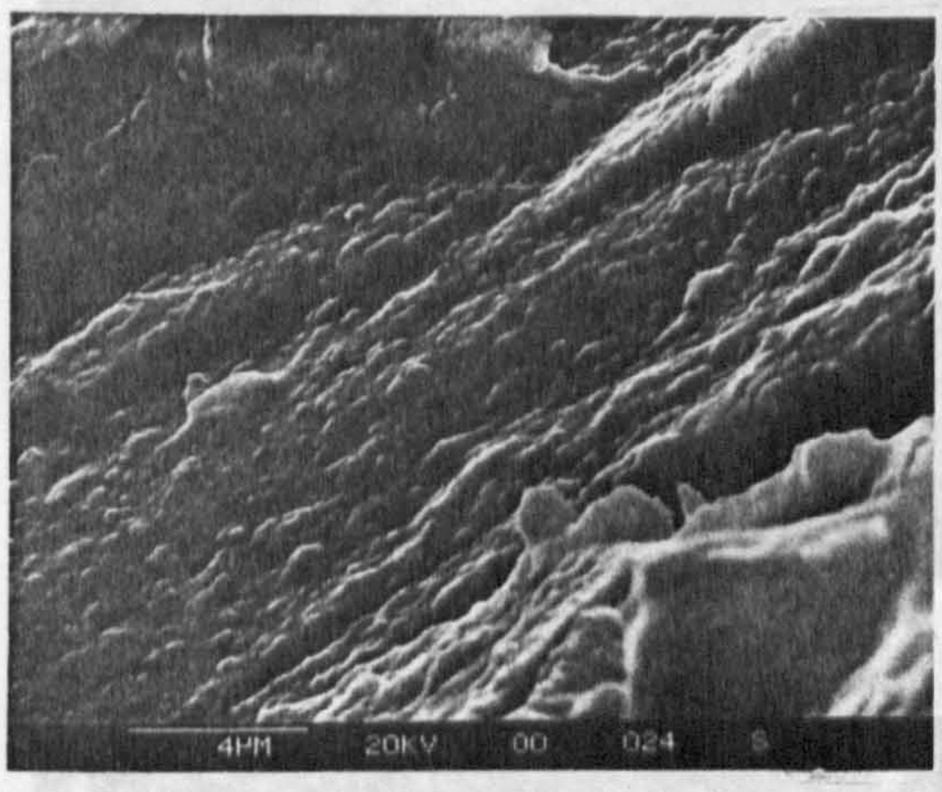

(d) Debris surface texture

Figure 5.13 Micrographs of ball five ceramic debris - continued

Delamination of the lower-ball from test six is microscopically analyzed, shown ad figure 5.14, captions (a) to (f). This lower ball delamination is a narrow path shape which concludes with a larger heart shape. Caption (a) shows the overview of the narrow path on the ball surface, caption (b) shows the heart shaped conclusion of the delaminated surface. The start of failure leading to the initial narrow path is shown as caption (c), brittle surface texture is positioned at a shallow depth from the ball surface. The brittle initiation area is shown in caption (c), is followed by a delamination along the path. Dents caused by plastic deformation on the ball surface is evident adjacent to the failed surface. A detailed view of the brittle initiation area is shown as caption (d), smooth surface and intact edge is visible. At the delamination heart shape conclusion, surface texture and failure depth is visible from caption (e). Edge detail of the delaminated area is shown as caption (f), micro-cracks are visible and increased failure depth is evident which implies subsurface crack propagation. Surface profile across the delamination path measured a depth of twenty microns, which is of the same order as other failures of this high viscosity oil test series.

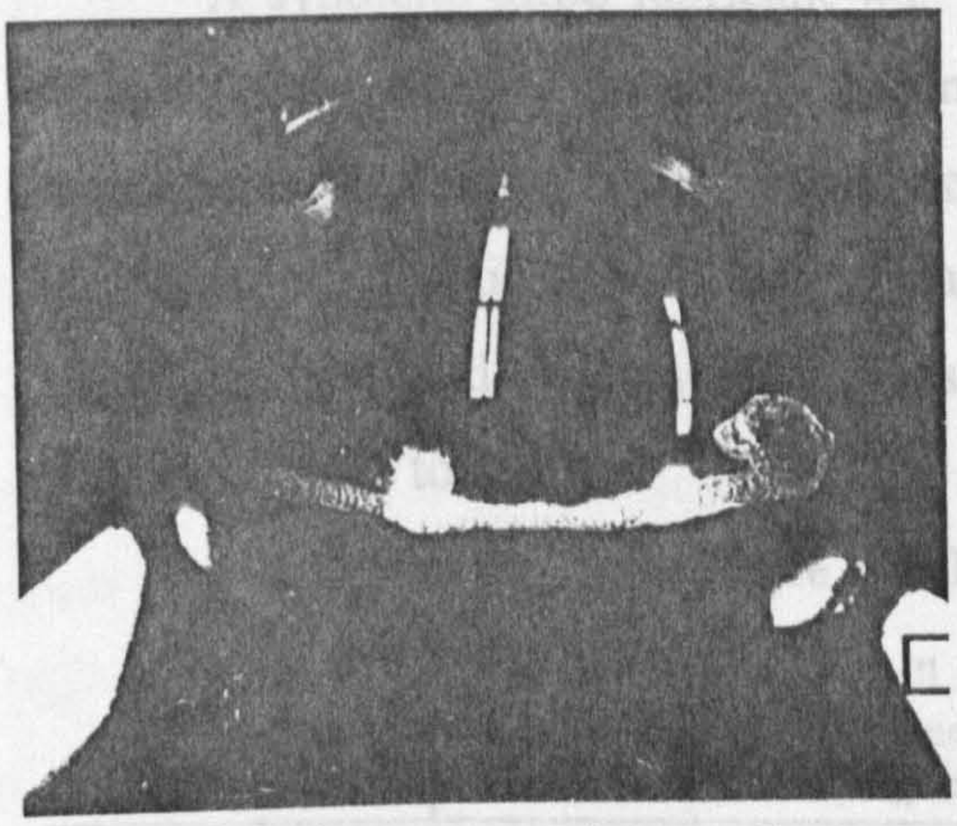

(a) Failure overview, x 5

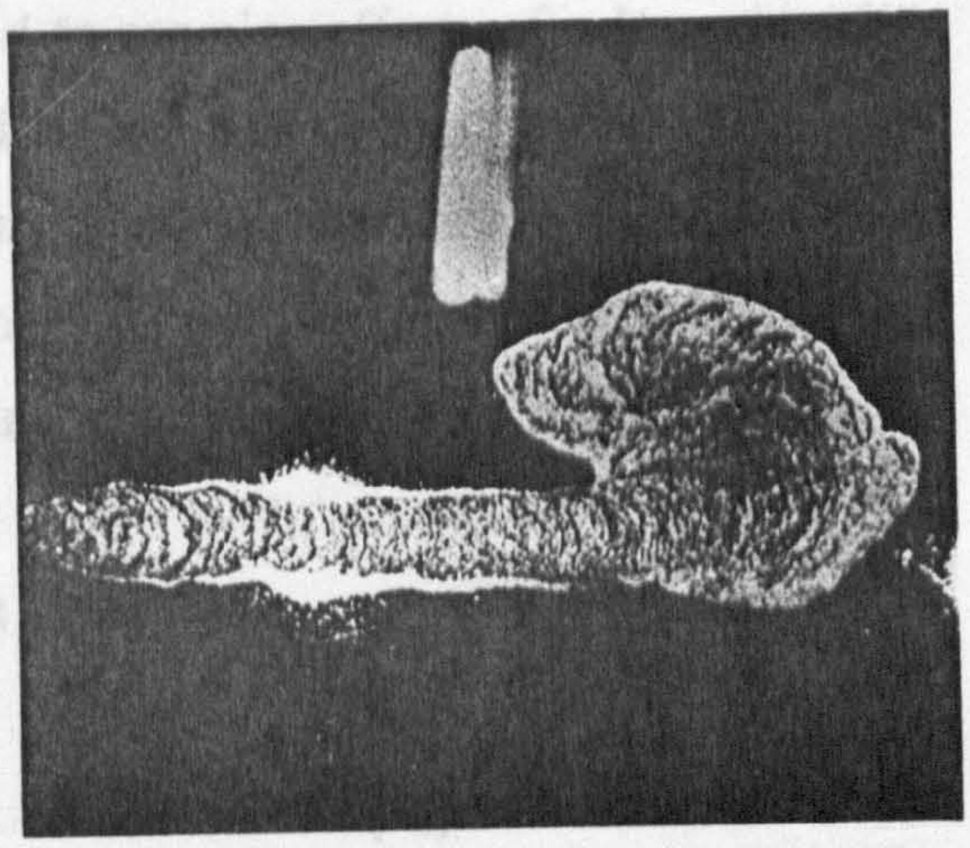

(b) Heart shape conclusion, x 15

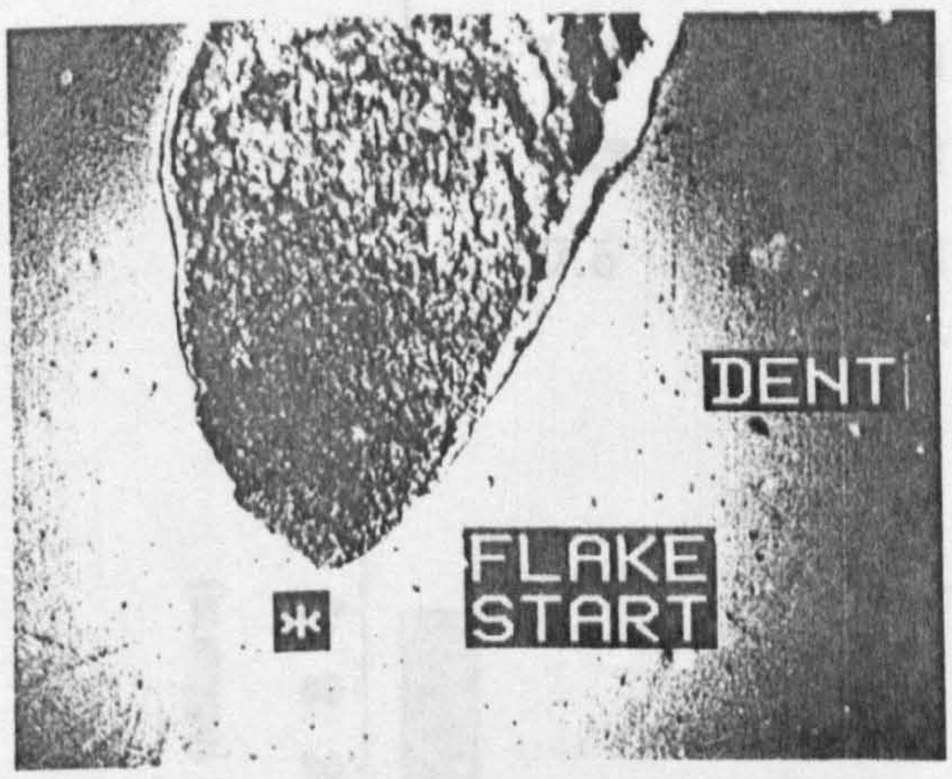

(c) Brittle failure initiation, x70

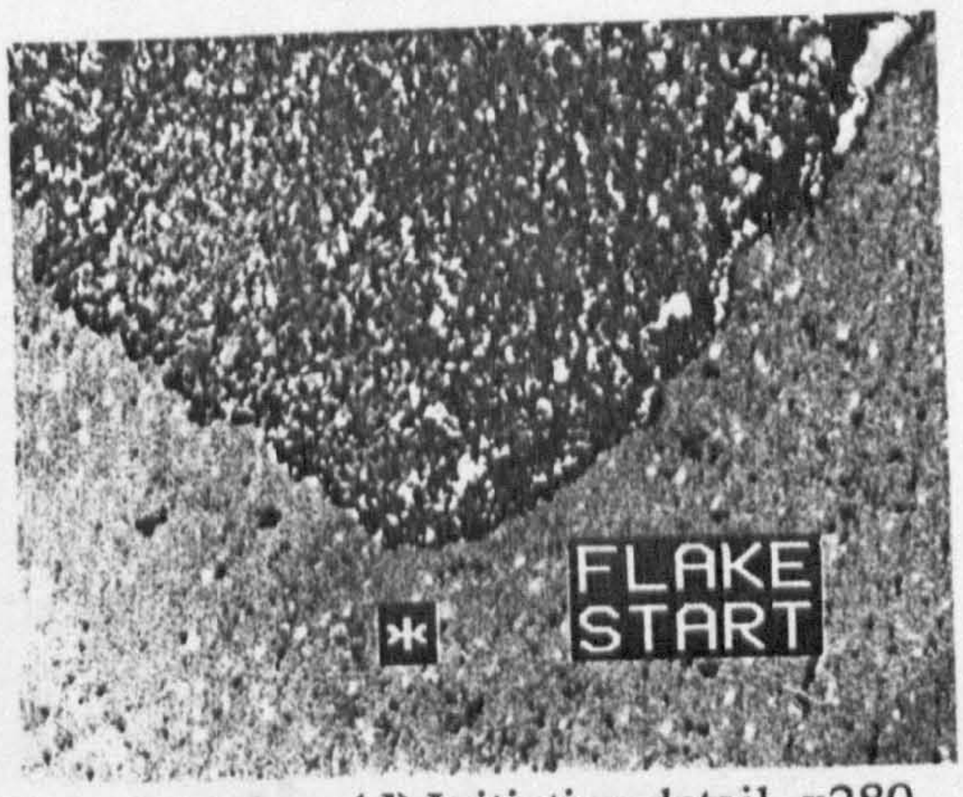

(d) Initiation detail, x280

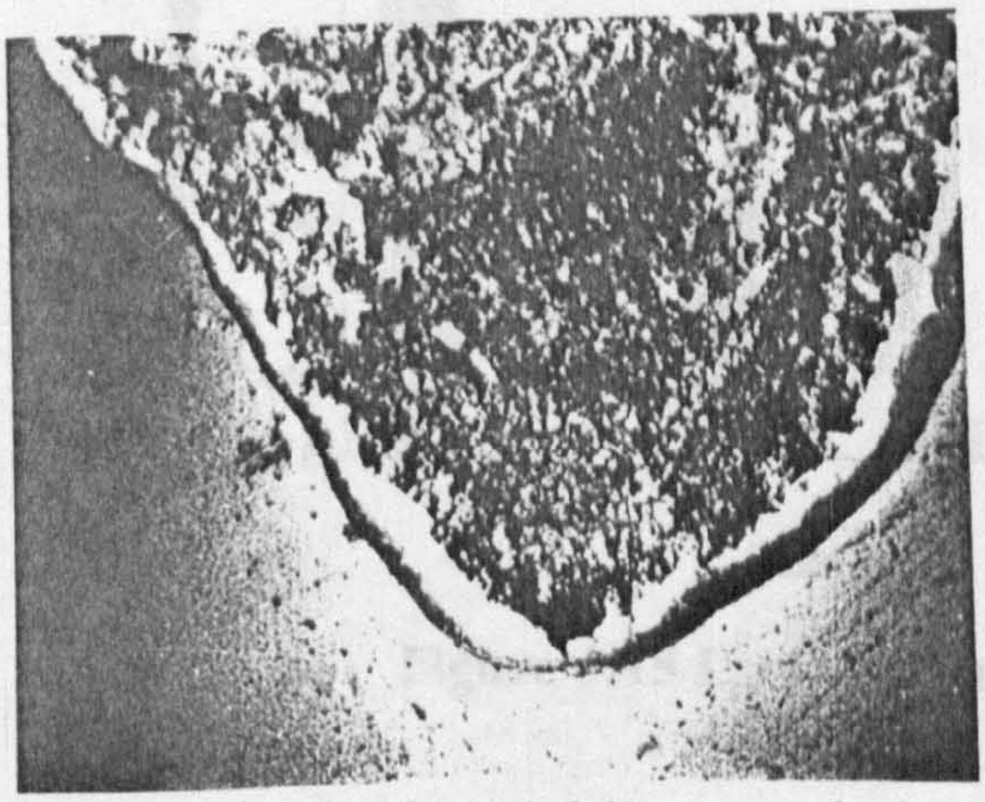

(e) Delaminated failure conclusion, x70

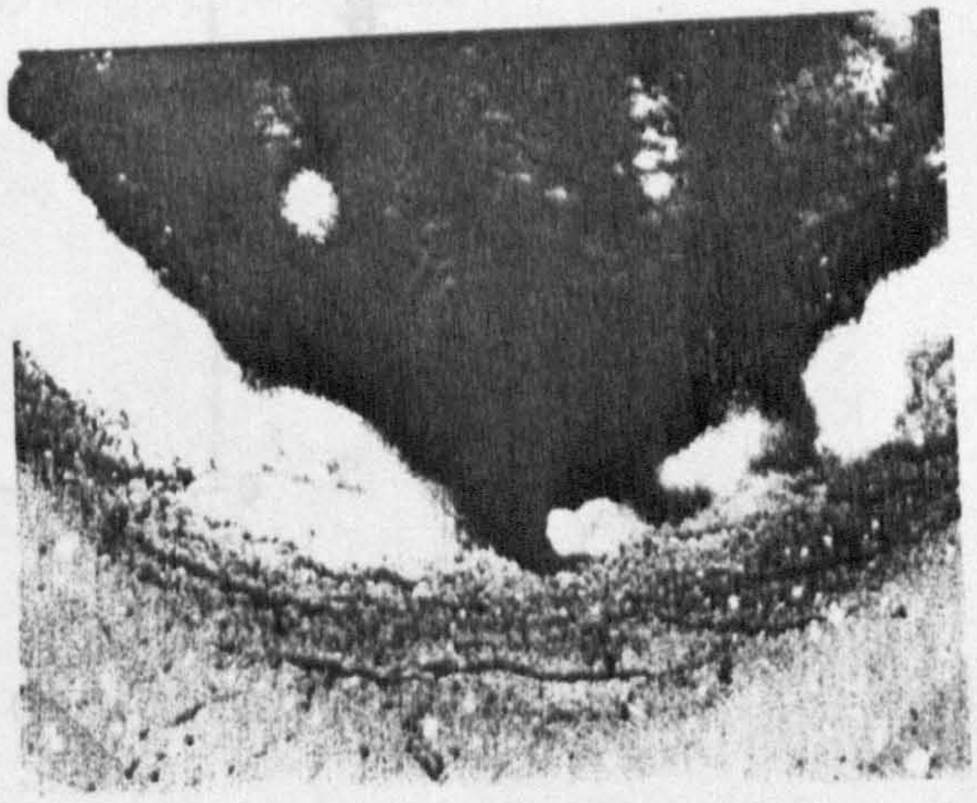

(f) Conclusion detail, x280

Figure 5.14 Microscopic analysis of test six lower-ball - captions (a) to (f)

5.1.4 Low Viscosity Oil Lubrication

A synthetic turbo lubricant was used to examine effects of a low viscosity oil on fatigue failure modes. Test conditions are described in table 5.4. Initial maximum compressive stress in test one was reduced to the value used in standard lubricant tests, section [5.1.2]. In remaining four tests the maximum compressive stress was gradually increased and resulting final temperatures reflect the stress levels and time to failure.

Table 5.4 Test Conditions

Test (10000 r.p.m.)	Maximum Compressive Stress (GPa)	Ball Roughness (Ra,μm)	Material	Final Temperature (°C)	Lubricant
1	7.1	0.008	UB	64	Exxon 2389
2	7.35	0.008	UB	68	Exxon 2389
3	7.48	0.008	UB	68	Exxon 2389
4	7.6	0.008	UB	66	Exxon 2389

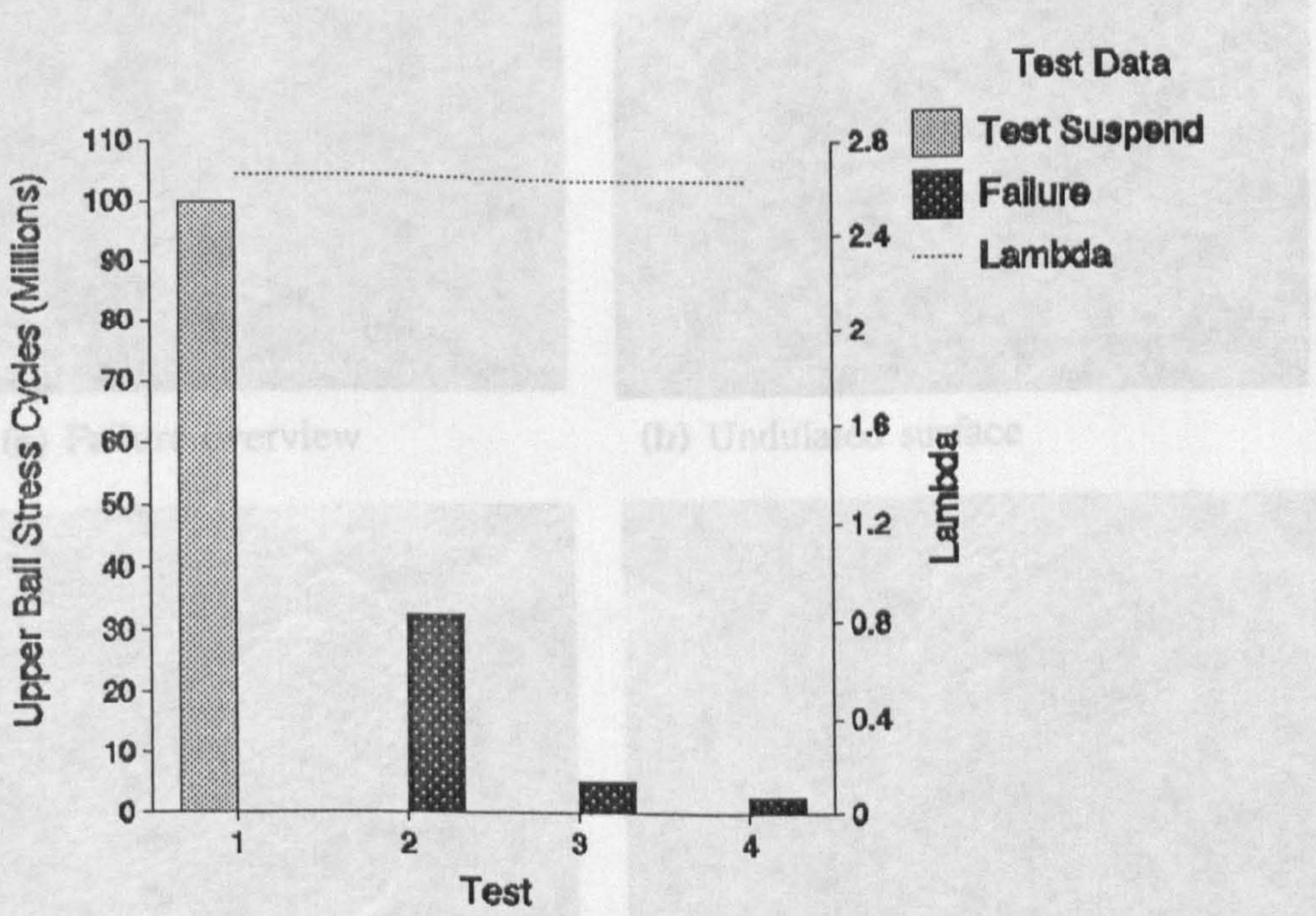

Figure 5.15 Low viscosity oil lubrication results

Results from ceramic/ceramic contact using the low viscosity lubricant are shown as figure 5.15. Test one was suspended after one hundred million upper-ball

stress cycles. No wear damage occurred to the upper or lower balls. Test two was stopped after over thirty million cycles with one lower ball delamination. Tests three and four were also terminated fail due to lower-ball delamination.

Lower-ball delamination produced in test two is analysed using a scanning electron microscope, (see figure 5.16, captions (a) to (d)). Caption (a) shows the failure overview which is of a heart shape with varying surface texture. The delaminated area is shown as caption (b), hardness indentation marks are visible, from which it is concluded that hardness remains constant on all intact and failed ball surfaces. The transition boundary from undulated fatigue surface to brittle surface is shown as caption (c). Smooth brittle surfaces may be seen in caption (d), at the top of the heart shape delamination.

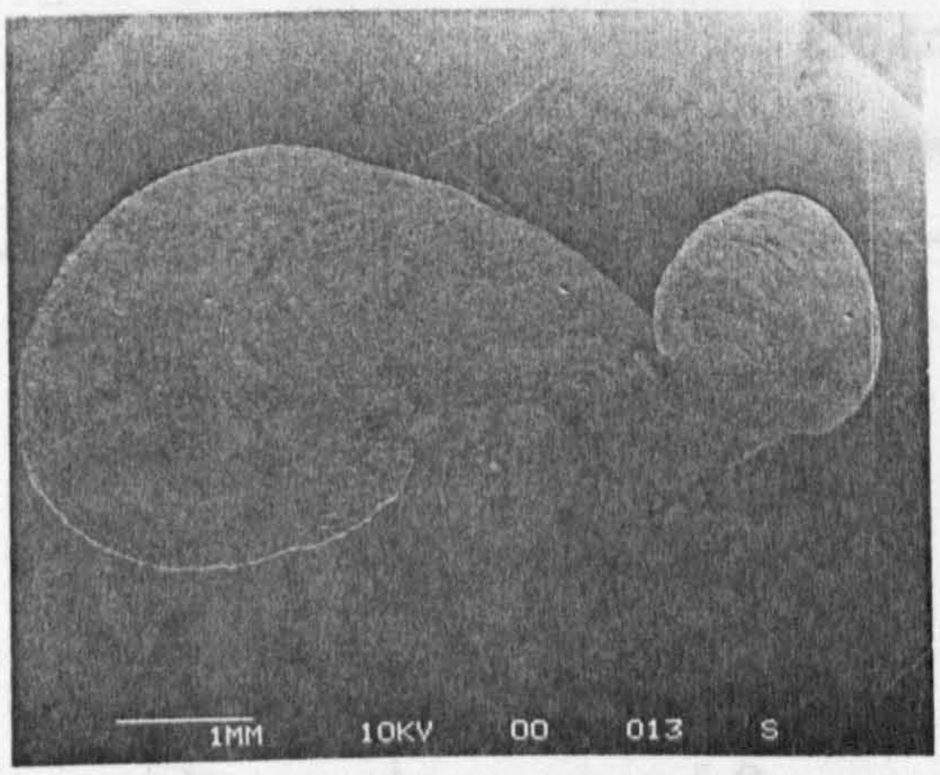

(a) Failure overview

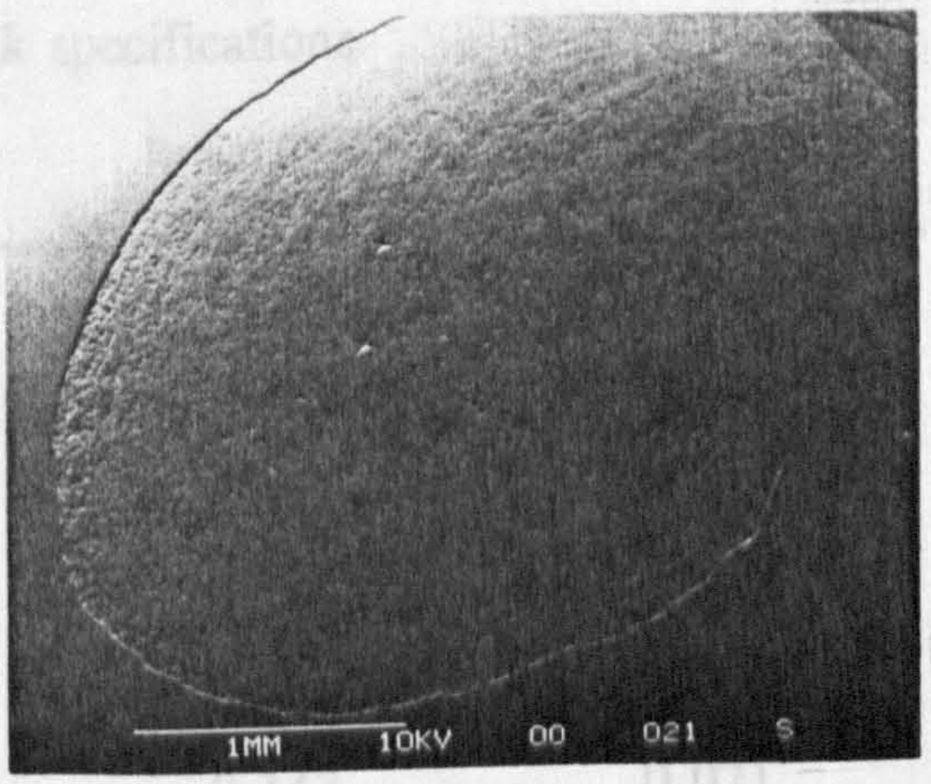

(b) Undulated surface

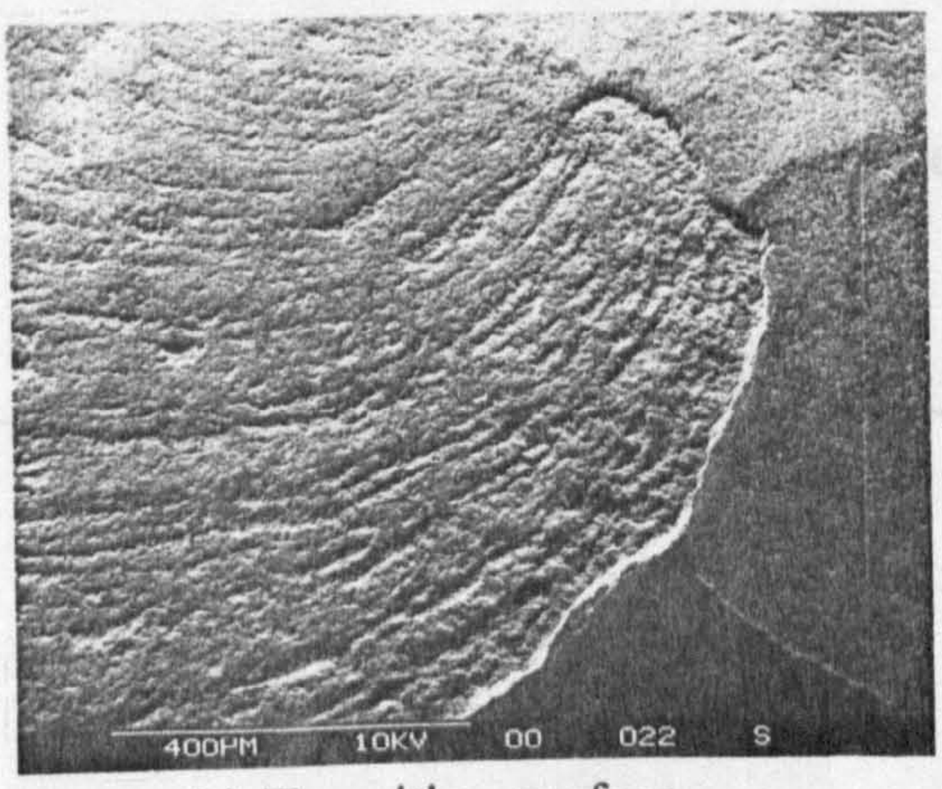

(c) Transition surface

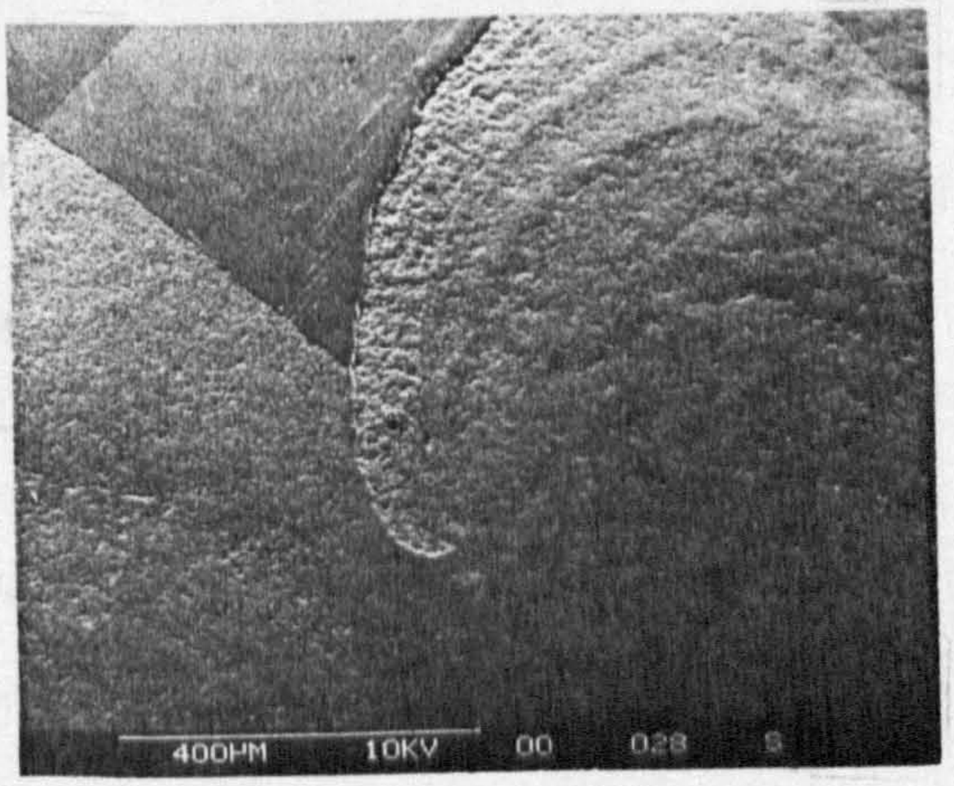

(d) Brittle surface

Figure 5.16 Micrographs of test two lower ball failure - captions (a) to (d)

5.2 Pre-Cracked Silicon Nitride Ball Tests

5.2.1 Crack Initiated By Sharp Indentor - Preliminary Experiments

Preliminary tests on artificially cracked ceramic balls, detailed in table 5.5, were tested. Radial crack and impression diagonal lengths are specified for each test ball in the table. In the case of test balls 'A' and 'B' it is significant that for small indentation loads, radial cracks are not present, implying plastic deformation. Test conditions are detailed in table 5.6, one upper steel ball contacts with three lower ceramic balls to simulate a hybrid ball-bearing. Test balls of varying damage were investigated keeping other test parameters constant to assess sensitivity of performance to crack length.

Table 5.5 Pre-crack specifications

Test Ball	Vickers hardness Indentation Load (kg)	Radial Crack Length (mm)	Impression Diagonal (mm)
A	0.5	N/A	0.023
B	0.5	N/A	0.023
C	2.5	0.103	0.053
D	2.5	0.100	0.053
E	5.0	0.150	0.071
F	5.0	0.143	0.071

Table 5.6 Test conditions

Test (5000 r.p.m.)	Maximum Compressive Stress (GPa)	Test Ball	Material: Steel Upper / Silicon Nitride Lower	Final Temperature (°C)	Lubricant
1	6.4	A, C, E	SKF3/UB	80	Exxon 2389
2	6.4	B, D, F	SKF3/UB	80	Exxon 2389

Results from preliminary tests are presented in figure 5.17. Apparent test failure mode is steel upper ball fatigue spall after reasonably long test times. Lubricant temperature in both tests reaches an equilibrium value before failure.

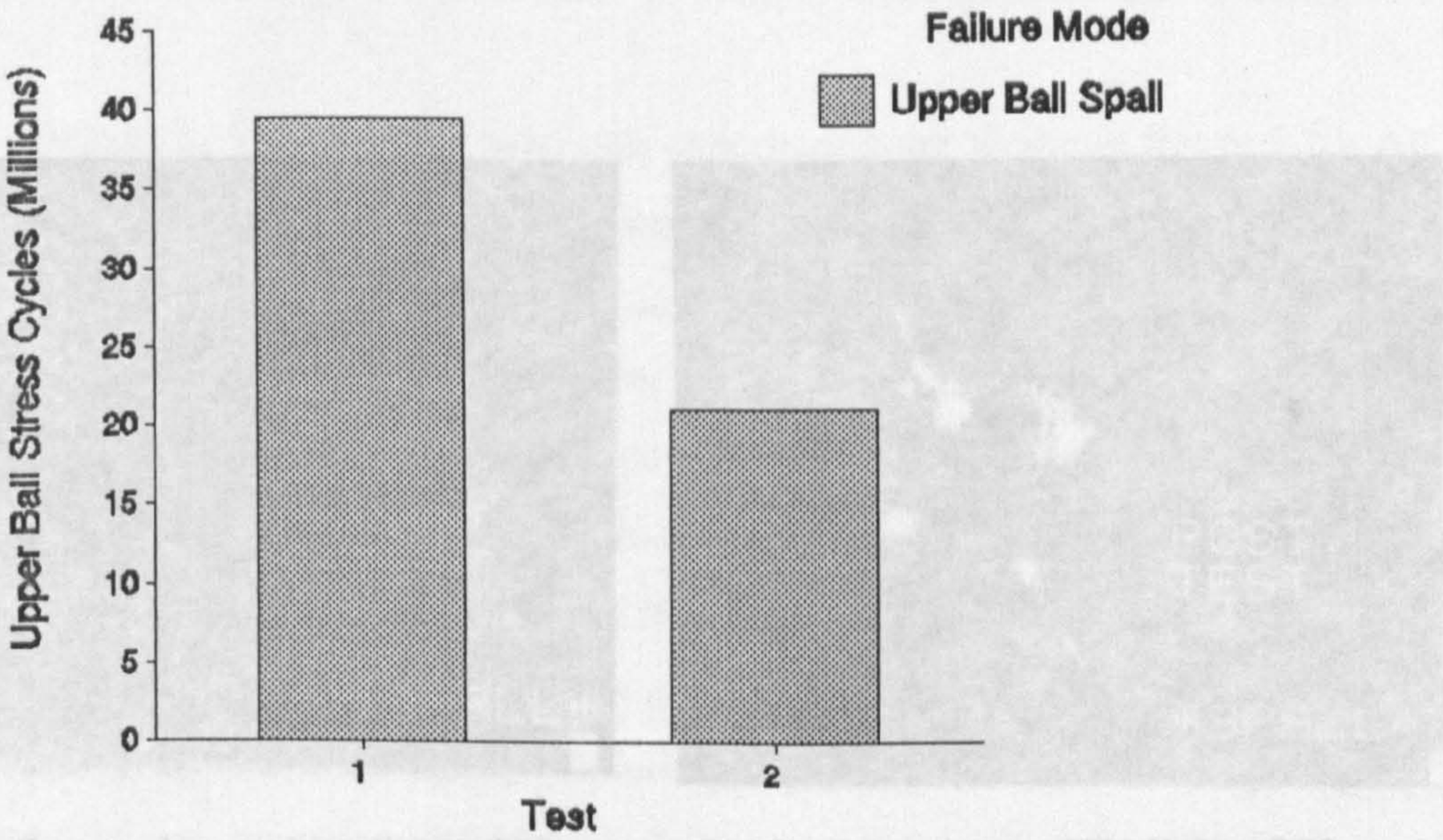

Figure 5.17 Sharp indentor preliminary results

Post test analysis of the ceramic balls revealed that damage occurred although test ceased upon the steel upper-ball spalling. Figure 5.18 shows photographs of ball 'F' under white and ultra violet light microscopy. This figure can be compared with the pre-test appearance of this ball, figures 4.6 and 4.7, in chapter four. Figure 5.19 shows micrographs of ball 'F' illustrating a partial spall and radial crack damage near the spall root. Measurement of post-test radial crack length revealed zero crack growth.

Detailed micro-analysis of all pre-cracked balls revealed that ball 'F' was the only partially spalled indentation. It is possible that ceramic debris from ball 'F' may have affected the steel upper-ball cycles to failure. After analyzing ball 'E', some evidence of crack delamination emerged from subsurface illumination adjacent to radial cracks.

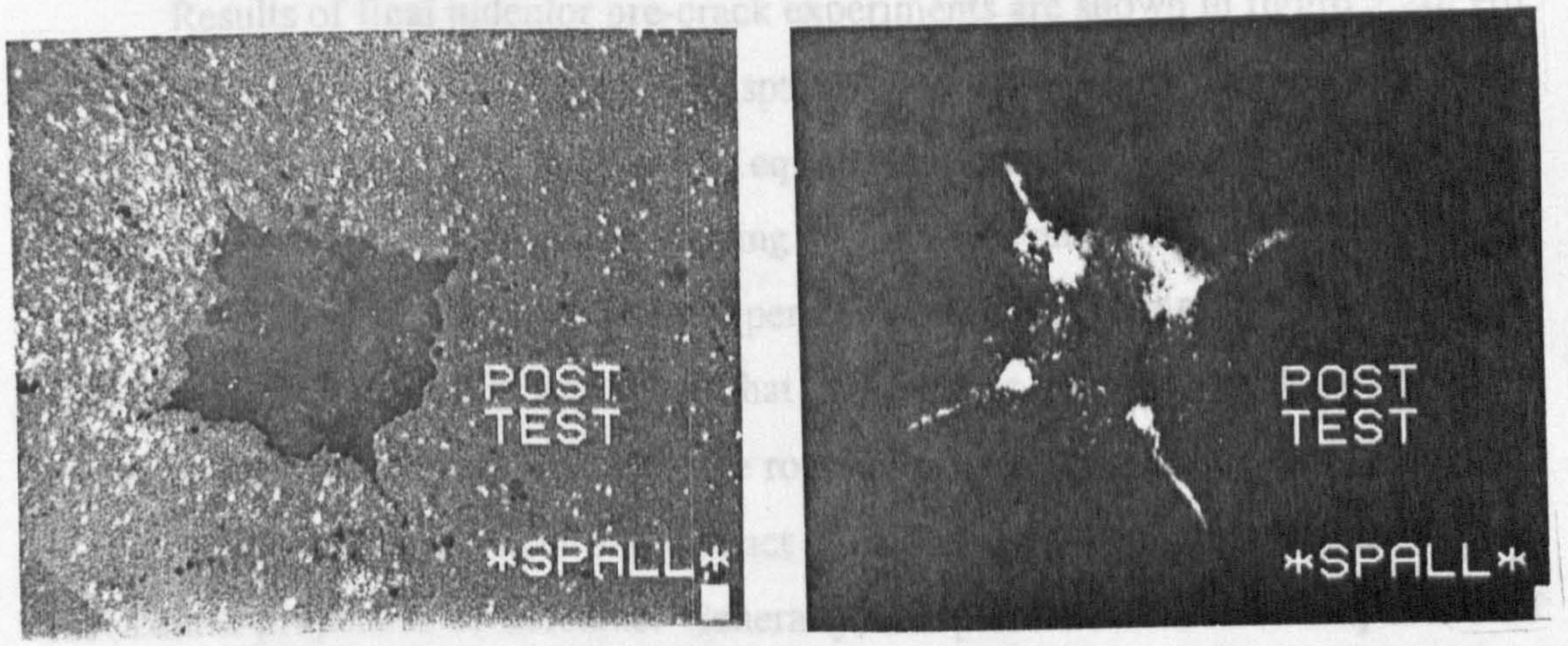

(a) Spall overview, white light x280 **(b)** Spall overview, UV light x280

Figure 5.18 Photograph of point pre-crack spall (Ball 'F')

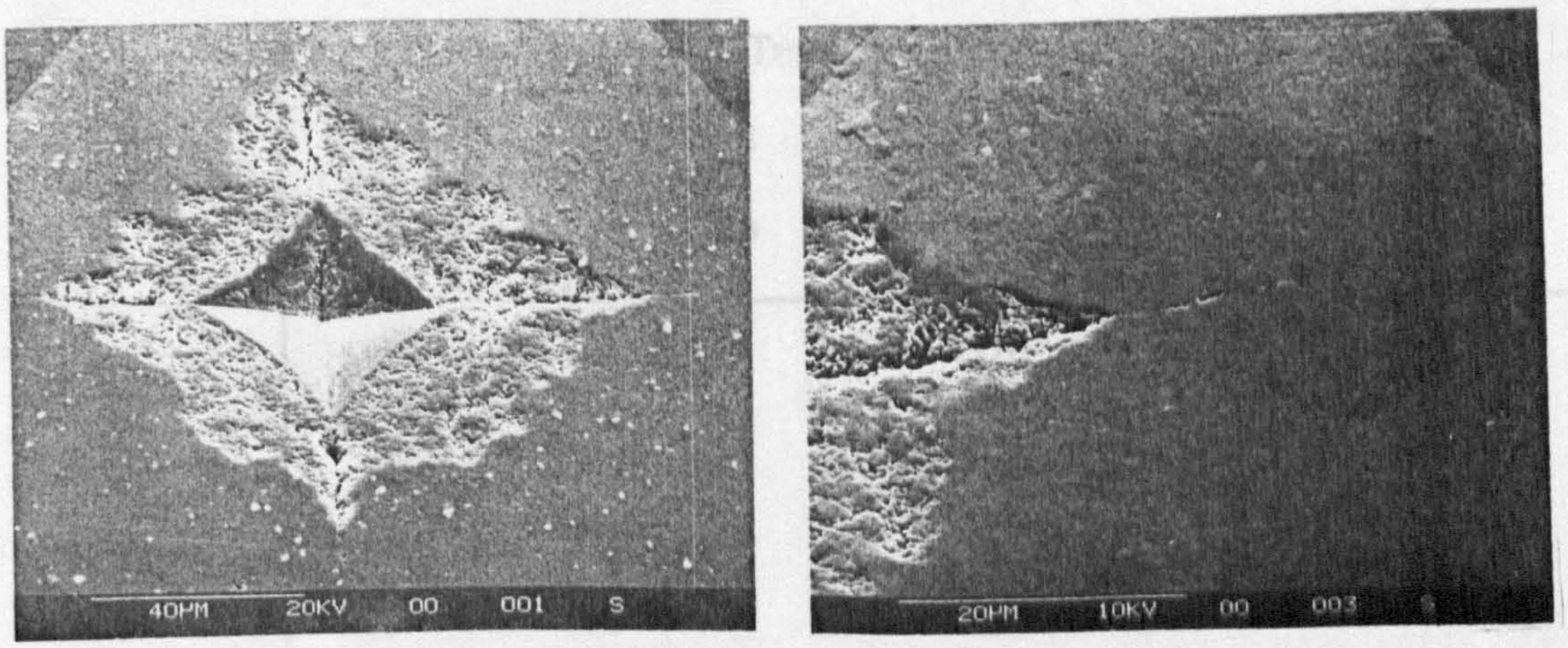

(a) Spall overview **(b)** Right radial crack

Figure 5.19 Micrograph of point pre-crack spall (Ball 'F')

5.2.2 Pre-Crack Initiated By Sharp Indentor - Final Experiments

Following preliminary results, lower-ball indentation load was set to 5 kg for all tests (see table 5.7). Each lower-ball was artificially cracked by nine equally spaced clusters of four indents. This spacing insures upper to lower-ball contact on damaged areas. Three lubricants: high viscosity, low viscosity and low surface energy, were used with constant load, to identify their possible effect on failure mode.

Results of final indentor pre-crack experiments are shown in figure 5.20. All tests were stopped when upper-ball spalled due to contact fatigue. Final test temperature (see table 5.7) implies that equilibrium conditions were reached during test one only while it was still increasing in tests two and three. Preliminary post test analysis showed that lower-ball experienced damage during test one and two. After close examination it was found that some minor damage may have occurred on the lower-balls of test three. Surface roughness of lower ceramic balls increased in test three; also upper steel ball contact path was worn. This reflects the limited lubrication properties of kerosine. Generally, the presence of debris suspended in the lubricant may be responsible for relatively short steel ball fatigue life, although it can be seen that the high viscosity lubricant which was used in test one restricts ball damage.

Table 5.7 Test conditions

Test (5000 r.p.m.)	Maximum Compressive Stress (GPa)	Lower Ball Hardness Indentation (kg)	Material: Steel Upper / Silicon Nitride Lower	Final Temperature (°C)	Lubricant
1	6.4	5.0	SKF3/UB	75	HiTec 174
2	6.4	5.0	SKF3/UB	40	Exxon 2389
3	6.4	5.0	SKF3/UB	48	Kerosine

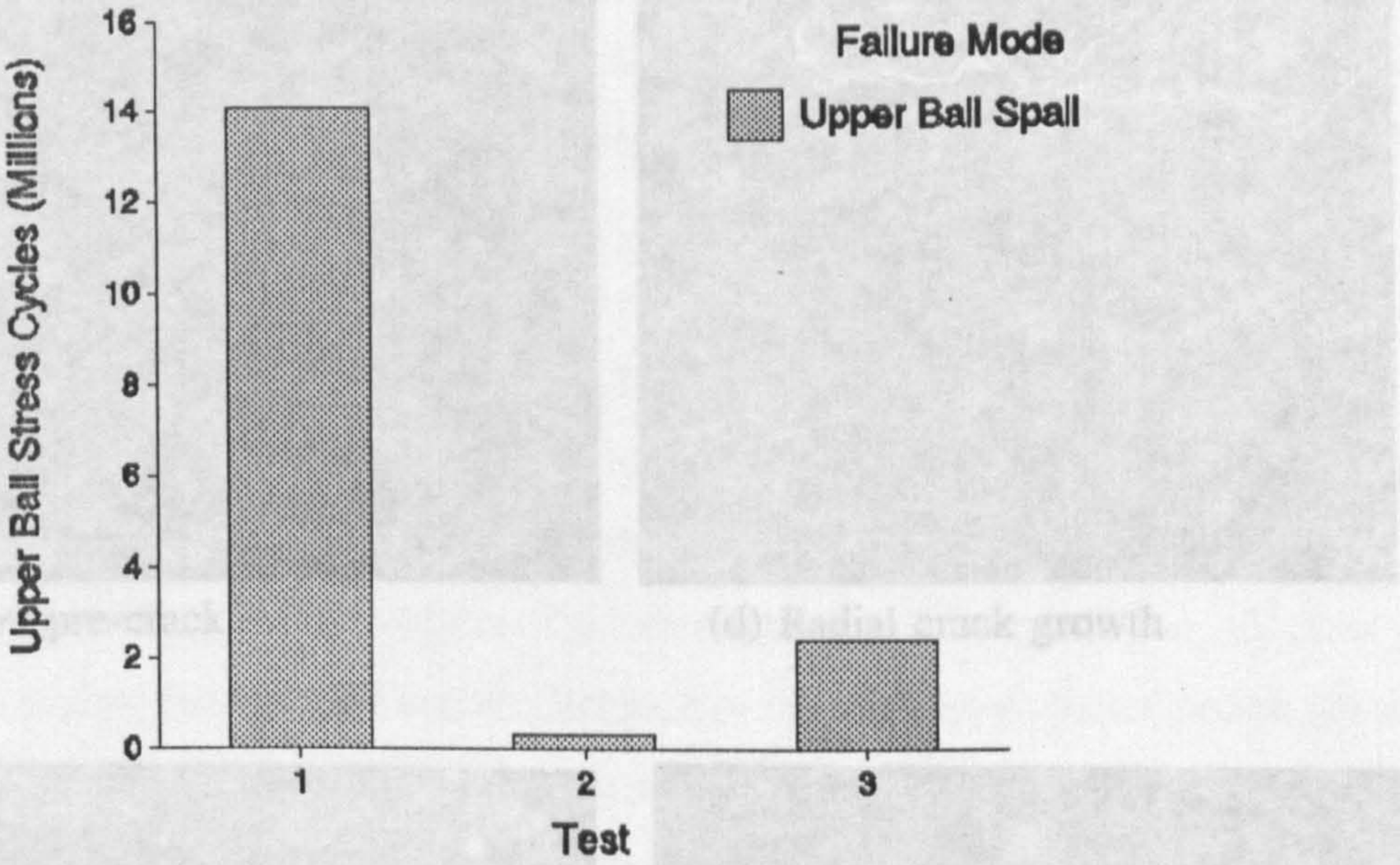

Figure 5.20 Sharp indentor final results

Detailed SEM investigation of tests balls was carried out. Figures 5.21 and 5.22, show micrographs of a ceramic lower-ball and steel upper-ball from test one. The ceramic lower-ball is illustrated in figure 5.21, captions (a) to (h). Caption (a) shows the pre-crack cluster and a delamination type failure. It is seen in captions (b) to (d), that radial cracks have propagated to connect together from two positions. Caption (e) shows the ball surface along a propagated radial crack; the presence of micro-cracks implies delamination below the apparently intact surface.

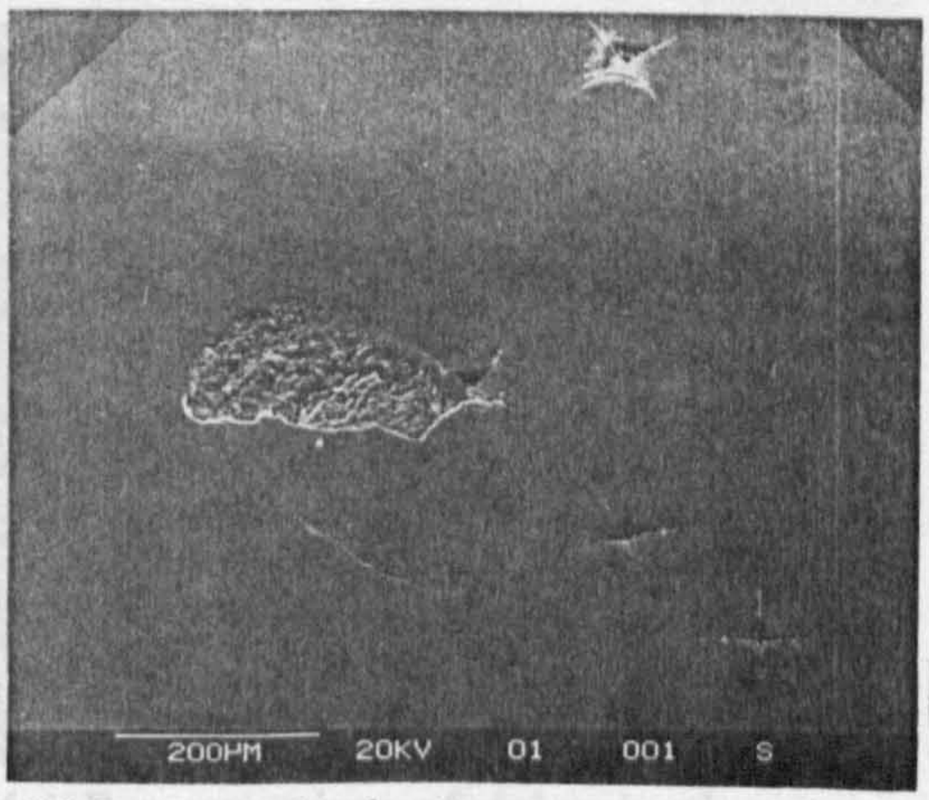

(a) Pre-crack cluster

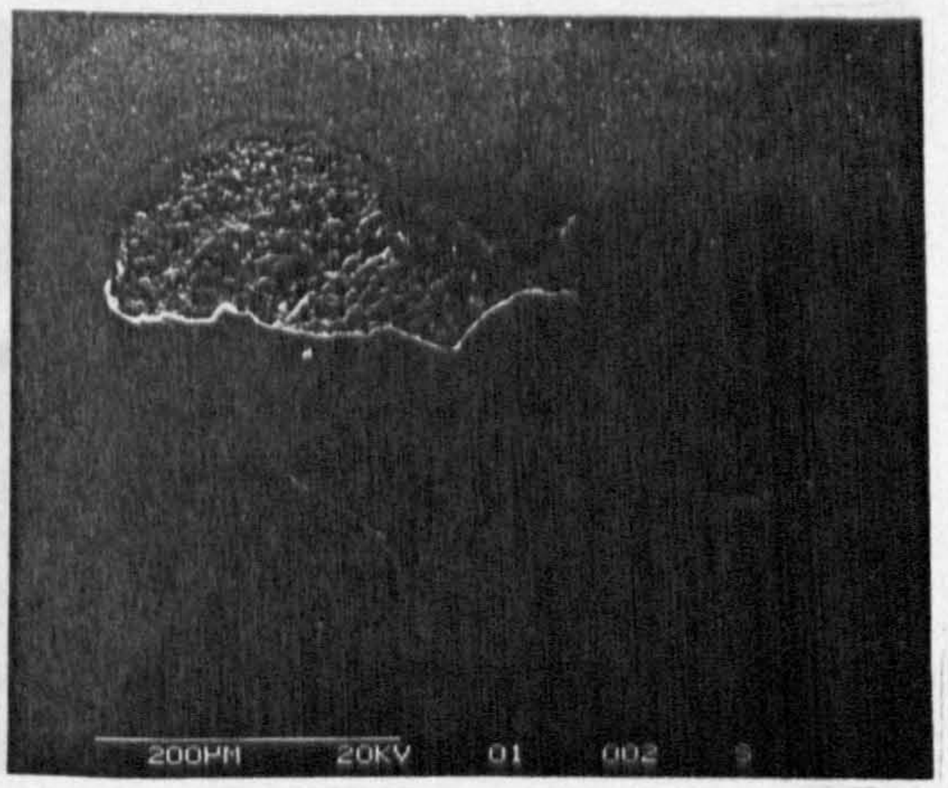

(b) Delamination and radial cracks

Figure 5.21 Micrographs of lower ceramic ball from test one - captions (a) to (h)

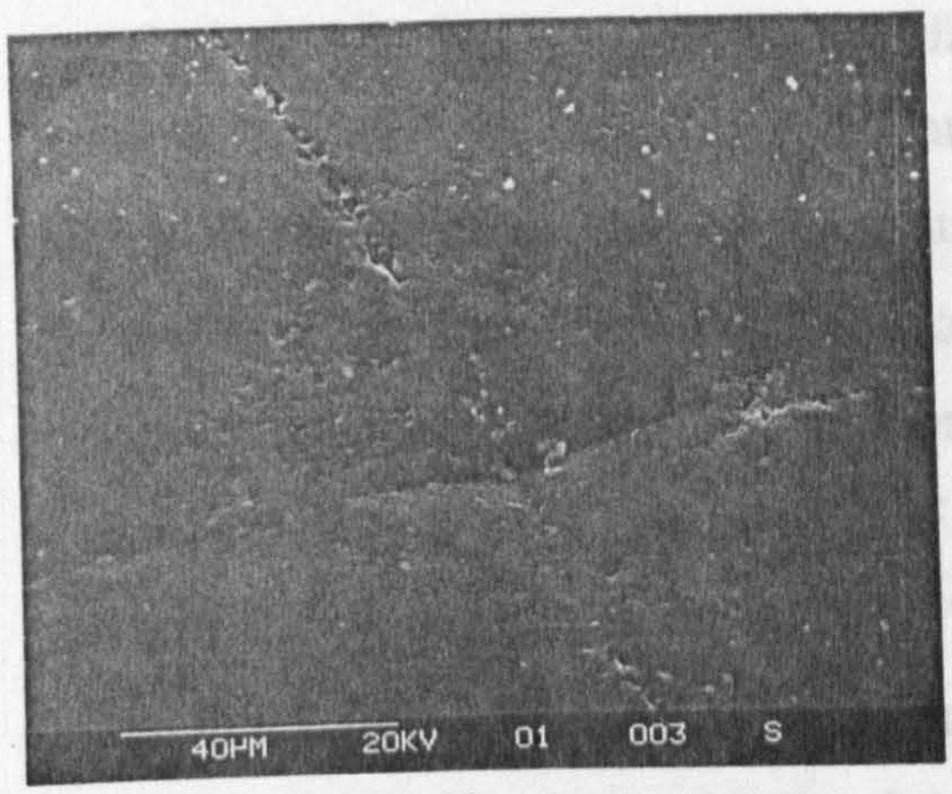

(c) Dent pre-crack

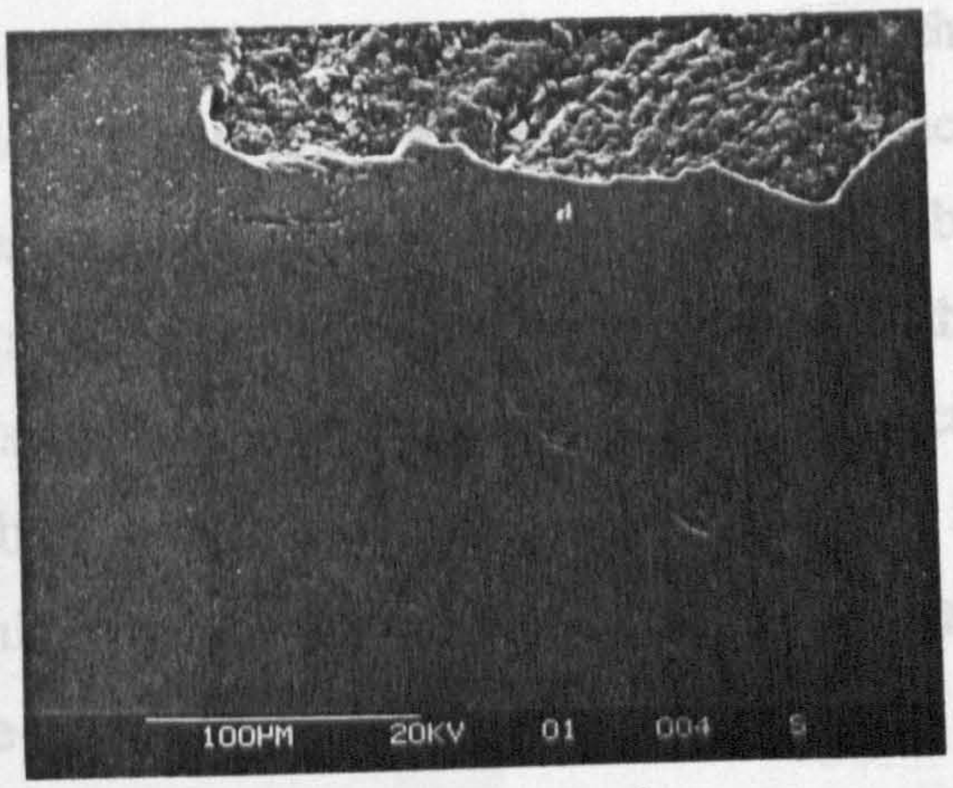

(d) Radial crack growth

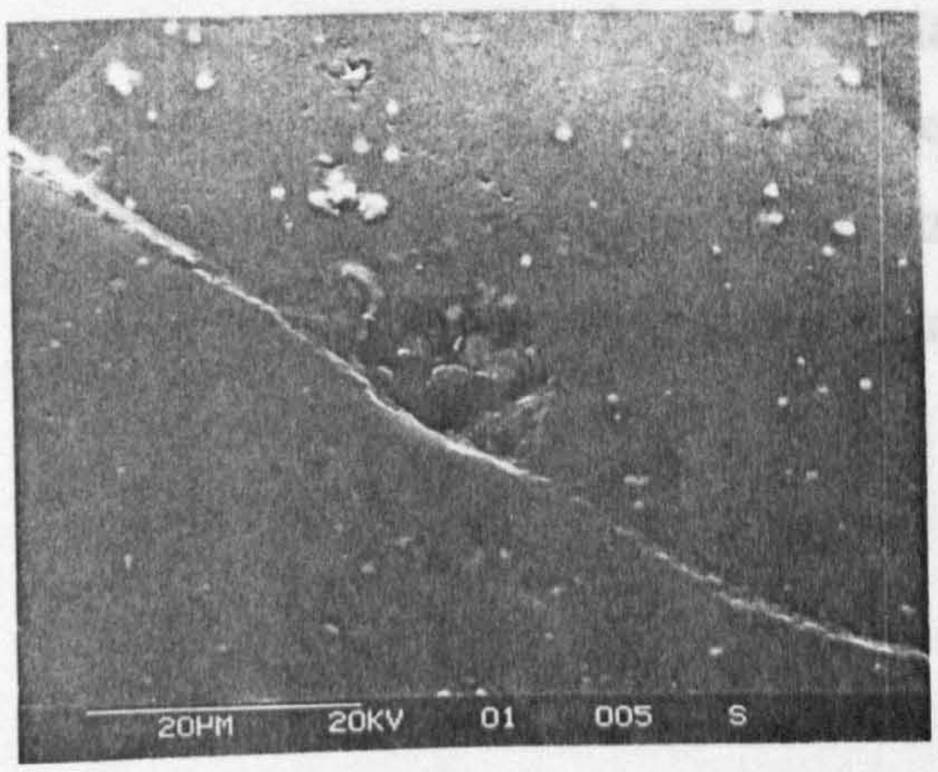

(e) Surface cracks

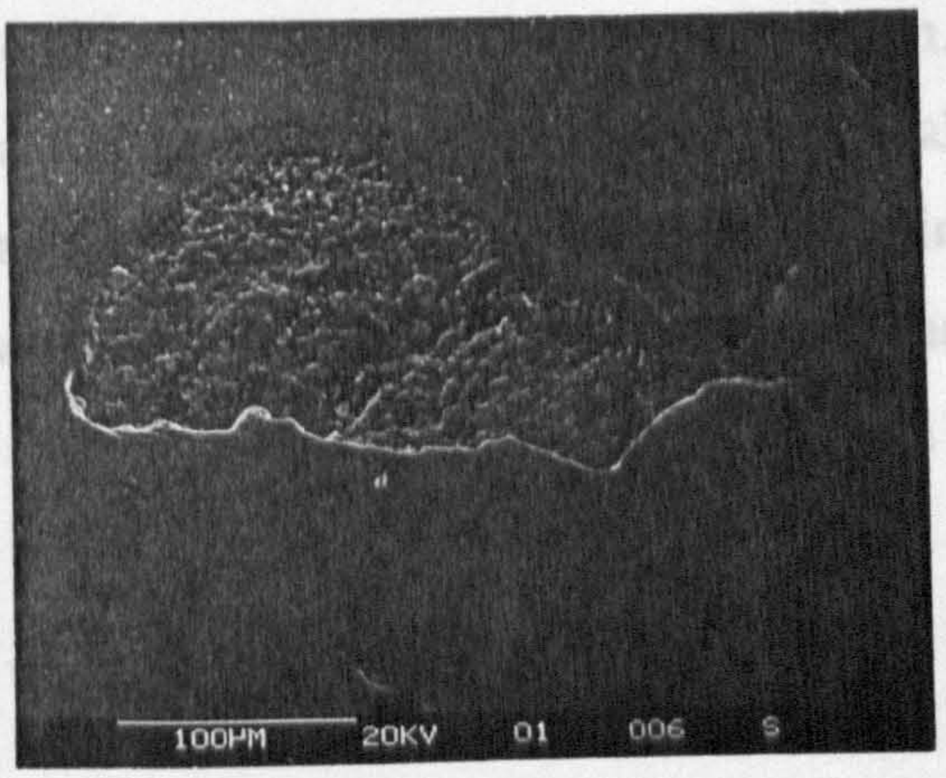

(f) Delamination area

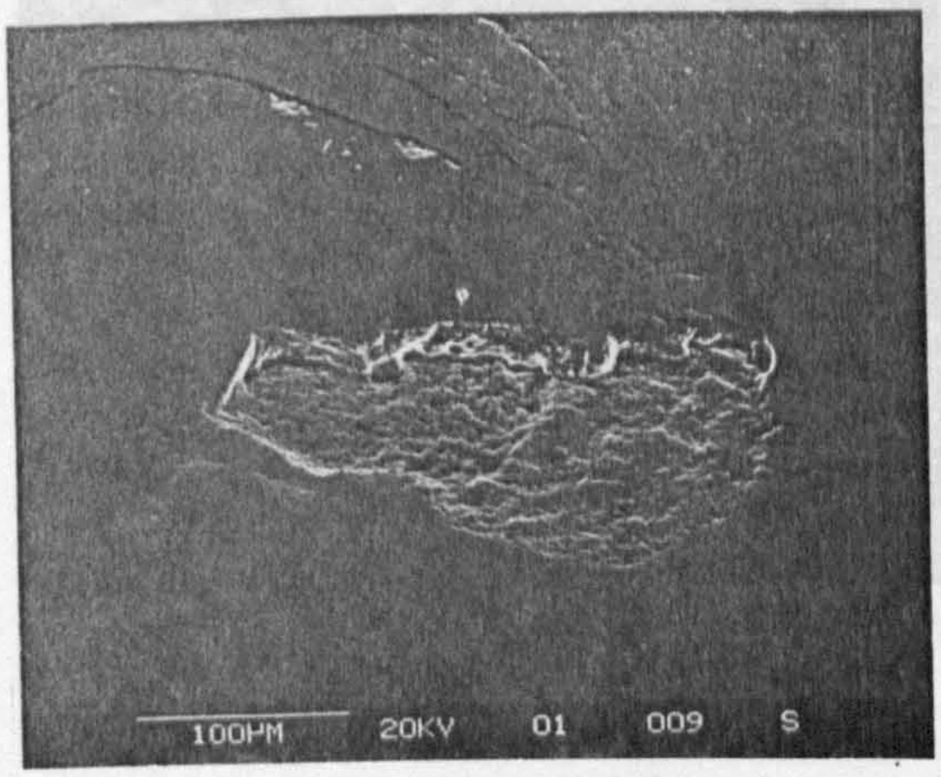

(g) Reverse view of delamination

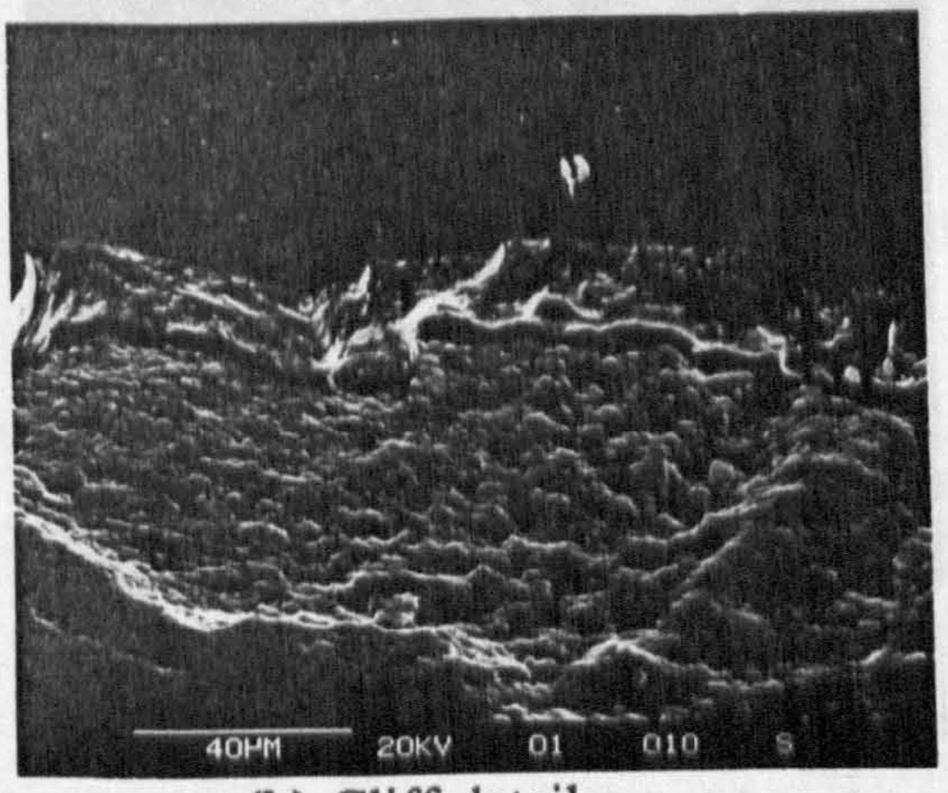

(h) Cliff detail

Figure 5.21 Micrographs of lower ceramic ball from test one - continued

Caption (f) of figure 5.21, shows an overview of the delamination area, undulations can be seen on this surface. The fact that radial cracks join the delamination area from separate indentations, points to the damage under the surface which further implies that the next stage of this failure would be complete by delaminated surface between pre-cracks. Reversed viewing position of the delamination area is shown in captions (g) and (h). It clearly shows a typical delamination type cliff edge and cliff base crack. The delamination direction is towards the propagated radial cracks. This confirms that failure mode consists in an initial crack propagation from radial pre-cracks the subsurface delamination.

Figure 5.22, shows details of the steel upper-ball from test one. Caption (a) shows a typical fatigue spall and contact path of the steel upper-ball. Caption (b) and (c) show a view from 90 degree rotation, looking along the rolling direction. Caption (b) depicts contact edge cracks and subsurface delamination with typical cliff base cracks. Surface micro-cracks adjacent to the cliff edge can be seen in caption (c). This further implies subsurface damage. Debris are also visible in the cliff base of the fatigue spall.

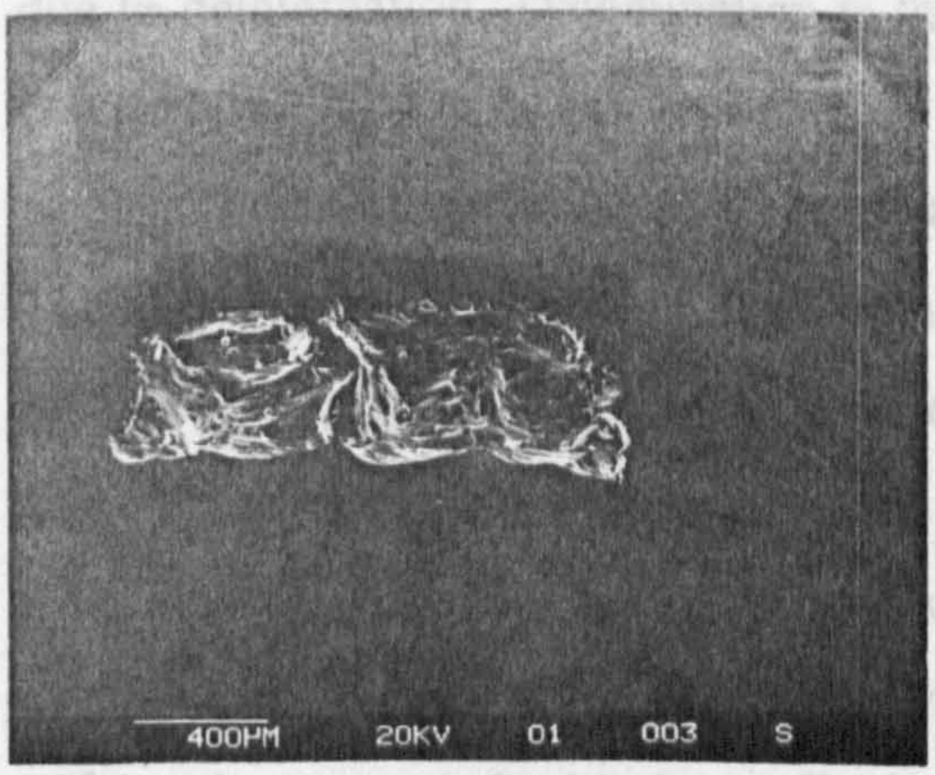

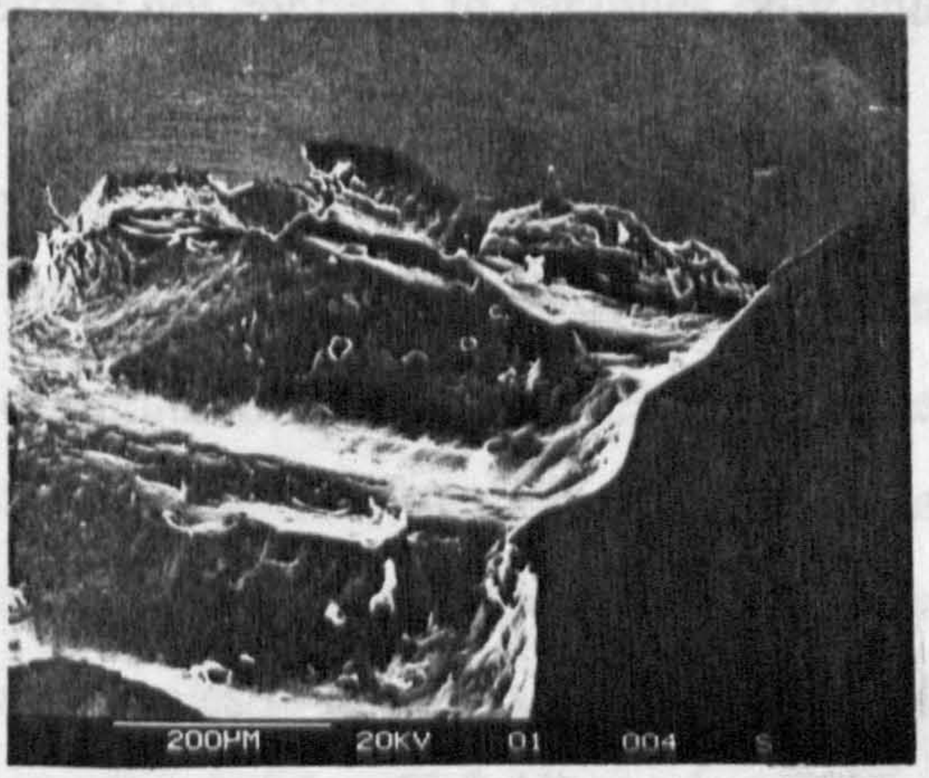

(a) Spall overview - steel upper ball **(b)** Spall edge - rolling direction

Figure 5.22 Micrographs of upper steel ball from test one - caption (a) to (c)

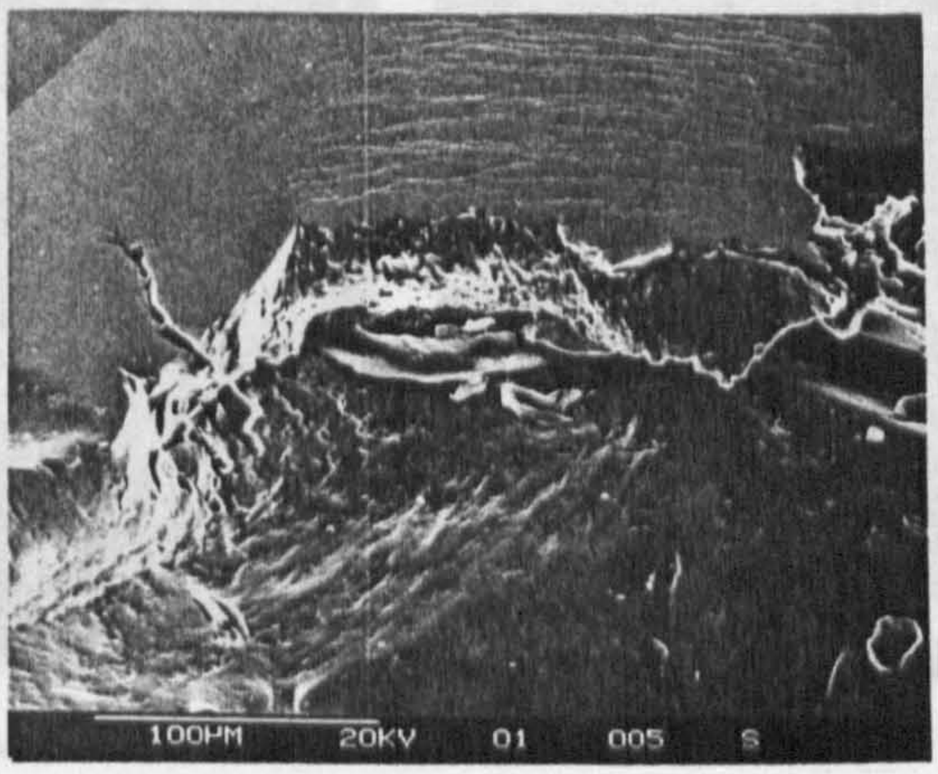

(c) Cliff detail

Figure 5.22 Micrographs of upper steel ball from test one - continued

The observations from test one provide evidence supporting new failure modes for both lower pre-cracked balls and upper steel ball. By testing with high viscosity oil, delamination occurs on lower pre-cracked balls. The high viscosity lubricant alters the fatigue failure mode by increasing the film thickness between the contacting surfaces. The spalling of the steel upper ball confirms that it also fails due to delamination. Delamination is therefore, not confined to ceramics only and is a genuine fatigue failure mode.

The results of lower-ball examinations for test two are shown in figure 5.23. The failed area, caption (a), shows that all pre-cracks in the cluster have been removed by a large deep spall. Edge of delamination spall is not evident as the crack propagates deep into the ceramic material. Caption (b) shows details of the spall surface. Striation-like texture is clearly visible. Steel upper-ball failure by fatigue spalling halted the test. The number of cycles to failure is severely reduced and can be compared with the preliminary results, (section [5.2.1]) obtained under the same conditions with identical low viscosity lubricant. This confirms that ceramic debris will markedly affect fatigue life of the steel upper-ball.

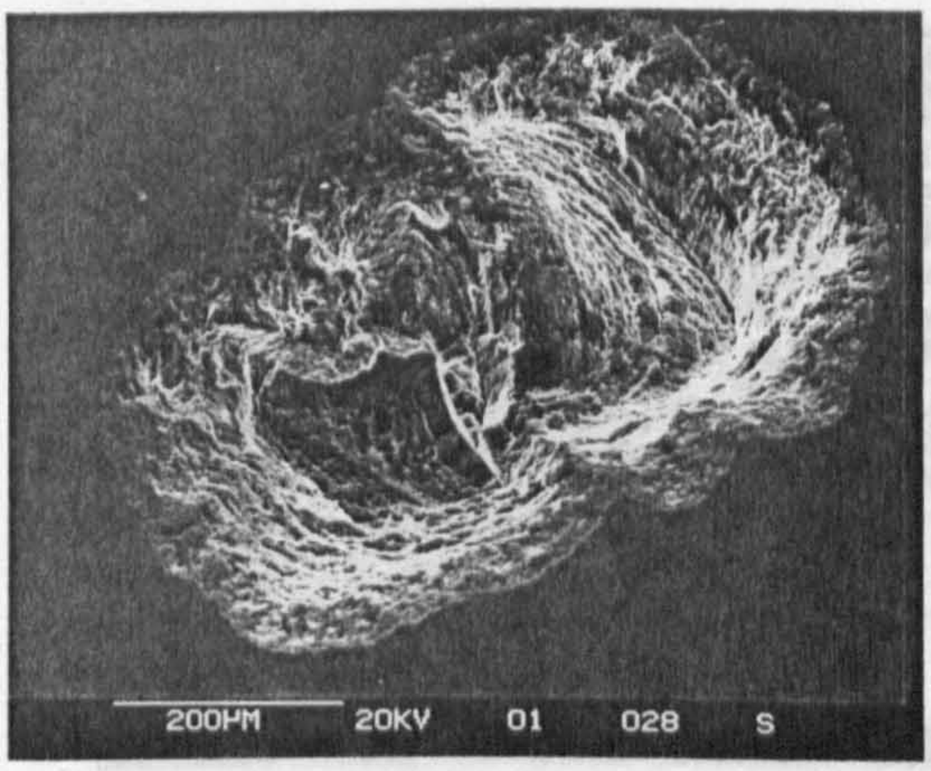

(a) Failed area

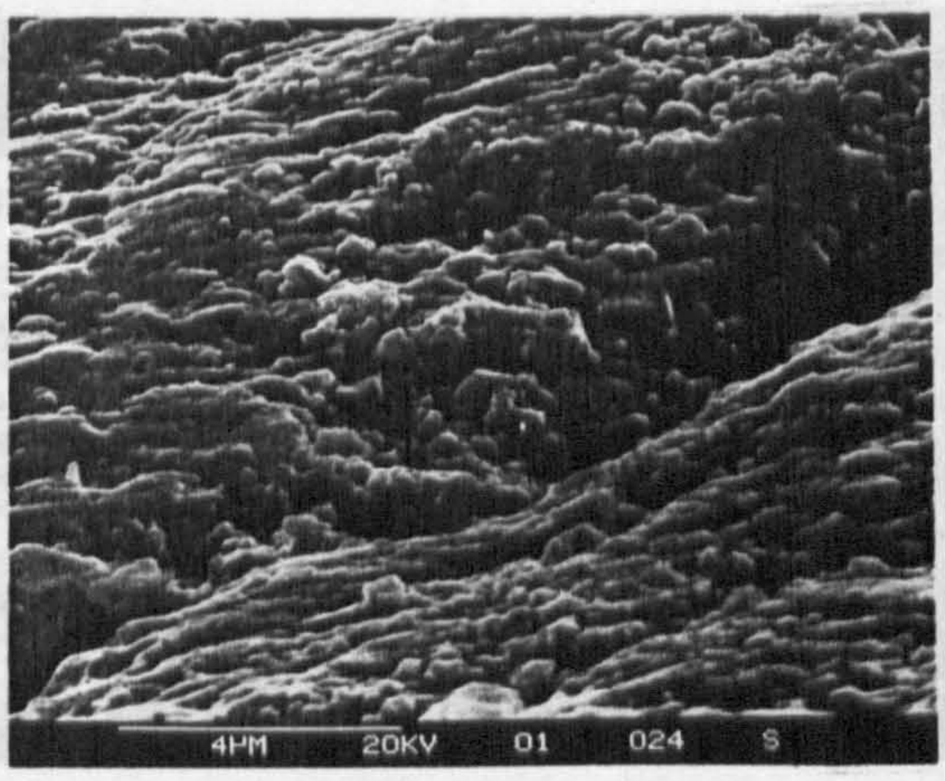

(b) Surface detail

Figure 5.23 Micrographs of lower ceramic ball from test two

The post-test investigation of test three, figure 5.24 captions (a) to (h), produced some surprising results after initial analysis yielded evidence of only minor damage. An overview of a pre-crack cluster, caption (a), shows limited damage due to radial pre-cracks. Close examination of a radial crack, caption (b), shows crack damage, and also wear on the ball surface. Near the radial crack, a bulge is observed protruding from the surface, caption (c). Even closer examination of the bulge, caption (d), shows cracks at the apex and trapped debris.

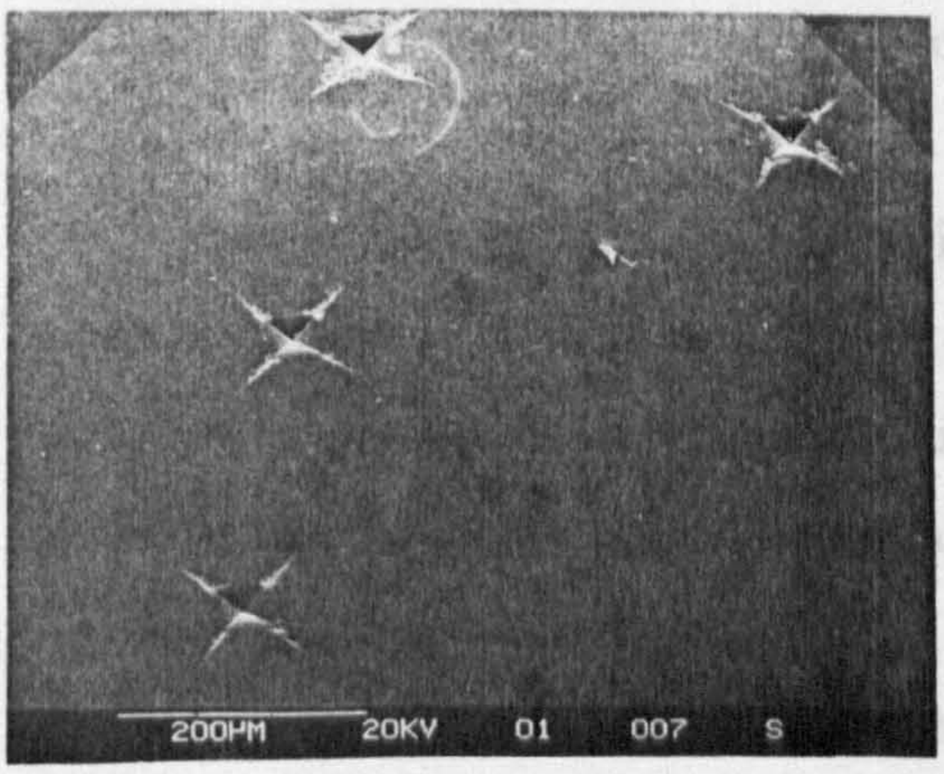

(a) Failed area

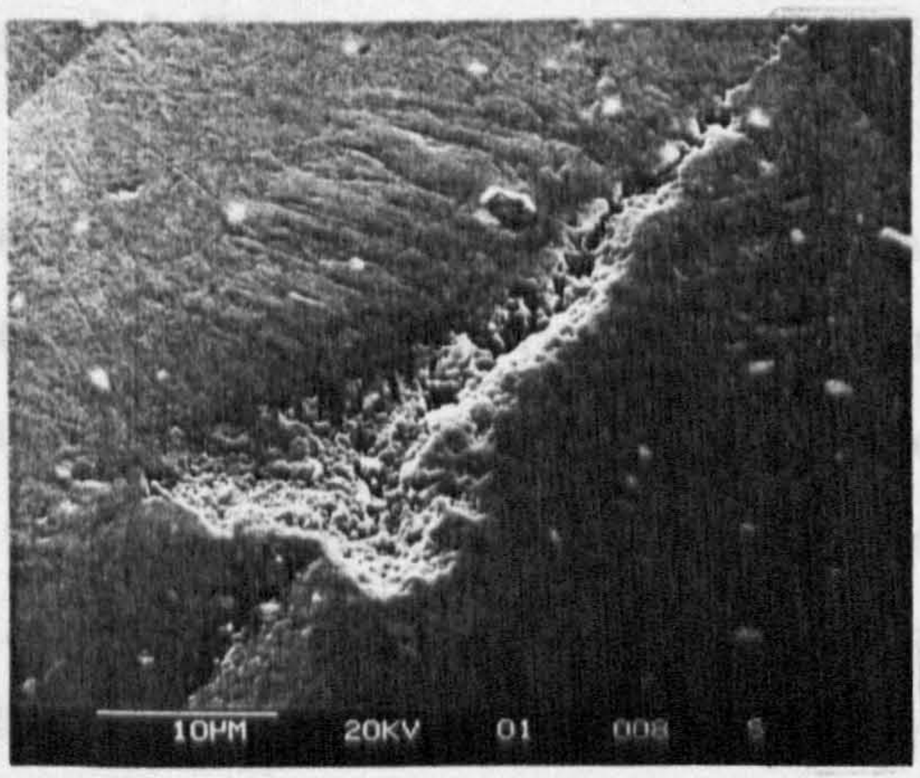

(b) Radial crack

Figure 5.24 Micrographs of lower ceramic ball from test three - captions (a) to (e)

(c) Radial crack - side view

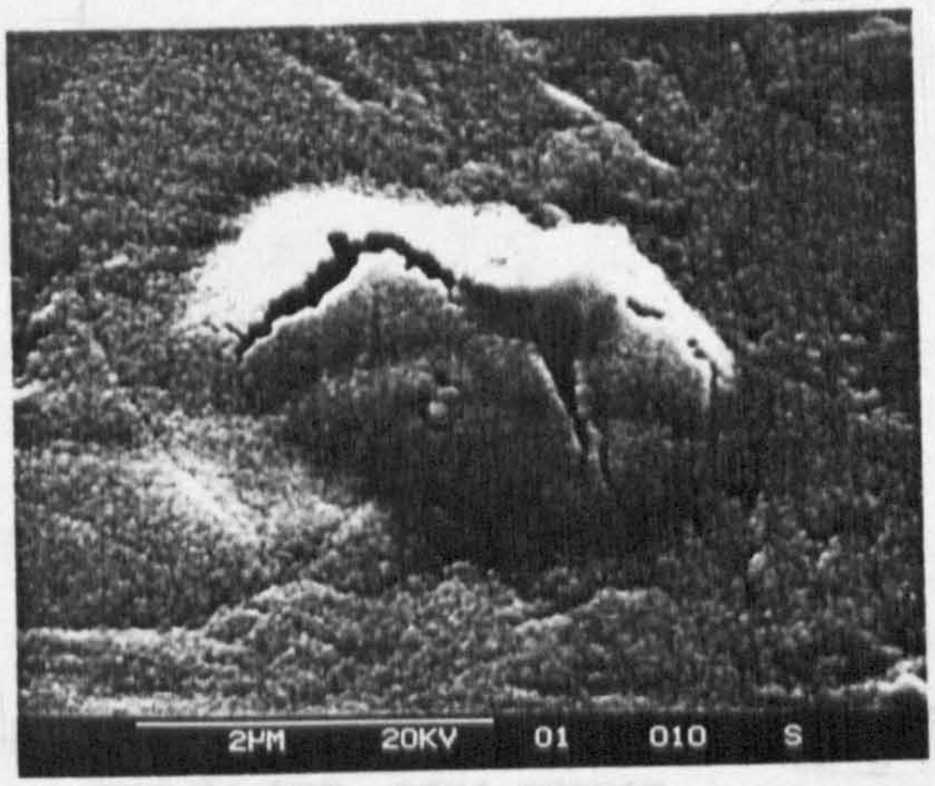

(d) Bulge detail

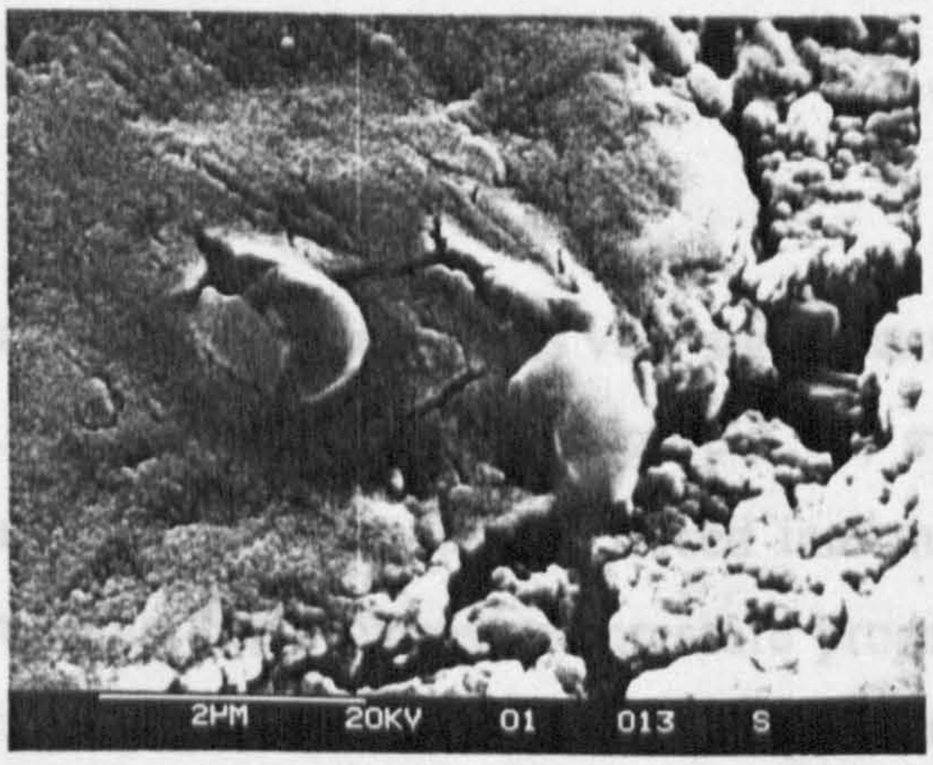

(e) Additional bulge example

Figure 5.24 Micrographs of lower ceramic ball from test three - continued

Bulges near radial cracks were identified on many lower-ball samples. An additional example is shown as caption (e) in figure 5.24. Debris in this case are identified as similar to the previous example, shown as caption (d). Results of Electron Probe Micro Analysis (EPMA) of the ball surface near the bulge and of the bulge debris, are shown in figure 5.25, captions (a) and (b). The chemical analysis shows that the debris trapped within the bulges are ferrous and hence must originate from the steel upper-ball.

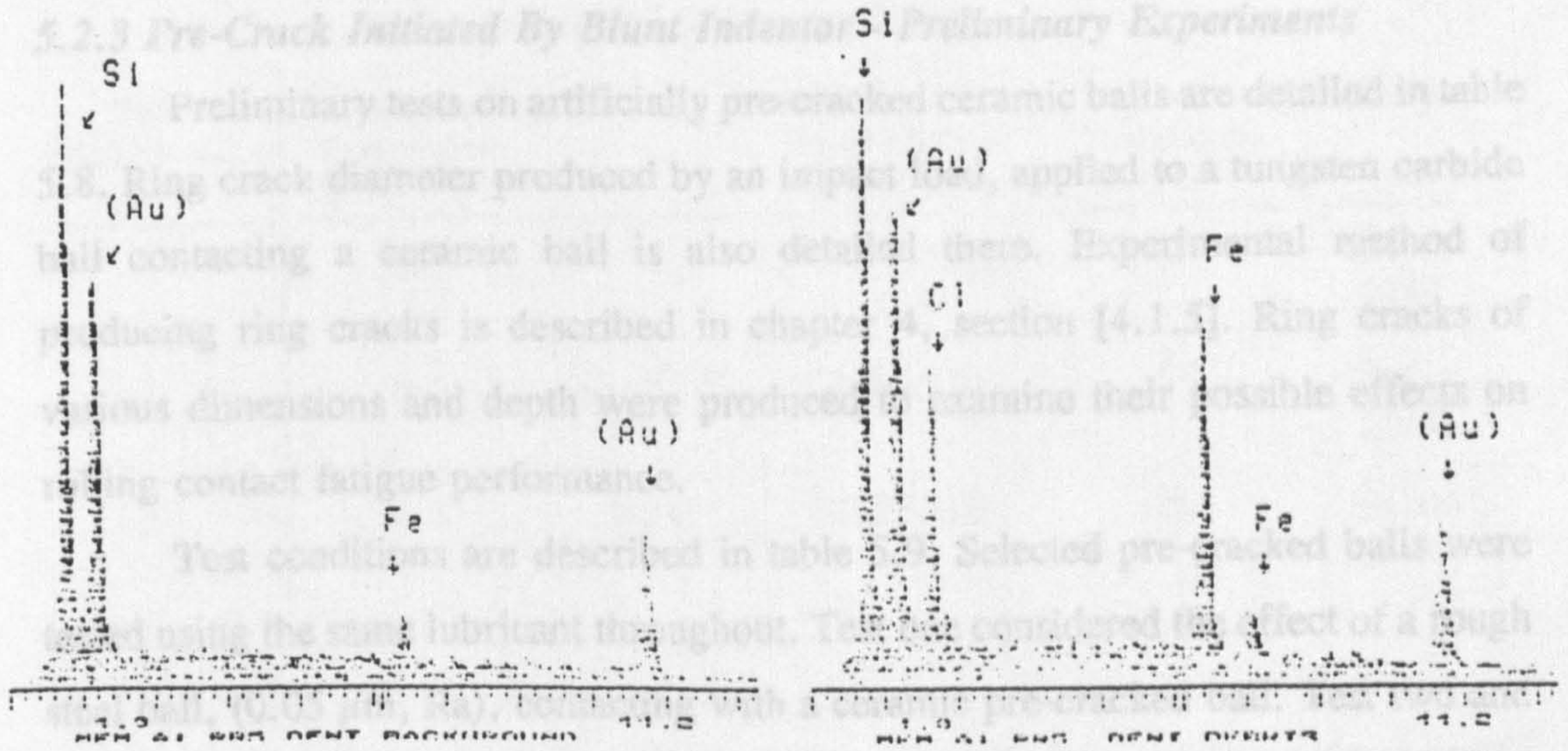

(a) Near bulge (b) Bulge debris

Figure 5.25 Chemical analysis

The result from chemical analysis is very significant for the identification of failure mechanism. The bulges, shown in figure 5.24, must be a result of steel debris suspended in the lubricant which is forced into the damaged radial crack space. The lubricant under high hydrostatic pressure propagates subsurface cracks from the lateral crack root. The steel debris trapped under the ball surface, suspended in the pressurised lubricant is forced up through the ceramic surface. This failure mode is typical for the test in which the upper-ball wear in addition to standard contact fatigue spall failure.

5.2.3 Pre-Crack Initiated By Blunt Indentor - Preliminary Experiments

Preliminary tests on artificially pre-cracked ceramic balls are detailed in table 5.8. Ring crack diameter produced by an impact load, applied to a tungsten carbide ball contacting a ceramic ball is also detailed there. Experimental method of producing ring cracks is described in chapter 4, section [4.1.5]. Ring cracks of various dimensions and depth were produced to examine their possible effects on rolling contact fatigue performance.

Test conditions are described in table 5.9. Selected pre-cracked balls were tested using the same lubricant throughout. Test one considered the effect of a rough steel ball, (0.05 μm, Ra), contacting with a ceramic pre-cracked ball. Test two and three consider were devoted to the effect of contacting a standard steel ball. Final test temperature reflects the number of cycles to failure; test one and two ceased before equilibrium temperature was reached.

Table 5.8 Pre-crack specifications

Test Ball	Drop Height (mm)	Drop Mass (g)	Top Ball Diameter - Tungsten Carbide (mm)	Ring Crack(s) Diameter (mm)
A	485	277	6.35	0.75 and 0.6
B	485	277	9.53	0.7
C	485	158	9.53	0.7
D	485	158	12.7	0.9 and 0.7
E	485	277	12.7	1.1 and 0.9
F	485	158	6.35	0.65

Table 5.9 Test conditions

Test (5000 r.p.m.)	Maximum Compressive Stress (GPa)	Test Ball	Material: Steel Upper / Silicon Nitride Lower	Final Temperature (˚C)	Lubricant
1	6.4	A	SKF3 (rough) /UB	60	Exxon 2389
2	6.4	D, E, F	SKF3/UB	58	Exxon 2389
3	6.4	B, C	SKF3/UB	80	Exxon 2389

Results from preliminary tests on balls with artificially produced ring cracks are presented as figure 5.26. Test one and three ended with an upper steel ball fatigue spall. The difference in fatigue life is probably due to the increased surface roughness. Preliminary post test analysis for lower-ball from test one and three did not reveal damage. Test two was stopped by lower-ball 'E' spalling from an artificial ring crack.

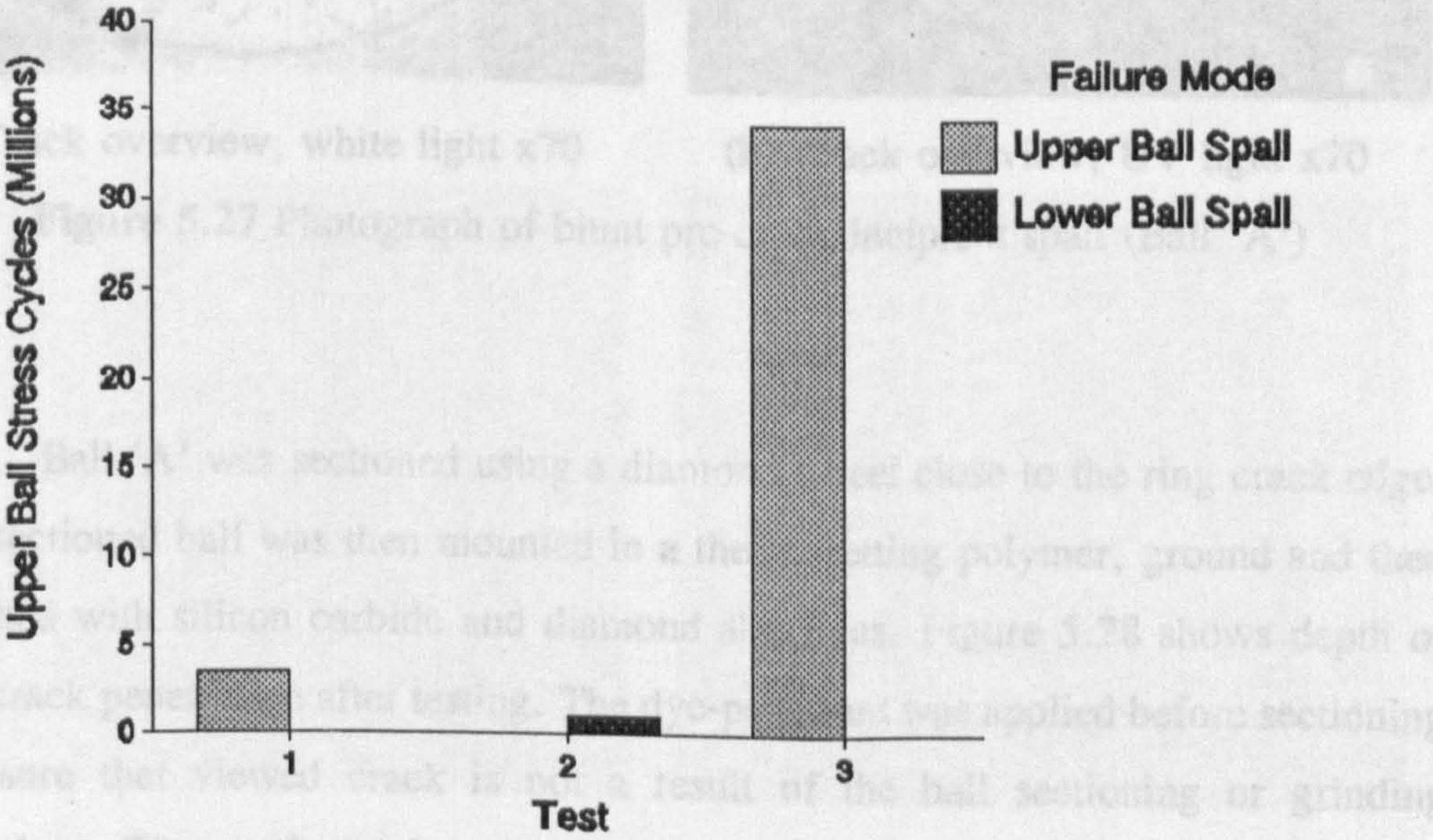

Figure 5.26 Blunt indentor preliminary results

Detailed microscopic examination of lower balls was carried out. The dye penetrant method, described in chapter four, section [4.1.4], was used to locate artificial pre-cracks and to estimate crack depth. Figure 5.27 shows the pre-crack on ball 'A' after testing. Caption (a) shows the pre-crack under normal light. The ring crack is clearly visible. The surface was subsequently damaged as this ball was tested with a rough steel upper ball which insured partial boundary lubrication. The ring crack is seen to be damaged and spall beginning to initiate. Damaged paths caused by debris are also evident. Caption (b) shows the same image under ultra violet light after the ball was treated with dye penetrant. The emitted light varying intensity at damaged position on the ring crack suggests internal crack growth.

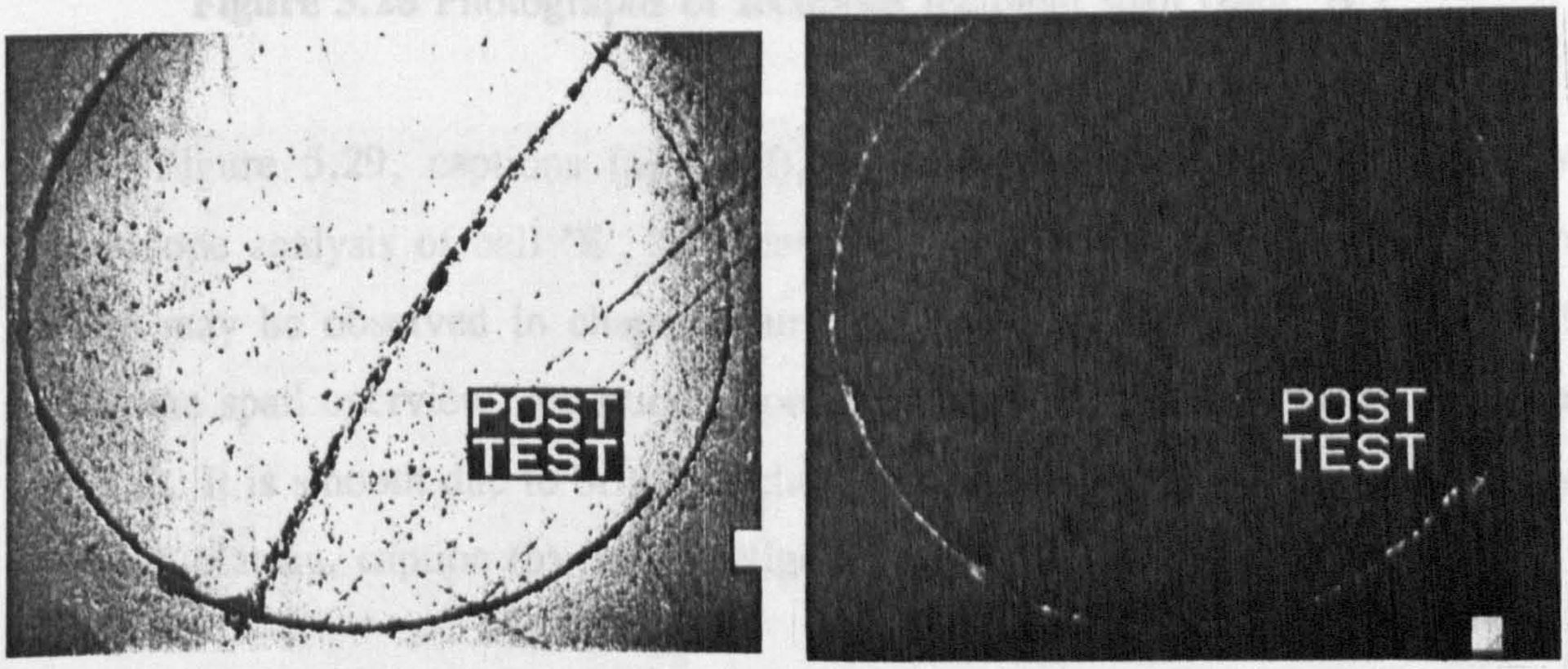

(a) Crack overview, white light x70 **(b)** Crack overview, UV light x70

Figure 5.27 Photograph of blunt pre-crack incipient spall (Ball 'A')

Ball 'A' was sectioned using a diamond wheel close to the ring crack edge. The sectioned ball was then mounted in a thermosetting polymer, ground and then polished with silicon carbide and diamond abrasives. Figure 5.28 shows depth of ring crack penetration after testing. The dye-penetrant was applied before sectioning to insure that viewed crack is not a result of the ball sectioning or grinding operations. The crack can be seen to have propagated from the initial cone root, probably driven by high pressure lubricant.

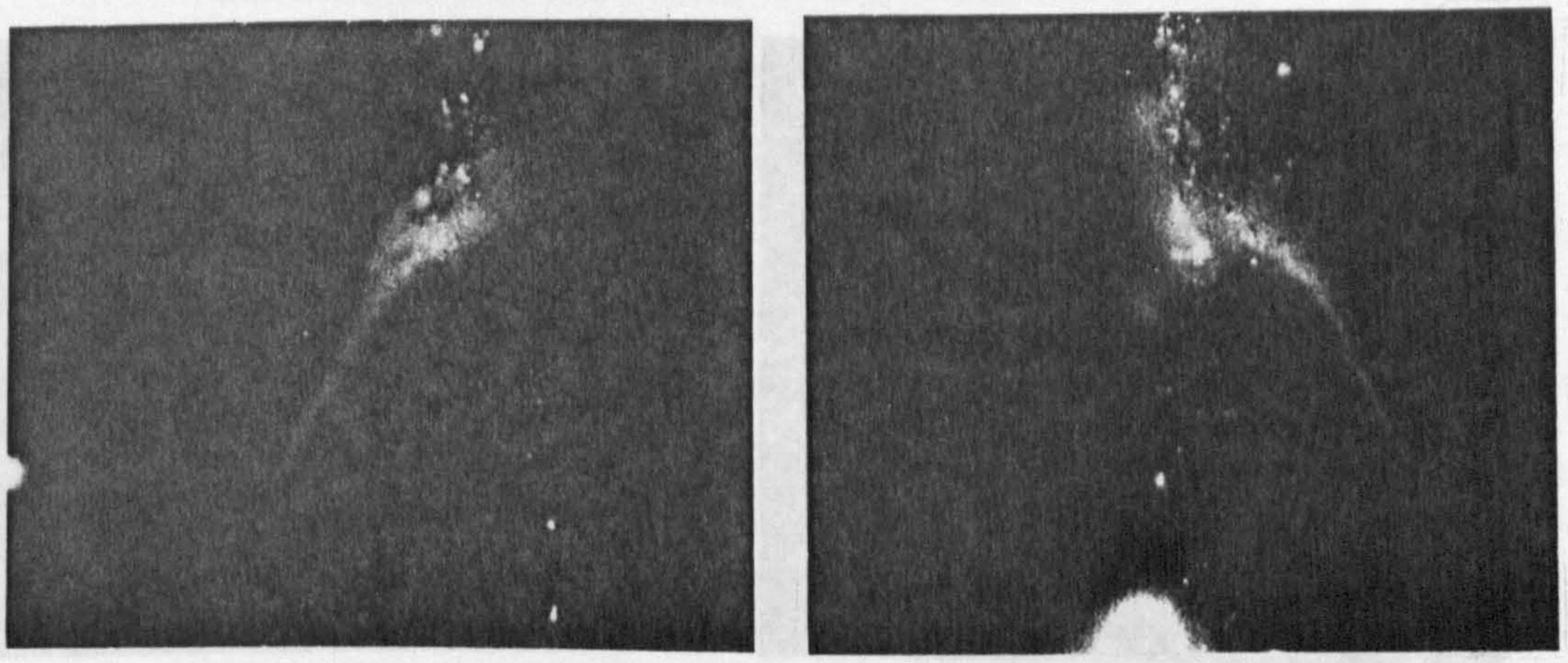

(a) Right crack section, UV x70 **(b)** Left crack section, UV x70

Figure 5.28 Photographs of sectioned incipient spall (Ball 'A')

Figure 5.29, captions (a) to (f), shows results from scanning electron microscope analysis of ball 'E', from test two. The pre-crack on ball 'E' before testing may be observed in chapter four, figure 4.9. Caption (a) of figure 5.29 shows the spall overview, the smooth cone surface , initiated from the ball surface crescent. It is smooth due to brittle fracture caused by impact. The undulations on the spall plateau, caption (b), imply fatigue fracture from pressurised lubricant.

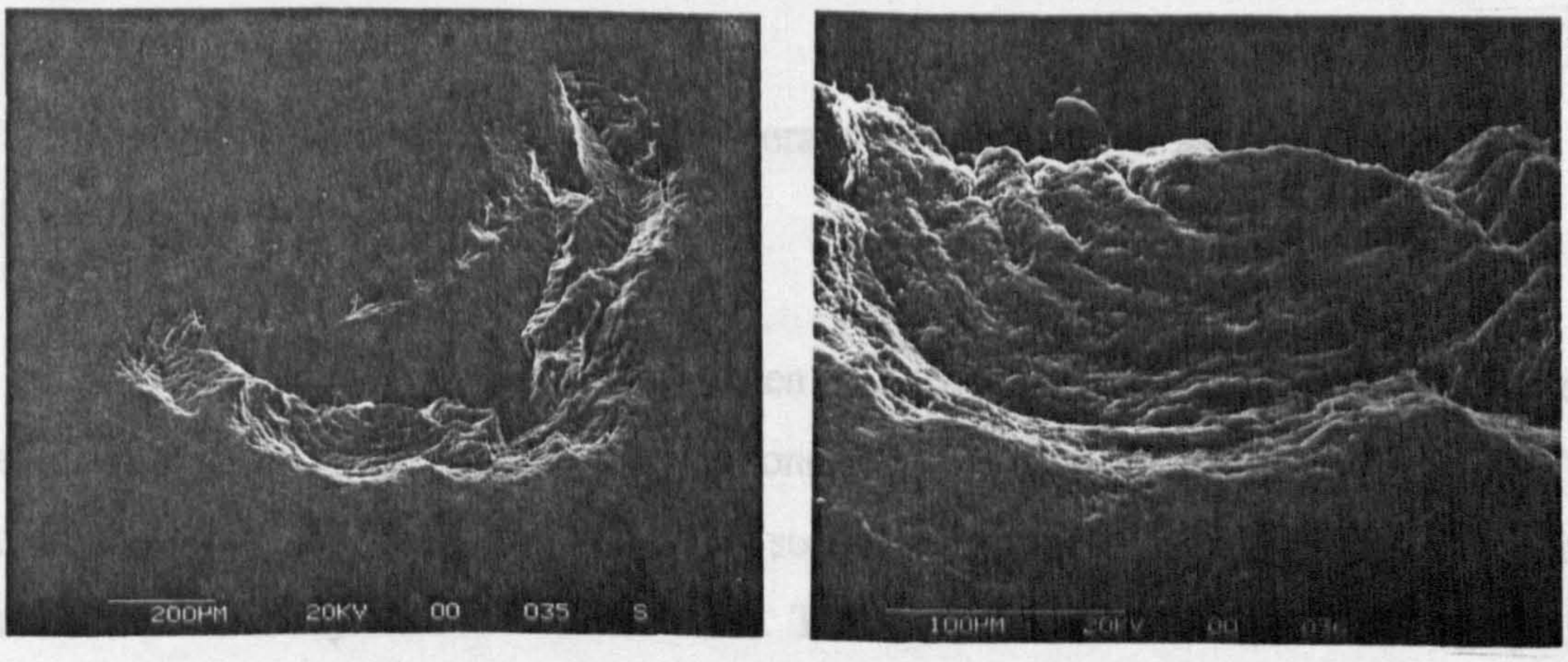

(a) Failure overview **(b)** Fatigued area

Figure 5.29 Micrographs of lower ceramic ball 'E' from test 2 - captions (a) to (f)

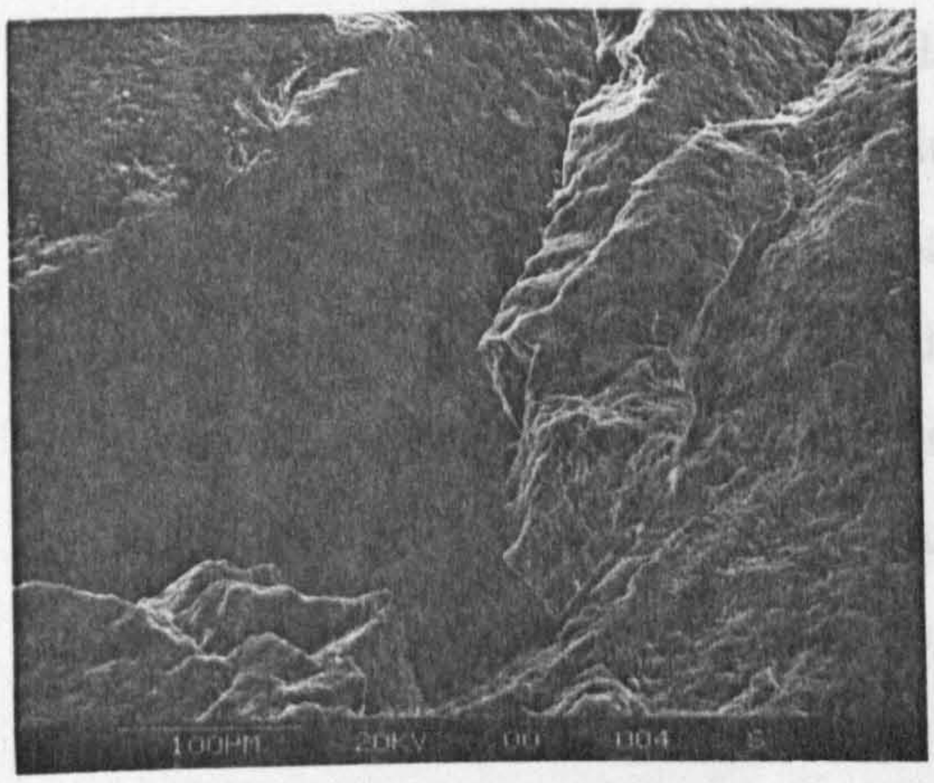

(c) Brittle ring-crack surface

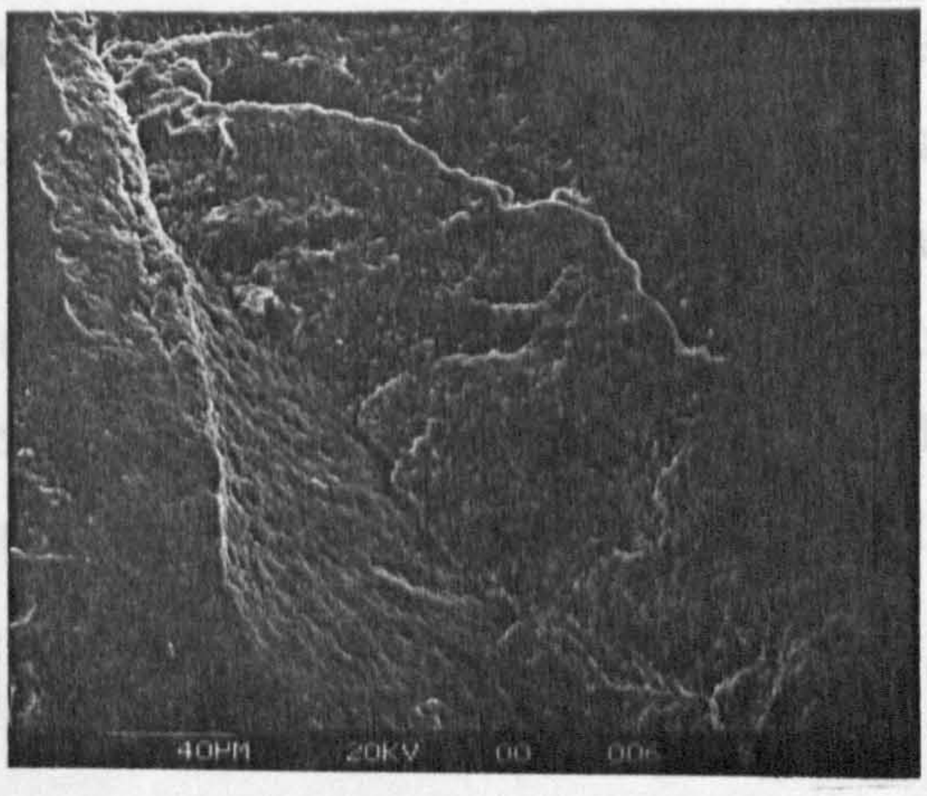

(d) Right side of spall

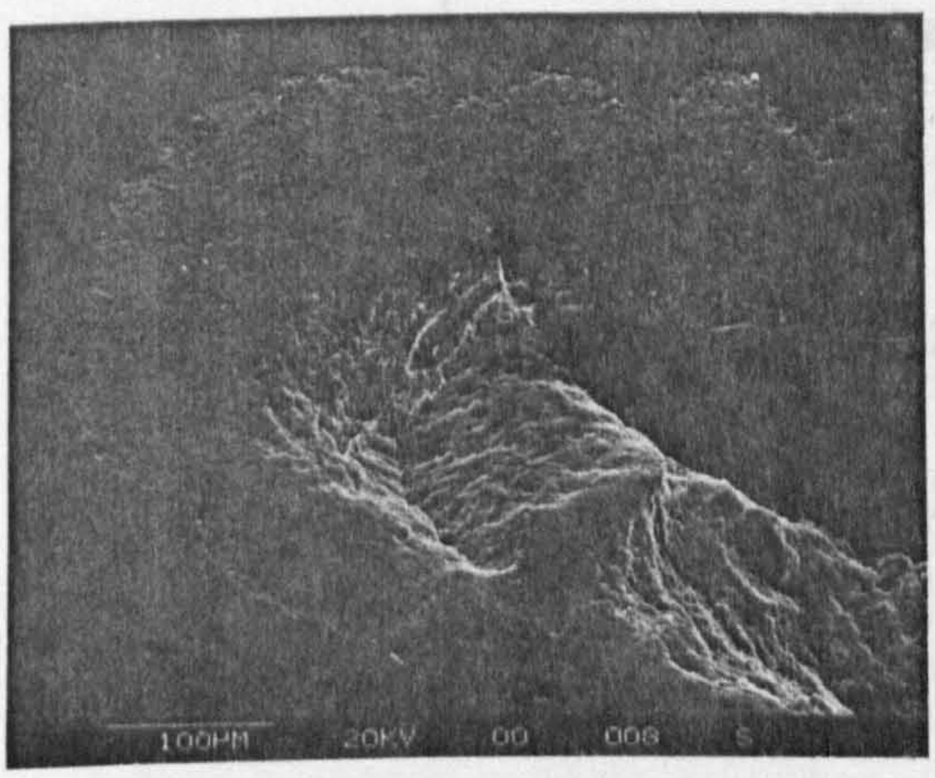

(e) Left side of spall

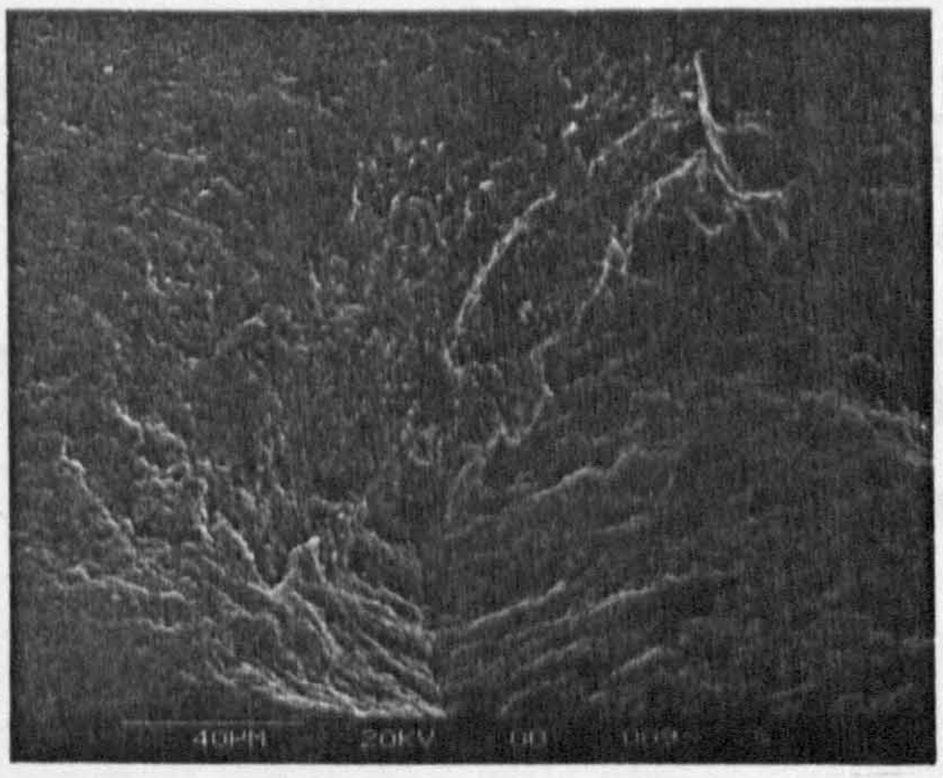

(f) Right side detail

Figure 5.29 Micrographs of lower ceramic ball 'E' from test 2 - continued

Debris formed in the spall are seen in figure 5.29, caption (c). These large sections are crushed within the contact zone after removal from the spall area. Left and right area of the spall ends are seen in caption (d) to (f), with fatigue undulations clearly visible in these areas. This initial study of the pre-cracked spall is quite encouraging as the failure mode is of a non-catastrophic nature and is also confined to the area near the initial ring-crack.

5.2.4 Pre-Crack Initiated By Blunt Indentor - Final Experiments

Following preliminary results, it was decided to set impact load the same as for ball 'E' which failed by a spalling mode in preliminary tests. Each lower ball was artificially pre-cracked to produce six equally spaced ring cracks. It was done by dropping a 277 gram mass, from 485 millimetres on 12.7 millimetre diameter tungsten carbide ball in contact with test ball. Test conditions were the same as those used for sharp indenter experiments. Three lubricants and constant load were used throughout testing. Temperature at the end of testing indicates that all three experiments were of short duration.

Table 5.10 Test conditions

Test (5000 r.p.m.)	Maximum Compressive Stress (GPa)	Tungsten Carbide Ball Diameter (mm)-Drop Mass 277 g, Drop Height 485 mm	Material: Steel Upper / Silicon Nitride Lower	Final Temperature (°C)	Lubricant
1	6.4	12.7	SKF3/UB	63	HiTec 174
2	6.4	12.7	SKF3/UB	44	Exxon 2389
3	6.4	12.7	SKF3/UB	40	Kerosine

Results from experiments on artificially induced ring cracks are shown in figure 5.30. All tests were halted when the upper steel ball failed due to a rolling contact fatigue. The number of cycles to failure for the three lubricants employed, decreases with decreasing oil viscosity. Also, the cycles to failure are much reduced when compared to tests on dented pre-cracked ceramic balls, described in section [5.2.2]. The comparative low life results are probably due to increased debris density suspended in the lubricant; the ring crack spall being much larger than the dent crack damage.

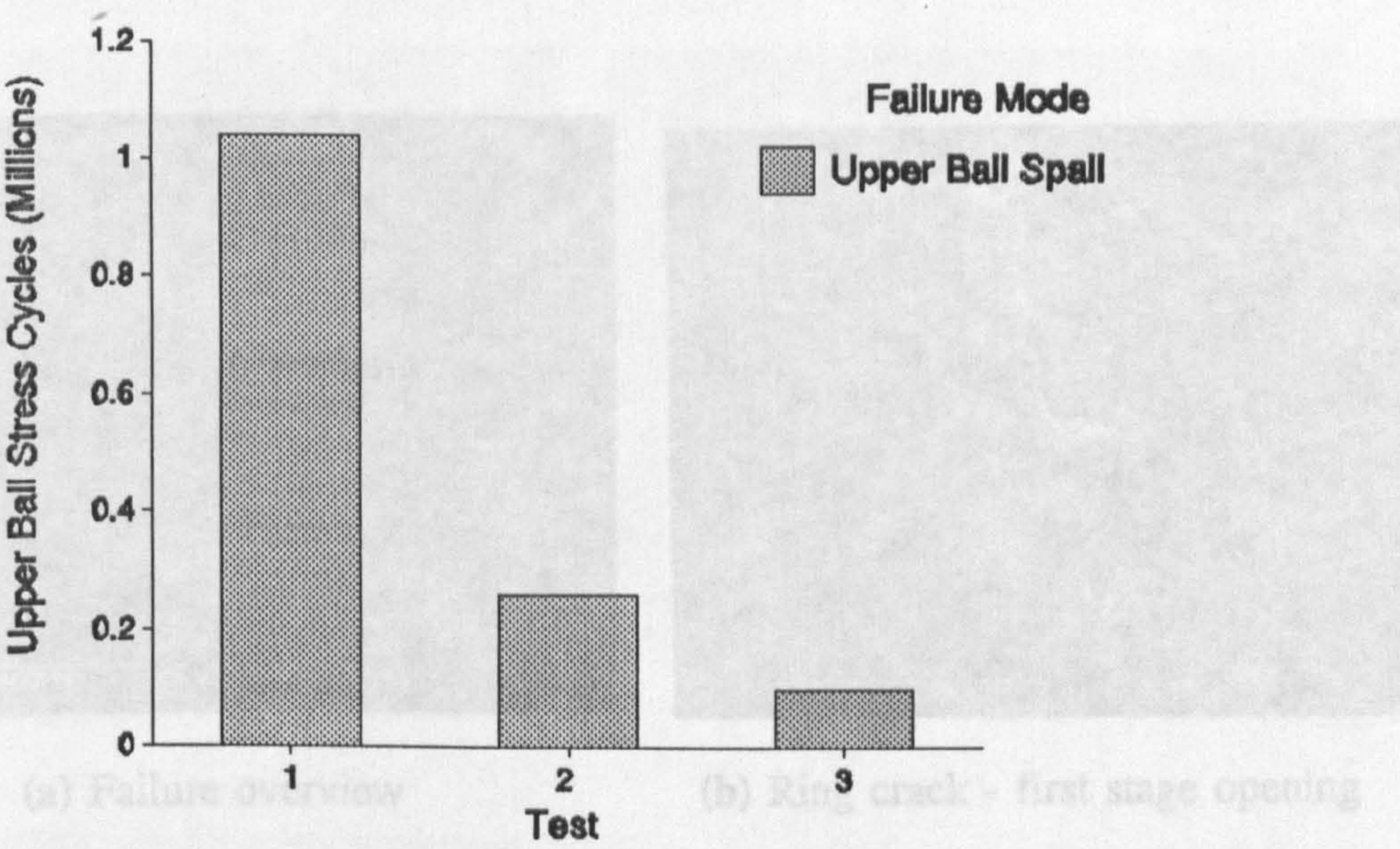

Figure 5.30 Blunt indentor final results

Initial analysis after the completion of test one showed that, in addition to steel ball spalling, many lower balls had also spalled at ring crack positions. Debris in powder like form were found suspended in the lubricant after filtration. Test two and test three also produced lower-ball spalling with upper steel ball failure. Additionally test three showed indications of upper steel ball wear.

Electron microscopy analysis of pre-cracks on lower-ball are shown in figures 5.31 to 5.36. Examples of spall stages are identified and described; stage one - initial damage, stage two - removal of ceramic material from the surface, stage three - partial spall and finally, fully developed fatigue spall. Stage one spall is shown in figure 5.31, captions (a) to (d). Caption (a) shows the ring crack overview, initial damage is shown as caption (b). Further material removal and secondary crack at ninety degrees to the ring-crack is shown as caption (c) . Caption (d) shows further material removal enabling lubricant to penetrant deep into the ceramic material.

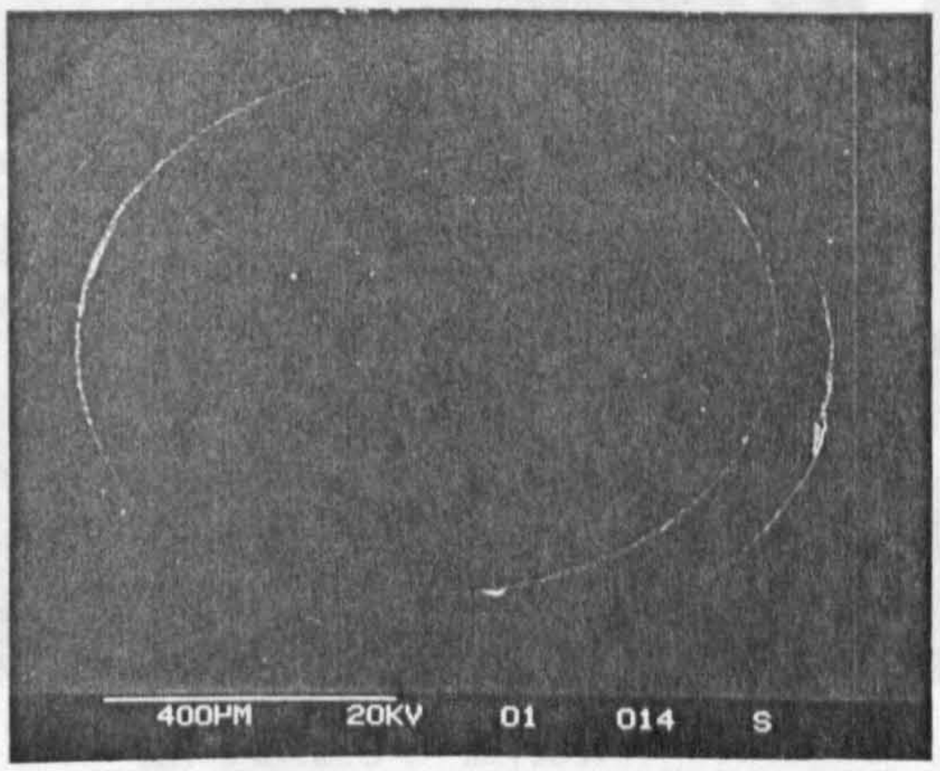

(a) Failure overview

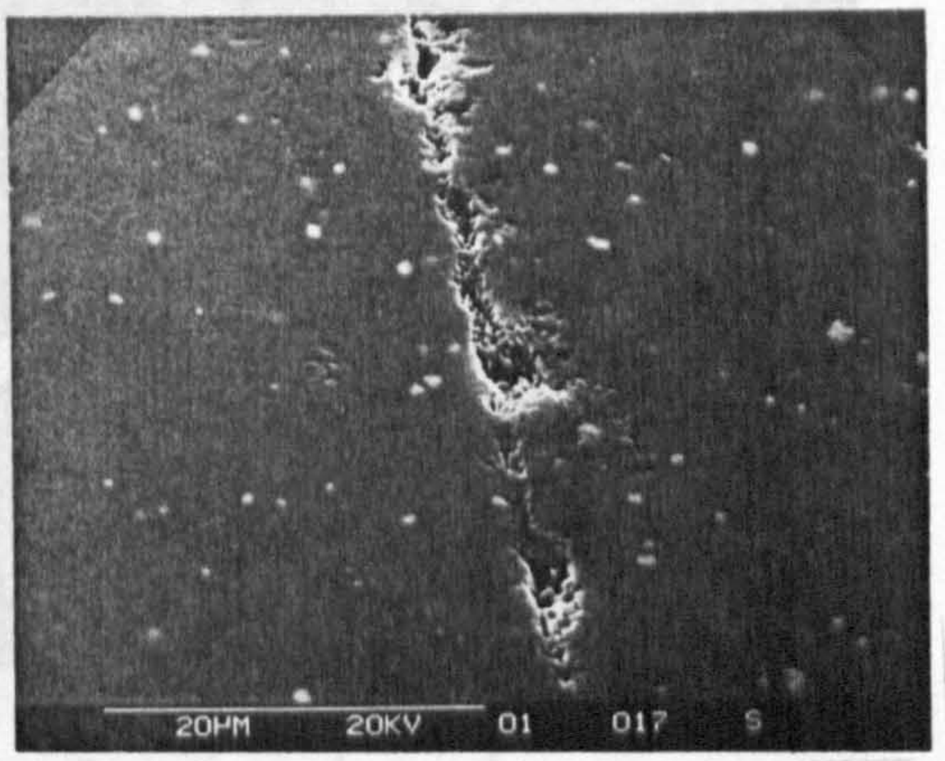

(b) Ring crack - first stage opening

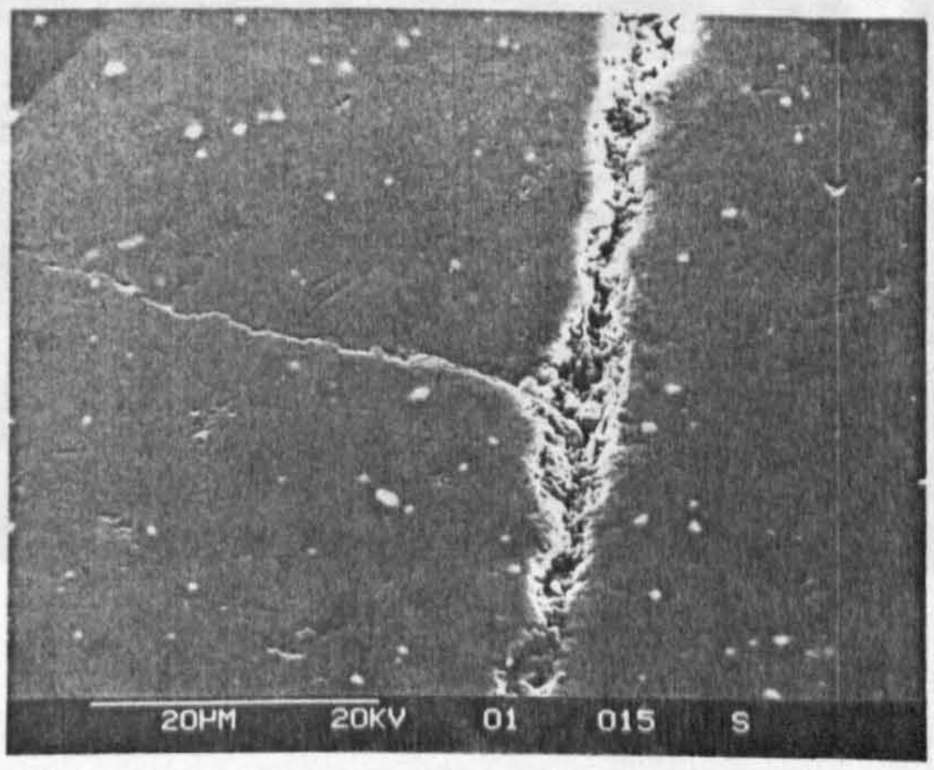

(c) Crack 90° to ring crack

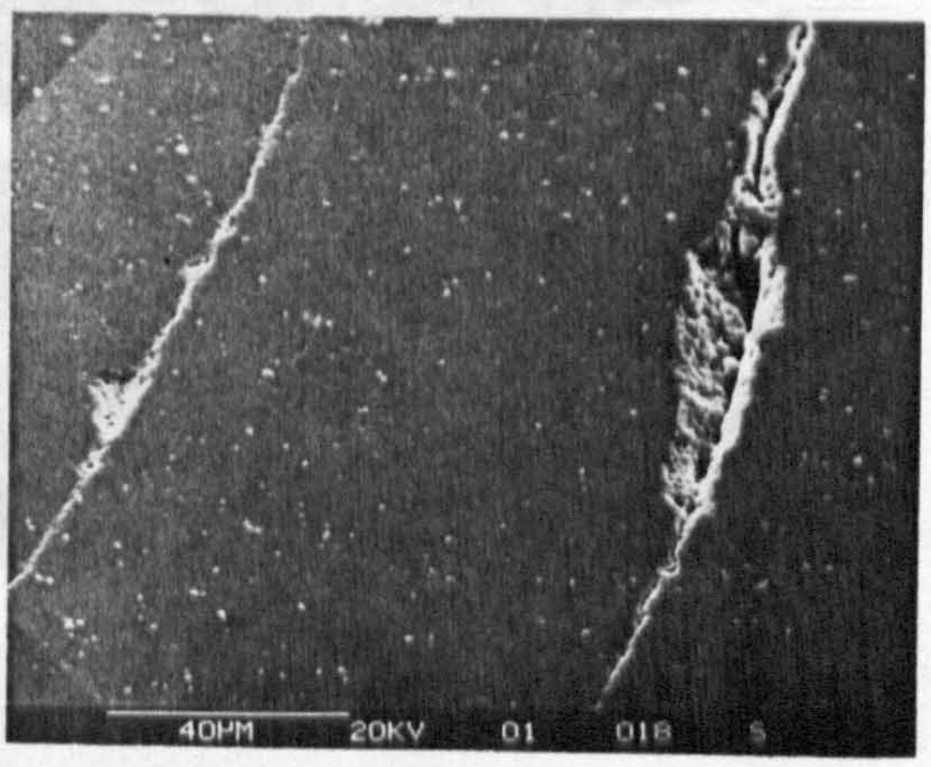

(d) Ring crack - second stage opening

Figure 5.31 Micrographs of stage one spall from test three - captions (a) to (d)

Second stage of failure, where material has began to be removed, is shown in figure 5.32, captions (a) to (e). Caption (a), shows the failure overview, details of ring crack and secondary damage is shown in captions (b) and (c). Detailed views of second stage damage is shown as captions (d) and (e). Debris are visible and incipient spall resulting from gradual removal of ceramic particles resulting is evident.

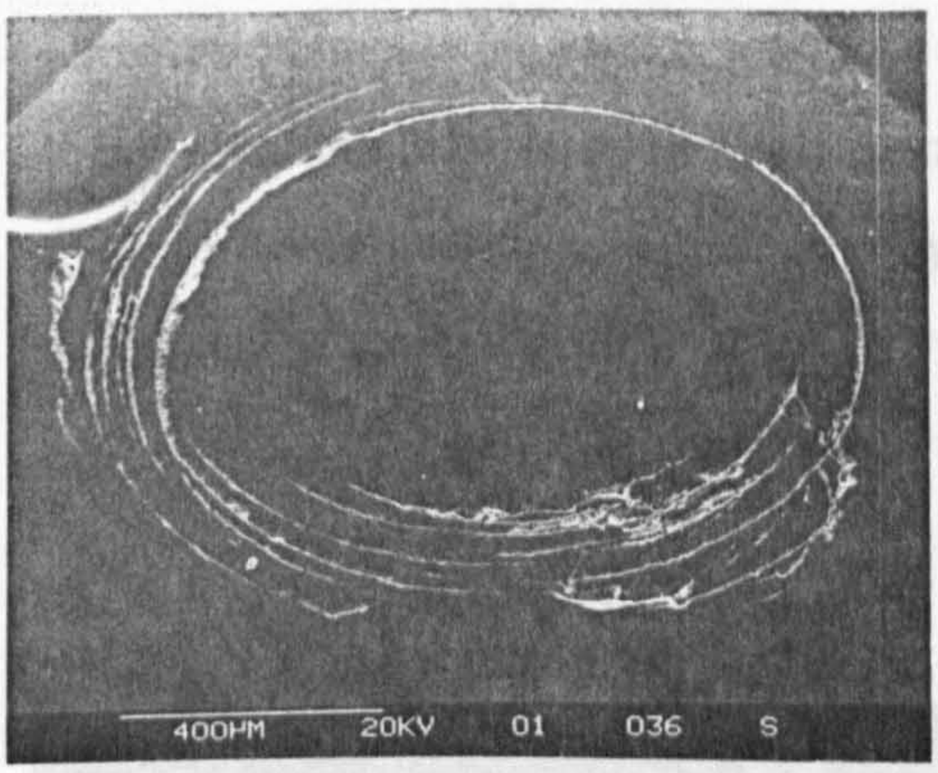

(a) Failure overview

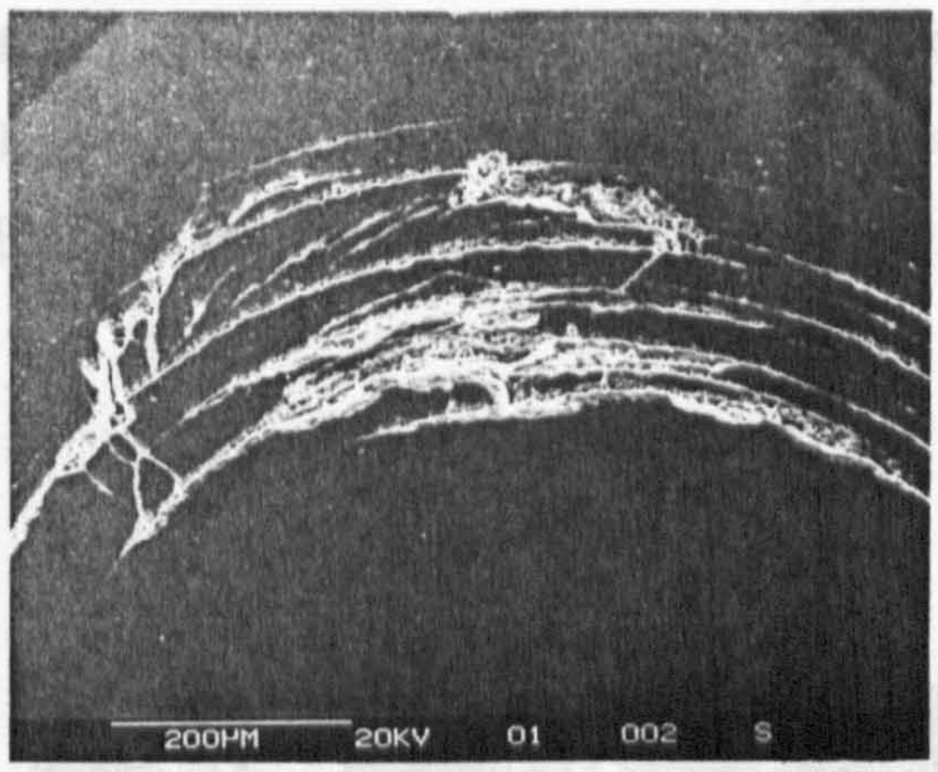

(b) Incipient spall area

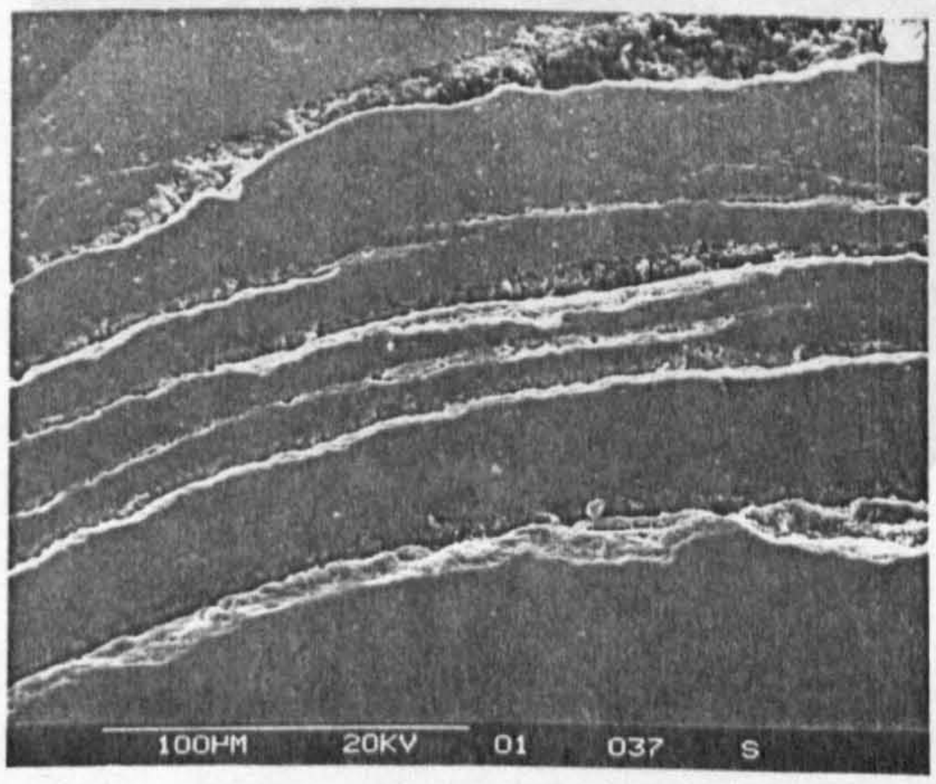

(c) Detail of ring cracks

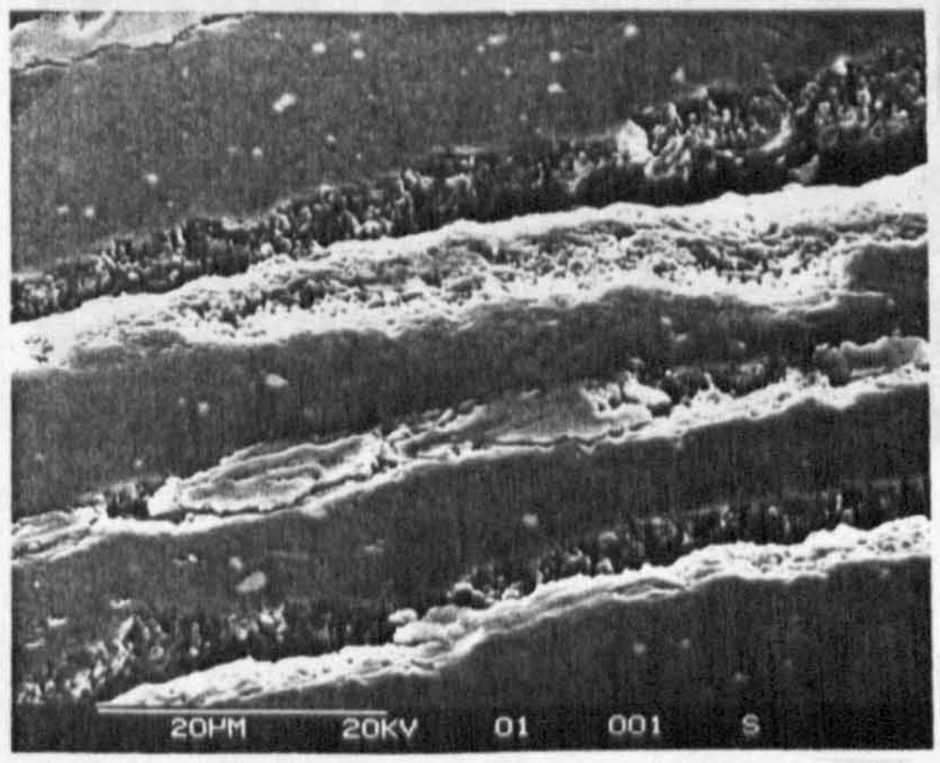

(d) Crack detail

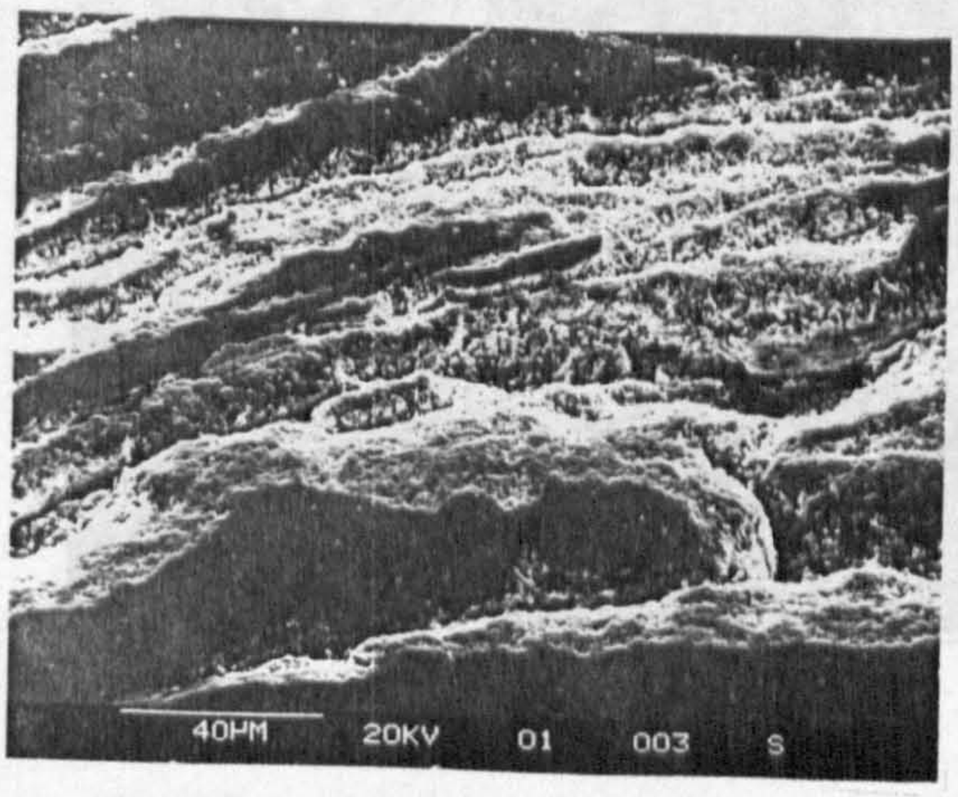

(e) Surface damage

Figure 5.33, captions (a) to (c), shows an example of a third stage spall. Caption (a) shows the overview of partial spall. A significant amount of material is removed from the ring area. Analysis of the failure at the edges, captions (b) and (c), shows the main ring crack and parallel secondary crack. After additional stress cycles the spall volume will inevitably increase due to material between ring and secondary crack removal.

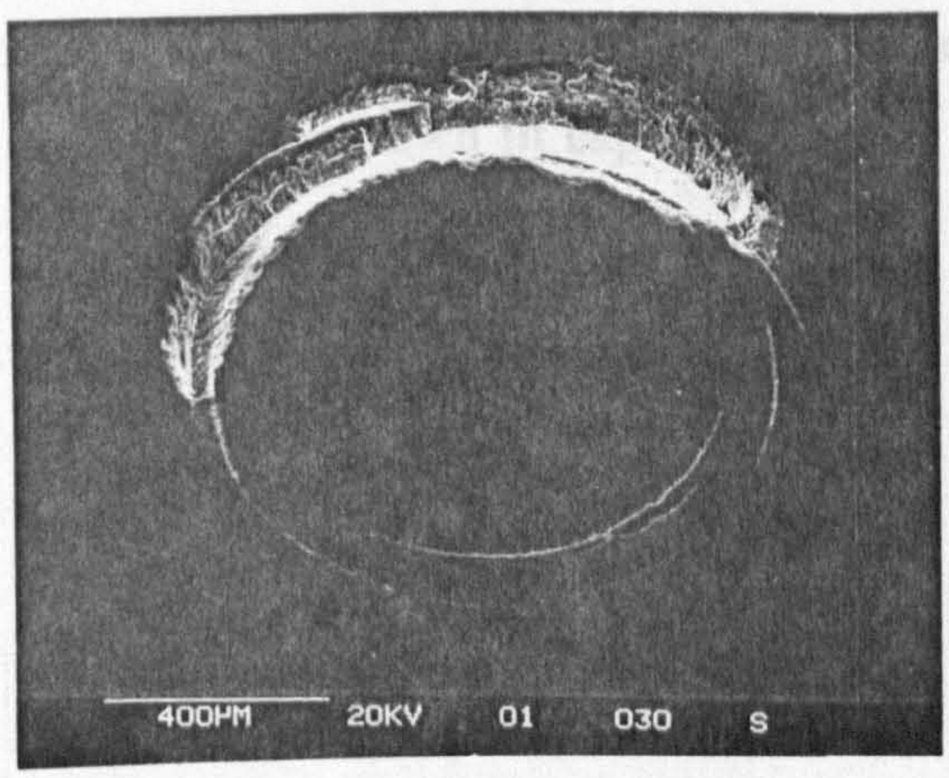

(a) Failure overview

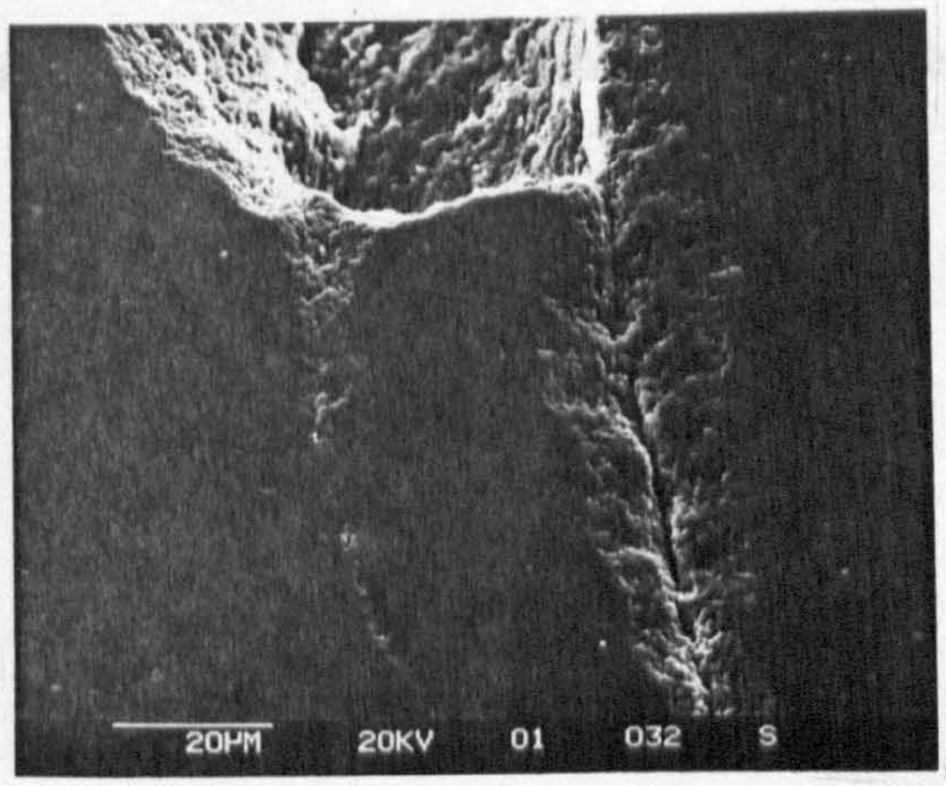

(b) Left edge

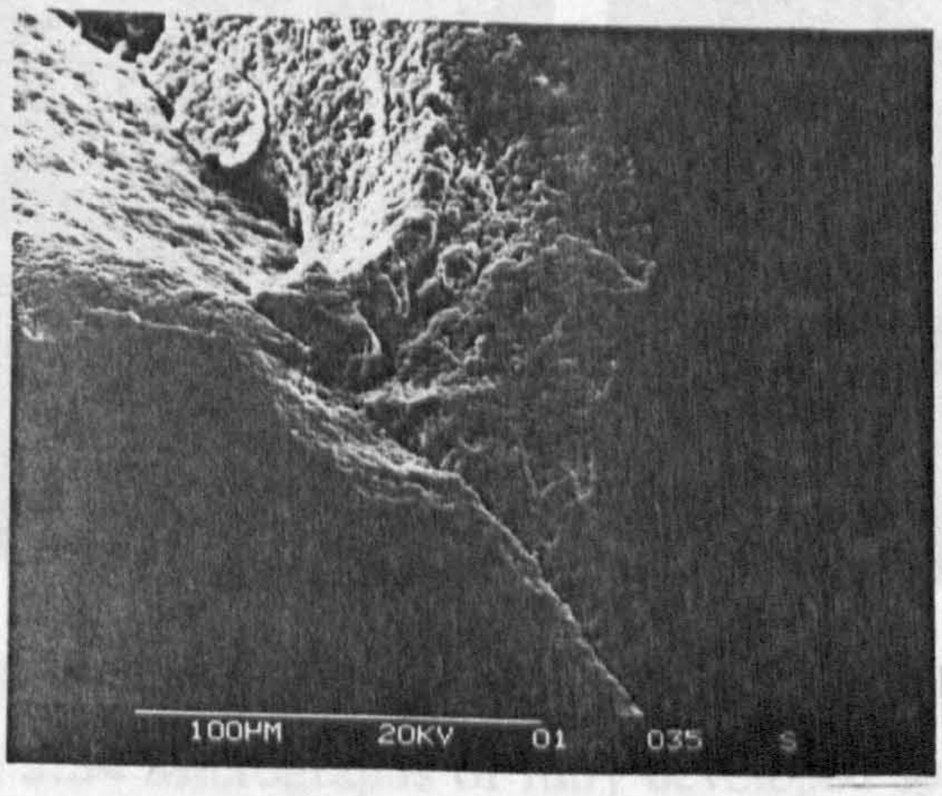

(c) Right edge

Figure 5.33 Micrographs of stage three spall from test two - captions (a) to (c)

A fully developed ring crack fatigue spall is shown in figure 5.34, captions (a) and (b). The smooth conical brittle fracture surface of the original ring-crack is evident. Final fracture resulting from subsurface micro-cracks (described by Cundill et al. (1992)) is taking place as the lubricant pressure produces large bending moment within the material. The smooth and beach-like marks on the cliff fracture edge indicate a combination of brittle and fatigue failure. Very low residual stresses, measured on the conical fracture face by Fujinawa et al. (1992), confirm a brittle fracture. Initial ring cracks running in parallel are responsible for the double edge effect, shown in caption (b).

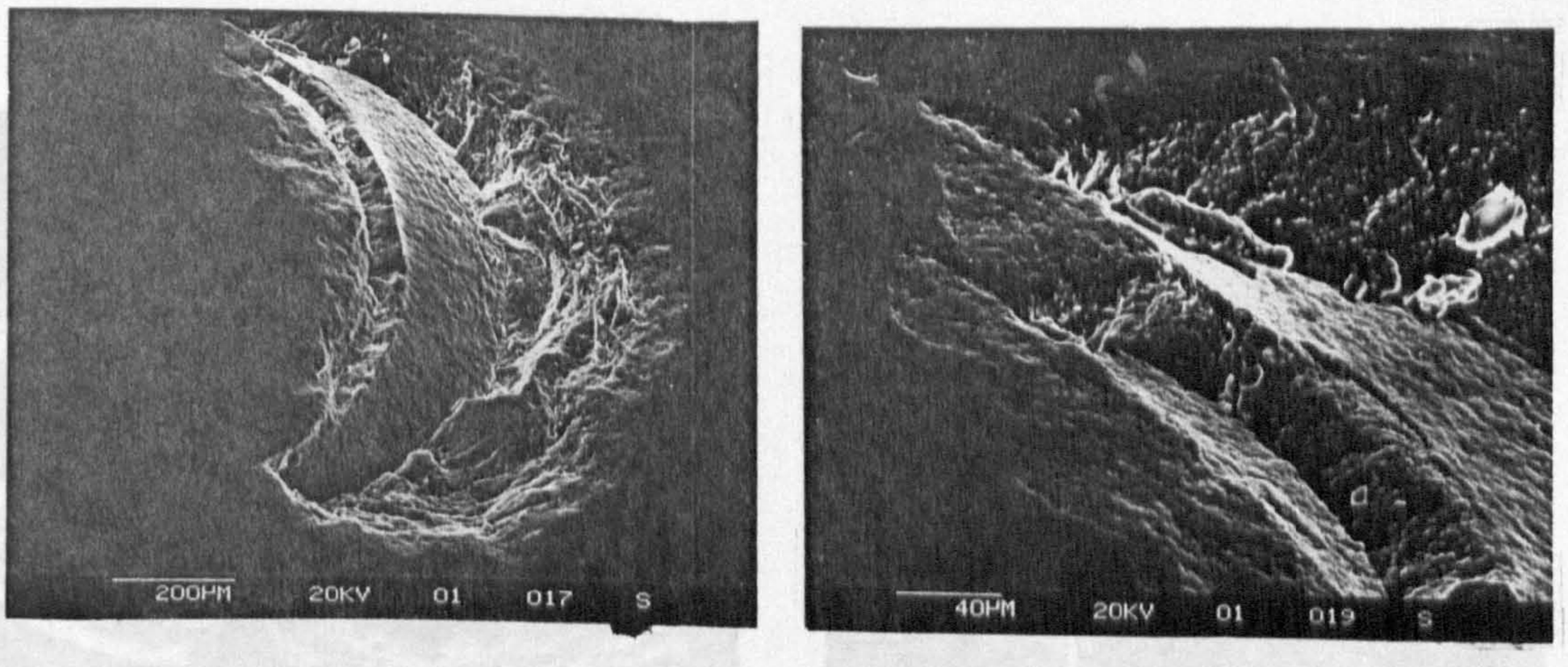

(a) Failure overview **(b)** Spall edge

Figure 5.34 Micrographs of fully developed spall from test one

Advanced ring crack spall with secondary damage, shown in figure 5.35, was produced from test three using kerosine as a lubricant. Captions (a) and (b) shows the spall overview and debris within a secondary spall. Close examination of the debris, caption (c), shows large volumes of material separated from the ball surface. A highly magnified view of the secondary spall shows crack branching on the ball surface.

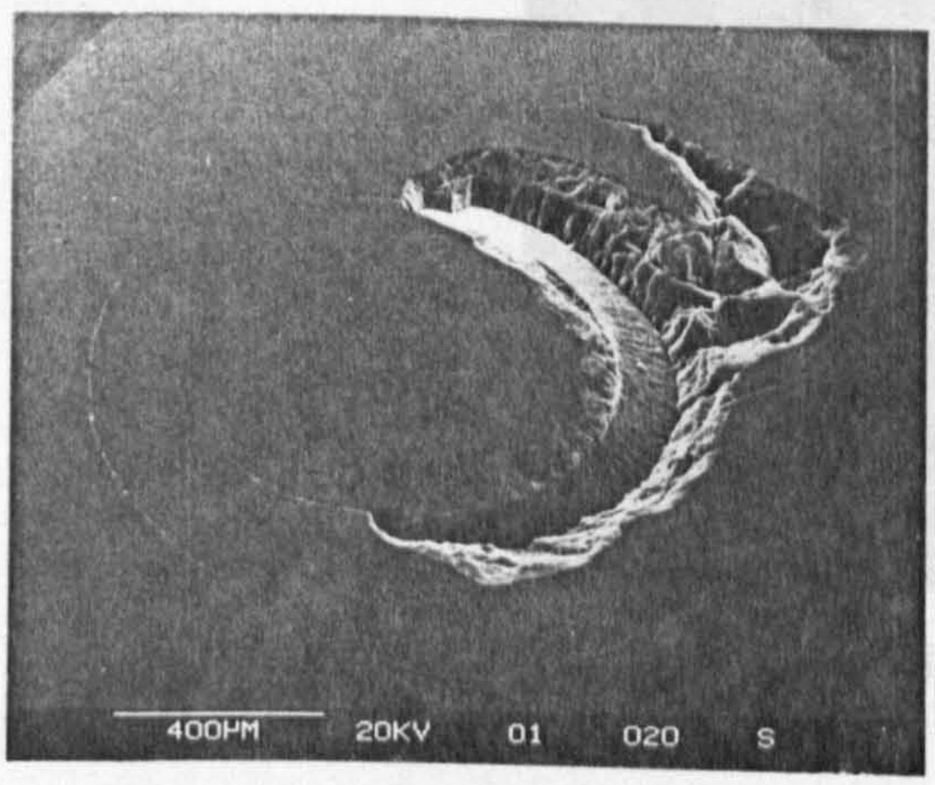

(a) Failure overview

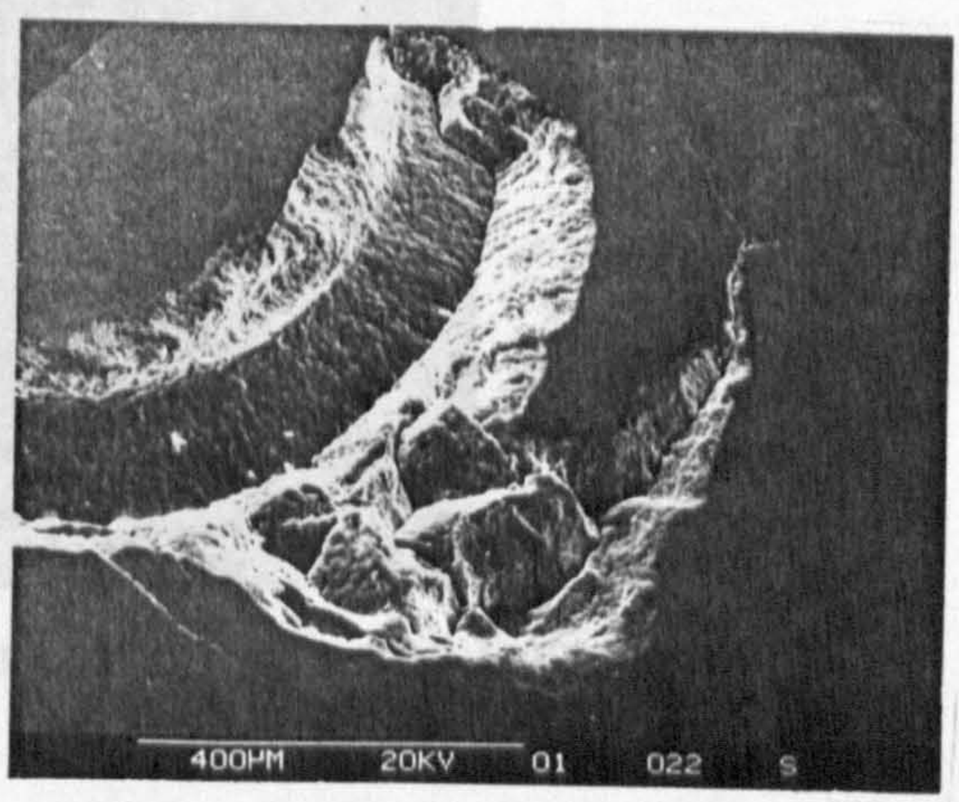

(b) Additional damage

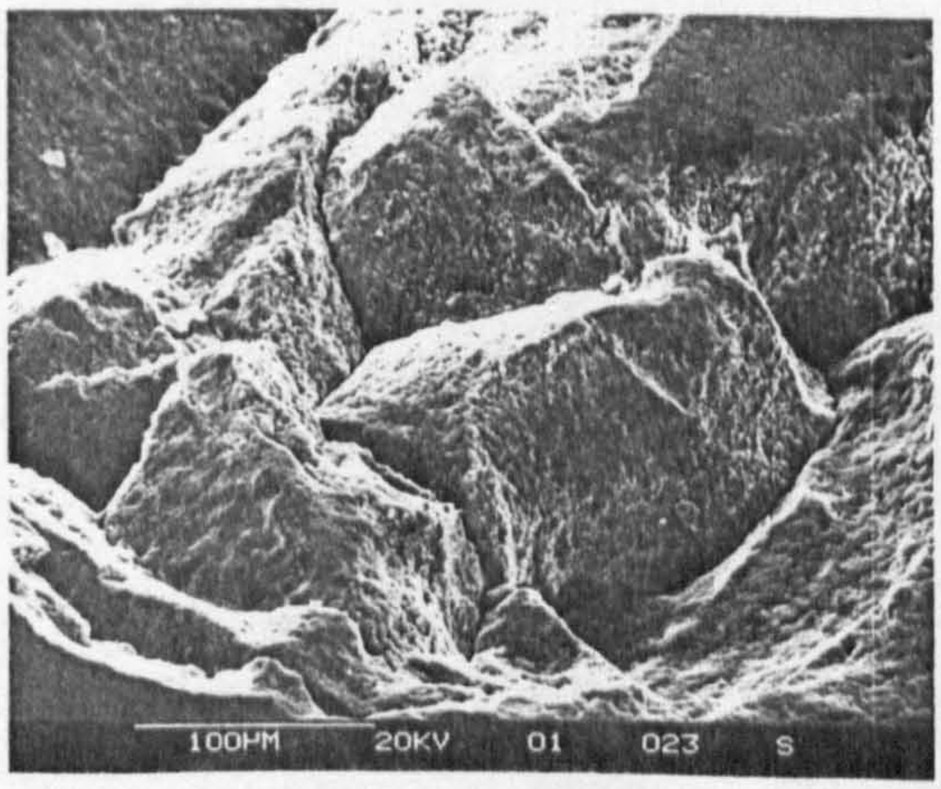

(c) Debris in damaged area

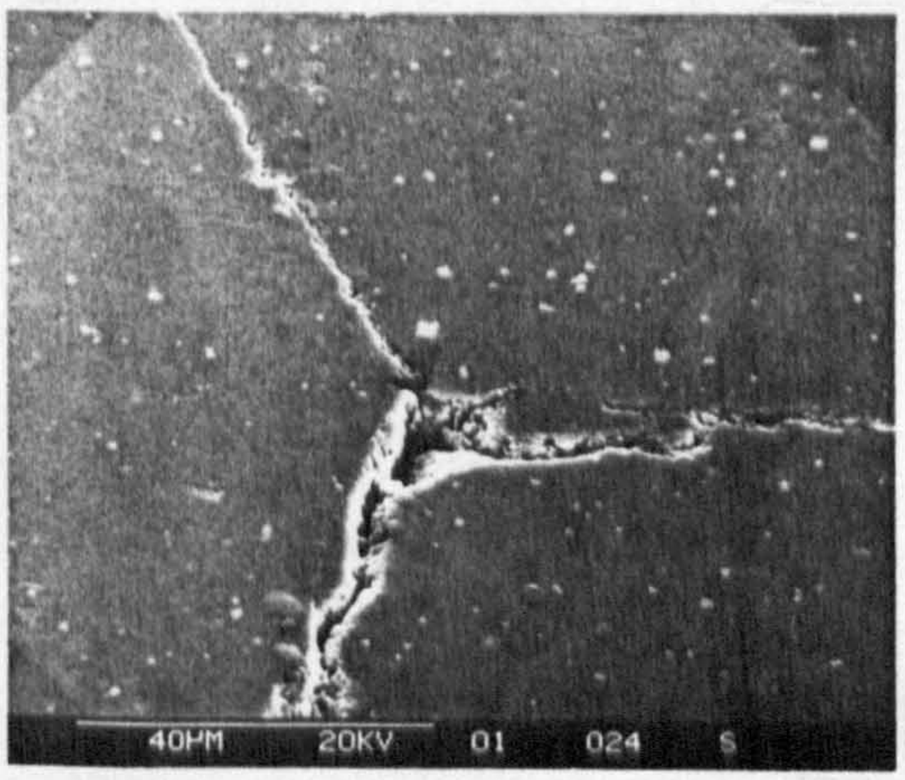

(d) Surface crack growth

Figure 5.35 Micrographs of advanced spall from test three - captions (a) to (d)

A double ring crack spall is illustrated in figure 5.36. This example shows how fully developed ring cracks may fail under random rolling directions, such as found in a conventional ball bearing.

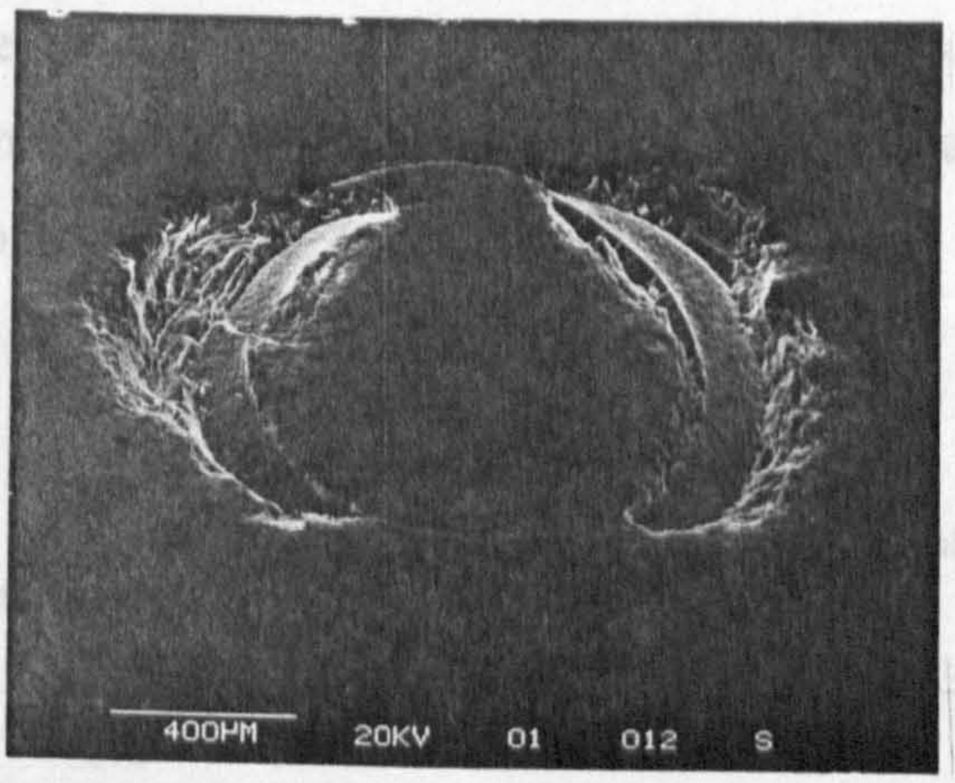

Figure 5.36 Micrograph of double ring crack spall from test one

5.3 Silicon Nitride Ball Tests Under Mixed Lubrication

5.3.1 Emulsified Oil Lubrication - Ceramic/Ceramic Contact

This preliminary test series is detailed in table 5.11. Results from tests are shown in figure 5.37, where damage caused by wear dominates the failure mode. All tests were sump lubricated and problems with maintaining effective lubrication level was experienced. Lubrication problems were probably caused by water evaporation at asperity flash temperature. Tests were terminated when an unacceptable noise level was attained, although test time was arbitrary for wear mode failure. Maximum cyclic stress levels were considerably reduced due to geometric conformability resulting from upper-ball wear.

Table 5.11 Test conditions

TEST (5000 r.p.m.)	Maximum Compressive Stress (GPa)	Average Ball Roughness (Ra,μm)	Material	Temperature Ambient/ Final (°C)
1	8.0	0.004	UB	26/74
2	7.3	0.004	UB	27/66
3	7.6	0.004	UB	33/46

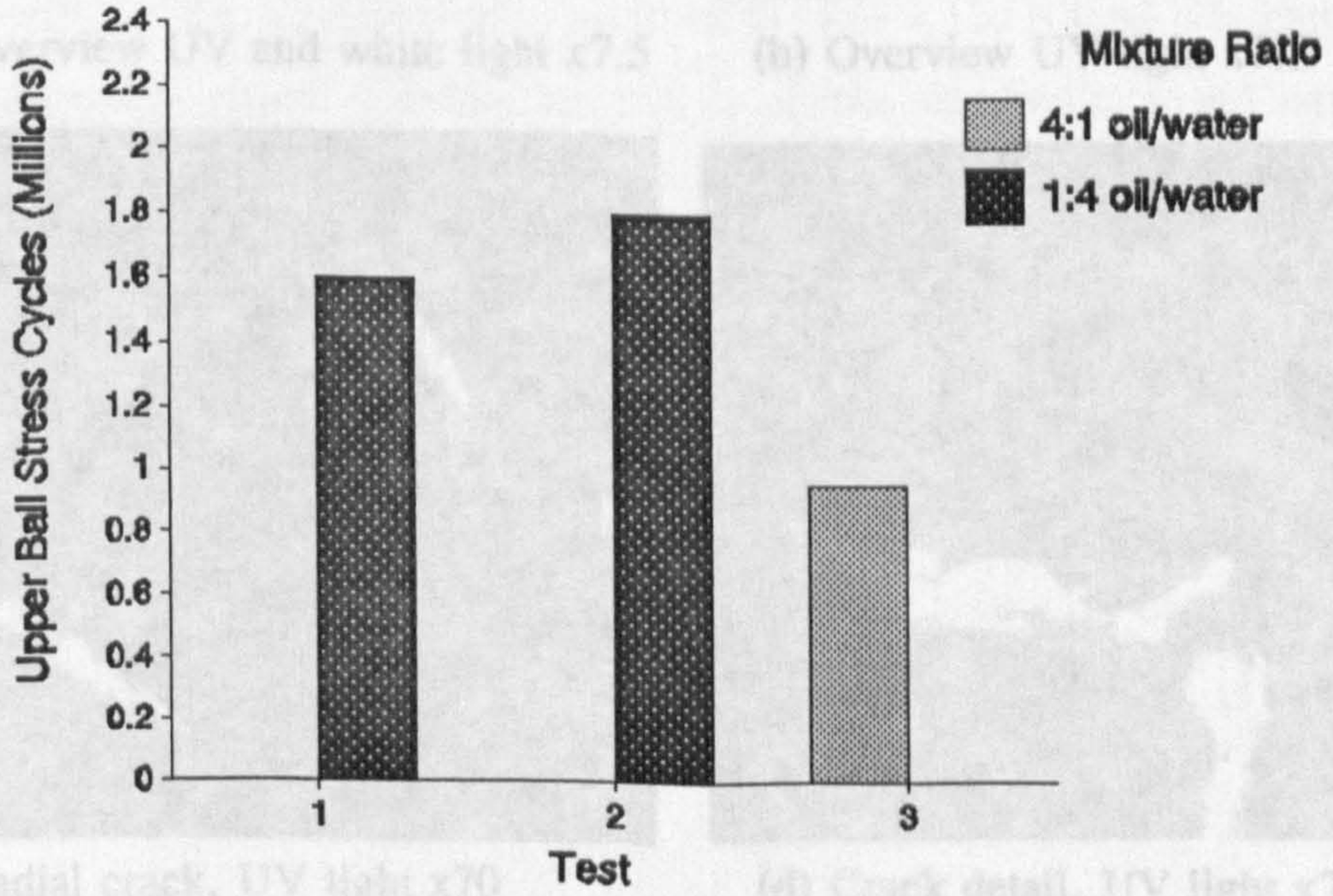

Figure 5.37 Emulsified oil results

Post test analysis by investigation of upper-ball wear path confirmed anticipated failure mode. Figure 5.38, shows results of microscopic analysis of a ball from test one using dye penetrant under white and ultra violet light. Radial cracks are evident on the wear path (see captions (c) and (d) of figure 5.38).

Surface roughness of all three lower balls from each test was measured, (see table 5.12). It can be seen that surface roughness of lower-balls deteriated considerably during test one and two. Lower-ball roughness of test three remained unchanged probably due to increased oil to water ratio.

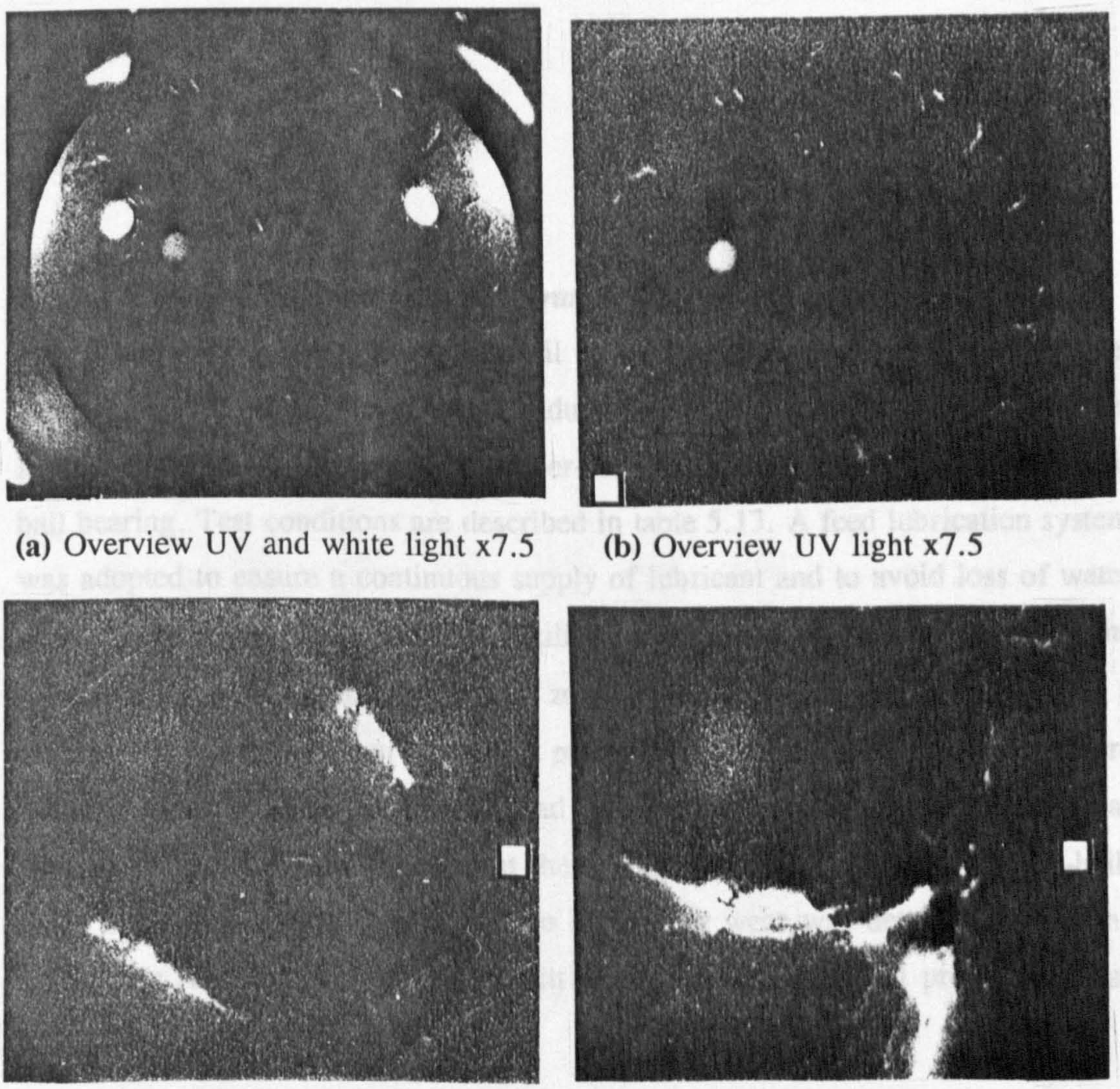

(a) Overview UV and white light x7.5

(b) Overview UV light x7.5

(c) Radial crack, UV light x70

(d) Crack detail, UV light x70

Figure 5.38 Microscopic analysis of wear path

Table 5.12 Lower-ball roughness analysis

TEST	Lower Ball Roughness (Ra,μm)		
	A	B	C
1	0.193	0.259	0.280
2	0.341	0.490	0.470
3	0.004	0.005	0.003

5.3.2 Emulsified Oil Lubrication - Ceramic/Steel Contact

Fatigue tests with emulsified oil as a lubricant of silicon nitride to steel contact are presented. Tests were conducted at 5000 r.p.m. with standard steel lower-balls and a standard ceramic upper-ball. This configuration models a hybrid ball bearing. Test conditions are described in table 5.13. A feed lubrication system was adopted to ensure a continuous supply of lubricant and to avoid loss of water due to evaporation. Ratio of oil to distilled water was one to one by volume. The lubricant was injected into the contact zone at a rate of 2.75 cc. per minute via a micro-pump. Results from tests are presented in figure 5.39. All tests were suspended at two million upper-ball load cycles. Maximum compressive stress was limited by the steel ball plasticity at these high rotational speeds. All upper-balls were microscopically analyzed, and no damage or wear was detected during any tests. This result shows that silicon nitride has good tribological properties in an emulsified lubricant environment.

Table 5.13 Test conditions

TEST (5000 r.p.m.)	Maximum Compressive Stress (GPa)	Average Ball Roughness (Ra,μm)	Material	Lubricant Mixture Ratio oil/water
1	5.4	0.01	NB/SKF3	1:1
2	5.7	0.01	NB/SKF3	1:1
3	6.0	0.01	NB/SKF3	1:1
4	6.2	0.01	NB/SKF3	1:1
5	6.4	0.01	NB/SKF3	1:1
6	6.6	0.01	NB/SKF3	1:1

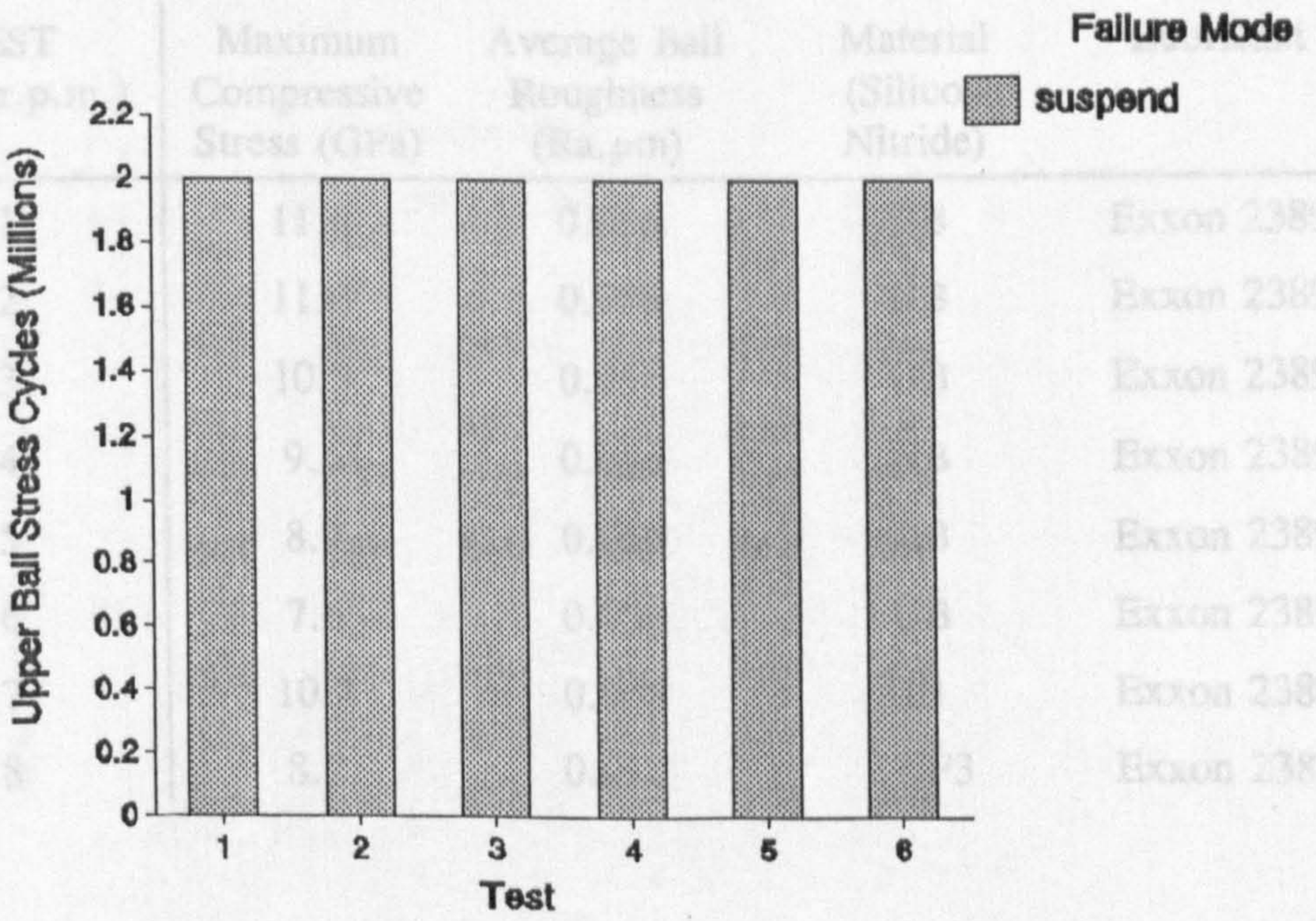

Figure 5.39 Emulsified oil results - ceramic/steel contact

5.4 Silicon Nitride Ball Tests With Varying Surface Roughness

A preliminary high-speed test of contacting rough ceramic balls at moderate load was conducted. This test terminated after ten million cycles. The upper-ball wear created surface conformability which reduced stress and, therefore, fatigue mode was not present. An additional preliminary test with ceramic/steel contact also produced gross wear, but this time to the lower steel balls.

Test details of low speed ceramic/ceramic contact with varying surface roughness are shown in table 5.14. Standard modified fatigue test of, steel/steel contact IP 300, was chosen for comparison. Tests from one to seven, described in table 5.14, show various surface roughness and applied stress. Test eight is a standard IP 300 test with steel/steel contact, the applied load (stress is reduced due to elasticity modulus reduction) is equal to that of test two.

Table 5.14 Test conditions

TEST (1450 r.p.m.)	Maximum Compressive Stress (GPa)	Average Ball Roughness (Ra,μm)	Material (Silicon Nitride)	Lubricant
1	11.6	0.056	UB	Exxon 2389
2	11.0	0.056	UB	Exxon 2389
3	10.3	0.056	UB	Exxon 2389
4	9.6	0.056	UB	Exxon 2389
5	8.7	0.056	UB	Exxon 2389
6	7.6	0.056	UB	Exxon 2389
7	10.3	0.008	UB	Exxon 2389
8	8.2	0.010	SKF3	Exxon 2389

Results from rough ball tests are shown in figure 5.40. All tests resulted in short cycles to failure. High stress levels used for test one to three show no difference in cycles to failure despite steady reduction of load. Tests four to seven steadily increase cycles to failure with decreasing applied load. Test seven of smooth ceramic balls at the same load as test three, showed that surface roughness affects cycles to failure at low speed. Steel/steel contact form test eight failed by spalling after 250 thousand stress cycles.

Test seven and eight confirm that at excessively high loads, roughness has a weak influence on cycles to failure. Steel contact behaves much better at excessive loads as the material has grater toughness and tensile stress resistance. However to compare the ceramic and steel rolling contact fatigue resistance for ball bearing applications based on this test is unrealistic, as typical maximum compressive stress experienced by ball bearings is between 2.0 and 3.0 GPa.

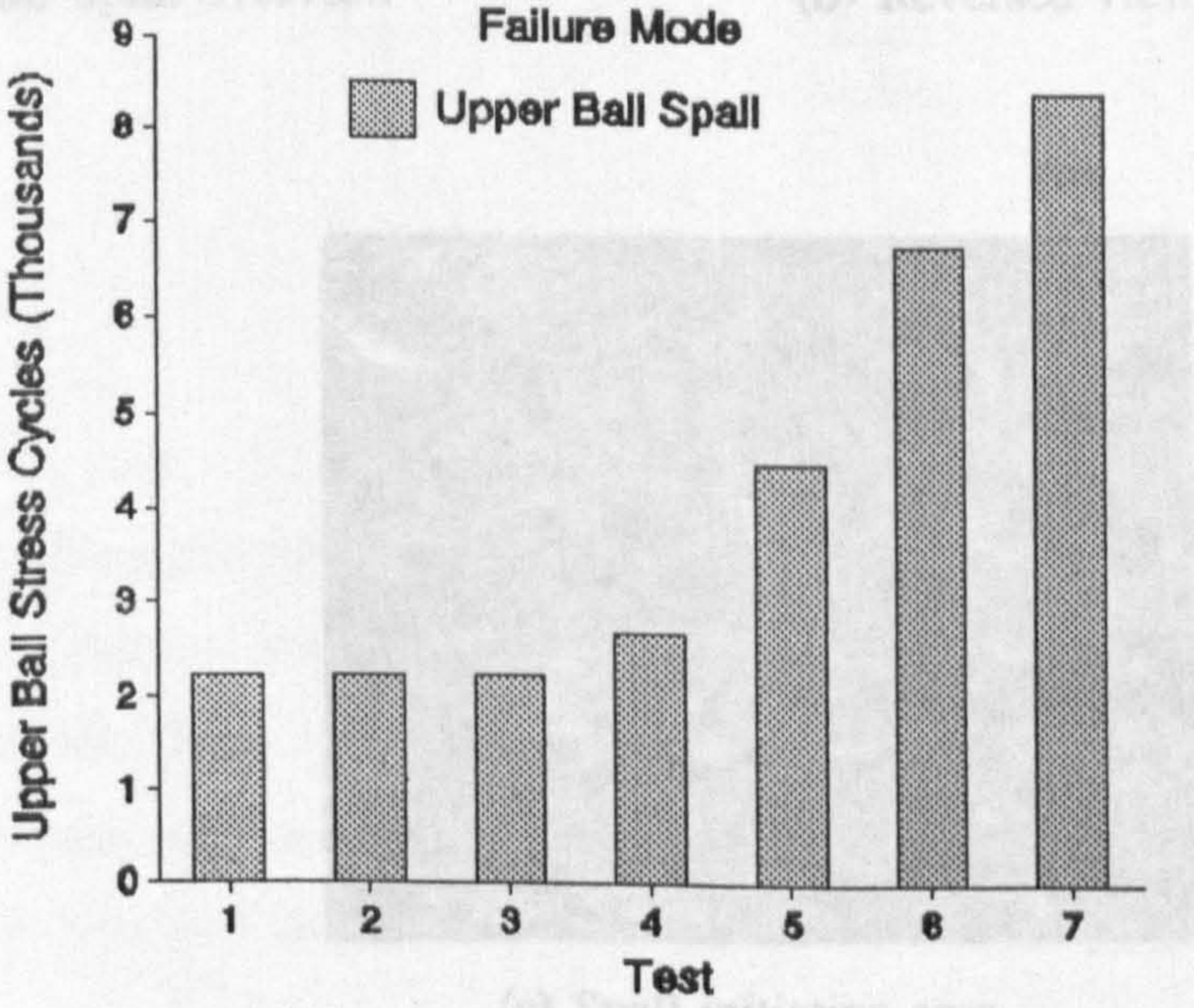

Figure 5.40 Rough ball test results

Figure 5.41 shows micrographs of a rough ceramic upper-ball spall from test three. Micrograph, caption (a), shows the general spall overview. Direction and height of undulations found on the base reflect spall depth and rolling direction. Reversed view, caption (b), shows the spall position on the contact path. Initial surface damage is shown as caption (c).

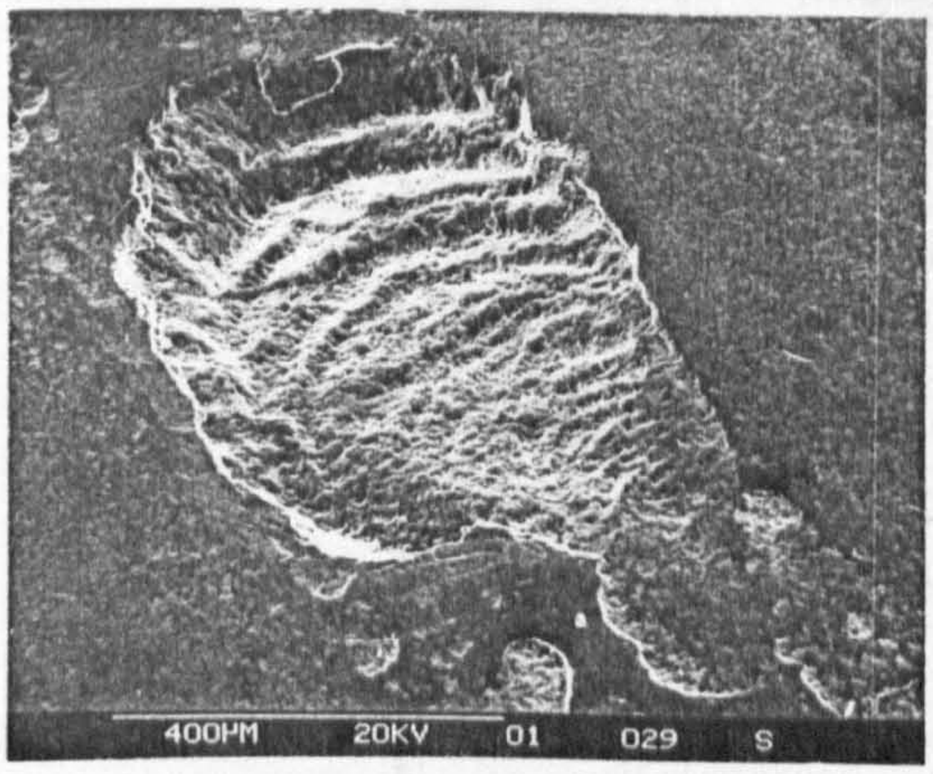

(a) Spall overview

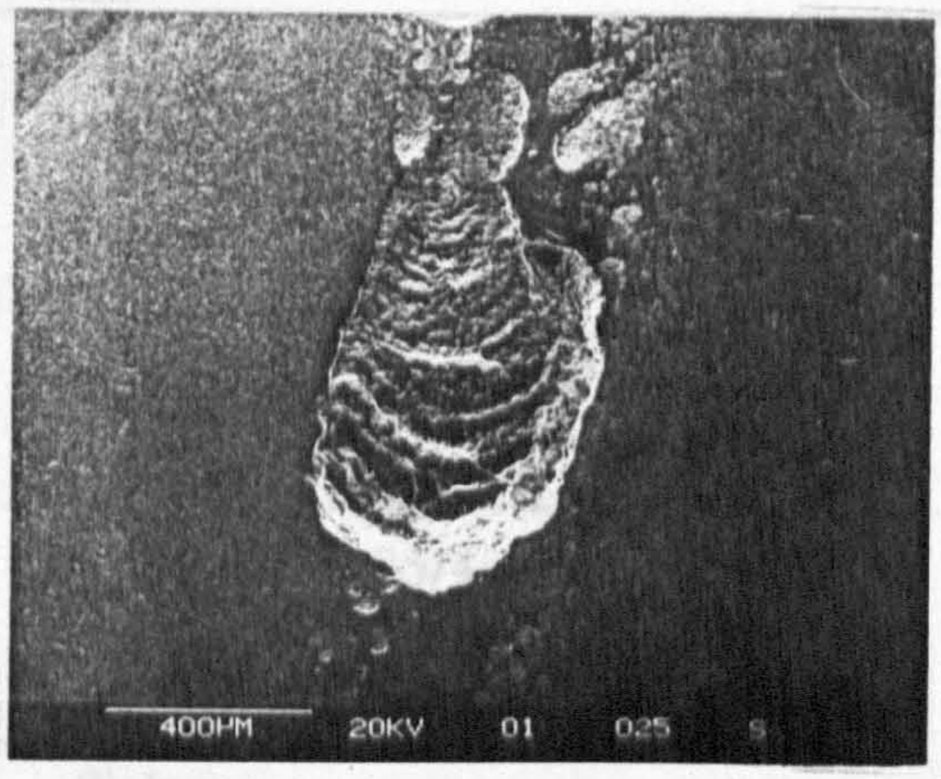

(b) Reversed view of spall

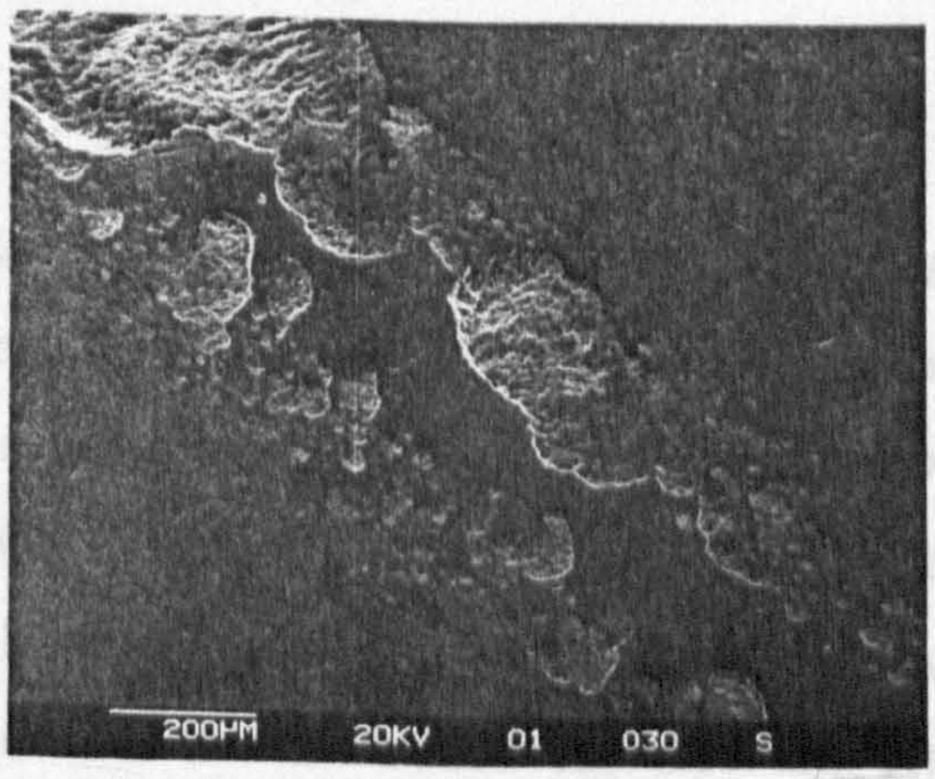

(c) Spall initiation area

Figure 5.41 Micrographs of upper ball spall from test three

5.5 Sialon Ball Tests

Contact fatigue tests on sialon ceramic balls are detailed in table 5.15. Tests at moderate speeds investigated failure modes with various contacts, loads and lubrication. Tests one to three concerned ceramic/steel contacts at varying contact pressure. Tests four and five considered ceramic/ceramic contacts at different pressures. The final test was unlubricated ceramic/ceramic contact.

Table 5.15 Test conditions

Test (5000 r.p.m.)	Maximum Compressive Stress (GPa)	Ball Roughness (Ra,μm)	Material: Upper / Lower	Temperature Ambient/Final (°C)	Lubricant
1	6.8	0.034 / 0.011	Sialon/ SKF3	22/72	Talpa 20
2	7.35	0.034 / 0.011	Sialon/ SKF3	22/67	Talpa 20
3	7.68	0.034 / 0.011	Sialon/ SKF3	22/95	Talpa 20
4	6.0	0.034	Sialon/ Sialon	25/44	Talpa 20
5	7.6	0.034	Sialon/ Sialon	23/44	Talpa 20
6	7.6	0.034	Sialon/ Sialon	n/a	Unlubricated

Results of sialon ball tests are shown in figure 5.42. Test one was suspended after reaching the pre-determined two million maximum cycles. Test two and three were stopped due to excessive noise. All three tests showed wear on the upper-ball contact path. Tests two and three produced damage to the steel lower balls in the from of wear and spalls. Lubricant was free from suspended wear debris in test one, while in tests two and three it was clouded with steel and ceramic particles.

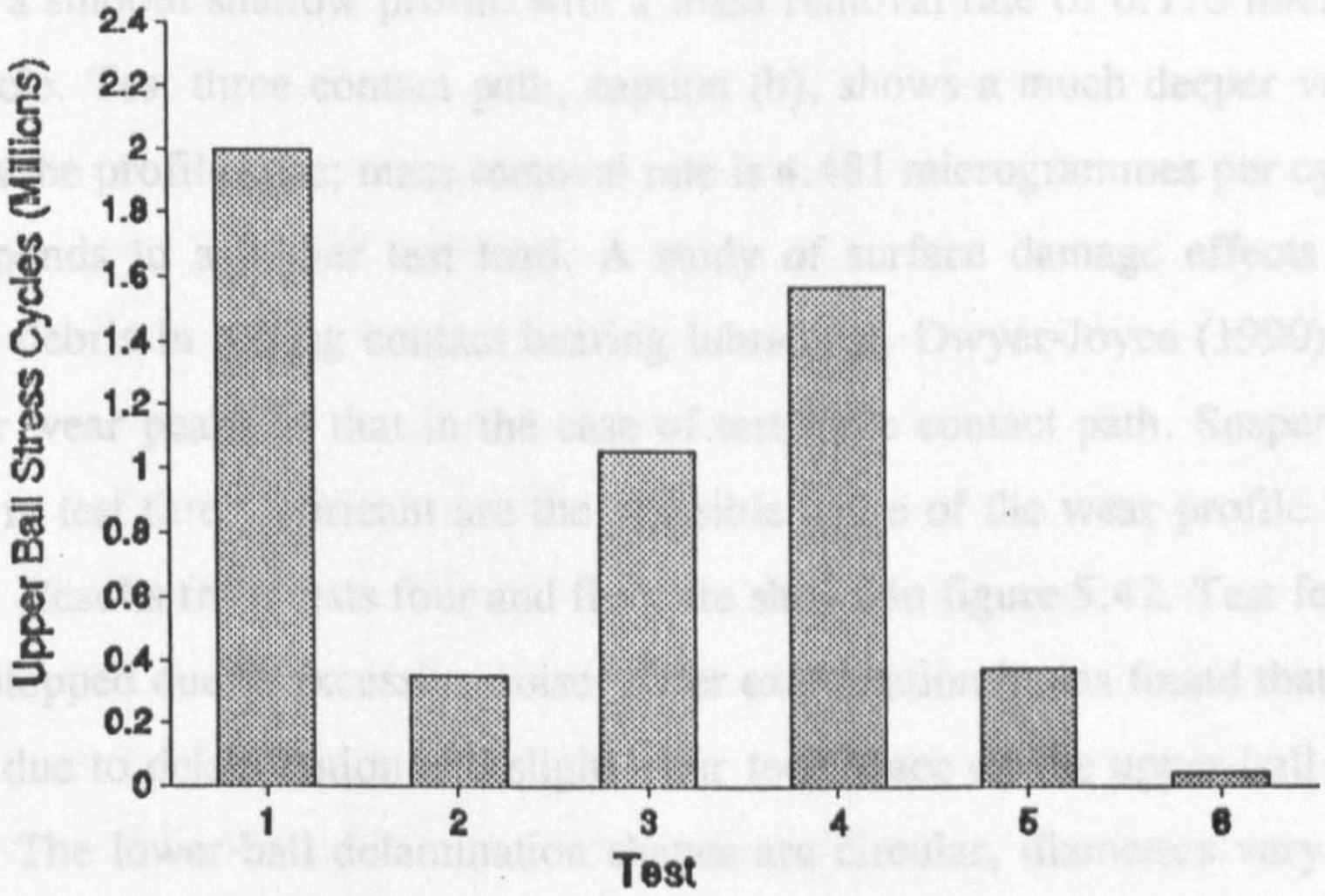

Figure 5.42 Sialon test results

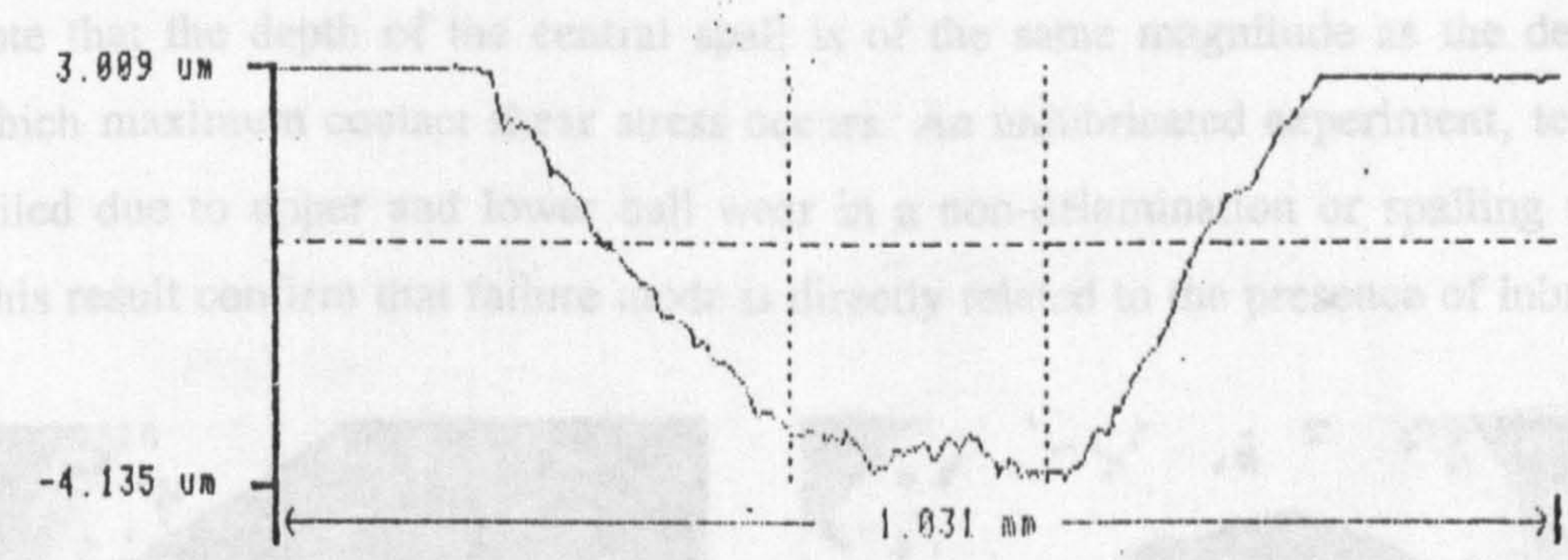

(a) Test one

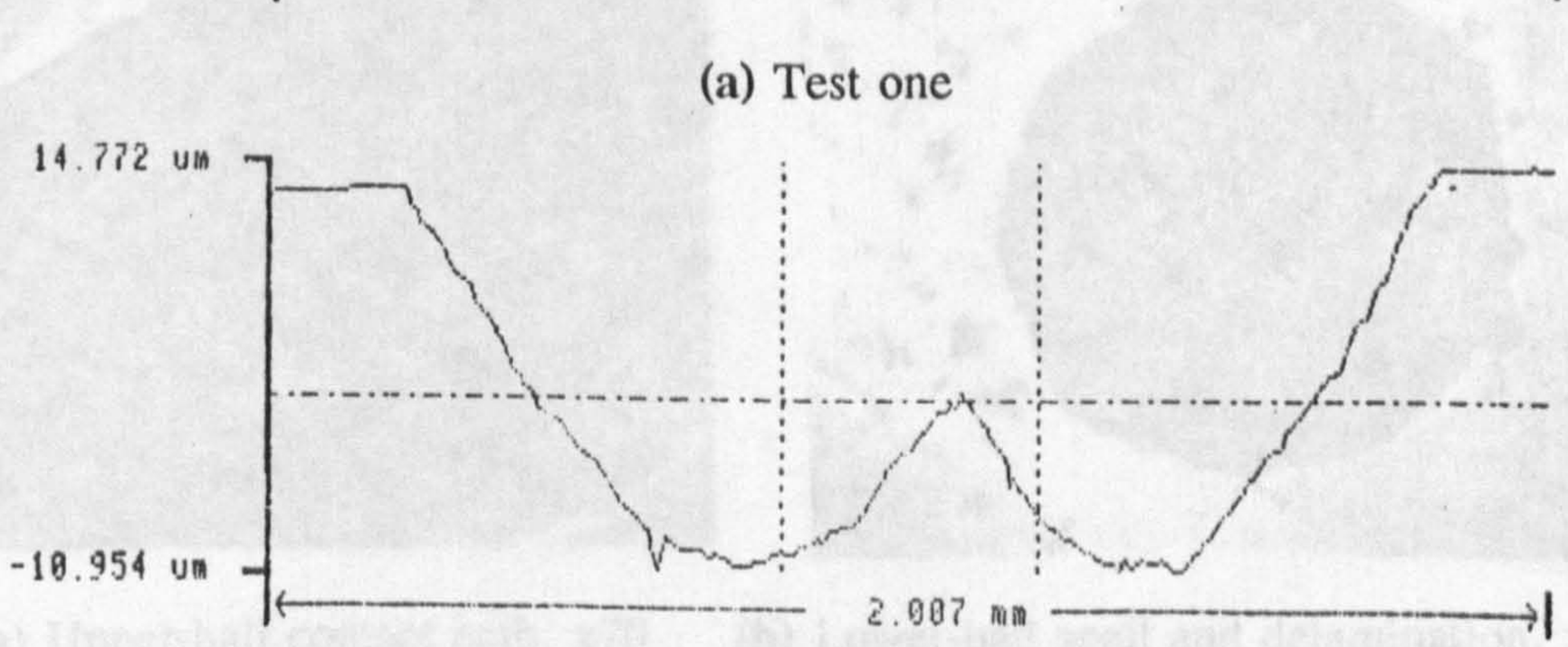

(b) Test three

Figure 5.43 Contact path wear profiles

Figure 5.43, captions (a) and (b) show wear profiles of the upper-ball contact paths resulting from test one and three. The contact path from test one, caption (a), shows a smooth shallow profile with a mass removal rate of 0.116 microgrammes per cycle. Test three contact path, caption (b), shows a much deeper valley and a peak at the profile base; mass removal rate is 4.481 microgrammes per cycle, which corresponds to a higher test load. A study of surface damage effects caused by friable debris in rolling contact bearing lubricants, Dwyer-Joyce (1990), describes similar wear peaks as that in the case of test three contact path. Suspended debris found in test three lubricant are the plausible cause of the wear profile shape.

Results from tests four and five, are shown in figure 5.42. Test four and five were stopped due to excessive noise. After examination it was found that lower-ball failed due to delamination and slight wear took place on the upper-ball (see figure 5.44). The lower-ball delamination shapes are circular, diameters vary from 0.57 millimetres to 2.28 millimetres and depth averages eight microns. A deep central spall within the delamination is also typical and varies from 0.07 millimetres to 0.64 millimetres in diameter and depth reaching eighty microns. It is also interesting to note that the depth of the central spall is of the same magnitude as the depth at which maximum contact shear stress occurs. An unlubricated experiment, test six, failed due to upper and lower ball wear in a non-delamination or spalling mode. This result confirm that failure mode is directly related to the presence of lubricant.

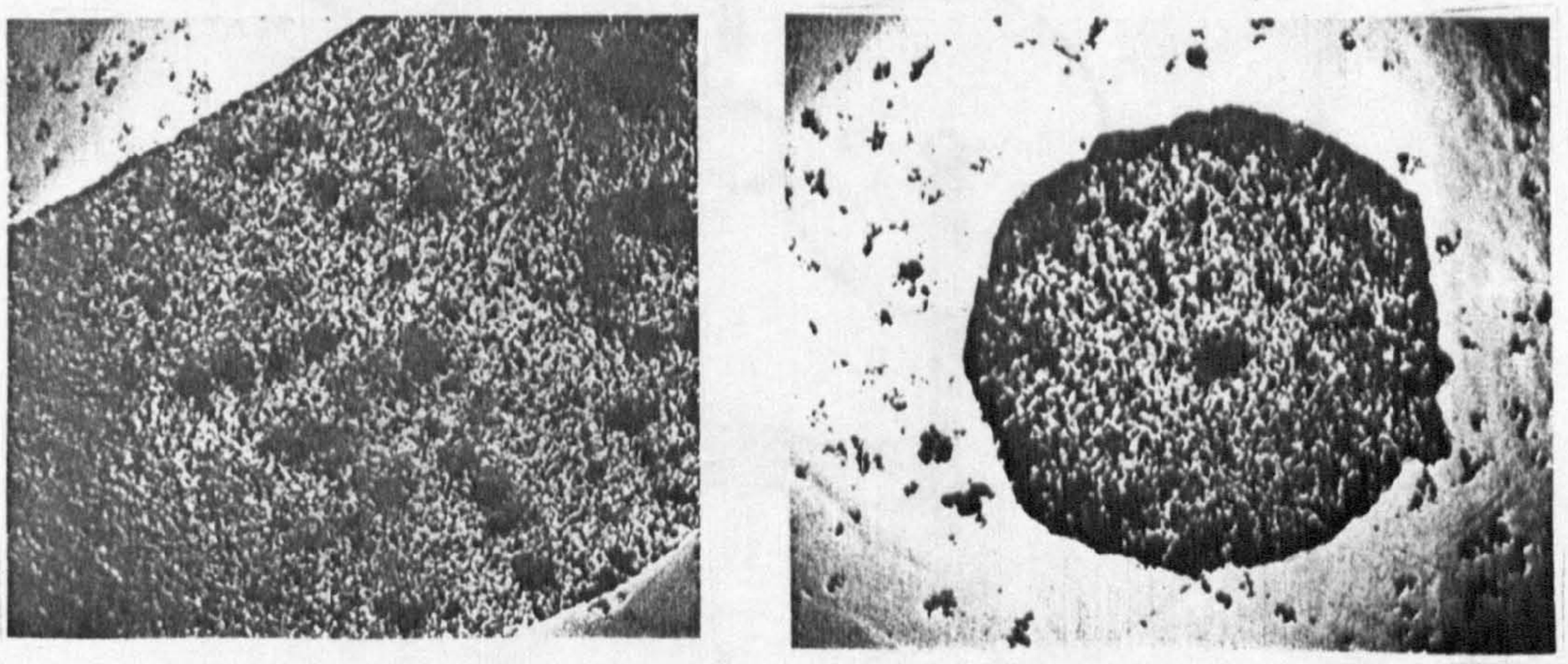

(a) Upper-ball contact path, x70 **(b)** Lower-ball spall and delamination, x 70

Figure 5.44 Photographs of test four upper and lower ball failure

5.6 Supplementary Silicon Nitride Rod Tests

5.6.1 Test Description

A supplementary rod/disc type rolling contact fatigue test is shown (schematically) in figure 5.45. A test rod of 9.53 millimetre diameter is clamped to a motor drive spindle. Rod eccentricity is checked by a dial test indicator clamped to the machine. Two 200 millimetre diameter discs with end radius ground to 12.7 millimetre diameter are rested on the test rod. A force of 2.9 kN is applied to the contact area via a turnbuckle and measured by a load cell.

Lubricant is dripped onto the contact area, the rod is rotated at 12,500 r.p.m. and drives the steel discs. Slip between the steel discs and test rod is measured by a stroboscope as 4.6 percent. Disc and rod alignment is adjusted after viewing the lubricant spray from the contact area. Test is stopped by a vibration sensitivity cell as in the modified four ball machine. Table 5.16 shows standard test data for this machine.

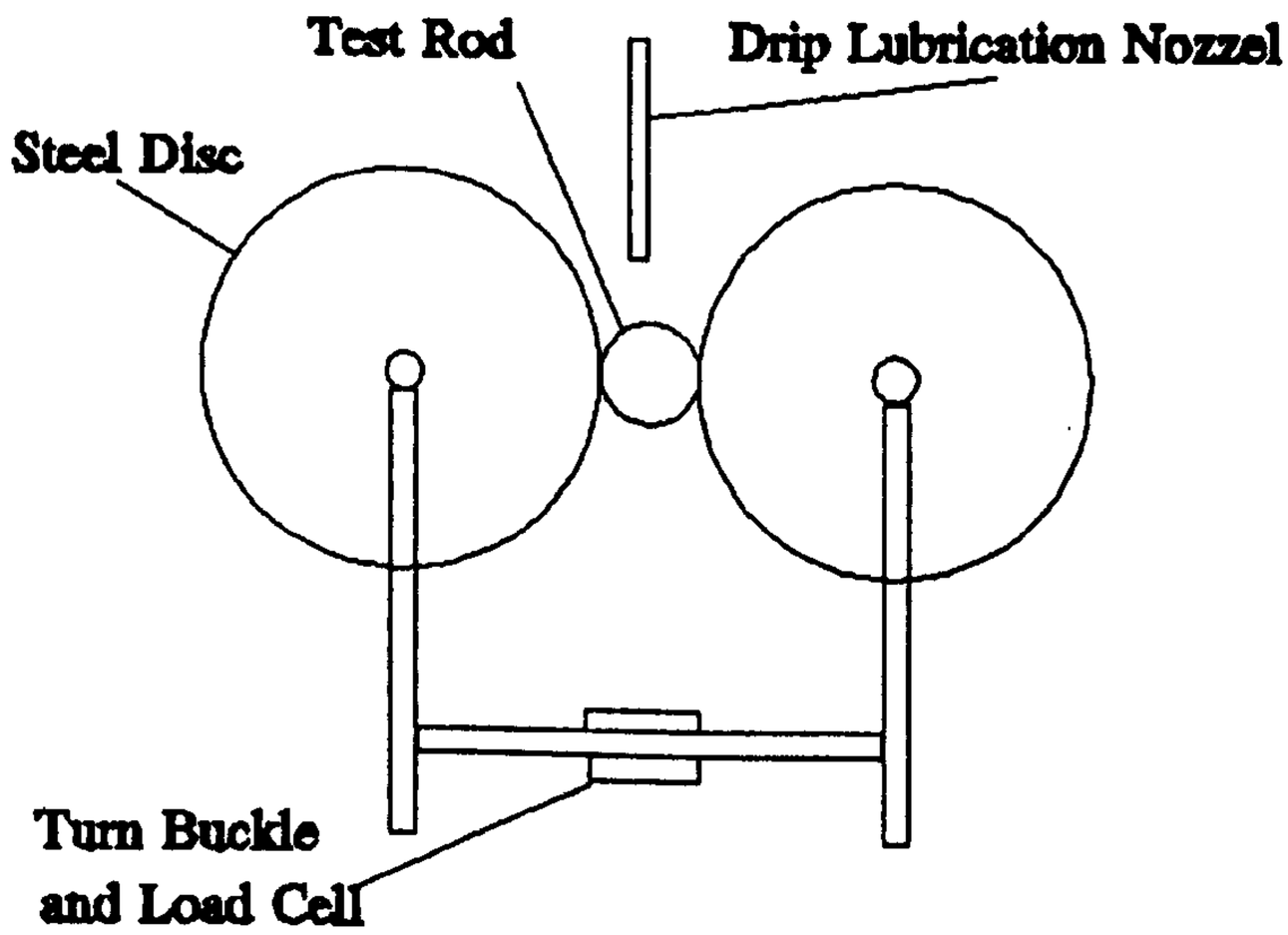

Figure 5.45 Rod Test Schematic Diagram

Table 5.16 Standard Test Data

Maximum Compressive Stress (GPa)	4.8 (steel rod)	5.4 (ceramic rod)
Surface Roughness (Ra,μm)	0.163 (steel disc)	0.100 (test rod)
Rod Speed (r.p.m.)	1250	
Lambda Ratio	1.6	

5.6.2 Standard Grade Material

Standard grade silicon nitride material tests are described in table 5.17. Test one was a validating test, with known fatigue performance of SKF3 grade bearing steel. Tests two and three were both fully dense ceramic which after considerable stress cycles were suspended or stopped due to steel disc spalling. Another ceramic, which contains micro-porosity, was used in tests four to seven. All tests were suspended after thirty million cycles to provide adequate screening and to avoid severe wear to the steel discs.

Table 5.17 Test Conditions

Test	Material	Test Stop Reason	Lubricant
1	SKF3 - Steel	Spall	Exxon 2389
2	CD - Ceramic	Spall (Disc)	Exxon 2389
3	CD - Ceramic	Suspend	Exxon 2389
4	NG - Ceramic	Suspend	Exxon 2389
5	NG - Ceramic	Suspend	Exxon 2389
6	NG - Ceramic	Suspend	Exxon 2389
7	NG - Ceramic	Suspend	Exxon 2389

Results from the standard tests are shown in figure 5.46. It is seen that the ceramic preformed better than the SKF3 steel and did not fail in any test. The tests of the ceramic containing micro-porosity show that although it is known that porosity is associated with premature contact fatigue failure, the density and pore size has a limiting influence. Figure 5.47 shows the contact path of test four where the micro-porosity is clearly visible. It can been seen from figure 5.47, caption (b) that the porosity on the contact path is no longer visible on the surface. It can be argued therefore that in this particular test configuration, debris from the contacting materials seem to fill in micro-pores.

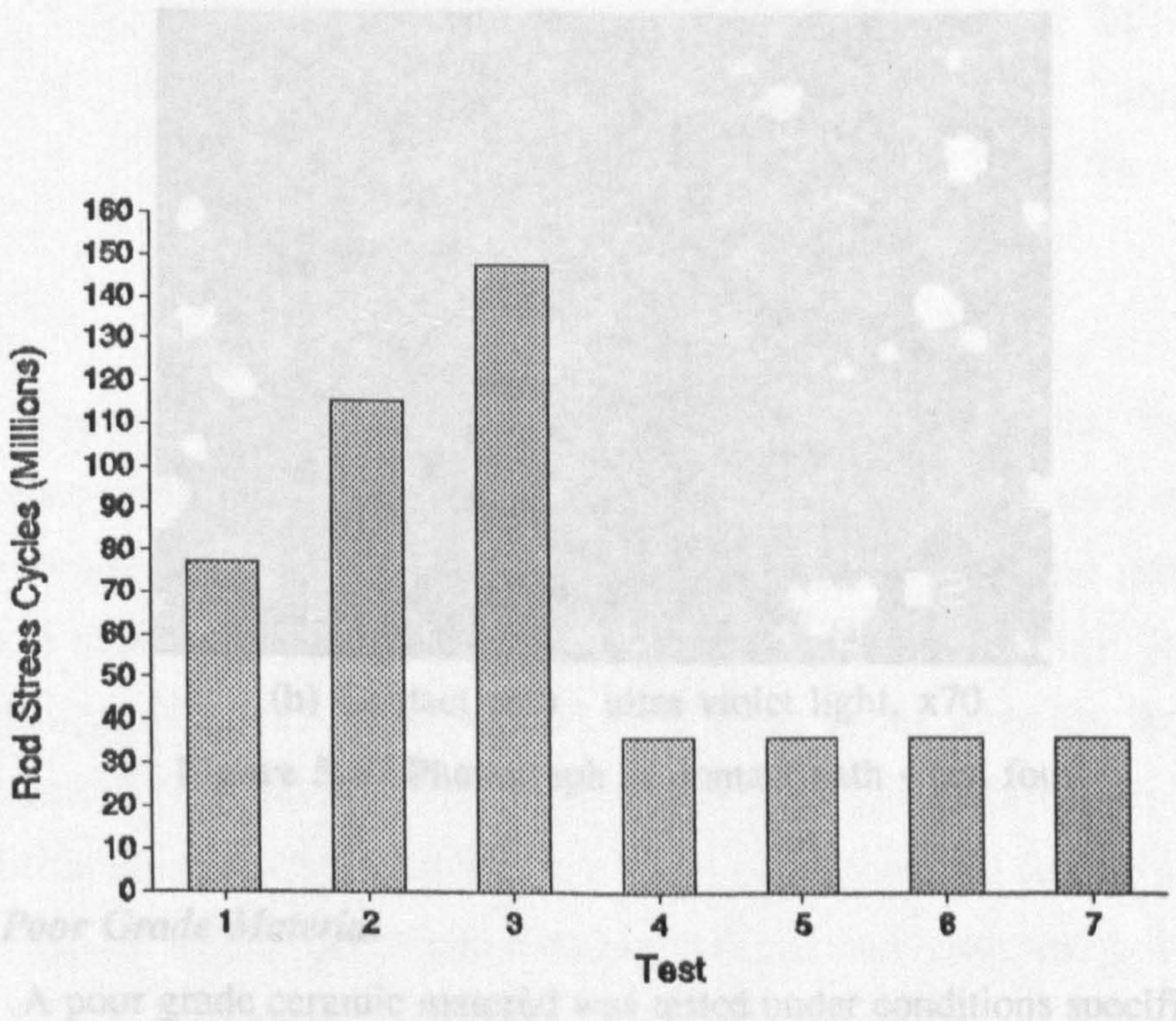

Figure 5.46 Standard material rod test results

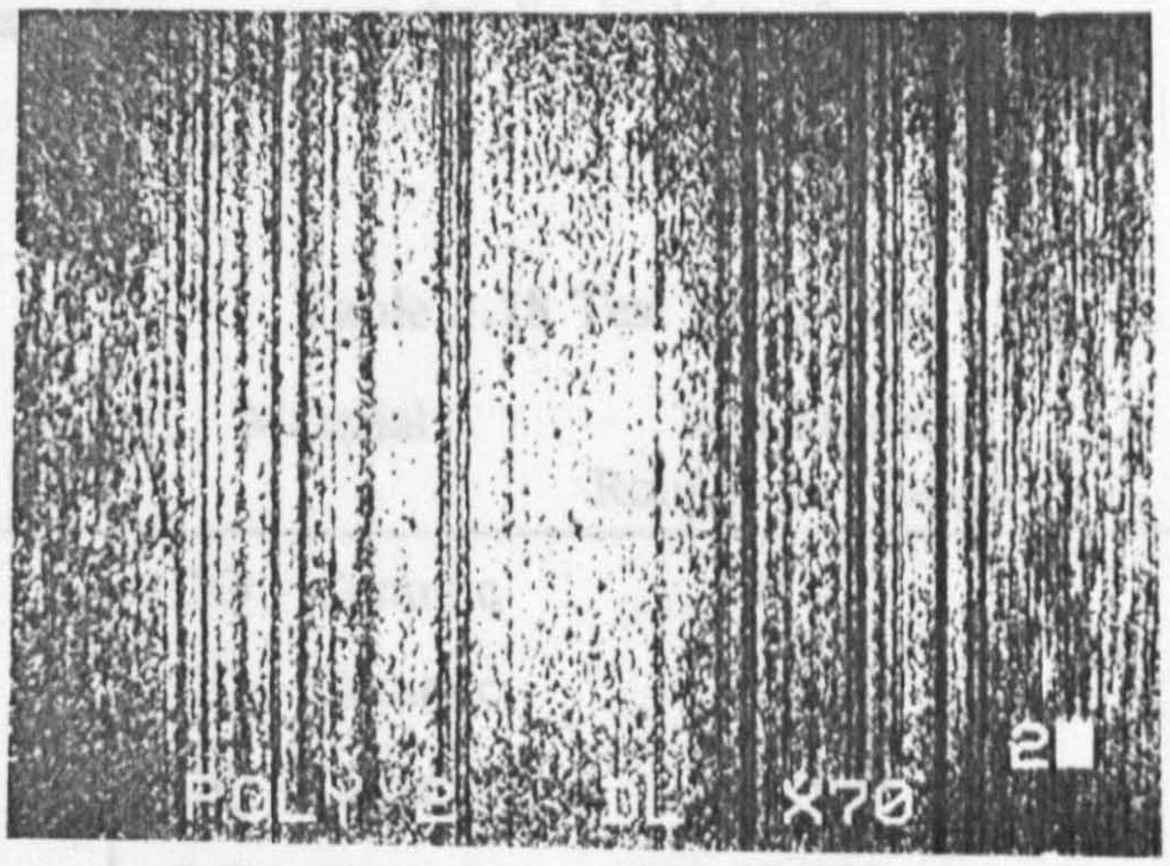

(a) Contact path - normal light, x70

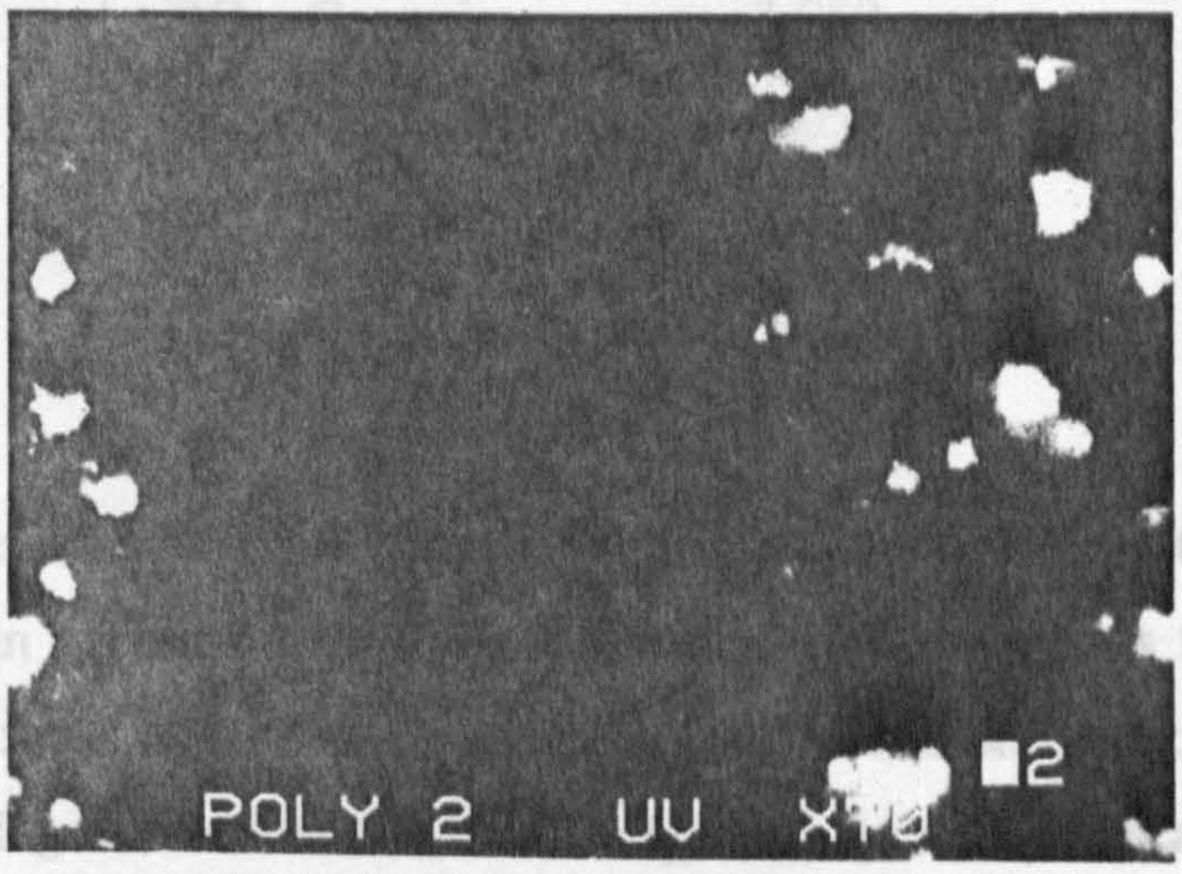

(b) Contact path - ultra violet light, x70

Figure 5.47 Photograph of contact path - test four

5.6.3 Poor Grade Material

A poor grade ceramic material was tested under conditions specified in table 5.18. The ceramic was designated as poor grade due to high porosity density, large porosity size and inclusions within the structure. Tests one to four examined the material fatigue life under standard conditions described in section [5.6.1]. The rod surface finish, for tests five to seven, was enhanced by diamond polishing in the presence of water. Test lubricant was then changed to Talpa 20 base oil which has greater viscosity than Exxon 2389 turbine oil. The modifications of tests five to

seven have the effect of bringing the lambda value to above three which implies little or none asperity contact at the disc/rod interface.

Table 5.18 Test Conditions

Test	Material	Rod Surface Roughness (Ra,μm)	Lubricant
1	DQ - Ceramic	0.100	Exxon 2389
2	DQ - Ceramic	0.100	Exxon 2389
3	DQ - Ceramic	0.100	Exxon 2389
4	DQ - Ceramic	0.100	Exxon 2389
5	DQ - Ceramic	0.050	Talpa 20
6	DQ - Ceramic	0.050	Talpa 20
7	DQ - Ceramic	0.050	Talpa 20

Test results are shown in figure 5.48. It can be seen that the material performance, in general, is poor when compared with previous tests on standard quality ceramic and steel. The results from tests five to seven show that the slight change in tribilogical conditions affects fatigue life quite dramatically. In this case, the rod survived at least twice the number of stress cycles when the lambda value was enhanced. This result shows that although material quality is very important, the material is extremely sensitive to the choice of lubricant and surface conditions.

Typical fatigue spalls from tests one to seven were measured and are shown in table 5.19. On most failed contact paths a number of fatigue spalls is evident. The comparison of spall dimensions shows no specific differences from varying test conditions. Scanning electron microscope observations are shown in figure 5.49. Caption (a) shows the failure overview of primary and secondary spalling. The wear path and exposed porosity adjacent to the spall can be seen in caption (b). Fatigue surface of the large spall is examined in captions (c) and (d). Surface undulations

are visible and exposed debris in the deepest section of the spall can also be seen. The small spall is examined in captions (e) and (f). The same surface features are visible, including debris position.

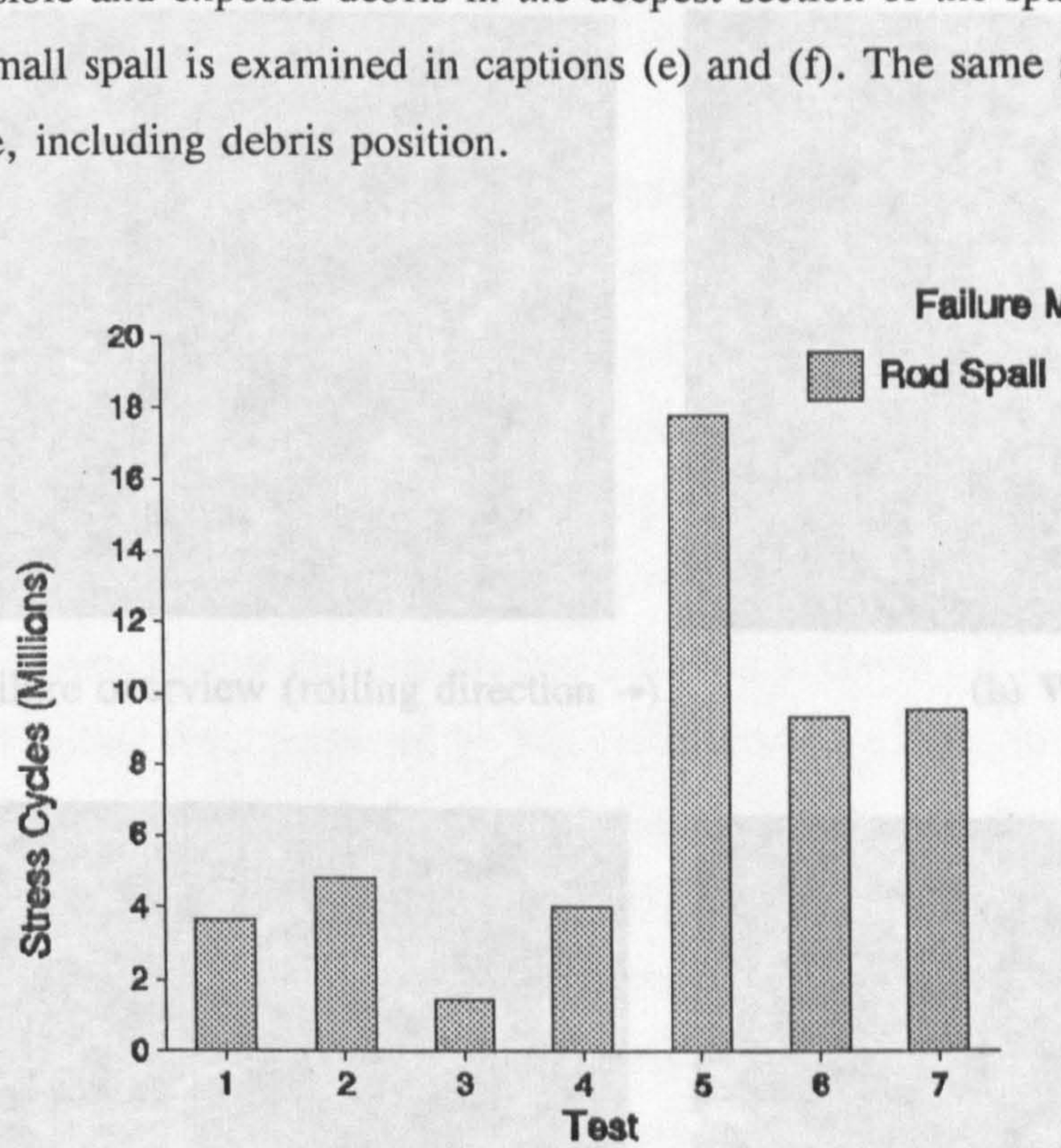

Figure 5.48 Poor grade material rod test results

Table 5.19 Spall analysis

Test	Spall Width - Across Contact Path (mm)	Spall Length - Along Contact Path (mm)	Spall Depth (mm)
1	0.67	0.46	0.034
2	0.71	0.46	0.030
3	0.79	0.64	0.082 (0.117 max.)
4	1.07	0.93	0.040 (0.080 max.)
5	0.81	0.57	0.100
6	0.53	0.43	0.030
7	0.5	0.64	0.040 (0.150 max.)

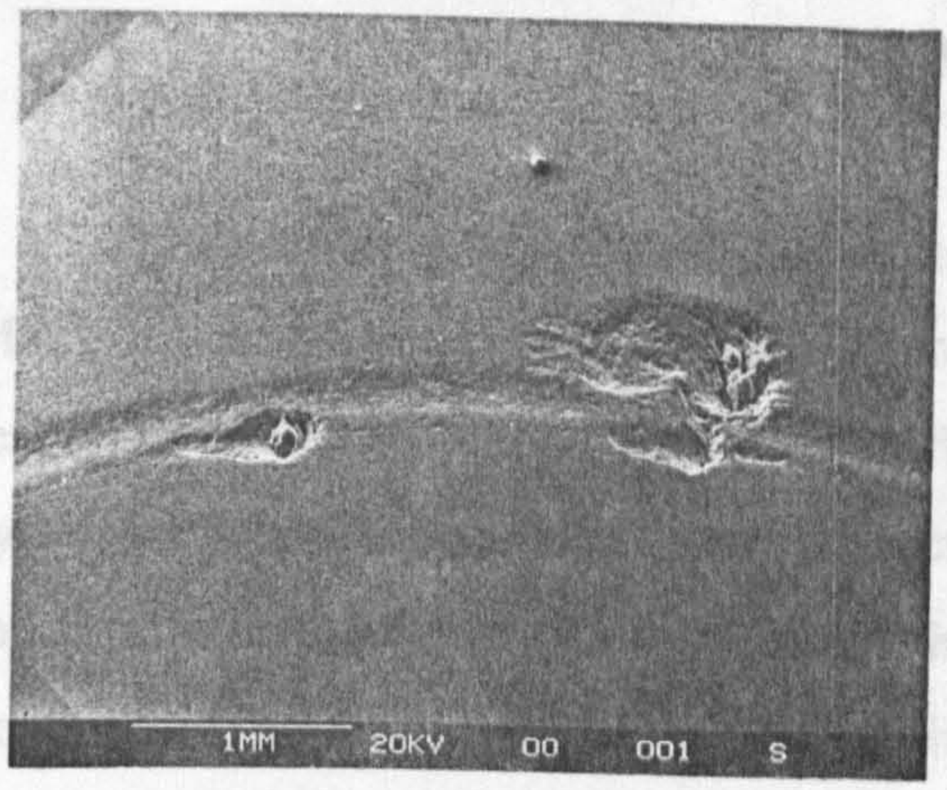

(a) Failure overview (rolling direction →)

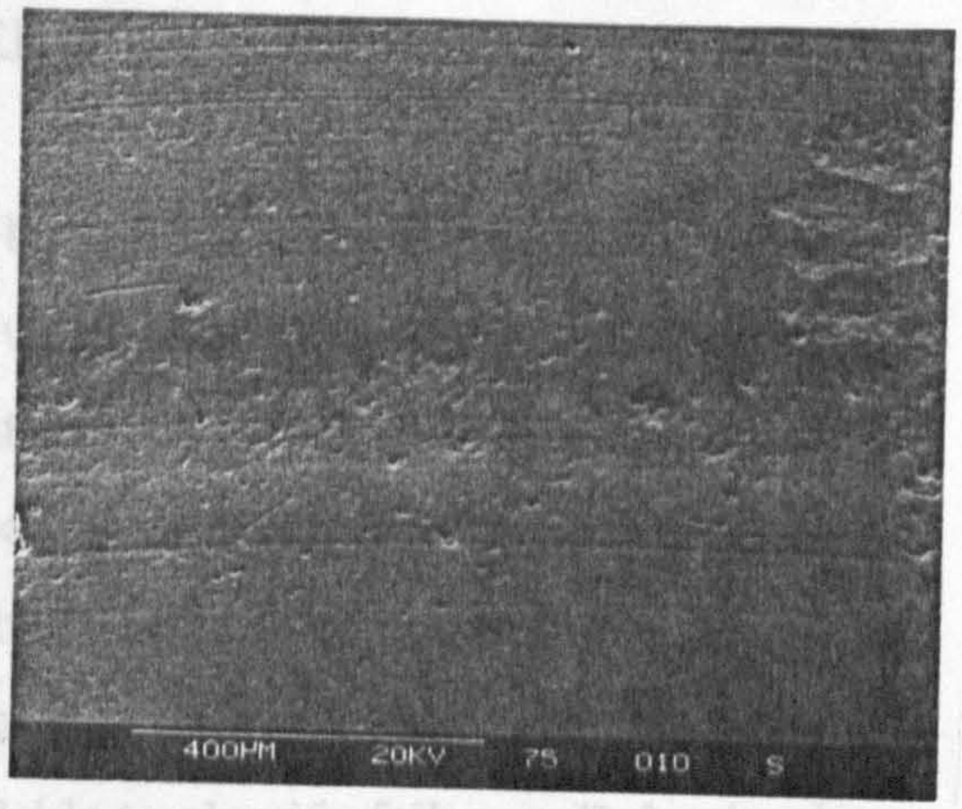

(b) Wear path

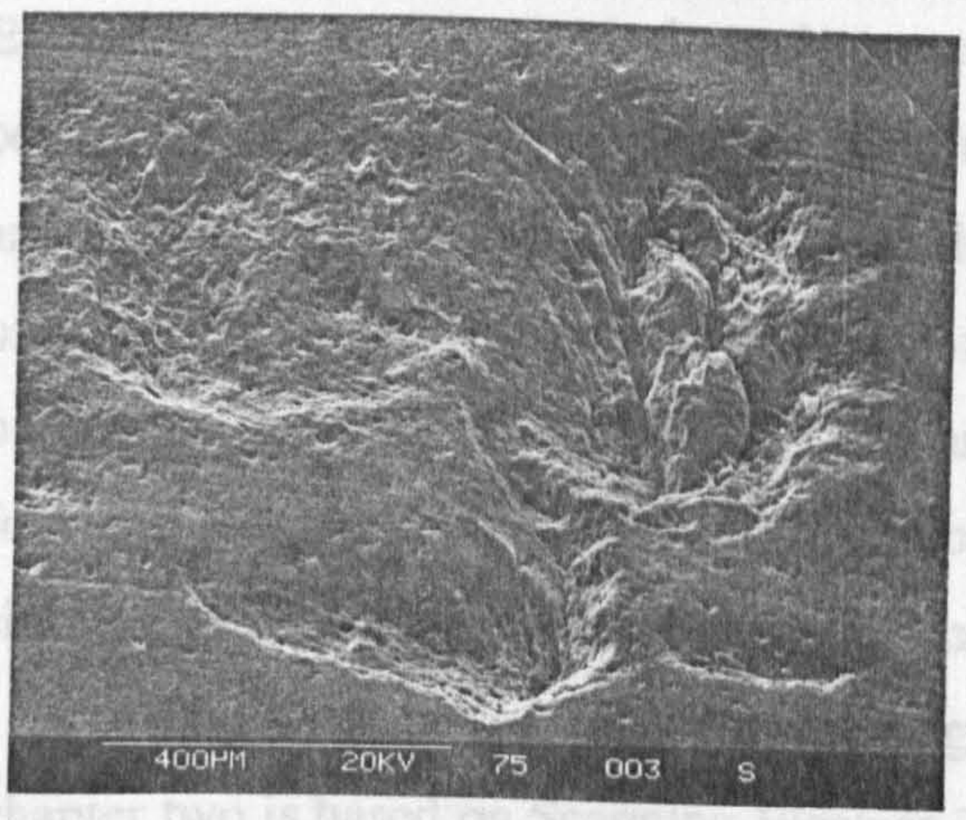

(c) Major spall overview

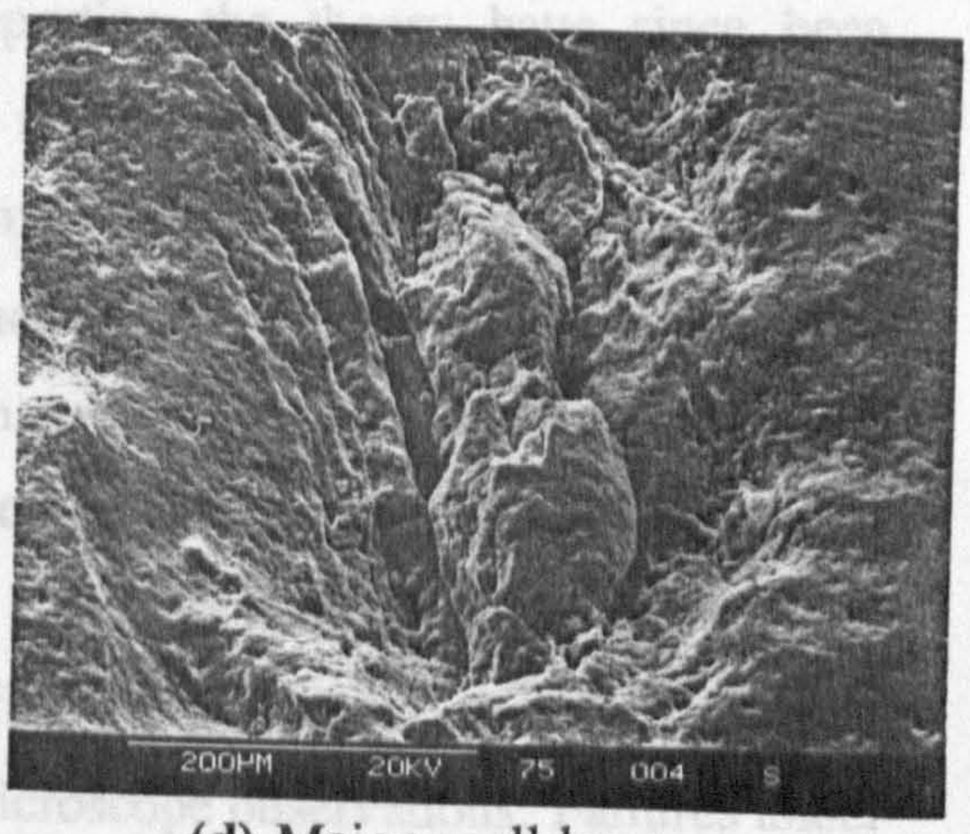

(d) Major spall base

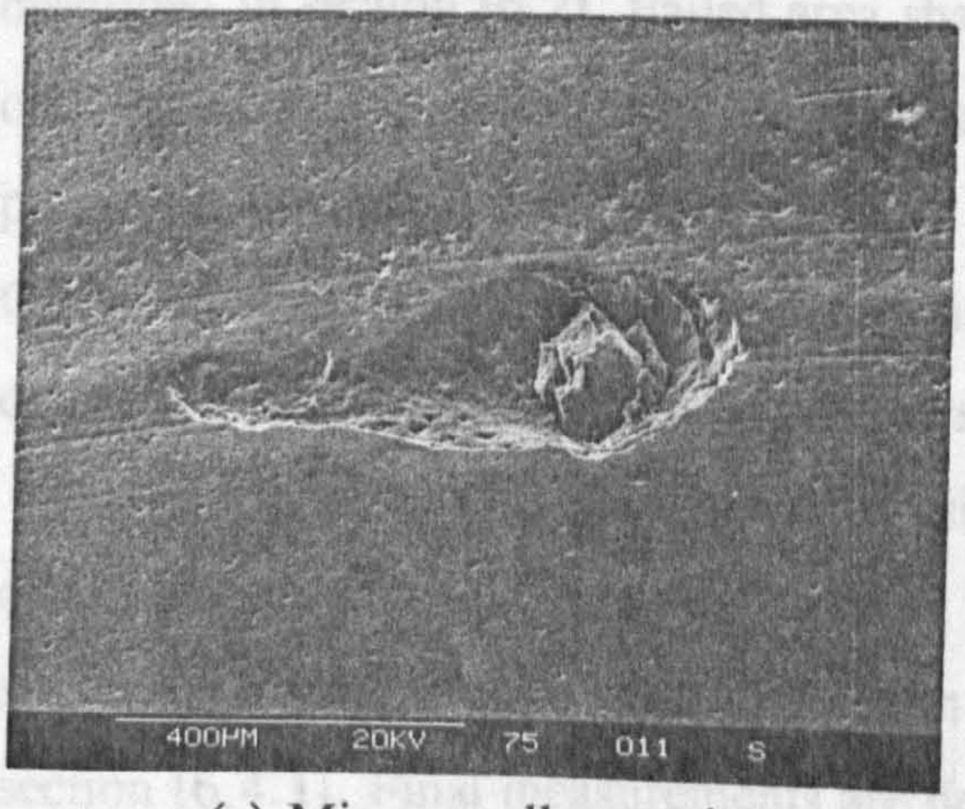

(e) Minor spall overview

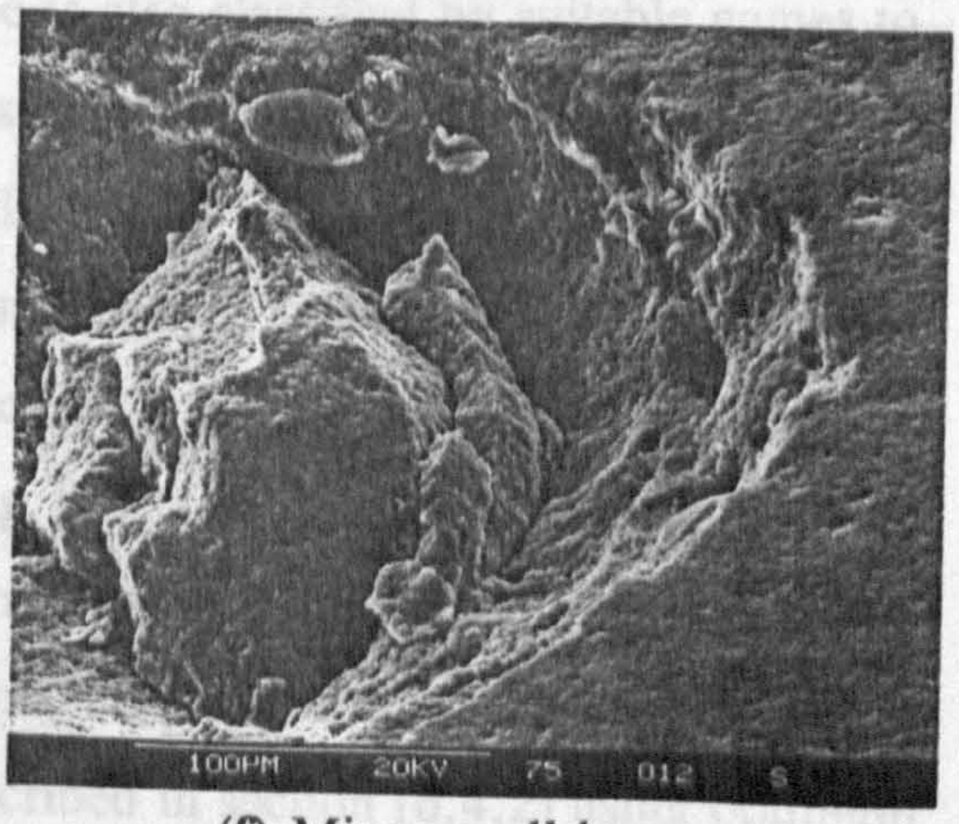

(f) Minor spall base

Figure 5.49 Micrographs of test four spall - captions (a) to (f)

Chapter 6
SURFACE STUDIES OF DELAMINATED BALLS

Delamination type failures are studied by various surface analysis techniques. Many different types of delamination failures were found after rolling contact fatigue testing described in chapter five. A classification framework has been developed to systemise delamination failures and is described in section [6.1]. These failures take the form of a flaking or delamination of the ball surface. As the modified four-ball machine is run at high speeds it is very difficult to observe crack propagation, and post test examination is the only method available to classify failures. Delamination theory of sliding wear proposed by Suh (1973) can be of assistance in this respect. Experimental and theoretical analyses supporting the theory have since been performed by Suh (1977), Jahanmir and Suh (1977), Fleming and Suh (1977), Suh and Saka (1980) and Suh (1986). The mechanism of delamination wear includes the propagation of cracks parallel to the surface at a depth governed by material properties and friction coefficient. Although rolling friction prevails in modified four-ball tests and delamination theory is based on sliding friction, nevertheless the similarities of the failure mechanism in both cases are compelling.

Classification of failures resulting from experimental tests described in chapter two is based on Scanning Electron Microscope observations. Failures under those testing conditions initiated and progressed by various mechanisms are described in section [6.2]. Failed area shape is also classified by suitable names to conveniently describe the damage. The classification of delaminated surfaces is also presented by the author (see Cundill et al. (1992) and Hadfield et al. (1992)). Chemical analyses of failed surfaces using energy dispersive and wavelength dispersive techniques are summarised in section [6.3].

Residual stress measurements using the X-ray diffraction technique are described in section [6.4]. Initial residual stress measurements using various X-ray sources, irradiated areas and diffraction planes are presented and discussed in section [6.4.1]. Final measurements are described in section [6.4.2] using optimum X-ray parameters. Residual stress measurements on all delamination types are

discussed and compared with failure depth. Results from the residual stress measurements are also presented by the author, (see Fujinawa et al. (1992)).

6.1 Classification of Delaminated Failures

6.1.1 Initiation and Propagation Type

Failures of ceramic balls under test conditions described in chapter 2 have been classified by initiation and propagation types of failure, shown in table 6.1. Four initiation groups and three propagation groups have been distinguished.

Table 6.1 Classification of crack propagation and initiation

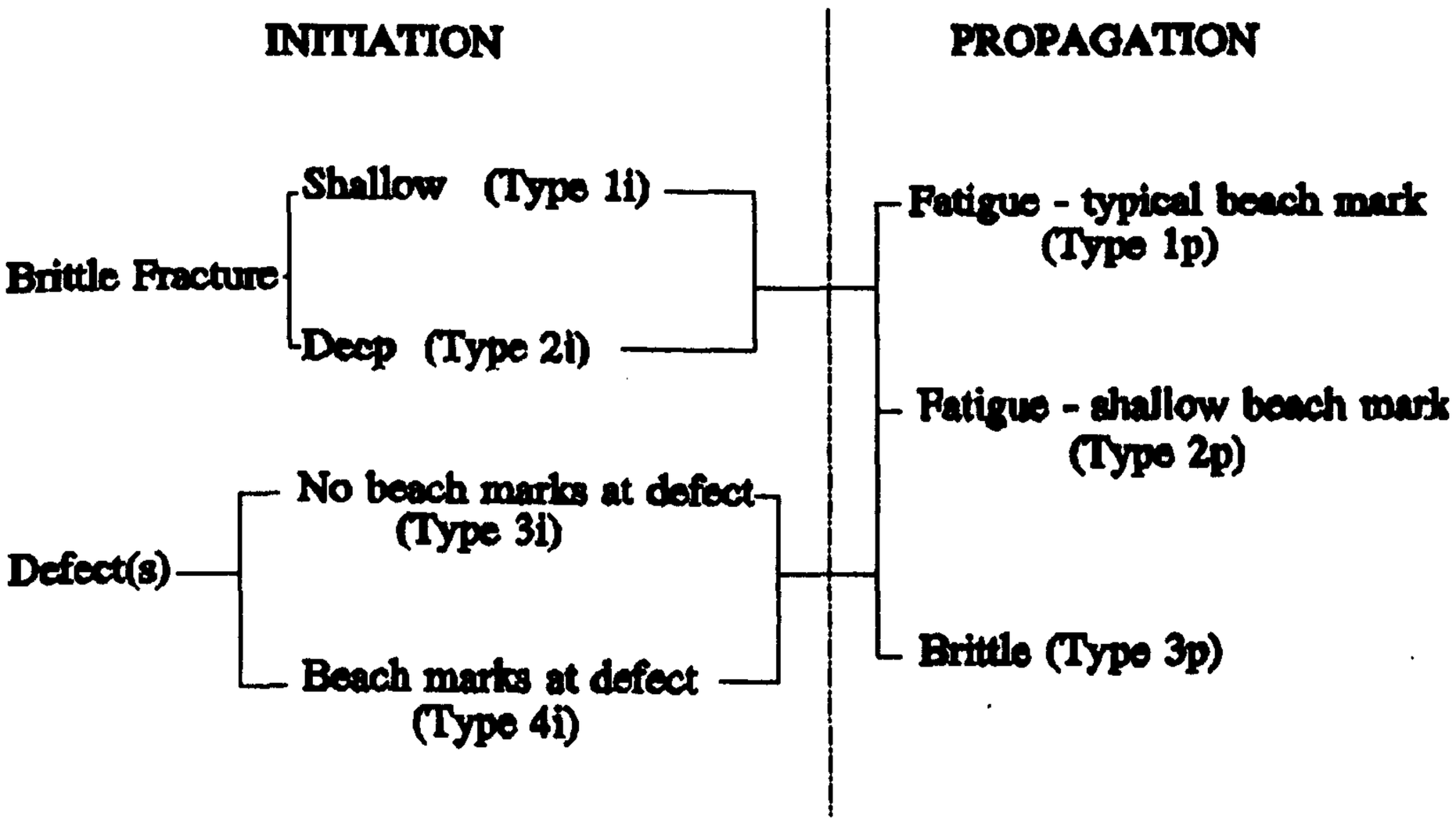

Crack initiation in ceramics under cyclic loading is not well known at present. Damage theory of materials begins with the premise that any material contains a multitude of defects in the form of micro-voids, Rabier (1989), which undergo extension due to loading and unloading. It is shown in table 6.1 that the four initiation types are arranged into two groups; brittle fracture and defects. Brittle

fracture initiation is proposed on the basis of post test surface examination. Conversely, it is accepted that conventional fatigue process ends by brittle fracture in the final stages of crack growth. Unstable crack initiation in this case is feasible due to the relatively brittle nature of ceramics. Shallow and deep initiation (Types 1i and 2i) are defined according to initiation depth below the surface; that is below or above 10 μm respectively. As classification is based upon post test examination, it is unclear if surface or subsurface initiation occurs. There is some evidence of both surface and subsurface initiation which is described in this chapter. Defect initiation is divided into groups, 'no beach marks at defect' (Type 3i) and 'beach marks at defect' (Type 4i). Beach marks described by Engel (1981), are undulations present on fatigue fractured surfaces. Beach marks found within the initiation region and classified type 4i, are commonly found on sialon ball failures. Type 3i defect initiated failure is diagnosed by premature cycles to failure and central spall at the centroid of the delaminated surface. Pre-cracks artificially positioned on ball surfaces are classified as type 3i initiation failures.

Mechanisms of cyclic fatigue propagation in ceramics have been proposed and reviewed frequently, most recently by Kishimoto (1991). Three propagation modes are identified from fractured ball surfaces. Type 1p, 'Fatigue - typical beach mark' is defined by undulations measuring above 10 μm peak to peak. Type 2p, 'Fatigue - shallow beach mark' is defined by undulations below 10 μm peak to peak. Brittle crack propagation is defined as failed surface with no undulations and relatively smooth surface.

6.1.2 Shape Nomenclature

Damages on ball surface are classified according to the general shape of the failed area, (see table 6.2), ie Eye, Heart, Leaf, Ring, Single Path, Double Path, Brittle Flake and Cracked Spall. Eye shape is found on type-4i3p failures, the centre initiates the final circular outer brittle failure. Heart shape is found on type-1i1p failures, the centre initiation band with fatigue growth from this region with typical beach marks. Leaf shape is found on type-1i2p and type-2i2p failures, initiation followed by central fatigue propagating to distinct paths. Ring shape is

found on type-3i2p failures, initiation occurs from brittle 'ring' cracks and propagates by fatigue to ball surface. Single and Double Path shapes are found on type-2i1p failures where brittle initiation is followed by fatigue propagation along a long narrow path arresting in a wide area. Brittle Flake shapes are found in type-1i3p and type-4i3p failures, combining brittle initiation with brittle or shallow fatigue propagation. Finally, Cracked Spall shape is found on type-1i1p and type-3i1p failures. Initiation takes place by brittle fracture, and propagation by fatigue causing spalling and secondary delamination failure.

Table 6.2 Shape nomenclature

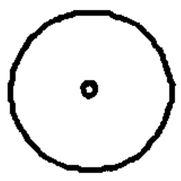	EYE	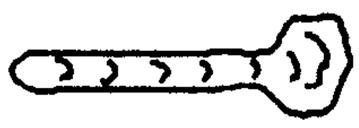	SINGLE PATH
	HEART		DOUBLE PATH
	LEAF		BRITTLE FLAKE
	RING		CRACKED SPALL

6.2 Examples of Delaminated Failures

6.2.1 Type-1 Initiation Failures

Type-1 initiation failure is generally described in section [6.1] as a brittle mode. This initiation type of failure is followed by one of the three delamination fatigue modes, ie. fatigue - typical (type 1i1p), fatigue - shallow (type 1i2p) and brittle (1i3p).

(6.2.1.1) Example of Type 1i1p Failure

Type 1i1p failures occur in ceramic/ceramic contacts on silicon nitride balls when tested with a high viscosity lubricant, and high contact stresses (7.0 to 10.0 GPa). The example shown in figure 6.1, captions (a) to (p), is a typical 'leaf' shape failure.

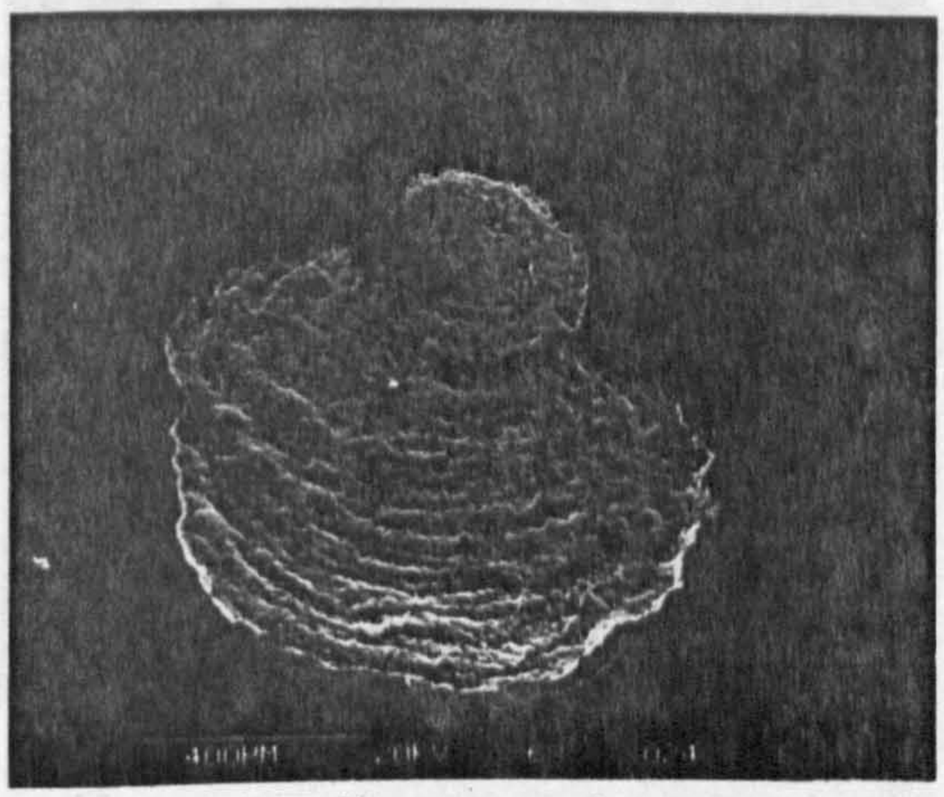

(a) Failure overview

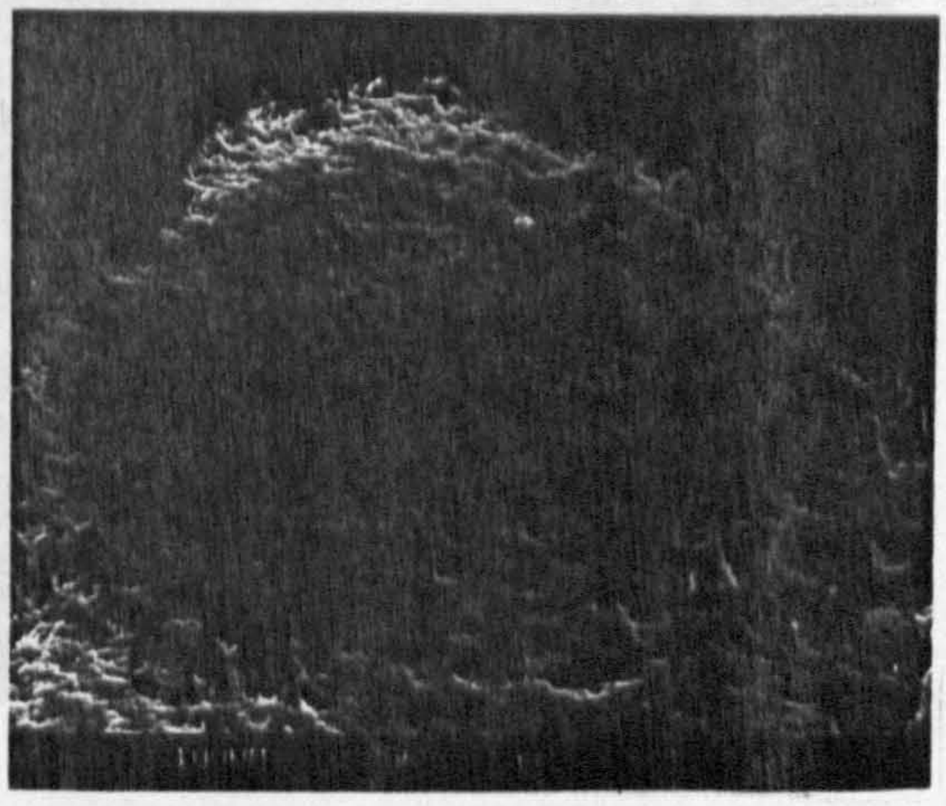

(b) Brittle area overview

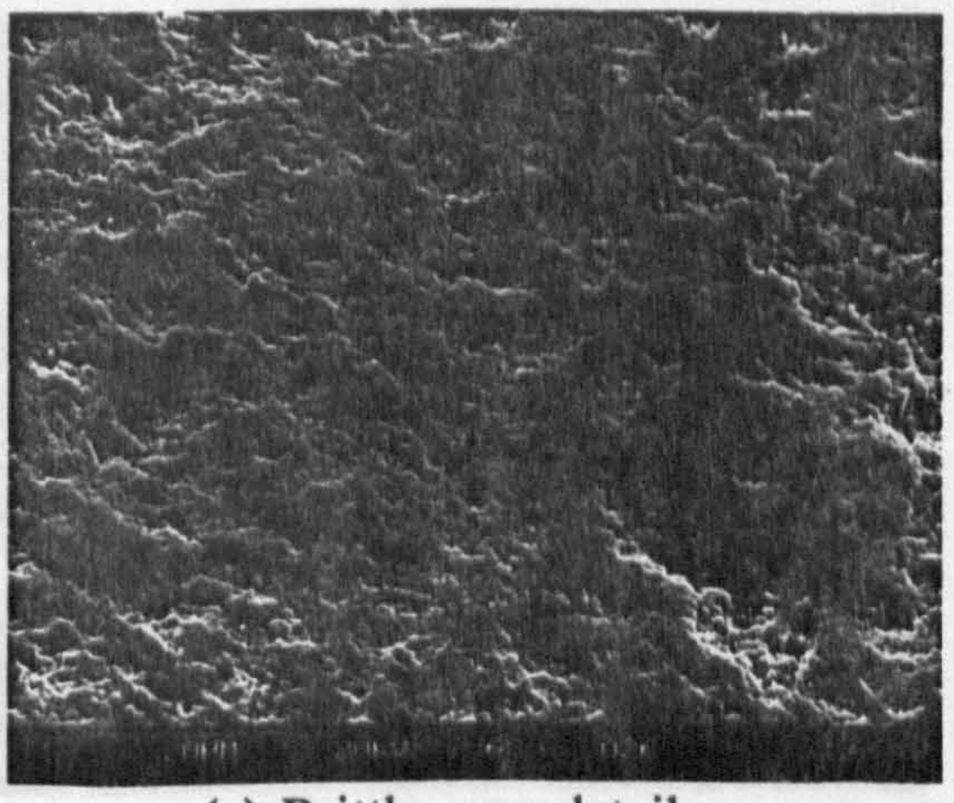

(c) Brittle area detail

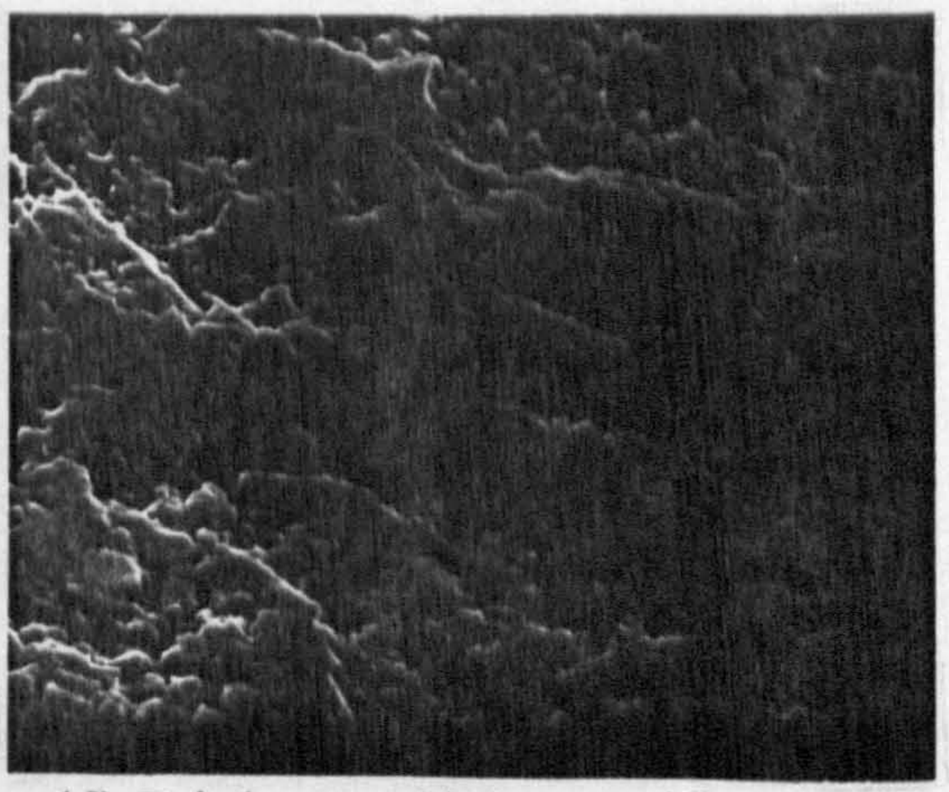

(d) Brittle area high magnification

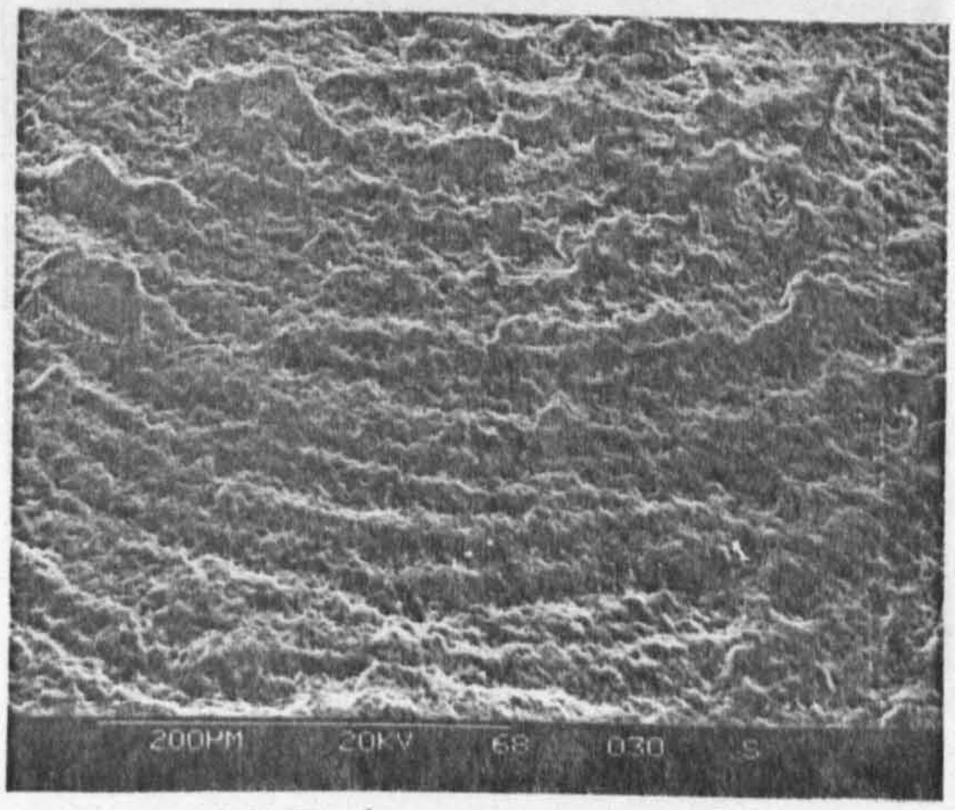

(e) Fatigue area

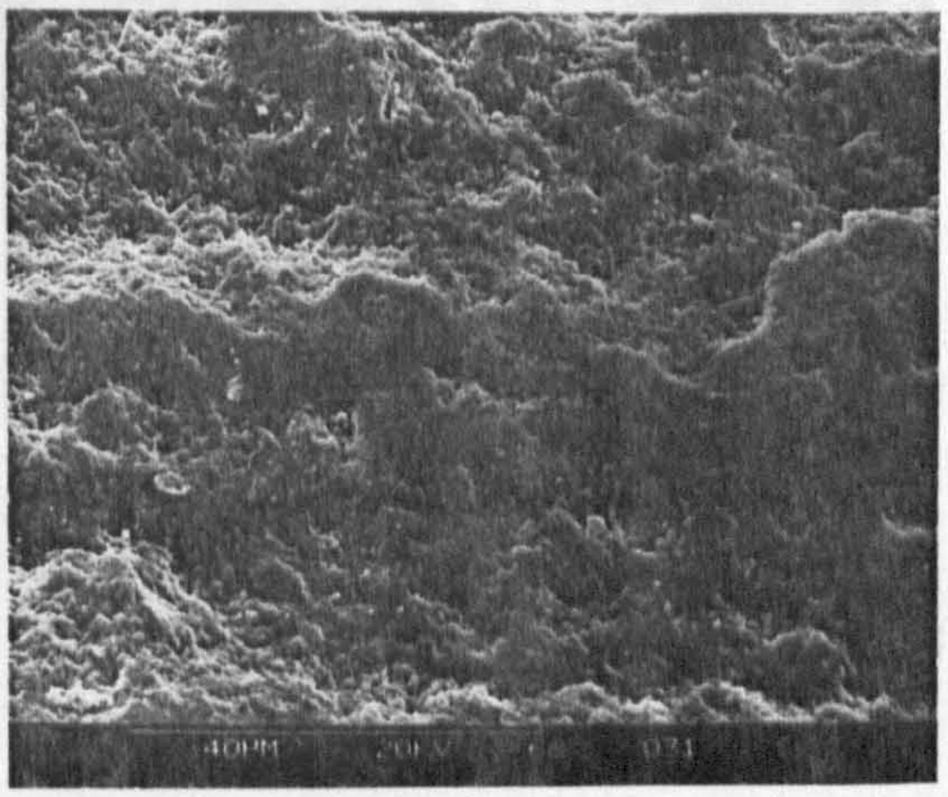

(f) Fatigue area surface

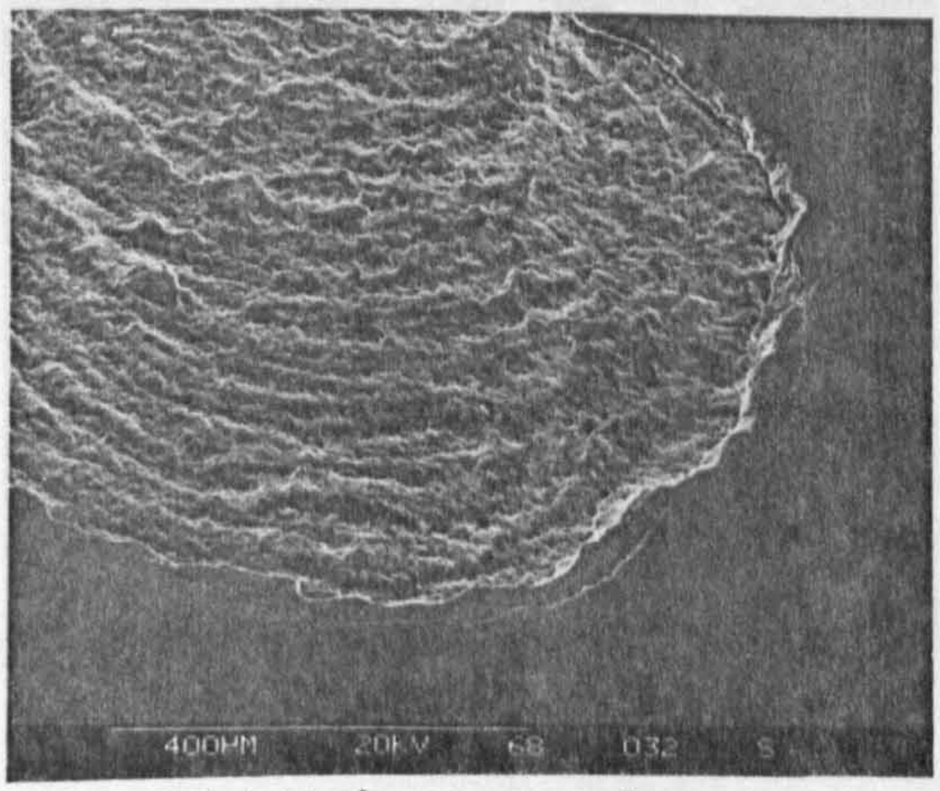

(g) Fatigue area edge

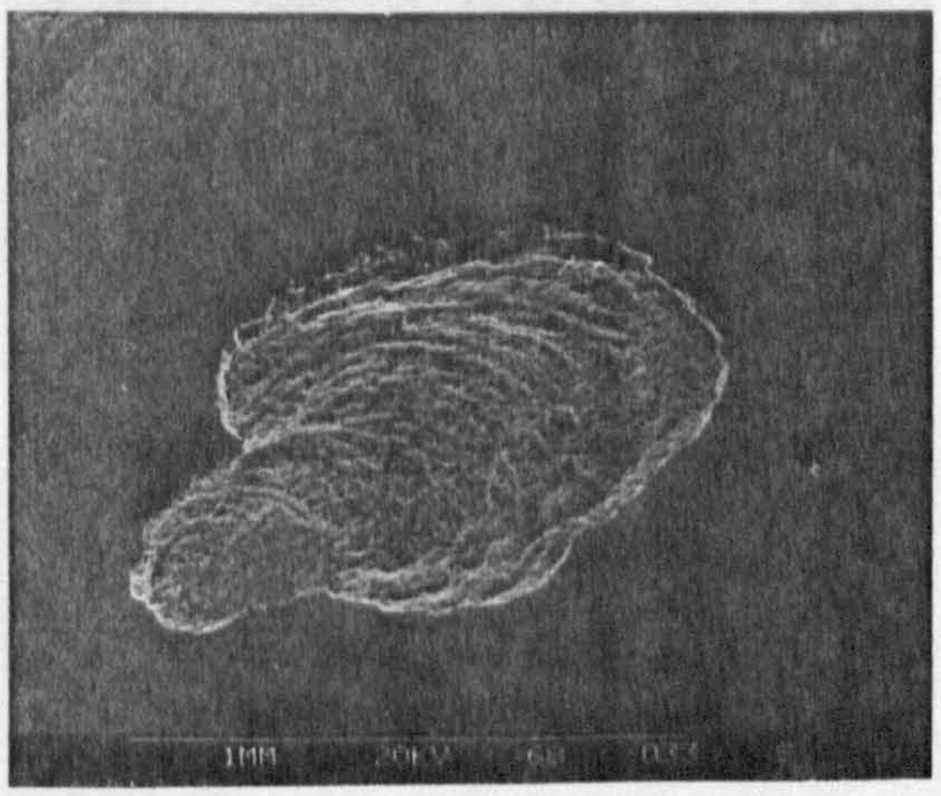

(h) Reversed view

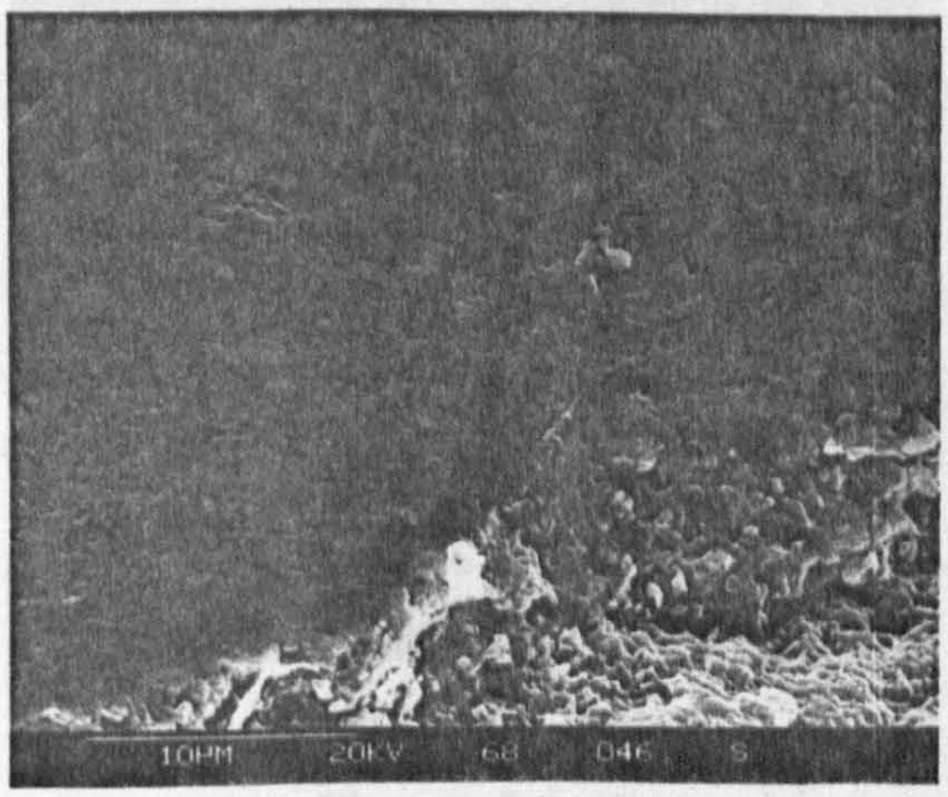

(i) Adjacent ball surface

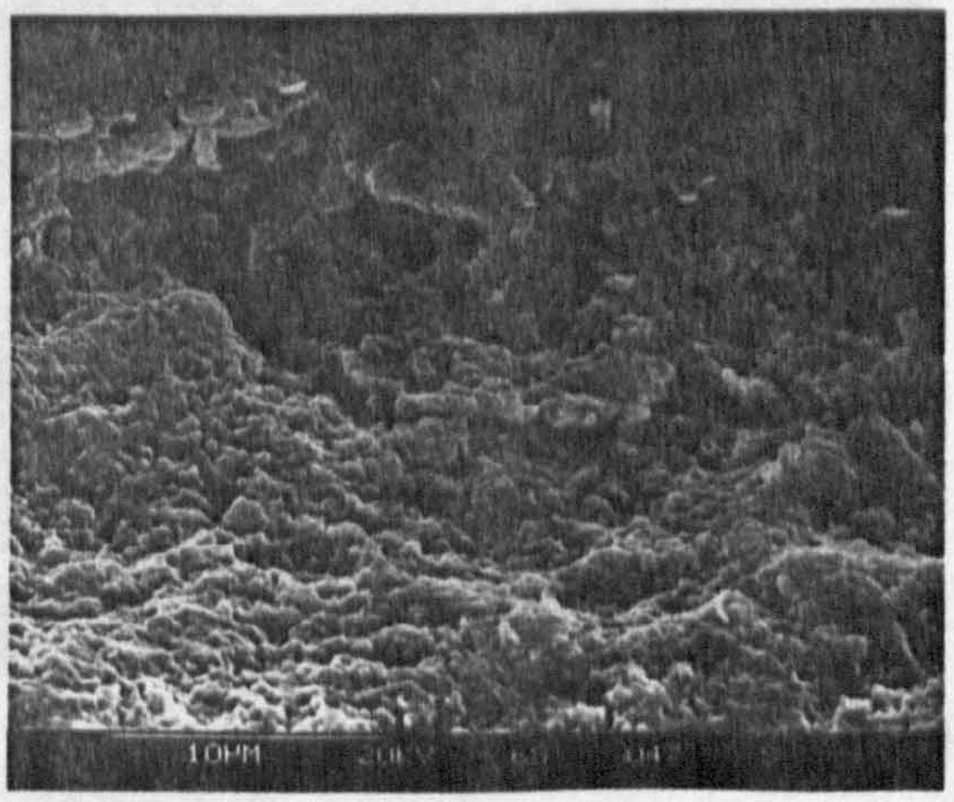

(j) Adjacent fatigue surface

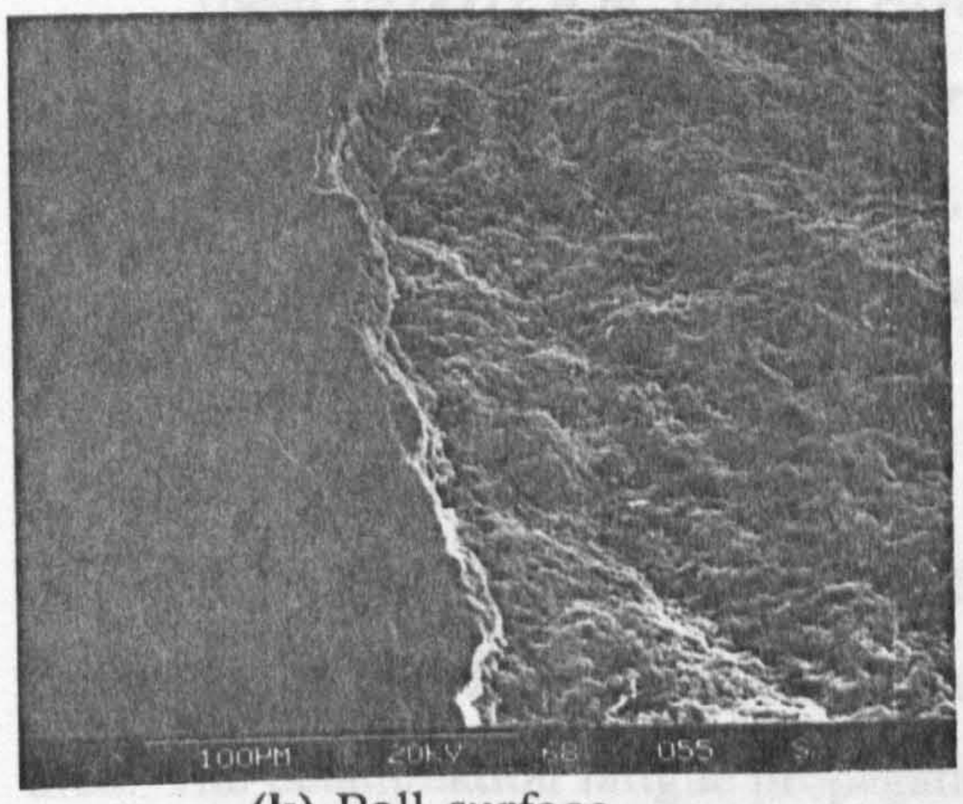

(k) Ball surface

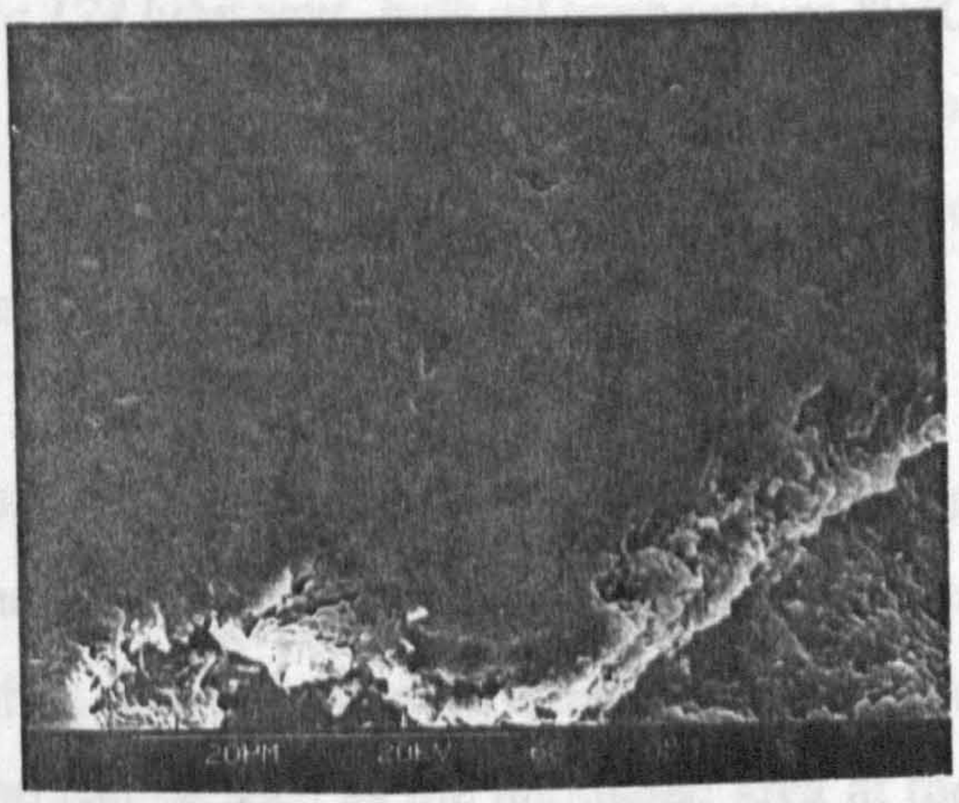

(l) Large surface crack

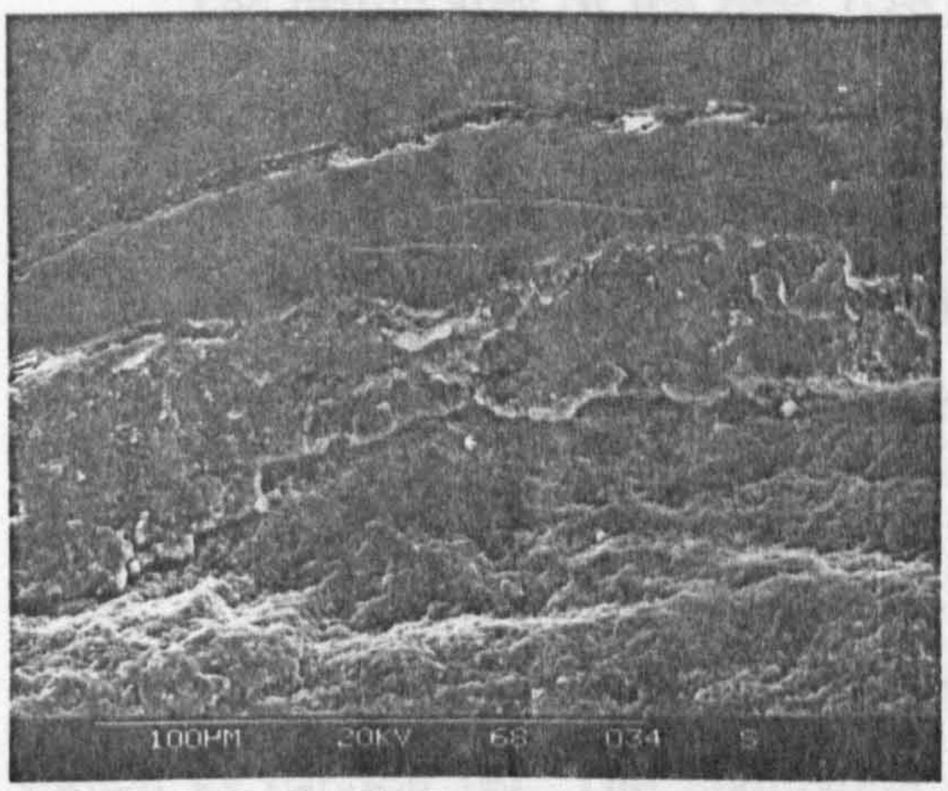

(m) Cliff edge

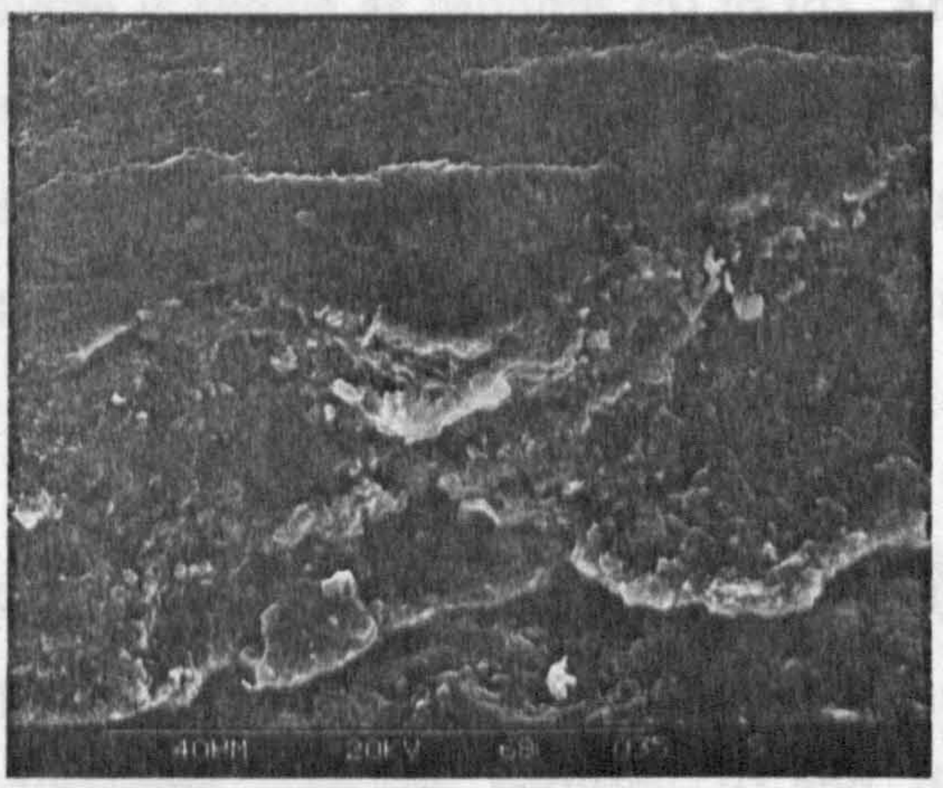

(n) Cliff edge high magnification

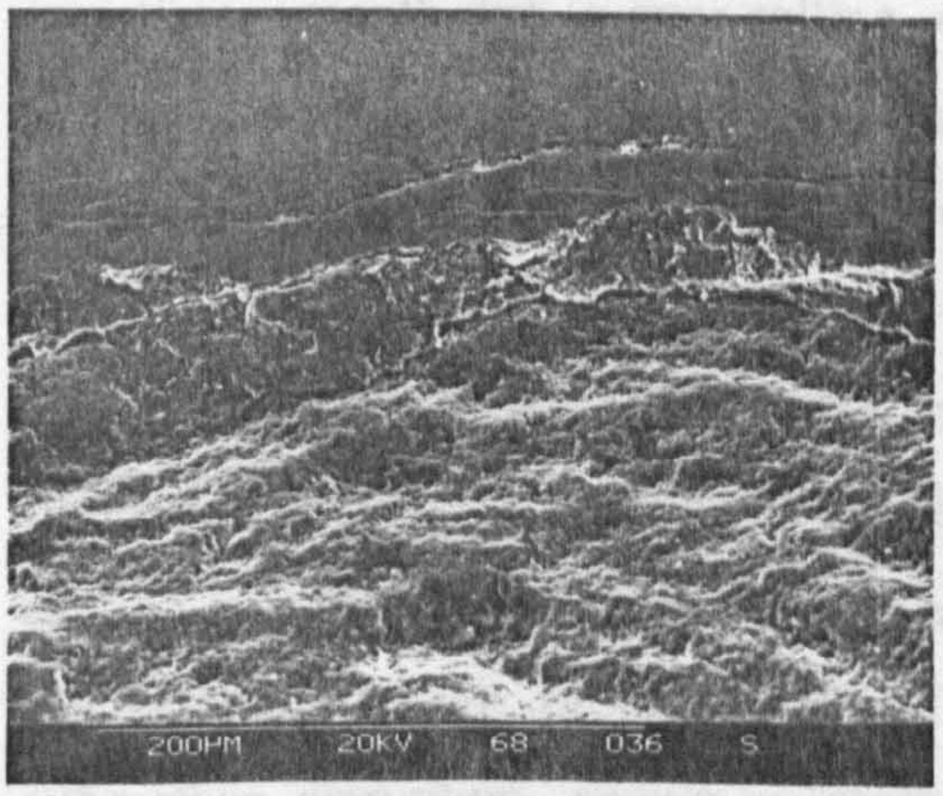

(o) Incipient failure

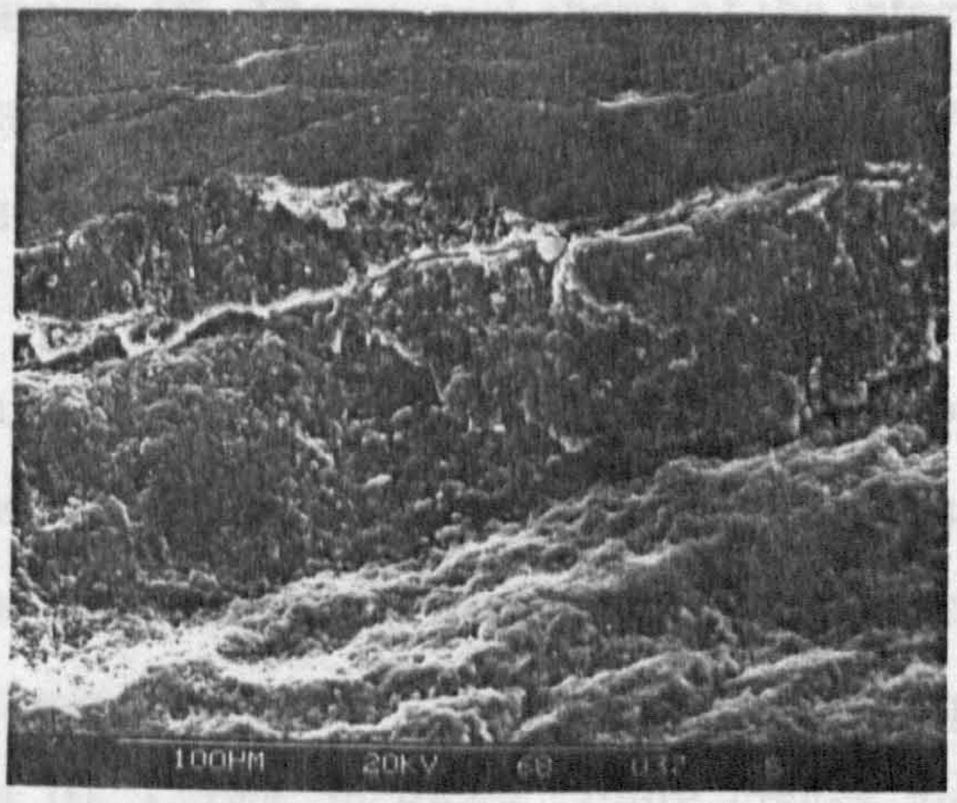

(p) Incipient failure high magnification

Figure 6.1 Example of type 1i1p failure - captions (a) to (p)

Test Conditions of figure 6.1: Ceramic/ceramic contact, machine spindle speed 10,000 r.p.m, inclosed HiTec 174 lubricant, bulk oil temperature 89°C - unheated, 1.4 million upper ball stress cycles, Hertzian maximum compressive stress - 9.6 GPa, theoretical lambda ratio - 6, Surface roughness (Ra) of upper and lower balls 0.008 μm.

Figure 6.1, captions (a) to (p), provides a detailed survey of a type 1i1p delamination failure. Caption (a) shows the failure overview. Approximate diameter of failed area is 900 μm. The brittle initiation area is evident at the top of the failure area. The delamination fatigue propagation can be seen as the undulated area at the middle and bottom of the failure.

The brittle area of the type 1i1p failure is shown as captions (b) to (d). An overview of the brittle area, caption (b), shows clearly the striation-free texture of the failure origin. High magnification of the brittle area, captions (c) and (d), shows the brittle area topography, where inter-granular smooth surface separation is apparent. The very high polished area at surface peaks is probably due to contact over-rolling.

Delamination surface fatigue on the propagated area is shown as captions (e) to (h). The general undulated area, propagating with concentric undulations, is shown as caption (e). The undulation wavelength measures between 10 and 20 microns from stereo imaging techniques and analyses. Undulation peaks are sometimes smooth due to over-rolling, caption (f). The general shape of the intact ball surface is shown as caption (g), where surface cracks can be seen close to the delaminated area. The directionality of the fatigue propagation is confirmed by the failure reversed view, caption (h).

The delaminated surface edge can be seen in detail in captions (i) to (p) of figure 6.1. Micro-cracks are evident on the ball surface adjacent to the delamination, caption (i). The random directionality and dimensions of the micro-cracks suggest inter-granular failure, probable cause of these cracks is tensile surface stress during subsurface disruption, shown as caption (j). Larger incipient failure cracks are illustrated from captions (k) to (p). An overview of the ball surface adjacent to

failure is shown as caption (k). Cracks with the length above 500 microns are visible emanating in the same direction as the undulations, captions (i) to (n). Cracks propagating from the base of the delamination cliff around the surface undulation are shown in caption (o). A more detailed view of an undulation crack is shown as caption (p).

(6.2.1.2) Example of Type 1i2p Failure

Type 1i2p failures occur in ceramic/ceramic contacts on silicon nitride balls when tested with a standard viscosity lubricant, and high contact stresses (7.1 to 7.6 GPa). The example shown in figure 6.2, captions (a) to (n), is a typical 'heart' shape failure.

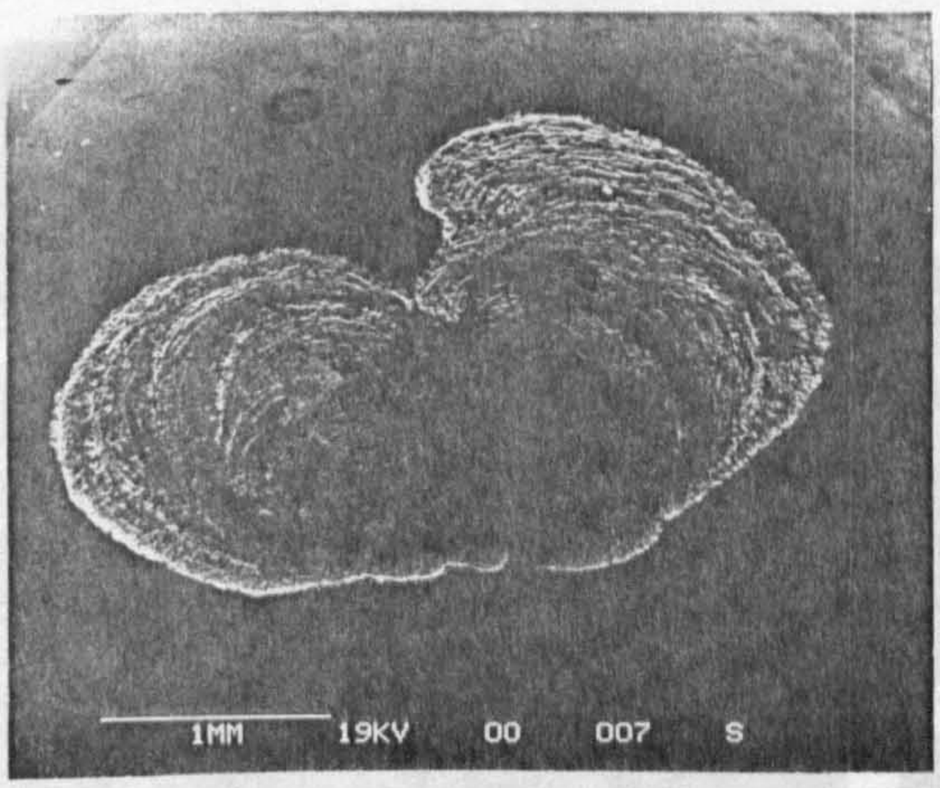

(a) Failure overview

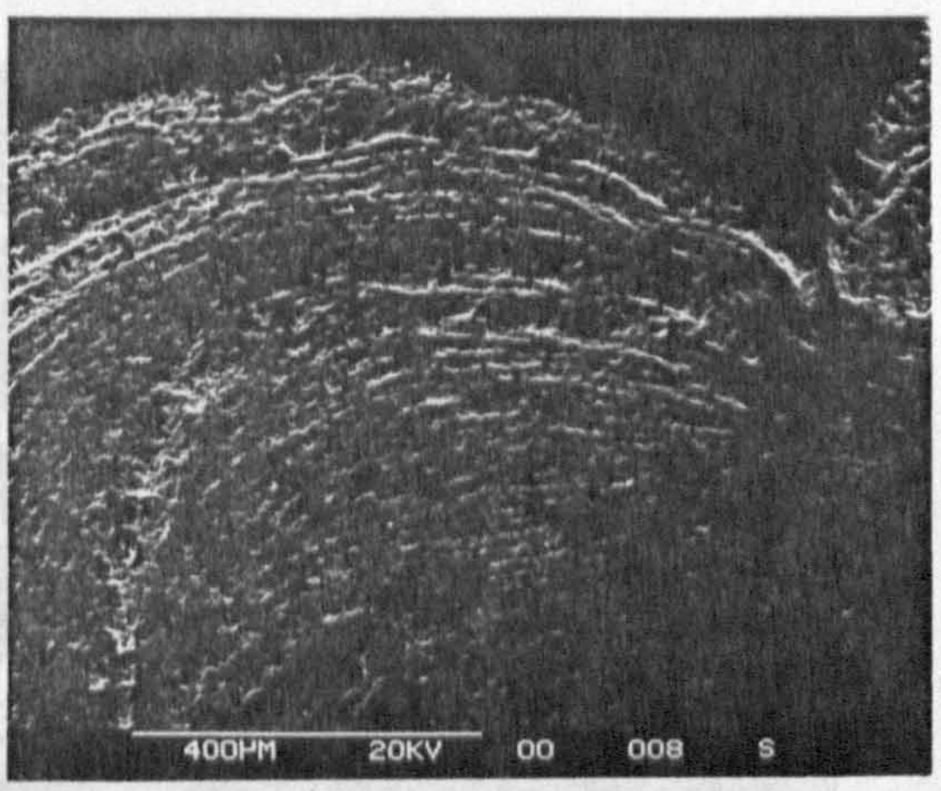

(b) Fatigue area overview

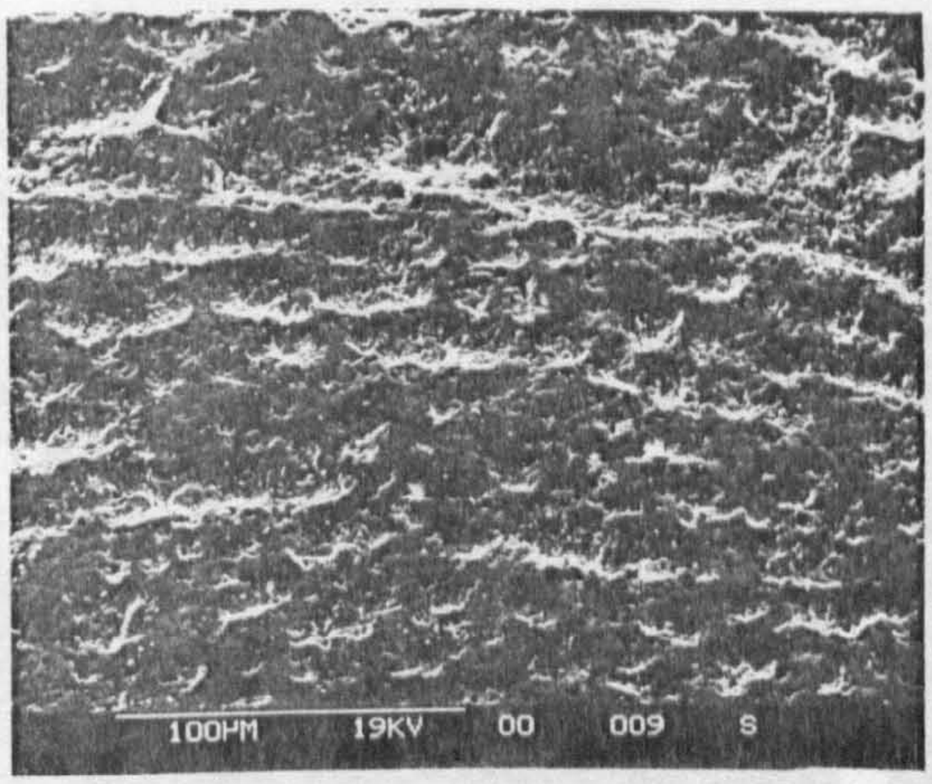

(c) Fatigue area high magnification

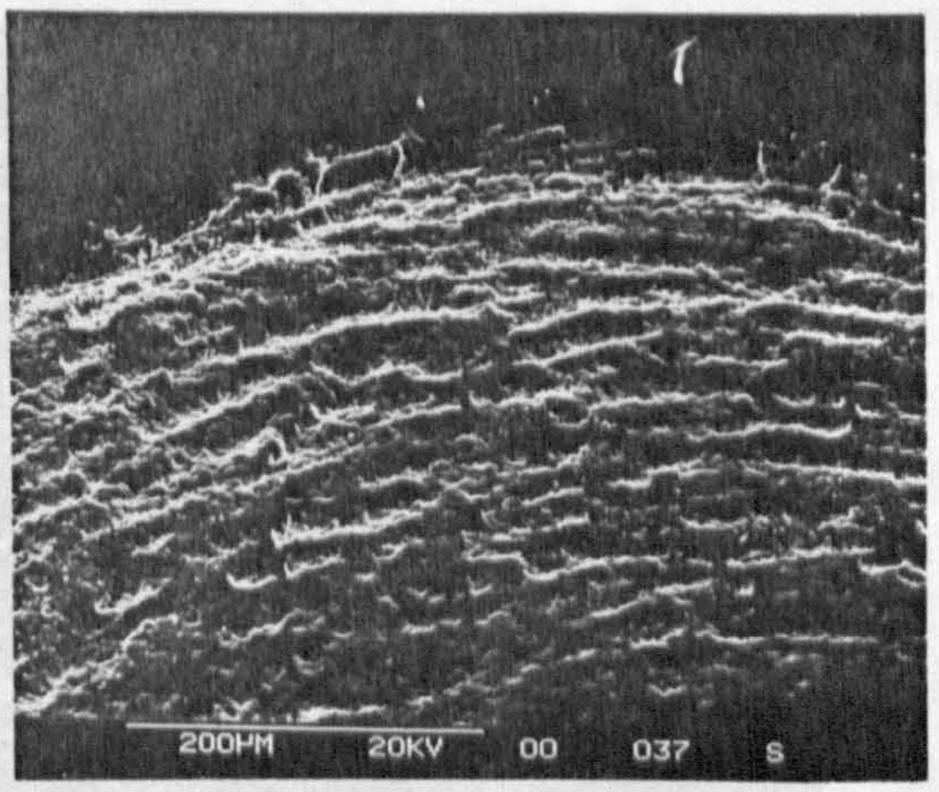

(d) Fatigue area edge

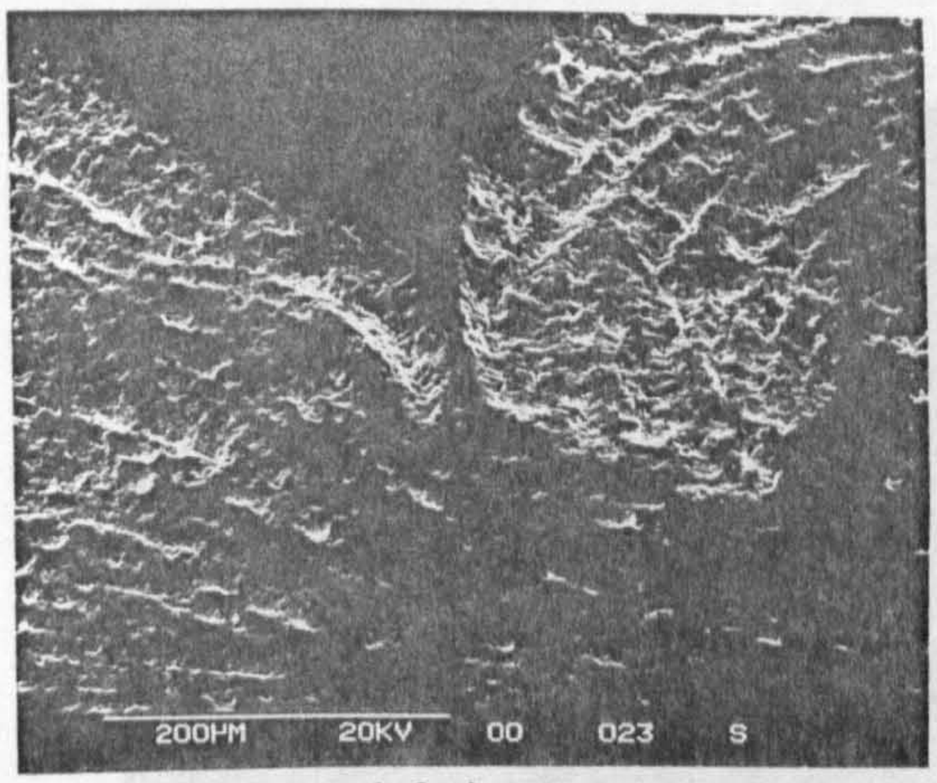

(e) Brittle and fatigue area (central)

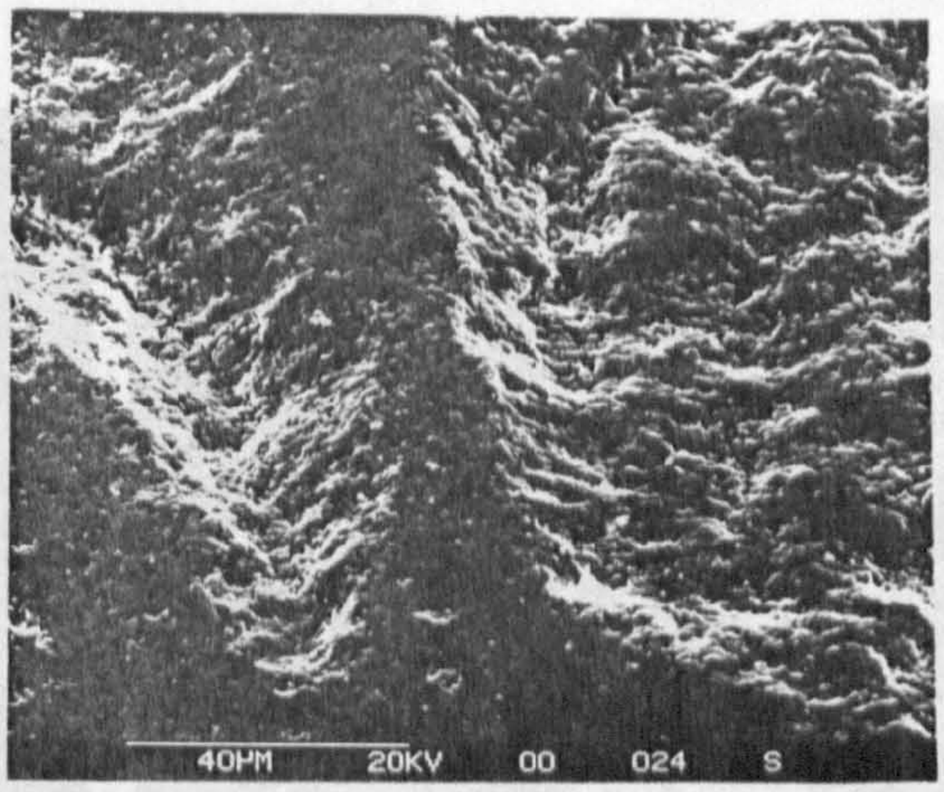

(f) Brittle and fatigue area

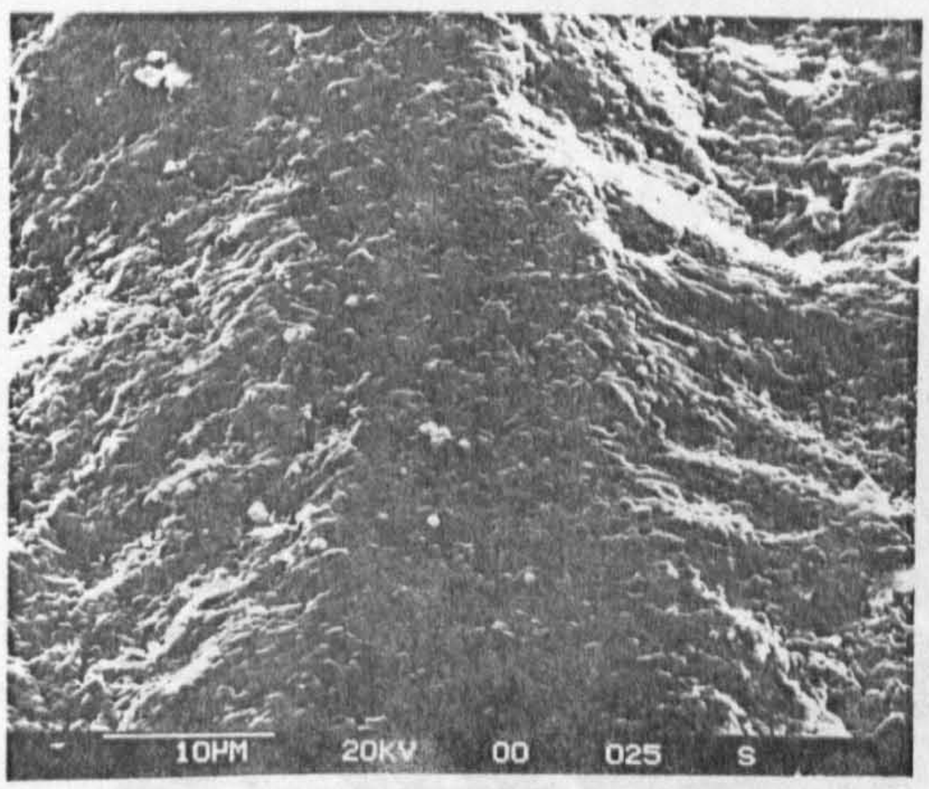

(g) Brittle area

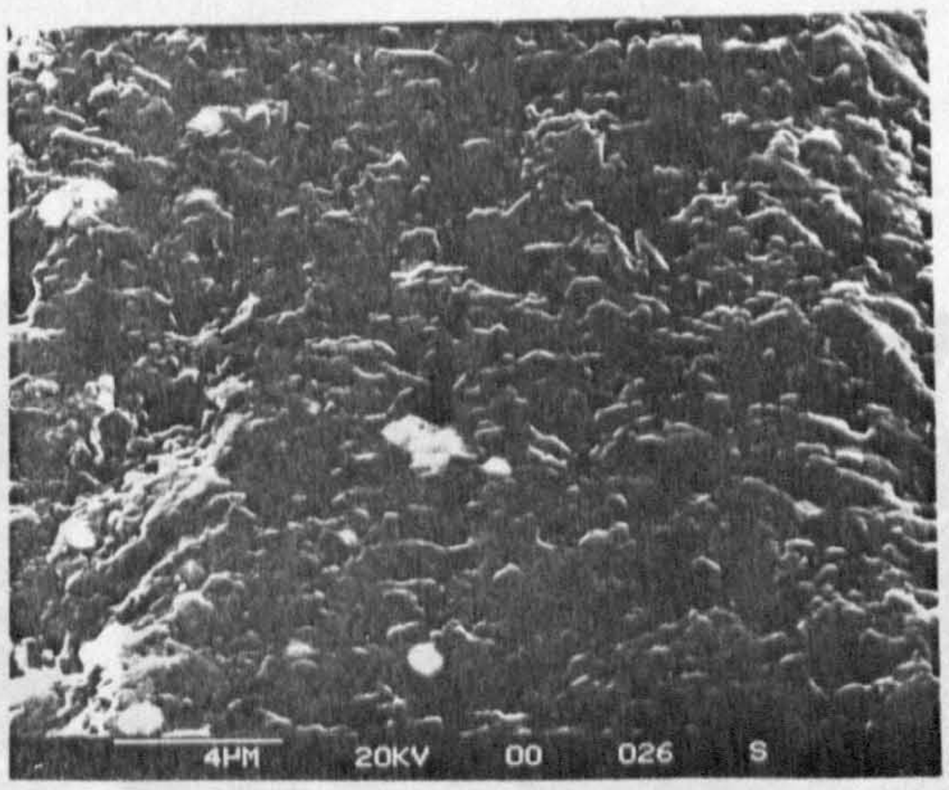

(h) Brittle area high magnification

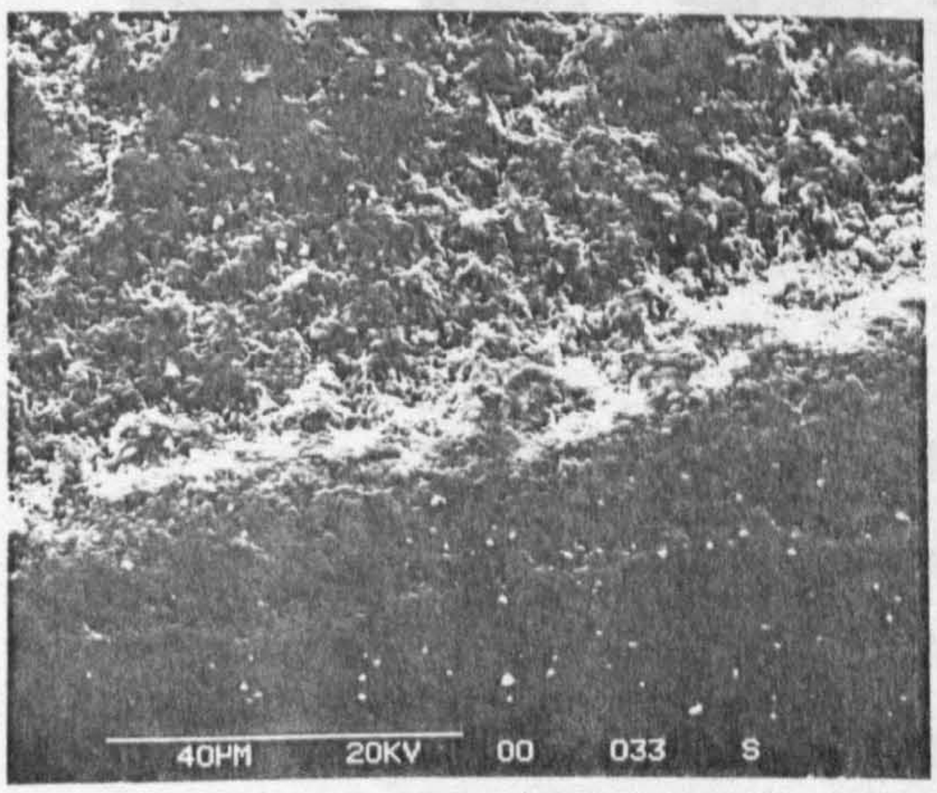

(i) Fatigue area edge (lower)

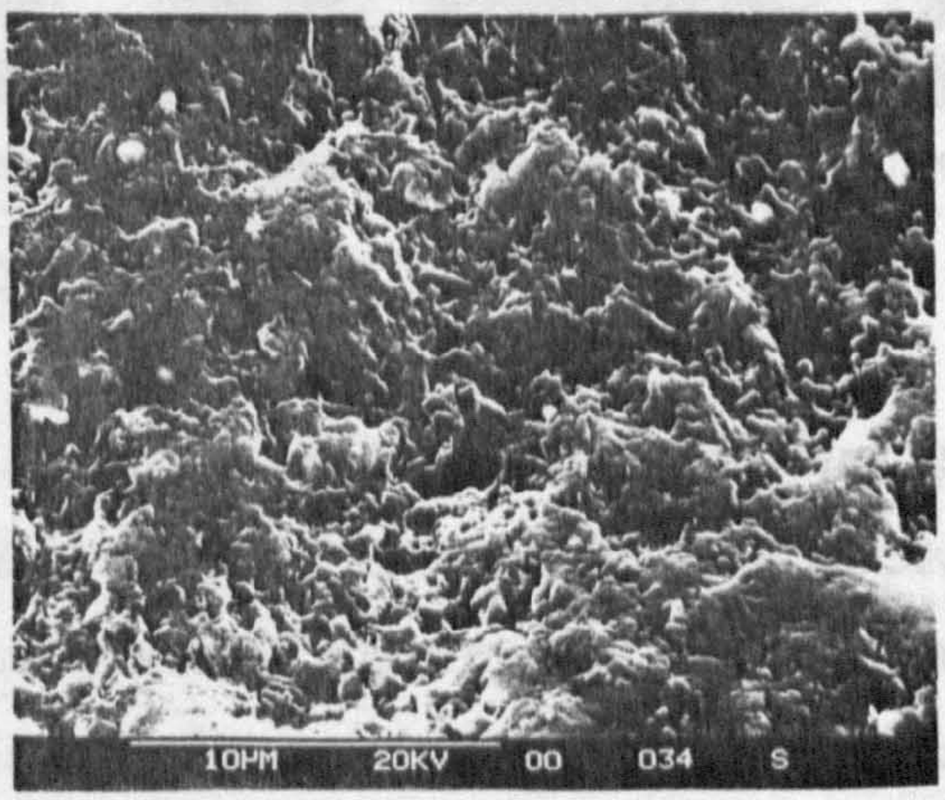

(j) Fatigue surface

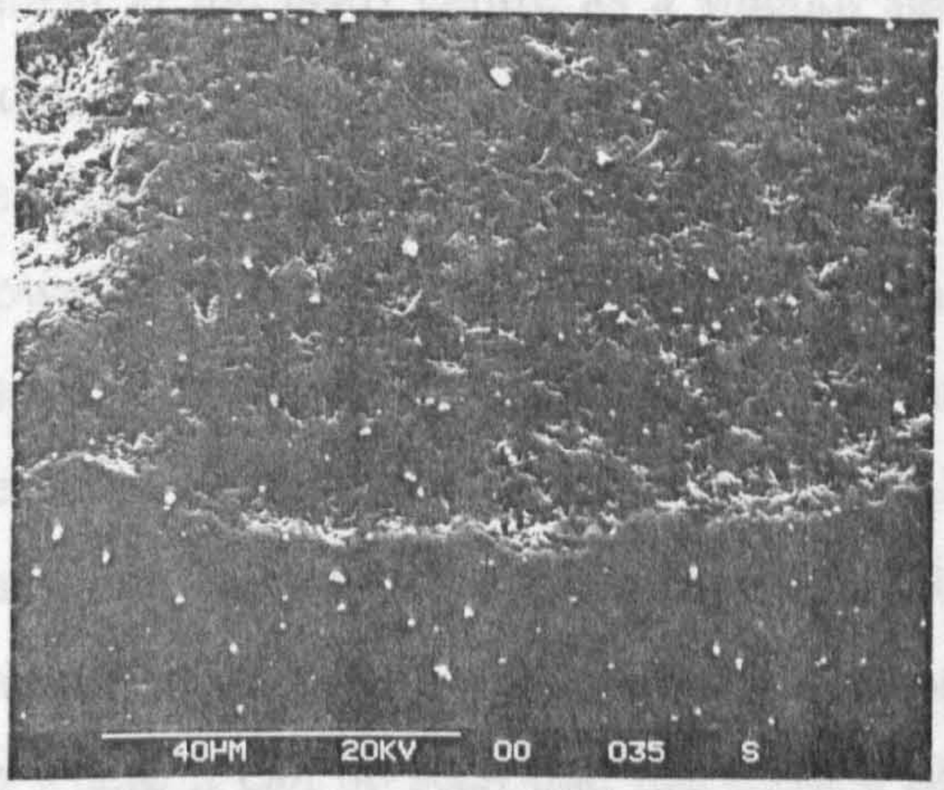

(k) Adjacent brittle area

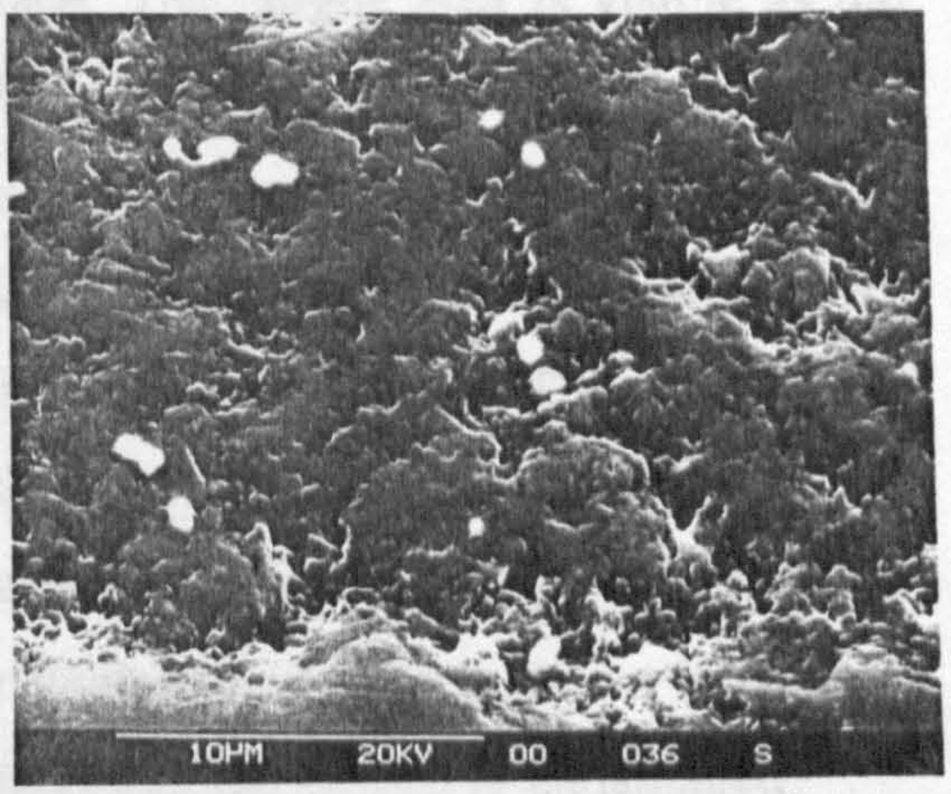

(l) Brittle surface

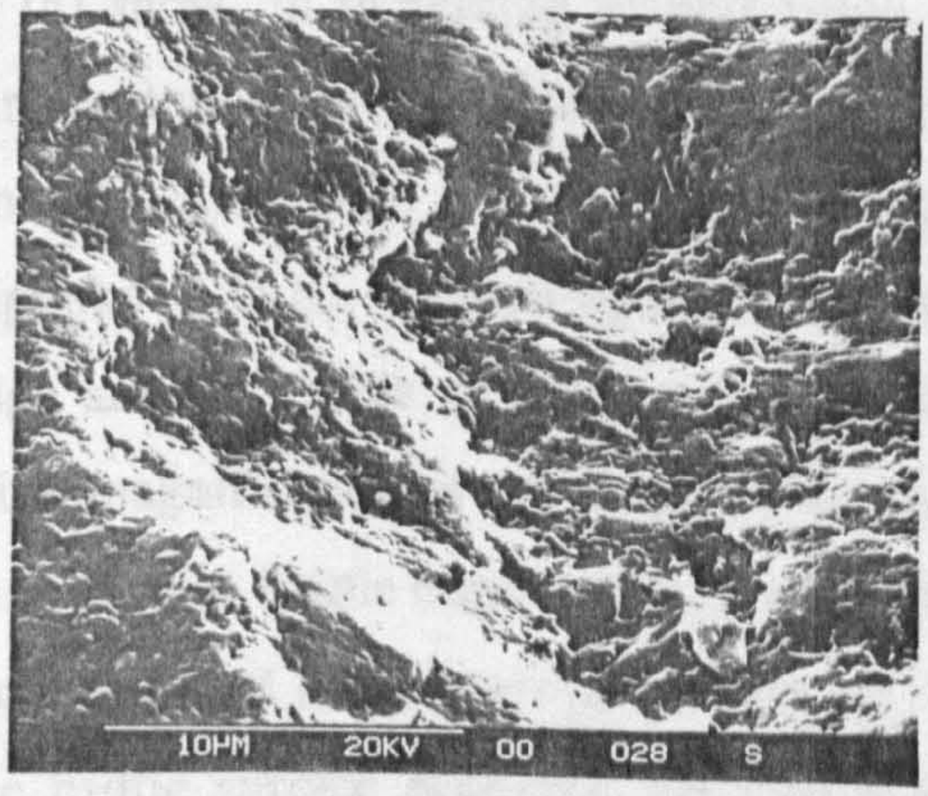

(m) Lower fatigue undulation

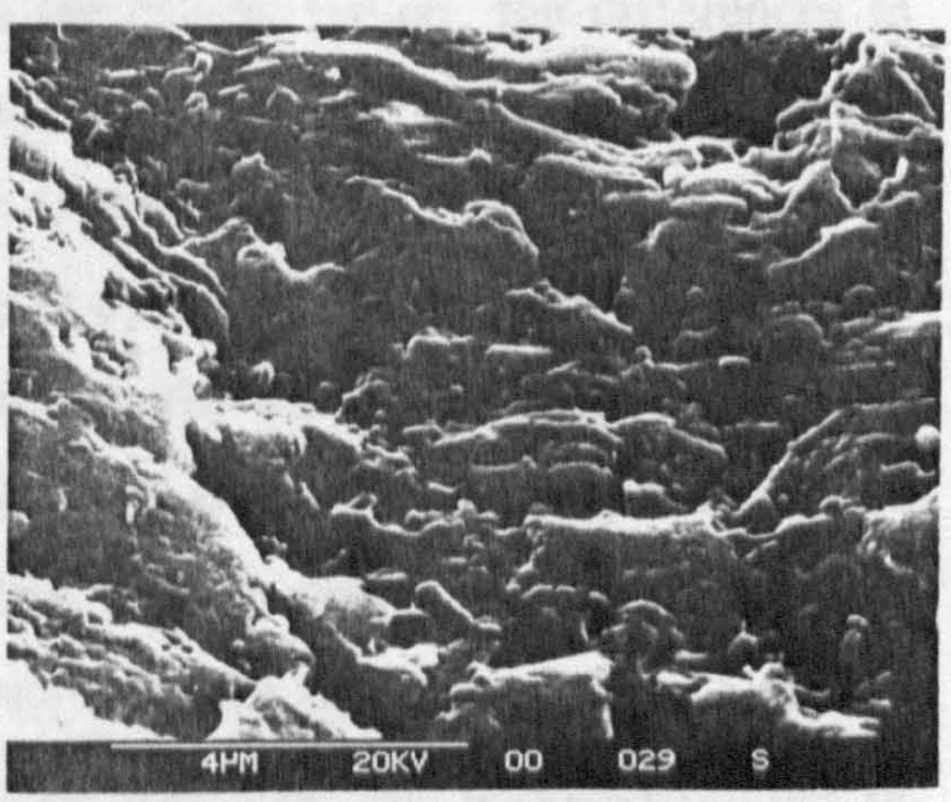

(n) Lower undulation high magnification

Figure 6.2 Example of type 1i2p failure - captions (a) to (n)

Test Conditions of figure 6.2: Ceramic/ceramic contact, machine spindle speed 10,000 r.p.m, inclosed standard oil lubricant, bulk oil temperature 68°C - unheated, 25.8 million upper ball stress cycles, Hertzian maximum compressive stress - 7.6 GPa, theoretical lambda ratio - 5.5, Surface roughness (Ra) of upper and lower balls 0.008 μm.

Figure 6.2, captions (a) to (n), describe a detailed microscopic survey of a type 1i2p delamination failure. Caption (a) shows overview of the 'heart' shape failure, with dimensions of 3.0 by 1.5 millimetres. The brittle initiation area is evident at the heart centre as a smooth surface. The fatigue area is visible as the undulation, concentric to the central region. Detailed observations of the fatigue area are shown in captions (b) to (d). A fatigue area from one half of the heart shape is shown in caption (b), where the directionality of the beach-like marks are clearly visible. Caption (c) shows the fatigue undulations in greater detail. The wave height measured by stereo imaging reaches a maximum of 10 microns peak to peak. This maximum undulation height distinguishes the delamination type as it is much lower than that described in section (6.2.1.1). The delamination edge is shown in caption (d) where it can be seen that the surface adjacent to the failure is undamaged.

The central brittle initiation area interfacing with the outer delamination undulations is presented in captions (e) to (h). An overview of the brittle and fatigue areas caption (e), shows the upper central position of the heart shape. Captions (f) to (h) show, in increasing magnification of the central region, the differences in surface topography. Caption (g) shows the rib-like fatigue area adjacent to the smooth brittle area. The fatigue area edge is compared with the brittle edge in captions (i) to (l). Caption (i) shows the fatigue area edge; micro-cracks on the ball edge are not visible and the brittle area proceeds the deeper delaminated surface. High magnification of the fatigue area, caption (j), shows a inter-granular fracture surface. The brittle edge interface with the ball surface, caption (k), shows a much shallower and smooth surface failure. Micro-cracks are again not evident although the brittle surface resemble the interface area found on the fatigue example of caption (i). A high magnification view of the brittle surface resembles previous brittle initiation areas. White specks on the surface are sintering additives.

Areas between delamination undulations were examined to find evidence of cyclic fatigue. One example of these investigations is shown as caption (m) and (n). A fatigue undulation base positioned near the brittle central region is shown in caption (m). Striation-like markings are found and can be seen in caption (n). The evidence of these observations show that these are potentially fatigue markings

although verification of this supposition is difficult due to the random nature and high speed contact stress.

(6.2.1.3) Example of Type 1i3p Failure

Type 1i3p failures occur in ceramic/ceramic contacts on silicon nitride balls when tested with a base mineral oil lubricant, and high contact stresses (6.0 to 7.1 GPa). The example shown in figure 6.3, captions (a) to (h), is a typical 'brittle flake' shape failure.

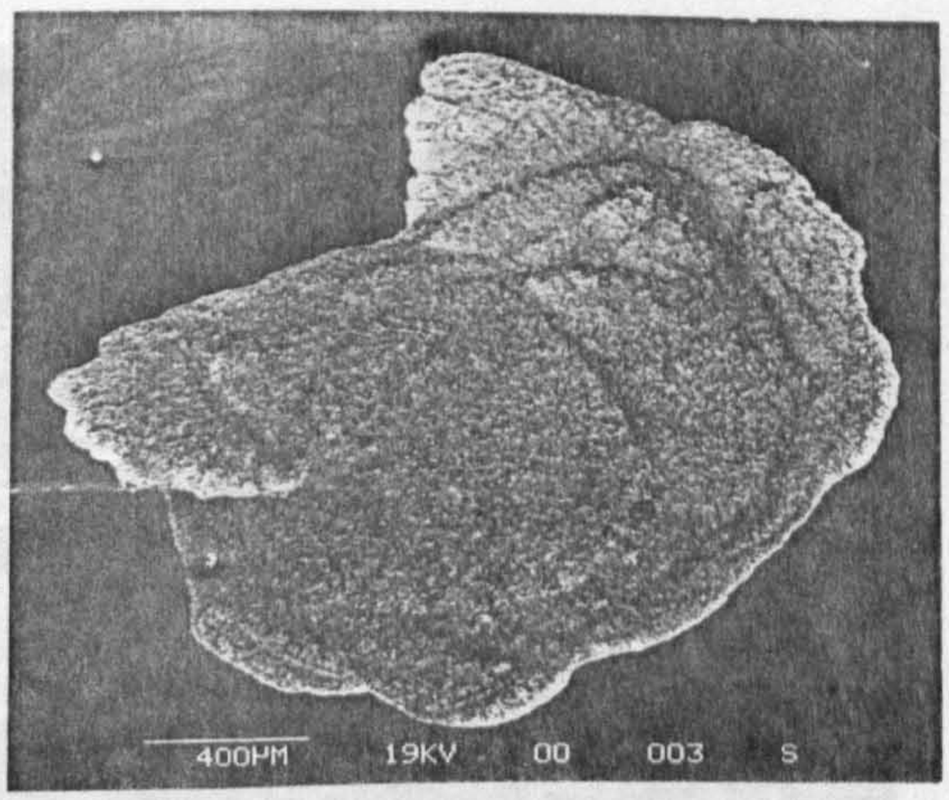

(a) Failure overview

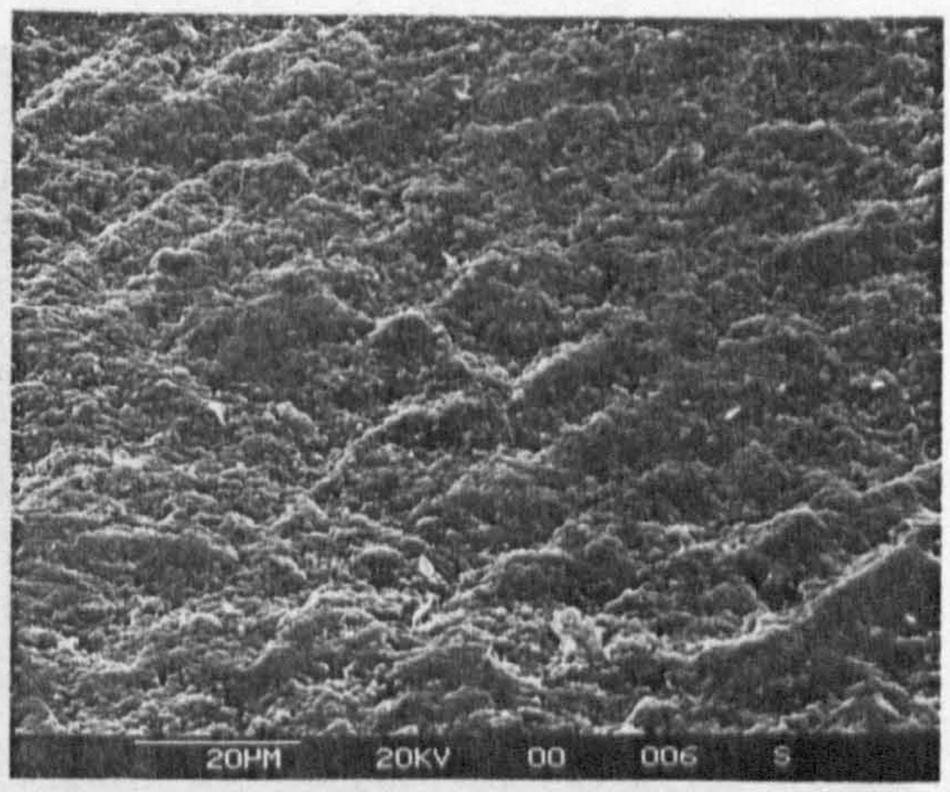

(b) Isolated shallow undulations

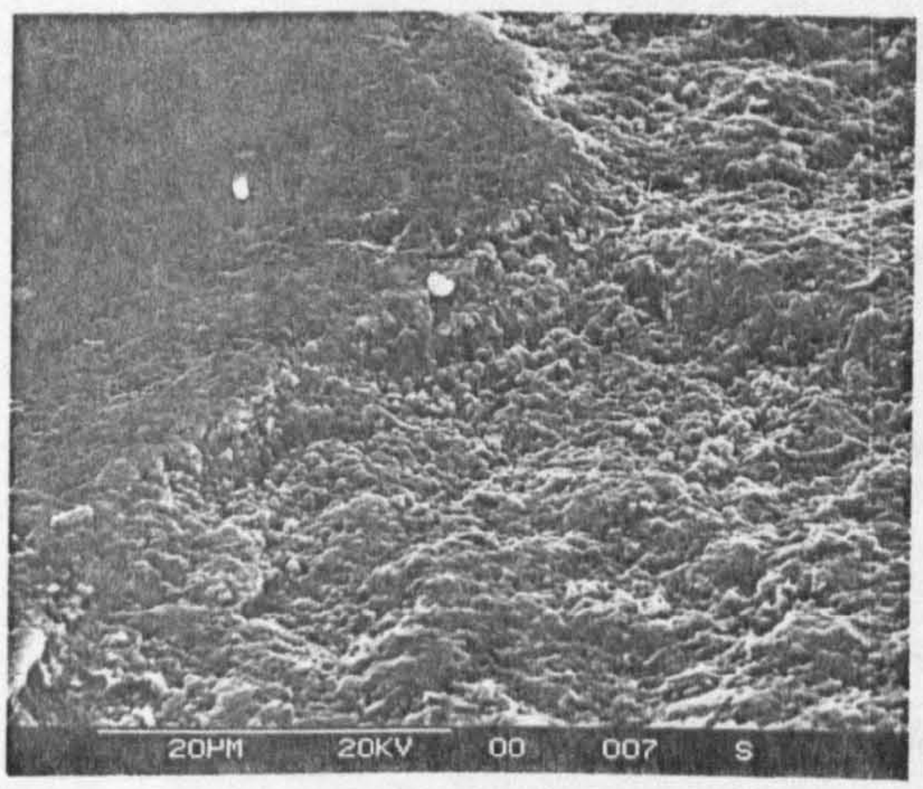

(c) Brittle area edge

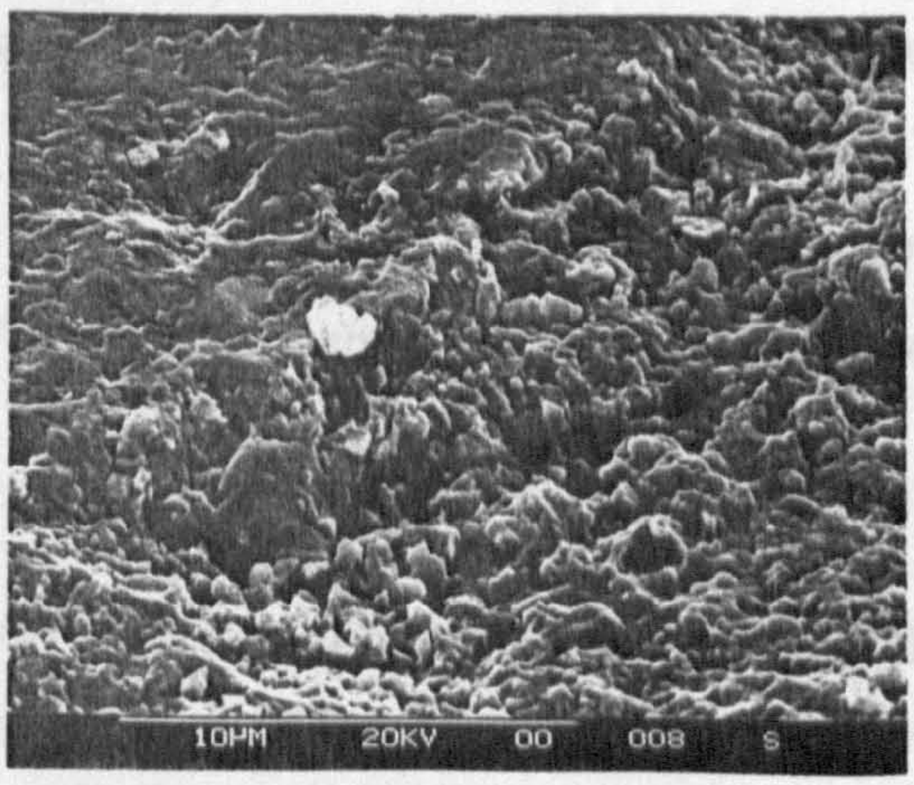

(d) Edge at high magnification

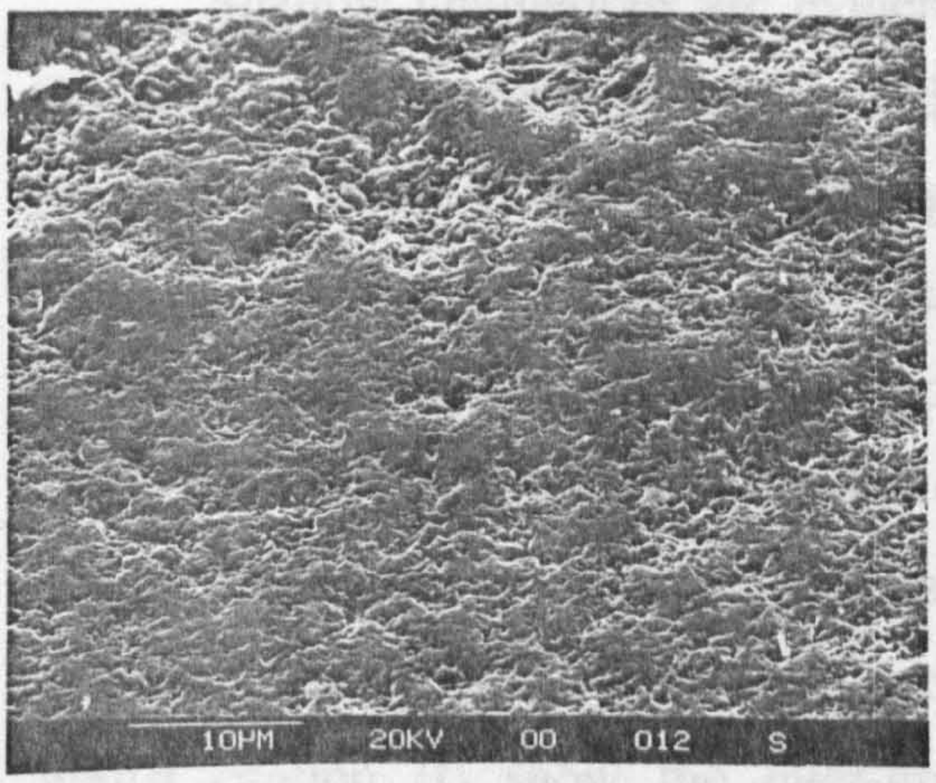

(e) Brittle area (top)

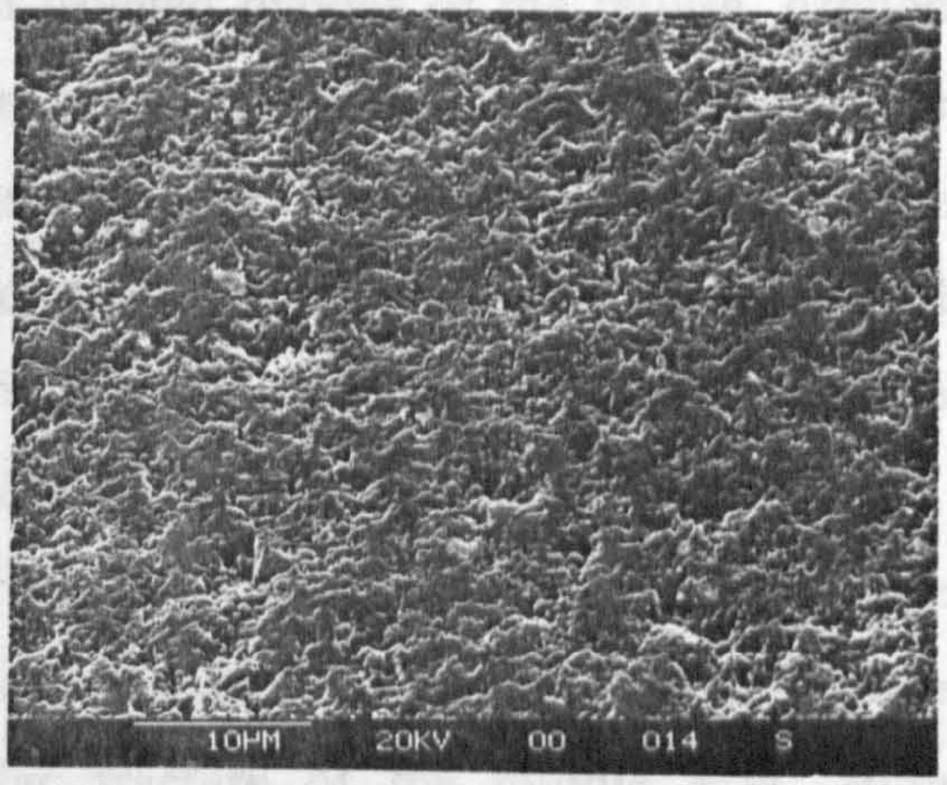

(f) Brittle area (middle)

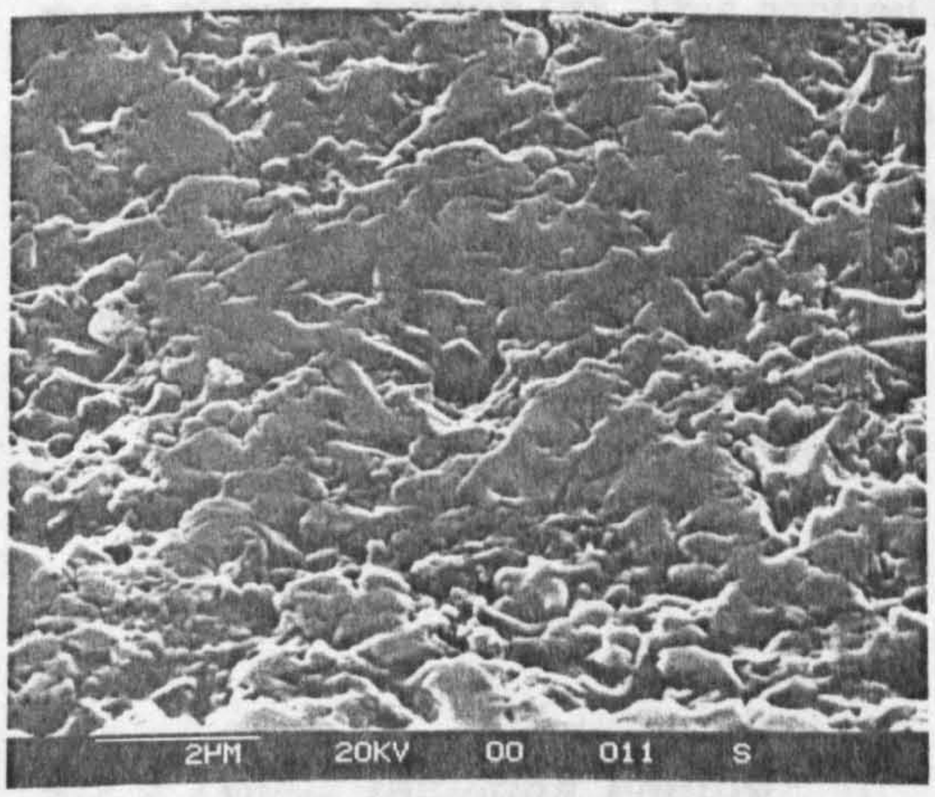

(g) Brittle area high magnification

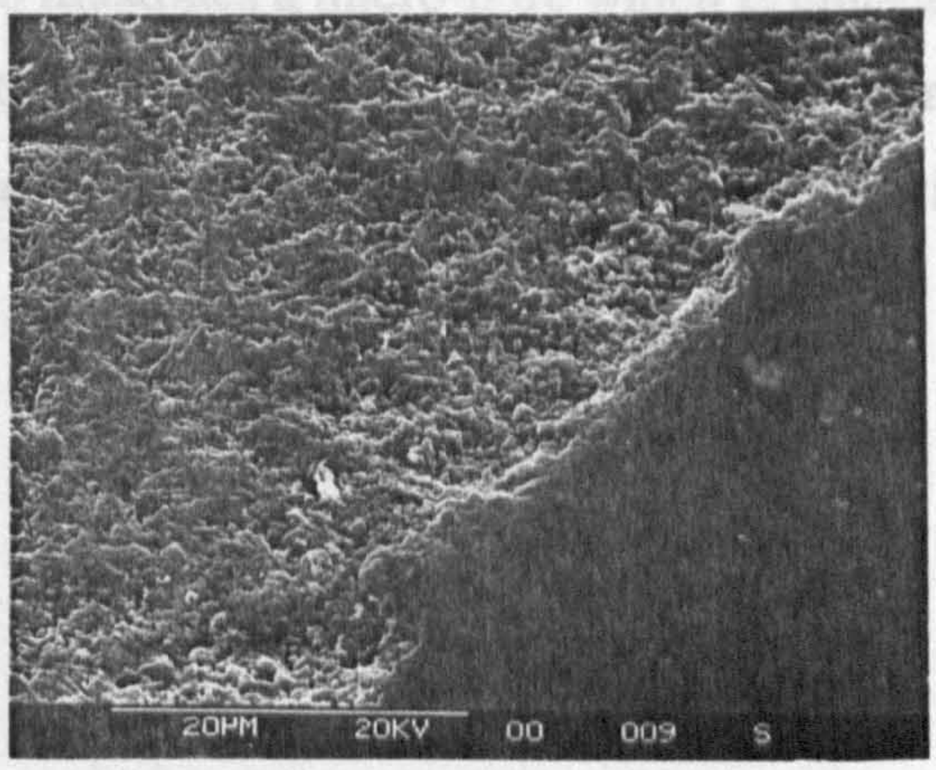

(h) Brittle area edge

Figure 6.3 Example of type 1i3p failure - captions (a) to (h)

Test Conditions of figure 6.3: Ceramic/ceramic contact, machine spindle speed 10,000 r.p.m, inclosed base oil lubricant, bulk oil temperature (59° C) - unheated, 1.6 million upper ball stress cycles, Hertzian maximum compressive stress - 7.1 GPa, theoretical lambda ratio -5.5, Surface roughness (Ra) of upper and lower balls 0.008 μm.

Figure 6.3, captions (a) to (h), presents a detailed survey of a type 1i3p delamination example. Caption (a) shows an overview of the failure with dimensions of 1.8 by 1.25 millimetres. The topography of brittle initiation and propagation over

the entire failure surface is evident from caption (a).

Shallow undulations are evident on isolated regions of the failure, caption (b), although the origin of failure initiation is not apparent. Surface cliff near the intact ball surface in the undulated regions show evidence of delamination fatigue failure, captions (c) and (d). Micro-cracks can be seen, caption (c), on the ball surface at increased magnification. Caption (d) shows material collapse. Subsurface crack positioned on the cliff base and on the ball surface is evident.

The brittle areas which dominate type 1i3p failures are surveyed, example are shown as captions (e) to (h). Captions (e) shows an over-rolled brittle surface whilst caption (f) show the inter-granular fracture of the middle area. High magnification of over-rolled brittle fracture shows surface smoothing and fracture more clearly, caption (g). This caption also illustrates a micro-pore which is unusual in the silicon nitride ceramic ball. The interface of the intact ball to brittle fracture surface is shown as caption (h). Limited surface damage to the ball surface is evident.

6.2.2 Type-2 Initiation Failure

This initiation type of failure is a brittle mode which penetrates relatively deep into the material. Crack propagation is evidenced by typical beech marks (type 2i1p) and by shallow beach marks (type 2i2p).

(6.2.2.1) Example of Type 2i1p Failure

Type 2i1p failures occur in ceramic/ceramic contacts on silicon nitride balls when tested with a high and low viscosity oil lubricants, and high contact stresses (6.0 to 10.0 GPa). The example shown in figure 6.4, captions (a) to (h), is a typical 'cracked spall' shape failure.

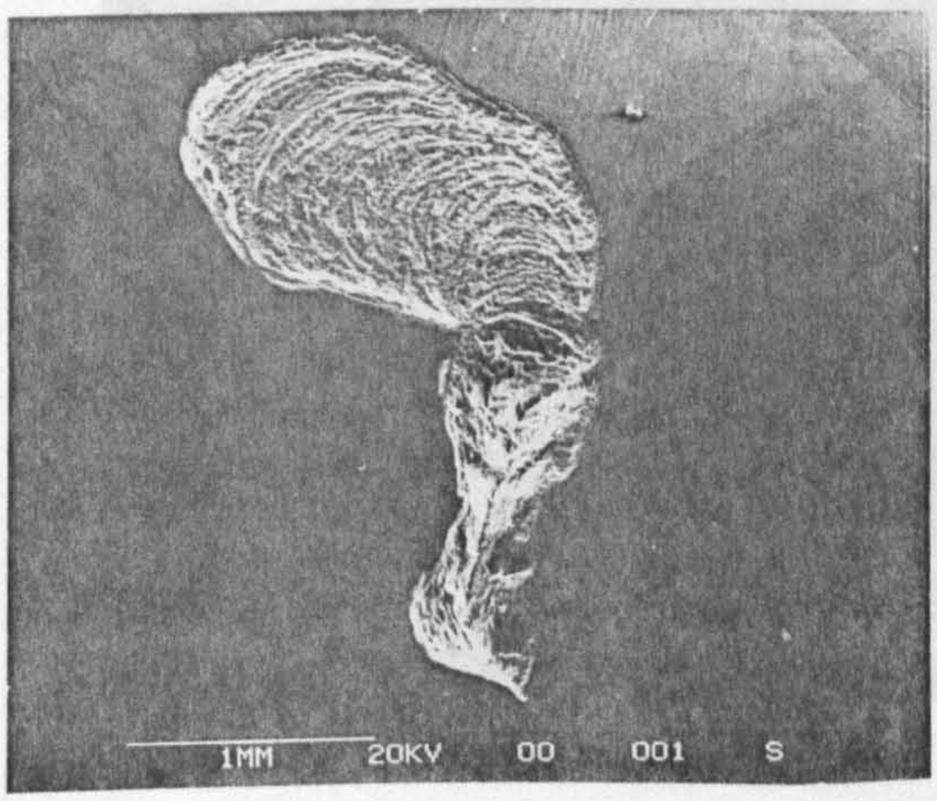

(a) Failure overview

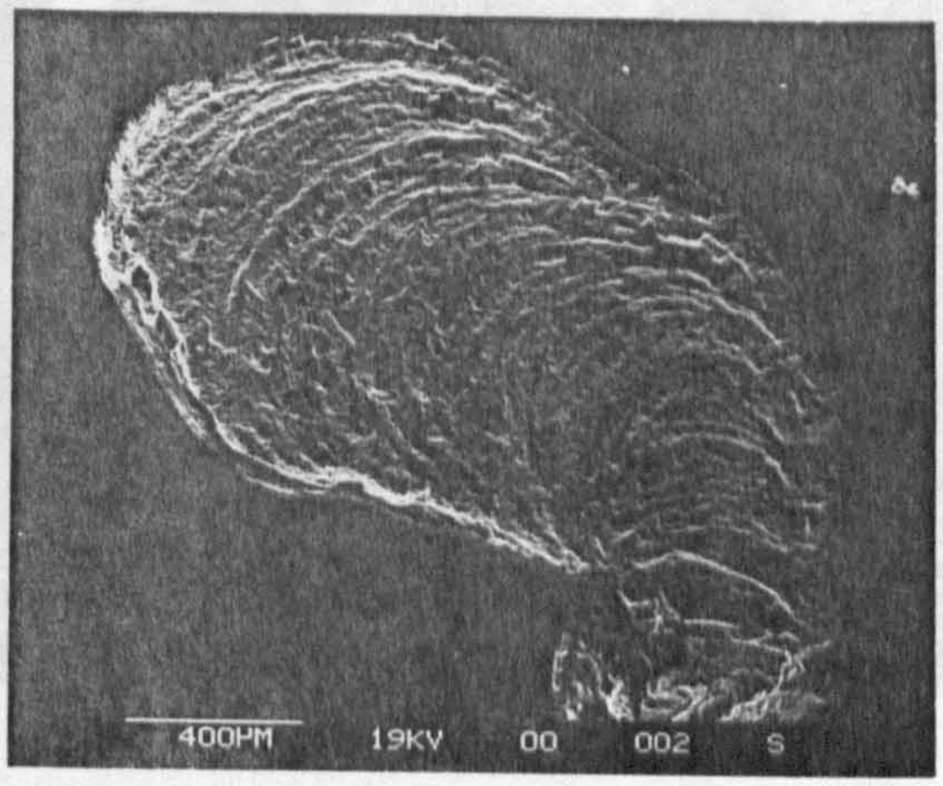

(b) Delamination area

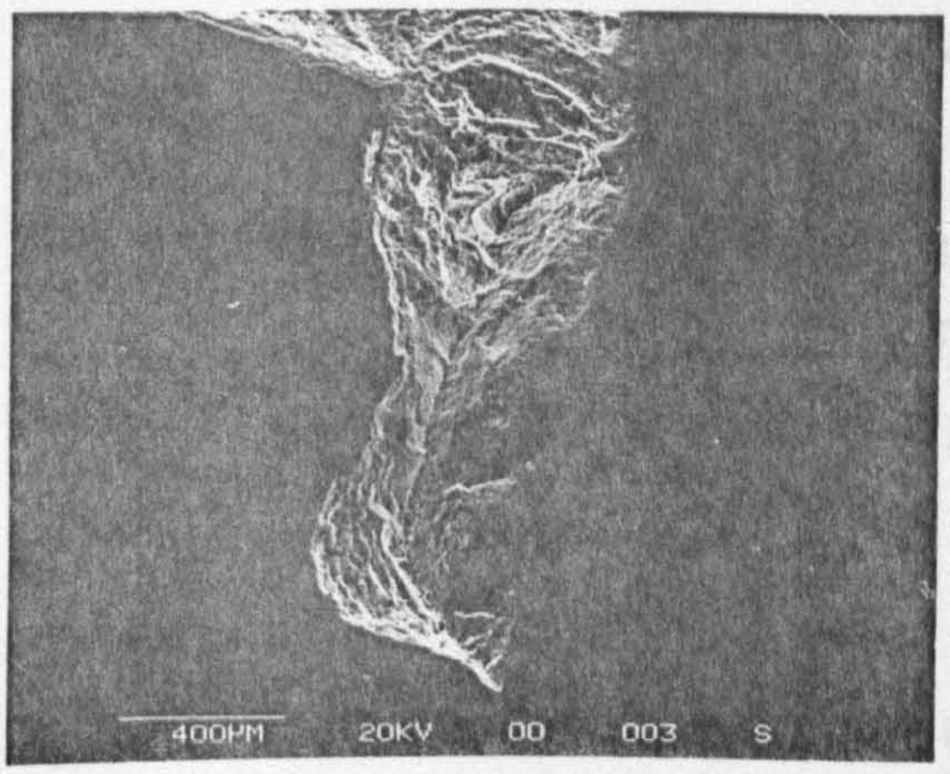

(c) Deep brittle failure

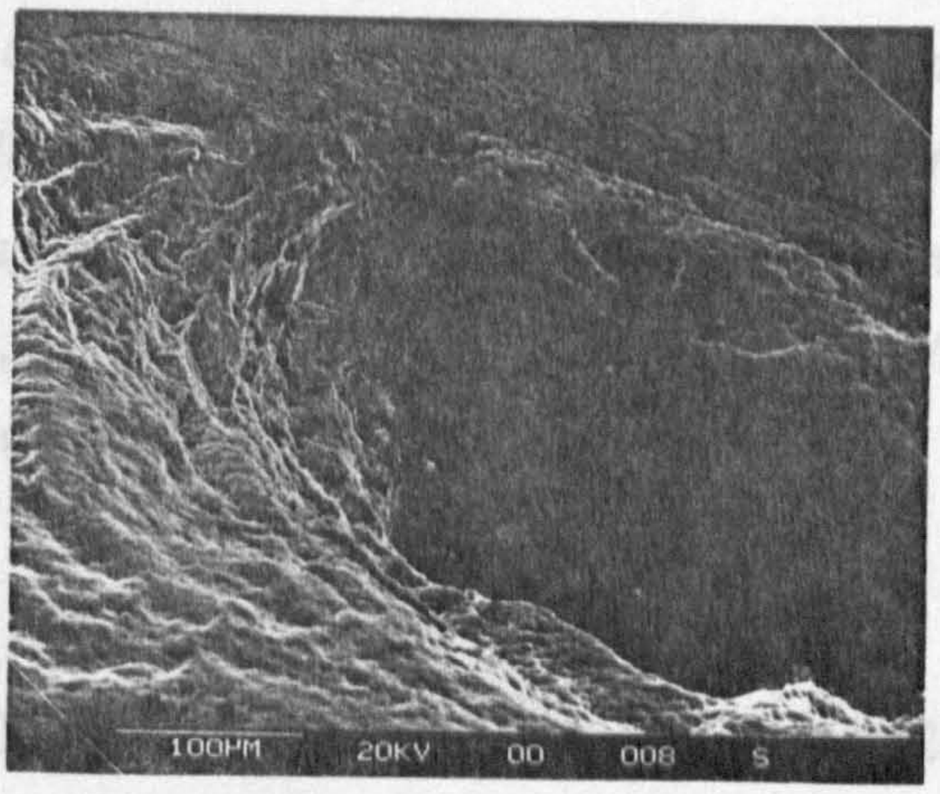

(d) Initiation bottom section

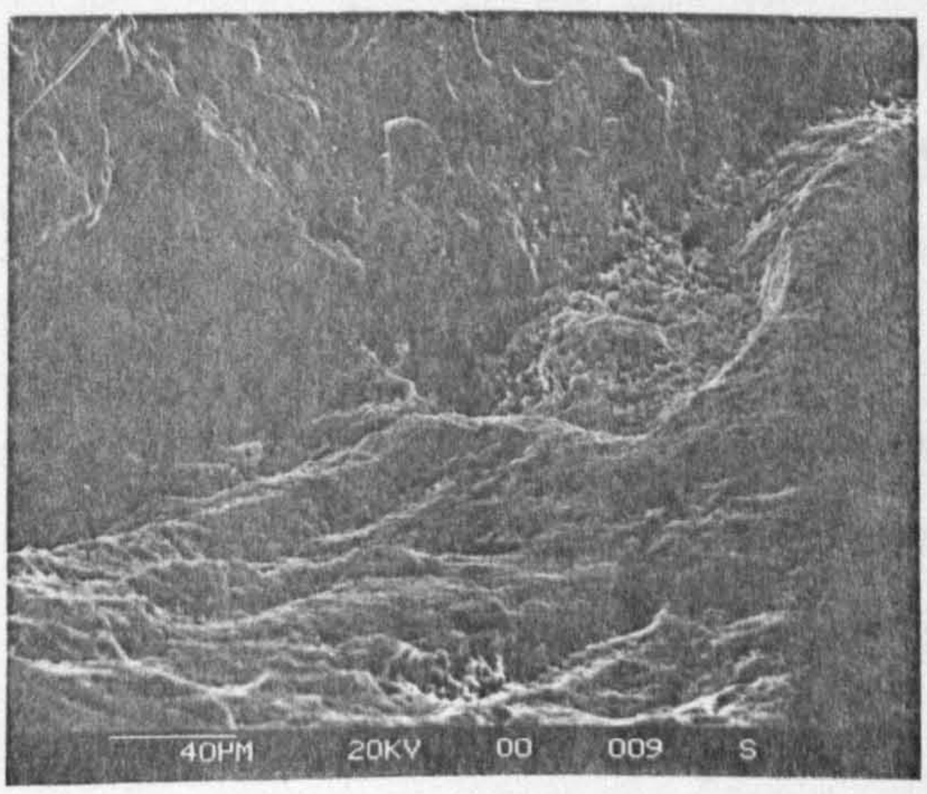

(e) Initiation top section

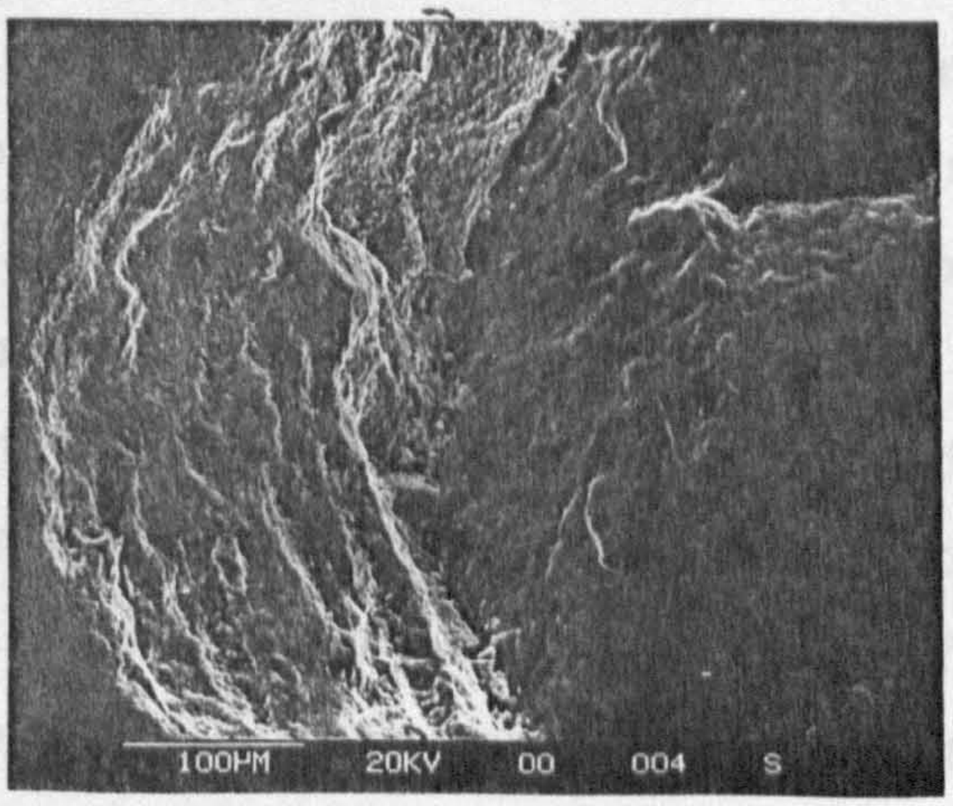

(f) Initiation middle section

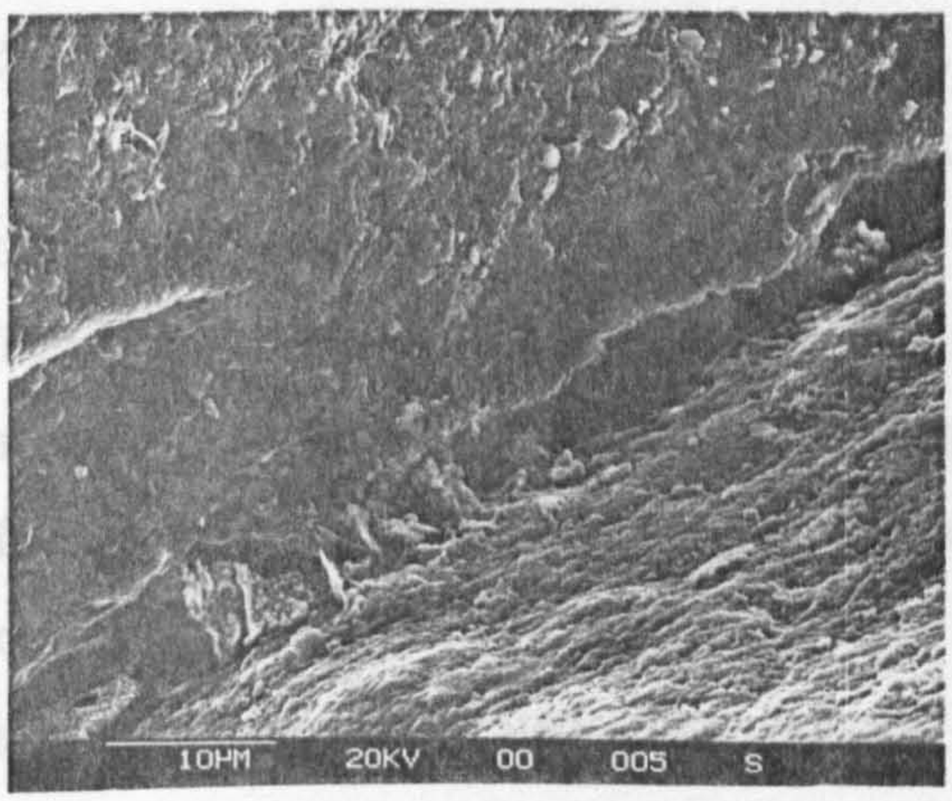

(g) Initiation crack

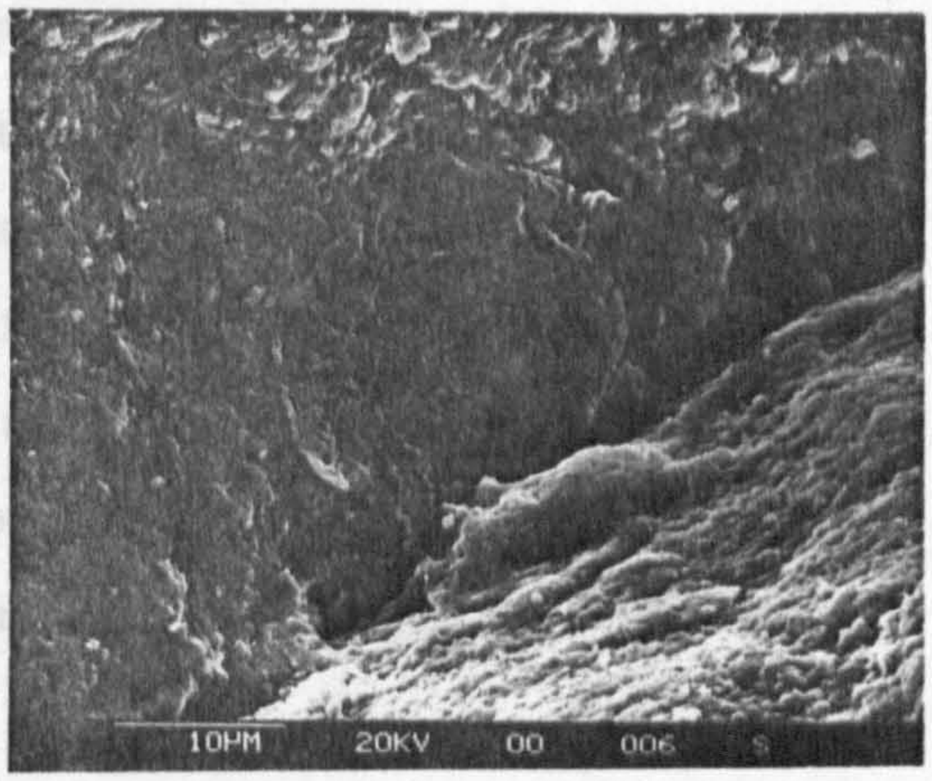

(h) Initiation crack brittle failure

Figure 6.4 Example of type 2i1p failure - captions (a) to (h)

Test Conditions of figure 6.4 Ceramic/ceramic contact, machine spindle speed 10,000 r.p.m, inclosed HiTec 174 oil lubricant, bulk oil temperature 83°C - unheated, 1.4 million upper ball stress cycles, Hertzian maximum compressive stress - 8.7 GPa, theoretical lambda ratio - 5.5, Surface roughness (Ra) of upper and lower balls 0.008 μm.

Figure 6.4, captions (a) to (h), gives a detailed survey of a type 2i1p delamination failure. Caption (a) shows the overview of a typical example; the failure is 2.5 millimetres in length. The deep initiation area is visible from the failure base which then propagates in a type-1 failure mode. The upper delamination propagation region, caption (b), is typical for the test tribological conditions used. The propagation area, of dimensions 1.0 by 1.5 millimetres, is covered with typical undulations which move away from the deep initiation area.

The remaining micrographs of figure 6.4, captions (c) to (h), detail the deep brittle initiation region. An overview of the deep brittle area, of dimensions 1.5 by 0.4 millimetres, caption (c), shows the general topography. A general survey of the deep initiation sections, captions (d) to (f), shows the area bottom, middle and top. Caption (d) shows the depth of the area as at least 300 microns which is a

magnitude increase on type-1 initiation failures. The failure propagation to the delamination area is shown as caption (e). The surface morphology within the deep initiation region consists of a smooth texture on one side and a fatigued area on the other, caption (f). This implies a ring or cone surface crack initiating the failure. The base crack position deep within the initiation area was examined, captions (g) and (h). The surface texture deep with that area, caption (g), implies inter-granular failure. Debris can be seen of dimensions above five microns and evidence of plastic deformation is shown in caption (h). The crack tip is not evident from the analysis and may have propagated some distance.

(6.2.2.2) Example of Type 2i2p Failure

Type 2i2p failures occur in ceramic/ceramic contacts on silicon nitride balls when tested with a low viscosity oil lubricant, and high contact stresses (7.1 to 7.6 GPa). The example shown in figure 6.5, captions (a) to (d), is also a typical 'cracked spall' shape failure.

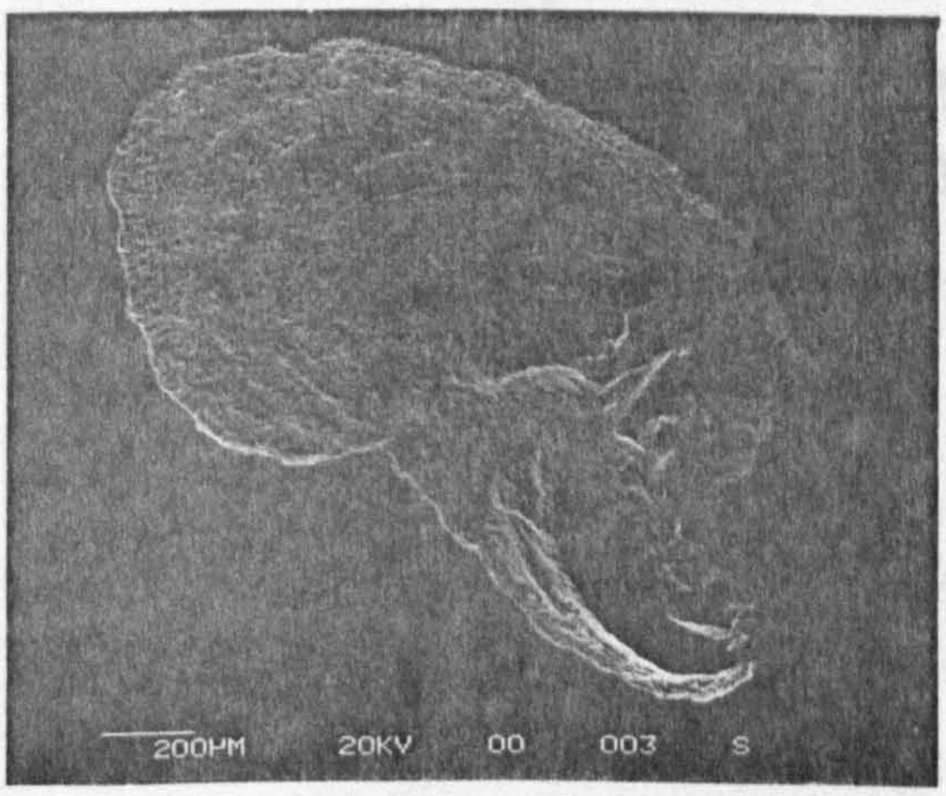

(a) Failure overview

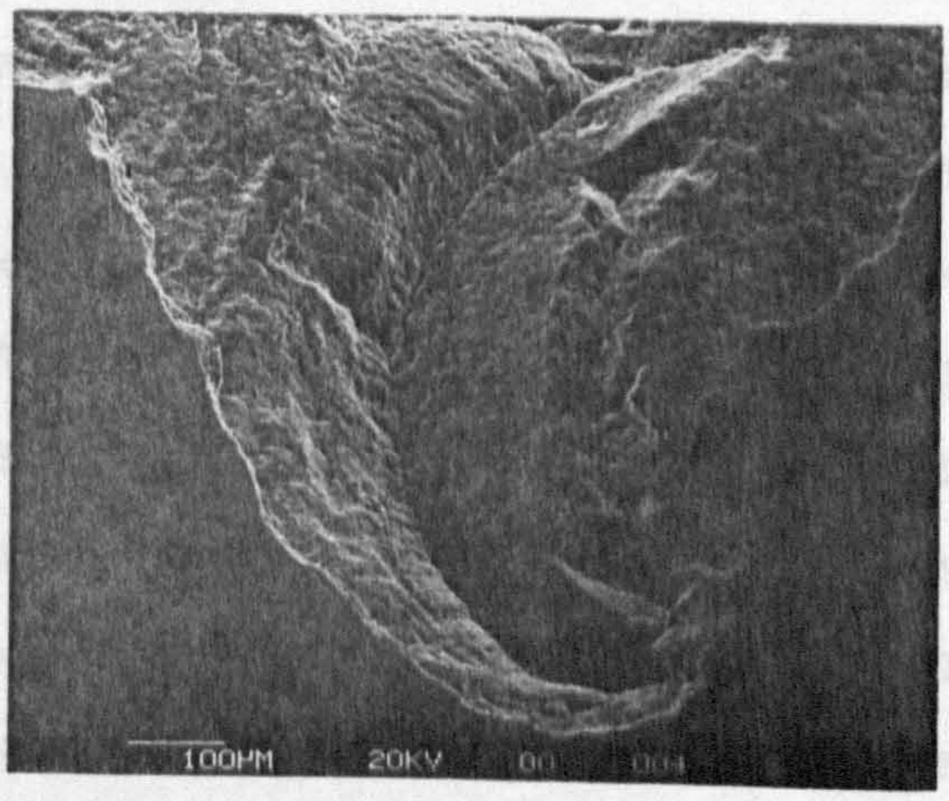

(b) Deep brittle initiation area

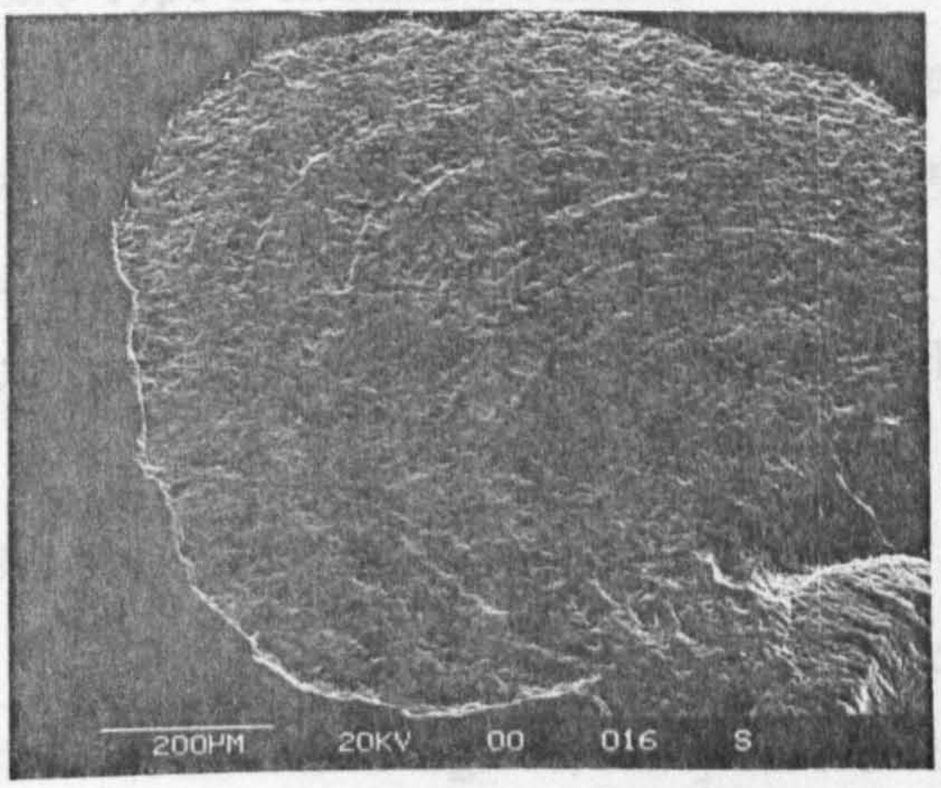

(c) Delamination area

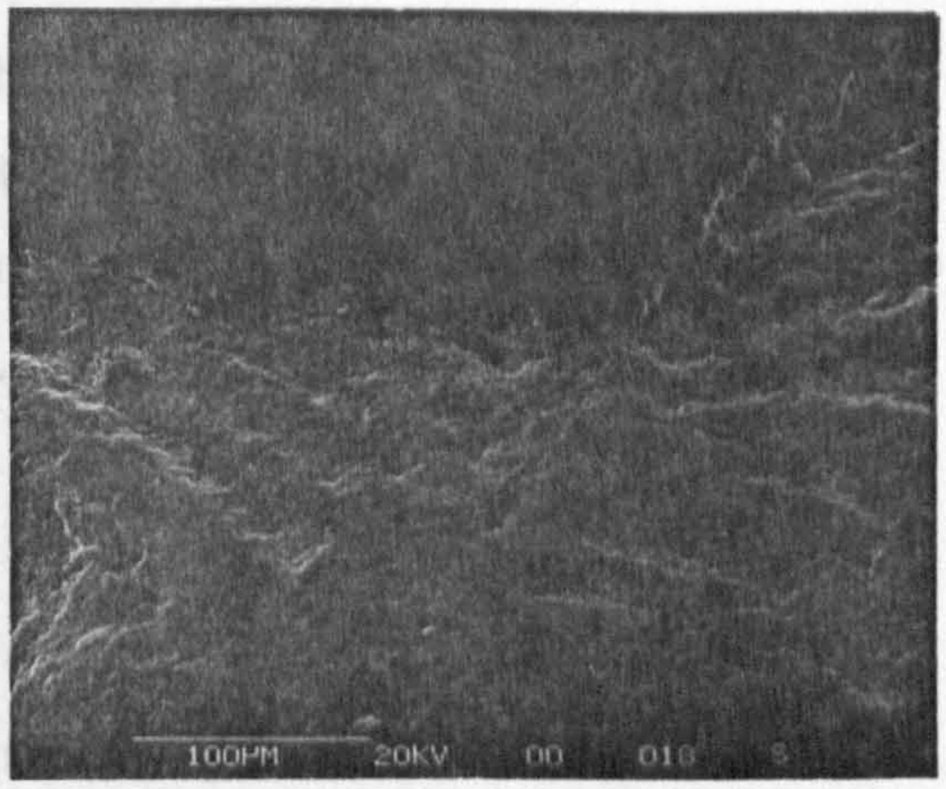

(d) Undulations adjacent to edge

Figure 6.5 Example of type 2i2p failure - captions (a) to (d)

Test Conditions of figure 6.5: Ceramic/ceramic contact, machine spindle speed 10,000 r.p.m, Feed (10 pulses per minute, 30 % stroke), Exxon 2389 oil lubricant, 3.7 million upper ball stress cycles, Hertzian maximum compressive stress - 7.35 GPa, theoretical lambda ratio - 5.5, Surface roughness (Ra) of upper and lower balls 0.008 μm.

Figure 6.5, captions (a) to (d), describes the observation details of a type 2i2p delamination failure. Caption (a) shows overview of the failure, which dimensions are 1.25 by 1.25 millimetres. The deep initiation area is seen at the failure base and type-2 delamination propagation is seen in the upper area. Caption (b) shows the deep initiation area, which is clearly a ring type shape, and smooth brittle fracture surface. The delaminated area, caption (c), shows shallow undulations of maximum wavelength ten microns which are typical for these loading conditions. A detail of the delamination failure shape, caption (d), shows a change in cliff edge direction and also a corresponding change in undulation direction. This failure is also significant as the test was conducted under controlled splash lubrication conditions. This implies that delamination fatigue is unaffected by the inclosed lubrication system.

6.2.3 Type-3 Initiation Failure

Type three initiation failure is described in section [6.1] as a defect initiation mode. This type of failure mode is propagated by typical type-1 delamination failure. Type-2 and type-3 propagation modes are possible although have not occurred during this present research work.

(6.2.3.1) Example of Type 3i1p Failure

Type 3i1p failures occur in ceramic/ceramic contacts on silicon nitride balls when tested with a high viscosity oil lubricant and high contact stresses (7.0 to 10.0 GPa). The example shown in figure 6.6, captions (a) to (l), is a 'leaf' shape failure.

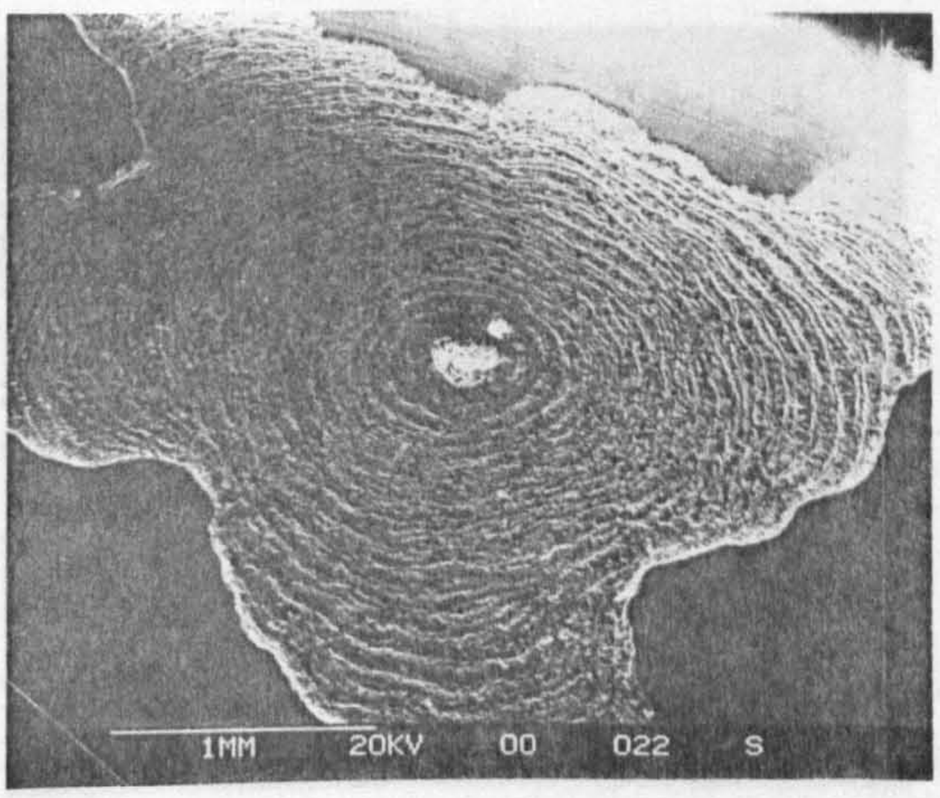

(a) Failure overview

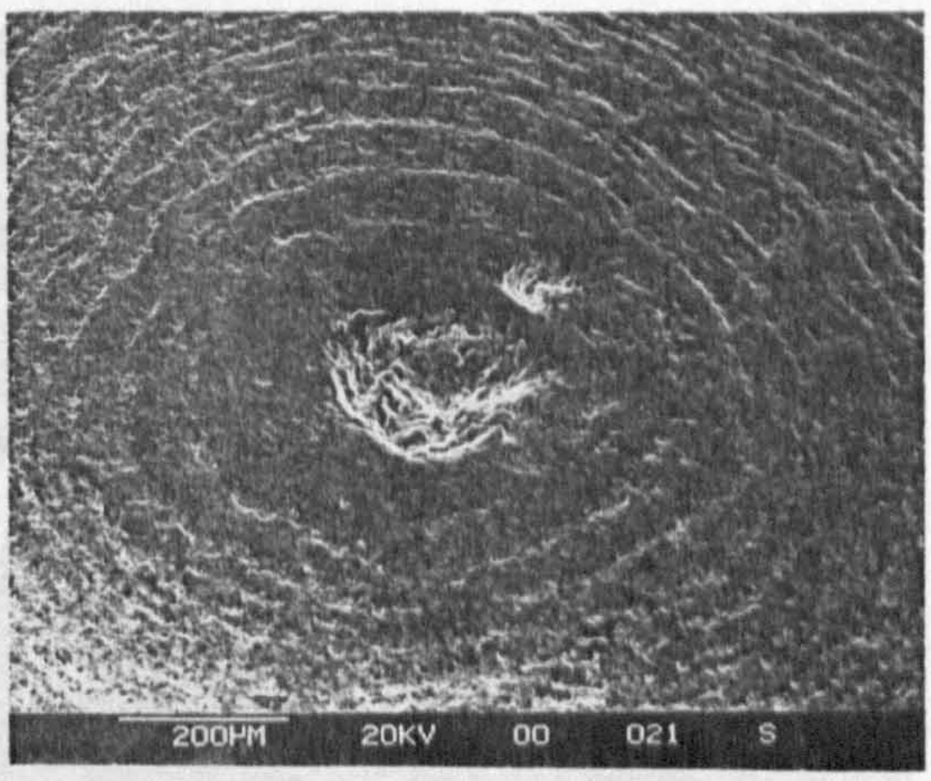

(b) Central initiation spall

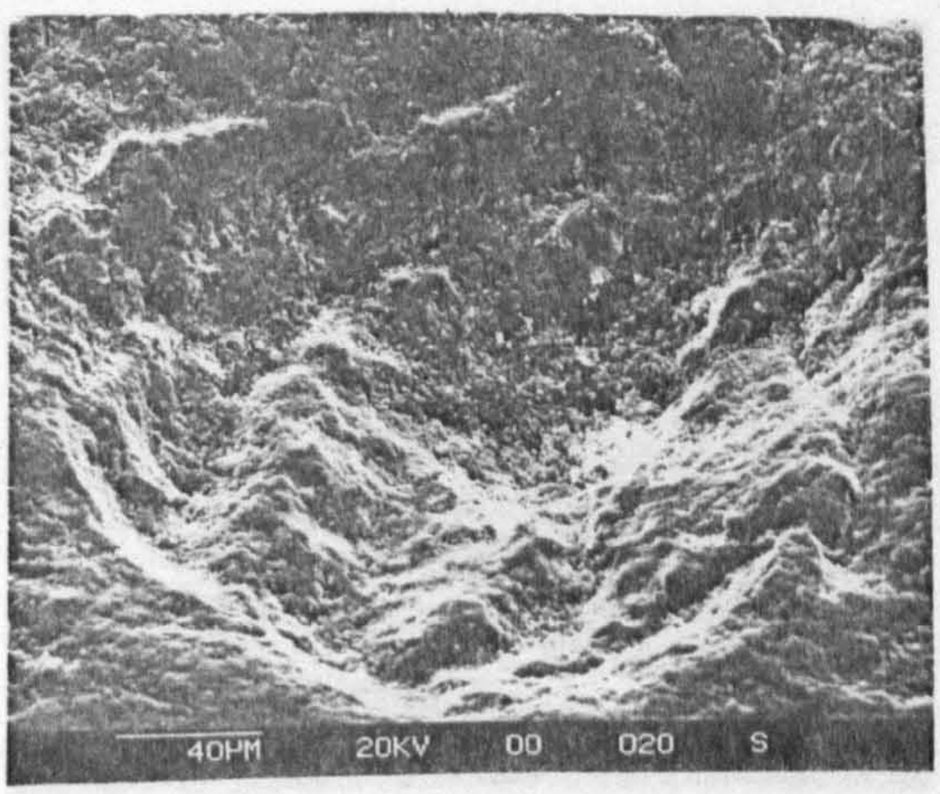

(c) Large central spall

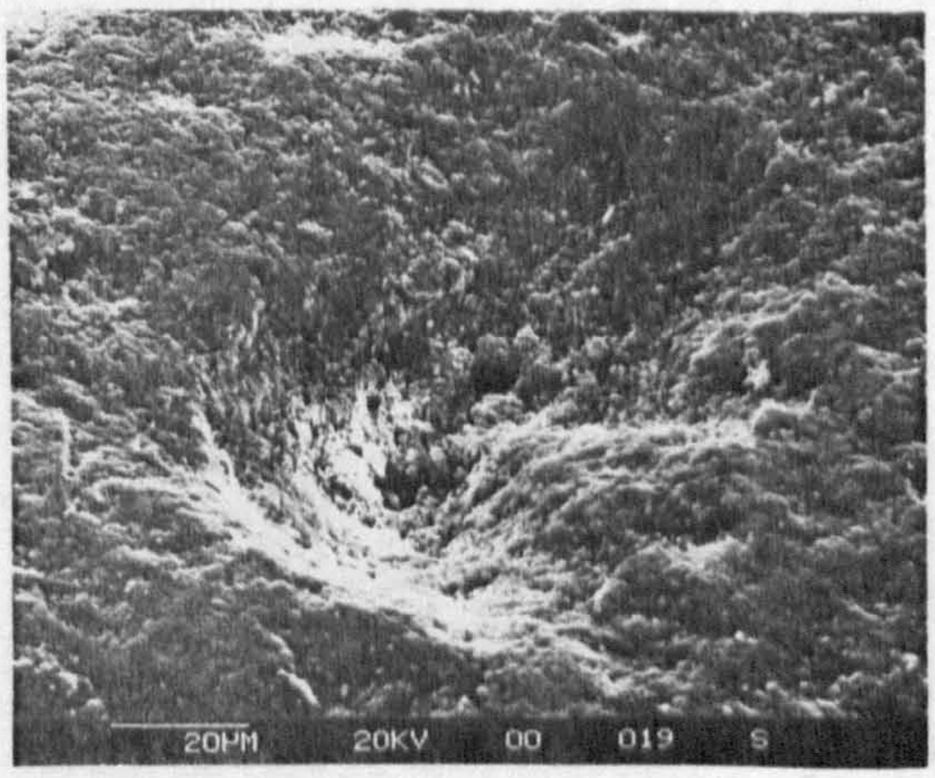

(d) Small central spall

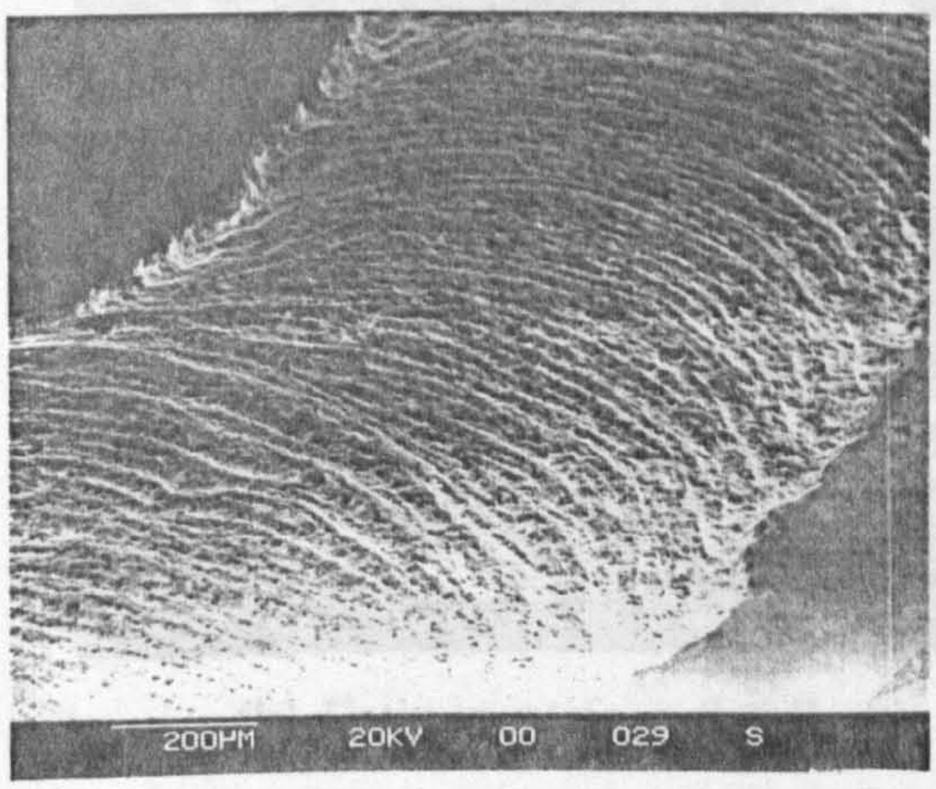

(e) Path entrance

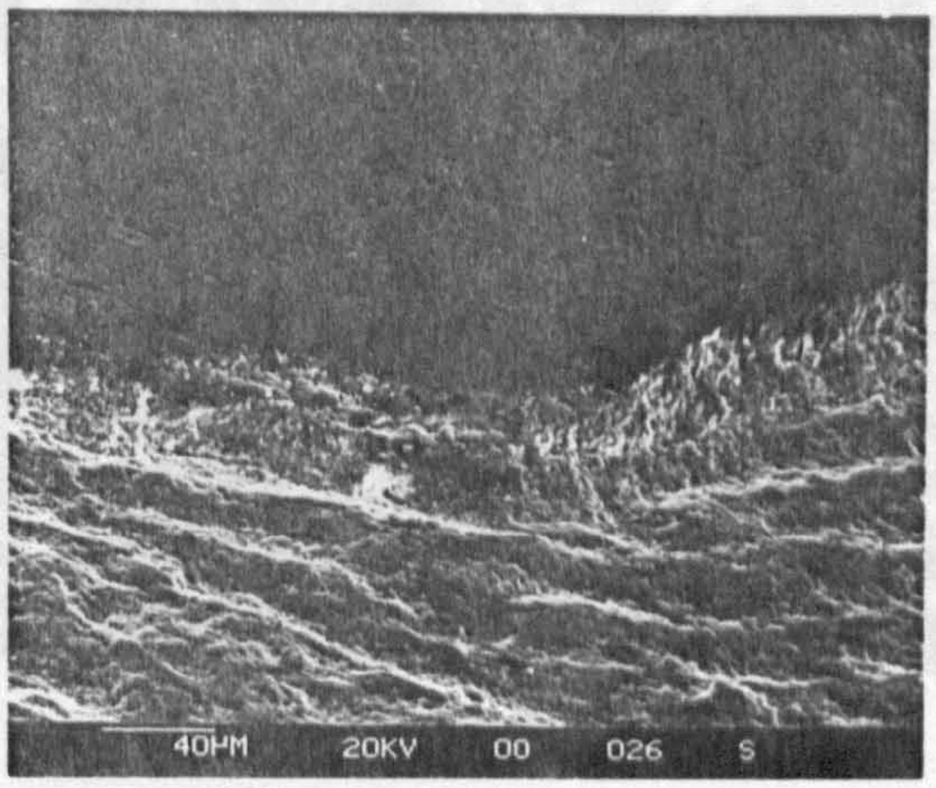

(f) Cliff at path entrance

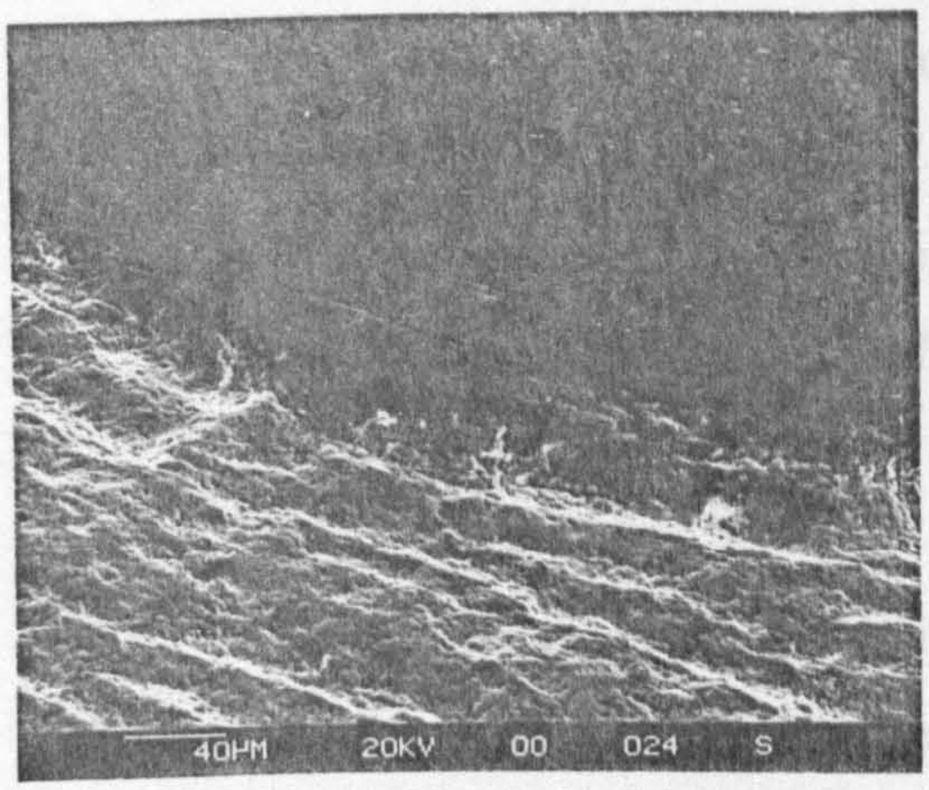

(g) Cliff with large surface crack

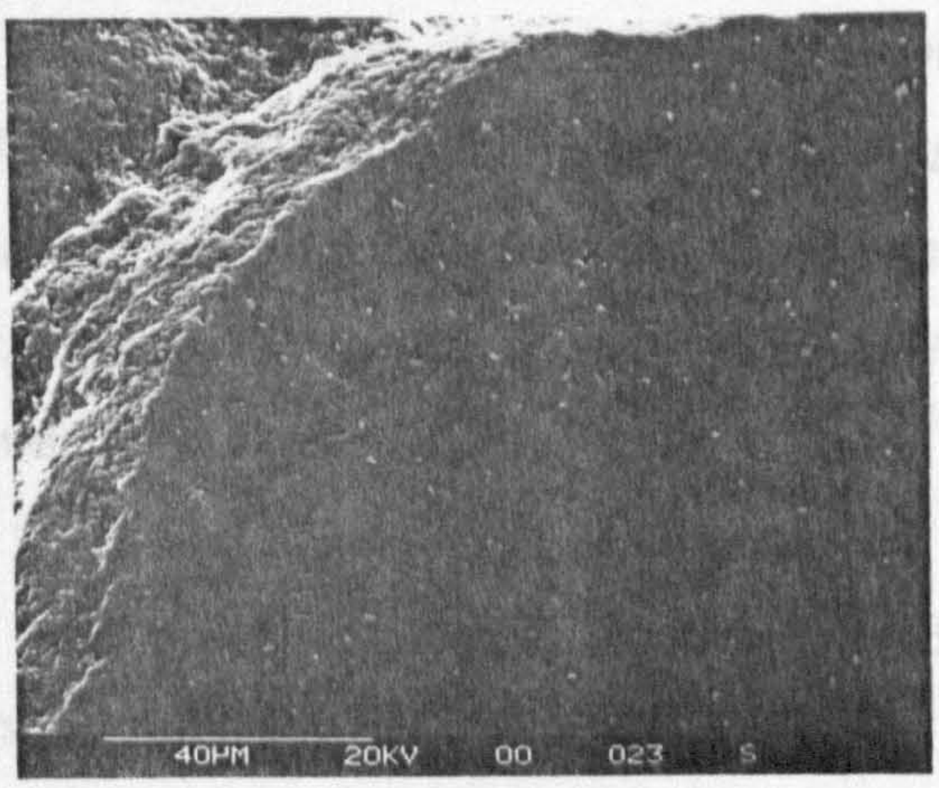

(h) Surface crack detail

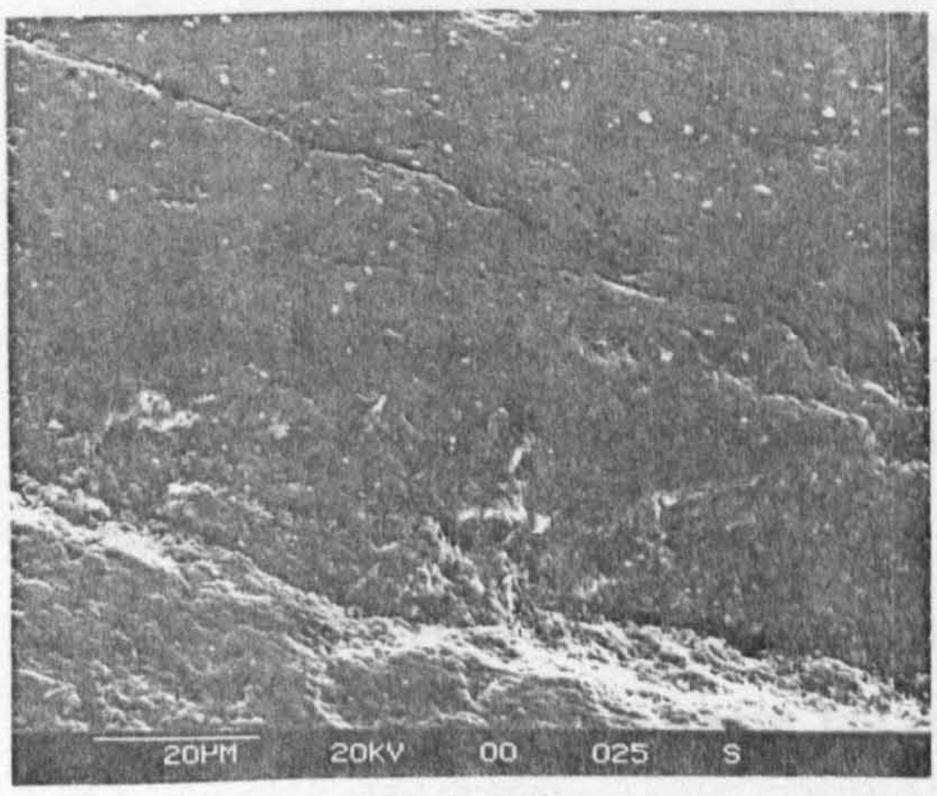

(i) Cliff detail

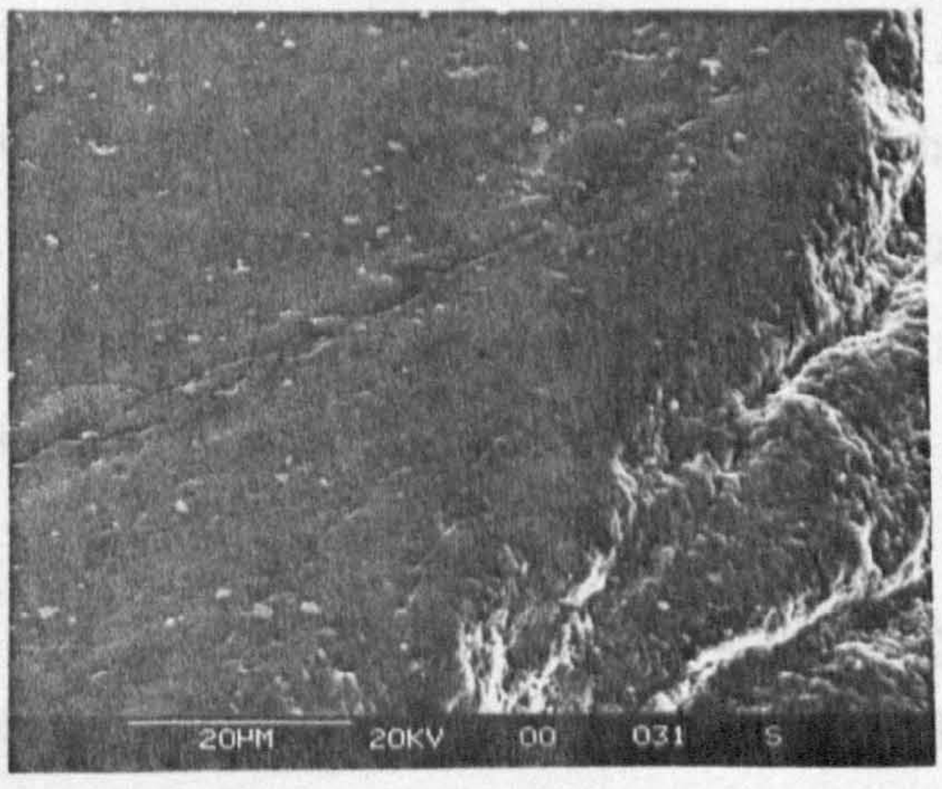

(j) Additional cracks

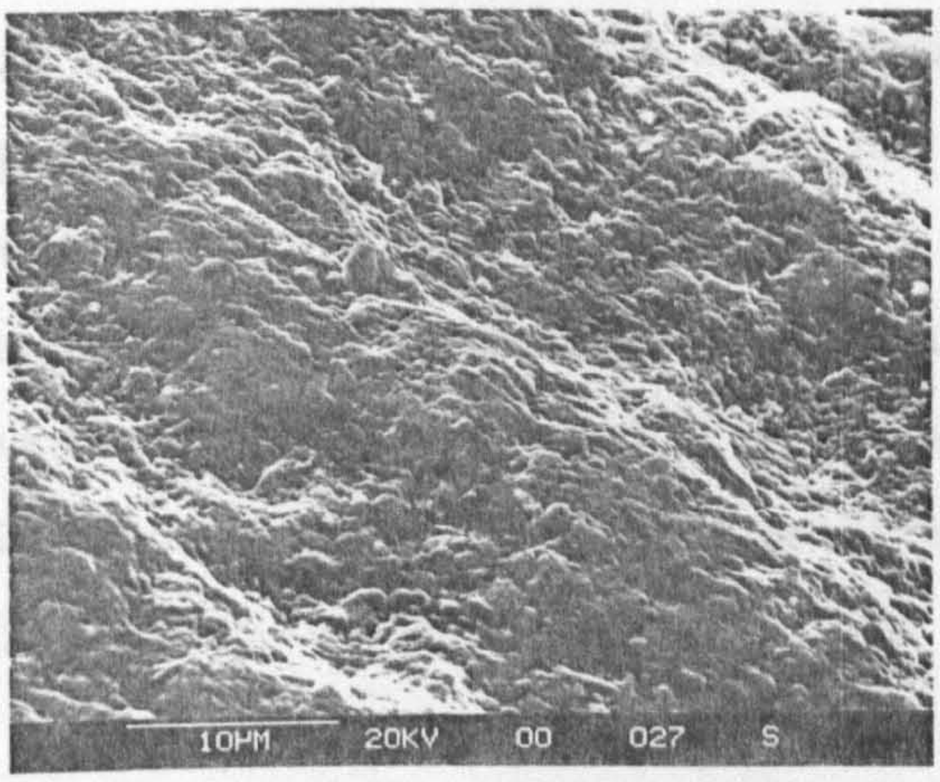

(k) Fatigue surface detail

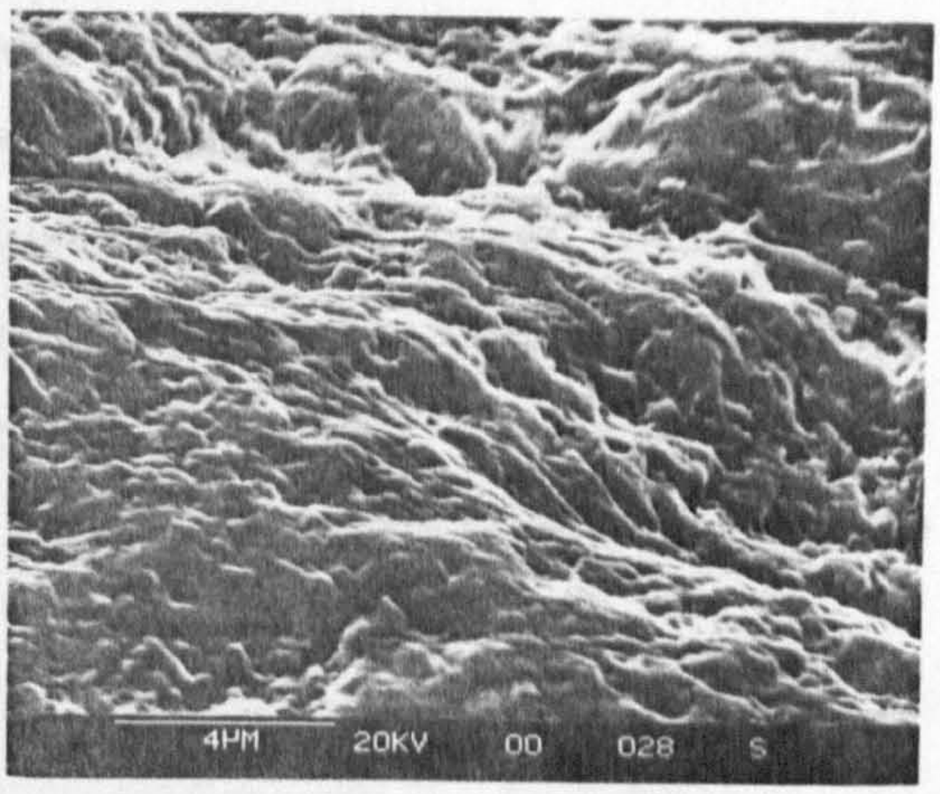

(l) Striation-like surface

Figure 6.6 Example of type 3i1p failure - captions (a) to (l)

Test Conditions for figure 6.6: Ceramic/ceramic contact, machine spindle speed 10,000 r.p.m, inclosed HiTec 174 oil lubricant, bulk oil temperature (78°C) - unheated, 1.6 million upper ball stress cycles, Hertzian maximum compressive stress - 7.9 GPa, theoretical lambda ratio - 6.0, Surface roughness (Ra) of upper and lower balls 0.008 μm.

Figure 6.6, captions (a) to (l), describes a detailed survey of a type 3i1p delamination failure. Caption (a) shows the failure overview. The failure area has a diameter of three millimetres and four paths propagating around the ball. The failure mechanism is suggested by the central spalls initiating failure and concentric undulations. The central initiation spalls are detailed in captions (b) to (d). An overview of the central initiation spalls, caption (b), suggests that the initial ball failure is from the large spall. The initial delamination undulation propagate concentrically from the large spall. Captions (c) and (d) show that the spall topography and, texture is smooth and, unlike previous initiation areas, this may be caused by inclusions or porosity.

Captions (e) to (l) describe the mechanism of type-1 delamination fatigue propagation. One region where the circular delamination divides into four paths, caption (e), shows that undulation directionality is continuous, although, with change

in the shape of the intact region the local undulation directionality also changes, caption (f). Large surface cracks are apparent on the intact ball surface , captions (g) and (h). Large cliff base cracks and ball surface cracks, captions (i) and (j) suggest a typical delamination fatigue driven by the lubricant under a high hydrostatic stress. Delamination undulations were measured, caption (k), as having wavelength twenty microns and distance between waves as fifteen microns. Striation-like surface topography similar to that previously described on a type 1i2p failure is also apparent (see caption (l)).

6.2.4 Type-4 Initiation Failure

Type four initiation failure is described in section [6.1] as a defect initiated mode. The initiation is caused by fatigue at a surface defect, in this case by material porosity. This type of failure mode is propagated by typical type-3 delamination failure.

(6.2.4.1) Example of Type 4i3p Failure

Type 4i3p failures occur in ceramic/ceramic contacts on sialon balls when tested with a base oil as lubricant and moderate contact stresses (5.4 to 7.2 GPa). The example shown in figure 6.7, captions (a) to (l), is a 'eye' shape failure.

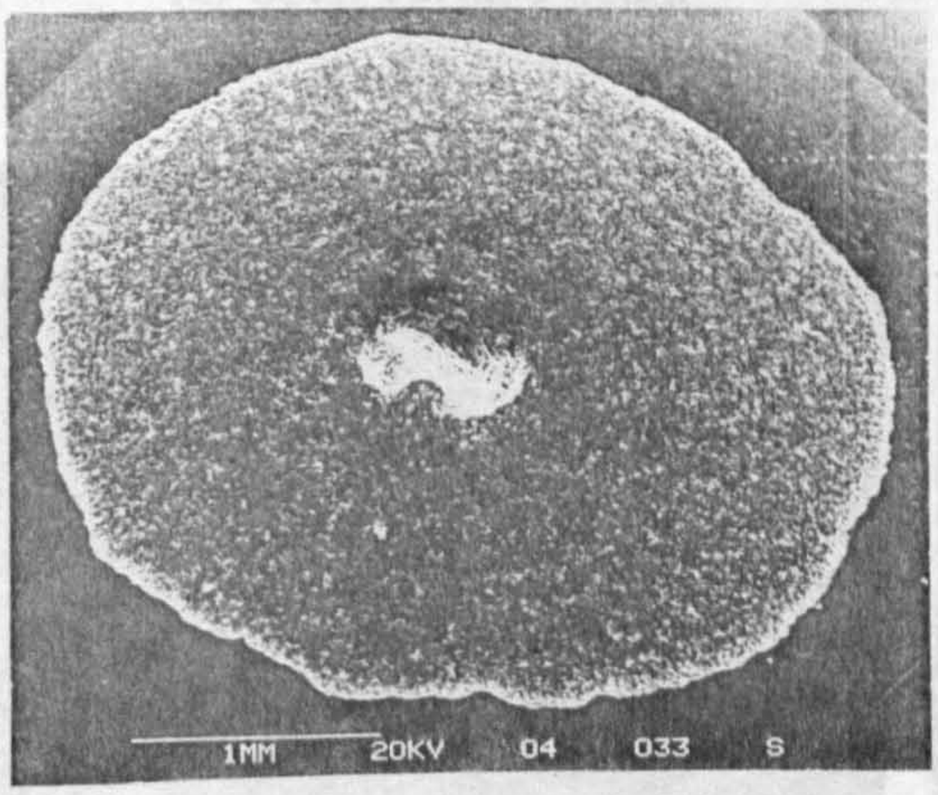

(a) Failure overview

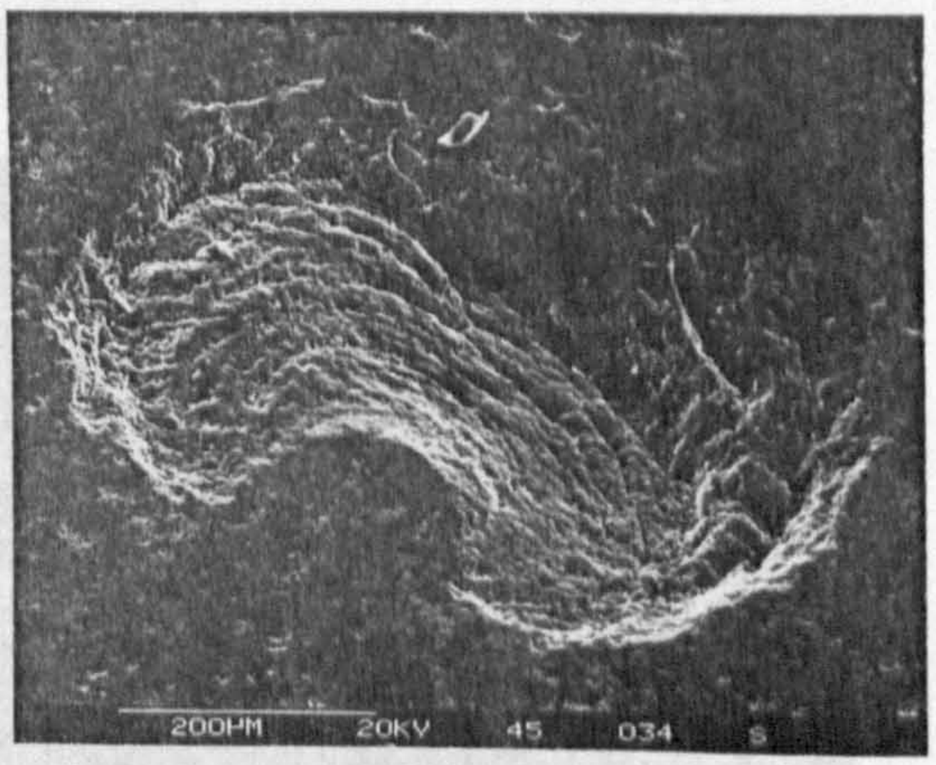

(b) Central initiation spall

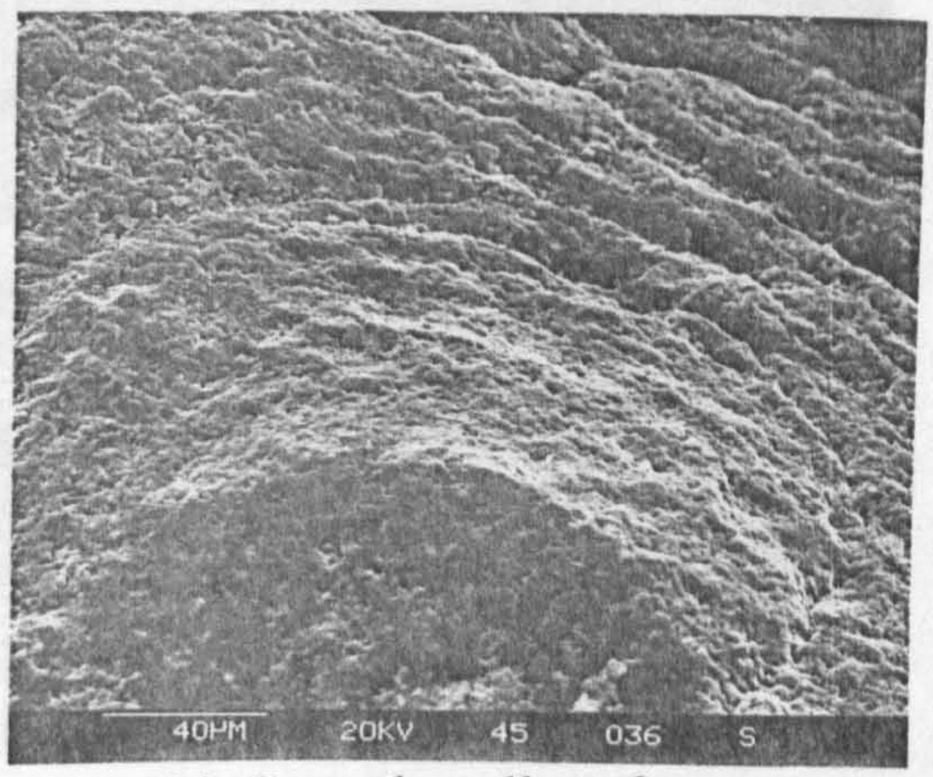

(c) Central spall surface

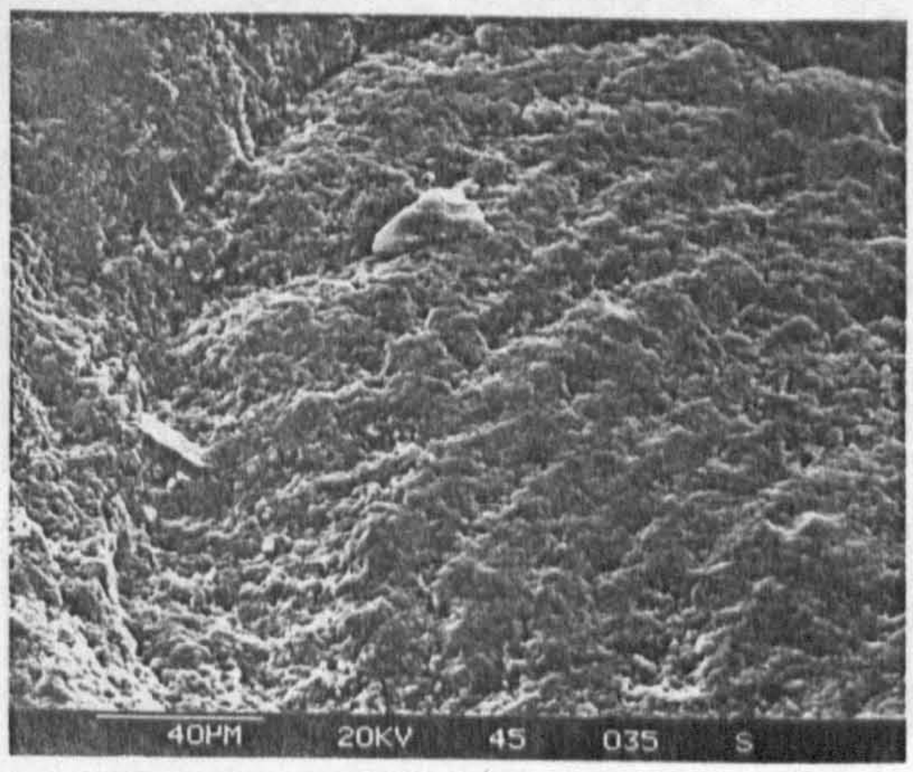

(d) Central spall base

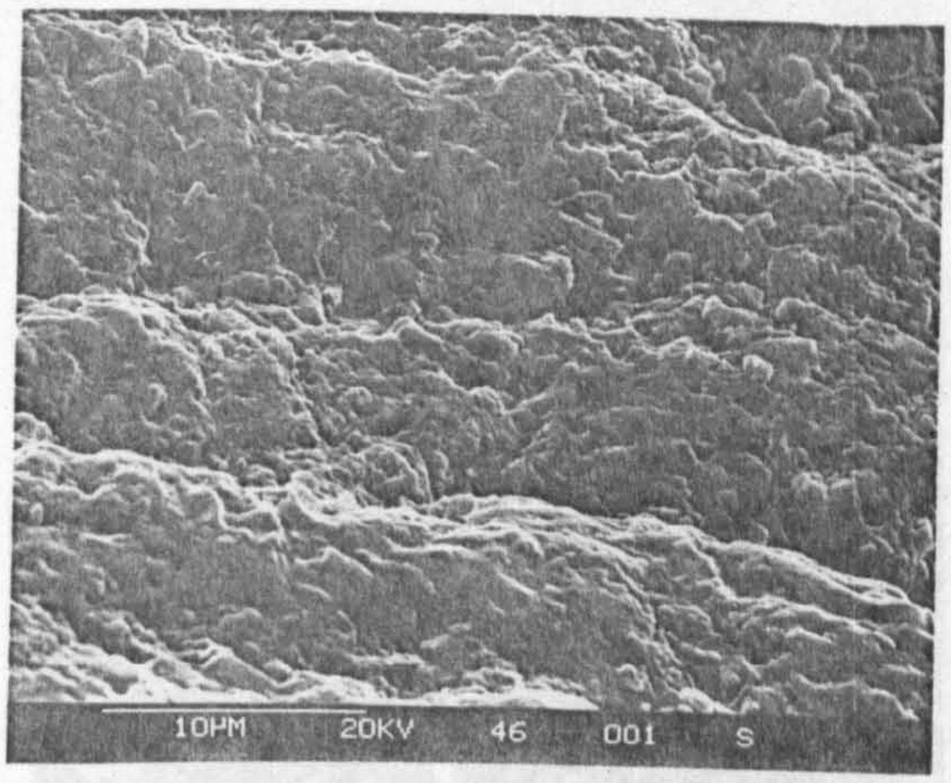

(e) Spall surface detail

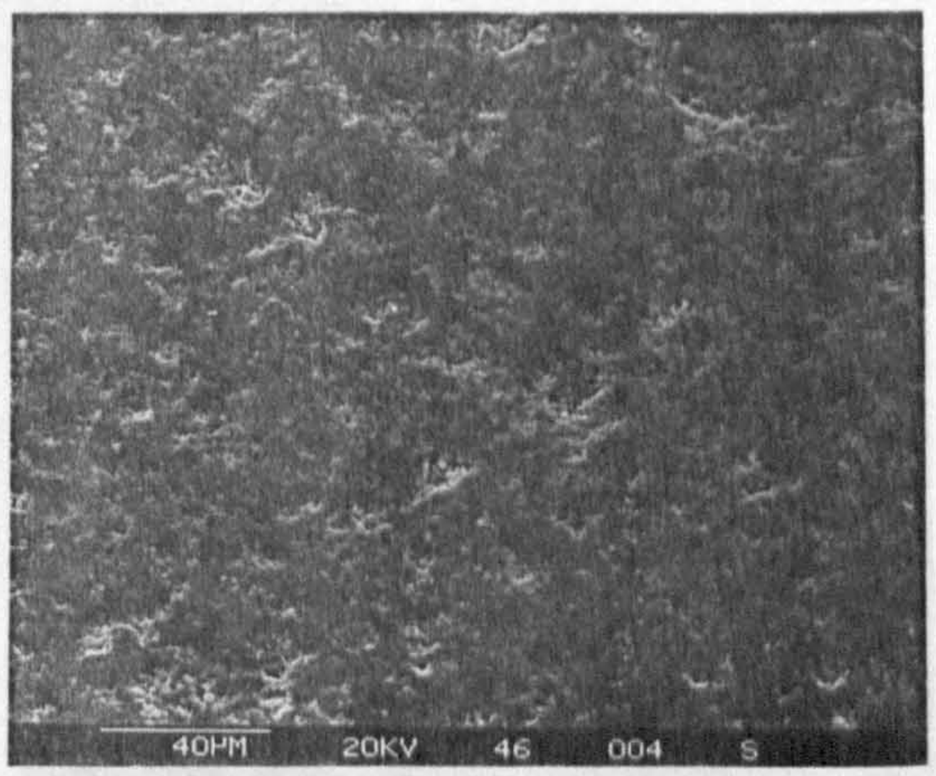

(f) Brittle delamination surface

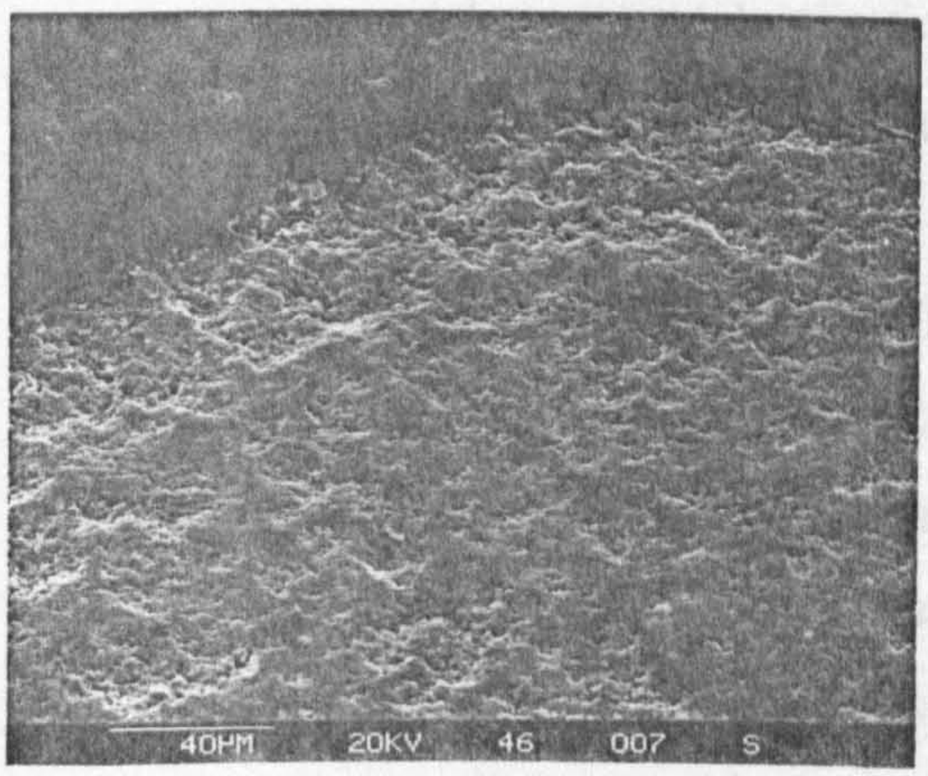

(g) General brittle surface

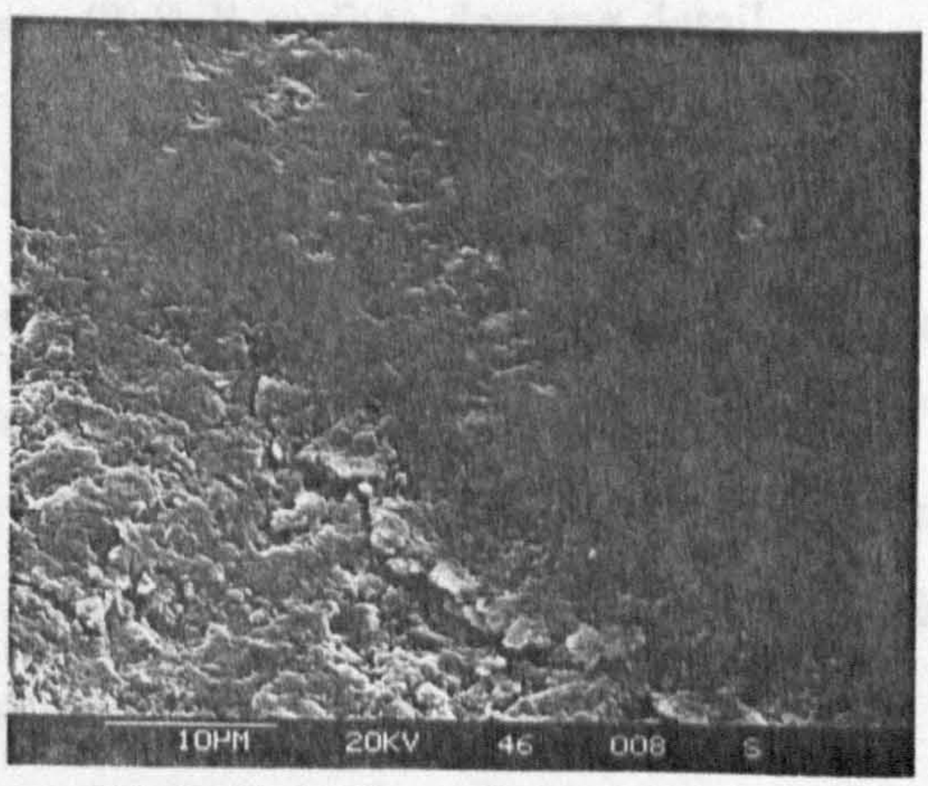

(h) Ball surface damage

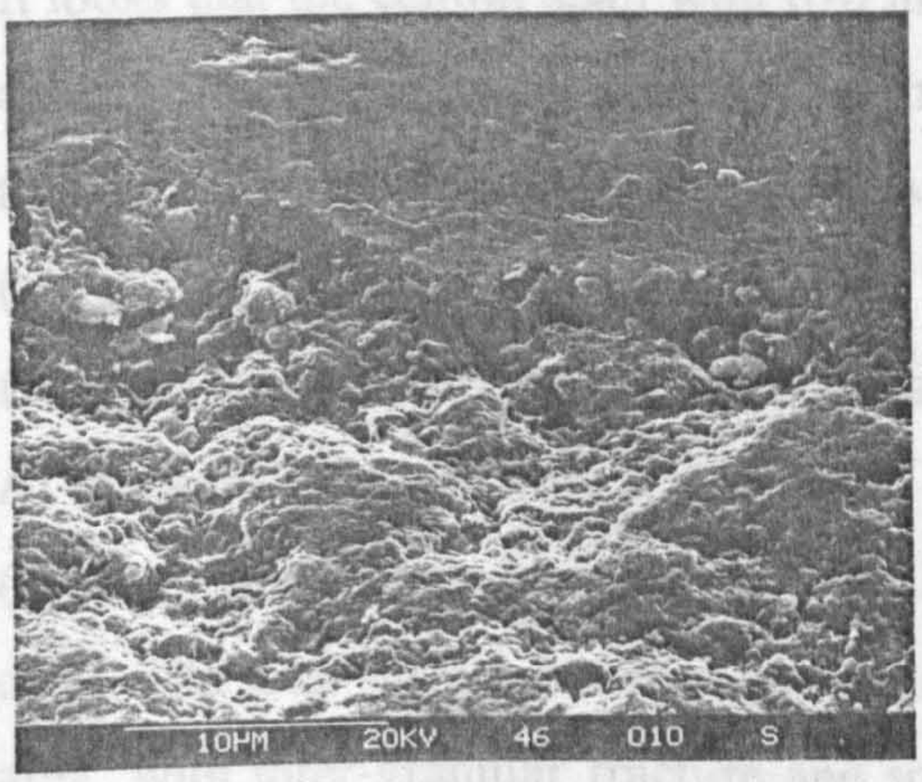

(i) Delamination cliff

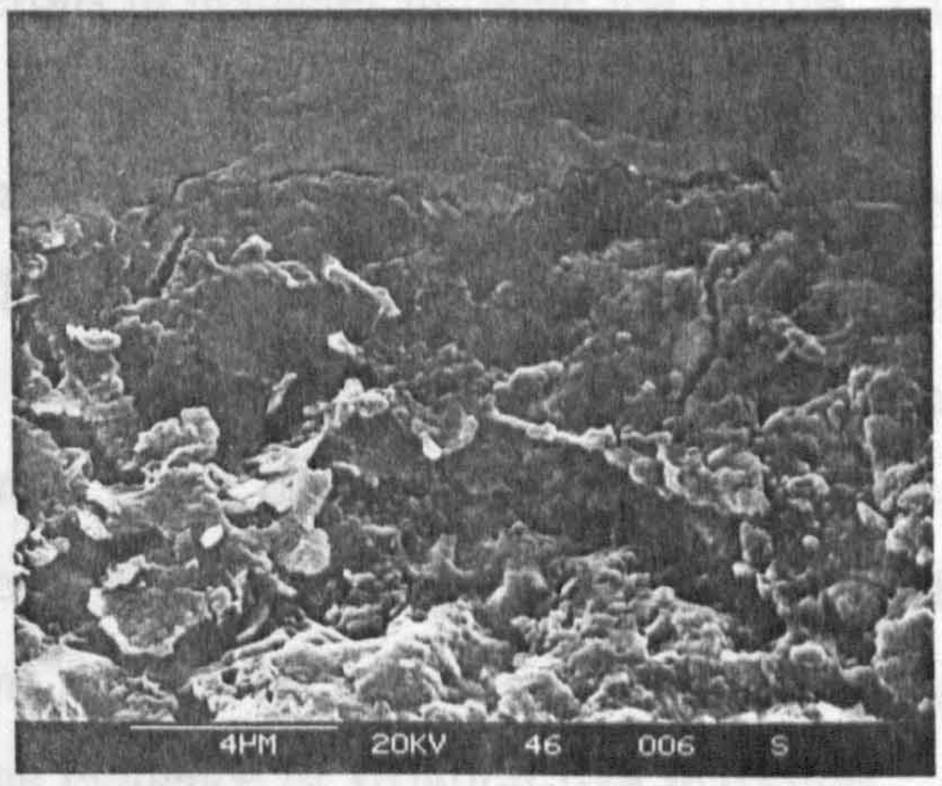

(j) Cliff detail

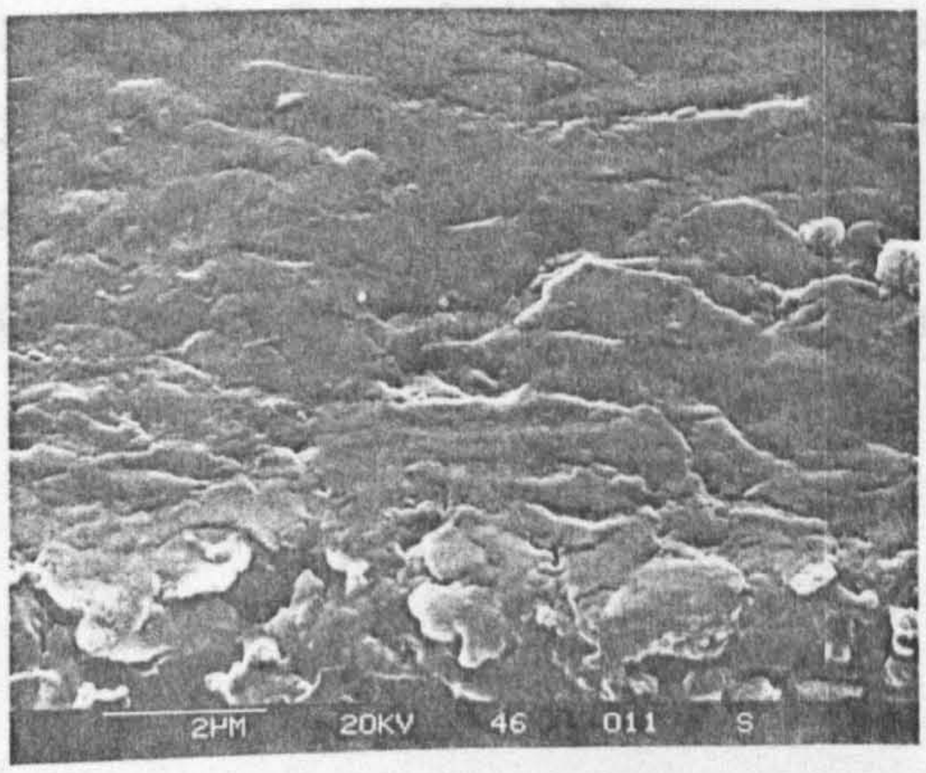

(k) Ball Surface adjacent to delamination

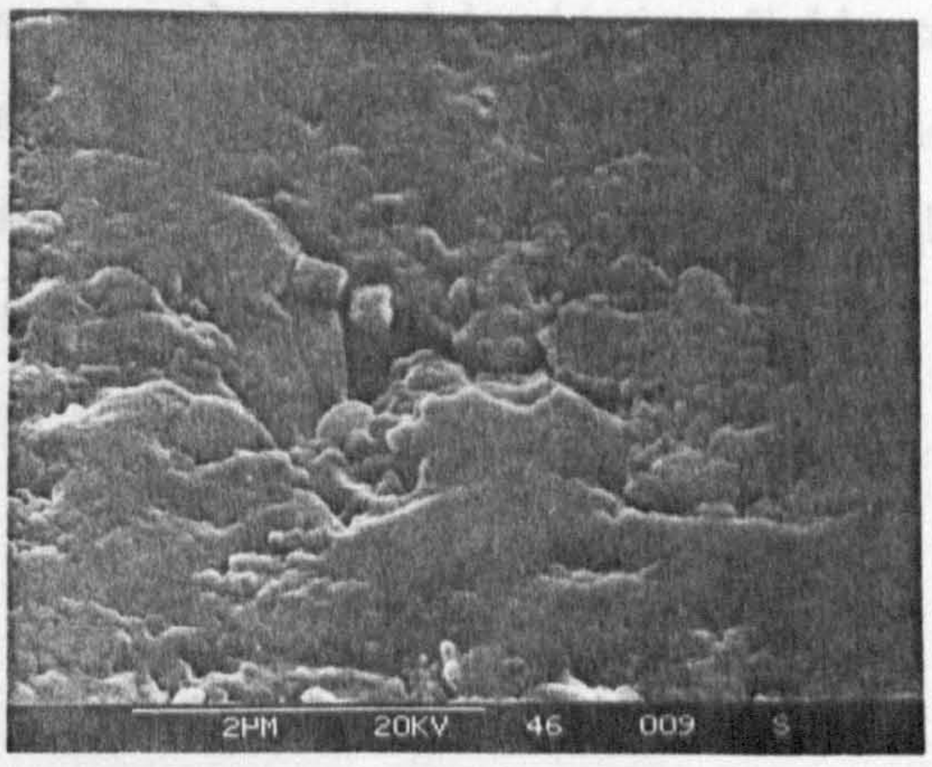

(l) Ball surface damage detail

Figure 6.7 Example of type 4i3p failure - captions (a) to (l)

Test Conditions from figure 6.7: Ceramic/ceramic contact, machine spindle speed 10,000 r.p.m, inclosed Base oil lubricant, bulk oil temperature (53°C) - unheated, 1.6 million upper ball stress cycles, Hertzian maximum compressive stress - 5.8 GPa, theoretical lambda ratio - 6.0, Surface roughness (Ra) of upper and lower balls 0.008 μm.

Figure 6.7, captions (a) to (l) describes in details type 4i3p delamination failure. Caption (a) shows the failure overview, with 3.25 millimetres in diameter. It looks that the central spall with 670 microns in diameter initiated the failure. The outer brittle surface was created from the ball subsurface. Captions (b) to (e) detail the central fatigue initiation area. An overview of the central fatigue spall, caption (b), clearly shows a fatigue mechanism. The crack of circular shape was propagated from the surface, caption (c), into the ball surface which shows typical undulations. At the spall base end with a concentric crack at the deepest spall position, caption (d), the material was removed by a cantilever effect which produced the sharp cliff edge. The spall surface between undulations, caption (e), represents a typical fatigue area, with inter-granular fracture and some evidence of striation-like markings.

The type-3 brittle fatigue delamination is detailed in figure 6.7, captions (f) to (l). The general smooth surface, caption (f), was probably produced by fast brittle fracture and some over-rolling. The surface adjacent to the intact ball surface, caption (g), shows the brittle area continuing throughout the delamination. Evidence of subsurface crack propagation is shown in captions (h) to (j) despite the shallowness of the delamination of eight microns. Extensive micro-cracks and ball surface damage close to the delamination suggest subsurface damage.

6.3 Chemical Analysis

6.3.1 Chemical Analysis of Type-1 Failure

Detailed observations of all delamination type failures are followed by chemical analysis. The chemical analysis is used to detect possible failure caused by material inhomogeneity such as concentration of sintering additives. Silicon, nitrogen and oxygen surface analysis is also used to detect any chemical disruption caused by delamination fatigue. A typical initiation area of a type 1i1p failure, is shown in figure 6.8. The brittle delamination failure surveyed at high magnification, caption (a), shows the initiation area. At the position of initiation, caption (b), a probe analysis was carried out to detect inclusions or debris damage.

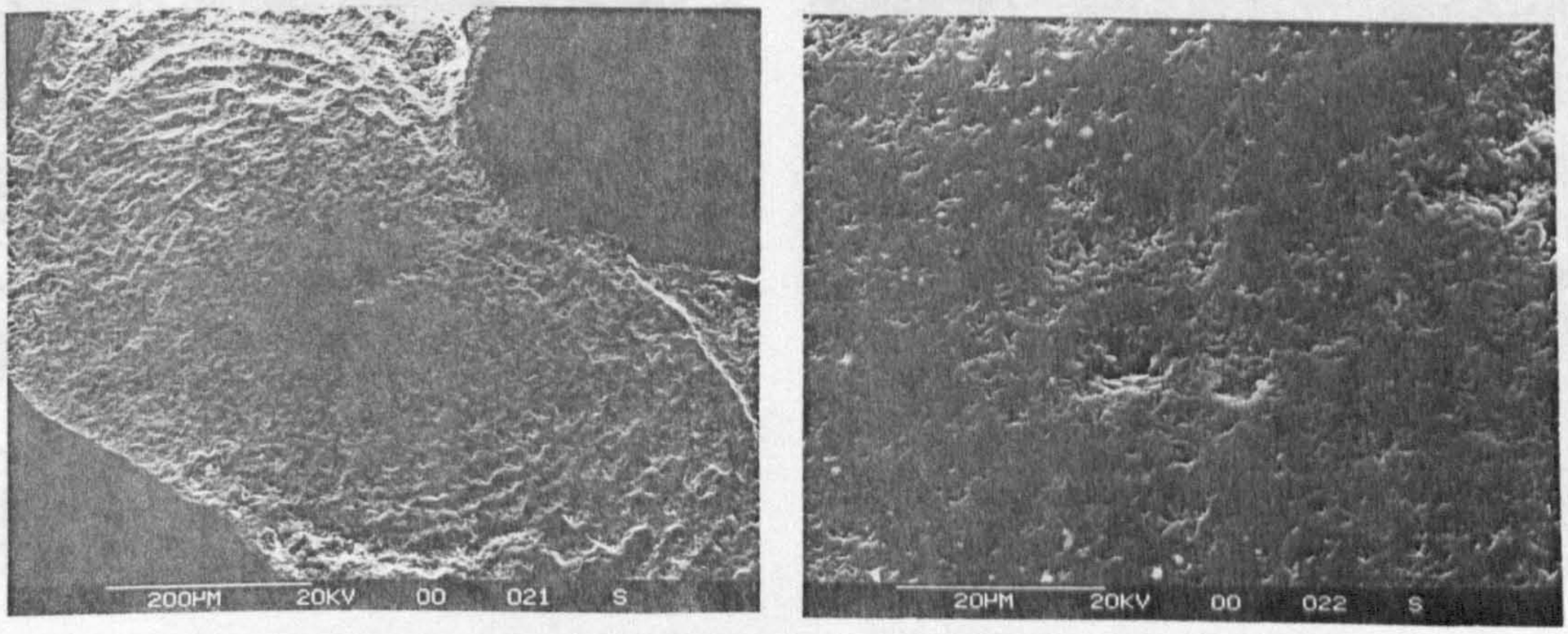

(a) Initiation area (b) Detailed view

Figure 6.8 Initiation area of type 1i1p failure

Test Conditions from figure 6.8: Ceramic/ceramic contact, machine spindle speed 10,000 r.p.m, inclosed HiTec 174 lubricant, bulk oil temperature 83°C - unheated, 1.4 million upper ball stress cycles, Hertzian maximum compressive stress - 9.6 GPa, theoretical lambda ratio - 6, Surface roughness (Ra) of upper and lower balls 0.008 microns.

The EPMA analysis of the initiation area of figure 6.8, caption (b) showed little chemical change within the initiation area. Slight changes in copper content were detected although this is not thought to have caused the brittle initiation. Elements of low atomic numbers such as nitrogen and oxygen are difficult to detect accurately using this analysis technique.

A more detailed surface chemical analysis by the WD system used to detect silicon, nitrogen and oxygen levels within the delaminated areas. Figure 6.9 shows results of surface analysis of the type-1 fatigue propagation delaminated area.

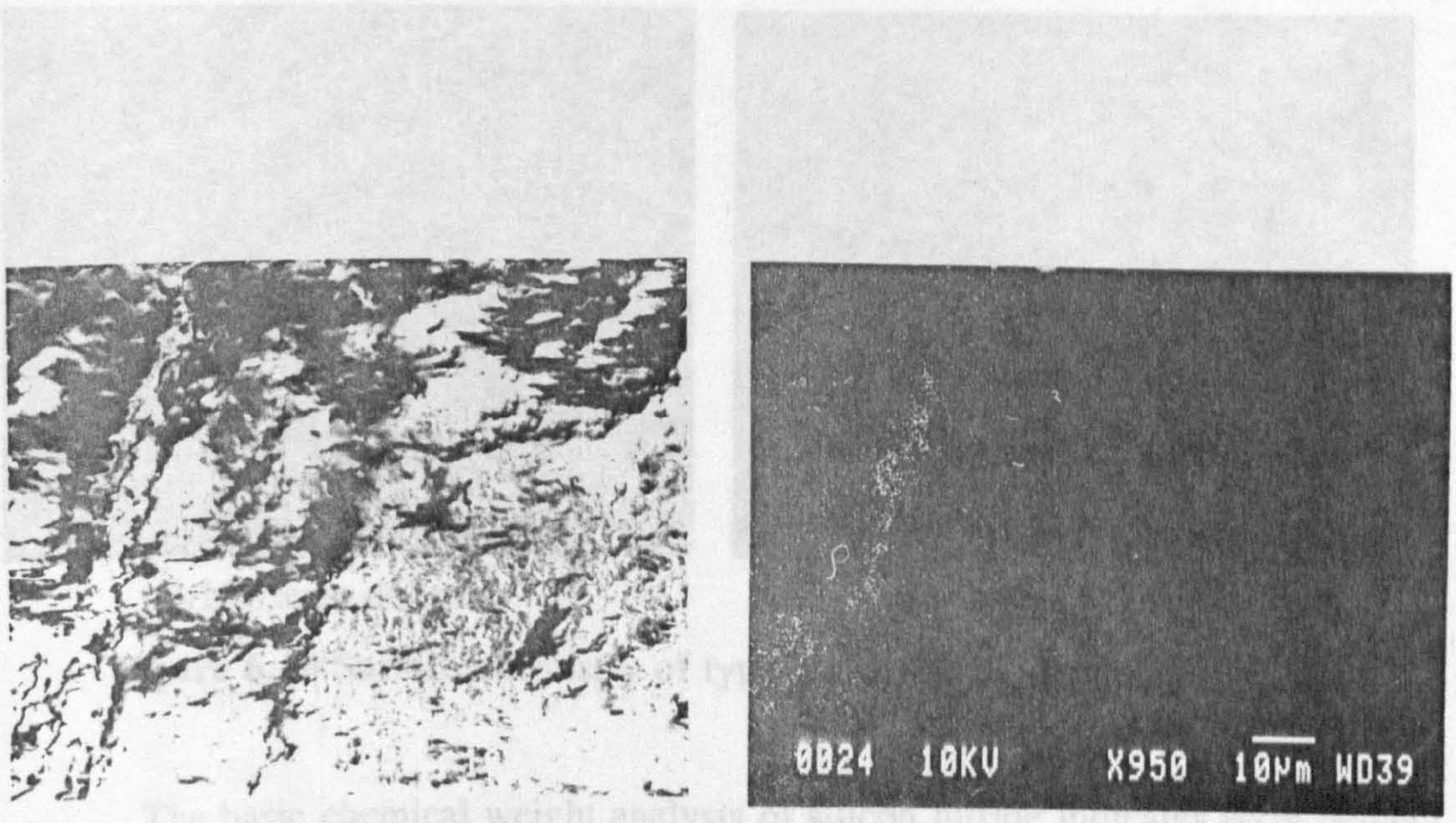

(a) Surface analyzed (b) Oxygen dot map

Figure 6.9 Surface chemistry of type 1i1p failure.

The general topography of fatigued surface analysed with the help of WD system; is shown in caption (a). Surface analysis of the oxygen content, caption (b), shows some evidence of oxidation along wear ridges. A more detailed quantitative analyses of silicon, nitrogen and oxygen content on the same delamination failure are presented in figure 6.10, captions (a) to (d).

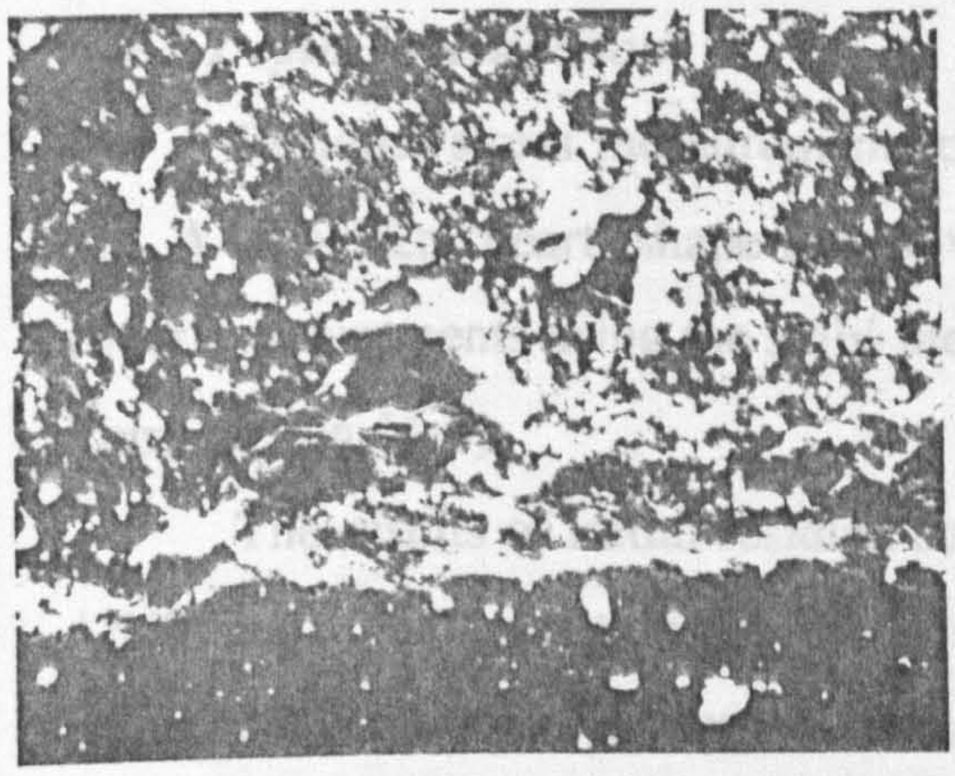

(a) Surface analyzed

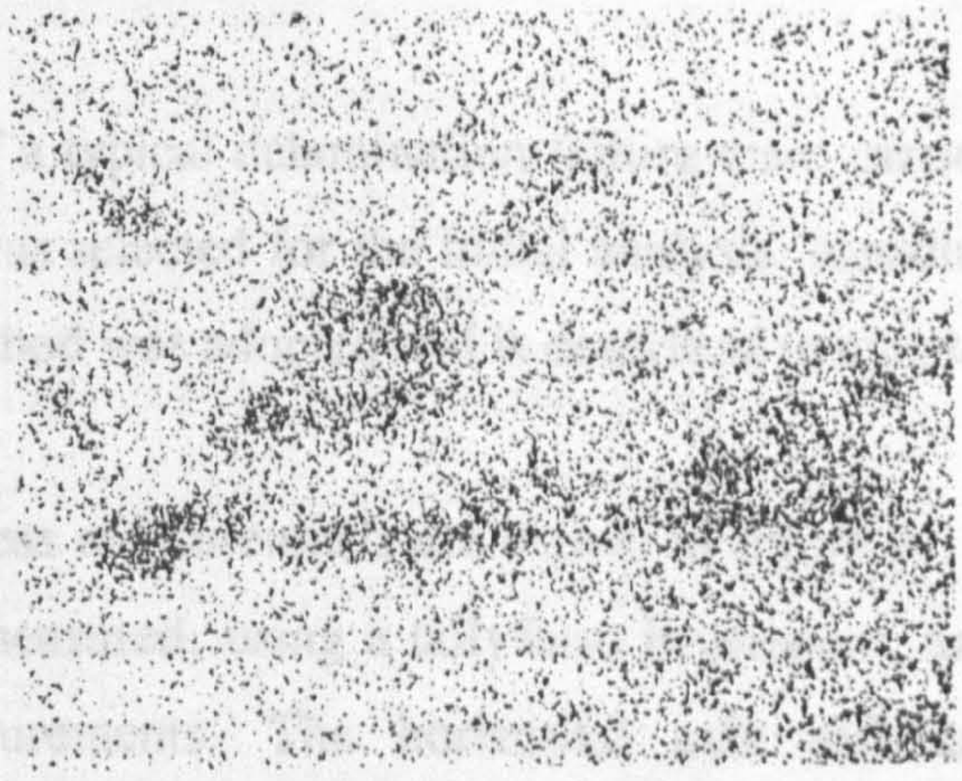

(b) Silicon dot map

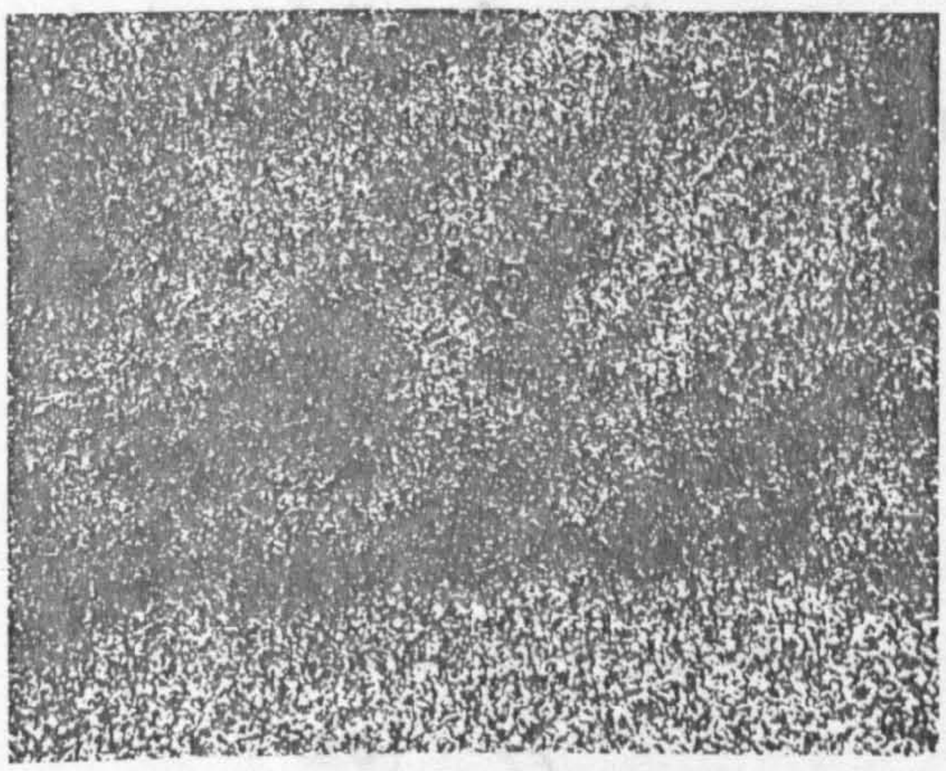

(c) Nitrogen dot map

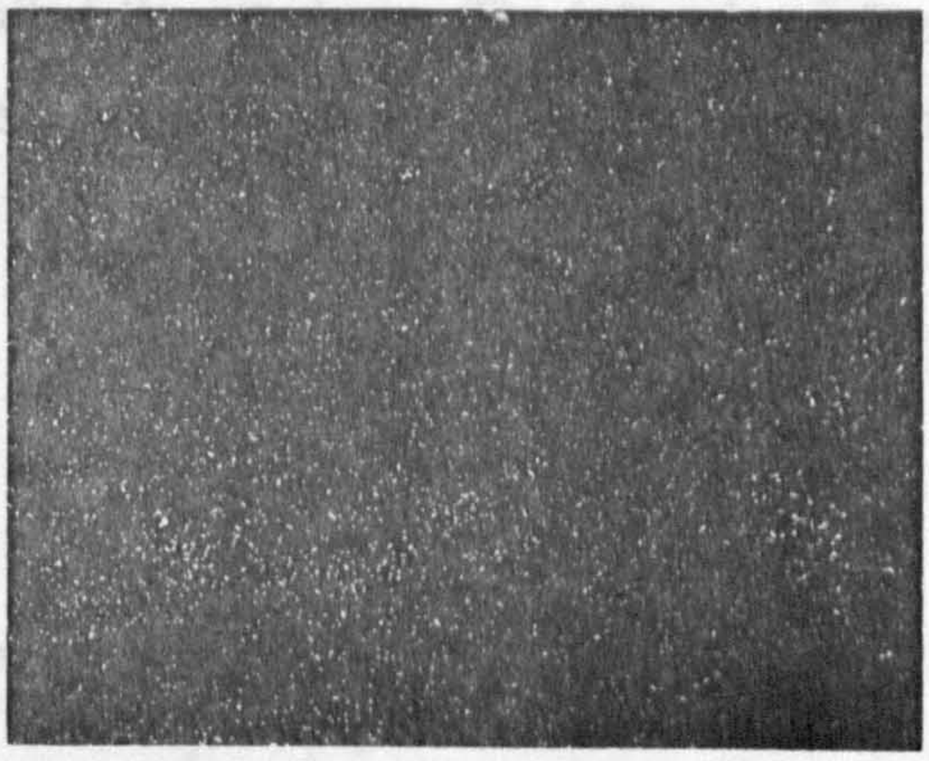

(d) Oxygen dot map

Figure 6.10 Surface chemistry of type 1i1p failure - captions (a) to (d)

The basic chemical weight analysis of silicon nitride indicates sixty percent silicon and forty percent nitrogen, ignoring sintering additives. The silicon and nitrogen analyses, captions (b) and (c), agree with the theoretical result although it is evident that unstable area exist in the delaminated surface. The oxygen level measured on an untested ball was less than one percent by volume. Caption (d) shows that the oxygen content is unstable in the disrupted area and reaches levels of two to three percent. The formation of silicon oxide on wear ridges is suggested as the reason for increased oxygen level as previously reported by Kato (1990). Under these extreme loads and rolling speeds the lubricant type may also have influenced the chemical instability of the ceramic.

6.4 Residual Stress Measurement

6.4.1 Depth Investigation

Residual stress measurements of a typical delamination failure were carried out. A type 1i2p 'heart' shape failure was selected for the initial analysis. Residual stress measurements using the $\sin^2\psi$ method was adopted and is described in chapter four, section [4.4].

The results of initial residual stress measurements are shown in figure 6.11. Additionally, delamination depth was measured, using a tallyform instrument, and compared with residual stress measurements. The horizontal axis indicates measurement position on the failure surface. Positions 'F' and 'C' are located on the intact ball surface adjacent to the failed 'heart' shape. The left axis of figure 6.11 indicates compressive residual stress measurements in MPa. The right axis represents the depth of failure profile in microns.

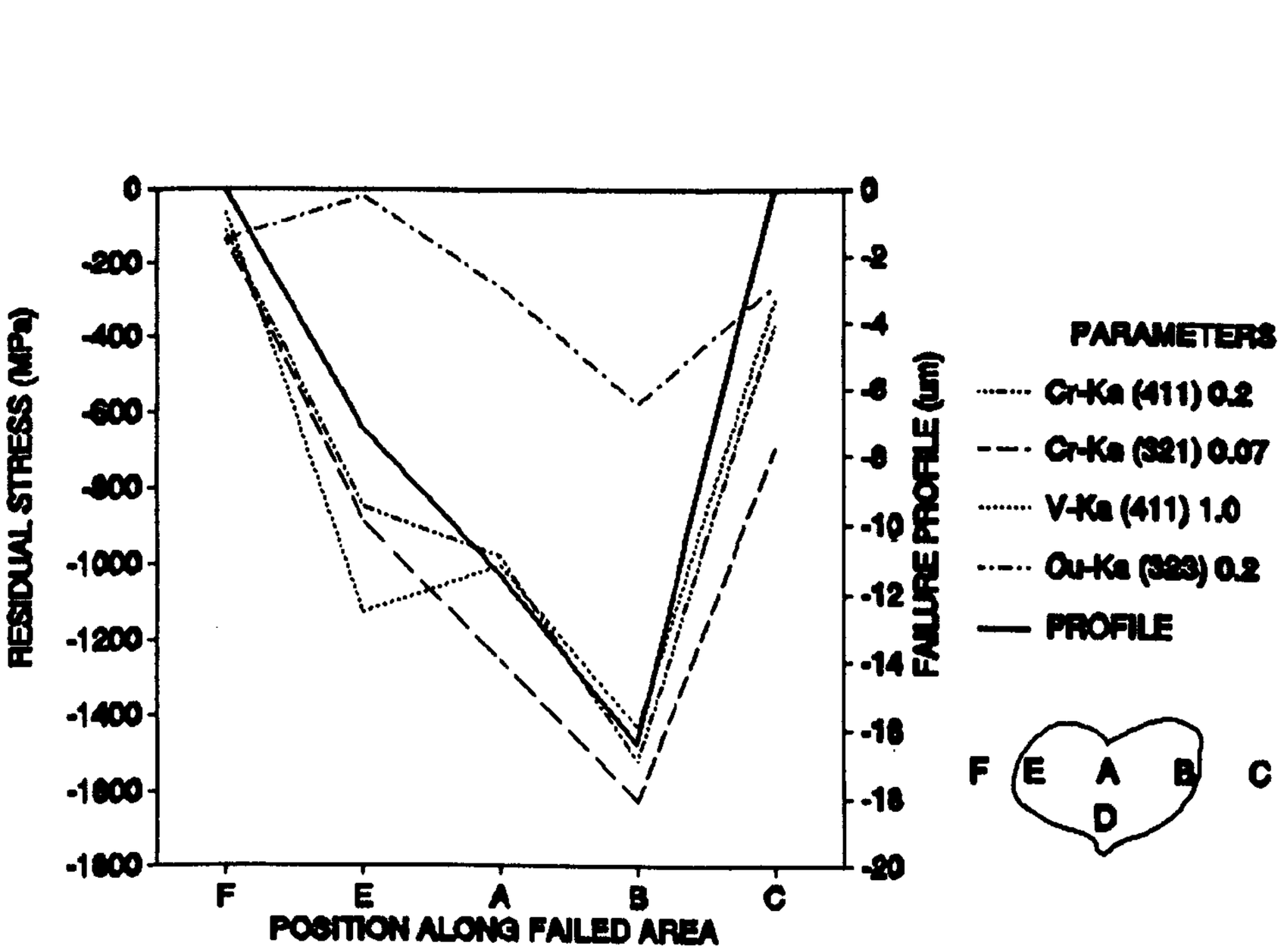

Figure 6.11 Residual stress and failure profile

The failure profile shown in figure 6.11 indicates increases of depth from position 'F' to 'C' of sixteen microns. Residual stress measurements were performed using various X-ray sources, shown in the legend. Stress measurements using chromium and vanadium X-ray sources on various diffractions planes and irradiated areas show general agreement. Copper X-rays results show much lower stress level. Copper X-rays were diffracted at 540 microns and chromium X-rays were diffracted at 175 microns below the delamination surface. This dependence of stress level on measurement position, figure 6.11, implies a high subsurface stress gradient of approximately 3 MPa per micron.

The compressive residual stresses measured at point 'C' confirm subsurface damage adjacent to the delaminated area. The residual stresses measured within the delamination area are within reasonable agreement considering the diversity of the measurement parameters. Residual stress increases from position 'E' to position 'B', which correlates with the delamination depth trend. The correlation of compressive residual stresses with failure depth suggests a shear stress type of failure.

6.4.2 Residual stress survey of delamination type failures

Following the preliminary residual stress measurements described earlier, a survey of ceramic ball failures will be conducted now. A constant set of X-ray parameters, table 6.3, was used to ensure consistent measurements. Measurements of delamination type failures are presented in figures 6.12 to 6.16.

Table 6.3 X-ray stress measurement parameters

Characteristic X-ray	Cr-Kα
Diffraction plane	(321)
Diffraction angle	125.54
Irradiation area (mm^2)	0.25
X-ray wavelength (Å)	2.29
Measurement Depth (μm)	175.0

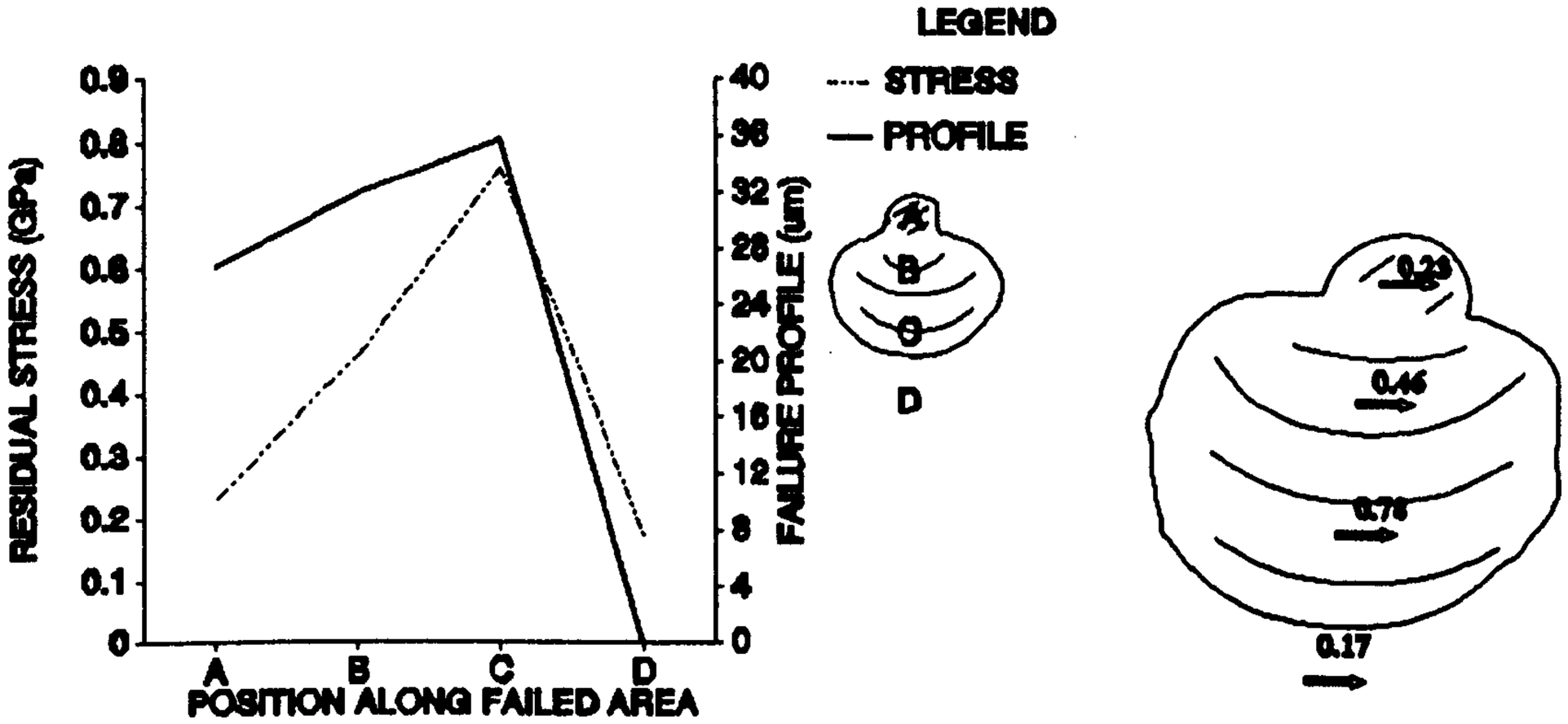

Figure 6.12 Residual stress (compressive) measurements of type 1i1p failure

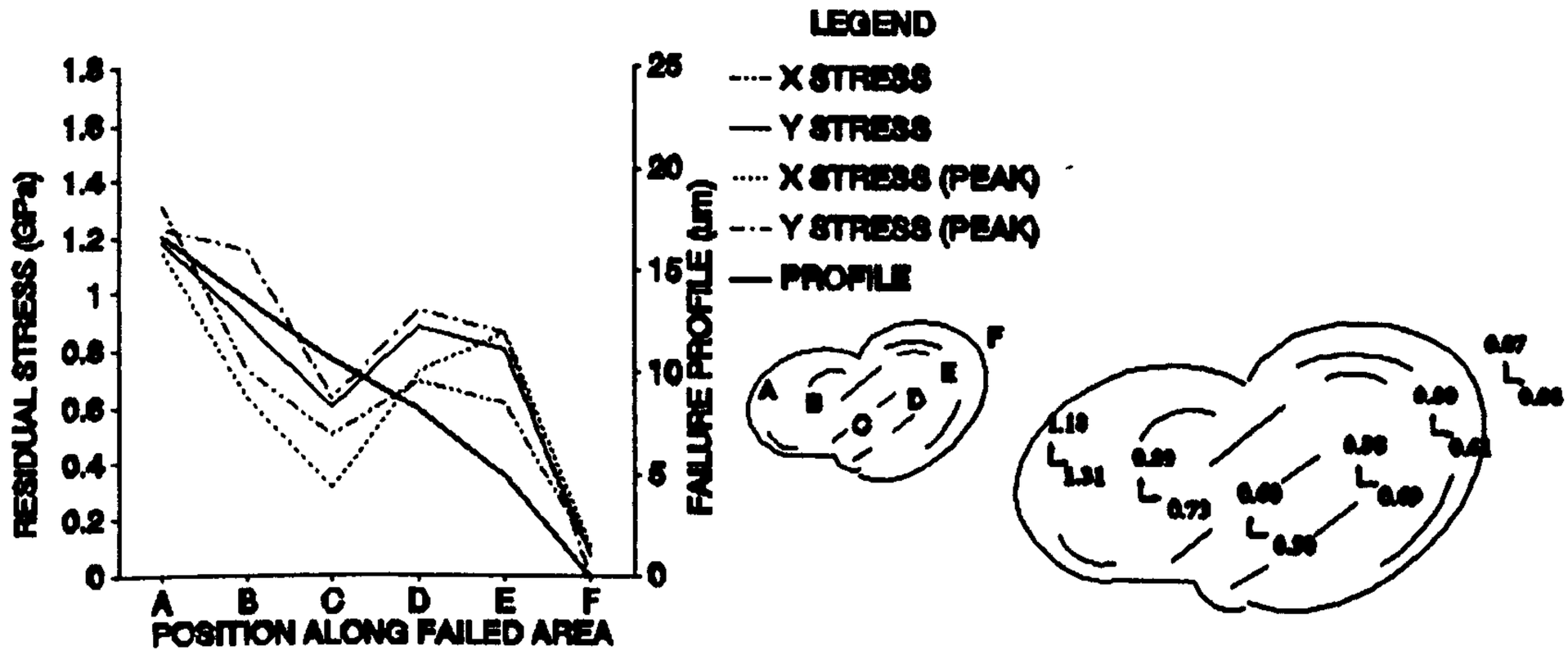

Figure 6.13 Residual stress (compressive) measurements of type 1i2p failure

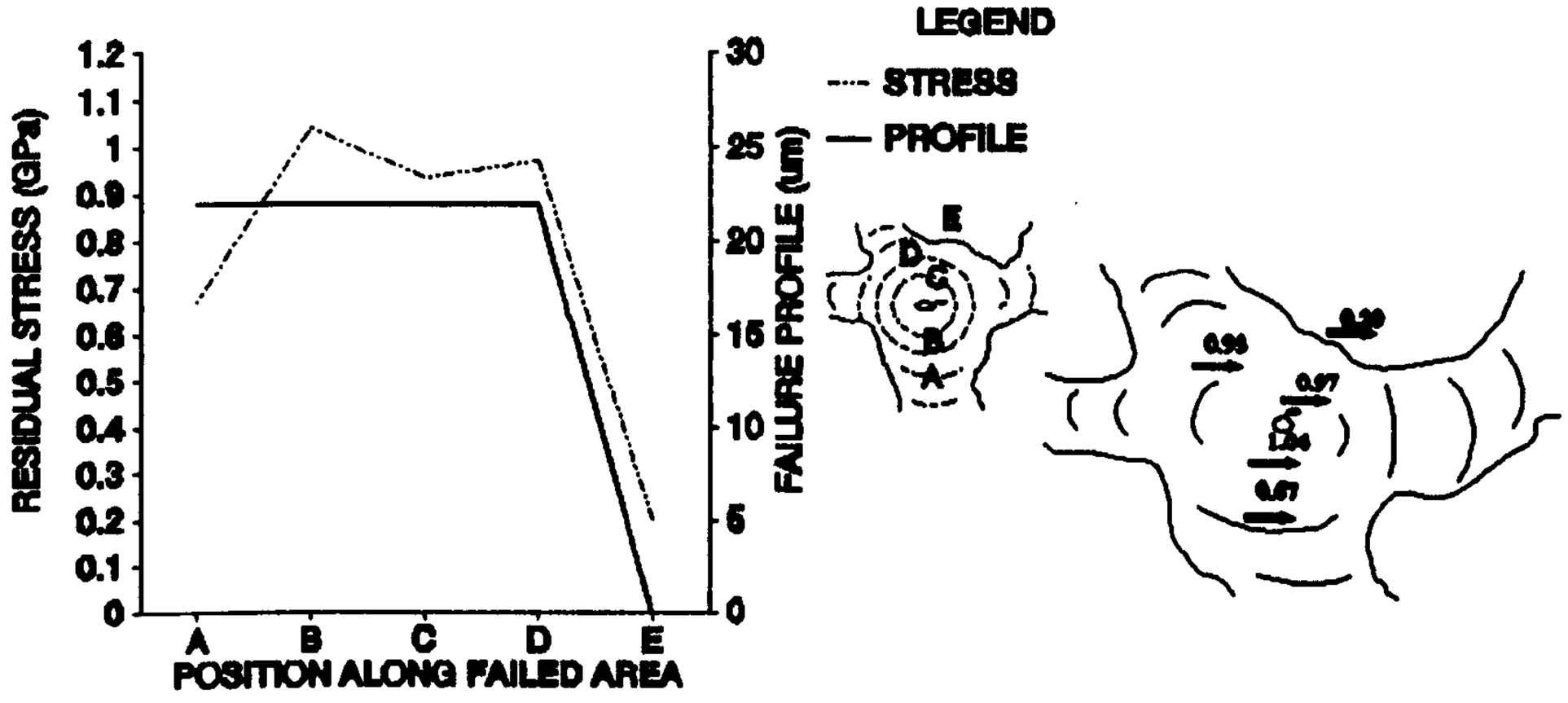

Figure 6.14 Residual stress (compressive) measurements of type 3i1p failure

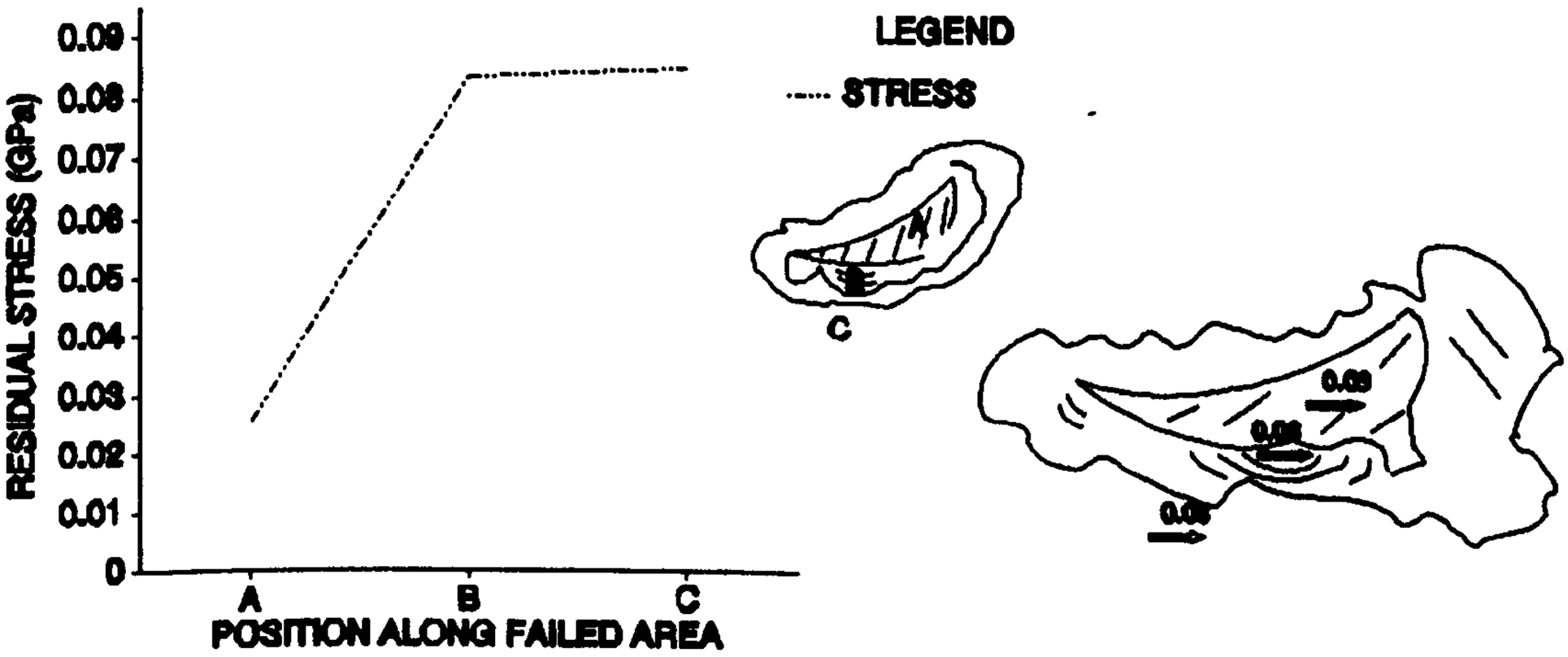

Figure 6.15 Residual stress (compressive) measurements of ring crack spall

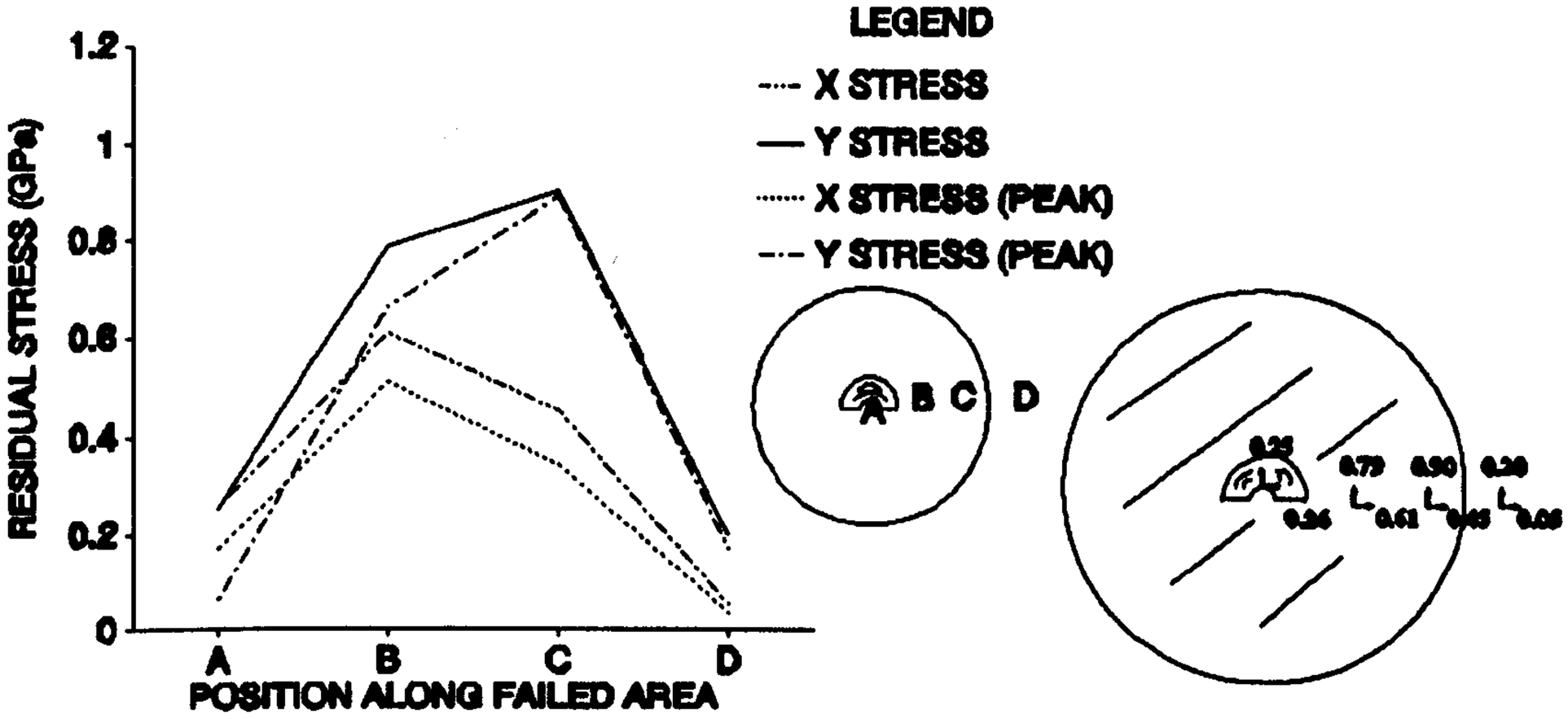

Figure 6.16 Residual stress (compressive) measurements of type 4i3p failure

Residual stress measurements of failure type 1i1p, figure 6.12, show increasing stress levels from initiation area to fatigue propagation area. Figure 6.13, shows results of type 1i2p delamination failure. Relatively high residual stress is recorded with the lowest values around the brittle initiation area. Defect initiated fatigue failure (type 3i1p), figure 6.14, shows uniform moderate residual stress with no stress reduction near the initiation area. An example of failure type 4i3p, central fatigue damage on initiation area with brittle crack propagation is shown as figure 6.16. Residual stress around the central initiation area increases along the brittle propagation surface.

Ring crack spall failure, figure 6.15, shows very low residual stress on both brittle initiation and fatigued surfaces. This confirms a supposition that a brittle cone crack propagated from the surface into the material. During testing, conventional spall type fatigue cracks driven towards the surface by pressurised lubricating oil produce final failure. Also, it is significant that this ball has not failed in a catastrophic mode.

These present results point to a close relationship between delaminated area depth and residual stress level. Figures 6.12, 6.13, and 6.14, illustrate failure profile obtained from detailed 'tallyform' measurements. The figures show that trends of increasing compressive residual stress correspond to increasing depth of failure surface. It should be noted that residual stress measurements were taken from diffraction plane at 175 μm below the surface, table 6.3. It can be seen that the maximum failure depth is 40 μm. Also, a high stress gradient exists and maximum shear stress is located approximately 120 μm below the ball surface. It is appreciated that if significant friction exists during testing then maximum shear stress will occur nearer to the surface and tensile stresses will occur on the contact circle edge. The high compressive stresses recorded, coupled with the possibility of high shear forces, favour subsurface initiation and consequent fatigue propagation.

Figures 6.13 and 6.16 illustrate the stress directionality. The results show that in some cases quite high differences in stresses are recorded at different sample orientations in common positions. The highest variation of stresses occur near delaminated surface edges. The reason why these differences occur may be due to actual stress field variation during failure or due to inherent material structure causing measurement variation.

Diffraction peak shape can assist in understanding of measurement directional sensitivity and uniformity. During measurements, large peak width or half breadth value was noted. This indicates that either particle size is small or random strain is large. As particle size is in the order of 1-2 μm, therefore random or lattice strain must be large. This random strain may be explained by the fact that inter-granular cracks have dominated micro-failure. Random strain will then be high due to combinations of shear and direct strains.

Chapter 7

DISCUSSION and CONCLUSIONS

7.1 Discussion

Modes of ceramic/ceramic and ceramic/steel contact fatigue failure have been studied. The modified four ball machine tests show that silicon nitride ceramic material is extremely resistant to contact fatigue failure. High speed tests on lubricated ceramic/steel contacts did not produce a spalling fatigue failure. Ring, radial and lateral pre-cracked silicon-nitride elements in contact with a bearing steel produced a spalling fatigue. High speed ceramic/ceramic contacts produced lubrication related delamination fatigue. High residual stresses were detected on surfaces failed due to delamination fatigue modes.

Delamination fatigue failure modes and conventional spall contact fatigue mode have been examined. Delamination fatigue modes are experienced during high speed, ceramic/ceramic contacts and lubricated, fatigue tests. The fatigue mechanisms of the delamination failure have been examined after classifying them into four types of initiation and propagation failure modes. Initiation failure modes are dependent on contact stress, surface condition, surface quality and material quality. Propagation failure modes are dependent on lubrication type and partially dependent on the factors which influence the initiation modes. Failure is experienced after up to sixty million upper-ball stress cycles. The number of lower-ball cycles to failure is difficult to estimate because of complicated contact conditions effecting the kinematics of the elements.

Pre-cracked balls (ring, lateral and radial) fail by spalling and secondary delamination. In the case of lateral and radial cracks, the fatigue failure mode is strongly related to the lubricant. High viscosity lubricant has produced radial crack growth and subsurface crack propagation causing a combined spalling and delamination failure mode. The upper steel ball also fails due to a spalling fatigue and delamination. Low viscosity lubricants produce a spalling failure surface and surface bulging. Chemical analysis shows steel debris in the bulge area, which implies lubricant driven subsurface damage. Tests using pre-damaged surfaces by

ring-cracks show a spalling fatigue mode.

Residual stresses measured by X-ray diffraction show that substantial compressive residual stresses exist within delaminated areas. Measurements of residual stress on delaminated areas with different X-ray sources indicate that a high subsurface stress gradient exists. Also, residual stress readings on apparently undamaged areas adjacent to delamination confirm existence of subsurface cracks previously observed. The compressive nature of measured stresses indicates mode 2 (sliding) or mode 3 (tearing) fatigue crack initiation and propagation. The measurements of residual stress have provided some validity to the delamination classification of the ceramic balls. Delamination profile depth may be related to residual stress magnitude.

7.2 Conclusions

(1) The ceramics chosen in this study, tested in extreme and varying rolling contact conditions, failed in a non-catastrophic mode.

(2) Chemical analysis shows that unstable silicon and nitrogen with slight increases of oxygen may occur during ceramic delamination.

(3) Residual stresses measured by X-ray diffraction show high compressive stresses exist within delaminated areas.

(4) High subsurface residual stresses exist on delamination areas. Depth of delamination is related to magnitude of residual stress.

(5) Non-catastrophic failure modes of ceramic elements have also been identified from pre-cracked rolling contact fatigue tests.

(6) A spalling fatigue failure mode is identified, in the case of ring pre-cracks.

(7) Balls with lateral and radial pre-cracks fail due to a fatigue process which is assisted by a lubricant and depends on its properties.

7.3 Recommended Further Work

A study of the effect of different roll/slip ratios on the fatigue failure modes is required. This could be investigated using ceramic cones instead of ceramic upper-ball. Cones of varying slope angles may produce a varying kinematic relationship.

Effects of varying hardness should be investigated as this factor is important to failure mode analysis. The main problem with this investigation is that bearing steel balls have lower hardness compared to silicon nitride. Also, it is difficult to vary the hardness of ceramics except by varying sintering additives during primary processing.

It is suggested that modified four-ball machine tests using tungsten carbide/silicon nitride contacts should be used to investigate the hardness parameter. The hardness of tungsten carbide may be increased to the same levels as silicon nitride and also can be varied more easily by altering the cobalt content.

During pre-crack analysis, it was found that ring cracks could not be initiated using steel/ceramic contacts, but, tungsten carbide/ceramic contacts proved successful. This result of hardness related failure is a good basis for justifying fatigue testing of tungsten carbide/ceramic contacts, which could tend to additional fatigue failure modes.

Additional rolling contact tests should be performed on a rolling disc machine. This will enable contacting surfaces to be controlled more easily. Data from this experiment may be used as a basis for theoretical analysis and modelling.

It has been shown that the lubricant type can strongly influence the fatigue failure mode. In the case of pre-cracked balls the influence of varying the crack penetration properties of the lubrication is required. Experiments using grease lubrication and debris contaminated lubricants is required. This also has important practical implications for ball-bearing manufactures.

Delamination wear theory for sliding contacts has been developed fully. The

application to rolling contacts should be developed and compared with the experimental results obtained from this study.

The measurement of undulation wavelength and height on delaminated surfaces should be investigated from a theoretical standpoint. The topographical observations imply that undulations may be studied by considering shear energy on the surface. It is suggested that wavelength and wave-height theories applied to fluids and wind energy may be analogous to the high shear forces and plastic flow of ceramics.

Appendix 1

THE MODIFIED FOUR-BALL MACHINE

The modified four-ball machine in pictorial and schematic representations are shown as figures A1.1 and A1.2. The machine has a proven history as being useful to investigate the rolling contact fatigue resistance of materials under various tribological conditions. Previously, this machine has been mainly used as an accelerated method to measure the rolling contact fatigue of bearing steels by various research staff. Barwell and Scott (1956), Krivoshein (1960) and Scott (1963) used the machine to evaluate the influence of lubrication type on steel ball rolling contact fatigue. A cone was used to replace the upper ball to evaluate pitting under different roll/slip conditions by Scott (1962). The machine is evaluated for use as an accelerated fatigue test by Scott and Blackwell (1963) who found it an acceptable rapid screening test. The Institute of Petroleum gathered various papers, Tourret and Wright (1977), which describes various test results, ball dynamics and kinematics using the modified four-ball machine.

The main element of the modified four-ball machine is an assembly shown in figure A1.3. The assembly consists of an upper-ball which drives three lower-balls around a hardened steel cup. Contact between of the upper/lower ball interface and lower-balls/steel cup interface is immersed with a suitable lubricant. A heater element pad beneath the cup assembly may be used to control lubricating oil bulk temperature and is measured by a 'K' type thermocouple. Dimensional relationships of the ball assembly are shown as figure A1.4. The configuration simulates an angular contact ball-bearing as the lower balls are free to roll and not held fast as in the conventional four-ball machine test. The contact between upper and lower balls is however different to an actual ball-bearing, due to the non-conforming geometry. The hardened steel cup represents a bearing outer-race, the three lower balls represent the balls within a bearing-race, (see figure A1.5). Bearing inner-race is represented by the upper-ball.

Ball assembly load is applied from a simple loading lever and dead weight, figure A1.6. A loading piston below the steel cup ensures correct alignment. A drive-spindle thrust bearing reacts the applied force which places the ball contact areas in compression. The standard weights may be placed on the loading lever at lever-arm ratios of 20:1 or 10:1. The lever-arm is balanced by a counter-weight adjustment before loading. The upper-ball is centrally located to the drive shaft by a spring-steel tapered collet.

The drive shaft rotates, via a belt-drive, from a shunt type electric motor. Spindle speed may be varied up to 20,000 rpm from high or low speed drives via a motor speed controller which also protects the shunt motor from excessive current. Test time and spindle revolutions are recorded by a timer and tachometer. The machine may be set to stop either at required revolution number or pre-set maximum vibration amplitude. The sensitivity of the vibration machine cut-out may be varied according to load and spindle speed conditions.

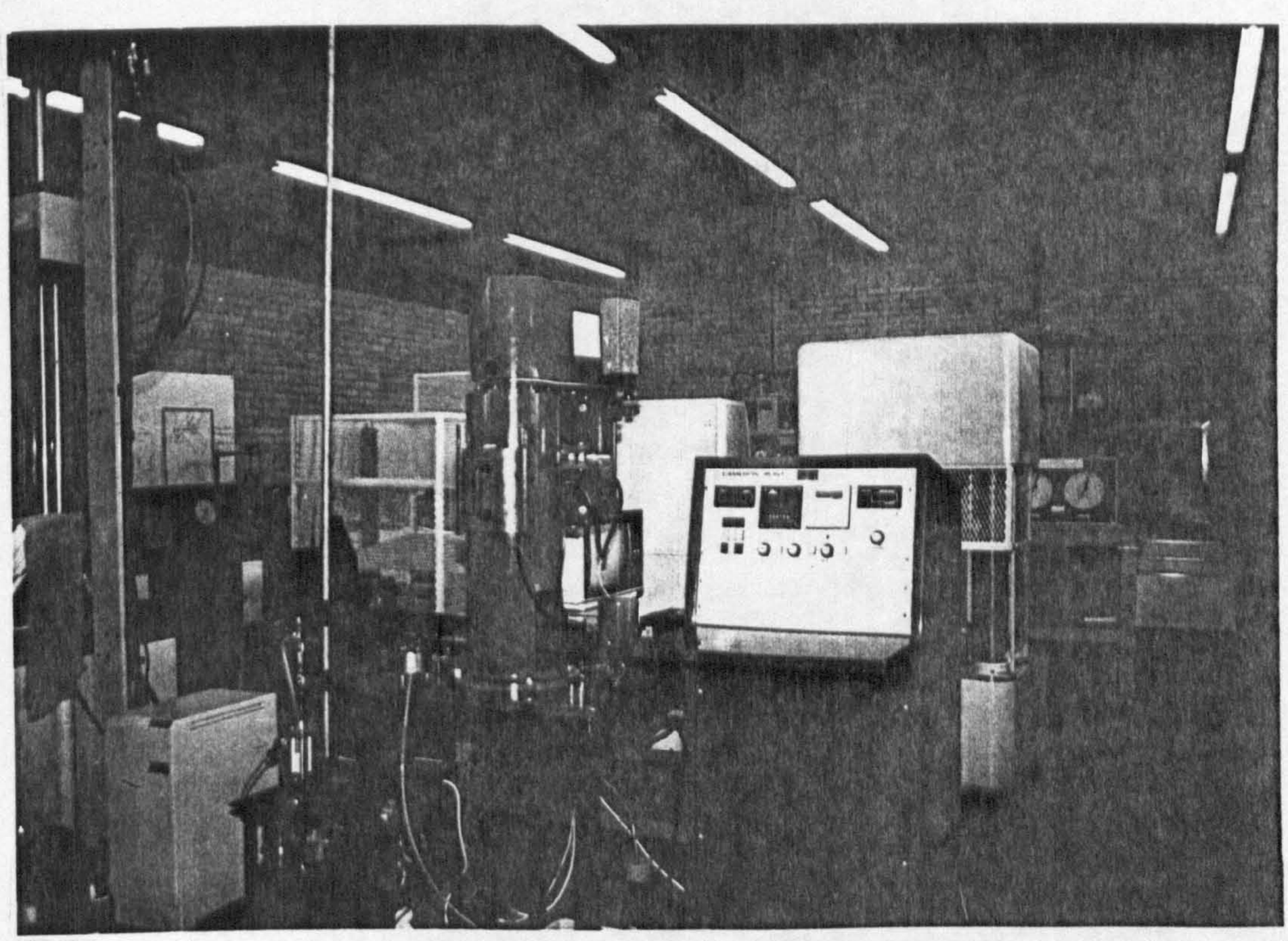

Figure A1.1 The modified four-ball machine

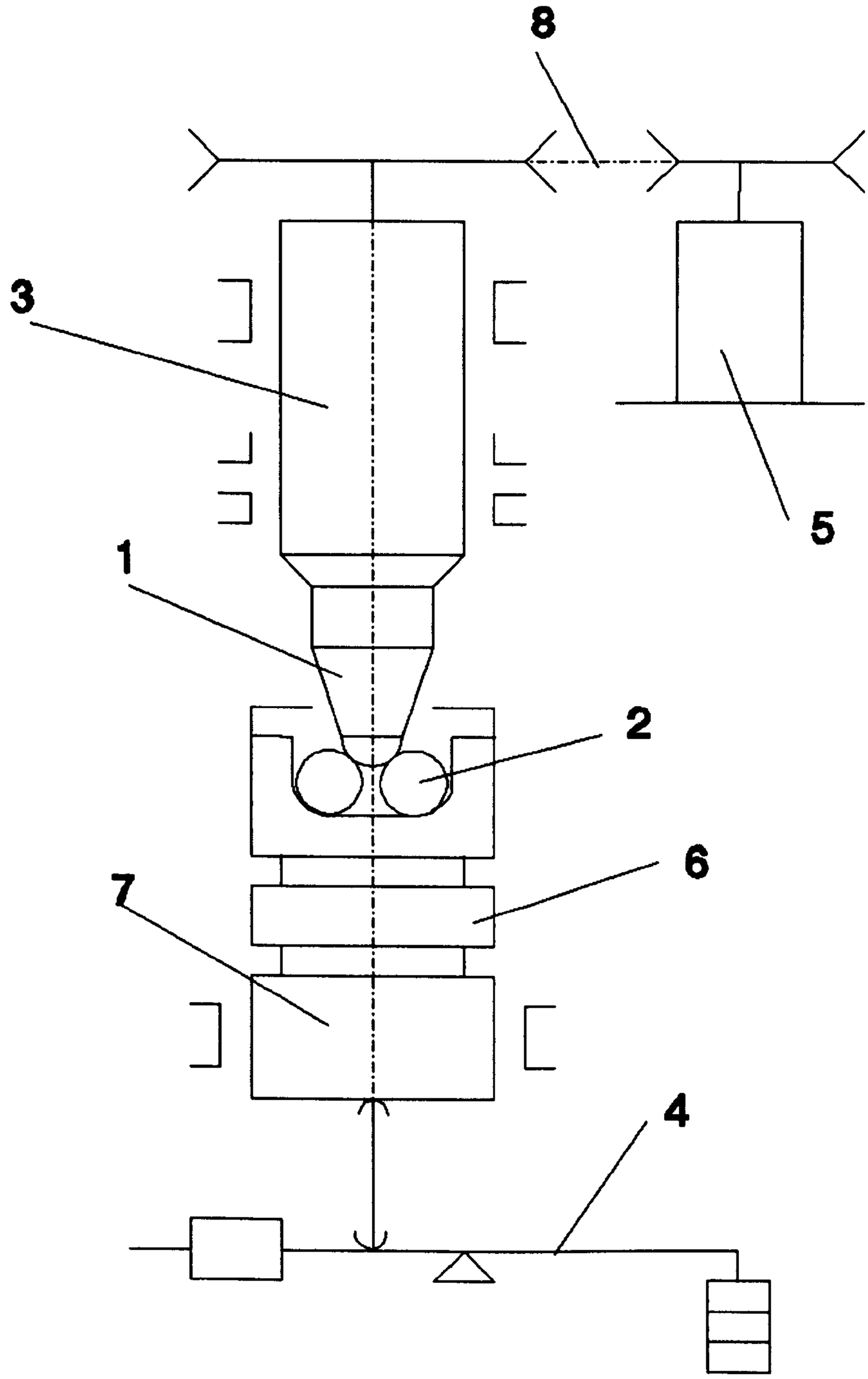

Figure A1.2 Schematic of the modified four-ball machine
1, upper-ball and collet; 2, lower-balls; 3, spindle; 4, loading lever;
5, driving motor; 6, heated plate; 7, loading piston; 8, belt drive.

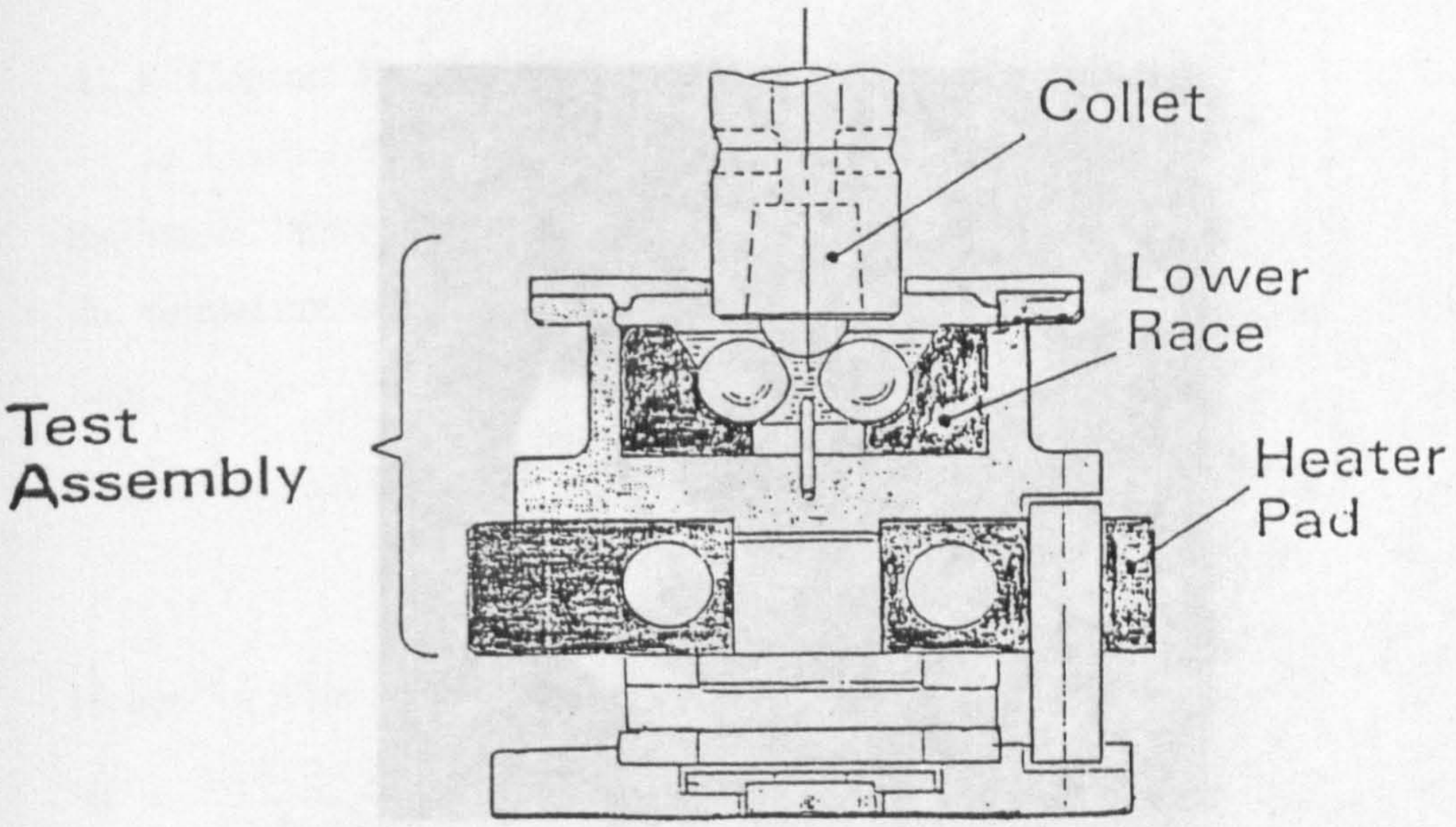

Figure A1.3 Schematic of Cup Assembly

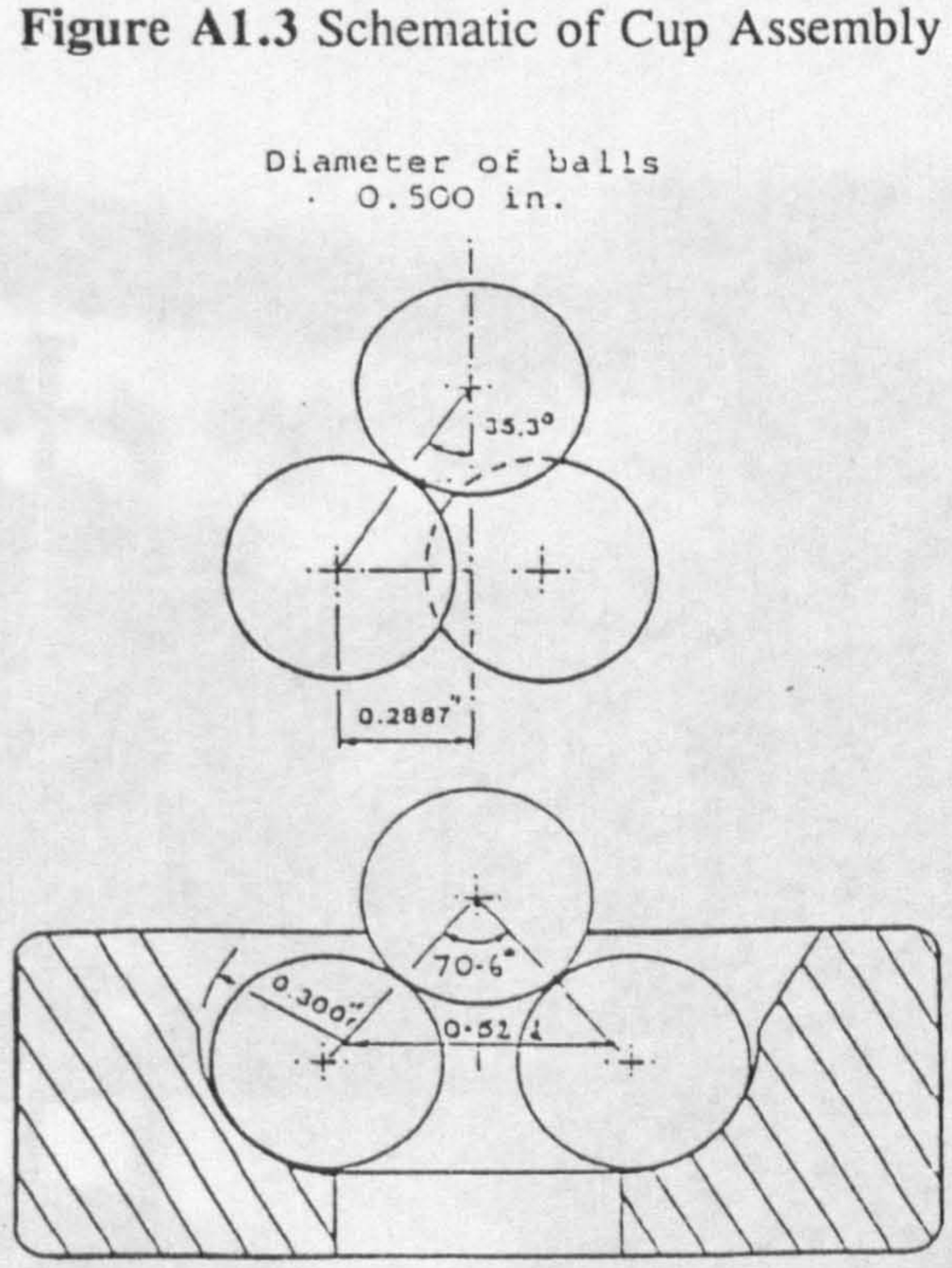

Figure A1.4 Dimensions of Ball Assembly

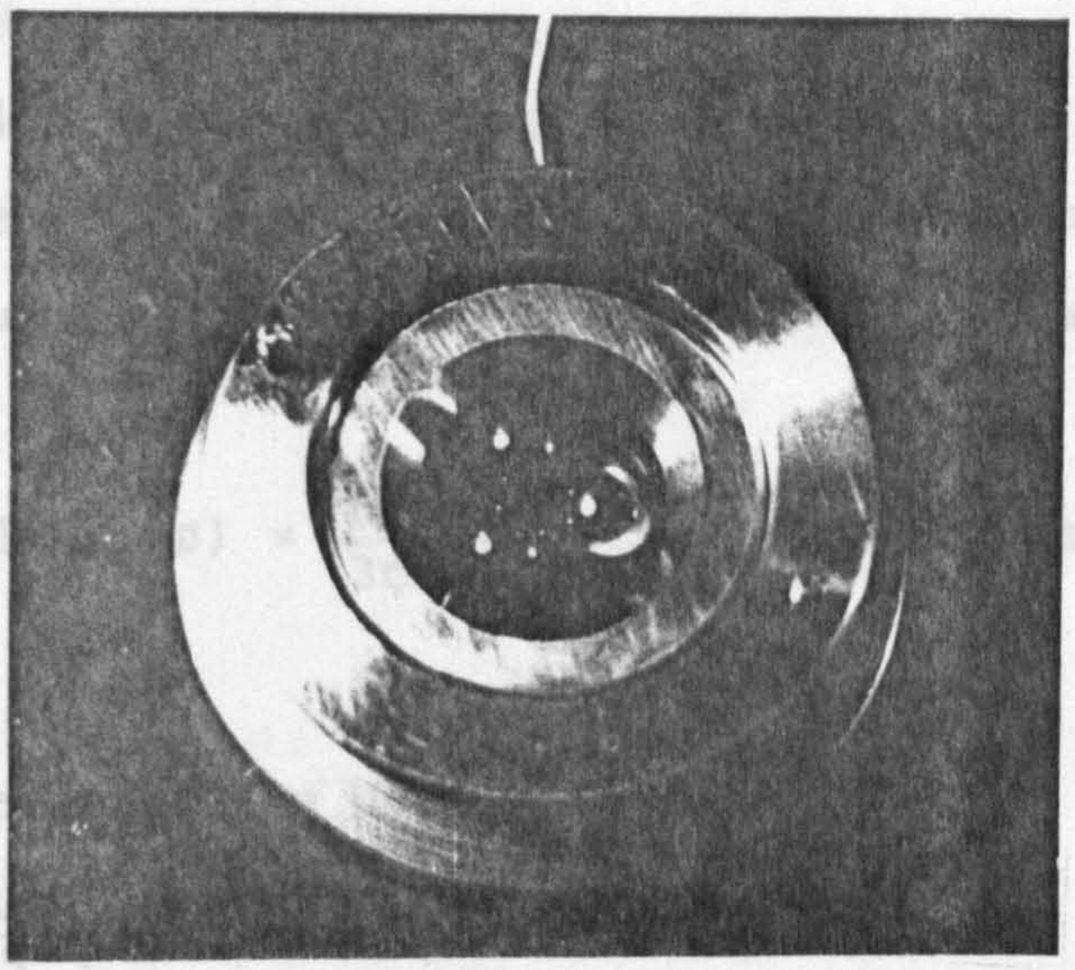

Figure A1.5 Steel Cup and lower ceramic balls

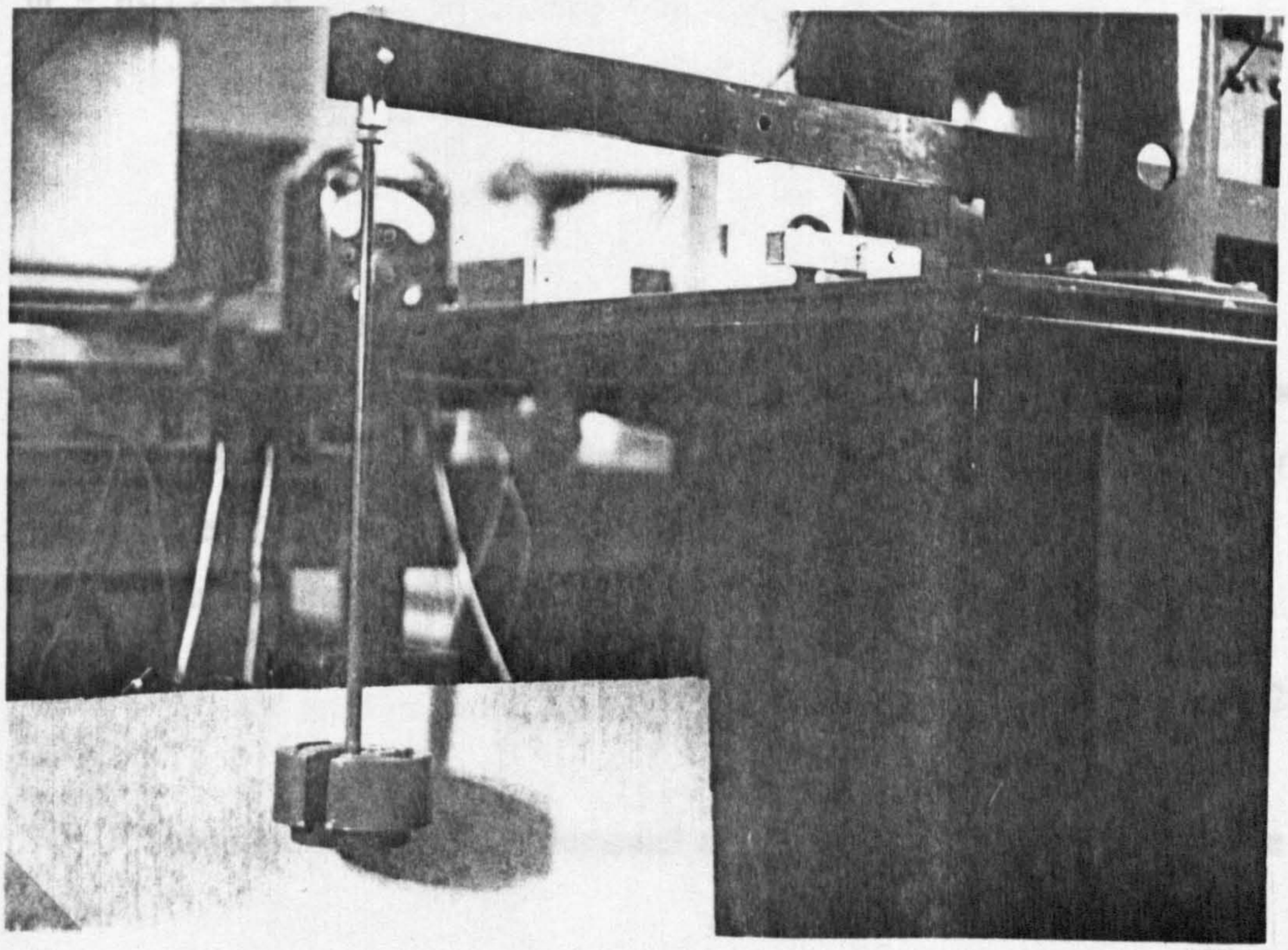

Figure A1.6 Fixed mass loading system

Appendix 2
ANALYSIS OF CONTACT

A2.1 Contact Force

Contact load is calculated from the mass, lever-arm ratio and angle of inclination between the upper and lower balls. The following calculation quantifies the normal contact force passing through the cup assembly for an average lever-arm load.

Contact normal load $(\varpi) = \frac{196.2M}{3\cos\theta_1}$ $(At\ 20{:}1\ Arm\ ratio)$ (A2.1)

Hence for a lever-arm load of 10Kg:-

$$\varpi = \frac{196.2(10.0)}{3\cos 35.3}$$

Therefore normal compressive force acting through contact surfaces is:-

$$\varpi = 801.34\ N$$

A2.2 Contact Stress

Theoretical model of the contact stresses between surfaces was first proposed by Hertz (1881) and more recently by Johnson (1985). This model indicates surface stresses due to deformation of contact points.

Consider a point force on an elastic half space:-

$$w = \frac{(1-\nu^2)}{(\pi E)}\left(\frac{P}{r}\right) \qquad \text{(A2.2)}$$

Substitute force P with elemental area which is a product of pressure and area:-

$$dw = \frac{(1-\nu^2)}{(\pi E)} p\ ds\ d\phi \qquad \text{(A2.3)}$$

By integrating, pressure distribution becomes:-

$$w = \frac{1-\nu^2}{\pi\ E} \iint_s p\ ds\ d\phi \qquad \text{(A2.4)}$$

By considering geometric deflection, leads to the contact equation:-

$$\frac{1}{\pi}\left[1-\frac{\nu_1^2}{E_1} + 1-\frac{\nu_2^2}{E_2}\right] \iint_s p\ ds\ d\phi = \delta - \frac{x^2}{2R'} - \frac{y^2}{2R''} \qquad \text{(A2.5)}$$

Hertz recognised, by analogy with electrostatic potential, that this equation would be satisfied by an ellipsoidal distribution of pressure.

$$p(x,y) = p_o\sqrt{1-\frac{x^2}{a^2}-\frac{y^2}{b^2}} \qquad \text{(A2.6)}$$

acting on an elliptical area of semi-axes a and b.

For circular contacts, maximum contact pressure (Hertz stress) is given by:-

$$p_o = \frac{1}{\pi}\left[6\ \frac{PE^2}{R^2}\right]^{1/3} \qquad \text{(A2.7)}$$

Also, the semi contact radius is given by:-

$$a = \left[\frac{3}{4}\ \frac{PR}{E'}\right]^{1/3} \qquad \text{(A2.8)}$$

Stresses may be found by considering the Airy stress function:-

$$\phi(r,\theta) = Ar\theta \sin\theta \qquad \text{(A2.9)}$$

The constant 'A' is found by equilibrium with the load 'P'. Then transforming to cartesian coordinates:-

$$\sigma_{xx} = -\frac{2P'}{\pi} \frac{x^2 z}{(x^2+z^2)^2} \qquad \text{(A2.10)}$$

$$\sigma_{zz} = -\frac{2P'}{\pi} \frac{z^3}{(x^2+z^2)^2} \qquad \text{(A2.11)}$$

$$\tau_{zx} = -\frac{2P'}{\pi} \frac{xz^2}{(x^2+z^2)^2} \qquad \text{(A2.12)}$$

Hertz contact equations are used to calculate stress magnitudes, stress positions and contact circle size. The standard equations for a non-conforming spherical contact are given as:-

Peak compressive pressure (normal to surface):-

$$p_0 = \left(\frac{6\varpi E'^2}{\pi^3 R'^2}\right) \qquad \text{(A2.13)}$$

Principal surface plane stresses:-

$$\sigma_x = \sigma_y = -\frac{p_0(1+2\nu)}{2} \qquad \text{(A2.14)}$$

Contact dimensions(circular):-

$$a = b = 0.88\sqrt[3]{\frac{\varpi R'}{E'}} \qquad \text{(A2.15)}$$

Maximum shear stress (at a depth 0.638a):-

$$\max \tau = \frac{1}{3}p_o \qquad \text{(A2.16)}$$

Maximum tensile stress (at radius a)

$$\max \sigma_t = \frac{(1-2\nu)p_o}{3} \qquad \text{(A2.17)}$$

Elastic contacts and effective radii must be calculated for different material and geometric configurations:-

a) Effective elastic constants

$$\frac{1}{E'} = \frac{1-\nu_1^2}{E_1} + \frac{1-\nu_2^2}{E_2} \qquad \text{(A2.18)}$$

Hence for ceramic-ceramic contact:- $\frac{1}{E'} = \frac{1-0.27^2}{315.0} + \frac{1-0.27^2}{315.0}$

$\therefore \quad E' = 169.885GPa$

For ceramic-steel contact:- $\frac{1}{E'} = \frac{1-0.27^2}{315.0} + \frac{1-0.3^2}{207.0}$

$\therefore \quad E' = 136.253GPa$

For steel-steel contact:- $\frac{1}{E'} = \frac{1-0.3^2}{207.0} + \frac{1-0.3^2}{207.0}$

$\therefore \quad E' = 113.736GPa$

b) Relative radius:-

$$\frac{1}{R'} = \frac{1}{R_1} + \frac{1}{R_2} \qquad \text{(A2.19)}$$

Hence for ball-ball contact $\frac{1}{R'} = \frac{1}{6.35} + \frac{1}{6.35}$

$\therefore \quad R' = 3.175 \ mm$

For ball-cup contact $\frac{1}{R'} = \frac{1}{6.35} - \frac{1}{6.72}$

$\therefore \quad R' = 115.33 \ mm$

Finally the Hertz equations may be quantified, the following calculation is for a ceramic-ceramic contact with a lever-arm load of 10.0 Kg:-

Peak compressive pressure (normal to surface):-

$$p_0 = \sqrt[3]{\frac{6\,(801.34)\,(165.3\ E9)^2}{\pi^3\,(3.175\ E{-}3)^2}} \qquad = \textbf{7.49 GPa}$$

Principal surface plane stresses:-

$$\sigma_x = \sigma_y = \frac{7.49\ (1+2\ (0.25))}{2} \qquad = \textbf{5.62 GPa}$$

Contact dimensions(circular):-

$$a = b = 0.88 \sqrt[3]{\frac{801.45\ \ 3.175E{-}3}{165.3E9}} \qquad = \textbf{0.22 mm}$$

Maximum shear stress (at a depth 0.638a):-

$$\max \tau = \frac{1}{3}\ \ 7.49 \qquad = \textbf{2.5 GPa at depth 0.14 mm}$$

Maximum tensile stress (at radius a)

$$\max \sigma_t = \frac{(1 - 0.5) \quad 7.49}{3} \qquad = \mathbf{1.25\ GPa}$$

Figures A2.1, A2.2 and A2.3 show graphs which illustrate maximum stress values calculated from the equations derived previously for ceramic/ceramic, hybrid and steel/steel contacts. The shape of the curves show that the stress is high for a relatively lower load particularly compressive and surface principal. As the load increases the stress gradients become quite shallow especially for tensile stress acting on the edge of the contact radius. It can be seen from the example calculation that compressive and surface principal stresses are the highest in magnitude. Fatigue is the failure of materials below yield or failure stress due to crack propagation, this involves separation of surfaces, the most important stresses are therefore shear and, in the case of brittle ceramic materials, tensile stresses.

All ceramic/ceramic contact stresses are considerable higher than for steel contact or indeed hybrid contacts. This is a result of the higher effective elasticity modulus. The principal shear stress which occurs centrally and subsurface, the maximum tensile stress which occur on the contact circle edge, both have small stress gradient. Principal shear stress depth below the surface, figure A2.4, indicates a position which is closer to the surface than steel or hybrid contacts.

The contact circle radius for various loads and material combinations is shown in figure A2.5. The ceramic contact radius is smaller for the same loads due to higher elastic modulus. This also implies that overall stress will be correspondingly higher. Reference tables from the graphs previously described for ceramic/ceramic, ceramic/steel and steel/steel contacts are shown in tables A2.1, A2.2 and A2.3.

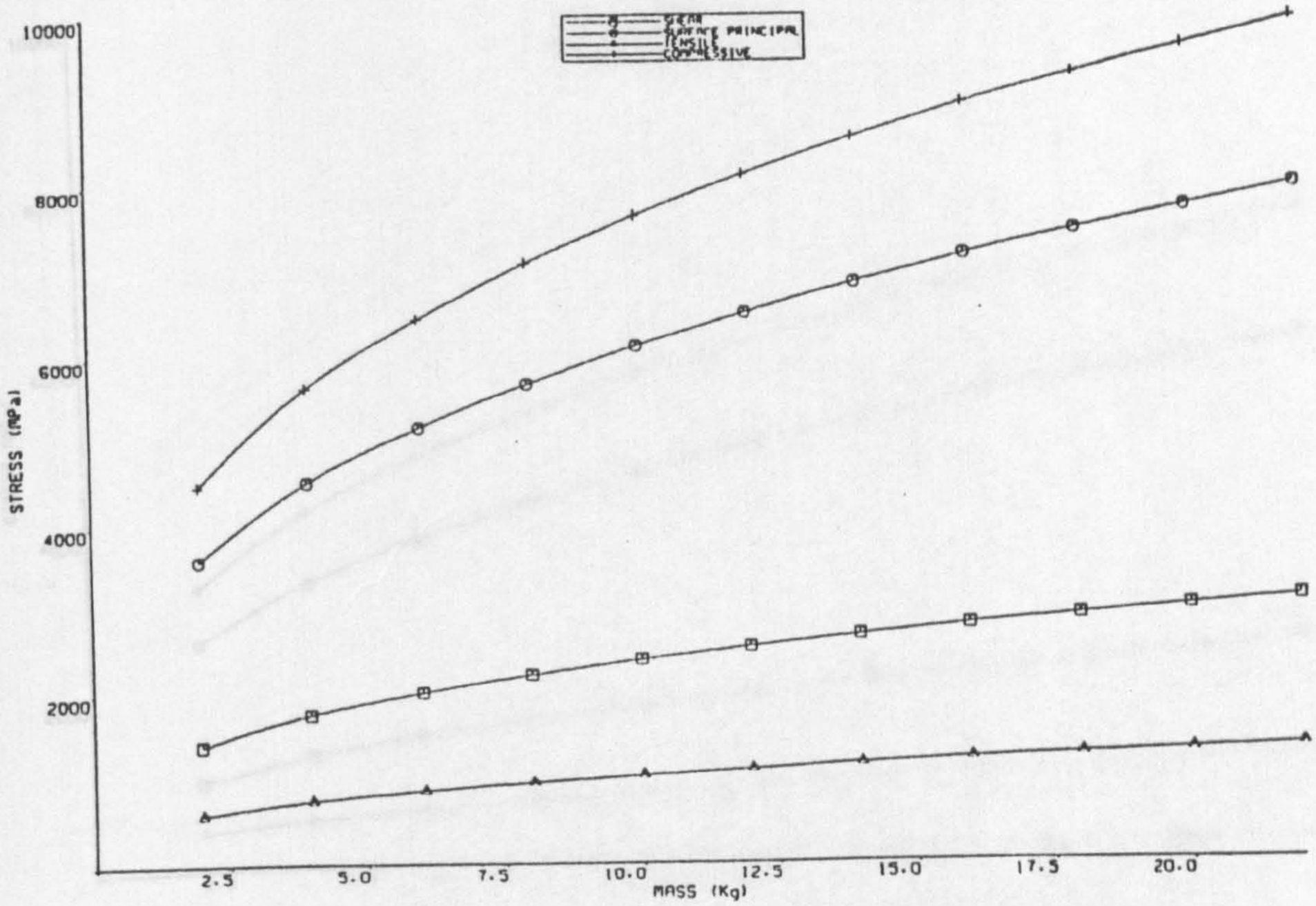

Figure A2.1 Maximum stresses for ceramic/ceramic contact

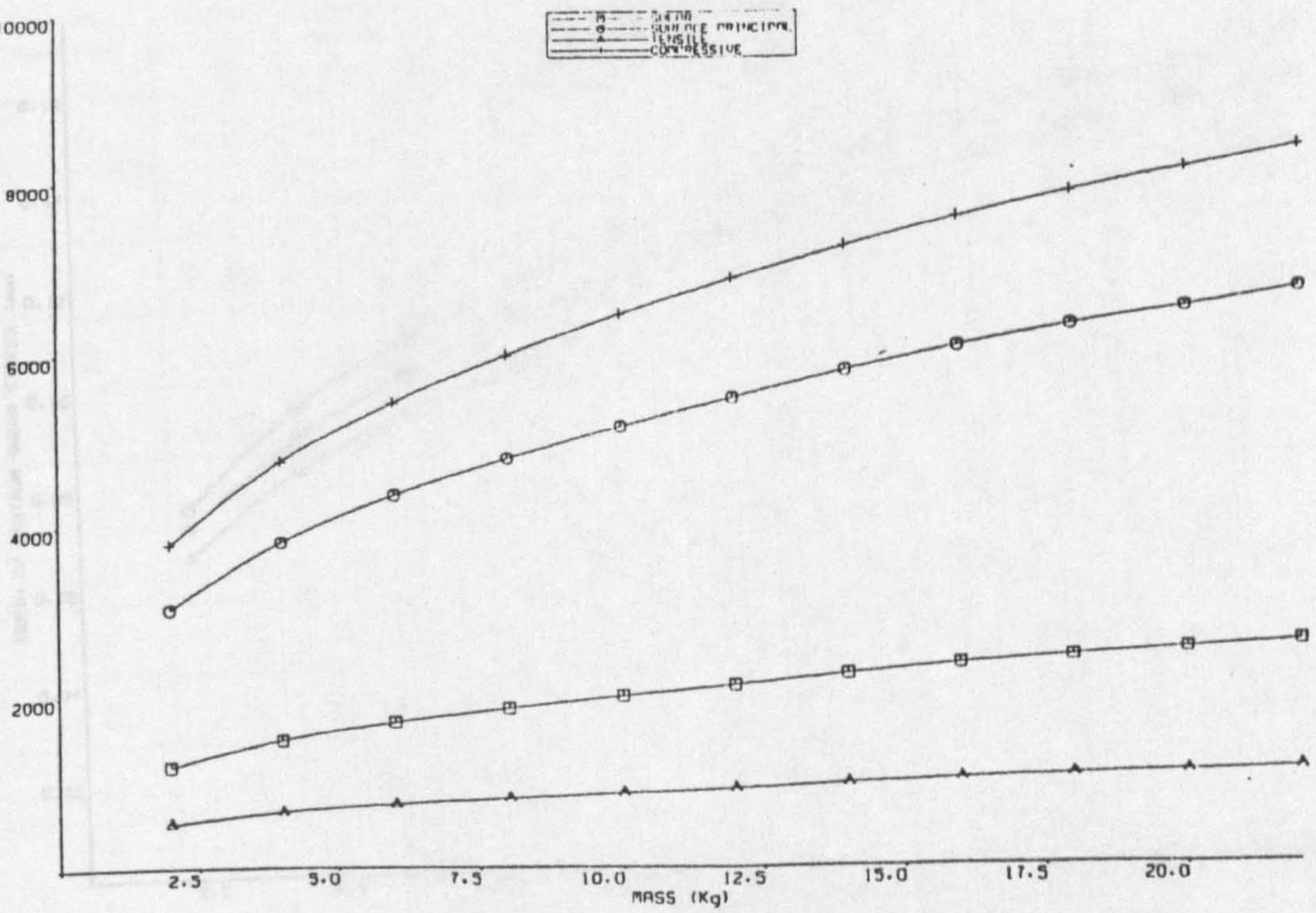

Figure A2.2 Maximum stresses for ceramic/steel contact

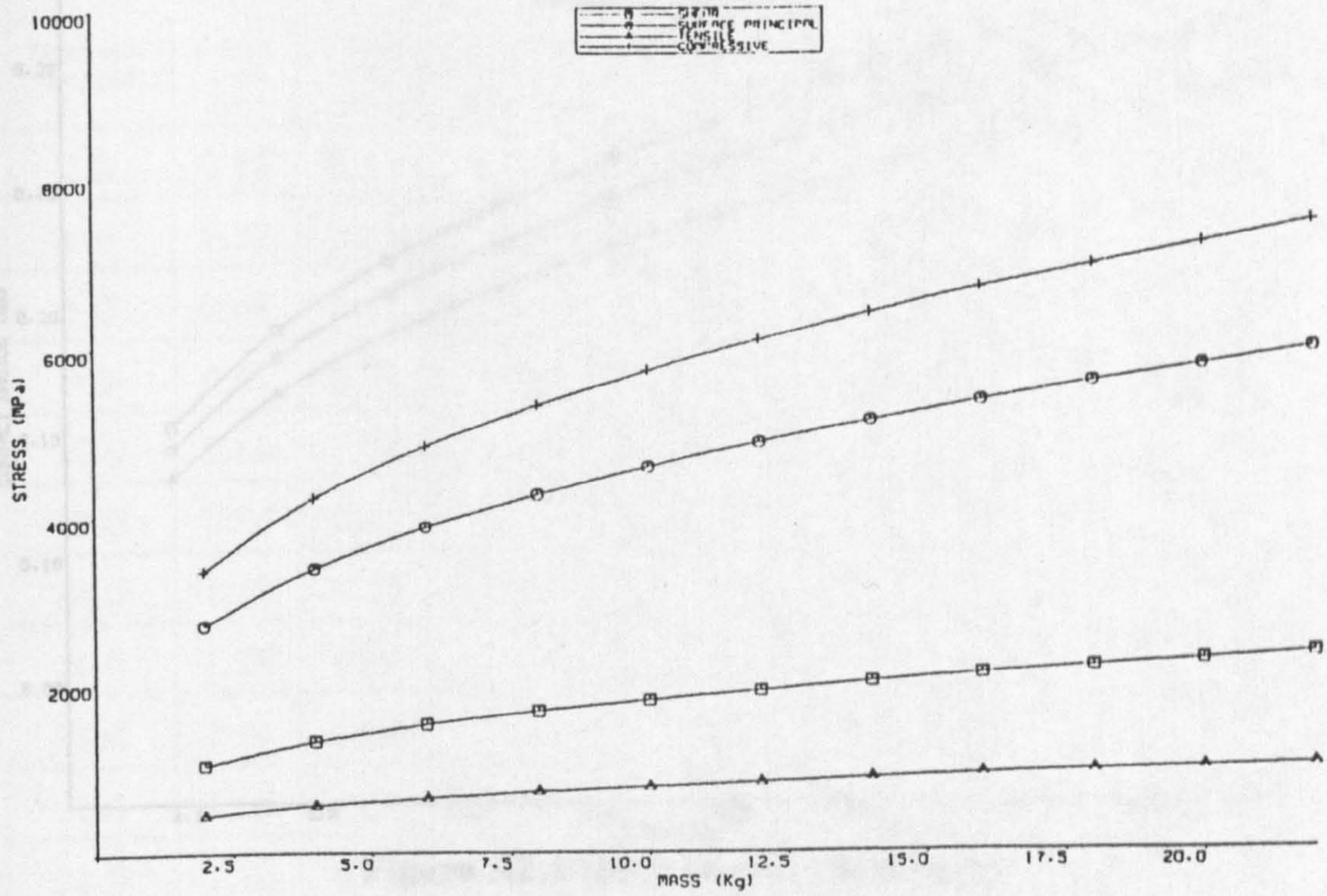

Figure A2.3 Maximum stresses for steel/steel contact

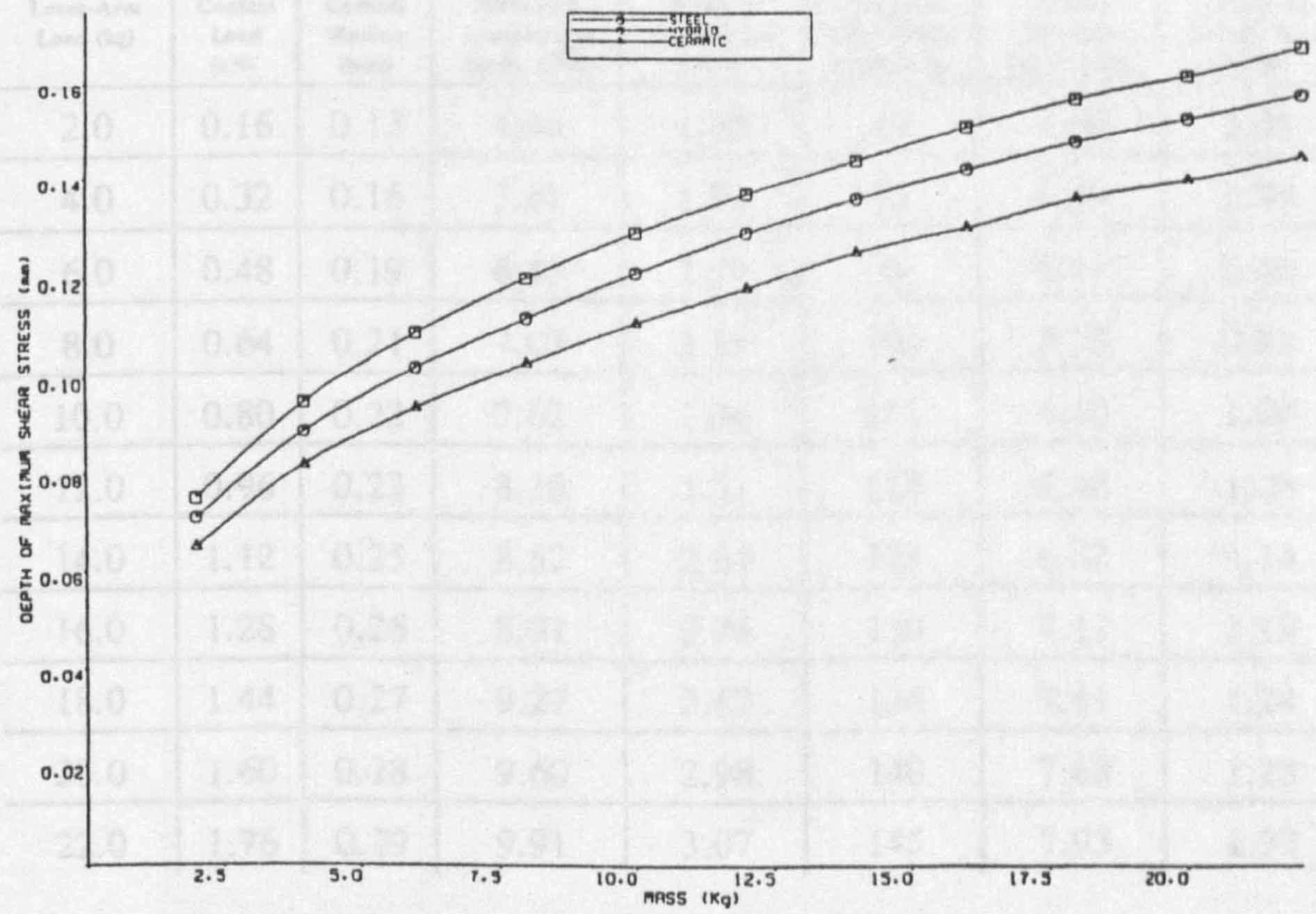

Figure A2.4 Maximum shear stress position below surface

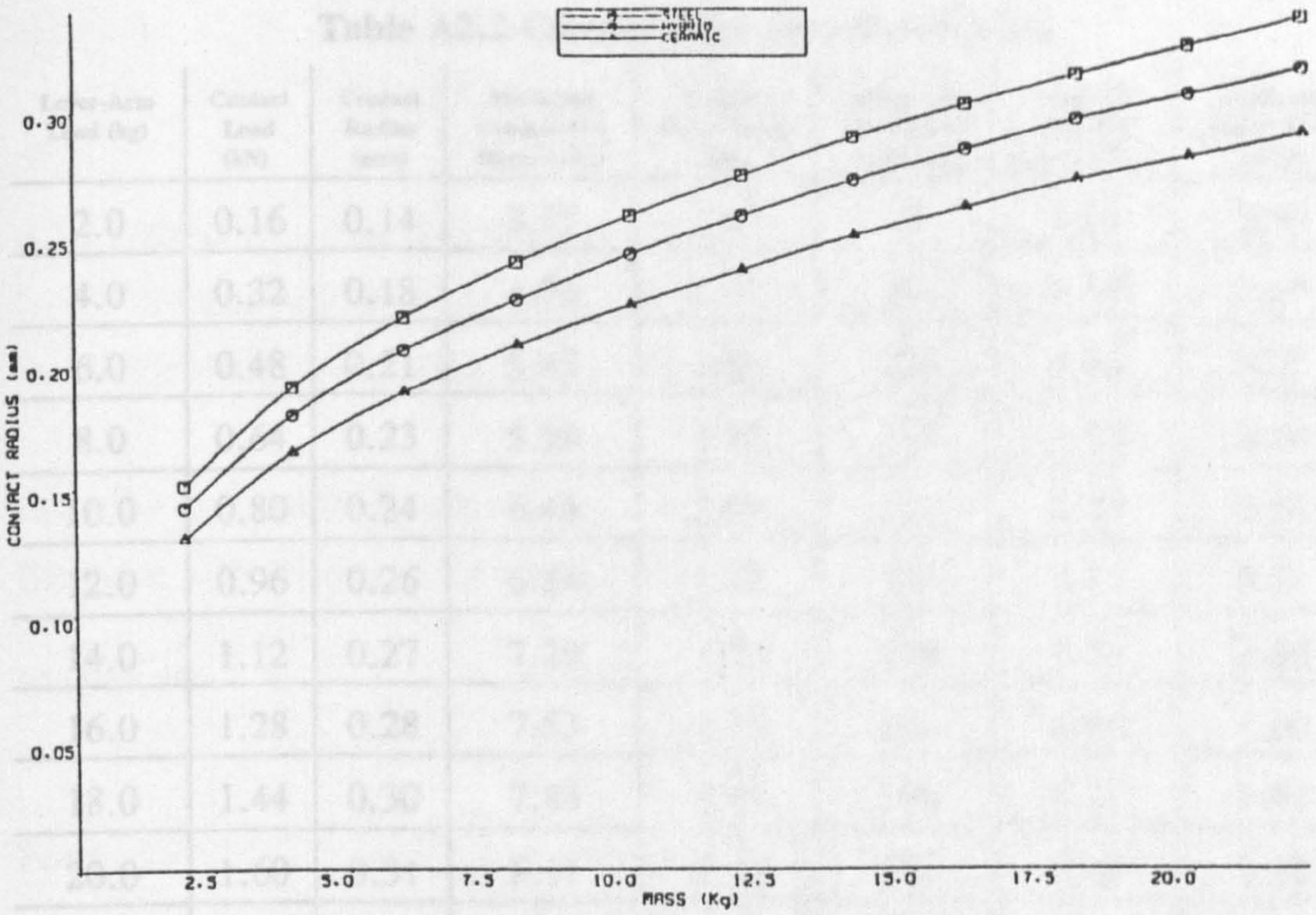

Figure A2.5 Hertz contact circle radius

Table A2.1 Ceramic/ceramic contact conditions

Lever-Arm Load (kg)	Contact Load (kN)	Contact Radius (mm)	Maximum Compressive Stress (GPa)	Maximum Shear Stress (GPa)	Maximum Shear Stress Depth (μm)	Surface Principal Stress (GPa)	Maximum Tensile Stress (GPa)
2.0	0.16	0.13	4.46	1.38	65	3.56	0.59
4.0	0.32	0.16	5.61	1.74	82	4.49	0.79
6.0	0.48	0.19	6.43	1.99	94	5.14	0.86
8.0	0.64	0.21	7.07	2.19	103	5.56	0.94
10.0	0.80	0.22	7.62	2.36	111	6.10	1.02
12.0	0.96	0.23	8.10	2.51	118	6.48	1.08
14.0	1.12	0.25	8.52	2.64	125	6.82	1.14
16.0	1.28	0.26	8.91	2.76	130	7.13	1.19
18.0	1.44	0.27	9.27	2.87	136	7.41	1.24
20.0	1.60	0.28	9.60	2.98	140	7.68	1.28
22.0	1.76	0.29	9.91	3.07	145	7.93	1.32

Table A2.2 Ceramic/steel contact conditions

Lever-Arm Load (kg)	Contact Load (kN)	Contact Radius (mm)	Maximum Compressive Stress (GPa)	Maximum Shear Stress (GPa)	Maximum Shear Stress Depth (μm)	Surface Principal Stress (GPa)	Maximum Tensile Stress (GPa)
2.0	0.16	0.14	3.77	1.17	71	3.01	0.50
4.0	0.32	0.18	4.74	1.47	89	3.80	0.63
6.0	0.48	0.21	5.43	1.68	102	4.34	0.72
8.0	0.64	0.23	5.98	1.85	112	4.78	0.80
10.0	0.80	0.24	6.44	2.00	121	5.15	0.86
12.0	0.96	0.26	6.84	2.12	129	5.47	0.91
14.0	1.12	0.27	7.20	2.23	136	5.76	0.96
16.0	1.28	0.28	7.53	2.33	142	6.03	1.00
18.0	1.44	0.30	7.83	2.43	148	6.27	1.04
20.0	1.60	0.31	8.11	2.52	153	6.49	1.08
22.0	1.76	0.32	8.38	2.60	158	6.70	1.12

Table A2.3 Steel/steel contact conditions

Lever-Arm Load (kg)	Contact Load (kN)	Contact Radius (mm)	Maximum Compressive Stress (GPa)	Maximum Shear Stress (GPa)	Maximum Shear Stress Depth (μm)	Surface Principal Stress (GPa)	Maximum Tensile Stress (GPa)
2.0	0.16	0.15	3.33	1.03	75	2.67	0.44
4.0	0.32	0.19	4.20	1.30	95	3.36	0.56
6.0	0.48	0.22	4.81	1.49	109	3.85	0.64
8.0	0.64	0.24	5.29	1.64	120	4.23	0.71
10.0	0.80	0.26	5.70	1.77	129	4.56	0.76
12.0	0.96	0.27	6.06	1.88	137	4.85	0.81
14.0	1.12	0.29	6.38	1.98	144	5.10	0.85
16.0	1.28	0.30	6.67	2.07	151	5.33	0.88
18.0	1.44	0.31	6.93	2.15	157	5.55	0.92
20.0	1.60	0.33	7.18	2.22	162	5.74	0.96
22.0	1.76	0.34	7.41	2.30	168	5.93	0.98

Appendix 3

FATIGUE FAILURE MODES

A3.1 Theory 1 - Maximum Shear Stress

A crack is initiated below the surface and is propagated to the surface. The maximum shear stress initiates the crack at a depth below the surface.

Location - on load axis, subsurface

Direction - 45 degrees w.r.t. loaded surface

Magnitude - $\tau_{max}=0.3p_0$ (A3.1)

Position - $Z_{max}=0.15\ a$ (A3.2)

Max. alternating component - $0.15p_0$ *about mean* (A3.3)

A3.2 Theory 2 - Maximum orthogonal shear stress:

A crack is initiated below the surface and is propagated to the surface. The maximum orthogonal shear stress initiates the crack at a depth below the surface.

Location - offset 0.85a from load axis, subsurface

Direction - parallel w.r.t. loaded surface

Magnitude - $\tau_{orth}= +0.25p_0 / -0.25p_0$ (A3.4)

Position - $Z_{orth}=0.25\ a$ (A3.5)

Max. alternating component - $0.25p_0$ *about mean* (A3.6)

A3.3 Theory 3 - Maximum Von Mises Stress:

A crack is initiated at the point of maximum Von Mises stress below the surface.

Location - on load axis, subsurface

Direction - Not applicable

Magnitude - $$\sigma_{VM\,max}=2\tau_{orth\,max} \quad \text{(A3.7)}$$

Position - $$Z_{VM\,max}=\frac{3}{2}Z_{orth\,max} \quad \text{(A3.8)}$$

Max. alternating component - $\tau_{orth\,max}$ *about mean* (A3.9)

A3.4 Theory 4 - Maximum Tensile Stress:

A crack is initiated on the surface due to tensile stresses at the contact edge. Lubricating oil forces a wedge which propagates the crack below the surface until the pit falls out due to bending moment.

Location - edge of contact area, on surface

Direction - radial from centre of contact area

Magnitude - $$\sigma_{t\,max}=\frac{(1-2\nu)}{3}p_0 \quad \text{(A3.10)}$$

Position - a (A3.11)

Max. alternating component - $$\sigma_{t\,max}=\frac{(1-2\nu)}{6}p_0 \quad \text{(A3.12)}$$

Appendix 4

THEORETICAL LUBRICATION REGIME

During lubricated testing the upper ball is separated from the three planetary balls by a thin film of oil. It is important to calculate this film thickness as it affects the wear, fatigue, friction, and pressure distribution. Calculations of film thickness is based on a combination of fluid mechanics and materials science. Much work has been produced on elastohydrodynamic lubrication, notably by Hirst and Richmond (1988), Archard (1973), Tallian (1972), Hirano et al (1971), Dowson and Higginson (1966), and Archard and Kirk (1960). By considering the problem of lubricated contact by dimensional analysis then the following parameters may be established.

Dimensionless parameters:-

Dimensionless materials parameter:

$$G = \xi E'' \tag{A4.1}$$

Dimensionless elipticity parameter:

$$k = \left(\frac{R_y}{R_x}\right)^{2/\pi} \tag{A4.2}$$

Dimensionless speed parameter:

$$U = \frac{\eta_o u}{E'' R_x} \tag{A4.3}$$

Dimensionless load parameter:

$$W = \left(\frac{F}{E'' R_x^2}\right) \tag{A4.4}$$

Dimensionless minimum film thickness is then given by the equation:-

$$H_{min} = 3.63\ U^{0.68}\ G^{0.49}\ W^{-0.073}\ (1-e^{-0.68k}) \qquad \text{(A4.5)}$$

This equation indicates the influence of various oil and material physical properties on film thickness. It should be noted that as the relationships of the various dimensionless groups are found experimentally and errors may increase when the equation is applied to ceramic materials especially the materials group.

Dimensionless minimum film thickness may now be evaluated using the following average physical properties:

$\xi \approx 2.3\ E{-}8\ m^2/N$

$\eta_0 = 0.015\ N\,m^2/s$

$u = 3.65\ m/s$

$R_x = 3.175\ E{-}3\ m$

$E'' = 331.0\ GPa$

$F = 800.0\ N$

$k = 1.0$

Then using the equation A4.5:-

$$H_{min}=3.63\,(5.21E{-}11)^{0.68}\,(7613.0)^{0.49}\,(2.3976E{-}4)^{-0.073}\,(1-e^{-0.68})$$

Hence the dimensionless minimum film thickness is:-

$$H_{min} = 2.673\ E\text{-}5$$

The value of dimensionless minimum film thickness is related to the surface roughness to describe lubrication mode.

Actual minimum film thickness is:-

$$h_{min} = H_{min}\ R_x \tag{A4.6}$$

Hence:

$$h_{min} = 8.487\ E\text{-}8\ m$$

The lambda ratio may then be calculated using a surface RMS roughness value of 10.0 nm for both contacting balls.

$$\lambda = \frac{h_{min}}{(\ \Delta_a^2+\Delta_b^2\ )^{0.5}} \tag{A4.7}$$

Hence:

$$\lambda = 6.0$$

This result implies that the experiment under the conditions described is operating with a full-film lubrication. In order to access when condition would be such that partial film or even boundary lubrication occurs, a number of variables must be investigated.

Appendix 5
KINEMATIC ANALYSIS

A5.1 Geometric calculations

Consider a standard test configuration using 1/2 inch upper and lower balls, cup radius 7.62 mm and cup external radius 14.2 mm. Equation (3.2) (section 3.2.1) may be used to calculate the basic contact angle 'alpha'.

alpha = 35.15 degrees

As the radius of the upper and lower balls are the same for this example then, by symmetry, angle 'alpha' will equal angle 'beta'. Using equation (3.3) (section 3.2.2) this may be verified.

beta = 35.15 degrees

Using equation (3.4) (section 3.2.2), 'gamma' may then be evaluated.

gamma = 19.7 degrees

A5.2 Upper-Ball Stress Cycle Factor

The upper-ball stress cycle factor 'L' may be calculated from equation (A5.1). This parameter is used to assess the total number of upper-ball stress cycles per machine spindle revolution.

$$\text{Stress cycles per rev } (L) = z\left(\frac{R_A + 2R_P}{2R_A + R_P}\right) \qquad \text{(A5.1)}$$

Hence $$L = 3\left(\frac{6.35 + 2(6.35)}{2(6.35) + 6.35}\right)$$

Therefore $$L = 2.25$$

Hence, for example, two million stress cycles applied to the upper-ball, require 0.889 million machine spindle revolutions.

Appendix 6
MECHANICAL PROPERTIES

Table A6.1 Physical and mechanical properties of silicon nitride

Property	Unit	Range	Calculation*	
Density	g/cc	3.0 - 3.5	3.25	
"	kg/m³	3000 - 3500	3250	
Elastic Modulus	GPa	280 - 330	310	
Poisson's Ratio	-	0.23 - 0.29	0.26	
Thermal Conductivity	W/m.°K	13 - 38	20	
Specific Heat	J/kg.°K	710 - 810	750	
Thermal Expansion	10 /°C	2.8 - 3.8	3.2	
Resistivity	Ohm.m	10 - 10	10	
Transverse rupture strength (20°C)	MPa	600 - 1000	900	
Compressive strength	MPa	2500 - 4000	3500	
Hardness	kg/m²	1400 - 1900	1600	(HV5)
Toughness	MPa/m	3 - 7	6.5	

* Typical or mid-range values recommended for use in calculations

Table A6.2 Typical properties of engineering ceramics and bearing steel

Material	Density gm/cc	Elastic Modulus GPa	Hardness kg/mm²	Toughness MPa$\sqrt{m}$	Failure Mode
Silicon Nitride	3.2	310	1400 - 1800	5 - 8	Spalling
Silicon Carbide	3.1	420	2000 - 2400	2 - 4	Fracture
Alumina	3.9	390	1800 - 2000	3 - 5	Fracture
Zirconia	5.8	210	1100 - 1400	8 - 12	Spalling
Steel*	7.8	200	1000	> 16	Spalling

* Standard bearing steel AISI 52100, or aircraft bearing steel - M50 high speed steel.

Appendix 7

SCANNING ELECTRON MICROSCOPE CALCULATIONS

A7.1 Thickness of Coating

Thickness of coating is given by equation (A7.1).

$$T = ma.Kv.t.k \qquad \text{(A7.1)}$$

A typical example of splutter coating a silicon nitride ball, using a gold target in argon gas, is shown below:

ma = 25 ma

Kv = 1.2 KV

t = 5.0 minutes

K = 5 for argon with gold target

hence $T = 25 \times 1.2 \times 5 \times 5$

therefore $\underline{T = 750\ \text{Å}}$

A7.2 Stereo Image height

Actual height from a stereo image is given by:

$$Z = \frac{P}{2\ Mg\ SIN\left(\frac{\alpha' - \alpha''}{2}\right)}$$

A typical example is shown below:

$$Z = \frac{0.45}{2\ SIN(5)\ 570}$$

therefore $\underline{Z = 4.5\ \mu m}$

Appendix 8

GENERAL PRINCIPLE OF X-RAY RESIDUAL STRESS MEASUREMENT

X-ray stress measurement is used to find residual surface stress on failed areas. The $\sin^2\psi$ method is employed which may be used on materials with a crystal structure. When a stress is applied to a material, the interatomic distance in the crystal will be extended or compressed within the elastic limit in proportion to the force. The X-ray diffraction technique is employed to measure the variations of the interplaner spacing in the crystal so that stress will be calculated. Using the Bragg's condition for diffraction (A8.1), strain may then be calculated (A8.2).

$$n\lambda = 2d \sin\theta \qquad \text{.....(A8.1)}$$

$$\epsilon = \frac{\Delta d}{d} = \cot\theta_0 \, \Delta\theta \qquad \text{.....(A8.2)}$$

Strain is calculated from the quantity of variations of the X-ray diffraction angle (A8.2). Stress on the surface is then calculated from the expression (A8.3).

$$\sigma = \frac{E}{1+\nu} \frac{\partial(\epsilon)}{\partial(\sin^2\psi)} = -\frac{E \cot\theta_0}{2(1+\nu)} \frac{\partial(\theta)}{\partial(\sin^2\psi)} \qquad \text{.....(A8.3)}$$

Equation (A8.3) is described by two constants 'K' and 'M', shown as equation (A8.4).

$$\sigma = K M \qquad \text{.....(A8.4)}$$

where $$K = -\frac{E \cot\theta_0}{2(1+\nu)}$$

and $$M = \frac{\partial(\theta)}{\partial(\sin^2\psi)}$$

The incident X-ray is varied typically 0, 10, 20 and 30 degrees. At these settings, the diffraction angle is measured and hence gradient 'M' is evaluated from a regression line. The constant elasticity parameter 'K' is evaluated from material properties and the stress-free diffraction angle.

Appendix 9
TYPE-1 INITIATION FAILURES

A9.1 Type 1i1p Failures

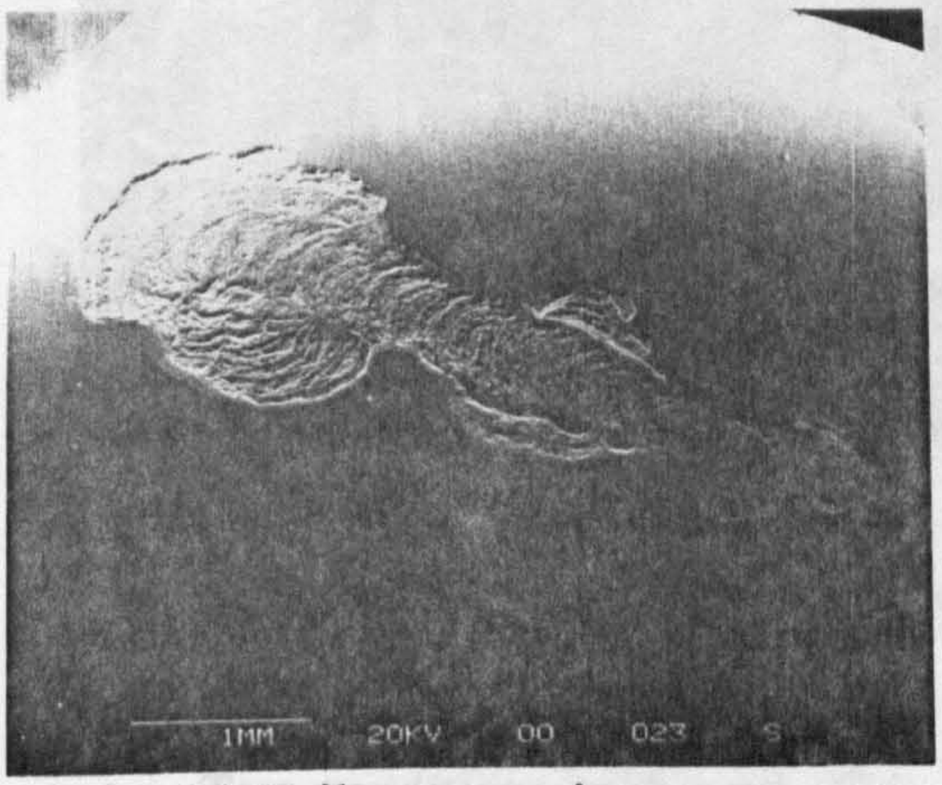

(a) Failure overview

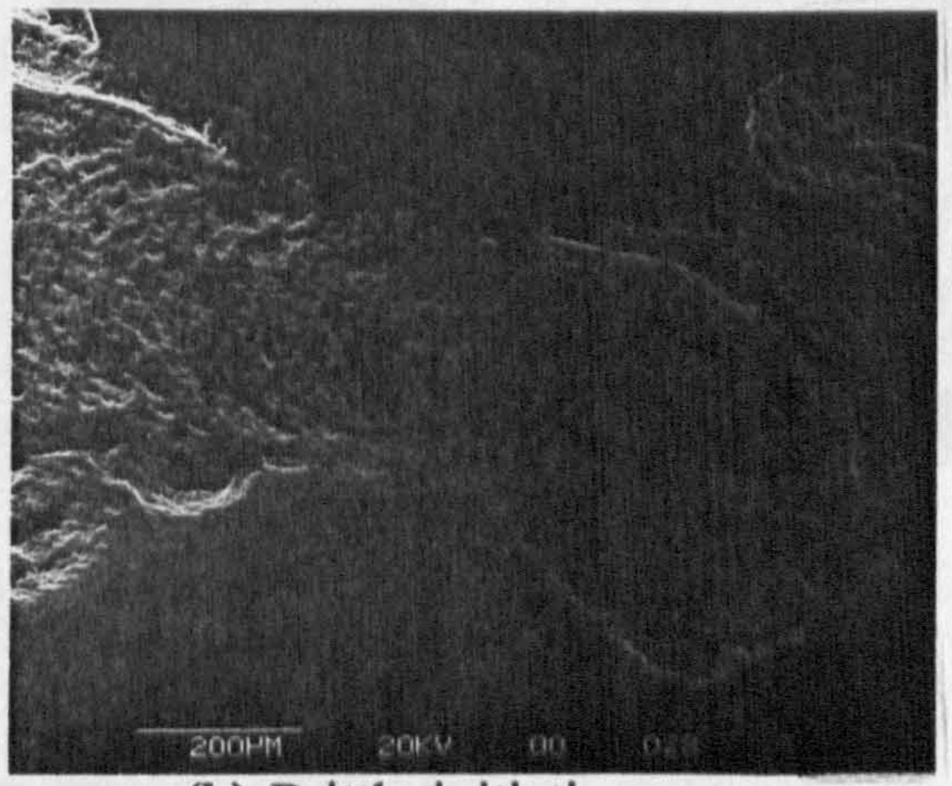

(b) Brittle initiation area

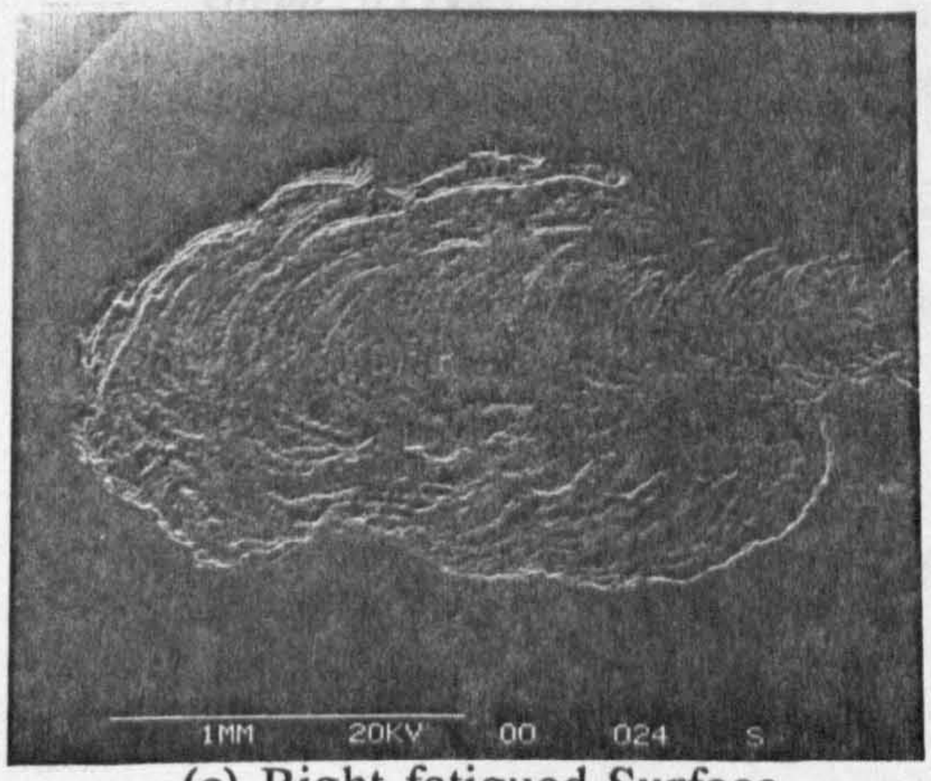

(c) Right fatigued Surface

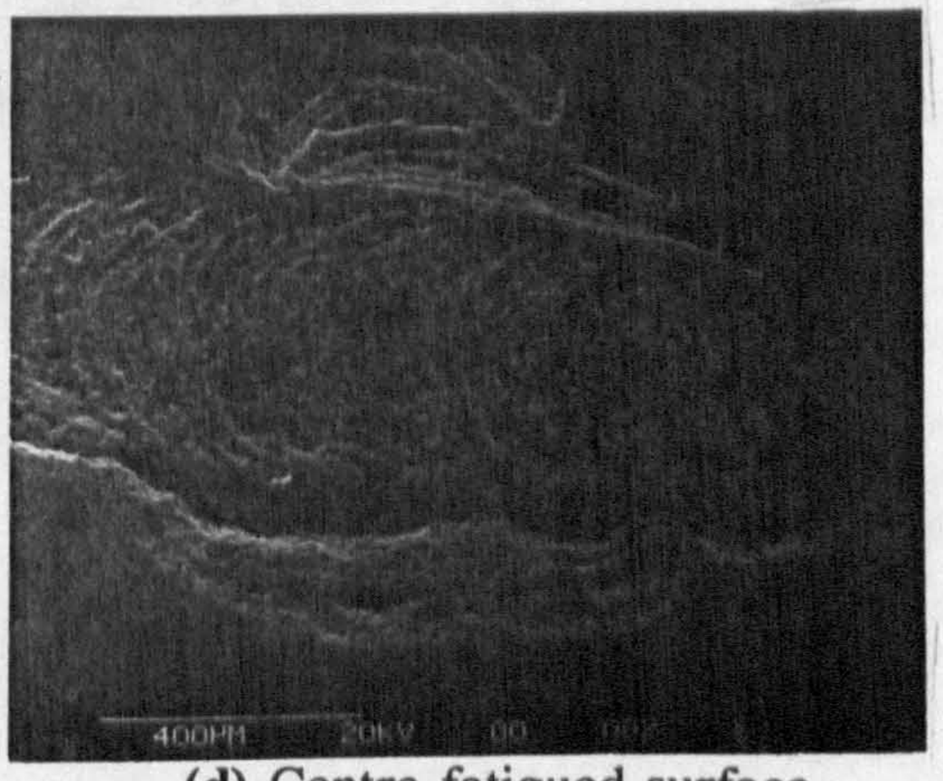

(d) Centre fatigued surface

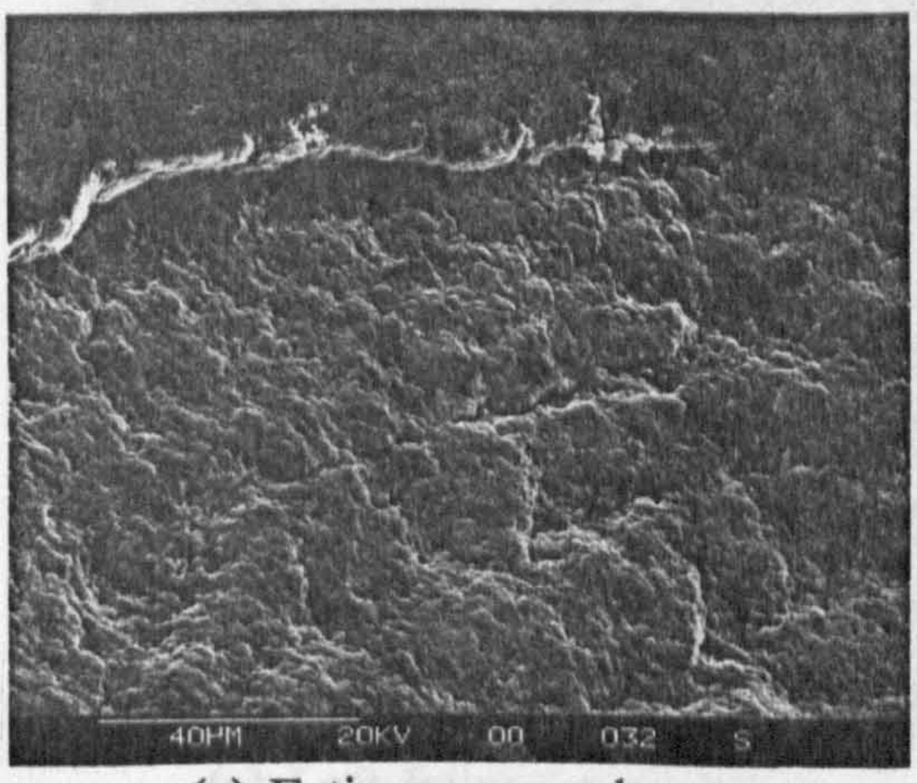

(e) Fatigue near edge

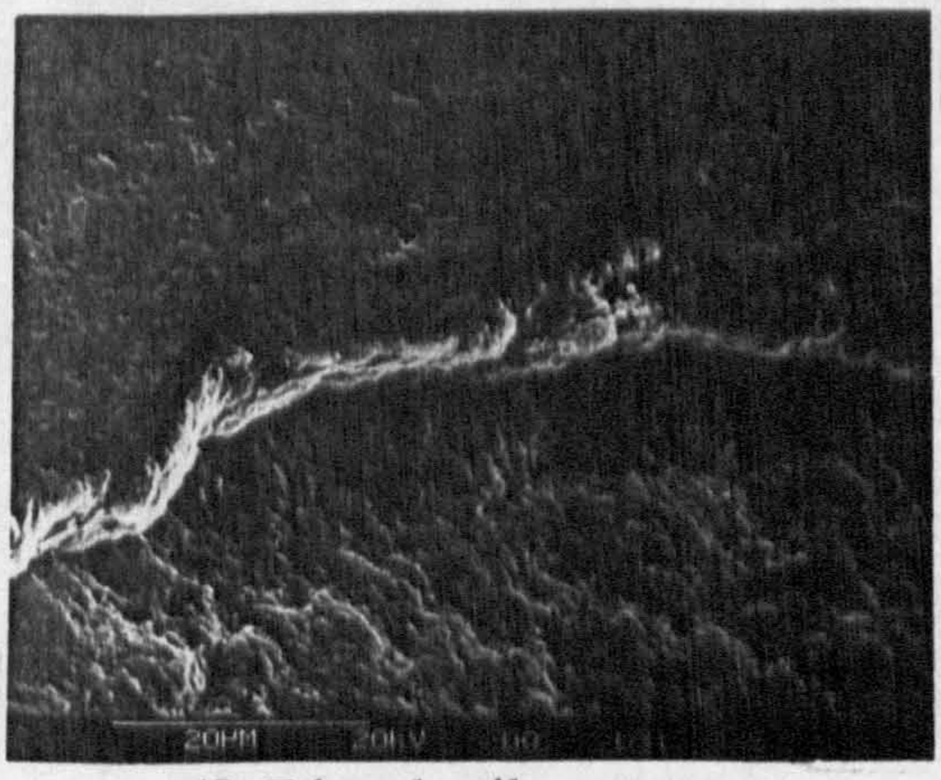

(f) Edge detail

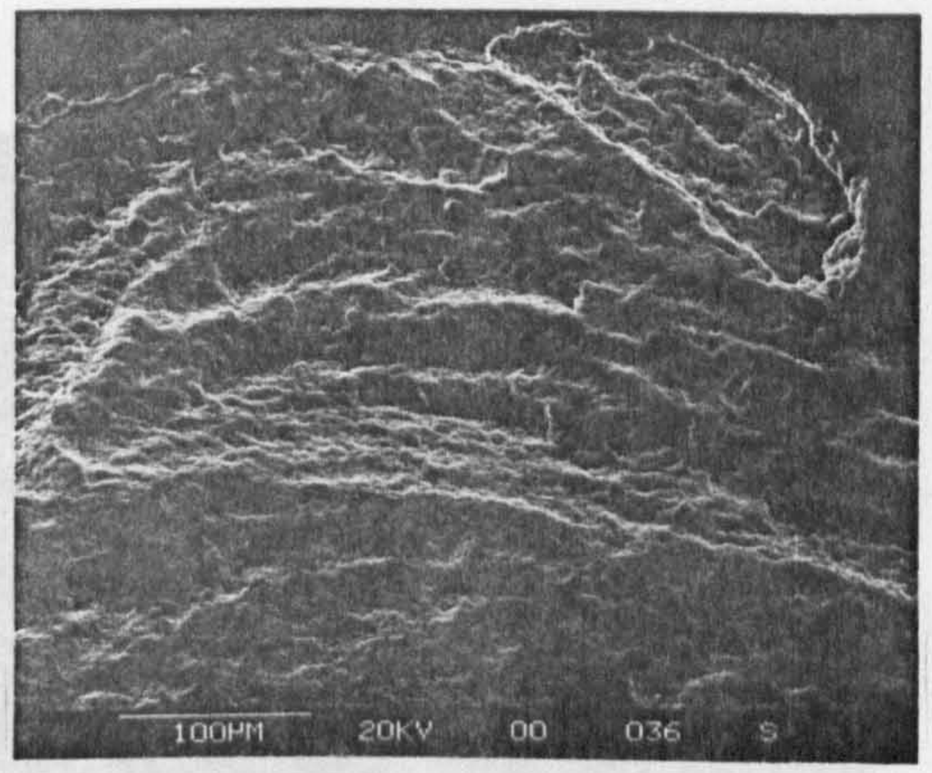

(g) Central fatigue detail

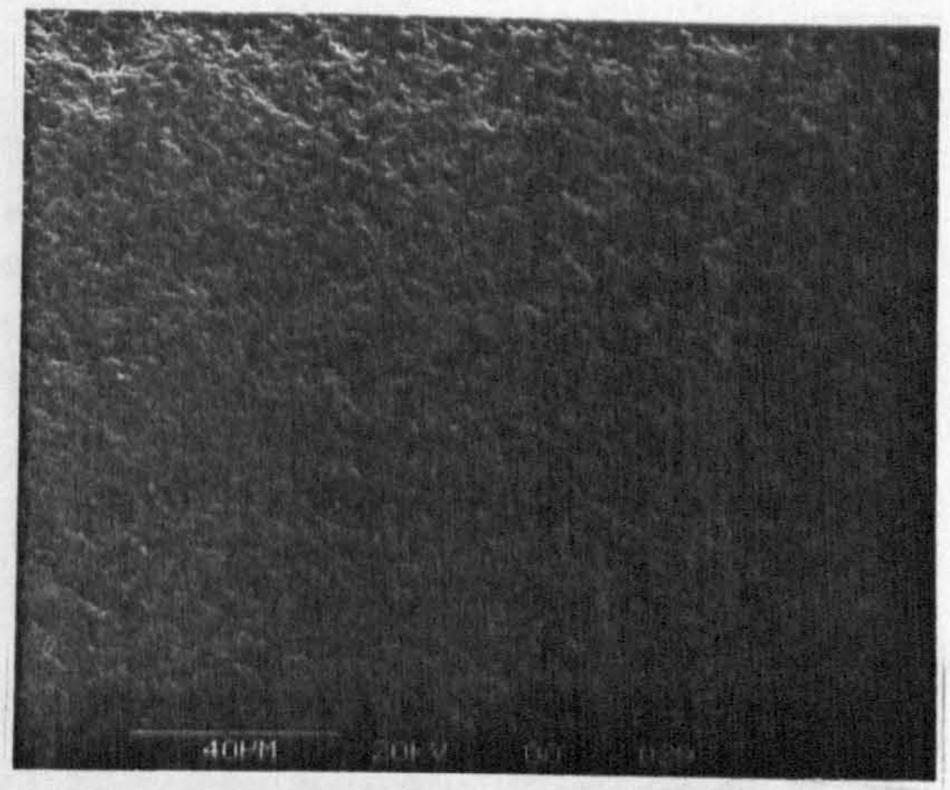

(h) Brittle surface detail

Figure A9.1 Example of type 1i1p failure - captions (a) to (h)

Test conditions of figure A9.1: ceramic/ceramic contact, machine spindle speed 10,000 r.p.m, HiTec 174 oil lubricant, bulk oil temperature 83°C - unheated, 45.7 million upper ball stress cycles, Hertzian maximum compressive stress - 8.7 GPa, theoretical lambda ratio - 6, Surface roughness (Ra) of upper and lower balls 0.008 μm.

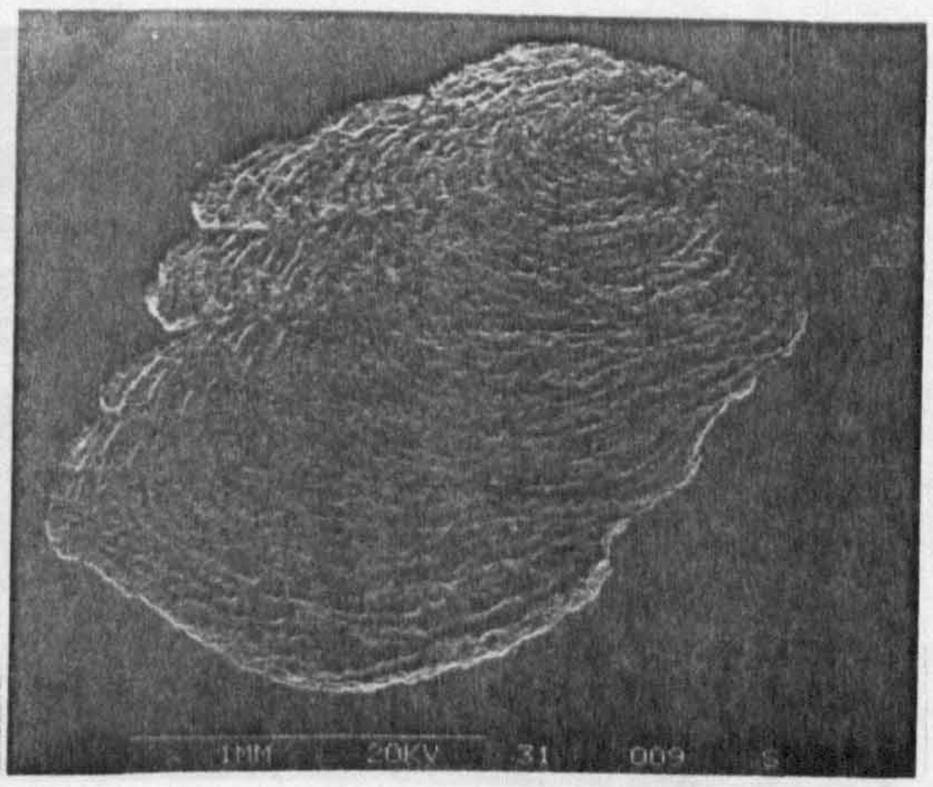

(a) Left failure overview

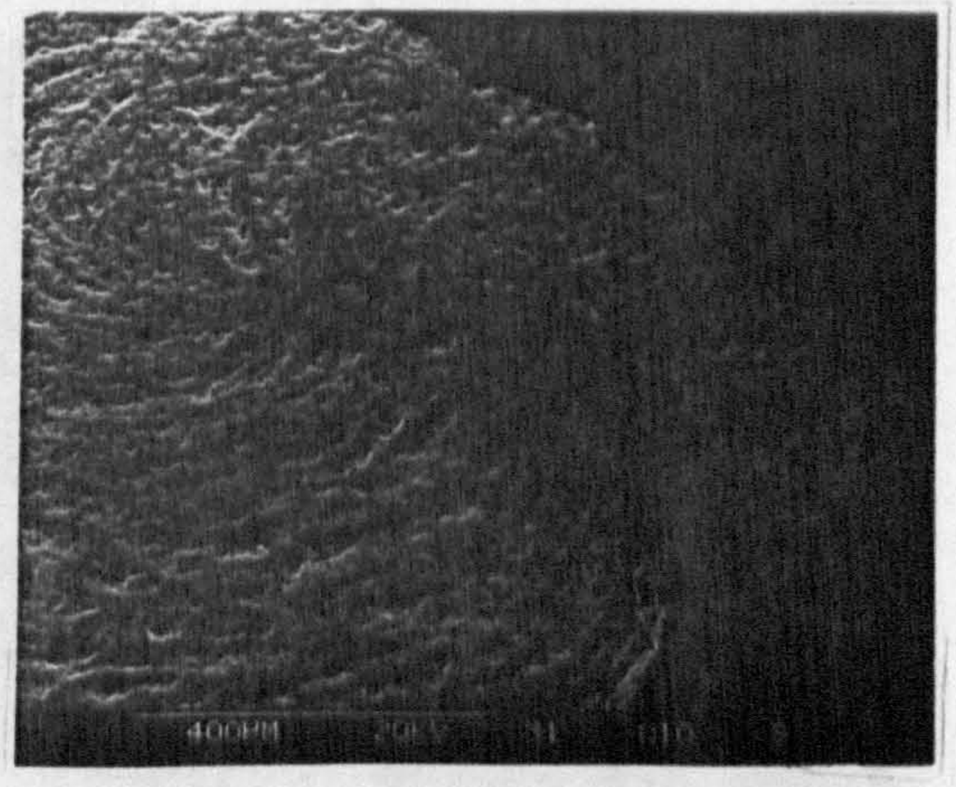

(b) Brittle initiation area

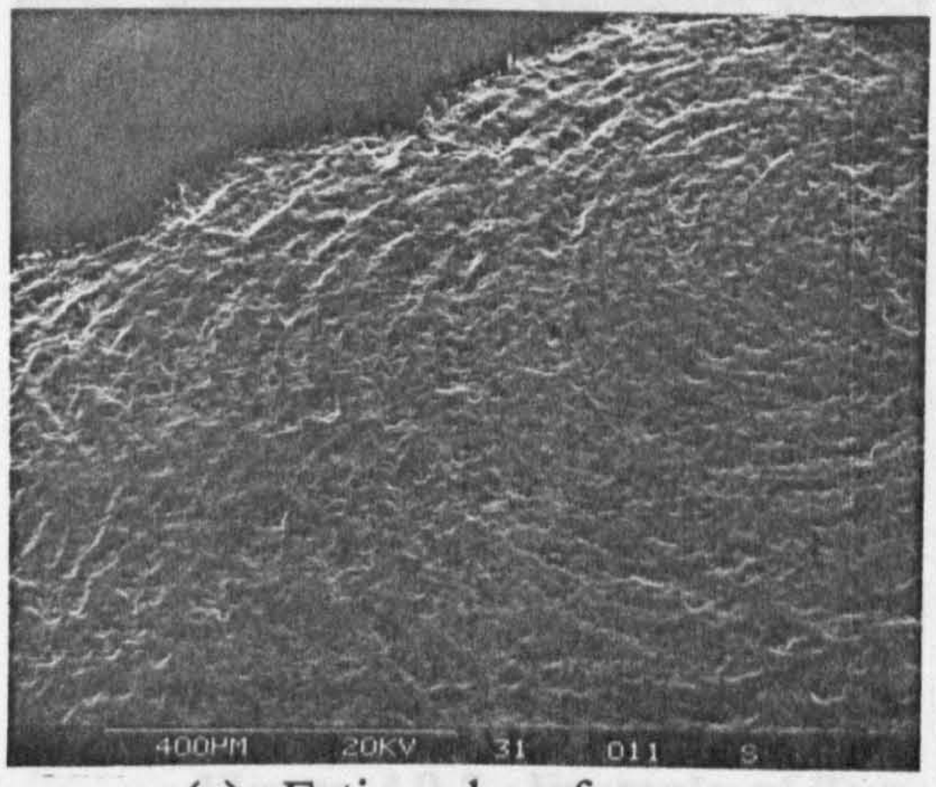

(c) Fatigued surface

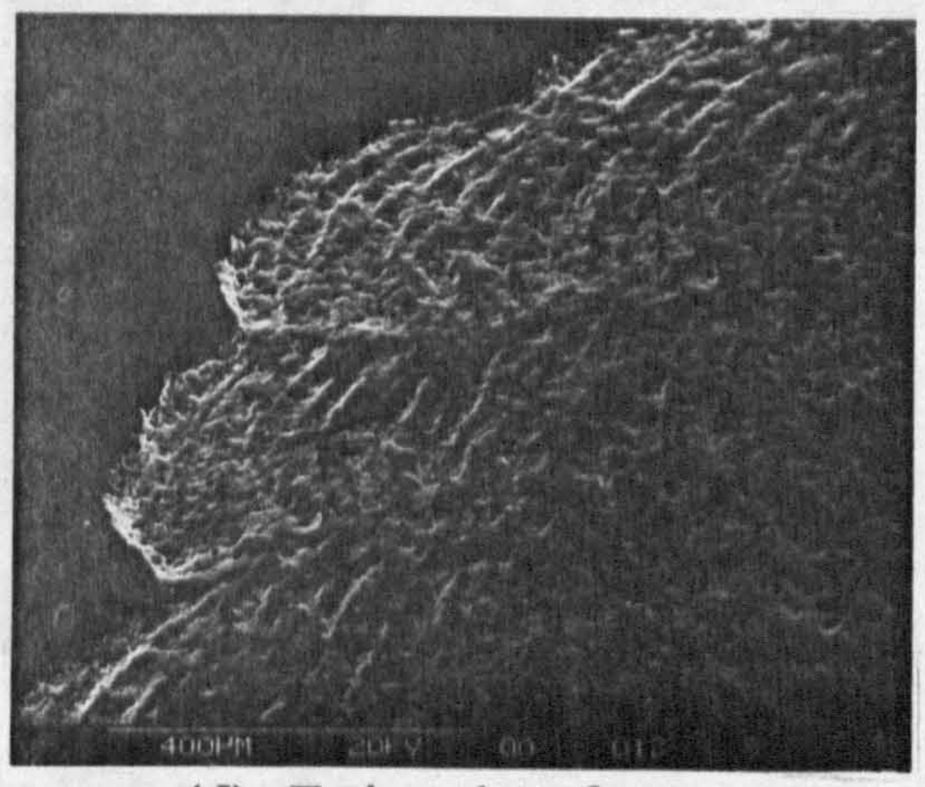

(d) Fatigued surface

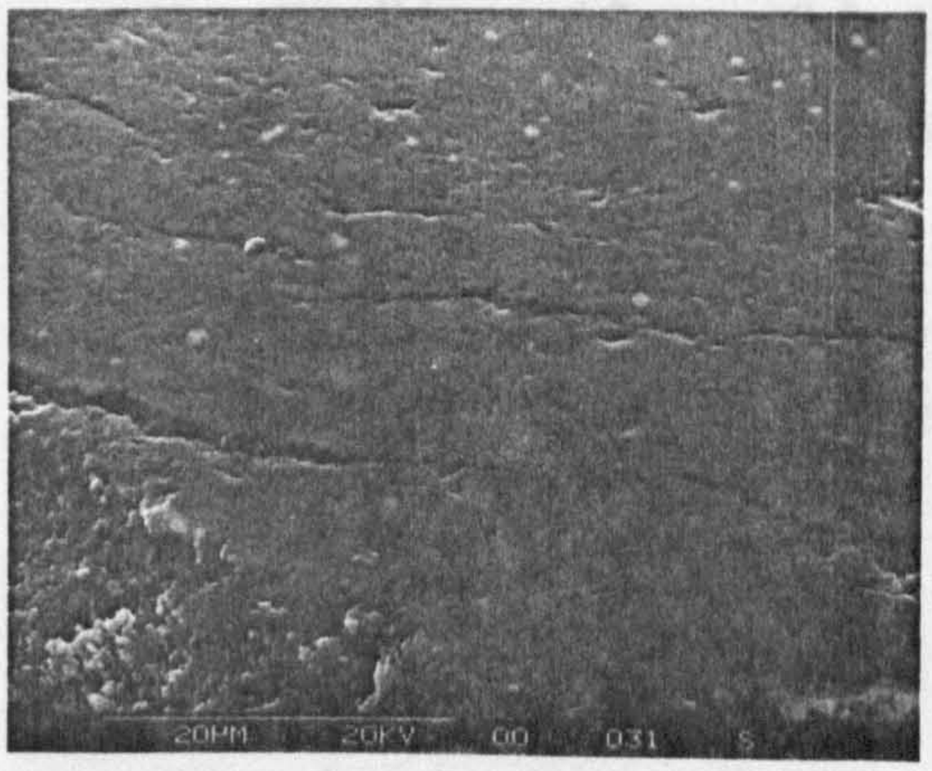

(e) Ball surface near edge

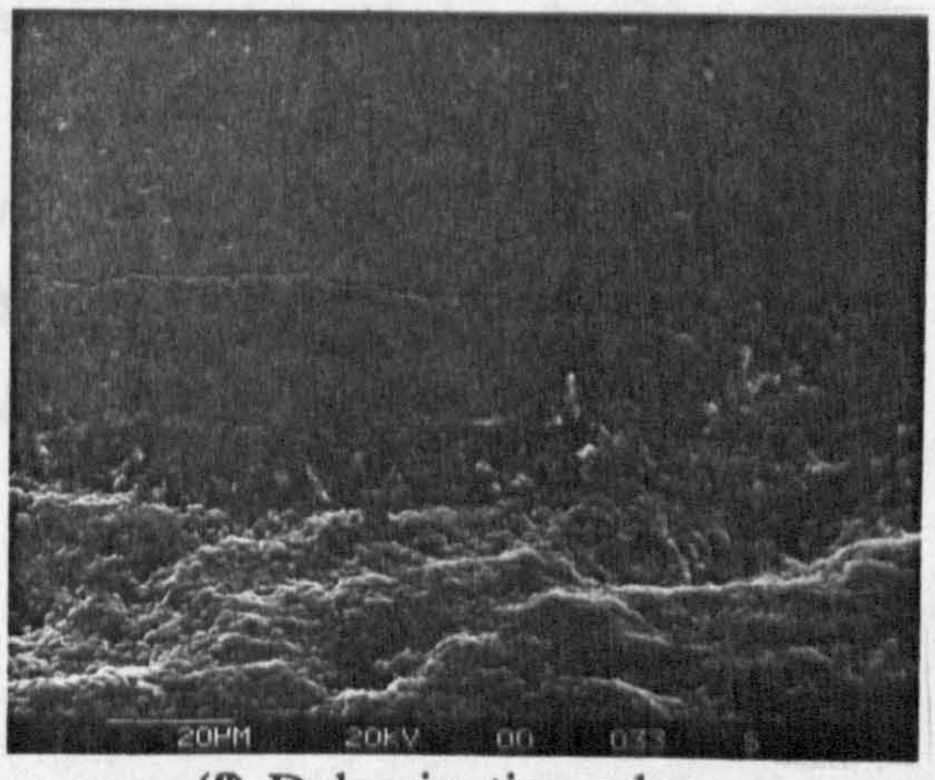

(f) Delamination edge

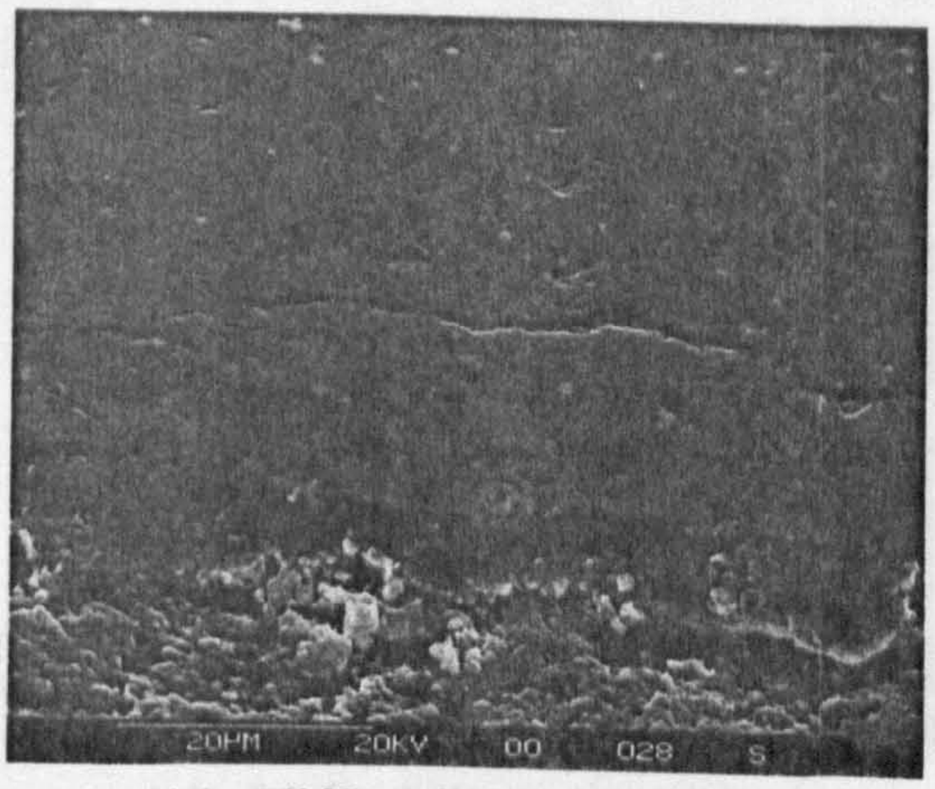

(g) Cliff and ball surface

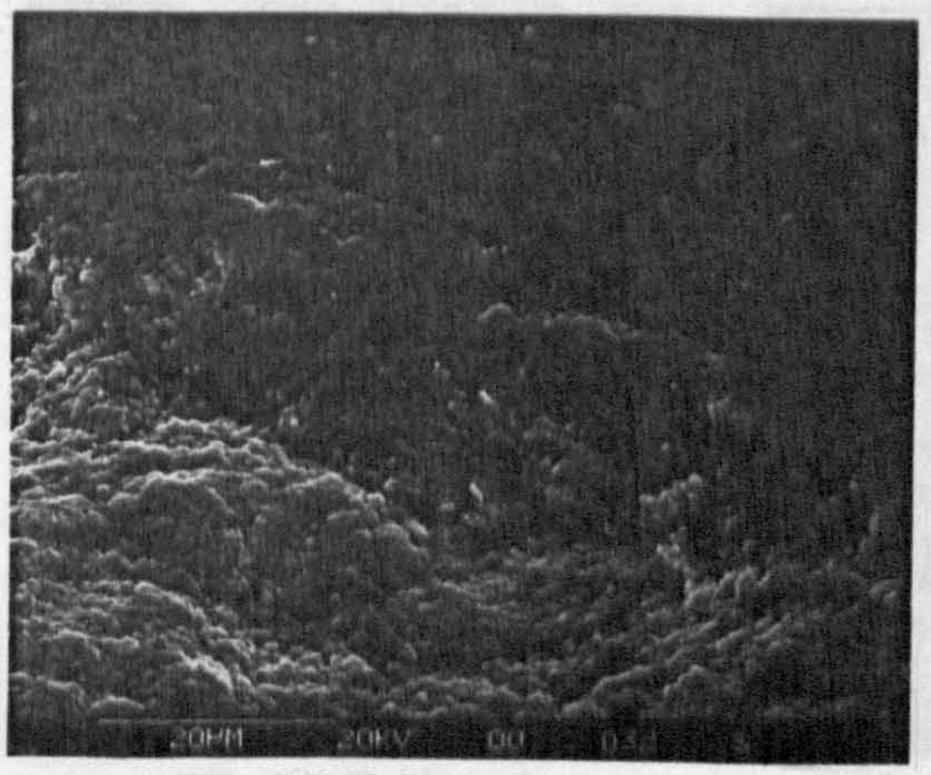

(h) Cliff fracture

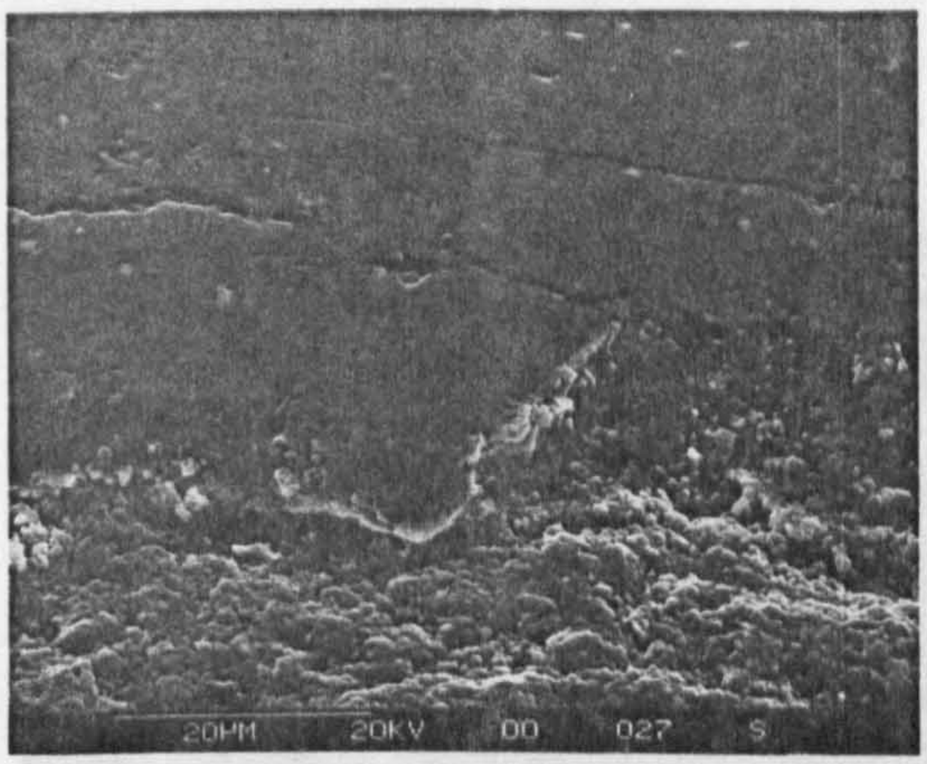

(i) Cliff fracture detail

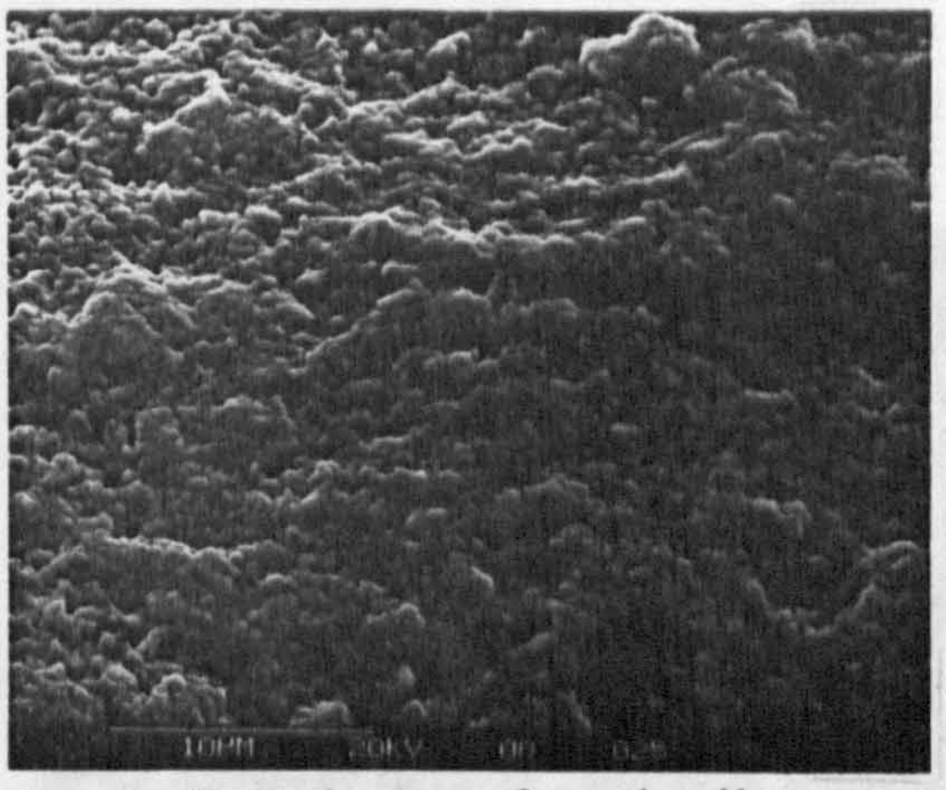

(j) Fatigue surface detail

Figure A9.2 Example of Type 1i1p Failure - Captions (a) to (j)

Test Conditions of figure A9.2: Ceramic/ceramic contact, machine spindle speed 10,000 r.p.m, HiTEc 174 oil lubricant, bulk oil temperature 83°C - unheated, 45.7 million upper ball stress cycles, Hertzian maximum compressive stress - 8.7 GPa, theoretical lambda ratio - 6, Surface roughness (Ra) of upper and lower balls 0.008 μm.

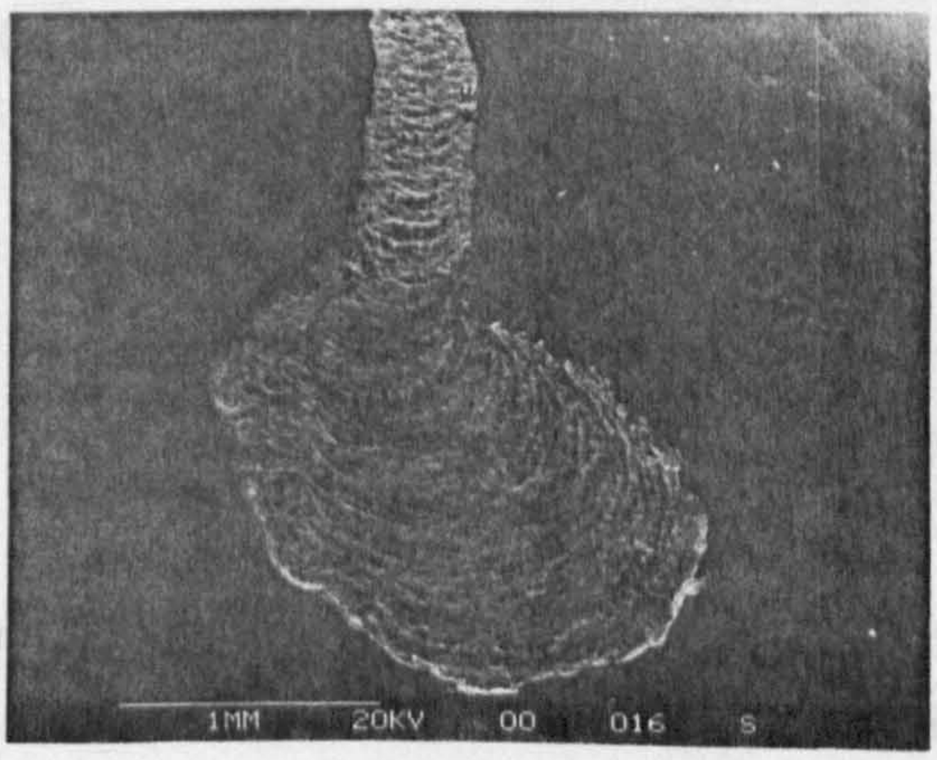

(a) Right failure overview

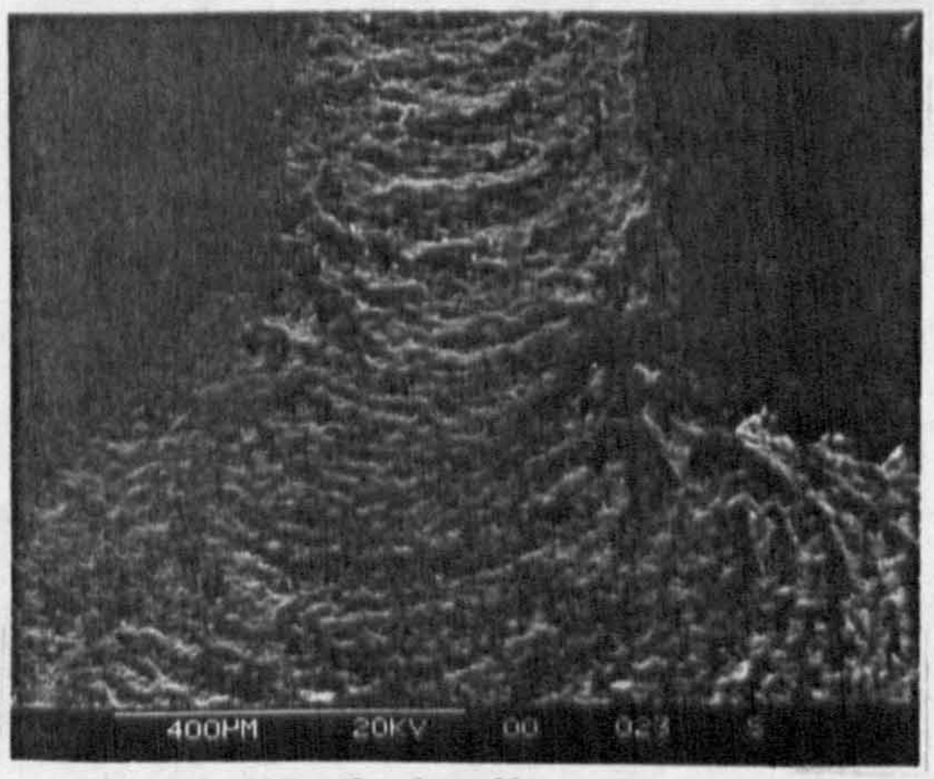

(b) Neck detail

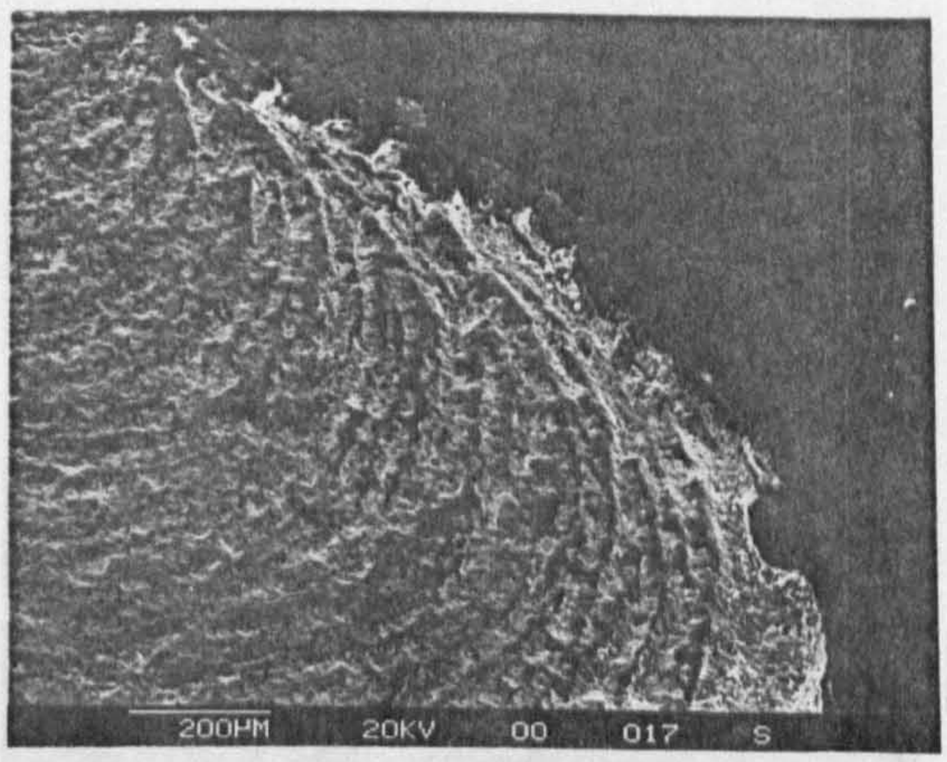

(c) Delamination detail-top right

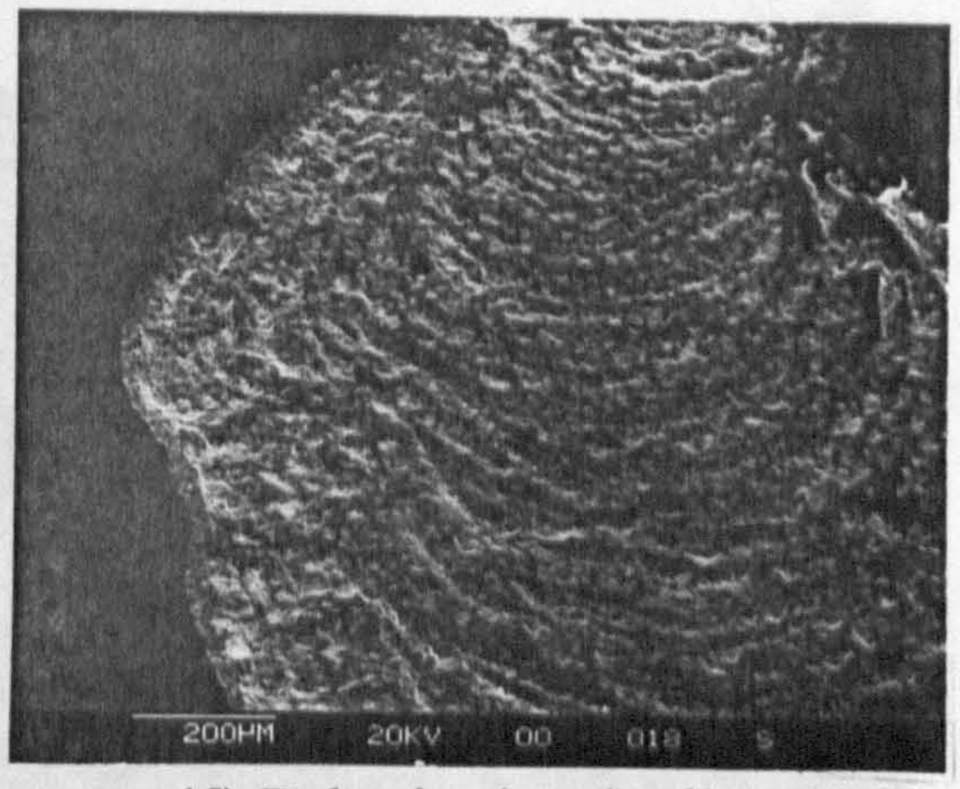

(d) Delamination detail-top left

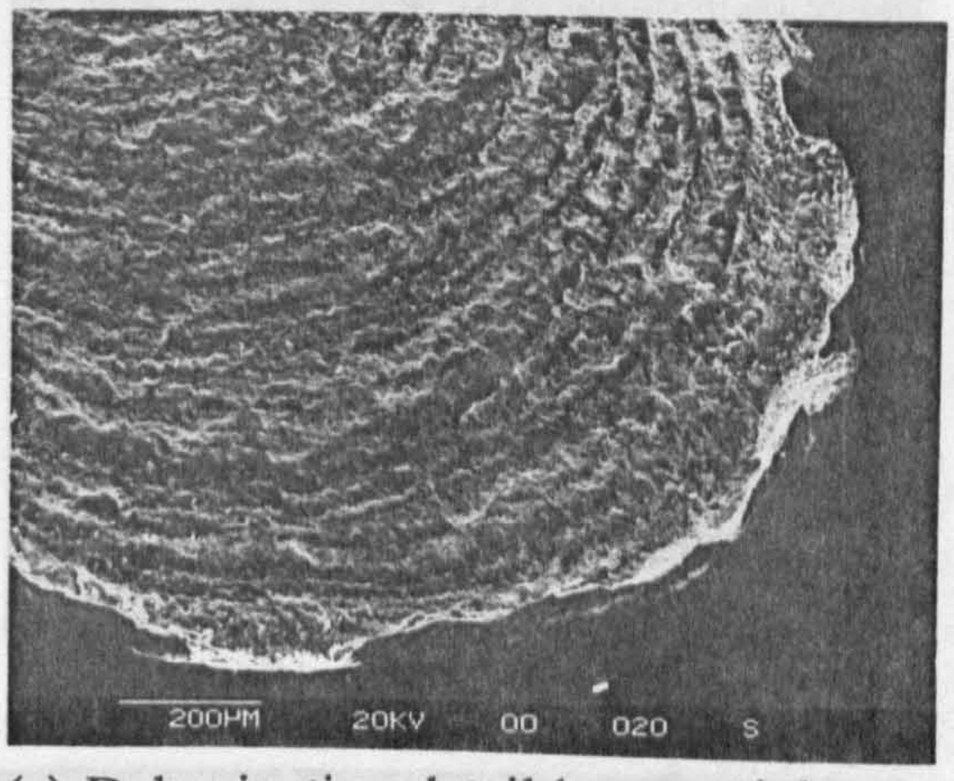

(e) Delamination detail-bottom right

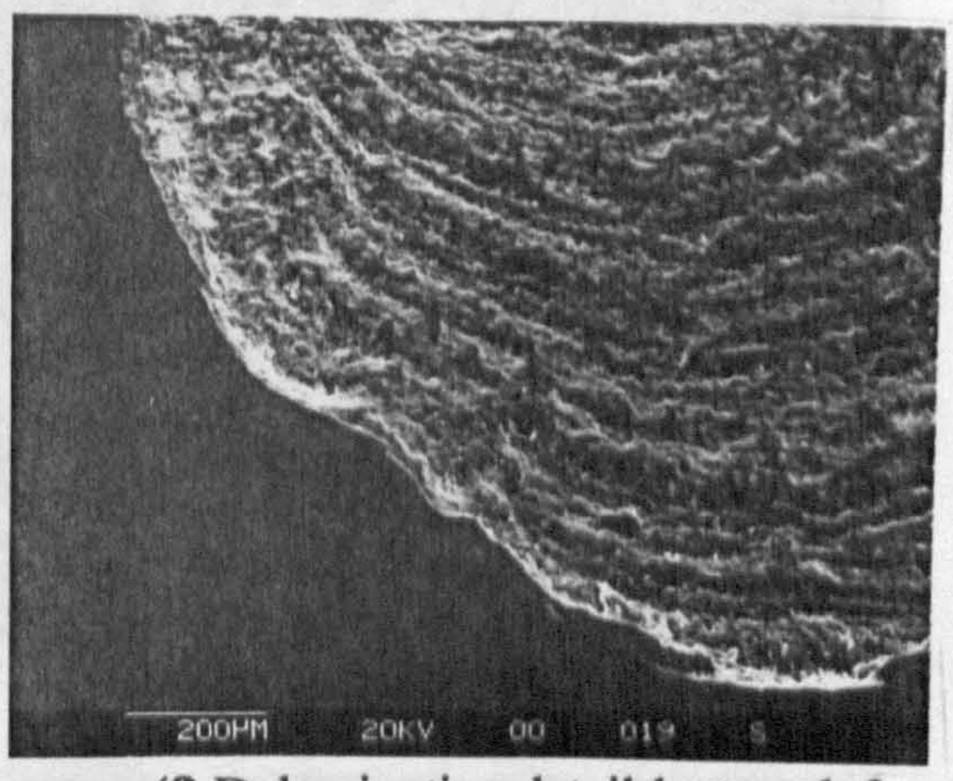

(f) Delamination detail-bottom left

Figure A9.3 Example of type 1i1p failure - Captions (a) to (f)

Test conditions of figure A9.3: Ceramic/ceramic contact, machine spindle speed 10,000 r.p.m, HiTec 174 oil lubricant, bulk oil temperature 83°C - unheated, 45.7 million upper ball stress cycles, Hertzian maximum compressive stress - 8.7 GPa, theoretical lambda ratio - 6, Surface roughness (Ra) of upper and lower balls 0.008 μm.

A9.2 Type 1i2p Failure

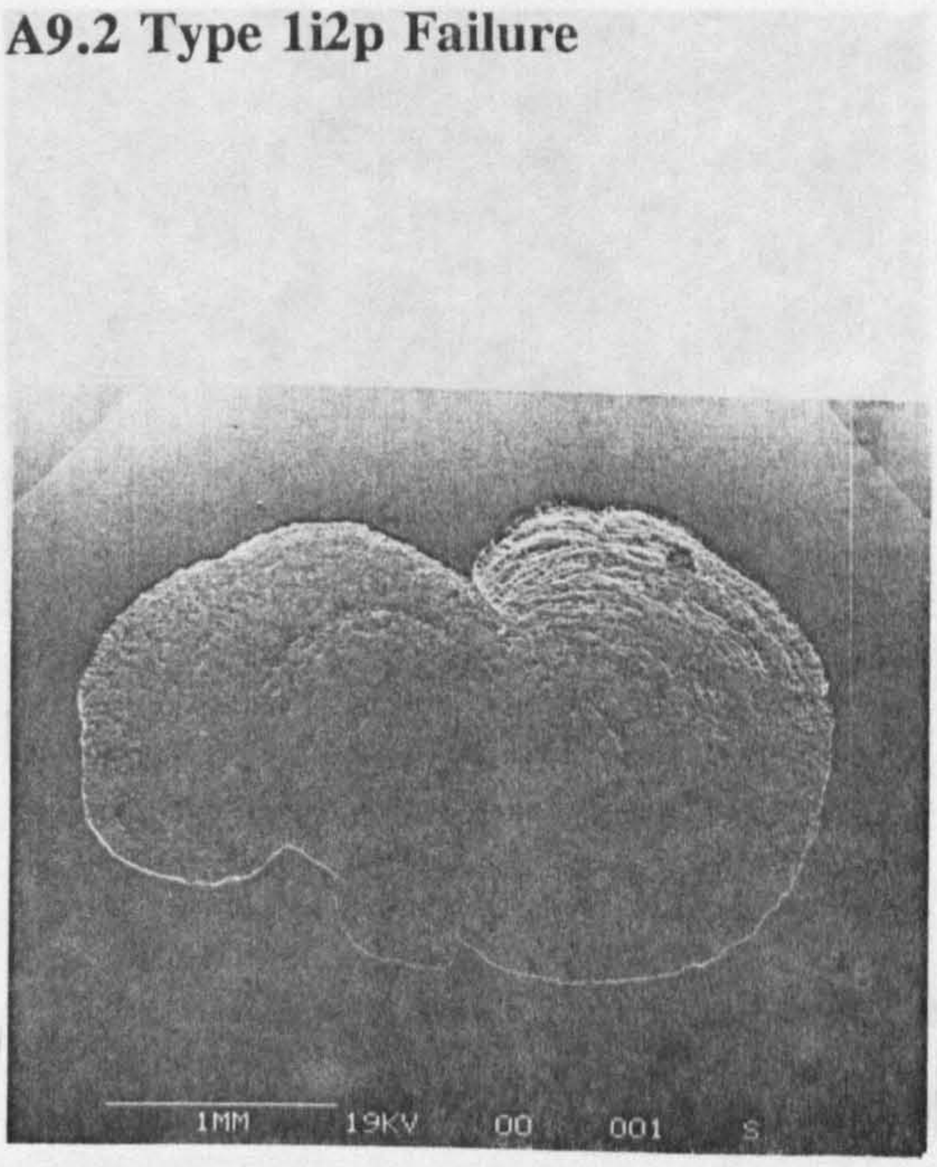

(a) Failure overview

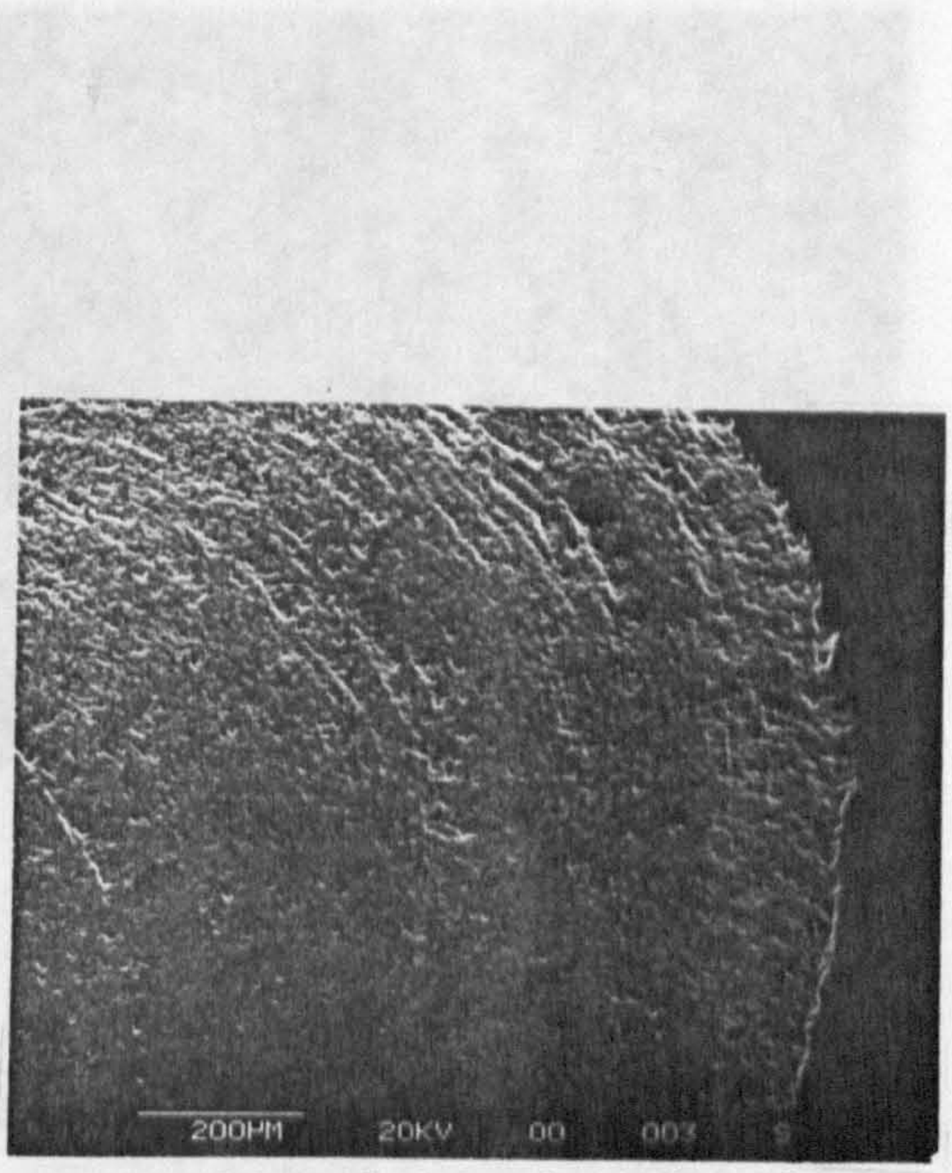

(b) Left delaminated surface

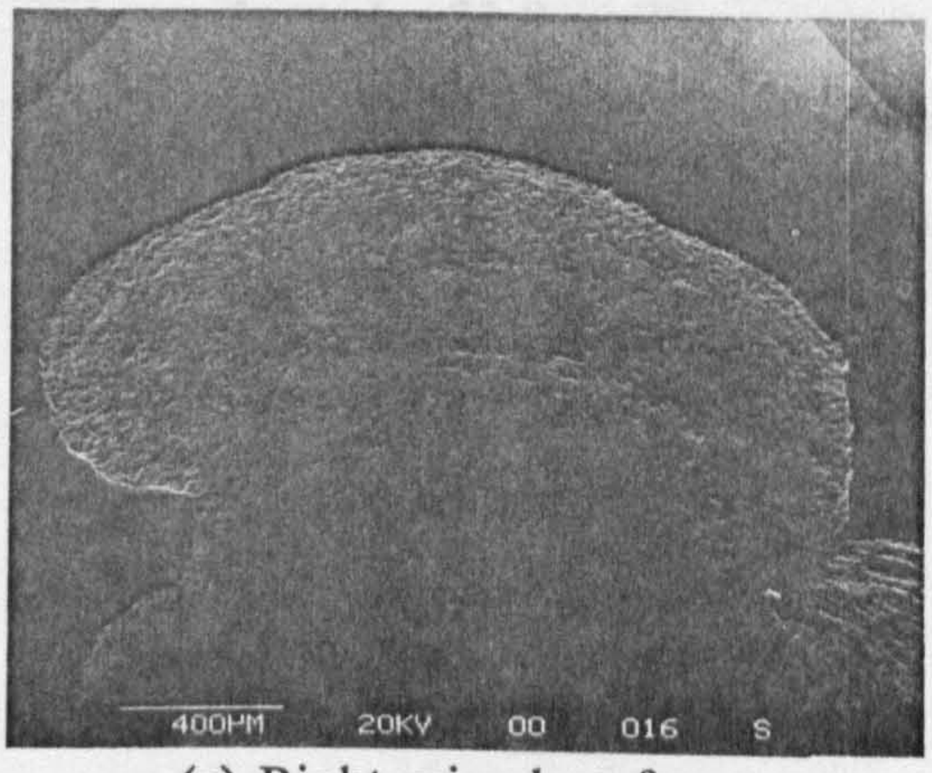

(c) Right mixed surface

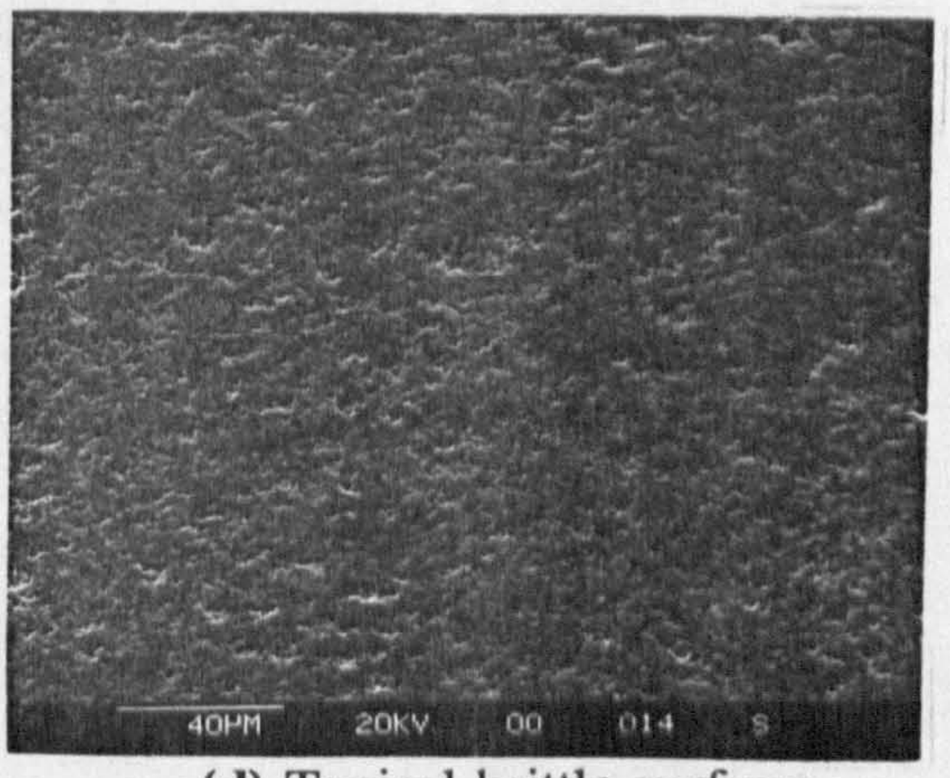

(d) Typical brittle surface

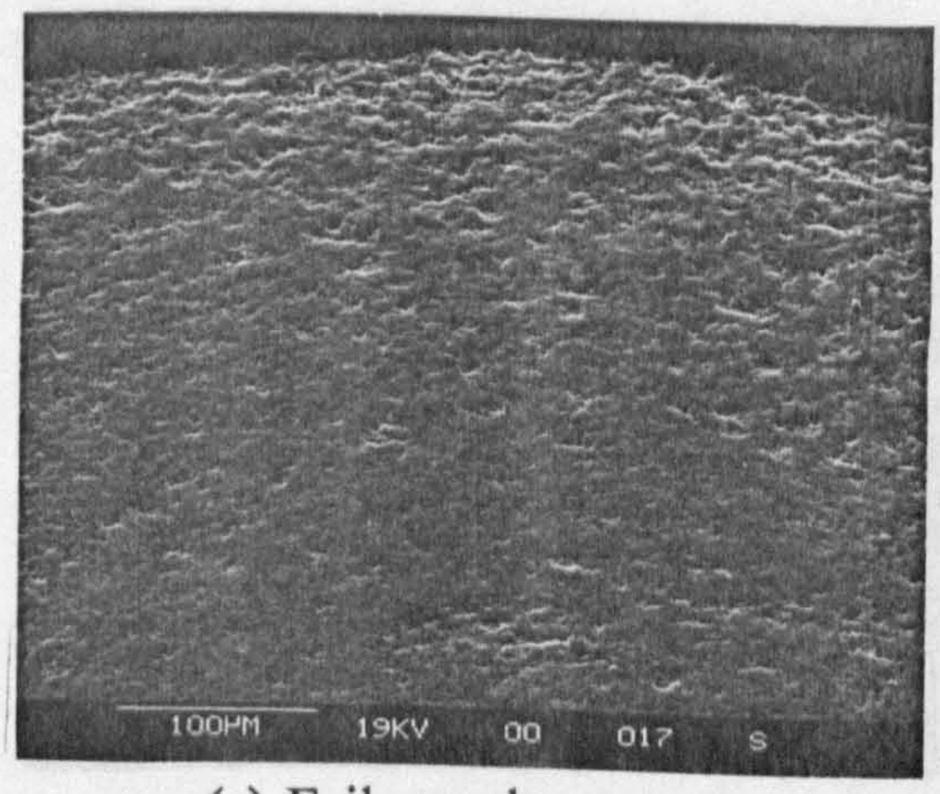

(e) Failure edge

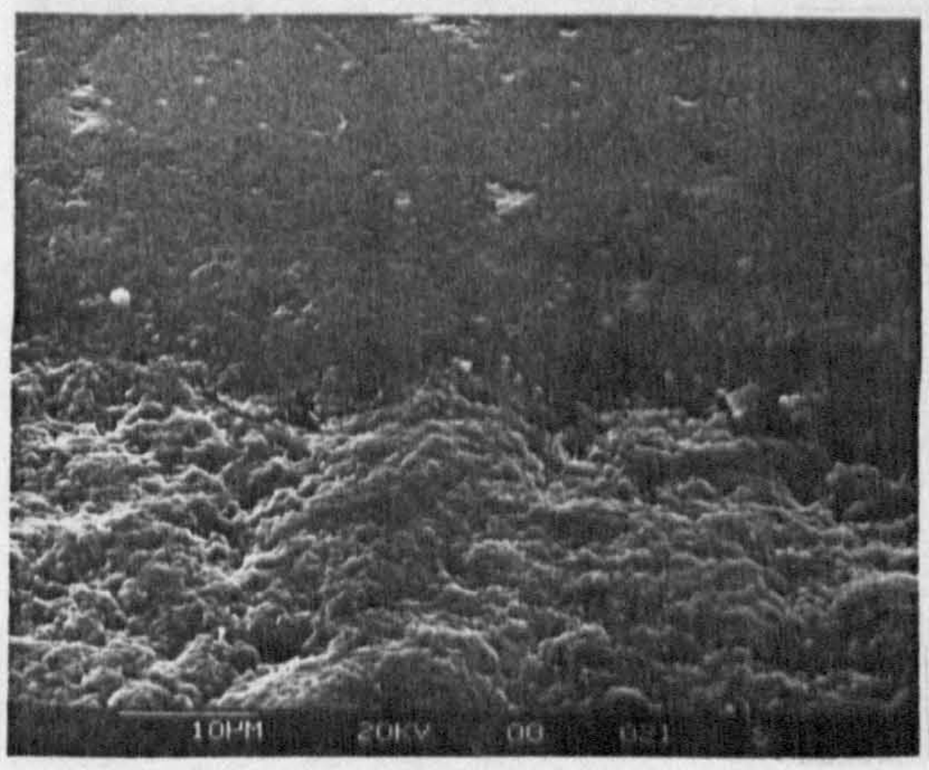

(f) Edge detail

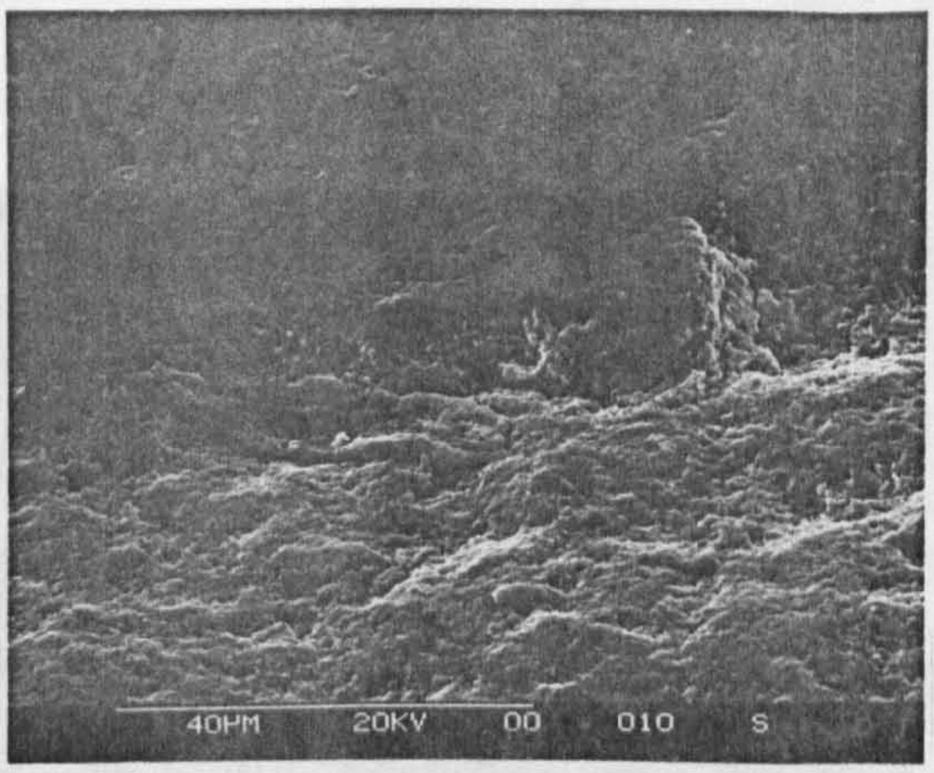

(g) Cliff edge

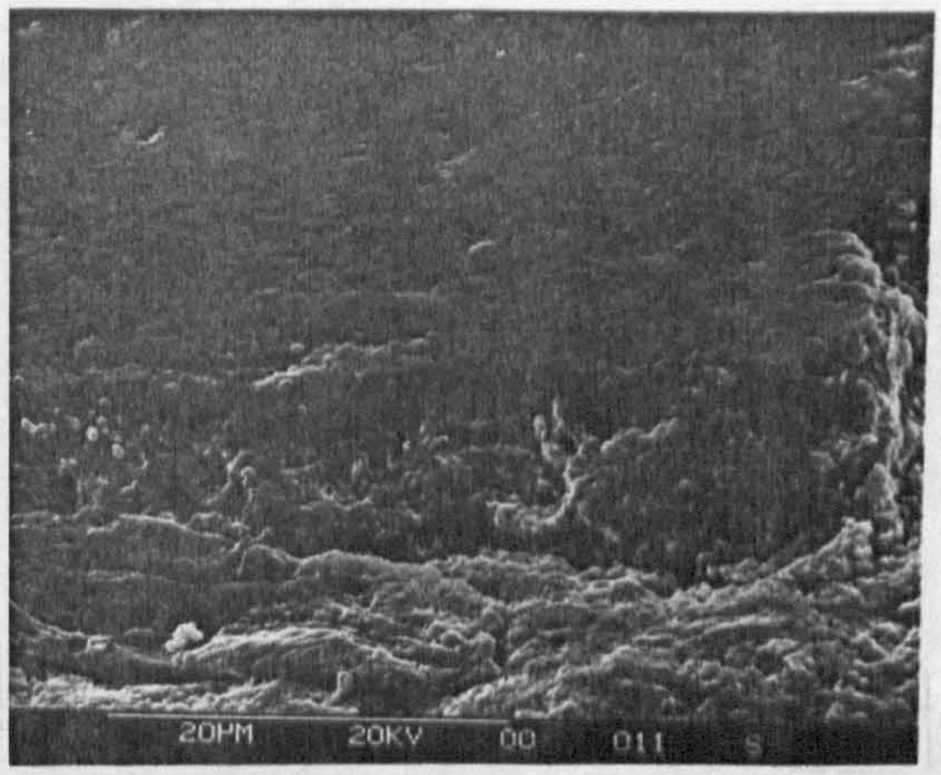

(h) Cliff edge detail

Figure A9.4 Example of type 1i2p failure - captions (a) to (h)

Test conditions of figure A9.4: Ceramic/ceramic contact, machine spindle speed 10,000 r.p.m, standard oil lubricant, bulk oil temperature 68°C - unheated, 33.8 million upper ball stress cycles, Hertzian maximum compressive stress - 7.35 GPa, theoretical lambda ratio - 6, Surface roughness (Ra) of upper and lower balls 0.008 μm.

A9.3 Type 1i3p Failure

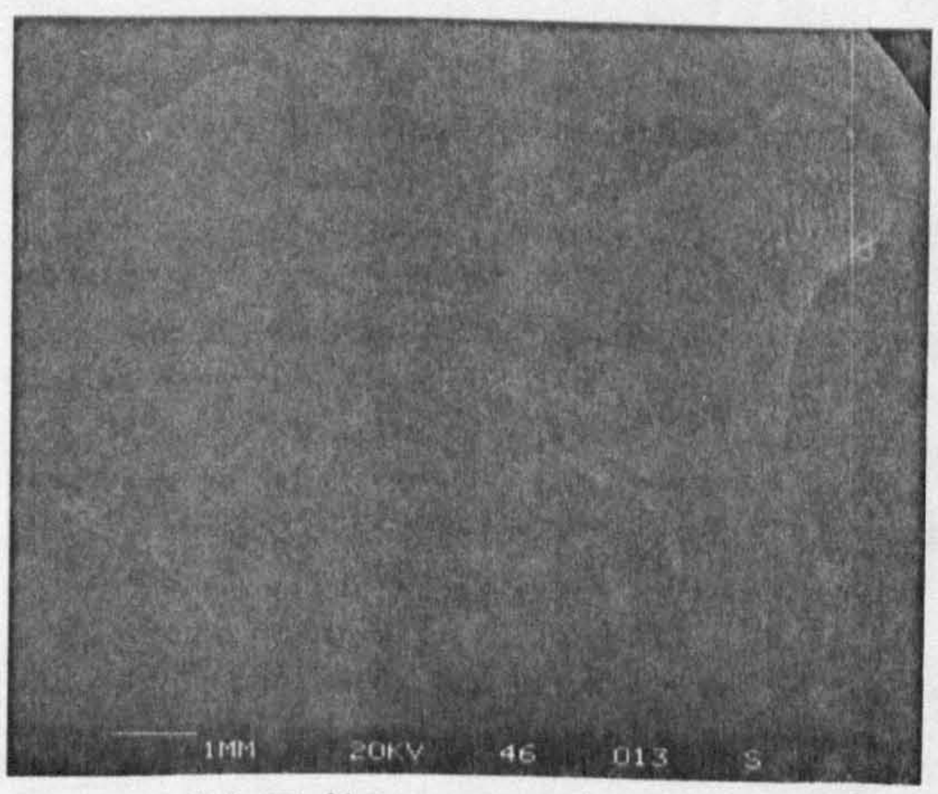

(a) Failure overview

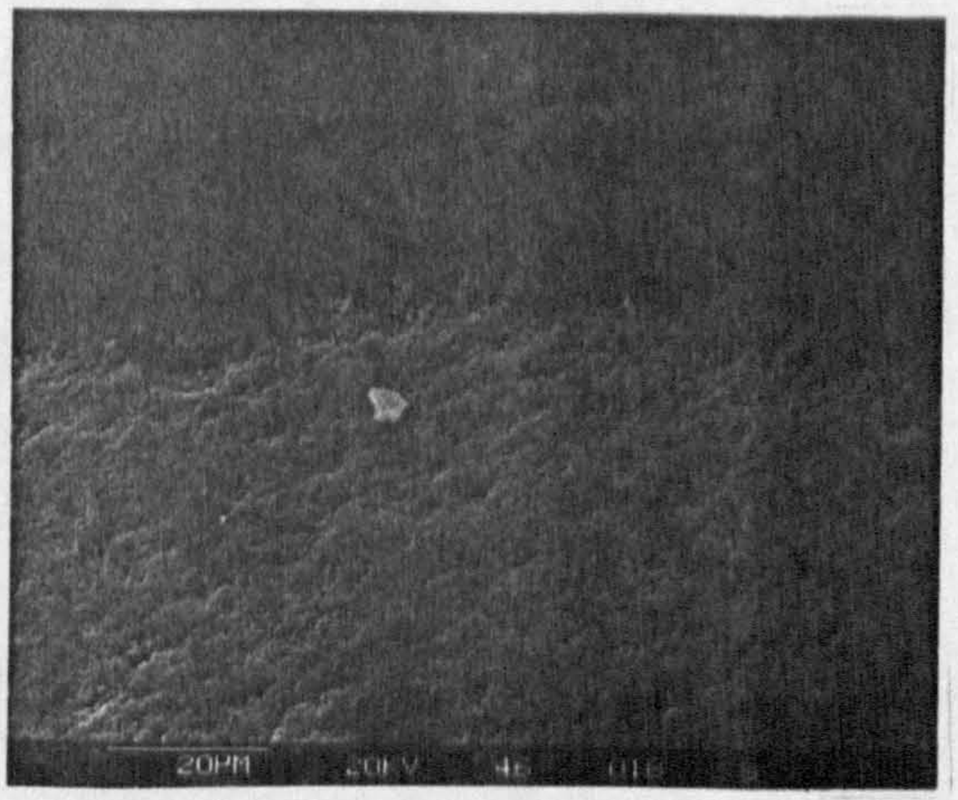

(b) Top edge

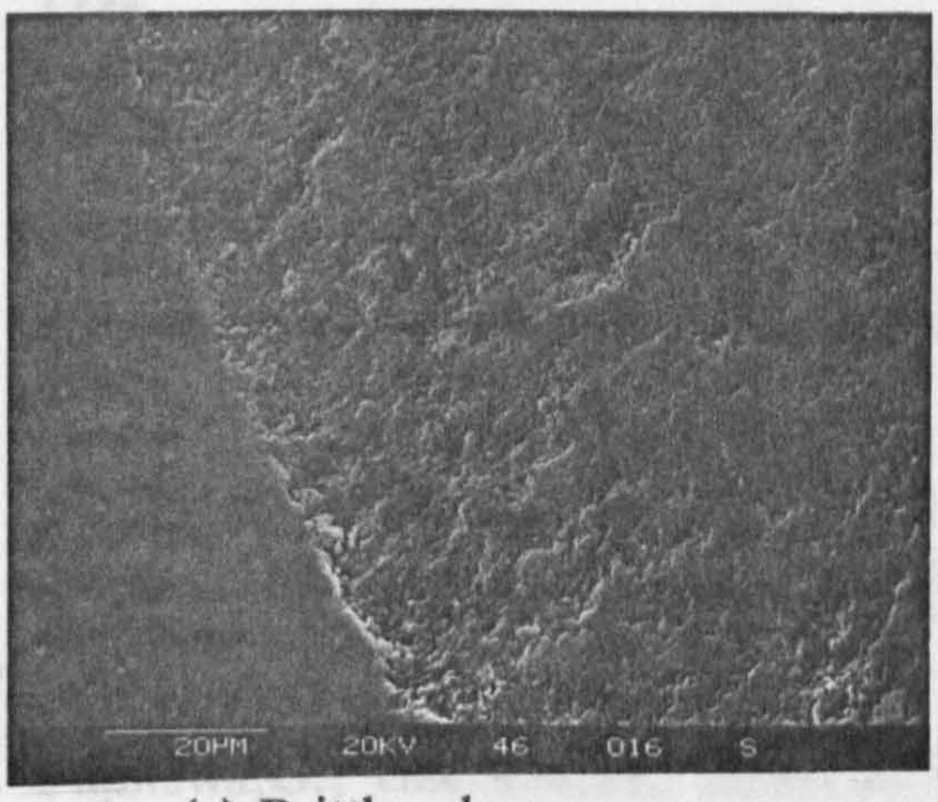

(c) Brittle edge

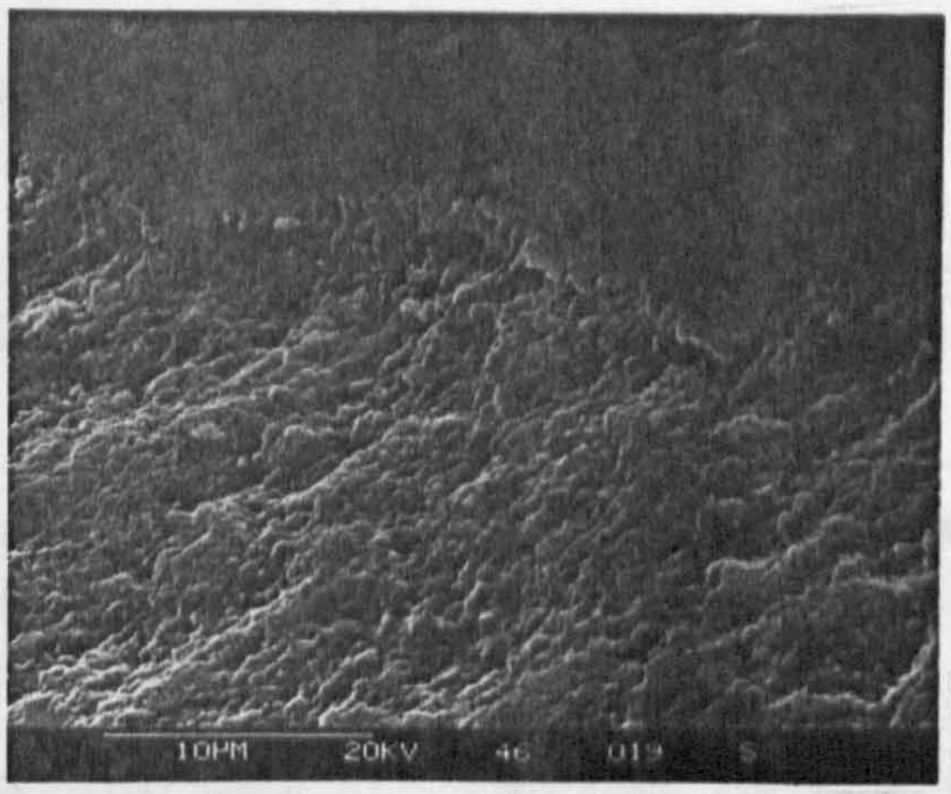

(d) Edge detail

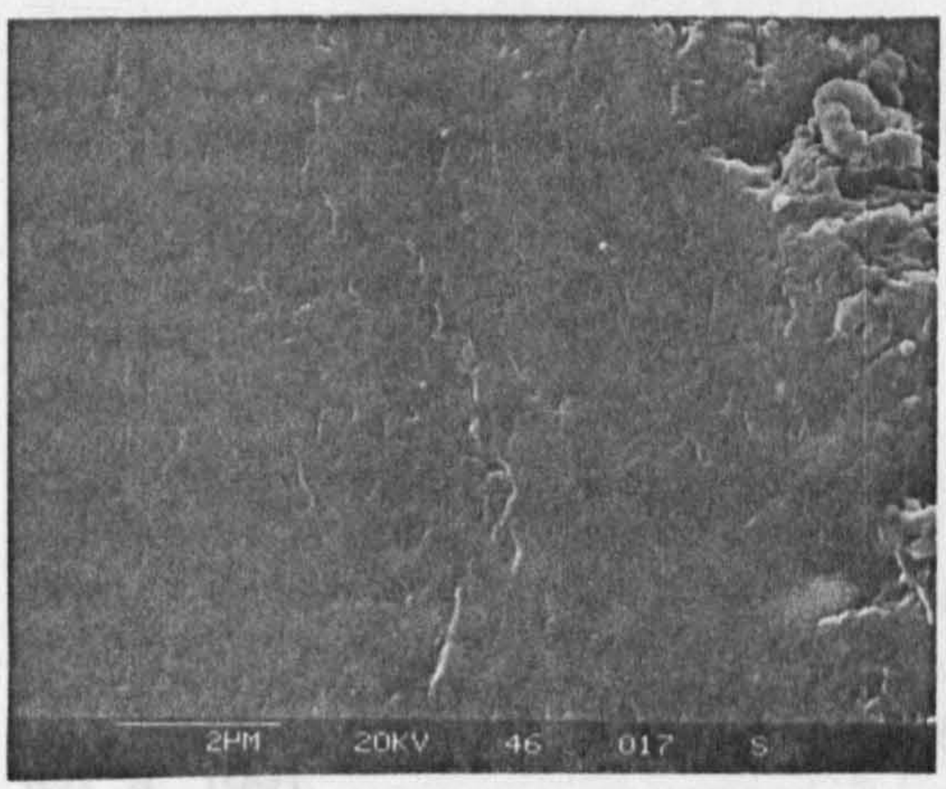

(e) Ball surface damage

(f) Neck detail

Figure A9.5 Example of type 1i3p failure - captions (a) to (f)

Test Conditions of figure A9.5: Ceramic/ceramic contact, machine spindle speed 10,000 r.p.m, base oil lubricant, bulk oil temperature 66°C - unheated, 6.1 million upper ball stress cycles, Hertzian maximum compressive stress - 7.1 GPa, theoretical lambda ratio - 5.5, Surface roughness (Ra) of upper and lower balls 0.008 μm.

REFERENCES

1992

Cundill,R.T., Hadfield,M., and Stolarski,T.A., "Delamination of Ceramic Balls in Rolling Contact" Ceramics International, Accepted June 1992.

Cundill,R.T., Hadfield,M., Horton,S. and Stolarski,T.A., **"Failure Modes of Pre-Cracked Ceramic Elements Under Rolling Contact"** Wear Journal, Sub. October 1992.

Cundill,R.T., Hadfield,M., Horton,S. and Stolarski,T.A., **"Failure Modes of Ceramic Elements With Ring-Crack Defects"** Tribology International, Accepted November 1992.

Fujinawa,G., Hadfield,M., Stolarski,T.A. and Tobe,S., **" Residual Stresses in Failed Ceramic Rolling Contact Balls"** Ceramics International, Accepted October 1992.

Hadfield,M., Stolarski,T.A. and Tobe,S., **"Analysis of Silicon Nitride Ball Failure Due to Rolling Contact Fatigue"** ICR 92, Birmingham, Vol 1, 297-302, September 7-10, 1992.

1991

Dowson,D., Taylor,C.M. and Xu.H., **"Elastohydrodynamic Lubrication of Ellipical Contacts with Spin and Rolling"** Proc. Instn. Mech. Engrs., Vol. 205, Part C: J. Mech. Eng. Sci., 165-174, 1991.

Kishimoto,H., **"Cyclic Fatigue in Ceramics"** JSME International, Series I, Vol. 34, No. 4, 1991.

Yingzhi,Li. and Hills,D.A., **"The Hertzian Cone Crack"** Trans. of the ASME, Vol. 58, 120-127, March 1991.

1990

Cundill,R.T., **"Rolling Element Bearings into the 21st Century"** IMechE Seminar, London, November 1990.

Dwyer-Joyce,R.S., Hamer,J.C. and Sayles,R.S., **"Surface Damage effects caused by Debris in Rolling Bearing Lubricants, with an Emphasis on Friable Materials"** IMechE Seminar, 16 Nov. 1990, ISBN 0 85298 752 8, pp. 1-8

Fischer,T.E., **"Friction and Wear of Ceramics"** Scripta METALLURGICA et MATERIALIA, Vol. 24, pp. 833-838, 1990

Kato,K., **"Tribology of Ceramics"** Wear, 136(1990) pp 117-133

Kodama,S., Akita,K., Misawa,H. and Tobe,S., **"A Model for Residual Stress Distribution in X-Ray Fractography"** J.S.M.S 1990.

Lucek,J.W. **"Rolling Wear of Silicon Nitride Bearing Materials"** ASME, 90-GT-165, Presented at the Gas Turbine and Aero-engine Congress and Exposition-June 11-14, 1990-Brussels,Belgium

1989

Bhargava,V., Hahn,G.T. and Rubin,C.A., **"Rolling Contact Deformation and Microstructural Changes in High Strength Bearing Steel"** Wear, 133(1989)

Braza,J.F., Cheng,H.S., Fine,M.E., Gangopadhyay,A.K., Keer,L.M. and Worden,R.E. **"Mechanical Failure Mechanisms in Ceramic Sliding and Rolling Contacts"** Tribology Transactions, Vol.32 (1989),1, 1-8

Braza,J.F., Cheng,H.S. and Fine,M.E., **"Silicon Nitride Wear Mechanisms: Rolling and Sliding Contact"** Tribology Transactions, Vol.32 (1989),4, 439-446

Fujiwara,T., Yoshioka,T., Kitahara,T., Koizumi,S., Takebayashi,H. and Tada,T., **"Study on Load Rating property of Silicon Nitride for Rolling Bearing Material"** J. JSLE 10(1989)81 - 86

Rabier,P.J., **"Some Remarks on Damage Theory"** Int.J.Engng Sci. Vol 27, No. 1, pp 29-54, 1989

Ueda,K., **"Contact-Stress Deformation and Fracture in Ceramics"** Jap. J. of Tribology, Vol 34, 123-131 No.2, 1989.

1988

Akazawa,M. and Kato,K. **"Wear Properties of Silicon Nitride in Rolling-Sliding Contact"** Wear,124(1988) 123-132

Aramaki,H., Shoda,Y., Morishita,Y. and Sawamoto,T., **"The Performance of Ball Bearings With Silicon Nitride Ceramic Balls in High Speed Spindles for Machine Tools"** J. of Tribology, October 1988, Vol. 110, 693-698

Ham,G., Rubin,C.A., Hahn,G.T. and Bhargava,V., **"Elasto-Plastic Finite Element Analysis of Repeated, Two-Dimensional Rolling-Sliding Contacts"**, Trans. ASME 44/Vol.110,Jan. 1988

Hurst,W. **"Traction in Elastohydrodynamic Contacts"** Proc. IMechE, Vol 202, No. C2, pp. 129-144

1987
Cranmer,D.C., **"Ceramic Tribology-Needs and Opportunities"** Tribology Transactions, Vol.31, 2 , 164-173

Todd,M.J. **"Spin Division and Estimation of Coulomb Torque in Angular Contact Ball Bearings"** IMechE 1987, C193/87, pp.933-944

Tunca,N. and Laufer,E.E., **"Wear Mechanisms and Finite Element Crack Propagation Analysis of High Speed Roller Bearings"** Wear,118(1987) 77-97

1986
Kim,S.S., Kato,K., Hokkirigawa,K. and Abe,H., **"Wear Mechanism of Ceramic Materials in Dry Rolling Friction"** Trans. of the ASME, J. of Tribology, October 1986, Vol.108, 522-526

Suh,N.P., **"Tribophysics"** Prentice-Hall, 1986

1985
Bhargava,V., Hahn,G.T. and Rubin,C.A., **"An Elastic-Plastic Finite Element Model of Rolling Contact - Part 1: Analysis of Single Contacts"**, Journal of Applied Mechanics (ASME Trans.), March 1985, Vol.52(1989) 65-74

Bhargava,V., Hahn,G.T. and Rubin,C.A., **"An Elastic-Plastic Finite Element Model of Rolling Contact - Part 2: Analysis of Repeated Contacts"**, Journal of Applied Mechanics (ASME Trans.), March 1985, Vol.52(1989) 75-82

Johnson,K.L. **"Contact Mechanics"** Cambridge Univ. Press, 1985

1984
Kikuchi,K., Yoshioka,T., Kitahara,T., Ozaki,K., Nakayama,K. and Fujiwara,T., **"Rolling Contact Fatigue Life of Ceramics for Rolling Bearing Materials"** J. of JSLE Int. Ed., Number 5, 1984, 137-142

Morrison,F.R., McCool,J.I., and Yonushonis,T.M., **"The Load-Life Relationship for M50 Steel Bearings with Silicon Nitride Ceramic Balls"** J. of the ASLE, Lubrication Engineering, March, 1984, 153-159

1983
Cundill,R., **"Light-Weight Material for the Rolling Elements of Aircraft Bearings"** Ball Bearing Journal 216:1983, 33-36

1981

Engel,L. and Klingele,H. **"An Atlas of Metal Damage"** Wolfe Pub. Ltd., 1981

1980

Hamburg,G., Cowley,P. and Valori,R.,**"Operation of an All-Ceramic Mainshaft Roller Bearing in a J-402 Gas-Turbine Engine"** J. ASLE, Lubrication Engineering, July 1981

Suh,N.P. and Saka,N **"Fundamentals of Tribology"** Proc. of the Int. Conf. on the Fundamentals of Tribology, MIT, June 1978, The MIT Press, 1980

1978

Hartnett,M.J., **"The Analysis of Contact Stresses in Rolling Element Bearings"** Trans. of the ASME, J. of Lub. Tech., No. 78-Lub-2, 1978.

Lucek,J.W. and Cowley,P.E., **"Investigation of the use of Ceramic Material in Aircraft Engine Bearings"** Dept. of Navy,Code AIR-52032A,Washington

1977

Fleming,J.R. and Suh,N.P., **"Mechanics of Crack Propagation in Delamination Wear"** Wear,44(1977)39-56

Jahanmir,S. and Suh,N.P., **"Mechanics of Subsurface Void Nucleation in Delamination Wear"** Wear,44(1977)17-38

Suh,N.P., **"An Overview of the Delamination Theory of Wear"** Wear,44 (1977) 1-16

Tourret,R and Wright,E.P. **"Rolling Contact Fatigue: Performance Testing of Lubricants"** Papers Presented at the Int. Symp., I. Petroleum, October 1976, London, Heyden & Son Ltd, 1977

1976

Reddecliff,J.M. and Valori,R., **"The Performance of a High-Speed Ball Thrust Bearing Using Silicon Nitride Balls"** Trans. of the ASME, J. of Lub. Tech., Oct 1976, 553-558

1975

Parker,R.J. and Zaretsky,E.V. **"Fatigue Life of High-Speed Ball Bearings With Silicon Nitride Balls"** Trans. of the ASME, J. of Lub. Tech., July 1975, pp.350

1973
Archard,J.F., **"Elastohydrodynamic Lubrication of Real Surfaces"** Tribology Feb.1973 8-14

Scott,D. and Blackwell,J., **"Hot Pressed Silicon Nitride as a Rolling Bearing Material - A Preliminary Assessment"** Wear, 24(1973)61-67

Suh,N.P., Wear, 25 (1973) 111-124.

1972
Tallian,T.E., **"The Theory of Partial Elastohydrodynamic contacts"** Wear, 21(1972), pp. 49-101

1971
Harris,T.A. **"Ball Motion in Thrust-Loaded, Angular Contact Bearings With Coulomb Friction"** Trans. of the ASME, J. of Lub. Tech., Jan. 1971, pp.32-36

Hirano,F., Sakai,T. and Kamitani,T., **"On a Significant Property of Lubricants Concerning Rolling Fatigue and Scoring"** Inst. of Mech. Eng. C66/71, pp. 86-96

Scott,D., Blackwell,J. and McCullagh,P.J., **"Silicon Nitride as a Rolling Bearing Material - A Preliminary Assessment"** Wear, 17(1971)73-82

1966
Dowson,D. and Higginson,G.R., **"Elasto-Hydrodynamic Lubrication"** Pergamon Press, 1966

1965
Hirano,F., **"Motion of a Ball in Angular-Contact Ball Bearing"** ASLE Trans 8, pp.425-434, (1965)

1963
Scott,D. and Blackwell,J. **"Accelerated Test for the Study of Materials Under Rolling Contact"** IMechE, Lub. and Wear Convention, 1963, pp. 291-298

Scott,D., **"Study of the Effect of Lubricant on Pitting Failure of Balls"** ImechE, Lub. and Wear Convention, 1963, pp. 463-468

Scott,D., **"The Effect of Material Properties, Lubrication and Environment on Rolling Contact Fatigue"** Proc of the Symp.on 'Fatigue in Rolling Contact', 1963, Paper 10, pp. 103-115

1961
Hirano,F. and Tanoue,H. **"Motion of a Ball in a Ball Bearing"** Wear,4 (1961), pp.177-197

1960
Archard,J.F. and Kirk,M.T., **"Lubrication at Point Contacts"** Royal Society Vol.261.A (1960) 532-549

Krivoshein,G.S., **"On Evaluating the Effect of Lubricants on the Fatigue Pitting of Steel"** Industr. Lab., 1960, Vol. 26, pp. 405-7

1956
Barwell,F.T. and Scott,D., **"Effect of Lubricant on Pitting Failure of Ball Bearings"** Engineering, July 6, 1956, pp. 9-12

1904
Hüber,M.T., **"Zur theorie de Beruhrung fester elastische Korper"** Ann. der Physics, Vol. 14, pp.153, 1904.

1881
Hertz,H. **"On the Contact of Elastic Solids"**, J. reine angew Math. (1881), 92, 56, pp.156-171

BIBLIOGRAPHY

Ajayi,O.O. and Ludema,K.C. **"Surface Damage of Structural Ceramics" Implications for Wear Modelling"** Wear, 124(1988) 237-257

Akazawa,M., Kato,K. and Umeya,K., "Wear Properties of Silicon Nitride in Rolling Contact" Wear,110(1986) 285-293

Anon. **"Ceramics Offer Better Bearings"** Engineering, Dec. 1986, 895-896

Anon. **"Progress with Ceramic Ball Bearings"** Ceramic Industries Int. August 1990, 41-44

Anon. **"Silicon Nitride for High-Performance Bearings"** Ceramic Bulletin, Vol. 69, No.7, 1990, 1113-1115

Arnov,V. and Mesyef,T., **"Wear in Ceramic/Ceramic and Ceramic/Metal Reciprocating Sliding Contact. Part 1"** Trans. of the ASME, J. of Tribology, 1985, 85-TRIB-9, pp.1-6

Baumgartner,H.R., **"Ceramics for High-Performance Applications"** Proc. of the Second Army Materials Technology Conf. Nov. 13-16,Hyannis, Massachusetts. 1973. edited; Burke,J.J., Gorum,A.E. and Katz,R.N.

Barnwell,F.T., **"Effect of Lubrication and Natural Superficial Layer after Prolonged Periods of Running"** Inst. Metals Monograph Series, 1953, No 13, pp. 101-122

Bayer,R.G. **"Prediction of Wear in a Sliding System"** Wear, 11(1968), 319-332

Bidwell,J.B. **"Rolling Contact Phenomena"** Proc. of a Symp. at General Motors, Warren, Michigan, Elsevier Pub. Co., 1962

Bhushan,B. and Sibley,L.B., **Silicon Nitride Rolling Bearings for Extreme Operating Conditions"** ASLE Trans., Vol.25, 4, pp. 417-428

Bowden,F.P. and Tabor,D., **"Friction and Lubrication of Solids"** Oxford Univ. Press, 1964

Chivers,T.C. and Gordelier,S.C., **"Fretting Fatigue and Contact Conditions: a rational explanation of palliative behaviour"** Proc. IMECHE, Vol. 199, No.C4, 104/85, 325-337

Chu,P.S. **"Research Note:Hysteresis Loss in Ball and Roller Bearings"** J. Mech. Eng. Sci., IMechE, Vol 18, No. 5, 1976, pp.254-255

Cottrell,A.H. **"The Mechanical Properties of Matter"** J.Wiley & Sons, 1964

Eldredge,K.R. and Tabor,D., **"The mechanism of Rolling Friction 1. The Plastic Range "** Proc. Royal Society, A, Vol. 229, (1955) 181-198

Engel,L. and Klingele,.H., **"An Atlas of Metal Damage"** Wolfe Science Books, ISBN 0 7234 0750 9.

Farrahi,G.H., Markho,P.H. and Maeder,G., **"A Study of Fretting Wear with Particular Reference to Measurement of Residual Stresses by X-ray Diffraction"** Wear, 148, 249-260, 1991.

Fischer,T.E. and Tomizawa,H. **"Interaction of Tribochemistry and Microfracture in the Friction and Wear of Silicon Nitride"** Wear, 105(1985) 29-45

Fonseka,G.U. and Krajcinovic,D. **"The Continuous Damage Theory of Brittle Materials - Part 2: Uniaxial and Plane Response Modes"** Trans. of the ASME, J. of Applied Mechanics, Dec. 1981, Vol.48, pp. 816-824

Habeeb,J.J., Blahey,A.G., and W.N.Rogers,W.N., **"Wear and lubrication of ceramics"** C132/87, IMechE 1987, 555-564

Hahn,G.T., Bhargava,V. and Chen,Q. **"The Cyclic Stress-Strain Properties, Hysteresis Loop Shape, and Kinematic Hardening of Two High-Strength Bearing Steels"** Metallurgical Transactions A, Vol. 21A, March 1990, pp. 653-665

Halling,J., **"A Contribution to the Theory of Friction and Wear and the Relationship Between Them"** Proc. IMechE, Vol 190, 43/76, 477-488

Hamilton,G.M., **"Plastic Flow in Rollers Loaded above the Yield Point"** Proc. ImechE, Vol 177, No 25, 1963.

Hampshire, J.M., **"The Role of Materials in the Design and Application of Rolling Contact Bearings"** Materials & Design, Vol.7, No.4, July/August 1986, 192-197

Hartnett,M.J., **"The Analysis of Contact Stresses In Rolling Element Bearings"** Trans. of the ASME, J. of Lub. Tech., 78-Lub-2, pp.1-5

Harnett,M.J., **"The Analysis of Contact Stresses in Rolling Element Bearings"** Jour. Lub. Tech. (ASME Trans.) Paper No. 78-Lub-2

Harris,T.A., **"Rolling Bearing Analysis"** J Wiley & Sons, 1984

Hearn,E.J. **"Mechanics of Materials"** Pergamon Press, 1985

Hills,D.A. and Ashelby D.W. **"A Fracture Mechanics Approach to Rolling Contact Fatigue"** Tribology Int., June1979, pp.115-119

Hirst,W. and Richmond, J.W., **"Traction in Elastohydrodynamic Contacts"** Proc. IMechE Vol.202 No.C2 129-144

Hisakado,T., **"Wear Mechanism of Ceramics and Surface Topography"** Trans. of the ASME, J.of Trib.,85-Trib-9,1-7

Johnson,K.L., **"Aspects of Contact Mechanics"** IMechE, 1987, C246/87, pp.919-932

Kimura,Y. and Okada,K. **"Sliding Damage of Silicon Nitride in Plane Contact"** Wear, 133(1989) 147-161

Knott,J.F. **"Fundamentals of Fracture Mechanics"** Page Bros. 1981

Kragelsky,I.V., Dobychin,M.N. and Kombalov,V.S. **"Friction & Wear Calculation Methods"** Pergamon Press, 1982

Krajcinovic,D. **"Constitutive Equations for Damaging Materials"** Trans. of the ASME, J. of Applied Mechanics, June 1983, Vol.50, 355-360

Krajcinovic,D. and Fonseka,G.U. **"The Continuous Damage Theory of Brittle Materials - Part 1: General Theory"** Trans. of the ASME, J. of Applied Mechanics, Dec. 1981, Vol.48, pp. 809-815

Kuznetsov,YE.A. and Gorokhovsky,G.A., **"The Depth of Propagation of Elastic Deformation in Rough Bodies Under Frictional Contact"** Wear, 3 (1980) 41-49

Lawn,B.R. and Wilshaw,T.R., **"Fracture of Brittle Solids"** Cambridge University Press, p.63, 1975.

Leckie,F.A. and Hayhurst,D.R., **"Creep Rupture of Structures"** Proc. of the Royal Society, Lon., Series A, Vol. 340, 1974, pp.323-347

Lieblein,J. and Zelen,M., **"Statistical Investigation of the Fatigue Life of Deep-Groove Ball Bearings"** J. Res. Bur. Stand., Vol. 57, No. 5, Nov. 1956, pp. 273-87

Likhtman,V.I., Shchukin,E.D. and Rehbinder,P.A., **"Physiochemical Mechanics of Metals"** Academy of Sciences of the USSR Inst. of Physical Chemistry, 1962, Israel Program for Scientific Translations, Jerusalem, pp.3 10(1964).

Ling,F.F. **"Surface Mechanics"** J. Wiley & Sons, 1973

Longching,C., Qing,C. and Eryu., **"Study on Initiation and Propagation Angles of Subsurface Cracks in GCr15 bearing Steel Under Rolling Contact"** Wear, 133(1989) 205-218

Lorosch,H., **"The Life of the Rolling Bearing under Varying Loads and Environmental Conditions"** Ball and Roller Bearing Engineering, 1981-1, pp. 17-23

Lorosch,H., Vay,J., Weigand,R., Gugel,E. and Kessel,H., **"Fatigue Strength of Balls Made from Hot-Pressed Silicon Nitride for High-Speed Rolling Bearings"** Ball and Roller Bearing Engineering, 1980-1, pp. 33-36

Lou,L.K.V., Mitchell,T.E. and Heuer,A.H. **"Impurity Phases in Hot-Pressed Silicon Nitride"** J. of the American Ceramic Society, Vol.61, No9-10, 392-396

McCool,J.I., **"Predicting Microfracture in Ceramics Via a Microcontact Model"** Trans. of the ASME, J. of Tribology, 85-Trib-10, 1-6

Merwin,J.E. and Johnson,K.L. **"An Analysis of Plastic Deformation in Rolling Contact"** Proc. IMechE, Vol 177, No.25, 1963, pp. 676-690

Miller,G.R., Keer,L.M. and Cheng,H.S. **"On the Mechanics of Fatigue Crack Growth due to Contact Loading"** Proc.R.Soc.Lond., A 397, 197-209(1985)

Moore,D.F. and Geyer,W. **"A Review of Hysteresis Theories for Elastomers"** Wear, 30 (1974), pp.1-34

Morales,W. and Buckley, D.H., **"Concentrated Contact Sliding Friction and Wear Behaviour of Several Ceramics Lubricated with a Perfluoroplyalkylether at 25 Degrees Celsius"** Wear,123 (1988) 345 -354

Nishihara,Y., Nakashima,H., Tsushima,N. and Ito,S., **"Factors That Affect Rolling Contact Fatigue Life of Ceramics and Rolling Contact Fatigue Life of Ceramic Balls and Rollers"** ASME, New York, 90-GT-377, 1990.

Parker,R.T. **"Rolling-Element Fatigue life of AMS 5900 Balls"** NASA Technical Paper 2080, 1983

Parker,R.J. and Hodder,R.S. **"Rolling-Element Fatigue Life of AMS 5749 Corrosion Resistant, High Temperature Bearing *Steel"*** *Trans.* of the ASME, J. of Lub. Tech., April 1978, Vol 100, pp.226-234

Pasdari,M. and Gentle,C.R., **"Analysis of a high-speed, Deep-groove ball bearing with ceramic balls"** IMechE 1987, C196/87, 851-858

Pater,A.D. and Kalker,J.J. **"The Mechanics of the Contact Between Deformable Bodies"** Delft Univ. Press, 1975

Peterson,M.B., **"Advancements in Tribological Materials 1937-1987-2002"** IMechE 1987, C249/87, 583-593

Scott,D., **"Studies in Rolling Surface Fatigue - The Four-Ball Machine with a ball-ended upper specimen"** Wear, 5 (1962), pp. 69-71

Scott,D., **"Lubricants at Higher Temperatures - Assessing the Effects on Ball Bearing Failures"** Engineering, 1958, May 23, pp. 660-663

Scott,D. and Blackwell,J. **"The Assessment of Ball Bearing Steels of Modified Chemical Composition"** Wear, 46(1978), pp.273-279

Sutor,P., **"Tribology of Silicon Nitride and Silicon Nitride-Steel Sliding Pairs"** Ceramic Engineering and Science Proceedings, July-August, 1984, 460-469

Stolarski,T.A., **"Adhesive Wear of Lubricated Contacts"** Tribology Int., Aug. 1979, 169-179

Stolarski,T.A., **"Tribology in Machine Design"** Heinemann Newnes, 1990

Stolarski,T.A., **"Fracture Mechanics and the Contact Between a Pair of Surface Asperities During Rolling"** Int.J.Engng Sci. Vol27,No2,pp169-179,1989

Suo,Z., **"Singularities, Interfaces and Cracks in Dissimilar Anisotropic Media"** Proc. R. Soc. Lond. A 427, 331-358(1990)

Tabor,D. **"The Hardness of Metals"** Oxford Univ. Press, 1951

Tabor,D. **"Gases, Liquids and Solids"** Penguin Books Ltd, 1970

Tabor,D., **"The mechanism of Rolling Friction 2. The Elastic Range "** Proc. Royal Society, A, Vol. 229, (1955) 198-220

Wedeven,L.D. and Harris,T.A. **"Rolling Element Bearings operating at the extremes"** Machine Design/August 6, 1987 pp72-76

Wedeven,L.D., Pallini,R.A. and Miller,N.C., **"Tribological Examination of Unlubricated and Graphite-Lubricated Silicon Nitride Under Traction Stress"** Wear,122(1988)183-205

Weigand,R., **"Ceramics-Tomorrow's Rolling Bearing Materials?"** Ball and Roller Bearing Engineering, Industrial Engineering 1988-1, 4-9

Yoshimura,H., Rubin,C.A. and Hahn,G.T. **"A Technique for Studying Crack Growth Under Repeated Rolling Contact"** Wear, 0043-1648/1984, 29-33

Yoshioka,T., Kitahara,T., Takebayashi,H. and Yuine,T. **"A New Method for Static Load Rating of Ceramic Rolling Bearing"** Wear, 133 (1989) 373-383

Zatetsky, E.V., **"Ceramic Bearings for Use in Gas Turbine Engines"** Trans. of the ASME, J.of Eng. for Gas Turbines and Power, January 1989,Vol.111/146-157

Zum Gahr,K.H., **"Sliding Wear of Ceramic-Ceramic-Steel and Steel-Steel Pairs in Lubricated and Unlubricated Contact"** Wear,133 (1989) 1-22